

# Journal of **Geophysics** Zeitschrift für **Geophysik**

**Volume 52 1983**

---

*Managing Editors*            **W. Dieminger, G. Müller, J. Untiedt**

*Editorial Board*            **K.M. Creer   Edinburgh, Scotland**  
**W. Dieminger   Lindau, F.R.G.**  
**C. Kisslinger   Boulder, Colorado**  
**Th. Krey   Hannover, F.R.G.**  
**G. Müller   Frankfurt, F.R.G.**  
**G.C. Reid   Boulder, Colorado**  
**J. Untiedt   Münster, F.R.G.**  
**S. Uyeda   Tokyo, Japan**

*Advisory Board*

<b>G. Angenheister, München</b>	<b>I. P. Kosminskaja, Moskwa</b>
<b>A. A. Ashour, Cairo</b>	<b>W. Krauss, Kiel</b>
<b>W. I. Axford, Lindau/Harz</b>	<b>St. Müller, Zürich</b>
<b>J. Behrens, Berlin</b>	<b>A. Roche, Strasbourg</b>
<b>V. Bucha, Praha</b>	<b>O. Rosenbach, Clausthal-Zellerfeld</b>
<b>J. Cain, Greenbelt, MD</b>	<b>S. Saxov, Aarhus</b>
<b>K. Fuchs, Karlsruhe</b>	<b>U. Schmucker, Göttingen</b>
<b>N. Fukushima, Tokyo</b>	<b>M. Siebert, Göttingen</b>
<b>V. Haak, Berlin</b>	<b>H. Soffel, München</b>
<b>B. Haurwitz, Fort Collins, CO</b>	<b>L. Stegena, Budapest</b>
<b>W. Jacoby, Frankfurt a.M.</b>	<b>H. Stiller, Potsdam</b>



**Springer International**

## Journal of Geophysics – Zeitschrift für Geophysik

This journal was founded by the Deutsche Geophysikalische Gesellschaft on the initiative of L. Mintrop in 1924 as the *Zeitschrift für Geophysik* and edited by G. Angenheister from Vol. 1–18 (1944). It reappeared in 1954 edited by B. Brockamp from Vol. 19–26 (1960), and edited by W. Dieminger from Vol. 27–33 (1961), and from Vol. 34 (1968) edited by W. Dieminger and J. Untiedt. After Vol. 40 (1970) the title was changed to *Journal of Geophysics – Zeitschrift für Geophysik*.

Published: Vols. 19–39 by Physica-Verlag, Würzburg, from Vol. 40 by Springer Berlin, Heidelberg, New York.

---

### Copyright

It is a fundamental condition that submitted manuscripts have not been published and will not be simultaneously submitted or published elsewhere. By submitting a manuscript, the authors agree that the copyright for their article is transferred to the publisher if and when the article is accepted for publication. The copyright covers the exclusive rights to reproduce and distribute the article, including reprints, photographic reproductions, microform or any other reproductions of similar nature, and translations.

Photographic reproduction, microform, or any other reproduction of text, figures, or tables from this journal is prohibited without permission obtained from the publisher.

The use of general descriptive names, trade names, trade marks, etc., in this publication, even if the former are not specifically identified, is not to be interpreted as exempt from the relevant protective laws and regulations and may accordingly be used freely by anyone.

### *Special Regulations for the USA*

The Article Fee Code on the first page of an article in this journal indicates the copyright owner's consent that in the USA copies may be made for personal or internal use, provided the stated fee for copying beyond that permitted by Section 107 or 108 of the United States Copyright Law is paid through the Copyright Clearance Center, Inc., 21 Congress Street, Salem, Mass. 01970, USA.

If a code does not appear, copies of the article may be made without charge, provided permission is obtained from the publisher.

The copyright owner's consent does not extend to copying for general distribution, for promotion, for creating new works, or for resale. Specific written permission must be obtained from the publisher for such copying.

### *Other Regulations*

Authors of this journal can benefit from library and photocopy fees collected by VG WORT if certain conditions are met. If an author lives in the Federal Republic of Germany or in West Berlin it is recommended that he contact Verwertungsgesellschaft WORT, Abteilung Wissenschaft, Goethestraße 49, D-8000 München 2, for detailed information.

Springer-Verlag Berlin Heidelberg New York

Printed in Germany by Universitätsdruckerei H. Stürtz AG Würzburg

© Deutsche Geophysikalische Gesellschaft, Clausthal-Zellerfeld, 1983



## Author Index

- Ahmad, M.M. 106  
 Ansonge, J. 109
- Baader, H.-R. 140  
 Baumjohann, W. 40  
 Brösche, P. 140
- Cambou, F. 150  
 Chroston, P.N. 14  
 Crasnier, J. 150  
 Czechowsky, P. 34
- Daly, P.W. 199  
 Deichmann, N. 109
- Elsner, R. 97  
 Evans, C.J. 14
- Fan, C.Y. 239
- Galperin, Yu.I. 150  
 Gladyshev, V.A. 150
- Gloeckler, G. 239  
 Götze, H.-J. 136  
 Gusev, A.A. 247
- Haerendel, G. 53, 61  
 Hahn, A. 71  
 Hövel, W. 140  
 Hovestadt, D. 239  
 Hufen, J.-H. 71  
 Hultquist, B. 203  
 Husebye, E.S. 119
- Ipavich, F.M. 239
- Jones, D. 158  
 Just, I. 247
- Kaila, K.U. 40  
 Keppler, E. 199  
 Khosa, P.N. 106  
 Kind, R. 7  
 Klecker, B. 239
- Kovrazhkin, R.A. 150  
 Kröger, P. 97  
 Kudela, K. 247  
 Kustov, A.V. 49
- Lalmani 106
- McElhinny, M.W. 85  
 Mereu, R.F. 119  
 Meurers, B. 136  
 Meyer, J. 71  
 Micheel, H.J. 97  
 Mykkeltveit, S. 119
- Nielsen, E. 40
- Odom, R.I. 7  
 Oksman, J. 49
- Papamastorakis, I. 53, 61  
 Pellinen, R.J. 40  
 Pugacheva, G.I. 247
- Rademacher, H. 7  
 Röttger, J. 34  
 Rüster, R. 34
- Saunders, M.A. 190  
 Sauvaud, J.A. 150  
 Schenk, H. 1  
 Schmidt, G. 34  
 Scholer, M. 176, 239  
 Senanayake, W.E. 85  
 Siebert, M. 71  
 Sofko, G. 40  
 Spjeldvik, W.N. 215  
 Starkov, G.V. 40, 49
- Uspensky, M.V. 40, 49
- Wielandt, E. 1  
 Wilhelm, H. 131  
 Wolf, D. 22
- Young, D.T. 167

## Subject Index

### *Auroral Particles*

- Global Pattern of Auroral Ion Precipitation: A Review of the Results from the AUREOLE-1 and AUREOLE-2 Satellites (Crasnier, J. et al.) 150

### *Auroral Zone Physics*

- Spatial Variations of Ionospheric Conductivity and Radar Auroral Amplitude in the Eastward Electrojet Region During Pre-Substorm Conditions (Uspensky, M.V., et al.) 40
- On the Dependence of Radar Aurora Amplitude on Ionospheric Electron Density (Starkov, G.V., et al.) 49

### *Black Forest*

- Evidence for Lamination in the Lower Continental Crust Beneath the Black Forest (Southwestern Germany) (Deichmann, N., Ansonge, J.) 109

### *Earth's Crust*

- Seismic Velocities of Granulites from the Seiland Petrographic Province, N. Norway: Implications for Scandinavian Lower Continental Crust (Chroston, P.N., Evans, C.J.) 14
- Investigations of the Internal Geomagnetic Field by Means of a Global Model of the Earth's Crust (Meyer, J., et al.) 71
- Evidence for Lamination in the Lower Continental Crust Beneath the Black Forest (Southwestern Germany) (Deichmann, N., Ansonge, J.) 109
- FENNOLOGRA Recordings at NORSAR (Mereu, R.F., et al.) 119

### *Earth's Flattening*

- Earth's Flattening Effect on the Tidal Forcing Field (Wilhelm, H.) 131

### *Earth's Rotation*

- Ocean Tides and Periodic Variations of the Earth's Rotation (Baader, H.-R., et al.) 140

### *Electromagnetic Induction*

- Inductive Coupling Between Idealized Conductors and Its Significance for the Geomagnetic Coast Effect (Wolf, D.) 22
- An Analogue Model of the Geomagnetic Induction in the South Indian Ocean (Papamastorakis, I., Haerendel, G.) 61

### *Error Analysis*

- Comparison of Errors in Local and Reference Estimates of the Magnetotelluric Impedance Tensor (Kröger, P., et al.) 97

### *Europe*

- The Upper Mantle Structure Under South-East Europe Derived from GRF Broadband Records of Greek Earthquakes (Rademacher, H., et al.) 7

### *Explosions Seismology*

- Evidence for Lamination in the Lower Continental Crust Beneath the Black Forest (Southwestern Germany) (Deichmann, N., Ansonge, J.) 109
- FENNOLOGRA Recordings at NORSAR (Mereu, R.F., et al.) 119

### *Flux Transfer Events*

- Recent ISEE Observations of the Magnetopause and Low Latitude Boundary Layer: A Review (Saunders, M.A.) 190
- Motion of Flux Transfer Events on 10 November 1977 Determined by Energetic Particles on ISEE 2 (Daly, P.W., Keppler, E.) 199

### *Geomagnetic Coast Effect*

- Inductive Coupling Between Idealized Conductors and Its Significance for the Geomagnetic Coast Effect (Wolf, D.) 22
- An Analogue Model of the Geomagnetic Induction in the South Indian Ocean (Papamastorakis, I., Haerendel, G.) 61

### *Geomagnetic Field*

- Investigations of the Internal Geomagnetic Field by Means of a Global Model of the Earth's Crust (Meyer, J., et al.) 71

### *Geomagnetic Variations*

- A Possibility to Distinguish Between Ionospheric and Magnetospheric Origin of Low Latitude Magnetic Perturbations (Papamastorakis, I., Haerendel, G.) 53
- An Analogue Model of the Geomagnetic Induction in the South Indian Ocean (Papamastorakis, I., Haerendel, G.) 61

### *Gravimeters*

- Some Results of Calibration Factor Determination of LaCoste and Romberg Gravity Meters (Model D) (Götze, H.-J., Meurers, B.) 136

- India**  
 A Possibility to Distinguish Between Ionospheric and Magnetospheric Origin of Low Latitude Magnetic Perturbations (Papamastorakis, I., Haerendel, G.) 53  
 An Analogue Model of the Geomagnetic Induction in the South Indian Ocean (Papamastorakis, I., Haerendel, G.) 61
- Ion Composition**  
 Heavy Ion Plasmas in the Outer Magnetosphere (Young, D.T.) 167  
 On the Dynamics of the Ring Current (Hultquist, B.) 203  
 Ionic Composition of the Earth's Radiation Belts (Spjeldvik, W.N.) 215  
 Energy and Charge Distribution of Energetic Helium Ions in the Outer Radiation Belt of the Earth (Klecker, B., et al.) 239
- Magnetosphere**  
 Preface 149  
 Global Pattern of Auroral Ion Precipitation: A Review of the Results from the AUREOLE-1 and AUREOLE-2 Satellites (Crasnier, J.) 150  
 A Technique for Studying Density Gradients and Motions of Plasmaspheric Irregularities (Jones, D.) 158  
 Heavy Ion Plasmas in the Outer Magnetosphere (Young, D.T.) 167  
 Energetic Particle Signatures Near Magnetospheric Boundaries (Scholer, M.) 176  
 Recent ISEE Observations of the Magnetopause and Low Latitude Boundary Layer: A Review (Saunders, M.A.) 190  
 Motion of Flux Transfer Events on 10 November 1977 Determined by Energetic Particles on ISEE 2 (Daly, P.W., Keppeler, E.) 199  
 On the Dynamics of the Ring Current (Hultquist, B.) 203  
 Ionic Composition of the Earth's Radiation Belts (Spjeldvik, W.N.) 215  
 Energy and Charge Distribution of Energetic Helium Ions in the Outer Radiation Belt of the Earth (Klecker, B., et al.) 239  
 High Energy Electrons at Altitudes 500 km Near the Equator (Just, L., et al.) 247
- Magnetotellurics**  
 Comparison of Errors in Local and Reference Estimates of the Magnetotelluric Impedance Tensor (Kröger, P., et al.) 97
- Magsat**  
 Investigations of the Internal Geomagnetic Field by Means of a Global Model of the Earth's Crust (Meyer, J., et al.) 71
- Mesospheric Winds**  
 VHF Radar Observations of Wind Velocities at the Arecibo Observatory (Röttger, J., et al.) 34
- Palaeomagnetism**  
 A Palaeointensity Method for Use with Highly Oxidised Basalts, and Application to Some Permian Volcanics (Senanayake, W.E., McElhinny, M.W.) 85
- Radar Aurora**  
 Spatial Variations of Ionospheric Conductivity and Radar Auroral Amplitude in the Eastward Electrojet Region During Pre-Substorm Conditions (Uspensky, M.V., et al.) 40  
 On the Dependence of Radar Aurora Amplitude on Ionospheric Electron Density (Starkov, G.V., et al.) 49
- Radiation Belts**  
 Ionic Composition of the Earth's Radiation Belts (Spjeldvik, W.N.) 215  
 Energy and Charge Distribution of Energetic Helium Ions in the Outer Radiation Belt of the Earth (Klecker, B., et al.) 239  
 High Energy Electrons at Altitudes 500 km Near the Equator (Just, L., et al.) 247
- Ring Current**  
 On the Dynamics of the Ring Current (Hultquist, B.) 203
- Rock Magnetism**  
 A Palaeointensity Method for Use with Highly Oxidised Basalts, and Application to Some Permian Volcanics (Senanayake, W.E., McElhinny, M.W.) 85
- Scandinavia**  
 Seismic Velocities of Granulites from the Seiland Petrographic Province, N. Norway: Implications for Scandinavian Lower Continental Crust (Chroston, P.N., Evans, C.J.) 14  
 FENNOLOGRA Recordings at NORSAR (Mereu, R.F., et al.) 119
- Seismic Surface Waves**  
 On Systematic Errors in Phase-Velocity Analysis (Wielandt, E., Schenk, H.) 1
- Seismic Velocities**  
 Seismic Velocities of Granulites from the Seiland Petrographic Province, N. Norway: Implications for Scandinavian Lower Continental Crust (Chroston, P.N., Evans, C.J.) 14
- Seismology**  
 On Systematic Errors in Phase-Velocity Analysis (Wielandt, E., Schenk, H.) 1  
 The Upper Mantle Structure Under South-East Europe Derived from GRF Broadband Records of Greek Earthquakes (Rademacher, H., et al.) 7  
 FENNOLOGRA Recordings at NORSAR (Mereu, R.F., et al.) 119
- Stratospheric Winds**  
 VHF Radar Observations of Wind Velocities at the Arecibo Observatory (J. Röttger, et al.) 34
- Synthetic Seismograms**  
 The Upper Mantle Structure Under South-East Europe Derived from GRF Broadband Records of Greek Earthquakes (Rademacher, H., et al.) 7  
 Evidence for Lamination in the Lower Continental Crust Beneath the Black Forest (Southwestern Germany) (Deichmann, N., Ansorge, J.) 109
- Tidal Forces**  
 Earth's Flattening Effect on the Tidal Forcing Field (Wilhelm, H.) 131
- Terrestrial Myriametric Radiation**  
 A Technique for Studying Density Gradients and Motions of Plasmaspheric Irregularities (Jones, D.) 158
- Tides**  
 Ocean Tides and Periodic Variations of the Earth's Rotation (Baader, H.-R., et al.) 140
- Upper Mantle**  
 The Upper Mantle Structure Under South-East Europe Derived from GRF Broadband Records of Greek Earthquakes (Rademacher, H., et al.) 7
- VHR Radar**  
 VHR Radar Observations of Wind Velocities at the Arecibo Observatory (Röttger, J., et al.) 34
- VLF Emissions**  
 Discrete Chorus Emissions Recorded at Nainital (Khosa, P.N., et al.) 106
- Whistlers**  
 Discrete Chorus Emissions Recorded at Nainital (Khosa, P.N. et al.) 106  
 In Memoriam 143, 145  
 Book Reviews 69, 147

# Journal of Geophysics Zeitschrift für Geophysik

8° 2 Net. 2748  
Z 4137 G4

Volume 52 Number 1 1983

**E. Wielandt, H. Schenk**

On Systematic Errors in Phase-Velocity  
Analysis 1

**H. Rademacher, R.I. Odom, R. Kind**

The Upper Mantle Structure Under South-East  
Europe Derived from GRF Broadband Records  
of Greek Earthquakes 7

**P.N. Chroston, C.J. Evans**

Seismic Velocities of Granulites from the Seiland  
Petrographic Province, N. Norway: Implications  
for Scandinavian Lower Continental Crust 14

**D. Wolf**

Inductive Coupling Between Idealized Con-  
ductors and Its Significance for the Geomagnetic  
Coast Effect 22

**J. Röttger, P. Czechowsky, R. Rüster,  
G. Schmidt**

VHF Radar Observations of Wind Velocities at the  
Arecibo Observatory 34

**M.V. Uspensky, R.J. Pellinen, W. Baumjohann,  
G.V. Starkov, E. Nielsen, G. Sofko, K.U. Kaila**  
Spatial Variations of Ionospheric Conductivity and  
Radar Auroral Amplitude in the Eastward Electro-  
jet Region During Pre-Substorm Conditions 40

**G.V. Starkov, J. Oksman, M.V. Uspensky,  
A.V. Kustov**

On the Dependence of Radar Aurora Amplitude  
on Ionospheric Electron Density 49

**I. Papamastorakis, G. Haerendel**

A Possibility to Distinguish Between Ionospheric  
and Magnetospheric Origin of Low Latitude  
Magnetic Perturbations 53

**I. Papamastorakis, G. Haerendel**

An Analogue Model of the Geomagnetic Induction  
in the South Indian Ocean 61

*Book Review* 69

*Indexed in Current Contents*

*Evaluated for Physics Briefs and INKA-PHYS  
data base*

51 o.l.

1-3, t, i



Springer International

252 J. Geophys. — ISSN 0340-062X — JGEOD4 52(1) 1-70 (1983) — February 1983

17. März 1983

Niedersächsische Staats-  
Universitätsbibliothek  
Göttingen

# Journal of Geophysics – Zeitschrift für Geophysik

Edited for the Deutsche Geophysikalische Gesellschaft by W. Dieminger, G. Müller, and J. Untiedt

This journal was founded by the Deutsche Geophysikalische Gesellschaft on the initiative of L. Mintrop in 1924 as the *Zeitschrift für Geophysik* and edited by G. Angenheister from Vol. 1–18 (1944). It reappeared in 1954 edited by B. Brockamp from Vol. 19–26 (1960), and edited by W. Dieminger from Vol. 27–33 (1961), and from Vol. 34 (1968) edited by W. Dieminger and J. Untiedt. After Vol. 40 (1970) the title was changed to *Journal of Geophysics – Zeitschrift für Geophysik*.

Published: Vols. 19–39 by Physica-Verlag, Würzburg, from Vol. 40 by Springer-Verlag GmbH & Co. KG Berlin, Heidelberg, New York.

**Manuscripts may be addressed to any of the Editors. For addresses see last cover page. Manuscripts should conform with the journal's accepted practice as described in the instructions to Authors.**

The Journal accepts

- Review Articles (invited by the Editors)
- Original Papers
- Short Communications
- Letters to the Editors
- Book Reviews

**in the field of Geophysics and Space Physics.**

## Copyright

It is a fundamental condition that submitted manuscripts have not been published and will not be simultaneously submitted or published elsewhere. By submitting a manuscript, the authors agree that the copyright for their article is transferred to the publisher if and when the article is accepted for publication. The copyright covers the exclusive rights to reproduce and distribute the article, including reprints, photographic reproductions, microform or any other reproductions of similar nature, and translations.

Photographic reproduction, microform, or any other reproduction of text figures, or tables from this journal is prohibited without permission obtained from the publisher.

The use of general descriptive names, trade names, trade marks, etc., in this publication, even if the former are not specifically identified, is not to be interpreted as exempt from the relevant protective laws and regulations and may accordingly be used freely by anyone.

## Special Regulations for the USA

Photocopies may be made for personal or internal use beyond that permitted by Section 107 or 108 of the U.S. Copyright Law, provided a fee is paid. This fee is \$0.20 per page or a minimum of \$1.00 if an article consists of less than five pages. Please pay this fee to the Copyright Clearance Center, Inc., 21 Congress Street, Salem, MA 01970, USA, stating the ISSN 0340-062X, volume, and first and last page numbers of each article copied.

The copyright owner's consent does not extend to copying for general distribution, for promotion, for creating new works, or for resale. Specific written permission must be obtained from the publisher for such copying.

## Other Regulations

Authors of this journal can benefit from library and photocopy fees collected by VG WORT if certain conditions are met. If an author lives in the Federal Republic of Germany or in West Berlin it is recommended that he contact Verwertungsgesellschaft WORT, Abteilung Wissenschaft, Goethestraße 49, D-8000 München 2, for detailed information.

## Subscription Information

Volumes 53 + 54 (3 issues each) will appear in 1983. The price of a volume is DM 168,00 or \$70.00. Prices for backvolumes are available on request. Correspondence concerning subscriptions should be addressed to the publisher.

**Members.** Members of the Deutsche Geophysikalische Gesellschaft are entitled to purchase the Journal for their own use at a privilege price of DM 98,00 payable with the Membership dues. Orders should be sent to the Society's office at the following address: Postfach 230, D-3392 Clausthal-Zellerfeld.

**North America.** Annual subscription rate: \$149.00, including carriage charges. Subscriptions are entered with prepayment only. Orders should be addressed to: Springer-Verlag New York Inc. Journal Sales Department 44 Hartz Way Secaucus, NJ 07094, USA Tel. (201) 348-4033, Telex 0023-125994.

**All Other Countries.** Annual subscription rate: DM 336,00, plus carriage charges. Airmail delivery on request only. For *Japan*, carriage charges (Surface Airmail Lifted) are DM 45,60; for *India* DM 36,60. Single issue price: DM 67,20 plus carriage charges. Orders can either be placed with your bookdealer or sent directly to: Springer-Verlag Heidelberger Platz 3 D-1000 Berlin 33 Tel. (0)30/82 07-1, Telex 1-83319.

**Changes of Address:** Allow six weeks for all changes to become effective. All communications should include both old and new addresses (with Postal Codes) and should be accompanied by a mailing label from a recent issue.

**Microform:** Microform editions are available from: University Microfilms International 300 N. Zeeb Road Ann Arbor, MI 48106, USA

## Production

Springer-Verlag  
Journal Production Department II  
Postfach 105280  
D-6900 Heidelberg 1  
Federal Republic of Germany  
Tel. (0)6221/487-339, Telex 4-61 690.

## Responsible for Advertisements

Springer-Verlag  
G. Sternberg  
Kurfürstendamm 237  
D-1000 Berlin 15  
Tel. (0)30/882 1031, Telex 1-85411.

## Printers

Universitätsdruckerei H. Stürtz AG Würzburg  
© the Deutsche Geophysikalische Gesellschaft, Clausthal-Zellerfeld, 1983  
Printed in Germany



**Springer International**

## On Systematic Errors in Phase-Velocity Analysis\*

E. Wielandt and H. Schenk

Institute of Geophysics, Swiss Federal Institute of Technology, 8093 Zürich, Switzerland

**Abstract.** We investigate the systematic error that is introduced into the phase and amplitude of a dispersed signal by the application of a gaussian time window. The most significant contribution to the phase error is proportional to the slope of the group delay (vs. frequency) curve and inversely proportional to the square of the window width. This error is normally negligible in the 15-100s long-period seismic band, but can be significant at periods longer than 240s for fundamental-mode Rayleigh waves. To first order, no phase error is associated with a slope of the amplitude spectrum. We derive a simple nonlinear formula that predicts the bias in the phase velocity to a few parts in ten thousand; it applies both to the moving-window and to the multiple-filter method.

**Key words:** Surface waves - Phase-velocity analysis

### The Problem

Two methods are widely used in phase velocity analysis of seismic surface waves. The moving-window method consists in isolating parts of the wavetrain from other seismic arrivals or noise with a set of time windows, and determining the Fourier phase at each frequency in the appropriate window. As stated by the convolution theorem of the inverse Fourier transform, this procedure is (for a given window) equivalent to convolving the signal spectrum with  $(2\pi)^{-1}$  times the Fourier transform of the window function. The resulting Fourier phases are in general different from the original ones whose spatial dependence defines the phase velocity. Phase velocities obtained with the moving-window method are therefore biased, and while the bias is small when the window is wide compared to the signal period, substantial errors can arise at very long periods where windows no more than a few periods wide must be used to separate subsequent surface-wave arrivals.

An alternative method for phase velocity analysis is the multiple-filter method. It consists in transmitting the seismic signal through a set of zero-phase bandpass filters, and evaluating the instantaneous phase of the filtered signals at or near the group arrival time. No time windowing is applied explicitly, but it is implied in

the duration of the transient response of the filters. There are some problems, both theoretical and practical, associated with this method. The instantaneous phase is in general different from the Fourier phase, and no simple relationship exists between them unless simplifying assumptions are made (such as constant amplitude and a linear group delay "curve"). It is therefore not quite obvious how the phase velocity is related to the instantaneous phase, and in fact the instantaneous phase of an unfiltered signal gives only a poor estimate of the phase velocity. Nevertheless the multiple-filter method is equivalent to the moving-window method provided that the time at which the phase is read, and the frequency to which it is associated, are correctly identified. This follows from the identity (Eq. (1) of Kodera et al., 1976):

$$s(t_0, \omega_0) = \frac{1}{2\pi} \int F(\omega) H(\omega - \omega_0) \exp(i\omega t_0) d\omega \\ = \exp(i\omega_0 t_0) \int f(t) h(t_0 - t) \exp(-i\omega_0 t) dt. \quad (1)$$

Here  $f(t)$  is the seismic signal,  $F(\omega)$  its Fourier transform,  $h(t)$  is a window function which we assume to be real and symmetric with respect to the origin, and  $H(\omega)$  is its Fourier transform that has the same property.  $s(t_0, \omega_0)$  is an estimate for the complex signal amplitude at time  $t_0$  and frequency  $\omega_0$ ; its computation is known as a frequency-time analysis (FTAN), and a two-dimensional display of its modulus is known as a Gabor matrix.

The time-domain integral represents the Fourier amplitude, at frequency  $\omega_0$ , of the signal  $f(t)$  in a time window centered at time  $t_0$ . The frequency-domain integral is an inverse Fourier transform; it represents the instantaneous complex amplitude, at time  $t_0$ , of the signal that was passed through a zero-phase bandpass filter centered at  $\omega_0$ . Equation (1) states that the two complex amplitudes are equal when the phases are referred to a common time origin. Thus, the moving-window and multiple-filter methods of frequency-time analysis are mathematically equivalent, and the phase corrections which we are going to derive apply to both methods.

Apart from a phase factor that refers the phase to  $t_0$  as the time origin, the estimate  $s(t_0, \omega_0)$  mathematically approaches the complex Fourier amplitude  $F(\omega_0)$  when we increase the window width to infinity so that  $H(\omega)$

\* Publication No. 396, Institute of Geophysics, Swiss Federal Institute of Technology

in Eq. (1) becomes  $2\pi$  times a delta function. Vice versa,  $s(t_0, \omega_0)$  becomes the instantaneous value  $f(t_0)$  when the time window  $h(t)$  is reduced to a delta function. In the analysis of real signals, the presence of noise would prevent us from reaching these limits; the integrals would diverge away from the desired values when the window width, or the bandwidth, are unreasonably increased. We therefore need methods to convert FTAN phase estimates obtained with a limited set of windows or filters into Fourier phases (for a phase velocity measurement) or into instantaneous amplitudes and phases (for a group velocity measurement).

Dziewonski et al. (1972) and Denny and Chin (1976) have proposed methods to measure group velocities of dispersed seismic signals without bias. The residual-dispersion method of Dziewonski et al. eliminates the phase bias as well, without determining it explicitly. Still, an independent investigation of the bias remains desirable, whether for the purpose of determining its magnitude, to derive criteria for the selection of windows, or for correcting phase velocities obtained with different methods. We have not found any useful formula for the difference between FTAN phase estimates and Fourier phases in the seismological literature. Such formulae were however developed in unpublished investigations by Nyman (1977) and Cara (1978) for gaussian multiple filters. Nyman takes into account third-order derivatives of the signal spectrum with respect to frequency, but assumes that the instantaneous phase is evaluated at the exact group arrival time, which is in general unknown. Cara solves the problem to second order in the phase and to arbitrary order in the amplitude spectrum with an infinite series. Their results cannot be compared to ours term by term due to their different mathematical form, except for the leading first-order term which agrees with our Eq. (13) in each case. The inclusion of derivatives higher than the second appears unrealistic from a practical point of view. We therefore restrict our investigation to derivatives of second order of the logarithmic signal spectrum. The resulting error formula (10) has a comparatively simple structure and permits us to discuss in some detail the functional dependences involved, especially the influence of the position and width of the window on the FTAN phase. The second-order formula is sufficiently accurate for practical applications in surface-wave seismology. Accuracy is however not our main point. As will be discussed later, the ‘‘systematic error’’ consists of one desired and one undesired component; only the latter needs be removed, but the distinction is to some degree subjective. A discussion of the ‘‘accuracy’’ of a method for bias correction is therefore not meaningful without reference to a specific problem.

### Prediction of the Systematic Error

Consider a plane dispersed wave that is recorded at a distance  $\Delta$  from the source:

$$\begin{aligned} f(t, \Delta) &= \frac{1}{2\pi} \int A(\omega) \exp[i(\omega t - k\Delta)] d\omega \\ &= \frac{1}{2\pi} \int F(\omega) \exp(i\omega t) d\omega. \end{aligned} \quad (2)$$

Assuming that the amplitude has no zeroes, we write the Fourier spectrum  $F(\omega)$  in the form

$$\begin{aligned} F(\omega) &= A(\omega) \exp(-ik\Delta) \\ &= \exp[a(\omega) - i\omega\tau_\phi(\omega)] \end{aligned} \quad (3)$$

where  $a(\omega) = \log A(\omega)$  and  $\tau_\phi(\omega) = k\Delta/\omega = \Delta/c(\omega)$ .  $c$  is the phase velocity and  $\tau_\phi$  the phase delay time. The signal (2) is analyzed in the time window

$$w(t) = h(t - t_0) = \exp[-(t - t_0)^2/\varepsilon^2] \quad (4)$$

of width  $\varepsilon$ . This is equivalent to convolving  $F(\omega)$  with

$$\begin{aligned} \frac{1}{2\pi} W(\omega) &= \frac{1}{2\pi} H(\omega) \exp(-i\omega t_0) \\ &= \frac{\varepsilon}{\sqrt{4\pi}} \exp\left[-\frac{\varepsilon^2}{4}\omega^2 - i\omega t_0\right]. \end{aligned} \quad (5)$$

The result at frequency  $\omega_0$  is

$$\begin{aligned} s(t_0, \omega_0) &= \frac{\varepsilon}{\sqrt{4\pi}} \int \exp\left[a(\omega) - i\omega\tau_\phi(\omega) \right. \\ &\quad \left. - \frac{\varepsilon^2}{4}(\omega_0 - \omega)^2 - i(\omega_0 - \omega)t_0\right] d\omega. \end{aligned} \quad (6)$$

To solve the integral, we replace the logarithmic amplitude  $a(\omega)$  and the phase  $\omega\tau_\phi(\omega)$  by their second-order Taylor expansions around  $\omega = \omega_0$ . This is the only approximation in the derivation of Eq. (10). Our result will therefore be exact to that degree to which  $a(\omega)$  and  $k(\omega)$  can be represented by second-order polynomials in the effective bandwidth of integration. Observing that  $\tau(\omega) = \frac{d}{d\omega}(\omega\tau_\phi)$  is the group delay time, we have

$$a(\omega) \cong a(\omega_0) + (\omega - \omega_0) a'(\omega_0) + \frac{1}{2}(\omega - \omega_0)^2 a''(\omega_0), \quad (7)$$

$$\begin{aligned} \omega\tau_\phi(\omega) &\cong \omega_0\tau_\phi(\omega_0) \\ &+ (\omega - \omega_0)\tau(\omega_0) + \frac{1}{2}(\omega - \omega_0)^2 \tau'(\omega_0). \end{aligned} \quad (8)$$

The constant term,  $\exp[a(\omega_0) + i\omega_0\tau_\phi(\omega_0)]$  can now be extracted from the integral; it represents the original Fourier coefficient  $F(\omega_0)$ . The remaining integral represents the error that was introduced by time-windowing.

$$\begin{aligned} \frac{s(t_0, \omega_0)}{F(\omega_0)} &= \frac{\varepsilon}{\sqrt{4\pi}} \int \exp\left[(\omega - \omega_0)(a' + i(t_0 - \tau)) \right. \\ &\quad \left. + \frac{1}{2}(\omega - \omega_0)^2 \left(a'' - \frac{\varepsilon^2}{2} - i\tau'\right)\right] d\omega. \end{aligned} \quad (9)$$

From now on  $a$ ,  $\tau$  and their derivatives are to be taken at  $\omega = \omega_0$ . We will assume that  $a(\omega)$  is real; the generalization to complex amplitudes (i.e., the inclusion of an initial phase at  $\Delta = 0$ ) affects the definition of the group arrival time but does not change our subsequent derivations.  $t_0 - \tau$  is the offset of the center of the window against the group arrival time  $\tau$ . The integral can be evaluated with standard methods provided that  $a''$ , if positive, is less than  $\varepsilon^2/2$ . The result is

$$\frac{s(t_0, \omega_0)}{F(\omega_0)} = \left(1 - 2\frac{a''}{\varepsilon^2} + 2i\frac{\tau'}{\varepsilon^2}\right)^{-1/2} \exp\frac{(a' + i(t_0 - \tau))^2}{\varepsilon^2 - 2a'' + 2i\tau'}. \quad (10)$$

The error depends only on the four dimensionless quantities

$$\alpha = \frac{a'}{\varepsilon}, \quad \beta = \frac{t_0 - \tau}{\varepsilon}, \quad \gamma = \frac{2a''}{\varepsilon^2}, \quad \delta = \frac{2\tau'}{\varepsilon^2}. \quad (11)$$

These normally have, in seismological applications, absolute values smaller than one, but are not always small enough to allow a linear expansion of Eq.(10). For a qualitative discussion, let us first assume that  $\alpha$  and  $\gamma$  are negligible, i.e. the amplitude spectrum is flat in the vicinity of  $\omega_0$ . The remaining two variables,  $\beta$  and  $\delta$ , measure how well the window is centered at the group arrival time, and how strongly the signal is dispersed in the window. For small dispersion,  $\delta \cong 0$ , the right-hand side of Eq.(10) reduces to the original window function

$$\frac{s(t_0, \omega_0)}{F(\omega_0)} \cong \exp[-(\tau - t_0)^2/\varepsilon^2] \quad (12)$$

as expected for an impulsive input signal. When  $\delta$  is not negligible but the window is centered, we have

$$\frac{s(t_0, \omega_0)}{F(\omega_0)} = (1 + 2i\tau'/\varepsilon^2)^{-1/2}. \quad (13)$$

The behaviour of the systematic error now depends on the magnitude of  $\delta$ . This quantity determines whether a change of the signal frequency can be resolved in the window or not. The resolving power of a gaussian time window of  $1/e$ -width  $\varepsilon$  for angular frequencies is  $\varepsilon^{-1}$  and the variance of the angular frequency of the signal in it is  $\varepsilon(2|\tau'|)^{-1}$ ; the latter can be resolved when  $2|\tau'| < \varepsilon^2$ , i.e.  $|\delta| < 1$ . When  $|\delta|$  is small, the phase error is proportional to  $\delta$  and the amplitude error to  $\delta^2$ .  $|\delta| = 1$  defines the width of an "optimum window" in which the signal has the smallest bandwidth. This is easily seen from Eq.(10) if we put  $a' = a'' = 0$ : the value  $\varepsilon = \sqrt{2|\tau'|}$  minimizes the real part of the exponent, and thus the modulus of  $s(t_0, \omega_0)$ , at any frequency  $\omega_0$  for which the window is not centered. The Fourier transform of the optimum window defines an optimum filter of bandwidth  $\sqrt{2|\tau'|}^{-1}$  for which the filtered signal has the shortest duration (Inston et al., 1971; Cara, 1973). With this optimum width, we obtain a phase bias of  $\mp\pi/8$ , depending on the sign of  $\tau'$ . When  $|\delta|$  is much larger than one, the signal is practically sinusoidal in the window; the amplitude becomes proportional to the window width, and the phase error approaches the limit  $\mp\pi/4$ . This is the well-known relationship between the instantaneous phase and the Fourier phase in the case of linear dispersion (compare Fig. 7.4 of Aki and Richards, 1980 and our Fig. 5).

A linear expansion of Eq.(10) is possible when all four quantities in Eq.(11) are small, i.e. when the window is sufficiently wide:

$$\frac{s(t_0, \omega_0)}{F(\omega_0)} \cong 1 + \varepsilon^{-2}(a'' + a'^2 - (t_0 - \tau)^2 + 2ia'(t_0 - \tau) - i\tau'). \quad (14)$$

This equation indicates that for  $\varepsilon$  large and  $t_0 = \tau$  the phase error depends only on the window width and on

the slope of the group delay curve; an eventual slope in the amplitude spectrum ( $a' \neq 0$ ) would not cause a phase error. This is in agreement with Nyman's (1977) and Cara's (1978) formulae. Considerations of symmetry suggest that this result is not restricted to gaussian windows; any centered symmetric window should provide a phase estimate independent of the amplitude spectrum to first order. However, phase errors related to  $a'$  have occasionally been observed (Dziewonski et al., 1972; Souriau-Thevenard, 1978). Since both our Eq.(10) and Nyman's formulae predict a phase error proportional to  $a'^2\tau'/\varepsilon^4$  when nonlinear terms are retained, such errors are likely to occur when the window is narrow. An alternative explanation would be that the error is not directly related to the measurement of the instantaneous phase at time  $t_0$ , but comes in when its time derivative (the instantaneous frequency) is evaluated and taken for  $\omega_0$ .

Equation (14) also has an application to free mode analysis. Time-variable filtering is sometimes used to separate different modes of oscillation prior to spectral analysis. It is then essential that the window width is chosen proportional to the optimum width (i.e. to the square root of the group delay time) so that the systematic error is constant. Otherwise, the error would enter into the eigenfrequencies and the amplitude decay rates. A window of increasing width can however be realized only for the first few Rayleigh arrivals.

When the window is offset from the arrival time, Eq.(14) predicts an additional phase error proportional to the window offset and to the slope of the amplitude spectrum. Amplitude equalization, as recommended by Cara and Hatzfeld (1976) for group velocity analysis, would eliminate this part of the error, but at the same time deteriorate the signal-to-noise ratio by spectral leakage from those frequencies where the noise predominates. It is probably better to leave the amplitudes unchanged, giving automatically less weight to those frequencies where the signal-to-noise ratio is inadequate.

In practice, the width of the window must often be chosen such that none of the Eqs.(12), (13) or (14) is applicable. By splitting the logarithm of the right-hand side of Eq.(10) into its real and imaginary parts, we find that the dependence of the phase error on the window offset is quadratic, and its dependence on the window width is characterized by an arctangent function. We shall however postpone the discussion until we have presented the results of a numerical test.

As indicated above, our results apply without any change to a multiple-filter analysis with the gaussian filters

$$H(\omega - \omega_0) = \frac{\varepsilon}{\sqrt{4\pi}} \exp\left[-\frac{\varepsilon^2}{4}(\omega - \omega_0)^2\right]. \quad (15)$$

We have then to interpret  $\omega_0$  as the center frequency of the filter, and  $t_0$  as the time at which amplitude and phase are read from the filtered seismogram.

## A Numerical Test

As a test seismogram we have used a synthetic wave-train (Fig. 1) representing a Rayleigh wave that has trav-

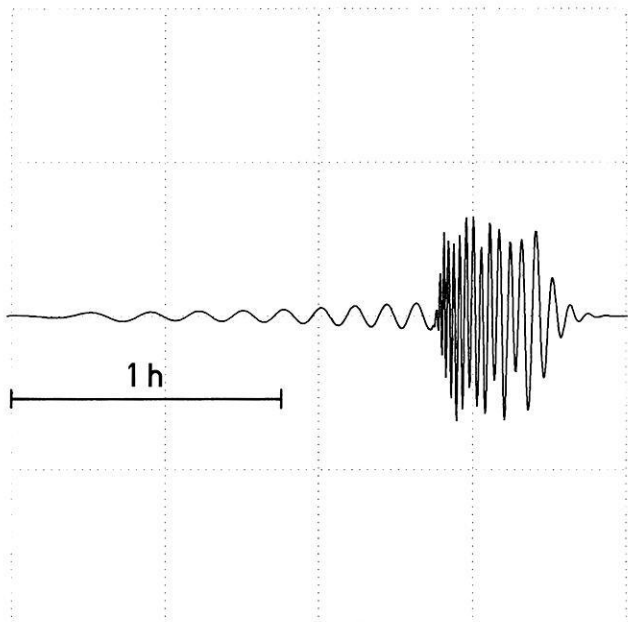


Fig. 1. The test seismogram

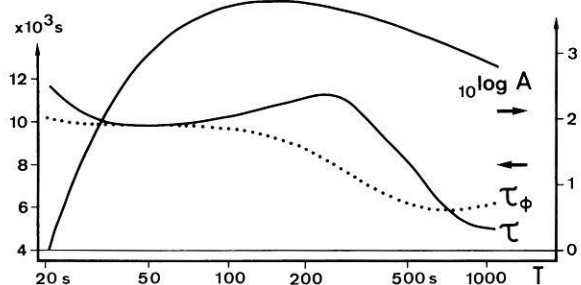


Fig. 2. Phase and group delay (lefthand scale), and log amplitude (righthand scale) of the test signal

elled over a distance of  $\Delta = 40,030$  km on a flat earth. Group velocities were fitted to those of the observed free spheroidal oscillations of the earth at periods longer than 150 s, and to those of model 1066B at shorter periods (both after Gilbert and Dziewonski, 1975). The use of cubic splines in the fit makes it possible to calculate the derivatives in Eq. (10) analytically as continuous functions. For the amplitude spectrum a simple mathematical form was specified,  $A(\omega) \sim \omega^2 \exp(-\omega \Delta / 2cQ)$ , with a phase velocity  $c = 4$  km/s and a  $Q$  factor of 100 (both being relevant only at the short-period end of the spectrum). Figure 2 shows the phase and group travel times and the amplitude spectrum.

Our program for dispersion analysis evaluates Eq. (6), replacing the integral with a sum over the coefficients of the Fast Fourier Transform of the signal. This is a very efficient method that requires only one Fourier transform for any number of frequencies and windows. The sample frequencies  $\omega_0$  and the window parameters  $t_0$  and  $\epsilon$  at each frequency can be chosen arbitrarily. Normally we set the window width equal to  $200\text{ s} + 2T$  at period  $T$ , a value that was found satisfactory in a practical application (Wielandt and Knopoff, 1982) at periods up to 400 s. At longer periods, one would probably have to use narrower windows in order

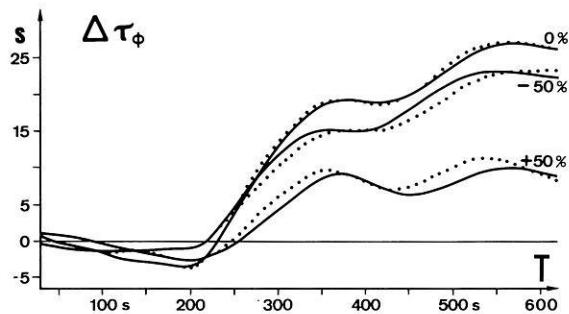


Fig. 3. Predicted and experimental errors of the phase delay time. Errors are positive when the windowed signal is delayed. Window width  $\epsilon$  (Eq. 4) is  $200\text{ s} + 2T$  at period  $T$ . The window centers are offset by  $-50\%$ ,  $0\%$  and  $+50\%$  of the width against the theoretical group arrival time. In this figure and all following, solid lines represent experimental values and symbols predicted values

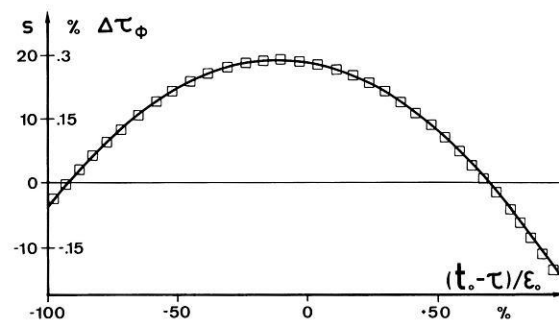


Fig. 4. Error of the phase delay at 400 s period versus window offset. 100% is an offset equal to the window width  $\epsilon$  which is 1,000 s. The vertical scale gives the error in seconds and as a fraction of the total phase delay; with a minus sign, this is also the relative error of the phase velocity

to separate subsequent Rayleigh arrivals, but we have no practical experience in this.

Observed and predicted errors of the phase delay time are compared in Fig. 3 for three sets of windows: one centered at the theoretical group arrival time and one each offset by  $+$  and  $-50\%$  of the width. The agreement is satisfactory, considering that the observational error per circuit is expected to be about 3 s rms for free modes (where several passes of the same wavetrain are averaged), and about twice as much for individual great-circle circuits. The systematic error is, in this example, negligible at periods shorter than 100 s, and becomes substantial only beyond 240 s. Even for window offsets as large as  $\pm 50\%$ , the term with  $a'(t_0 - \tau)$  in Eqs. (10) and (14) does not produce a significant error at the short-period end of the spectrum where the amplitude decays rapidly (Fig. 2). Experiments with less regular amplitude spectra confirm that the influence of the amplitude on the phase error is in fact very small. Since in practice amplitude and phase spectra are not independent of each other, it appears unrealistic to study their influences separately in much detail.

An unexpected result is that at long periods the systematic error is close to a maximum when the window is centered, and decreases when the window is

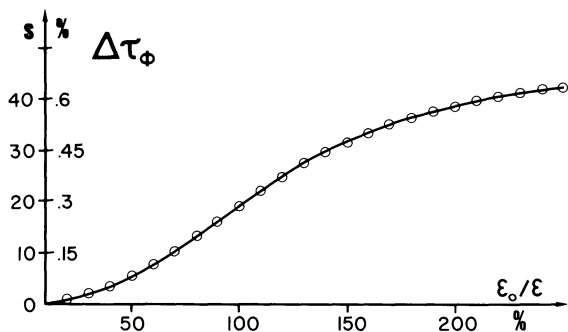


Fig. 5. Error of the phase delay at 400 s period versus window width, with no offset. Note the reciprocal scale;  $\epsilon_0 = 1,000$  s is the normal width

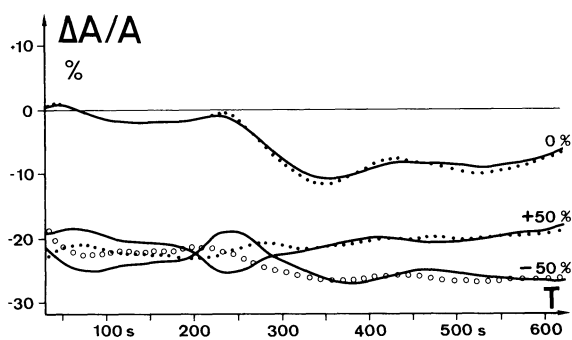


Fig. 6. Amplitude error versus period, for the same windows as in Fig. 3

offset. This is more clearly seen from Fig. 4 where the error at 400 s period is plotted versus the relative offset,  $(t_0 - \tau)/\epsilon$ . For offsets of approximately  $-90\%$  and  $+70\%$ , the systematic error vanishes in this example. We do not recommend this as a method to eliminate the bias. One might however consider adjusting the window so that the maximum of the error curve at about  $-10\%$  offset, rather than the center of the window, coincides with the expected group arrival time; a small error in the latter would then not cause an uncontrolled bias.

The error in phase delay time at 400 s period as a function of the window width is plotted in Fig. 5. In order to be able to display the limiting behaviour for wide windows, we have chosen a reciprocal scale for the width, i.e. the scale is linear with respect to the bandwidth. The error increases in proportion to  $\epsilon^{-2}$  when  $\epsilon$  is large, but approaches a limit when the width is reduced below the normal value, as predicted by Eq. (13). The normal window width lies just between two regions of asymptotic behaviour, a fact that makes a general discussion of Eq. (10) difficult.

Figure 6 shows the relative amplitude error as a function of period for the same three sets of windows as in Fig. 3. As expected, the Fourier amplitude of the windowed signal is normally smaller than that of the original one, and reduces further when the windows are offset. Discrepancies between experimental and predicted values are somewhat larger than for the phase velocity; they are apparently related to the neglected second derivative of the group delay time.

## Application to Real Signals

In contrast to the synthetic signal used to test Eq. (10), real signals often exhibit rapid oscillations in the amplitude and phase spectra for which the expansions (7) and (8) may not be accurate. One might try to include higher derivatives in the Taylor expansions; however one would then have the problem of extracting the values of these derivatives from the experimental data. Even  $a''$  and  $\tau'$  in Eq. (10) may be difficult to evaluate when the signal is noisy. For a practical application of Eq. (10), one has normally to use synthetic or smoothed experimental spectra where higher-order terms in the Taylor expansions are not very significant.

Fortunately, it turns out that the bias correction derived from a smooth spectrum is all we need. Time-windowing a dispersed signal has at the same time a desired and an undesired effect. The desired effect is the elimination of signal components and noise outside the time window; the undesired effect is the phase bias that results from spectral smoothing when the phase spectrum does not have a constant slope (i.e. the group delay is not constant). The two effects are in principle undistinguishable from each other. Only by referring to our a priori knowledge of what a dispersed seismic signal should look like are we able to define which degree of spectral smoothing is appropriate. Removing completely the phase distortion introduced by the frequency-time analysis would defeat the very purpose of this method. In general, the application of a second-order correction formula is probably a good compromise. For a more careful investigation, a scheme incorporating a differential analysis between observed and synthetic wavetrains would permit the a priori definition of the desired smoothness of the spectrum, and then the complete elimination of the systematic error for that spectrum. Remaining differences between the observed and synthetic signals would be considered as random noise whose suppression does not constitute a systematic error. The residual-dispersion method of Dziewonski et al. (1972) can be used in this way, but other methods are conceivable. It does not make much difference whether we first subtract the synthetic phase from the observed one and then analyze the resulting "residual-phase" seismogram, or first analyze the two signals separately and then form the phase difference. The effects of spectral leakage may be somewhat different, but numerical tests indicate that there is no significant difference between the two schemes with respect to their sensitivity to noise.

The systematic error can be studied directly with experimental data when a program for dispersion analysis is available that puts out a complete filtered version of the experimental seismogram. Using the latter as an input signal in the next step, we may pass the same signal through the filter repeatedly, and observe the small changes in amplitude and phase it undergoes every time. This is a very instructive experiment because it provides at the same time information on the magnitude of the systematic error and on the quality of the data (which can be judged from the stability of the error). Moreover, extrapolating backward from the phase after  $n=1, 2, 3, \dots$  passes to  $n=0$ , we obtain an unbiased estimate for the unfiltered signal. The experi-

ment (with seismograms from Wielandt and Knopoff, 1982) confirms what we have discussed above: a synthetic signal provides a valid estimate of the experimental phase bias at frequencies where the signal is good; the scatter in the phase is undesirably enhanced by removing the experimental bias at frequencies where the signal-to-noise ratio is bad.

### Other Systematic Effects

While phase delays measured with plane surface waves on a stratified halfspace can be interpreted directly in terms of the velocity-depth structure, this is not so simple on a sphere. Even in the case of a laterally homogeneous, non-rotating sphere, a correction for the incomplete polar phase shift must be applied to the observed phase delay before the latter can be converted into a phase velocity (Schwab and Kausel, 1976; Wielandt, 1980). The correction depends on the source-receiver geometry and on the radiation pattern of the source, and can amount to 1% of the phase velocity at 400s period. This correction normally has the same sign as that investigated in the present paper, so a substantial bias (in the sense of an apparent negative anomaly of the velocity) can accumulate when both are neglected. Another, although minor correction must be considered for the ellipticity and rotation of the earth (Dahlen, 1976). The purpose of all these corrections is to make phase velocities observed in different regions of the earth and with different methods comparable to each other. Their interpretation in terms of regional elastic properties of the earth is of course another, largely unsolved problem. Nevertheless, it is clear that lateral variations of the phase velocity are very small at periods between 200 and 400s, possibly of the order of 1%. Evidence for such anomalies should not be accepted before the corrections in question have been applied, or demonstrated to be insignificant.

*Acknowledgements.* We wish to thank Michel Cara for some valuable information, Douglas C. Nyman for a copy of his unpublished manuscript on dispersion analysis, and Walter Zürn for a careful double check of our results.

### References

- Aki, K., Richards, P.G.: Quantitative Seismology - Theory and Methods. San Francisco: W.H. Freeman Co. 1980
- Cara, M.: Filtering of dispersed wavetrains. *Geophys. J. R. Astron. Soc.* **33**, 65-80, 1973
- Cara, M.: Etude du manteau supérieur à partir des harmoniques des ondes de surface. Thèse de Doctorat d'Etat, Université de Paris 6, 1978
- Cara, M., Hatzfeld, D.: Vitesse de groupe de l'onde de Rayleigh de part et d'autre de la ligne Açores-Gibraltar. *Ann. Géophys.* **32**, 85-91, 1976
- Dahlen, F.A.: Reply. *J. Geophys. Res.* **81**, 4951-4956, 1976
- Denny, M.D., Chin, R.C.Y.: Gaussian filters for determining group velocities. *Geophys. J. R. Astron. Soc.* **45**, 495-525, 1976
- Dziewonski, A., Mills, J., Bloch, S.: Residual dispersion measurement - a new method of surface-wave analysis. *Bull. Seismol. Soc. Am.* **62**, 129-139, 1972
- Gilbert, F., Dziewonski, A.: An application of normal mode theory to the retrieval of structural parameters and source mechanisms from seismic spectra. *Philos. Trans. R. Soc. A* **278**, 187-269, 1975
- Inston, H.H., Marshall, P.D., Blamey, C.: Optimization of filter bandwidth in spectral analysis of wavetrains. *Geophys. J. R. Astron. Soc.* **23**, 243-250, 1971
- Kodera, K., de Villedary, C., Gendrin, R.: A new method for the numerical analysis of non-stationary signals. *Phys. Earth Planet. Int.* **12**, 142-150, 1976
- Nyman, D.C.: Dispersion analysis and the Gaussian frequency-time filter. Unpublished manuscript, Institute for Geoscience, University of Texas at Dallas, 1977
- Schwab, F., Kausel, E.: Long-period surface wave seismology: Love wave phase velocity and polar phase shift. *Geophys. J. R. Astron. Soc.* **45**, 407-435, 1975
- Souriau-Thevenard, A.: Le manteau supérieur sous la France et les régions limitrophes au nord. Thèse de Doctorat d'Etat, Université de Paris 6, 1978
- Wielandt, E.: First-order asymptotic theory of the polar phase shift of Rayleigh waves. *Pure Appl. Geophys.* **118**, 1214-1227, 1980
- Wielandt, E., Knopoff, L.: Dispersion of very-long-period Rayleigh waves along the East Pacific Rise: Evidence for S-wave velocity anomalies to 450km depth. *J. Geophys. Res.* **87**, 8631-8641, 1982

Received June 2, 1982; Revised version November 12, 1982  
Accepted November 15, 1982

# The Upper Mantle Structure Under South-East Europe Derived from GRF Broadband Records of Greek Earthquakes

H. Rademacher, R.I. Odom\*, and R. Kind

Seismologisches Zentralobservatorium Gräfenberg, Krankenhausstraße 1, 8520 Erlangen, Federal Republic of Germany

**Abstract.** Broadband recordings from the GRF (Gräfenberg) Array of the strongest earthquakes from Greece are examined. A *P*-wave seismogram section of a number of events in the range between 1,300 and 2,100 km epicentral distance is constructed. The dominant feature in this section is the second arrival, which is the reflection from the 400 km discontinuity. Characteristic amplitude changes of this phase across the array are observed. The apparent velocity across the array of the first arriving *P* phase is very slow, indicating a slower upper mantle in SE Europe than in other regions. There is also a very weak indication of a third phase. The resulting model of the upper mantle, which was derived with the aid of theoretical seismograms, shows a pronounced discontinuity at a depth of 400 km. The time difference between the observed first two phases can be used for a fast estimation of the epicentral distance.

**Key words:** Greek earthquakes – Upper mantle structure – Broadband seismograms – Synthetic seismograms

## Introduction

The GRF-Broadband Array in the southeastern part of the Federal Republic of Germany has provided digital seismic recordings since 1976 from the first subarray, and from the complete array of 13 vertical and 6 horizontal Wielandt seismometers since March 1980. See Harjes and Seidl (1978) and Seidl and Kind (1982) for a description of the array and its instrumental and seismological concept. Figure 1 shows the geographical distribution of the 13 seismometer sites. The existing data base of the GRF Array opens new possibilities for investigations of local (Kind, 1979b), regional (Müller et al., 1978; Räckers and Müller, 1982; Stoll, 1980) and teleseismic (Kind and Seidl, 1982; Hanka, 1982; Upadhyay and Duda, 1980) events. The purpose of this paper is to examine the GRF data base of the strongest Greek earthquakes. Greece is the most active seismic area in Europe. The distance from Greece to the GRF Array ranges from about 1,200 to 2,100 km, which is very suitable for studies of the upper mantle. The north-south extension of the array, however is less than 100 km. Therefore the GRF records of one Greek earthquake provide a seismogram section of only a relatively small distance interval.

\* Present address: Department of Geological and Geophysical Sciences Princeton University, Princeton, New Jersey 08540, USA

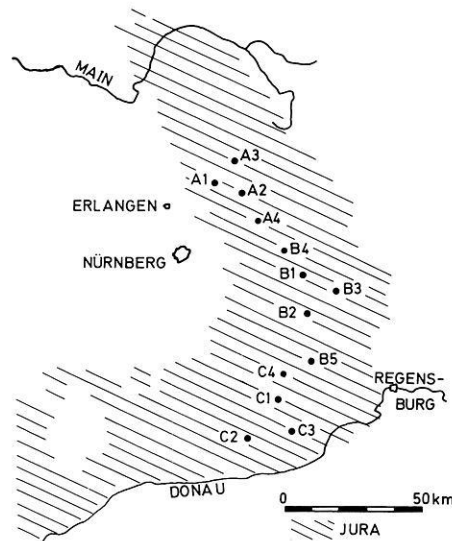


**Fig. 1.** Map of the GRF array stations. All stations have vertical Wielandt seismometers. In addition the stations A1, B1 and C1 have two horizontal instruments. The site of station A1 is also the site of the SRO station GRFO

We have attempted to construct a more extended seismogram section by combining GRF records of different earthquakes into one seismogram section. Such an attempt can only be successful if the localization of the events is good enough and if the earthquakes are similar enough.

## The Data

Besides several other authors McKenzie (1972) investigated the tectonic setting of the eastern Mediterranean region. Following his interpretation the region between  $36^\circ$  and  $43^\circ$  N and between  $18^\circ$  and  $33^\circ$  E is dominated by the Aegean Plate, with plate boundaries to the Eurasian Plate in the North, the African Plate in the South and the West, and the Turkish and the Black-Sea Plate in the East and in the Northeast. The dominant seismically active areas in that region are the Hellenic Arc, the normal-faulting zone on the west coast of Asia Minor, a NE-striking zone crossing the Greek mainland and an extension zone in northern Greece where the Thessaloniki events of June 1978 occurred. The main tectonic features are plotted after McKenzie (1972) in Fig. 2 together with the locations of the earth-

quakes examined in this paper. The basic data of the earthquakes are given in Table 1. In most GRF recordings of Greek earthquakes two onsets are clearly visible during the first 20 s of the seismogram. The signal shape of the second onset shows a clear dependence on the azimuth, while the time difference between the first and the second onset is distance dependent. An example of the azimuth dependence is shown in Fig. 3 in which events 12 and 36 are plotted with the same time scale and with the same configuration of array stations. The traces in Figs. 3 and 4 are time shifted so that a plane wave arriving with a slowness of  $11.5 \text{ s}^\circ$  from an azimuth of  $140^\circ$  would line up. The time marks apply to the bottom trace A3. It can be seen that for event 12, located in the Gulf of Corinth, the signal shape of the second onset (marked P4) changes dramatically south of station B3. For event 36 no such change could be detected. Although event 36 has longer periods than event 12, the observation of the change of the signal shape remains true

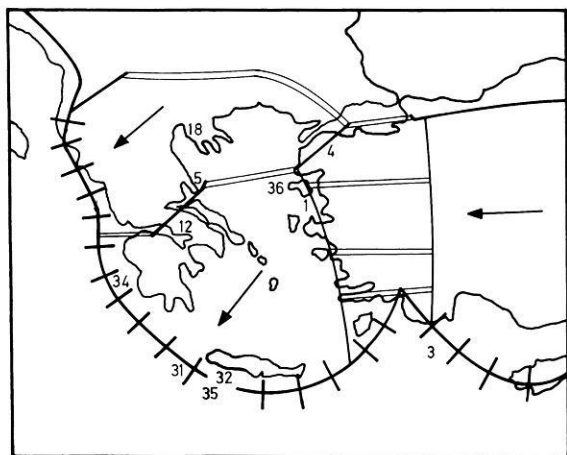


**Fig. 2.** Tectonic map of Greece and western Turkey after McKenzie (1972) with the locations of the earthquakes used in this study. The numbers refer to the event numbers in Table 1

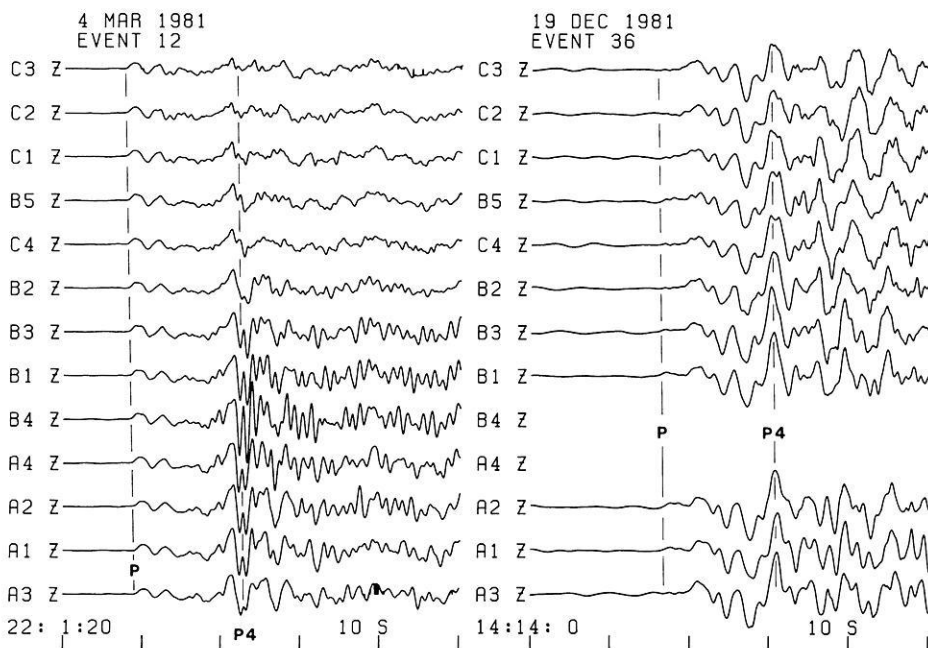


**Fig. 3.** GRF Array broadband records of the events 12 and 36. All traces are shifted according to a slowness of  $11.4 \text{ s}^\circ$  and an azimuth of  $140^\circ$ . The time scale applies to station A3. The phase P4 is strongly distorted in the southern part of the array for event 12, whereas P4 of event 36 is coherent across the whole array. One amplitude scale is used for all seismograms

for other events with a higher frequency content. The epicentral distance for both earthquakes is around 1,600 km. The time difference of 12 s between the onsets of the two phases at station A3 in Fig. 3 is also the same for both earthquakes. Another example is shown in Fig. 4, where the events 35 and 3 are plotted. Earthquake 35 was located south of Crete, which is roughly the same azimuth as for event 12. As in event 12 the signal shape changes abruptly south of station B3. This could not be seen in the seismograms of event 3, which is located off the south coast of Asia Minor. The two phases in Fig. 3 cannot be found in Fig. 4. They have already merged into one signal. This point is discussed in the next section. We have looked at many more events from Greece and found that all records of events following the Hellenic Arc from the border of Albania to the region east of Crete, including the Gulf of Corinth events, have a distinct decay of the amplitudes of the second phase at the southern part of the GRF array. Events from the eastern part of the Aegean Sea and the coast of Asia Minor, however, do not show such a pattern. The reason for this peculiar behaviour of the signal shape remains unknown, it could be focusing or defocusing effects. In most cases, the second phase has strong amplitudes. Only events from western Greece show the described decay in the southern part of the array. Therefore we consider this as an anomaly. It seems likely, however, that lateral inhomogeneities relatively close to the receivers are the cause, rather than inhomogeneities in the source region. It could possibly be connected to the roots of the Alps, because the Alps are the largest tectonic inhomogeneity along the ray path.

### Construction of a Seismogram Section

The examples in Figs. 3 and 4 are not unique. It was observed in the routine data analysis at the GRF observatory, that most events from Greece have a similar strong second onset, and that the time difference between the first two onsets varies. Also the slowness across the array of these

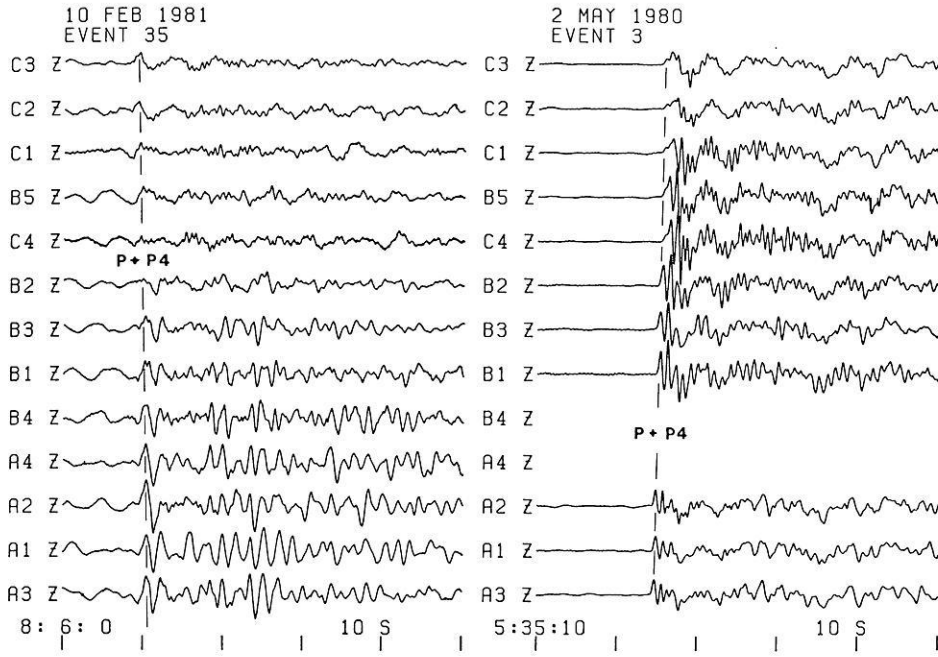


**Fig. 4.** The same as in Fig. 3 for the events 35 and 3. The phases *P* and *P4* have already merged into one phase at these distances. The phase *P+P4* is distorted for event 35 in the southern part of the array and it is relatively coherent for event 3. This is typical for GRF records for events from Greece: The phases *P4* or *P+P4* are strongly distorted in the southern part of the array for events from western and southern Greece. They are more coherent for events from the eastern Aegean Sea and the coast of Asia Minor. The reason for this seems to be lateral inhomogeneities, possibly underneath the Alps

**Table 1.** List of earthquakes used in this study (after PDE)

No.	Date	Origin time			Location		Depth km	Distance to A1 in km	$m_b$
		HH	MM	SS	Deg N	Deg E			
1	06 14 79	11	44	45.9	38.81	26.53	23	1,712	5.8
3	05 02 80	05	30	58.1	36.65	29.80	32	2,168	5.1
4	05 16 80	00	37	29.7	39.96	27.37	65	2,008	5.0
5	07 09 80	02	10	16.5	39.23	22.93	10	1,487	5.1
12	03 04 81	21	58	05.9	38.21	23.29	29	1,597	6.0
18	05 23 78	23	34	11.4	40.76	23.27	33	1,368	5.7
31	09 11 77	23	19	23.7	35.05	23.03	33	1,889	5.8
32	06 15 79	11	34	15.6	34.96	24.24	33	1,950	5.6
34	06 22 82	03	04	28.8	37.18	21.19	30	1,603	5.0
35	02 10 81	08	01	59.6	34.38	23.78	38	1,986	4.6
36	12 19 81	14	10	50.7	39.24	25.23	10	1,603	6.2

two phases is different. Therefore it seemed promising to assemble a number of records from different earthquakes into one figure. As we discussed in the previous section, the signal shape varies across the array for some events, but the amplitude decay is restricted to the southern part of the array. To avoid problems with the amplitudes in the construction of the seismogram section, it seems reasonable to use only recordings from the undisturbed subarray A for the compilation. The required origin times and epicenter locations have been taken from the PDE bulletin (see Table 1). The resulting seismogram section is shown in Fig. 5. Events 35 and 36 have not been included, for aesthetic reasons; other earthquakes used in this study have the same distances. The long-period signal in front of the first onset of event 5 is due to surface waves of another earthquake. Nevertheless this event was used, because it is the only earthquake at that distance. The maximum amplitude of each event is normalized to the same size. The slownesses, averaged over many events, of the two first arrivals across the array are 13.6 and 11.5 s/°, respectively (corresponding to 8.1 and 9.6 km/s). One should expect,

that the two phases in Fig. 5 should, at least approximately, line up along these apparent velocities. However this obviously does not occur in Fig. 5. There are at least three reasons for the deviations: insufficient accuracy in the determination of the epicenters, errors in the source time, and errors in the source depth. Differences in the source depths of the events have not been taken into account in the construction of Fig. 5, since most events are shallow. The possible errors are of course not independent from one another. No decision could be made, as to which of them is dominant, because there is no dense network of local stations in the epicentral region. Most seismologists would probably think, that the errors in source time and source depths have the strongest influence. We have tried to rearrange the seismogram section in Fig. 5 in order to line up the phases along travel time curves with the measured array velocities. Event 1 was used as our master event, because origin time and epicenter determination by PDE and ISC agreed very well. Also the determined source depths vary only within a few kilometers in both bulletins. In a first attempt to rearrange the seismograms in Fig. 5, we kept event 1 fixed,

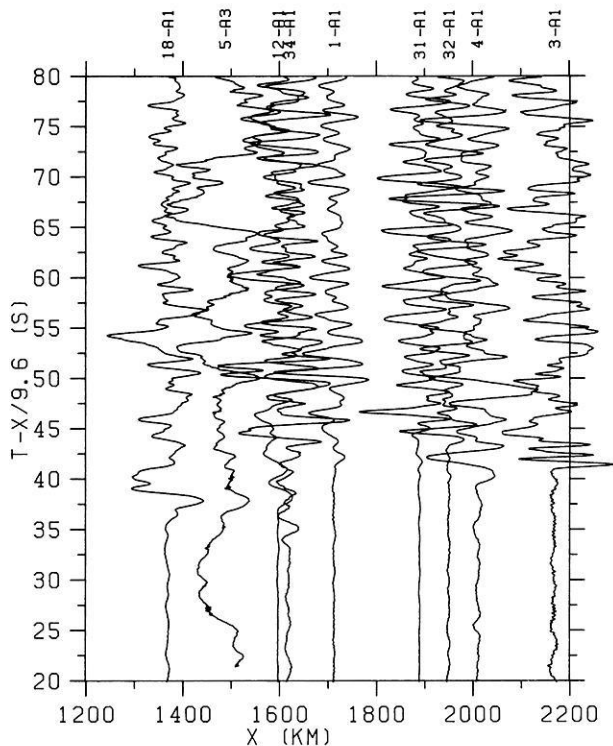


**Fig. 5.** Seismogram section of the vertical components of GRF broadband records from nine Greek earthquakes. The numbers on the upper border refer to Table 1. Compression is in the direction of increasing distance. The signs of the events 4 and 34 are reversed. Origin times and epicenters are taken from the PDE bulletin. The onsets of the first two phases do not line up at all

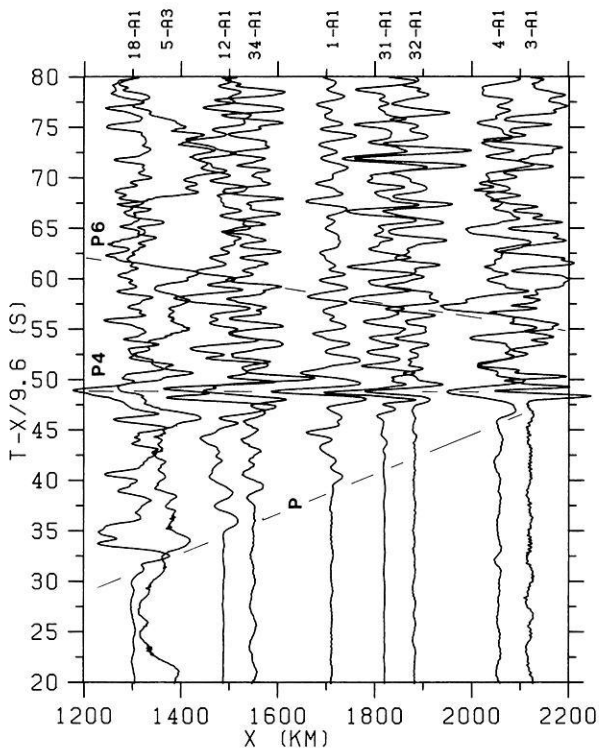


**Fig. 6.** A reconstruction of the seismogram section of Fig. 5, where the phases *P* and *P4* line up along straight lines with velocities of 8.1 and 9.6 km/s, respectively

kept the distances of all other events fixed too, and lined up the *P*-wave arrivals along a velocity of 8.1 km/s. As a result of that shift, the second phase lined up approximately along a straight line with a velocity of 9.5 km/s. The resulting time shifts reached up to 10 s. In a second attempt we kept event 1 fixed again and lined up the first two phases along the velocities of 8.1 and 9.6 km/s respectively, allowing the time and distance to vary. As a result, the two phases line up exactly along the two velocities, but we had to shift the distances up to 90 km (event 12) and the times up to 5 s. The corrections applied in both cases seemed surprisingly large, but it is not the purpose of this paper to discuss the accuracy of the hypocentral data. The corrected seismogram sections obtained with both methods are very similar. Therefore we think that the existing uncertainties do not significantly effect the inversion of the data. The seismogram section corrected with the second method is shown in Fig. 6. The first two phases are marked *P* and *P4*. There is a weak indication of a third phase (marked *P6*) in Fig. 6, which will be discussed later. Although we reversed the sign of events 4 and 34 the general similarity of the different events in Fig. 6 seems surprising if one keeps in mind that essential source parameters are different for the individual events and that they originate in different tectonic settings.

Although our rearrangement seems somewhat unconventional, Fig. 6 shows a clear improvement compared with Fig. 5. A conclusion from that is, that the time difference of the first two onsets of Greek events can be used for a rough estimation of the epicentral distance, similar perhaps to the use of *S* minus *P* times for local events. Of course the azimuth cannot be determined this way. However the pattern of the signal shape across the array (discussed in the previous section) may indicate whether the event occurred in the eastern or western part of Greece. Therefore a preliminary determination of the region within Greece, where an earthquake originates, seems to be possible, using GRF data only. This may have advantages for a fast estimation of the epicenter. The seismogram section in Fig. 6 also provides the basis for the investigation of the structure of the upper mantle underneath southeastern Europe.

### Interpretation of the Upper Mantle Phases

In many papers dealing with the structure of the upper mantle the existence of a strong discontinuity at a depth of about 400 km has been shown. Reflections from that boundary should lead to a more or less clear change in the slope of the travel time curve at approximately 20°. Hales (1972) gives an overview of several models derived for the USA. He showed models without any jump in the velocity-depth curve around 400 km. On the other hand he reviewed models with rather sharp discontinuities. King and Calcagnile (1976) investigated Soviet nuclear explosions with NORSAR data. In their model KCA they derived a discontinuity in a depth of 420 km with a jump in the *P*-wave velocity from 8.66 km/s to 9.27 km/s. England et al. (1977) looked at seismograms from earthquakes in SE-Europe recorded at NORSAR and Eskdalemuir. They found only a slight increase at 480 km depth. Mayer-Rosa and Mueller (1973) derived a model for the upper mantle under Europe, using body and surface waves. In their investigation they found a gradient zone only, between

310 km (8.8 km/s) and 540 km (9.5 km/s). On the other hand Baer (1979) found a very steep gradient between 405 km (8.82 km/s) and 420 km (9.55 km/s) in his investigation of earthquakes in SE-Europe with recordings of the Swiss Earthquake Service. Burdick and Helmberger (1978) derived an upper mantle model for the Western United States basically from long-period earthquake records. Their model has two first order discontinuities at 400 and 670 km depth. They used amplitude and signal shape information in their investigation. In more recent studies Given and Helmberger (1980) have re-examined the upper mantle structure underneath NW-Eurasia by means of WWSSN recordings of Soviet nuclear explosions. In contrast to KCA they found a low velocity zone between 150 and 200 km in their model K8. On the other hand the velocity jump at 420 km was not as strong as in KCA. Burdick (1981) derived two models, one for a stable continent (S8), for which he used WWSSN recordings at stations in the eastern USA of events in California, Idaho and on Bermuda. In his other model (T9) he used two Greek earthquakes of 1967 and recordings from WWSSN stations in Europe. Both models show a velocity jump at around 400 km. T9 has a low velocity channel, S8 has no such structure.

With the method described by Kind (1978; 1979a) theoretical seismograms have been computed for several models of the upper mantle. The following parameters have been set for the computation of the theoretical seismograms for all models: The source depth was set equal to zero, in order to avoid problems with depth phases like  $pP$ . The earthquakes in Fig. 6 have different source depths, which makes the recognition of  $pP$  difficult. The same applies for the source orientations, they are also different for each event. We have assumed a strike slip dislocation source (strike NW-SE) for all computations. This source orientation is similar to the orientation of the source of event 36, according to the PDE. A ramp function with sine smoothed corners (see Kind, 1978 for details) was chosen as the displacement source time function. This ramp seems to be sufficient for our purpose, since we do not intend to study the signal shape in detail.

There are essentially two phases visible in Fig. 6, which are labelled  $P$  and  $P4$ .  $P$  is certainly the direct  $P$  wave.  $P4$  is reflected energy from the 400 km discontinuity. This phase is the dominant feature in the observed data. This indicates, that the 400 km discontinuity must also dominate the model. The very weak indication of a third phase (marked  $P6$ ) could be – at first sight – interpreted as energy coming from a discontinuity below 400 km. In many other models of the upper mantle (i.e. KCA, K8, T9, and S9) a second velocity jump is assumed between 600 and 700 km. Trying to fit a travel time curve to  $P6$ , we had to lift that discontinuity to 560 km. To get enough energy back to distances of 1,500 km or less, the velocity jump has to be around 10% (from 8.9 to 9.8 km/s). The signal of a reflection from that discontinuity dominates the synthetics at distances of more than  $20^\circ$ , but there are no data available at GRF from that distance range and at southeastern azimuths. Because we think that the evidence in our data for a reflection from a second velocity jump in the lower part of the upper mantle is too weak, we will concentrate our modelling to depths not deeper than 400 km.

The comparison between observed and theoretical seismograms will not be done on a quantitative base. We will only compare relative amplitudes of different phases in one

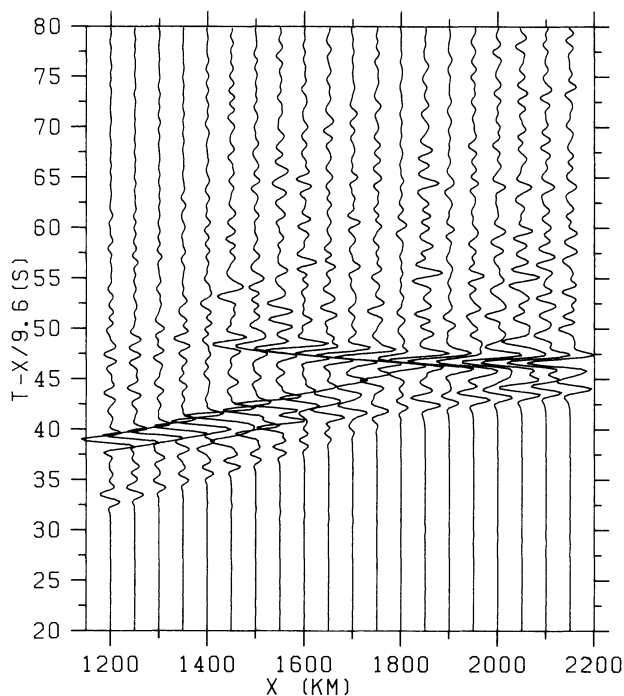
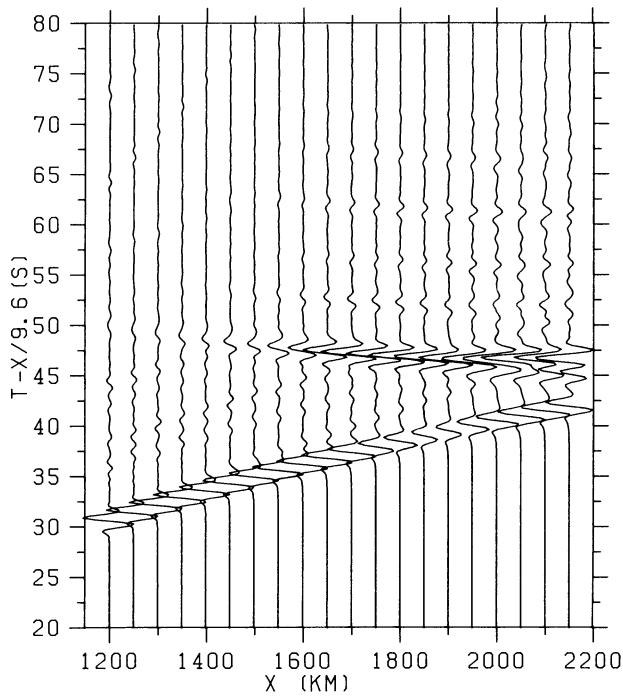


Fig. 7. Theoretical seismograms for the model of Baer (1979). The model produces too much energy between the phases  $P$  and  $P4$  at short distances. This is probably due to too many discontinuities above 400 km

seismogram qualitatively. This is common practice in explosion seismology, and we will adopt this technique. Each seismogram in the observed and computed sections is normalized to its maximum, so we are compensating for the different magnitudes of the recorded seismograms.

Figure 7 shows a seismogram section with synthetics computed with the model of Baer (1979). A comparison with Fig. 6 shows that this model does not fit our data well. In particular there is too much energy between  $P$  and  $P4$  at small distances. This is probably due to reflections from the many sharp discontinuities above 400 km in Baer's model. The absence of clear phases between  $P$  and  $P4$  in Fig. 6 indicates that the upper mantle in the investigated region has only smooth gradients above the 400 km discontinuity. Synthetics computed for KCA are shown in Fig. 8. This model, which is much simpler than the model of Baer, shows some similarity with our data, although their data came from another tectonic region. Synthetics computed with the model T9 from Burdick (1981) are shown in Fig. 9. As in KCA there is much more similarity with our data in this section than for Baer's model, but there are also some features, that cannot be seen in the data. In contrast to Fig. 6 the direct  $P$ -wave is dominating the section. The velocity of that phase is somewhat higher than in our data, but the slowness of the second phase is nearly the same. Also the two phases at about 60 s reduced travel time cannot be detected in our data. The best agreement with our data can be achieved with the model ROK shown in Fig. 10. The models KCA and T9 are also included in that figure. The velocity-depth data of ROK are listed in Table 2. The theoretical seismograms for this model are shown in Fig. 11. A qualitative comparison between the observed section in Fig. 6 and the computed section in Fig. 11 reveals



**Fig. 8.** Theoretical seismograms for the model KCA of King and Calcagnile (1976). This theoretical section is already fairly similar to the observed section in Fig. 6

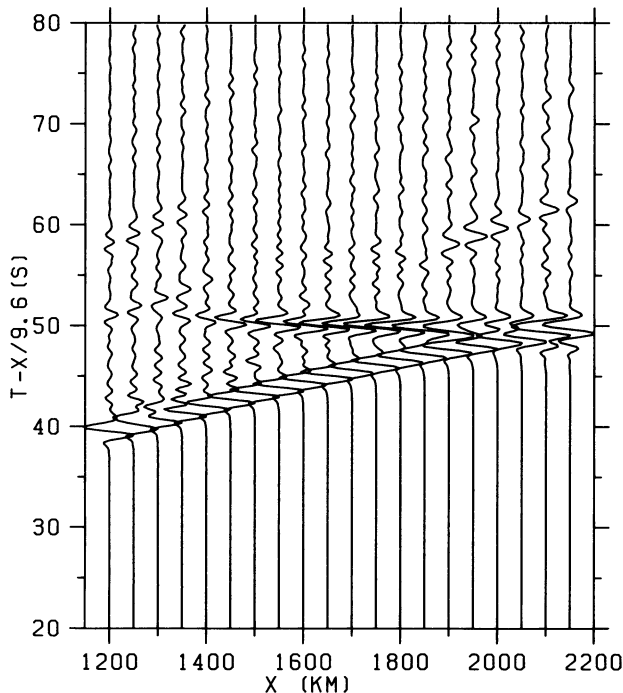


**Fig. 9.** Theoretical seismograms for the model T9 of Burdick (1981). There is a good similarity between the slowness of the second phase in the synthetics and in the observed data set, but the time difference between the first two phases is clearly too small

a large amount of similarity. The phase *P4* dominates in both sections, *P* is clearly smaller than *P4*.

When comparing the models KCA, T9 and ROK, one can see that only ROK brings enough energy for the second

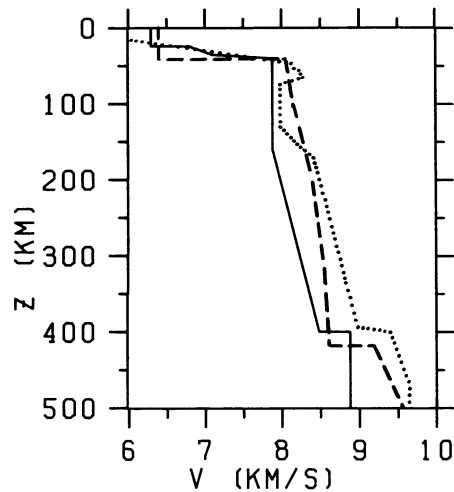


**Fig. 10.** Different velocity-depth functions for upper mantle models. The model ROK (solid line) is derived in this paper. KCA is the dashed line. The model T9 is represented by the dotted line

**Table 2.** List of the velocity-depth model ROK derived in this paper

Depth (km)	<i>P</i> -Velocity (km/s)
0	6.3
24	6.3
24	6.8
35	7.1
40	7.9
160	7.9
400	8.5
400	8.9

phase to small distances. KCA is the fastest model; it has the largest apparent velocities for both phases. Because KCA was derived from data collected in an old shield region, that result can be expected. The slowness of the phase *P4* agrees very well in T9 and in ROK. There is however a big difference in the direct waves of T9 and ROK. The velocity of that phase in T9 is much higher than in our data, but the arrival time is later than observed. The second phenomenon is due to the low velocity channel in T9. We do not find any hint of such a channel in our data because the multiple reflections from that channel, which can be seen in Fig. 9 at about 60 s reduced travel time, do not occur in Fig. 6. The difference in the slowness of the *P* phase, however, has to remain unexplained for the moment. Further studies of earthquakes at smaller distances have to be carried out in future to solve that problem, but the GRF data base for that region is still too small in the moment. It should be mentioned that the absolute travel times of the observed data in Fig. 6 and the theoretical data in Fig. 11 (model ROK) do not agree exactly. This follows from the problems mentioned earlier with the accuracy of the hypocentral data, and it does not influence the results of this paper significantly.

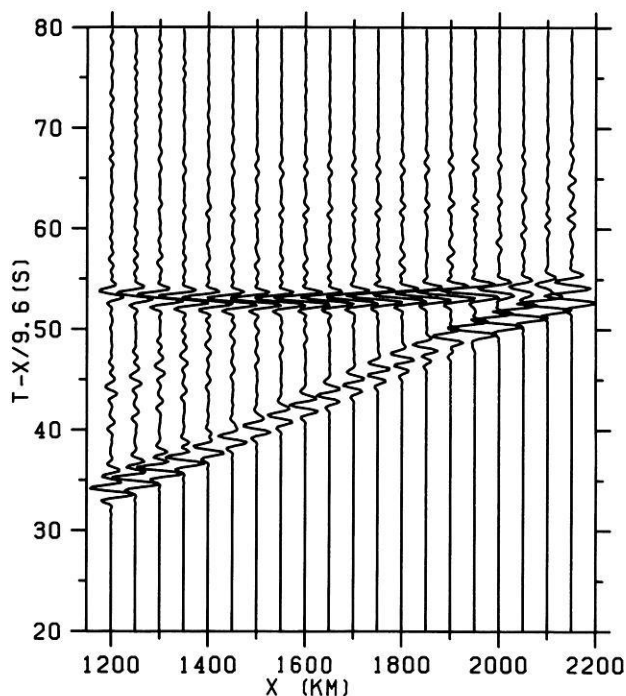


Fig. 11. Theoretical seismograms for the upper mantle model derived in this paper. The most essential features in this figure agree qualitatively well with the data in Fig. 6

## Conclusions

We have attempted to develop a method for upper mantle studies, which utilizes GRF array observations of a number of earthquakes from Greece and assembles them into one record section. The main sources of errors of the method are the errors of the localization of the hypocenters and of the origin times. We have attempted to improve the localizations and source times of the events, but a more detailed study of this problem is required, preferably using local Greek data. We have observed reflections from one upper mantle discontinuity in our data. With the aid of theoretical seismograms, we derived an upper mantle model which explains the main features of the data very well. The localization errors of the events influence the depths of the discontinuities only. The velocities are not influenced by these errors, because they follow from apparent velocities, measured for many events across the array. Inhomogeneities close to the array, which influence these apparent velocities, have been noticed, but they are believed to be small in the northern part of the array. A comparison of our upper mantle model with a model for a stable platform region (King and Calcagnile, 1976) reveals that the model underneath the younger tectonic area of south-eastern Europe is considerably slower in general.

*Acknowledgements.* This research was supported by the Deutsche Forschungsgemeinschaft. One of the authors (R.I.O) would like to acknowledge the support of the Alexander-von-Humboldt foundation.

## References

- Baer, M.T.: Kalibrierung des neuen Stationsnetzes des Schweizerischen Erdbebendienstes im Hinblick auf die Verbesserung der Lokalisierung seismischer Ereignisse mit Epizentralentfernungen bis 100 Grad. Ph.D.-Thesis, ETH Zürich, 1979
- Burdick, L.J.: A comparison of the upper mantle structure beneath north America and Europe. *J. Geophys. Res.* **86**, 5926–5936, 1981
- Burdick, L.J., Helmberger, D.V.: The upper mantle P velocity structure of the Western United States. *J. Geophys. Res.* **83**, 1699–1712, 1978
- England, P.C., Worthington, M.H., King, D.W.: Lateral variation in the structure of the upper mantle beneath Eurasia. *Geophys. J. R. Astron. Soc.* **48**, 71–79, 1977
- Given, J.W. and Helmberger, D.V.: Upper mantle of Northwestern Eurasia. *J. Geophys. Res.* **85**, 7183–7194, 1980
- Hales, A.L.: The travel times of P waves and their relevance to the upper mantle velocity distribution. *Tectonophysics* **13**, 447–482, 1972
- Hanka, W.: Analysis of broad-band Rayleigh waves: a possibility for seismic discrimination. *J. Geophys.* **51**, 165–179, 1982
- Harjes, H.-P., Seidl, D.: Digital recording and analysis of broadband seismic data of the Graefenberg (GRF) Array. *J. Geophys.* **44**, 511–523, 1978
- Kind, R.: The reflectivity method for a buried source. *J. Geophys.* **44**, 603–612, 1978
- Kind, R.: Extensions of the reflectivity method. *J. Geophys.* **45**, 373–380, 1979a
- Kind, R.: Observations of sPn from Swabian Alb earthquakes at the GRF Array. *J. Geophys.* **45**, 337–340, 1979b
- Kind, R., Seidl, D.: Analysis of broadband seismograms from the Chile-Peru Area. *Bull. Seismol. Soc. Am.* **72**, 2131–2146, 1982
- King, D.W., Calcagnile, G.: P-wave velocities in the upper mantle beneath Fennoscandia and Western Russia. *Geophys. J. R. Astron. Soc.* **46**, 407–432, 1976
- Mayer-Rosa, D., Mueller, St.: The gross velocity-depth distribution of P- and S-waves in the upper mantle of Europe from earthquake observations. *Z. Geophys.* **39**, 395–410, 1973
- McKenzie, D.: Active tectonics of the Mediterranean Region. *Geophys. J. R. Astron. Soc.* **30**, 109–185, 1972
- Müller, G., Bonjer, K.-P., Stöckl, D., Enescu, D.: The Romanian earthquake of March 4, 1977. I. Rupture process inferred from fault-plane solution and multiple-event analysis. *J. Geophys.* **44**, 203–218, 1978
- Räkers, E., Müller, G.: The Romanian earthquake of March 4, 1977. III. Improved focal model and moment determination. *J. Geophys.* **50**, 143–150, 1982
- Seidl, D., Kind, R.: Das instrumentelle und seismologische Konzept des Graefenburg-Array. *Geol. Jahrb.* *E23*, 207–220, 1982
- Stoll, D.: Determination of focal parameters of five 1976 Friuli earthquakes from Rayleigh wave spectra. *Boll. Geofis. Teor. Appl.* **22**(85), 3–12, 1980
- Upadhyay, S.K., Duda, S.J.: Source parameters of earthquakes from the Himalayan Region. *J. Geophys.* **48**, 67–79, 1980

Received September 2, 1982; Revised version November 10, 1982  
Accepted November 11, 1982

# Seismic Velocities of Granulites from the Seiland Petrographic Province, N. Norway: Implications for Scandinavian Lower Continental Crust

P.N. Chroston and C.J. Evans

School of Environmental Sciences, University of East Anglia, Norwich, Norfolk, U.K.

**Abstract.** Compressional and shear wave velocities have been measured in the laboratory at up to 1.0 GPa effective pressure on a suite of granulite facies rocks from the Seiland Petrographic Province. The suite may be of Precambrian age and the measurements were made to test a proposal that the suite represents lower continental crust. Compressional wave velocities at 0.4 GPa effective pressure range from 6.41–6.97 km s<sup>-1</sup> with a mean of 6.71 km s<sup>-1</sup>. Measurements of the parameter  $\frac{\partial V}{\partial T_p}$  suggest a value of  $-0.8 \times 10^{-3}$  km s<sup>-1</sup> °C<sup>-1</sup>, and the temperature corrected mean velocity of about 6.5 km s<sup>-1</sup> at 20 km depth is comparable to that found in parts of the lower crust in Scandinavia. The mean Poisson's ratio of 0.29 at 0.4 GPa is slightly higher than that found (0.276), but could be reduced if heterogeneity in the suite and the effect of higher pressures are taken into account. The occurrence of lower continental crust as a thrust slice in the Province is consistent with current ideas on the geological evolution of this area.

**Key words:** Norway – Seiland – Laboratory measurements – Seismic velocities – Granulites – Lower continental crust

## Introduction

Broad constraints for the interpretation of the lower continental crust have been provided by general geological considerations, and by experimental studies on the petrology and physical properties of rocks. It is recognized, for example, that the average compressional wave velocity through the lower crust lies mainly in the range 6.5–7.5 km s<sup>-1</sup> (Christensen and Fountain, 1975), and that it is likely to be composed of granulites with lesser amounts of igneous rocks ranging in composition from granite (charnockite) to gabbro (pyroxene granulite) (Smithson, 1978). Further, the variability of seismic velocities in refraction studies and the results from deep reflection sounding experiments indicate a heterogeneous lower crustal structure (Smithson et al., 1980).

These constraints have been used by a number of workers in an attempt to interpret suites of exposed rock as lower crust, or even as complete crustal sections. In Britain, for example, Hall and Haddad (1976) and Hall and Simmons (1979) have compared the seismic velocities of the high grade Lewisian gneisses of the N.W. Highlands

with the velocities of the lower crustal layer revealed on the LISPB (Bamford et al., 1978) and NASP seismic profiles (Smith and Bott, 1975). Evans (1980) has also compared the properties of the Ox Mountain granulites with the lower crustal velocities of the Midland Valley (Assumpcao and Bamford, 1978). In the Alps, a section across the Ivrea zone has been proposed as a section through the crust (Fountain, 1976), and the seismic velocity structure based on laboratory measurements compared favourably with that obtained from seismic experiments (Choudhury et al., 1971).

In Scandinavia, granulite facies terrains are found both in the Fennoscandian shield and in the Caledonides. The high-grade gneisses of Lofoten-Vesteralen (see e.g. Griffin et al., 1978) are an example of the former, whilst the latter include the granulites of the Jotun nappe (Strand, 1972) and of the Seiland Petrographic Province (Hooper, 1971). So far, however, there has been no systematic study of the physical properties, particularly seismic velocities, of these or other granulite terrains in Scandinavia to enable a comparison with lower crustal properties. In this paper, we describe the results of measurements of the seismic velocities of granulites from the Seiland Petrographic Province, and discuss their implications in the light of a proposal that part of the Province may represent lower continental crust of Precambrian age.

## The Seiland Petrographic Province

In order to compare a surface suite of rocks with the deep crust a number of geological constraints have to be satisfied. These include the appropriate metamorphic grade for a deep crustal level, a comparable stratigraphic age, and an adequate explanation for their present (surface) disposition.

The Seiland Petrographic Province (Barth, 1953) shows a complex history of deformation, metamorphism, and igneous intrusive activity. The Province covers the islands of Stjernøy, Seiland, and Sørøy, and much of the Loppen District (Fig. 1), and is believed to be entirely contained within the Kalak nappe complex (Sturt and Roberts, 1978) in the north Norwegian Caledonides. The nappe tectonically overlies the autochthonous Precambrian rocks of the Fennoscandian Shield, which are exposed in tectonic windows in the Caledonides to the south-east of the area. Metasediments (psammites, pelites, marbles and garnet bearing gneisses) of Lower Palaeozoic age (Holland and Sturt, 1970) occur mainly in the west of the Province and

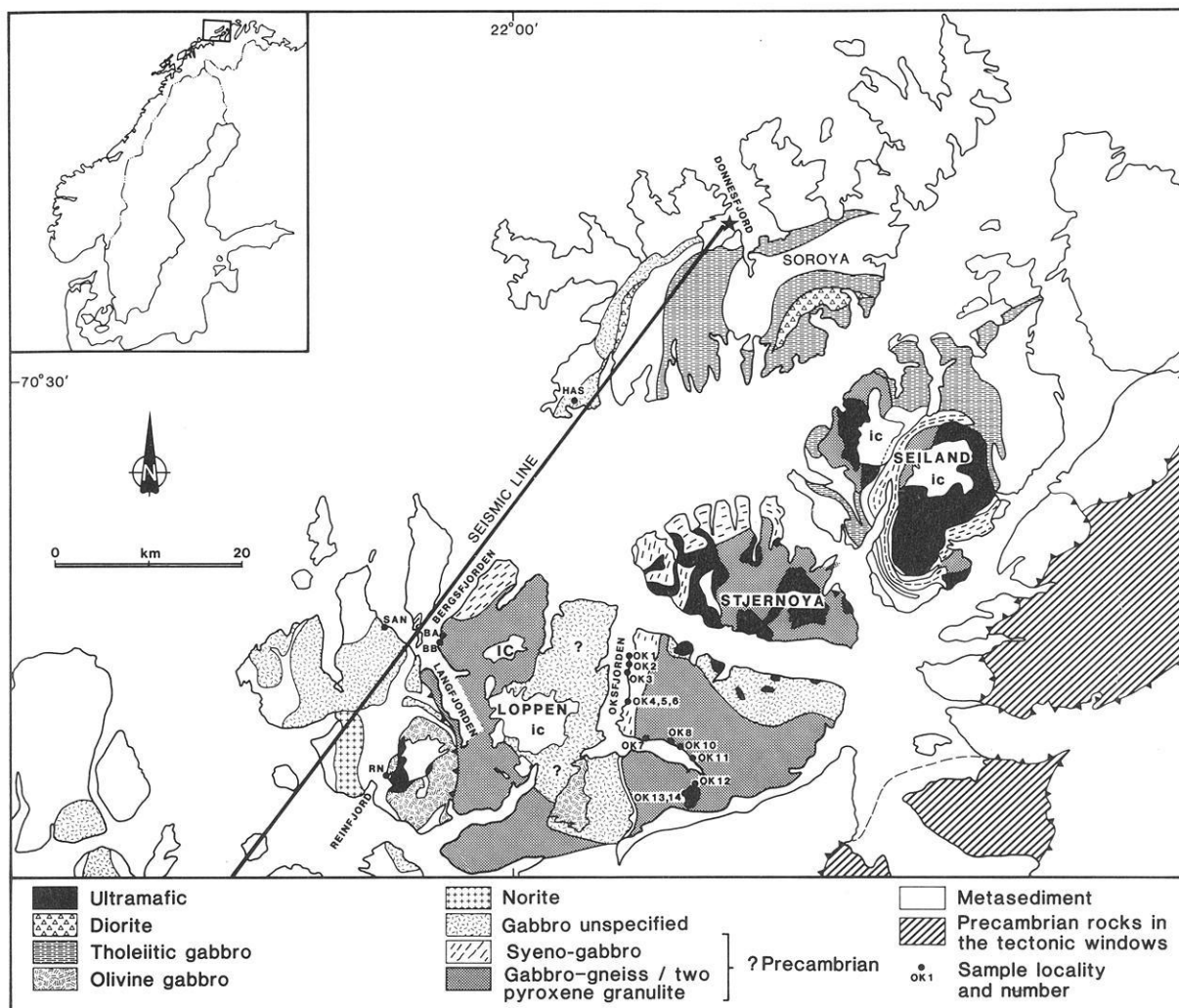


Fig. 1. General geology of the Seiland Petrographic Province, N. Norway, with sampling sites and location of the seismic line

on Sørøy, and in the rest of the area as minor intercalations. Igneous and meta-igneous rocks, however, dominate the area. Gabbros, anorthosites and peridotites with clear igneous textures are found throughout and on Sørøy, Seiland and Stjernøy they were intruded under amphibolite facies conditions, reaching the peak of the metamorphism at about 530 m.y. ago (Pringle, 1971).

The Palaeozoic age of the bulk of the rocks of the Province clearly precludes them from comparison with deep crustal rocks of the Precambrian Shield. However, the extensive area of mafic rock covering the east side of the Loppen District and Stjernøy displays a suite which was clearly metamorphosed under granulite facies conditions (Oosterom, 1963; Hooper, 1971; Brueckner, 1973). These rocks have not so far been studied in detail but are believed to consist primarily of a gabbro gneiss complex with some syenite gneiss. The gabbro gneiss complex is dominantly an augite-labradorite gabbro granulite but also includes interlayered olivine gabbro, norite, anorthosite gabbro with garnet biotite gneiss, and amphibolite. In addition, the complex includes smaller unfoliated bodies of gabbro syenite, anorthosite, hornblendite and peridotite (Krauskopf, 1954). An important feature of these rocks is that dating of the foliated mafic granulites (Brueckner, 1973) suggests that some of these gneissic rocks may be of Precambrian age

(ca. 1,065 m.y.). Although the results were questioned by Pringle (1975), there is little doubt that at least part of the meta-igneous province may be much older than the Caledonian intrusives, and is more comparable with parts of the Precambrian Shield.

The origin of the Province has been the subject of some controversy. Following the discovery of the positive 100 mgal gravity anomaly associated with it, Brooks (1970) suggested that the rocks of Seiland and Stjernøy represented the top of a mafic-ultramafic culmination under Sørøy and which had been transported by thrusting to the south-east. An alternative suggestion, using the granulite facies metamorphism as evidence, was that the anomaly is essentially due to an upward bulge of the "Conrad" discontinuity, and that the mafic complex may represent lower crust. Many ideas have, however, been based on principles of plate tectonics. Harland and Gayer (1972) suggested that the complex could represent a Caledonian suture, though this was dispelled by Brooks (1971). Ramsay (1973) believed that the vast volumes of mafic and ultramafic rocks indicated an attempt at producing a constructive plate margin and proposed a "stillborn marginal ocean". More conventionally, perhaps, the sedimentation, deformation, metamorphism and igneous intrusions can all be explained as a deep section above an eastward dipping subduction zone

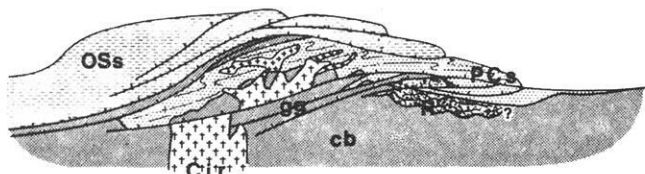


**Fig. 2.** Diagrammatic profile depicting the tectonic structure of the area of the Seiland Province, northern Norway (after Sturt et al., 1978) (OSs: Ordovician-Silurian sediments; PCs: Precambrian sediments; Cir: Caledonian intrusive rocks; cb: crystalline basement; gg: gabbro gneiss)

at an Andean type continental margin (Robins and Gardner, 1974). Thus, although the province is recognized as one of the most distinctive features of the Caledonian geology of northern Norway, its origin is somewhat uncertain.

The high-grade gabbro gneisses of Loppen and Stjernøy are, however, clearly an integral part of the Province. Their present upper crustal position is essentially due to major (late Caledonian) thrusting (see Fig. 2) and they might, therefore, represent an excellent exposure of lower crustal rocks, perhaps typical of at least part of the Fennoscandian Shield. The prime objective of this paper is to compare

**Table 1.** Mineralogy and texture of the samples studied. (Key: PF, plagioclase feldspar; Opx, orthopyroxene; Cpx, clinopyroxene; Amp, amphibole; Bio, biotite; Op, opaques; apat, apatite; qtz, quartz; sph, sphene; ol, olivine; serp, serpentine; tr, trivial; gs, grain size)

Sample No.	PF	Opx	Cpx	Amp	Bio	Op	Other	Texture
<i>Gabbro gneisses (granulites)</i>								
OK1	26		2	68	4		tr, apat	gs 0.5 mm, granoblastic but weak foliation, mortar texture on grain boundaries
OK2	59		24		17			gs 0.25–1 mm, granoblastic but moderate foliation defined by mica
OK3	60		tr	23	16	1		gs 0.5–1 mm, granoblastic but moderate foliation defined by mica and amphibole or feldspar rich bands. Plag shows bent twinning, extensive mortar texture on grain boundaries
OK4	16		26	39	11	8	tr, qtz	gs 0.1–1 mm, rounded porphyroclasts of plag, amp and pyx in fine grained mortar texture. Moderate foliation defined by amphibole. Bent twinning in plag
OK5	63	16	13	1	1	6		gs 0.5–2 mm, granoblastic but partially mylonized to give thin strings of mortar texture. Plag deformed, weak foliation
OK6	30		23	45	1	1		gs 0.5 mm. Virtually undeformed granoblastic rock, some bent twinning in plag
OK7	66	6	11	6	1	10	tr, sph	Relict coarse porphyroclasts of plag, in polygonal granoblastic texture. No foliation.
OK8	42	12	23	11	tr	11	ap. 1	gs 0.1 mm but relict porphyroclasts of pyx up to 2 mm. Strong foliation defined by feldspar and pyx rich bands with granoblastic texture
OK10	33		12	46		9		Intensely mylonized rock. Strong foliation defined by plag lenses in granoblastic amp. rich material (0.2 mm) highly altered, some relict porphyroclasts of cpx (3 mm)
BA2	38	4	28	1	19	10		gs 0.25–1 mm, granoblastic, unfoliated
BB1	43	2	9	24	15	7		gs 0.25–1 mm, granoblastic with weak foliation defined by feldspar and pyx rich bands, trace of mortar texture
BB3	44	3	24	10	15	4		0.25 mm granoblastic aggregate of pyroxene, foliation defined by mica and amp. orientation and by feld. and pyx. rich bands
BB4	50	10	14	13	11	2		gs 0.25 mm, granoblastic aggregate of pyroxene, weak foliation defined by mica and amp. orientation
<i>Gabbros</i>								
HAS4	53	16	25	tr		6		gs 0.5–1 mm, no foliation, igneous texture
SAN1	49	11	30		2	4	Chl 4	gs 0.5–1 mm, igneous texture, some alteration with chlorite veins.
SAN2	52	10	33		2	2	Chl 1	gs 0.5–1 mm, igneous texture, minor alteration
<i>Ultramafics</i>								
RN7	1	32	57			1	Ol 7 Serp 2	Large crystals pyx (1–3 mm) with minor plag (0.1 mm), igneous texture, no foliation
OK12	2	1	67	6		5	Ol 14 sph 5	Large crystal pyx and Ol (2–3 mm), no foliation, igneous texture, little alteration

the seismic properties of this mafic suite with the lower crust of the Shield.

### Selection of Samples

Samples have been collected from both the gabbro gneiss complex, and for comparative purposes, from the Caledonian intrusives (Fig. 1). For the latter, samples were taken from the Hasvik gabbro on Sørøy, from the Sandlands-Middagsfjell gabbro, and from ultramafic intrusions in Øksfjord and Reinfjord (Fig. 1). Within the mafic gneiss complex, nearly all of the samples collected were of gabbro-granulites which dominate the complex. The samples were taken from the pyroxene granulite on the east side of Bergsfjord (Hooper, 1971) from Krauskopf's (1954) "gabbro gneiss I" complex on the east side of Øksfjord (gabbro gneiss in Fig. 1) and from his "gabbro gneiss III" complex (syenite gabbro in Fig. 1). The "gabbro gneiss I complex" is chiefly composed of augite-labradorite gabbro granulite. It is probably comparable with the two-pyroxene granulite found on the east side of Bergsfjord and with similar rocks on Stjernøy, and appears from the geological map (Norges Geologiske Undersøkelse, 1974) to dominate the whole mafic gneiss complex. The "gabbro gneiss III" complex occurs down the east side of Øksfjorden and here, the gabbro gneiss is interlayered with garnet biotite gneiss, amphibolite and pyroxene-plagioclase-hornfels (Krauskopf, 1954). The gabbro gneiss complex is clearly heterogeneous and a full representative collection could not be taken, and the samples selected represent essentially varieties of the dominant pyroxene-granulite lithology. The mineralogy of the samples is shown in Table 1. All of the samples from the gabbro-gneiss complex show a primary granulite-facies mineralogy and granoblastic texture, and most show varying degrees of retrogressive metamorphism. Sample OK-5, for example, shows small amounts of amphibole and sample OK-1 is now effectively an amphibolite, with no primary pyroxene present. In addition most samples show signs of secondary deformation, with deformed plagioclase and some cataclasis, perhaps due to its uplift end emplacement during the evolution of the Seiland Province.

### Method

Cores of 25 mm diameter were taken from the samples and were cut with smooth perpendicular ends to a length of approximately 25 mm. Two cores were taken from most rocks, one parallel to the foliation and one perpendicular to it. In some cases, a 25 mm core was redrilled to give a 16 mm diameter core at right angles to the larger core. Compressional and shear wave velocities were measured at the University of East Anglia (UEA) and the University of Washington (UW) using a pulse transmission method similar to that of Birch (1960). At the University of East Anglia, lithium niobate compressional and shear wave transducers were used, operating at a frequency of 1 MHz. The latter transducers give a good shear wave arrival with a smaller compressional wave forerunner. Transit times were measured using a Hewlett-Packard timer-counter (linked to an oscilloscope) and after corrections for sample compressibility and transducer delay compressional wave velocities could be measured to an absolute accuracy of better than 2% and shear wave velocities to better than

5%. Plexol oil was used for the confining pressure medium and a maximum pressure of 0.4 GPa could be attained. All the samples were saturated in 0.5 M NaCl solution and pore water pressure equal to atmospheric pressure was used throughout. Measurements at the University of Washington used a similar system, but separate measurements of compressional and shear wave velocities were made using PZT-5 transducers for the compressional wave measurements and AC-cut quartz transducers for the shear wave measurements. The samples were screened in copper mesh to allow any pore fluid under pressure to escape. Both compressional and shear wave velocities could be measured to an accuracy of 2%.

On the UEA system, velocities were measured with increasing confining pressure at intervals of 0.025 GPa up to the maximum confining pressure (0.4 GPa) and then with decreasing pressure to (virtually) atmospheric pressure. On the UW system, velocities were measured at 0.02 GPa intervals at up to 0.1 GPa and then at 0.1 GPa intervals up to 1 GPa confining pressure. There was nearly always close agreement ( $\pm 0.05 \text{ km s}^{-1}$ ) between velocities on the increasing and decreasing part of the cycle at pressures above 0.2 GPa.

### Seismic Velocities Across the Mafic Complex and Comparison with Lower Crustal Velocities

The potentially complex nature of the lower continental crust (Smithson, 1978) makes the seismic velocity of a particular rock type of only limited value, and in order to make a meaningful comparison with the field seismic velocities, an effective mean velocity for the complex needs to be calculated. This mean velocity can be calculated from in situ velocity measurements or from estimating the proportions of the different rock types involved and whose individual velocities are known from laboratory measurements.

There are, however, difficulties with the former method. In particular, short seismic lines (a few hundred metres long) on complexes at or near the surface may give low velocities because the low confining pressures may leave cracks open, although Smithson and Shrive (1975) found a good comparison between laboratory velocities and those measured from seismic lines some 1,150 m long. Ideally, much longer lines are required to acquire velocities from rocks at greater depth where the influence of cracks on the seismic velocities is small. In 1972, a simple seismic refraction line some 200 km long was made across the western part of the Province to investigate the upper crustal structure of this area. Shots were fired from Donnesfjord (on the northern side of Sørøy) and from Lyngenfjord, about 100 km to the south-west of the Province (Chroston et al., 1976). The shots from Donnesfjord were also recorded on the east and south-east side of the mafic complexes of Stjernøy and Seiland. However, interpretation of the arrivals appeared to show no increased velocity through these areas compared to the velocity of the metasediments ( $6.18 \text{ km s}^{-1}$ ). Such a result is consistent with the interpretation (Brooks, 1970; Chroston, 1974) that the mafic rock extends only to shallow depth, being truncated by the major thrust which outcrops to the south-east. The analysis in this paper therefore is based only on the laboratory measured velocities.

The results of the laboratory measurements are shown

in Table 2 and Table 3 summarizes the velocities and elastic properties at a confining pressure of 0.4 GPa and 1.0 GPa. The “gabbro-gneisses” show a wide range of velocities at 0.4 GPa, from 6.41–6.97 km s<sup>-1</sup> (mean 6.71 km s<sup>-1</sup>), and with Poisson’s ratios from 0.24 to 0.33 (mean 0.29). Some of the samples are significantly anisotropic. The sample OK-1, for example, shows a difference between the two cores of 0.43 km s<sup>-1</sup> at 0.4 GPa. This can, however, be entirely explained by the difference in density between the cores. Anisotropy in other samples is not so strong, but in some cases is slightly greater than differences due to possible measurement error, and the velocities from field seismic experiments over this rock suite could vary significantly with propagation direction.

The few gabbros measured also give a wide range of velocities 6.56–7.22 km s<sup>-1</sup>. Shear wave velocities could only be measured on samples from the Sandlands-Middagsfjell gabbro. The high Poisson’s ratios (ca. 0.30) are consistent with other workers’ measurements on gabbroic rock (e.g. Birch, 1961). As might be expected, ultramafic rocks give the highest velocities (up to 7.96 km s<sup>-1</sup>) and

the mean of these samples would be expected to be higher for fresh samples.

The data show that in nearly all cases the increase in compressional and shear wave velocities is less than 0.1 km s<sup>-1</sup> between 0.4 GPa and 1.0 GPa, and that the change in Poisson’s ratio is not more than 0.02. This increase in velocity due to pressure is likely to be counteracted by temperature effects. Temperature effects on compressional wave velocities have been measured by a number of workers (Hughes and Maurette, 1957; Kroenke et al., 1978; Stewart and Peselnick, 1977; Kern, 1978) and a study of their results shows a considerable divergence of the parameter  $\left(\frac{\partial V_p}{\partial T_p}\right)$ .

A systematic study by Christensen (1979) suggested a value of about  $-0.59 \times 10^{-3}$  km s<sup>-1</sup> °C<sup>-1</sup>. We have also measured the effect on some of the Seiland Province rocks, and the results are shown in Fig. 2. The confining pressure was held at 0.4 GPa and the temperature increased (over a period of 12 h) to 250° C and then reduced, with velocity measurements made at 25° C intervals. Only the decreasing part of the thermal cycle is shown in the diagram as transient

**Table 2.** Compressional and shear wave velocities (km s<sup>-1</sup>), corrected for dimension changes

Sample	Core	Propo- gation*	Bulk Density ( $\times 10^3 \text{ kg m}^{-3}$ )	0.04 GPa		0.1 GPa		0.2 GPa		0.4 GPa		0.6 GPa		0.8 GPa		1.0 GPa	
				$V_p$	$V_s$	$V_p$	$V_s$	$V_p$	$V_s$	$V_p$	$V_s$	$V_p$	$V_s$	$V_p$	$V_s$	$V_p$	$V_s$
<i>Gabbro gneisses</i>																	
OK1	1	X	3.01	6.05	—	6.36	—	6.60	—	6.75	—	—	—	—	—	—	—
	2	Z	2.87	6.01	—	6.07	—	6.16	—	6.32	—	—	—	—	—	—	—
OK2	1	X	3.05	6.39	3.60	6.52	3.67	6.61	3.72	6.68	3.75	6.71	3.77	6.74	3.79	6.74	3.79
	2	Z	3.08	6.27	3.33	6.36	3.42	6.44	3.48	6.52	3.54	6.54	3.58	6.56	3.61	6.56	3.62
OK3	1	X	2.88	6.21	3.12	6.34	3.21	6.45	3.28	6.60	3.45	—	—	—	—	—	—
OK4	1	X	2.95	6.56	3.39	6.64	3.47	6.74	3.55	6.82	3.65	6.85	3.70	6.90	3.73	6.90	3.74
OK5	1	Z	3.01	6.37	3.41	6.54	3.53	6.62	3.55	6.68	3.63	6.71	3.74	6.74	3.89	6.73	3.93
	2	X	2.80	6.25	3.37	6.33	3.45	6.38	3.52	6.34	3.55	6.47	3.60	6.50	3.62	6.41	3.62
OK6	1	X	3.03	6.69	3.62	6.80	3.75	6.89	3.84	6.97	3.92	7.01	3.98	7.03	4.01	7.04	4.01
OK7	1	Z	2.99	6.70	3.43	6.79	3.49	6.87	3.54	6.91	3.59	6.93	3.61	6.93	3.62	6.94	3.64
	2	X	2.91	6.75	3.55	6.82	3.60	6.86	3.63	6.89	3.66	6.90	3.69	6.92	3.71	6.93	3.72
OK8	1	X	3.16	6.41	3.56	6.62	3.71	6.76	3.75	6.91	3.79	—	—	—	—	—	—
OK10	1	Z	3.11	6.65	3.61	6.86	3.67	6.94	3.72	7.01	3.79	7.44	3.82	7.33	3.84	7.18	3.85
	2	X	3.11	6.52	3.44	6.61	3.52	6.69	3.58	6.77	3.66	6.84	3.71	6.86	3.74	6.87	3.76
	3	Z	3.03	6.82	3.69	6.88	3.74	6.95	3.78	7.00	3.81	7.05	3.33	7.07	3.84	7.10	3.85
BA2	1	Z	3.03	6.17	3.67	6.24	3.46	6.40	3.53	6.45	3.58	6.45	3.63	6.47	3.65	6.46	3.65
	2	X	3.04	6.16	3.65	6.30	3.71	6.37	3.75	6.45	3.78	6.48	3.80	6.50	3.83	6.52	3.84
	3	X	3.01	6.23	3.36	6.33	3.48	6.45	3.53	6.59	3.60	—	—	—	—	—	—
BB1	1	X	3.05	6.10	3.52	6.22	3.67	6.35	3.73	6.41	3.75	—	—	—	—	—	—
BB3	1	Z	3.04	6.31	3.36	6.54	3.47	6.73	3.50	6.95	3.53	—	—	—	—	—	—
BB4	1	X	3.13	6.55	3.42	6.64	3.50	6.71	3.56	6.87	3.58	—	—	—	—	—	—
<i>Gabbros</i>																	
HAS4	1		2.89	7.02	—	7.08	—	7.16	—	7.22	—	—	—	—	—	—	—
SAN1	1		3.04	6.79	3.56	6.86	3.61	6.92	3.62	6.95	3.63	—	—	—	—	—	—
SAN2	1		3.02	6.21	3.10	6.37	3.40	6.45	3.48	6.56	3.50	—	—	—	—	—	—
<i>Ultramafics</i>																	
RN7	1		3.29	7.65	4.57	7.78	4.57	7.81	4.57	7.96	4.57	—	—	—	—	—	—
OK12	1		3.27	7.33	3.58	7.42	3.68	7.51	3.70	7.70	3.74	—	—	—	—	—	—

\* X: Parallel to foliation, Z: perpendicular to foliation

**Table 3.** Elastic constants calculated from mean  $V_p$ ,  $V_s$  and  $\rho$ 

Sample	Pressure GPa	$P$ $\times 10^3 \text{ kg m}^{-3}$	Mean $V_p$ $\text{km s}^{-1}$	Mean $V_s$ $\text{km s}^{-1}$	$V_p/V_s$	$\sigma$	$\emptyset$ $(\text{Km s}^{-1})^2$	$K$ GPa	$\mu$ GPa	$E$ GPa	$\lambda$ GPa
OK2	0.4	3.08	6.60	3.65	1.81	0.28	28.50	79.5	41.0	105.1	52.1
	1.0	3.10	6.67	3.71	1.80	0.28	26.14	81.0	42.7	108.9	52.6
OK3	0.4	2.88	6.60	3.45	1.91	0.31	27.69	79.8	34.3	89.8	56.9
OK4	0.4	2.96	6.82	3.65	1.87	0.30	28.75	85.1	39.4	102.5	58.8
	1.0	2.98	6.90	3.74	1.84	0.29	28.96	86.3	41.7	107.7	58.5
OK5	0.4	2.92	6.51	3.59	1.81	0.28	25.20	73.6	37.6	96.5	48.5
	1.0	2.94	6.57	3.78	1.74	0.25	24.11	70.9	42.0	105.2	42.9
OK6	0.4	3.04	6.97	3.92	1.78	0.27	28.09	85.4	46.7	118.5	54.3
	1.0	3.07	7.04	4.01	1.76	0.26	28.12	86.3	49.4	124.4	53.4
OK7	0.4	2.96	6.90	3.63	1.90	0.31	30.04	88.9	39.0	102.1	62.9
	1.0	2.98	6.94	3.68	1.89	0.31	30.10	89.7	40.4	105.3	62.8
OK8	0.4	3.17	6.91	3.79	1.82	0.28	28.60	90.6	45.5	117.0	60.3
OK10	0.4	3.10	6.93	3.75	1.85	0.29	29.27	90.8	43.6	112.7	61.7
	1.0	3.12	7.05	3.82	1.85	0.29	30.25	94.4	45.5	117.6	64.0
BA2	0.4	3.05	6.50	3.65	1.78	0.27	24.49	74.7	40.6	103.2	47.6
	1.0	3.08	6.49	3.75	1.73	0.25	23.37	72.0	43.3	108.2	43.1
BB1	0.4	3.07	6.41	3.75	1.71	0.24	22.34	68.6	43.2	107.0	39.8
BB3	0.4	3.05	6.95	3.53	1.97	0.33	31.69	96.7	38.0	100.8	71.3
BB4	0.4	3.14	6.87	3.58	1.92	0.31	30.12	94.5	40.2	105.8	67.7
SAN1	0.4	3.05	6.95	3.63	1.91	0.31	30.73	93.7	40.2	105.5	66.9
SAN2	0.4	3.03	6.56	3.50	1.87	0.30	26.70	80.9	37.1	96.6	56.2
RN7	0.4	3.30	7.96	4.57	1.74	0.25	35.51	117.2	68.9	172.9	71.3
OK12	0.4	3.28	7.70	3.74	2.06	0.35	40.64	133.4	45.8	123.3	102.9

$\sigma$ , Poisson's ratio;  $\emptyset$ , seismic parameter;  $K$ , bulk modulus;  $\mu$ , shear modulus;  $E$ , Young's modulus;  $\lambda$  Lamé's constant

effects are likely to be negligible (Evans et al., 1978). The average gradients of  $-0.8 \times 10^{-3} \text{ km s}^{-1} \text{ } ^\circ\text{C}^{-1}$  are higher than those found by Christensen (1979). Assuming a thermal gradient of about  $10^\circ \text{ C km}^{-1}$ , a reduction in velocity of about  $0.12 \text{ km s}^{-1}$  at 15 km depth (0.26 GPa effective pressure) and about  $0.24 \text{ km s}^{-1}$  at 30 km depth would be expected. The effect of temperature on shear wave velocities is uncertain, and the assumption is made that Poisson's ratio is not significantly effected.

All of the velocities of the samples from the "gabbro gneiss complexes" are within the range of velocities observed for the lower continental crust (Christensen and Fountain, 1975). In Scandinavia, earlier seismic refraction experiments suggest a simple two-layer crust (Sellevoll, 1973). Upper crustal velocities range from  $6.0\text{--}6.3 \text{ km s}^{-1}$ , and lower crustal velocities from  $6.5\text{--}6.8 \text{ km s}^{-1}$ . In some areas, a higher velocity of about  $7.1 \text{ km s}^{-1}$  has also been determined at the base of the crust. In northern Norway, the one seismic line across the Province obtained uncertain  $P^*$  arrivals giving a crudely estimated lower crustal velocity of  $6.9 \text{ km s}^{-1}$  (Chroston et al., 1976).

Some caution should, however, be applied in using these velocities. The quality of the seismic experiments varies considerably, with only more recent ones producing detailed recording with multiple coverage of the line. In addition, modern interpretation techniques, when applied to older data, may modify the crustal model. The results of the Blue Road Project (Lund, 1979) suggest low velocity layers in the upper crust in the vicinity of the Caledonides with,

over the Precambrian Shield, a gradational change in velocity across the "Conrad discontinuity" and significant velocity gradients in the upper and lower crust. A comparison of one of the Blue Road profiles and an interpretation of Lofoten-Vesteralen data (Sellevoll and Thanvarachorn, 1977) and with the laboratory results is shown in Fig. 3. Here the laboratory variations with pressure have been translated into velocity-depth functions assuming the effective pressure law (effective pressure = confining pressure - pore water pressure) and also assuming an average crustal density of  $2,800 \text{ kg m}^{-3}$  and that the pore water pressure is hydrostatic. The Blue Road lower crustal velocities are significantly higher than the mean of laboratory velocities, especially when temperature is taken into account, and in this case the lower crust would have to be significantly more mafic on average than the Seiland rocks to explain the discrepancy. The lower crustal velocity from Lofoten-Vesteralen, however, compares favourably with the mean of the Seiland suite. In general the estimated velocity of the mafic gneisses is in accord with lower crustal velocities on the Shield.

All of the velocities discussed above are compressional wave velocities and it is unfortunate that good shear wave velocity estimates have not generally been obtained for the Scandinavian refraction lines. An estimate of the average shear wave velocities for the upper and lower crust has, however, been made in Sweden for earthquake epicentre determinations (Båth, 1971). For the upper crust, a shear wave velocity of about  $3.58 \text{ km s}^{-1}$  and a Poisson's ratio

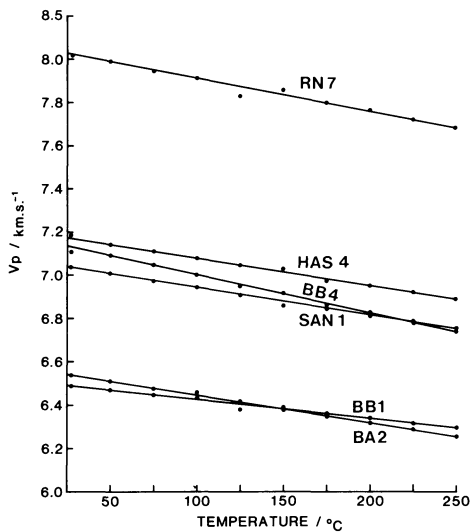


Fig. 3. Effect of temperature on compressional wave velocities on selected samples. All velocities are measured at an effective pressure of 0.4 GPa

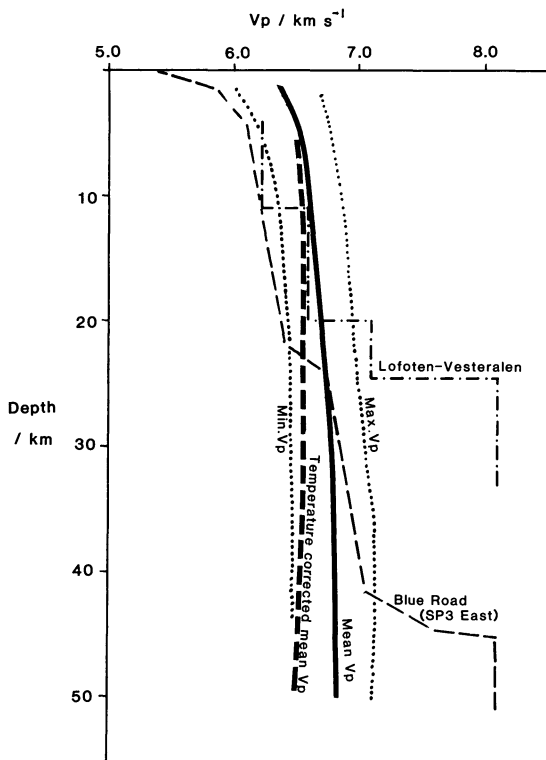


Fig. 4. Comparison of velocity depth profile based on the laboratory data with the Lofoten-Vesteralen profile and a Blue Road velocity depth profile. Possible temperature effects on the laboratory velocities are also shown

of 0.256 has been calculated. For the lower crust, the average shear wave velocity was  $3.69 \text{ km s}^{-1}$  and the Poisson's ratio 0.276.

This latter value is smaller than the mean of the Poisson's ratio of the granulites, though it is within the range of the calculated values. Two other factors, however, would result in a lower mean Poisson's ratio for the complex. Firstly, the Poisson's ratio decreases with increased pressure, and calculations on the velocity data show that a reduction of the ratio up to 0.03 is found between the effec-

tive pressures of 0.4 GPa and 1.0 GPa. Secondly, the lithologies sampled do not include the quartz rich layers which were reported by Krauskopf (1954), both of which would reduce the overall Poisson's ratio. The proportion of these rocks is believed to be minor, however, and their effect may be offset by the presence of anorthosite (with a Poisson's ratio of about 0.30). Taking these factors into account, the overall Poisson's ratio of the granulite samples is very similar to that found for the lower crust.

## Discussion

The geology, petrology and physical properties of the mafic gneiss complex as displayed in the Loppen District appear to satisfy well the constraints established for the identification of lower continental crust, and the complex has many similarities to the model proposed by Smithson and Brown (1977). The rocks are dominantly pyroxene granulites, but minor amounts of syenite gneiss, syenite, garnet syenite, amphibolite, and anorthosite are present, as well as garnet-biotite gneiss. The heterogeneous geology is in accord with the results of deep reflection experiments (Smithson et al., 1980). In the area the rocks have crystallized in the granulite facies (Hooper, 1971; Brueckner, 1973) and the estimated mean compressional wave velocity across the mafic gneisses based on laboratory measurements is comparable with the lower crustal velocities from Scandinavia.

The principal problem, however, concerns the tectonic emplacement of the proposed crustal suite, particularly in the light of the varying hypotheses on the origin of the Province. Assuming the suite is of Precambrian age, then one might expect to find a tectonic discontinuity between it and the surrounding Palaeozoic sediments and Caledonian intrusions. Such a structure may exist in the Loppen District, where west of Langfjord, metasediments and gabbro are thrust over pyroxene granulites (Hooper, 1971 and pers. comm.), but we are not aware if a comparable structure has been revealed to the east of the mafic suite.

In his interpretation of the 100 mgal gravity anomaly over the Province, Brooks (1970) provided two basic model interpretations of the anomaly. In the first, described above, it could be explained by an upward bulge of the "Conrad" discontinuity and/or a Moho bulge, and the mafic/ultramafic complex represents the sliced-off top of the bulge. In the second, one could also model the anomaly by extending the surface complex down to the NW so that effectively it represents a major thrust wedge of mafic rock. Detailed gravity surveys over the Loppen District (Chroston, 1974) lends some support for the former model, but the emplacement of the complex may be explained reasonably by either. Indeed, the latter model has some similarities to that suggested for the lower crustal rocks of the Jotun nappe (Smithson et al., 1974). It is emphasised, however, that although this suite appears to satisfy both the geological and geophysical constraints for deep crustal rocks, they may not be representative of the lower crust of the entire shield area. The variation in velocities found on refraction lines suggests a significant lithological variation, and measurements of velocities of suites from Lofoten-Vesteralen and from the Jotun nappe, which are currently in progress, should provide further information on this problem.

*Acknowledgements.* The velocity measurements to 1.0 GPa were made when one of us (PNC) was a visiting scholar at the Geophysics Programme, University of Washington. The authors are grateful to Professor N.I. Christensen for the use of the high pressure facili-

ties at the University of Washington and to Jim Schultz (at UW), Terry Manning (at UEA) and Frank Robinson (at UEA) for technical assistance.

## References

- Assumpcao M., Bamford D.: LISP-V: Studies of crustal shear waves. *Geophys. J.R. Astron. Soc.* **54**, 61–73, 1978
- Bamford D., Nunn K., Prodehl C., Jacob B.: LISP-IV: Crustal structure of Northern Britain. *Geophys. J.R. Astron. Soc.* **54**, 43–60, 1978
- Barth T.F.W.: The layered gabbro series at Seiland, Northern Norway. *Norg. Geol. Unders.* **184**, 191–200, 1953
- Båth M.: Seismic wave velocities of the Swedish crust. *Pure Appl. Geoph.* **88**, 75–91, 1971
- Birch F.: The velocity of compressional waves in rocks to 10 kilobars, Part I. *J. Geophys. Res.* **65**, 1083–1102, 1960
- Birch F.: The velocity of compressional waves in rocks to 10 kilobars, Part II. *J. Geophys. Res.* **66**, 2199–2224, 1961
- Brooks M.: A gravity survey of coastal areas of West Finnmark, Northern Norway. *Q. J. Geol. Soc. Lond.* **125**, 171–192, 1970
- Brooks M.: Positive Bouguer anomalies in some orogenic belts. *Geol. Mag.* **107**, 399–400, 1971
- Brueckner H.K.: Reconnaissance Rb-Sr investigation of salic, mafic and ultramafic rocks in the Øksfjord area, Seiland Province, Northern Norway. *Norsk. Geol. Tids.* **53**, 11–23, 1973
- Choudhury M., Giese P., de Visintini G.: Crustal structure of the Alps: some general features from explosion seismology. *Boll. Geofis.* **13**, 211–240, 1971
- Christensen N.I.: Compressional wave velocities in rocks at high temperature and pressure, critical thermal gradients, and crustal low velocity zones. *J. Geophys. Res.* **84**:6849–6857, 1979
- Christensen N.I., Fountain D.M.: Constitution of lower continental crust based on experimental studies of seismic velocities in granulite. *Geol. Soc. Am. Bull.* **86**, 227–236, 1975
- Chroston P.N.: Geological interpretation of gravity data between Tromsø and Øksfjord (Finnmark). *Norg. Geol. Unders.* **312**, 59–90, 1974
- Chroston P.N., Brooks M., Sellevoll M.A.: A seismic refraction line across the Seiland Igneous Province, Northern Norway. *Norsk Geol. Tids.* **56**, 211–216, 1976
- Evans C.J.: The seismic velocities of the Ox mountain granulites of Ireland and the implication for the interpretation of the crustal structure of north Britain. *Geophys. J. R. Astron. Soc.* **183**, 417–426, 1980
- Evans C.J., Lee C.D., Chroston P.N.: Transient effects in laboratory measurements of compressional wave velocity and electrical conductivity. *Nature* **276**, 485–487, 1978
- Fountain D.M.: The Ivrea-Verbano and Strona-Ceneri zones, northern Italy: a cross section of the continental crust—new evidence from seismic velocities of rock samples. *Tectonophysics* **33**, 145–165, 1976
- Griffin W.L., Taylor P.N., Hakkinen J.W., Heier K.S., Iden I.K., Krogh E.J., Malm O., Olsen K.L., Ormaasen D.E., Tvetan E.: Archaean and Proterozoic crustal evolution in Lofoten-Vesteralen, N. Norway. *J. Geol. Soc. London* **135**, 629–647, 1978
- Hall J., Al Haddad F.M.: Seismic velocities in the Lewisian metamorphic complex, northwest Britain – ‘in situ’ measurements. *Scottish J. Geol.* **12**, 305–314
- Hall J., Simmons G.: Seismic velocities of Lewisian metamorphic rocks at pressures to 8 kbar: relationship to crustal layering in north Britain. *Geophys. J.R. Astron. Soc.* **58**, 337–347, 1979
- Harland W.B., Gayer R.A.: The Arctic Caledonides and earlier oceans. *Geol. Mag.* **109**, 289–314, 1972
- Holland C.H., Sturt B.A.: On the occurrence of archaeocyathids in the Caledonian metamorphic rocks of Sørøy and their stratigraphical significance. *Norsk Geol. Tids.* **41**, 109–155, 1970
- Hooper P.R.: The mafic and ultramafic intrusions of S.W. Finnmark and N. Troms. *Norg. Geol. Unders.* **269**, 147–158, 1971
- Hughes D.S., Maurette C.: Variation of elastic wave velocities in basic igneous rocks with pressure and temperature. *Geophysics* **22**, 23–31, 1957
- Kern H.: The effect of high temperature and high confining pressure on compressional wave velocities in quartz-bearing and quartz-free igneous and metamorphic rocks. *Tectonophysics* **44**, 183–203, 1978
- Kroenke L.W., Manghani M.H., Rei C.S., Fryer P., Ramanantandro R.: Elastic properties of selected ophiolitic rocks from Papua New Guinea. Nature and composition of Oceanic Lower Crust and Upper Mantle. In: *The Geophysics of the Pacific Ocean Basin and its Margin*. Amer. Geophys. Union Geophysical Monograph **19**, G.H. Sutton, ed.: pp. 415–421, 1978
- Krauskopf K.F.: Igneous and metamorphic rocks of the Øksfjord area, West Finnmark. *Norg. Geol. Unders.* **188**, 29–50, 1954
- Lund C.E.: Crustal structure beneath the Blue Road profile, northern Scandinavia, derived from compressional wave velocity distribution. *Geol. Foren. Stockh. Forh.* **101**, 191–204, 1979
- Norges Geologiske Undersøkelse, Hammerfest: Berggrunskart 1:250,000, Publication NGU 301, 1974
- Oosterom M.G.: The ultramafic and layered gabbro sequence in the granulite facies rocks on Stjernøy, Finnmark. *Leidse Geol. Meded.* **28**, 1–96, 1963
- Pringle I.R.: A review of radiometric age determinations from the Caledonides of West Finnmark. *Norg. Geol. Unders.* **269**, 191–196, 1971
- Pringle I.R.: A comment: reconnaissance Rb-Sr investigation of salic, mafic and ultramafic rocks in the Øksfjord area, Seiland Province, Northern Norway. *Norsk Geol. Tids.* **55**, 97–100, 1975
- Ramsay D.M.: Possible existence of a stillborn marginal ocean in the Caledonian orogenic belt of north-west Norway. *Nature Phys. Sci.* **245**, 107–109, 1973
- Robins B., Gardner P.M.: The magmatic evolution of the Seiland Province, and Caledonian plate boundaries in northern Norway. *Earth Planet. Sci. Lett.* **26**, 167–178, 1974
- Sellevoll M.A.: Mohorovicic discontinuity beneath Fennoscandia and adjacent parts of the Norwegian Sea and the North Sea. *Tectonophysics* **20**, 359–366, 1973
- Sellevoll M.A., Thanvarachorn P.: A seismic reconnaissance study of the earth's crust in the Lofoten-Vesteralen area, N. Norway. In: Heier K.S. *The Norwegian Guotraverse Project*. *Norg. Geol. Unders., Trondheim* 1977
- Smith P.J., Bott M.H.P.: Structure of the crust beneath the Caledonian foreland and Caledonian belt of the North Scottish region. *Geophys. J.R. Astron. Soc.* **40**, 187–205, 1975
- Smithson S.B.: Modelling continental crust: structural and chemical constraints. *Geophys. Res. Lett.* **5**, 749–752, 1978
- Smithson S.B., Brewer J.A., Kaufman S., Oliver J.E., Zaurilak R.C.: Complex archaean lower crustal structure revealed by COCORP crustal profiling in the Wind River Range, Wyoming. *Earth Planet. Sci. Lett.* **46**, 295–305, 1980
- Smithson S.B., Brown S.K.: A model for lower continental crust. *Earth Planet. Sci. Lett.* **35**, 134–144, 1977
- Smithson S.B., Ramberg I.B., Grønlie G.: Gravity interpretation of the Jotun nappe of the Norwegian Caledonides. *Tectonophysics* **22**, 205–222, 1974
- Smithson S.B., Shrive P.N.: Field measurements of compressional wave velocities in common crystalline rocks. *Earth Planet. Sci. Lett.* **27**, 170–176, 1975
- Stewart R., Peselnick R.: Systematic behaviour of compressional velocity in Franciscan rocks at high pressure and temperature. *J. Geophys. Res.* **83**, 831–839, 1978
- Strand T.: *The Norwegian Caledonides*. In: *Scandinavian Caledonides*, De Sitter L.U. ed.: pp. 1–148. New York: Wiley 1972
- Sturt B.A., Roberts D.: Caledonides of northernmost Norway (Finnmark). In: *Caledonian-Appalachian region of the North Atlantic Region*. *Geol. Sci. Canada, Paper* 78–13, 17–24, 1978
- Sturt B.A., Pringle I.R., and Ramsay D.M.: The Finnmarkian phase of the Caledonian Orogeny. *J. Geol. Soc.* **135**, 597–610, 1978

# Inductive Coupling Between Idealized Conductors and Its Significance for the Geomagnetic Coast Effect

Detlef Wolf

Department of Physics, University of Toronto, Toronto, Ontario, Canada, M5S 1A7

**Abstract.** A problem of current interest is the inductive coupling between an ocean, a solid earth conductor and a conductosphere. The anomaly of this configuration is modelled by (i) the inductive response of a system consisting of two thin half planes and an underlying thin whole plane and (ii) the superposition of the responses of two related systems, each consisting of only one of the two half plane and the whole plane. The configuration is two-dimensional, and the planes are perfectly conducting. These two assumptions allow the derivation of rigorous solutions for the induced magnetic fields by conformal mapping methods. A comparison between the anomalies (i) and (ii) permits the determination of the degree of inductive coupling between the idealized conductors. This establishes a reference for estimating the inductive coupling between more realistic conductors and may therefore assist in the interpretation of complicated magnetic variation anomalies in coastal regions. Our substitute configurations can also be used directly for the rapid modelling of the inductive response of the earth in the vicinity of coastlines. This is demonstrated by analyzing some field data from the recent literature.

**Key words:** Electromagnetic induction — Inductive coupling — Geomagnetic coast effect — Conformal mapping

## Introduction

The behaviour of the geomagnetic variation vector in the vicinity of coastlines is characterized by the fact that it is closely confined to a certain plane, which has been called the preferred plane. This plane often strikes approximately parallel to the continental margin, and its orientation is nearly independent of the polarization and frequency characteristics of the inducing field. The whole phenomenon has been coined the geomagnetic coast effect and was first described by Parkinson (1959). Clearly, this effect is related to the sharp conductivity contrast between sea-water and adjacent rocks. However, there is evidence for the interference by other conductivity anomalies in coastal regions. These have sometimes been correlated with temperature anomalies in the upper mantle along recent subduction zones due to a cold, descending lithospheric slab or partial melting

(Schmucker et al., 1966; Greenhouse et al., 1973; Honkura, 1978). In other cases they are believed to be signatures of mineralogical or petrological changes in the lower crust, such as hydrous minerals or ancient plate boundaries (Hyndman and Hyndman, 1968; Edwards and Greenhouse, 1975).

The exact determination of the inductive response of a real (three-dimensional) ocean is a difficult task. Reliable solutions may be obtained from scale model experiments (Dosso, 1973). Alternatively, analytical or numerical solutions can be used, such as for three-dimensional induction in a thin layer of finite conductivity, overlying a homogeneous or layered half space (Vasseur and Weidelt, 1977; Dawson and Weaver, 1979). This raises the question as to how to “deduct” the response of the model ocean from the actually observed coastal anomaly in a realistic manner. Such a reduction is necessary, if an interpretation of the observed anomaly in terms of the conductivity structure of the lower crust or upper mantle alone is required. An obvious way to allow for the influence of the ocean is to subtract its anomaly. But this simple procedure neglects any inductive coupling existing even between insulated conductors, which may be significant. This has already been emphasized by Price (1964) and Rikitake (1966).

To shed some light on this problem, two deliberately simple classes of models (in the following denoted as cases A and B), which are nevertheless characteristic for actual conductivity structures near coastlines, are considered here. They involve only perfectly conducting half and whole planes of two-dimensional configuration. It is shown that the extent of inductive coupling is different for the two cases, which leads us to distinguish between what we call an additive case A and a coupled case B. These ideal configurations can serve as useful standards, as they establish an upper limit on the inductive coupling to be expected for more realistic models.

## Application of Conformal Mapping to Electromagnetic Induction

Conformal mapping methods have been applied to problems of geomagnetic induction by Schmucker (1964; 1970a), Greenhouse et al. (1973), Weidelt (1981)

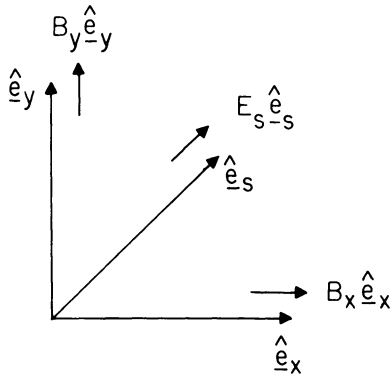


**Fig. 1.** Co-ordinate system used:  $s$  designates the direction tangential to strike, whereas  $x$  and  $y$  designate the horizontal and vertical directions, respectively, in a plane normal to strike (also see text)

and others. The mathematical principles are given in Morse and Feshbach (1953) and Koppenfels and Stallmann (1959). For our purposes, we adopt the following assumptions.

(i) The geometry of the induction problem is two-dimensional, i.e. an arbitrary function  $f$  of the Cartesian space co-ordinates, can be written as  $f=f(x, y)$  (Fig. 1).

(ii) The  $E$  polarization case applies (Fig. 1).

(iii) The conductors are perfect, and the non-conducting region of the  $(x, y)$  plane is a simply connected domain.

Since the interior of the perfect conductors is assumed to be source-free, the boundary conditions at any interfaces between perfectly conducting and non-conducting regions are

$$\hat{e}_n \cdot \mathbf{B} = 0, \quad (1)$$

$$\hat{e}_n \times \mathbf{H} = \mathbf{K}, \quad (2)$$

where  $\mathbf{K}$  is the surface current density and  $\mathbf{H}$  the magnetic field, with  $\mathbf{B} = \mu_0 \mathbf{H}$  as the magnetic induction.  $\hat{e}_n$  designates the unit vector normal to the interface. As displacement currents are neglected, we can write the magnetic induction in terms of a vector or scalar potential, respectively

$$\mathbf{B} = \nabla \times \psi, \quad (3)$$

$$\mathbf{B} = \nabla \phi. \quad (4)$$

But since we consider  $E$  polarization, we have  $\psi = \psi \hat{e}_s$ . Here  $\hat{e}_s$  denotes the unit vector in the strike direction (Fig. 1).  $\psi = |\psi|$  is a magnetic stream function. Considering the component forms of Eqs. (3) and (4), it can also be shown that  $\phi(x, y)$  and  $\psi(x, y)$  satisfy the Cauchy-Riemann conditions and are therefore harmonic functions. As this opens the possibility of using conformal mapping methods, we introduce complex quantities and define an analytical magnetic potential by

$$\Omega(z) = \Omega(x + iy) = \phi(x, y) + i\psi(x, y). \quad (5)$$

But as  $d\Omega/dz = \partial\phi/\partial x + i\partial\psi/\partial x$ , the analytic magnetic field is then given by

$$B(z) = B(x + iy) = B_x(x, y) - iB_y(x, y), \quad (6)$$

where the component forms of Eqs. (3) and (4) have been used. The concept of solving two-dimensional boundary-value problems of potential theory by conformal mapping can now be stated as follows. As a start, a trivial boundary-value problem is formulated in a complex auxiliary plane, the  $w$  plane. This auxiliary plane is then “deformed” as necessary, such that the solution of the actual boundary-value problem in the complex  $z$  plane is obtained. Mathematically, this transformation is represented by a conformal mapping  $w(z)$ , where  $w = u + iv$  and  $z = x + iy$ . If  $\Omega(w)$  is the solution for the potential in the  $w$  plane, the required solution in the  $z$  plane can then be written as  $\Omega(z) = \Omega(w(z))$ , where  $w(z)$  must be known. That  $\Omega(z)$  in fact constitutes the solution for the actual boundary-value problem can be proven if the mathematical properties of the functions  $\Omega(w)$  and  $w(z)$  are exploited.

### Solutions for some Perfectly Conducting Thin Sheet Configurations

#### Significance of Perfect Conductors

In this section, some induction problems are formulated in terms of perfectly conducting half and whole planes in a non-conducting environment. In view of the conductivity distribution of the real earth, this is obviously a highly idealized model. However, there are important facts that justify this choice.

For electromagnetic induction phenomena, a distribution of perfectly conducting and non-conducting regions constitutes the inductive limit, i.e. inductive effects completely dominate resistive effects. Since we are going to estimate the degree of electromagnetic interaction between galvanically insulated conductors, a distribution of perfect conductors is a useful limit to consider.

On the other hand, a particular geophysical interpretation can be attached to our induction problem. It is the situation in which a laterally discontinuous solid earth conductor is adjacent to an ocean and both are underlain by a highly conducting region at some depth. Even though there is evidence for such situations in several coastal regions (e.g. Bailey et al., 1974; Edwards and Greenhouse, 1975), no systematic investigation of the electromagnetic interaction between such conductors has been attempted so far. Lines et al. (1973) solved a related problem numerically, but the emphasis was on the detectability of an anomalous upper mantle beneath an ocean. Their formulation of the coupling problem was not rigorous, and only a special and complicated model was examined. For investigating inductive coupling, simple but versatile combinations of thin sheets are more promising, because the number of free parameters remains small. If only the inductive limit is considered, we thus have distributions of perfectly conducting half and whole planes, which are discussed here.

However, the representation of real conductors by ideal models of this kind has some notable implications. If, for example, a perfectly conducting half plane is considered, the conductor it replaces must be thick relative to its own skin depth, but also thin relative to the skin depth of its host. According to Bailey

(1977), for oceans and earth conductors of a regional scale, there is no frequency such that this condition applies strictly. On the other hand, if we confine ourselves to the interpretation of the in-phase part of the observed response, we are led to the concept of perfect substitute conductors. The general relation between a distribution of perfect substitute conductors and the corresponding imperfect conductivity distribution of the real earth cannot be expressed in simple terms. But considering results obtained for a layered earth (Schmucker, 1970b; Weidelt, 1972), the top interface of a perfectly conducting substitute region ought to mark approximately the mean depth of the induced in-phase currents in the real earth.

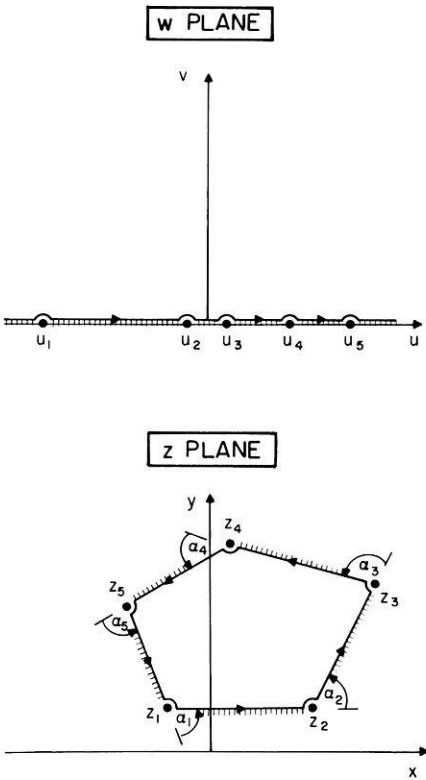


Fig. 2. Schwarz-Christoffel transformation (also see text)

Construction of Conformal Mappings

We consider some elementary two-dimensional configurations which involve only parallel and perfectly conducting half and whole planes. To derive the solutions for these configurations, conformal mapping theory is applied using the Schwarz-Christoffel transformation. An alternative approach based on the Cauchy integral formula has been outlined by Wolf (1982a).

The Schwarz-Christoffel transformation (Morse and Feshbach, 1953; Koppenfels and Stallmann, 1959) describes the mapping of the upper half of the  $w$  plane onto the interior of an arbitrary polygon of the  $z$  plane. Figure 2 illustrates the situation for a polygon with five vertices. In general we have  $z_\mu = z(u_\mu)$ , where  $\mu = 1, \dots, m$ , for the co-ordinates of the vertices.

Here the surfaces of all (two-dimensional) conductors are assumed to coincide with the contours of in-

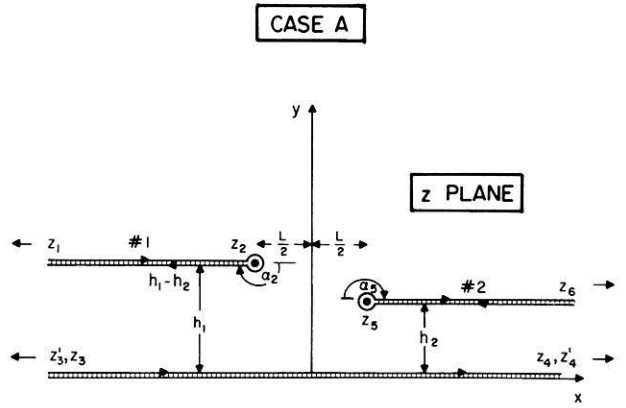


Fig. 3. Conductor configurations (degenerate polygons) for case A. Three distinct combinations of one or two conducting half planes and one conducting whole plane are possible (conductors are hatched): Model A.L.1: Half plane 1 ( $x < -L/2, y = h_1$ ) and whole plane ( $y = 0$ ). Model A.R.2: Half plane 2 ( $x > +L/2, y = h_2$ ) and whole plane ( $y = 0$ ). Model A.L.1/R.2: Half plane 1 ( $x < -L/2, y = h_1$ ), half plane 2 ( $x > +L/2, y = h_2$ ) and whole plane ( $y = 0$ )

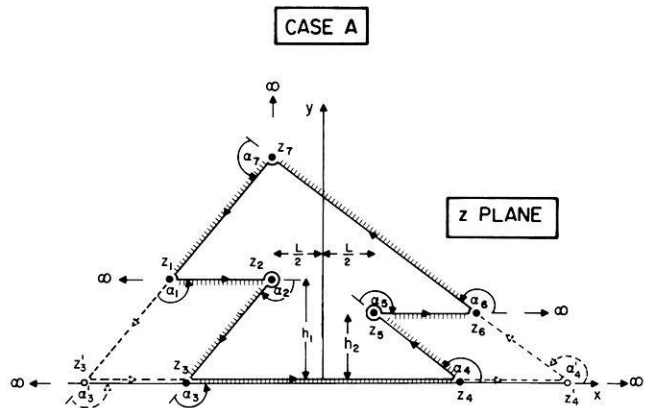


Fig. 4. Ordinary polygons corresponding to the three degenerate cases of Fig. 3. Three distinct polygons are shown: Model A.L.1: Vertices at  $z_1, z_2, z_3, z_4, z_7$ . Model A.R.2: Vertices at  $z'_3, z_4, z_5, z_6, z_7$ . Model A.L.1/R.2: Vertices at  $z_1, z_2, z_3, z_4, z_5, z_6, z_7$

tegration in the  $w$  or  $z$  planes (see the hatching in Figs. 2-6, especially the cross-sections of perfectly conducting half and whole planes in Figs. 3 and 5). In particular, we consider two basic cases, which are designated as case A (Figs. 3 and 4) and case B (Figs. 5 and 6). In this section, the transformation formulae  $z(w)$  for the different models included in cases A and B are summarized. The origin and orientation of the co-ordinate system adopted is evident from Figs. 3-6, which also show the meaning of the geometrical parameters  $h_1, h_2$  and  $L$  appearing in the formulae. More details on the mathematical aspects can be found in Wolf (1982a).

Case A comprises the models of three distinct polygons, certain parts of which are congruent. If the vertices approach infinity as indicated in Fig. 4, three corresponding degenerate polygons (combinations of half and whole planes) result (Fig. 3).

## CASE B

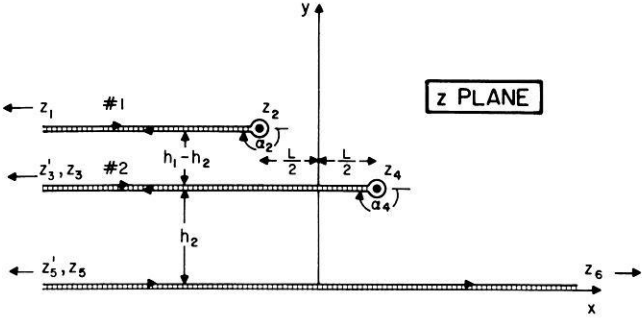


Fig. 5. Conductor configurations (degenerate polygons) for case B. Three distinct combinations of one or two conducting half planes and one conducting whole plane are possible (conductors are hatched): Model B.L.1: Half plane 1 ( $x < -L/2$ ,  $y = h_1$ ) and whole plane ( $y = 0$ ). Model B.L.2: Half plane 2 ( $x < +L/2$ ,  $y = h_2$ ) and whole plane ( $y = 0$ ). Model B.L.1/L.2: Half plane 1 ( $x < -L/2$ ,  $y = h_1$ ), half plane 2 ( $x < +L/2$ ,  $y = h_2$ ) and whole plane ( $y = 0$ )

## CASE B

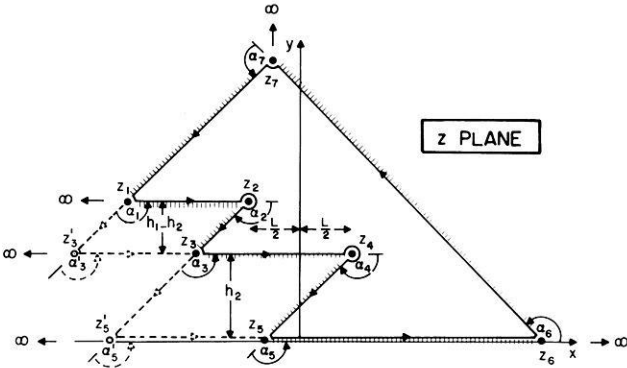


Fig. 6. Ordinary polygons corresponding to the three degenerate cases of Fig. 5. Three distinct polygons are shown: Model B.L.1: Vertices at  $z_1$ ,  $z_2$ ,  $z_5$ ,  $z_6$ ,  $z_7$ . Model B.L.2: Vertices at  $z_3$ ,  $z_4$ ,  $z_5$ ,  $z_6$ ,  $z_7$ . Model B.L.1/L.2: Vertices at  $z_1$ ,  $z_2$ ,  $z_3$ ,  $z_4$ ,  $z_5$ ,  $z_6$ ,  $z_7$

Model A.L.1: Half plane 1 has its edge at  $z_2 = -L/2 + ih_1$  and extends towards  $x = -\infty$  ( $L = \text{“left”}$ ). The whole plane is at  $y = 0$ . The transformation formula is

$$z(w) = w + a + \frac{h_1}{\pi} \left[ \ln(w+a) - \ln \frac{h_1}{\pi} + 1 \right] - \frac{L}{2}. \quad (7)$$

Parameter  $a$  is defined by  $z_3 = z(u_3) = z(-a)$ , where  $u_3$  is arbitrary. This model has been considered by Schmucker (1970a) in his attempt to explain the Californian coastal anomaly.

Model A.R.2: Half plane 2 has its edge at  $z_5 = +L/2 + ih_2$  and extends towards  $x = +\infty$  ( $R = \text{“right”}$ ). The whole plane is at  $y = 0$ . The transformation formula is

$$z(w) = w - a - \frac{h_2}{\pi} \left[ \ln(w-a) - \ln \frac{h_2}{\pi} + 1 - i\pi \right] + \frac{L}{2}. \quad (8)$$

Parameter  $a$  is defined by  $z_4 = z(u_4) = z(a)$ , and  $u_4$  may be chosen at will.

Model A.L.1/R.2: Half planes 1 and 2 and the whole plane are located as before. Now we have the transformation

$$z(w) = w + \frac{h_1}{\pi} \ln \frac{w+a}{\sqrt{2h_1 a/\pi}} - \frac{h_2}{\pi} \ln \frac{w-a}{\sqrt{2h_2 a/\pi}} + \frac{h_1-h_2}{2\pi} + ih_2. \quad (9)$$

Here parameter  $a$  is not arbitrary but implicitly given by

$$L = 2\sqrt{k_1} + \frac{h_1}{\pi} \ln \frac{\left[ \sqrt{k_1} + \left( a - \frac{h_1-h_2}{2\pi} \right) \right]^2}{2h_1 a/\pi} + \frac{h_2}{\pi} \ln \frac{\left[ \sqrt{k_1} + \left( a + \frac{h_1-h_2}{2\pi} \right) \right]^2}{2h_2 a/\pi}, \quad (10)$$

where  $k_1 \equiv \frac{(h_1-h_2)^2}{4\pi^2} + \frac{(h_1+h_2)a}{\pi} + a^2$ . It is related to  $u_3$

and  $u_4$  by  $z_3 = z(u_3) = z(-a)$  and  $z_4 = z(u_4) = z(a)$ . The special symmetrical configuration  $h_1 = h_2$  of this model has already been discussed by Schmucker (1964, 1970a) with reference to the anomaly caused by a (two-dimensional) island structure. The responses of models A.L.1 and A.R.2 can be superimposed and compared with the response of model A.L.1/R.2.

Case B also consists of three distinct polygons, certain parts of which are congruent. Referring to Figs. 5 and 6, we distinguish the following models.

Model B.L.1: Half plane 1 has its edge at  $z = -L/2 + ih_1$  and extends towards  $x = -\infty$  ( $L = \text{“left”}$ ). The whole plane is at  $y = 0$ . This model is identical with model A.L.1 and Eq. (7) represents the proper transformation. But now parameter  $a$  is defined by  $z_5 = z(u_5) = z(-a)$ , where  $u_5$  is arbitrary.

Model B.L.2: Half plane 2 has its edge at  $z_4 = +L/2 + ih_2$  and extends towards  $x = -\infty$  ( $L = \text{“left”}$ ). The whole plane is at  $y = 0$ . This model is closely related to models A.L.1 and B.L.1. The transformation formula is

$$z(w) = w - a + \frac{h_2}{\pi} \left[ \ln(w-a) - \ln \frac{h_2}{\pi} + 1 \right] + \frac{L}{2}. \quad (11)$$

Parameter  $a$  is again arbitrary and related to  $u_5$  by  $z_5 = z(u_5) = z(a)$ .

Model B.L.1/L.2: Half planes 1 and 2 and the whole plane are located as before. We have the transformation formula

$$z(w) = w + \frac{h_1-h_2}{\pi} \ln \frac{w+a}{\sqrt{2(h_1-h_2)a/\pi}} + \frac{h_2}{\pi} \ln \frac{w-a}{\sqrt{2h_2 a/\pi}} + \frac{h_1}{2\pi}. \quad (12)$$

Parameter  $a$  is not arbitrary but given by

$$L = 2\sqrt{k_2} + \frac{h_1 - h_2}{\pi} \ln \frac{\left[ \sqrt{k_2} + \left( a - \frac{h_1}{2\pi} \right) \right]^2}{2(h_1 - h_2) a / \pi} - \frac{h_2}{\pi} \ln \frac{\left[ \sqrt{k_2} + \left( a + \frac{h_1}{2\pi} \right) \right]^2}{2h_2 a / \pi} \quad (13)$$

with  $k_2 \equiv \frac{[h_2 + (h_1 - h_2)]^2}{4\pi^2} - \frac{[h_2 - (h_1 - h_2)] a}{\pi} + a^2$ . The interrelation between  $a$ ,  $u_3$  and  $u_5$  is evident from a consideration of  $z_3 = z(u_3) = z(-a)$  and  $z_5 = z(u_5) = z(a)$ . Eqs. (7), (11) and (12) allow us again to compare the sum of the responses of models B.L.1 and B.L.2 with the response of model B.L.1/L.2.

### Inversions of Mappings and Solutions for Magnetic Potential

As was emphasized above, the problem of obtaining solutions for the models of cases A and B reduces to deriving the solutions  $\Omega(w)$  for the boundary-value problem in the  $w$  plane and obtain the transformations  $w(z)$ . The corresponding inverse functions  $z(w)$  for the various models have been presented above. Thus, if  $\Omega(w)$  is known, it remains to calculate  $w(z)$  from  $z(w)$ .

In the  $w$  plane we assumed a perfectly conducting whole plane at  $v=0$  (see Fig. 2). A simple solution for this configuration is a potential that yields a homogeneous magnetic field of unit strength in the  $u$  direction. Thus

$$\Omega(w) = w, \quad (14)$$

$$B(w) = 1. \quad (15)$$

Transformation to the  $z$  plane yields

$$\Omega(z) = w(z), \quad (16)$$

$$B(z) = \frac{dw}{dz}. \quad (17)$$

If we consider the different mappings  $z(w)$ , we realize that, for  $z \rightarrow \infty$ , we again have a homogeneous and horizontal field of unit strength. Our different conductor configurations in the  $z$  plane are therefore subject to a uniform inducing field. This is the magnetic source field most widely assumed. A discussion of the limitations of this assumption has been given by several authors, e.g. Price (1964).

However, to obtain solutions  $\Omega(z)$  or  $B(z)$  at any point in the  $z$  plane, our solutions  $z(w)$  must be inverted numerically. Here we have used the Newton-Raphson iteration scheme. This algorithm has also been employed to calculate parameter  $a$  by inverting Eqs. (10) and (13). With  $w(z)$  thus determined, we can then calculate  $\Omega(z)$  and  $B(z)$  according to Eqs. (16) and (17). But due to Eqs. (5) and (6), the quantities  $\phi$ ,  $\psi$ ,  $B_x$ ,  $B_y$  are also determined, and we can consider various transfer functions as necessary.

## Inductive Coupling Between Ocean, Earth Conductor and Conductosphere

### General Remarks

Now we present some results for the models described above. To facilitate our discussion, a common normalization of the magnetic field components is adopted. We define as normal the field at a point far away from the lateral discontinuity, where the conductivity structure is effectively one-dimensional.

The following decompositions of the total field components can then be performed (Schmucker, 1964; 1970a).

$$B_x = B_{x_n} + B_{x_a}, \quad (18)$$

$$B_y = B_{y_n} + B_{y_a}. \quad (19)$$

Here  $B_{y_n} = 0$ , because the source fields are uniform. Due to the linearity of the Maxwell equations and in the limit of perfect conductivity we can then write in terms of two quantities,  $S_{xx}$  and  $S_{yx}$ ,

$$B_{x_a}(t) = S_{xx} B_{x_n}(t), \quad (20)$$

$$B_{y_a}(t) = S_{yx} B_{x_n}(t). \quad (21)$$

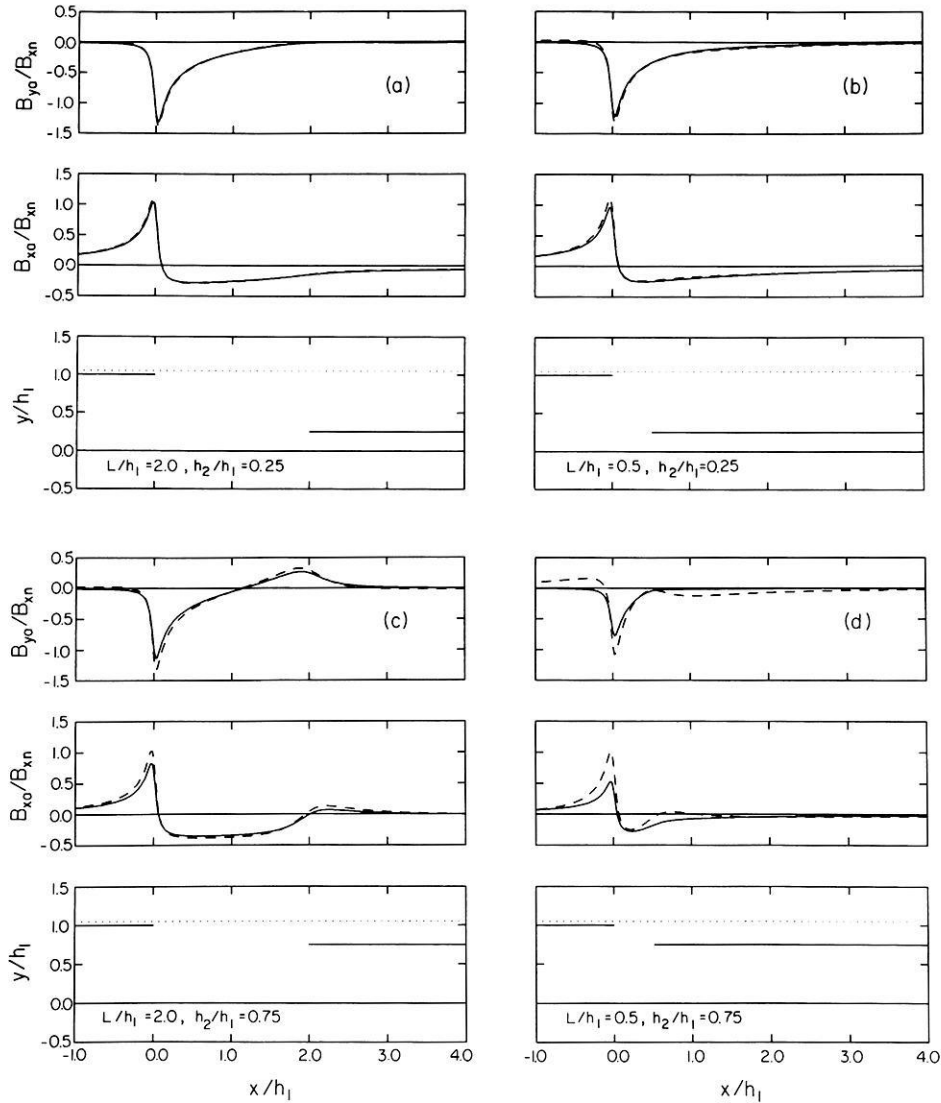
$S_{xx}$  and  $S_{yx}$  are the (real) horizontal and vertical Schmucker transfer functions, respectively. Other response parameters, such as the Parkinson transfer function, i.e.  $B_y/B_x$ , could also be used. But for our purposes, the Schmucker transfer functions are more useful, as their common normalization gives a true representation of the degree of the inductive coupling. The interrelation between several real transfer functions (induction vectors) has recently been discussed by Wolf (1982b).

All lengths are normalized relative to the separation  $h_1$  between half plane 1 and the whole plane, and the inductive response for several values of the ratios  $h_2/h_1$  and  $L/h_1$  is investigated. However, to gain some basic insight first, the normalized field distribution for two characteristic configurations of models A.L.1/R.2 and B.L.1/L.2 are shown in Figs. 7 and 8, respectively. The forcing of the field vectors about the edges of the half planes is very conspicuous. This behaviour is related to the fact that the magnetic field must be tangential to the surfaces of the perfect conductors. The screening effect of the half planes is also displayed, but some magnetic flux "leaks" into the region between the half planes and the whole plane.

When interpreting our results below, emphasis is placed on the inductive coupling between the conductors. More specifically, we compare the sum of the responses of two models, each one involving only one half plane parallel to a whole plane, with the response of the corresponding complete model consisting of both half planes and the whole plane. Theoretically, the latter response is not identical to the sum of the two individual responses, because of a redistribution of the current systems in all three conductors due to their interaction.

To give our results some geophysical relevance, we let half plane 1 represent an ocean and half plane 2 a laterally discontinuous earth conductor. The underlying whole plane is associated with the conductosphere, i.e.





**Figs. 10a–d.** *Top:* Sum of Schmucker vertical transfer functions for models A.L.1 and A.R.2 (dashed) and Schmucker vertical transfer function for model A.L.1/R.2 (solid). *Center:* As top but for Schmucker horizontal transfer functions. *Bottom:* Corresponding conductor configurations (solid) and position of measuring profile (dotted). For further explanations see text

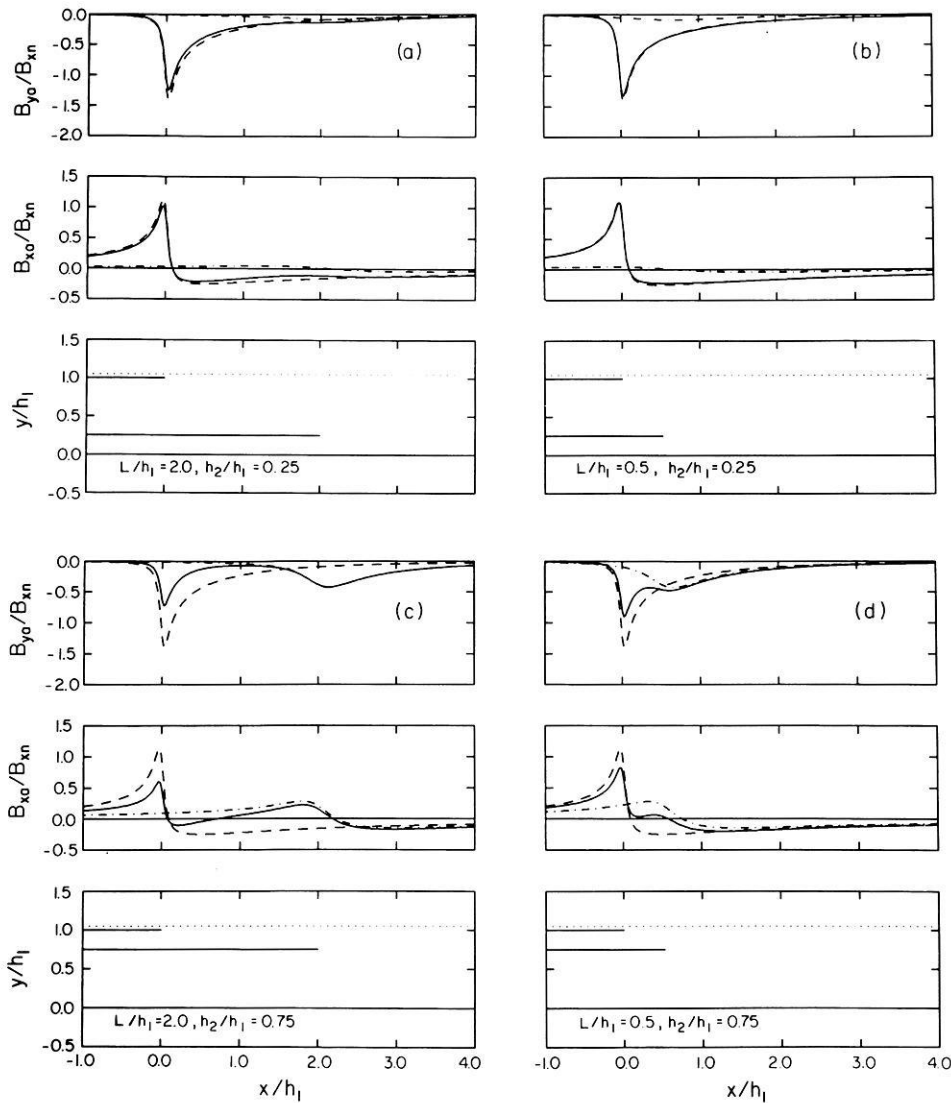
below the surface of a real ocean and no singularities are observed along ocean-continent boundaries.

#### Case A: Numerical Results and Discussion

The configurations considered belong to models A.L.1, A.R.2 or A.L.1/R.2. Here the perturbation of the edge anomaly of a laterally discontinuous earth conductor (model A.R.2) by an adjacent ocean (model A.L.1) is of most interest to us. A different interpretation would be to consider the perturbation of the “ordinary” ocean anomaly (model A.L.1) by including an earth conductor (model A.R.2) at some distance from the coast. In either case, the resulting response (model A.L.1/R.2) is a combination of the effects of both the linear superposition of the individual current systems and their redistribution due to their mutual interaction.

The responses of many conductor configurations have been calculated during these investigations. However, a limited number of geometries suffices for a demonstration of the general behaviour, and only combinations of the following ratios are considered:  $L/h_1 = 0.5, 2.0$  and  $h_2/h_1 = 0.25, 0.75$ , which gives a total of four configurations.

Let us first discuss the characteristics of the Schmucker vertical transfer function, i.e. the normalized (anomalous) vertical field. Then the ocean anomaly is negative throughout, whereas the edge anomaly of the earth conductor is always positive (Figs. 9a–d). If linear superposition holds, the magnitude of the latter anomaly therefore decreases by the magnitude of the ocean anomaly. The top panels of Figs. 9a–d allow us to compare the normalized vertical field of the four configurations of model A.L.1/R.2 (solid line) with that of the corresponding four configurations without an ocean (model A.R.2, dot-dashed line). If we focus on the section of the profile above the edge of the earth conductor, we can observe the following. Usually, the vertical field of the complete configuration (solid) approximates the sum of the vertical fields of the two individual configurations very closely, i.e. the edge anomaly of the earth conductor (dot-dashed) is in fact diminished by the magnitude of the anomaly of the ocean (dashed). The response of a deep earth conductor ( $h_2/h_1 = 0.25$ ) close to the edge of the ocean ( $L/h_1 = 0.5$ ) is therefore completely masked by the comparatively strong response of the latter (Fig. 9b). On the other hand, for a shallow earth conductor ( $h_2/h_1 = 0.75$ ) close



**Figs. 11a–d.** *Top:* Schmucker vertical transfer functions for model B.L.1 (dashed), model B.L.2 (dot-dashed) and model B.L.1/L.2 (solid). *Center:* As top but for Schmucker horizontal transfer functions. *Bottom:* Corresponding conductor configurations (solid) and position of measuring profile (dotted). For further explanations see text

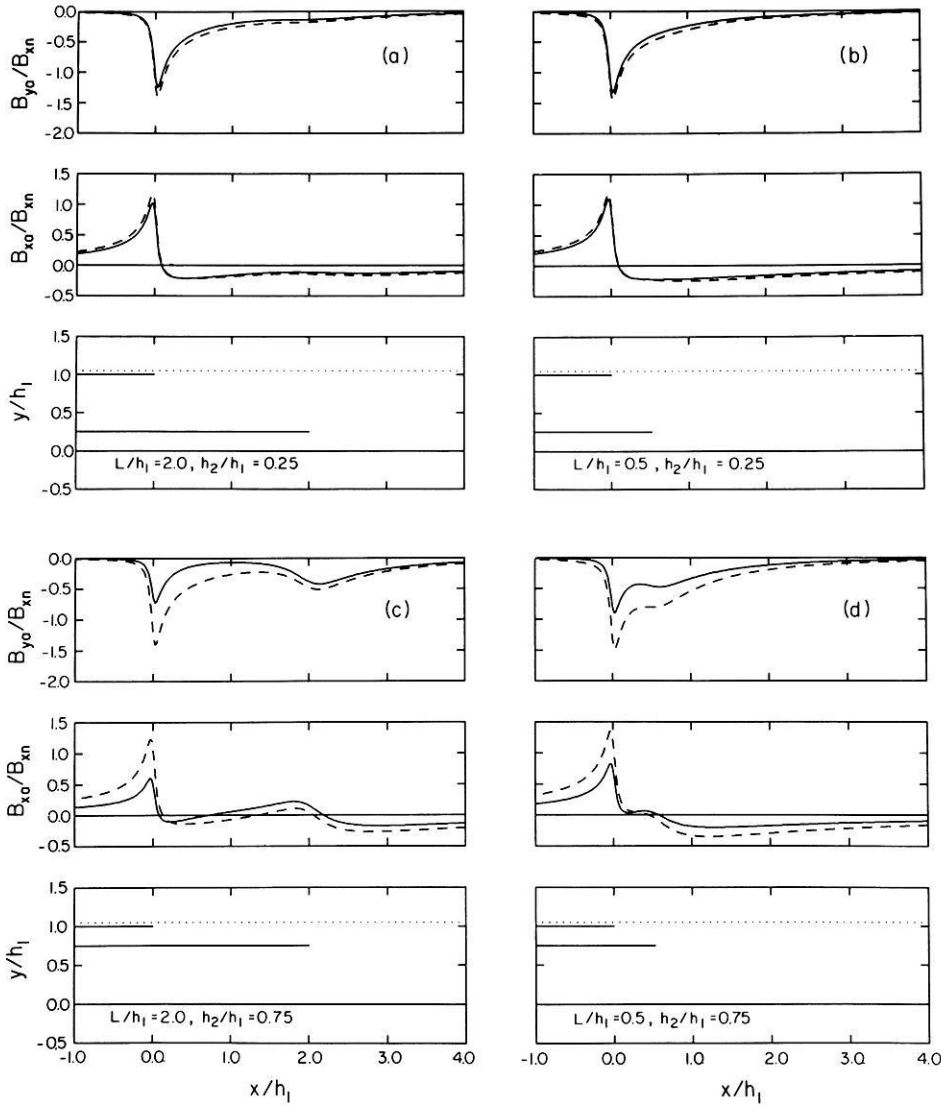
to the edge of the ocean ( $L/h_1=0.5$ ), some electromagnetic interaction can be identified (Fig. 9d). This is not surprising, because the distance between the edges of half planes 1 and 2 is now comparable with or less than either half plane's separation from the conducting whole plane underneath.

We have also calculated the Schmucker horizontal transfer functions, which are equal to normalized anomalous horizontal fields, for the same configurations (Figs. 9a–d, centre panels, respectively). Since the ocean anomaly is negative in the region above the earth conductor, linear superposition causes a downward shift of the edge anomaly of the earth conductor by the magnitude of the ocean anomaly. From the individual figures it is obvious that, for a deep continental conductor ( $h_2/h_1=0.25$ ), additivity of the anomalies holds to a very good approximation (Figs. 9a and b). But again its response is almost completely masked by the comparatively strong response of the ocean. However, if the earth conductor is shallow ( $h_2/h_1=0.75$ ), its edge anomaly becomes very conspicuous (Figs. 9c and d). The anomalous horizontal fields are roughly additive, except when the edges of half planes 1 and 2 are very close ( $L/h_1=0.5$ ).

To distinguish the effect of interaction more clearly, the sum of the magnetic fields according to models A.L.1 and A.R.2 (dashed lines) has been calculated and compared with the magnetic field of model A.L.1/R.2 (solid lines). The results are shown in Figs. 10a–d for the four configurations, for vertical (top panels) and horizontal transfer functions (centre panels). The nearly complete additivity of the anomalies for a deep earth conductor ( $h_2/h_1=0.25$ ) is corroborated by Figs. 10a and b. But, if it is shallow ( $h_2/h_1=0.75$ ), some inductive coupling can be identified. It mainly causes an attenuation of the peak values of the anomalies, as compared with the corresponding peaks of the superimposed anomalies (Figs. 10c and d).

#### Case B: Numerical Results and Discussion

Now the configurations are those of models B.L.1, B.L.2 or B.L.1/L.2. The earth conductor (half plane 2) extends from below the ocean (half plane 1) towards the land. In interpreting the following model curves, we again concentrate on the perturbation of the inductive response of a laterally discontinuous earth conductor (model B.L.2) by an ocean (model B.L.1), which leads



**Figs. 12a-d.** *Top:* Sum of Schmucker vertical transfer functions for models B.L.1 and B.L.2 (dashed) and Schmucker vertical transfer function for model B.L.1/L.2 (solid). *Center:* As top but for Schmucker horizontal transfer functions. *Bottom:* Corresponding conductor configurations (solid) and position of measuring profile (dotted). For further explanations see text

to the complete model B.L.1/L.2. A different interpretation is, as before, to consider the perturbation of the undisturbed ocean response (model B.L.1) by an additional earth conductor (model B.L.2). This causes an attenuation of the ocean response due to the decrease of the ocean's separation from the coupling surface below. Our discussion is again limited to configurations with the following geometrical parameters:  $L/h_1 = 0.5, 2.0$  and  $h_2/h_1 = 0.25, 0.75$ , which yields a total of four configurations.

Normalized vertical fields are presented in the top panels of Figs. 11a-d, respectively. When interpreting the individual figures, the following points should be borne in mind. Both ocean and earth conductor cause negative vertical fields. Thus, for linear superposition, the magnitude of the edge anomaly of the earth conductor increases by the magnitude of the ocean anomaly. We may, near the edge of the earth conductor, compare the complete response (model B.L.1/L.2, solid line) with the response of the corresponding configuration without an ocean (model B.L.2, dot-dashed line). Then we realize that linear superposition does not hold as accurately as for case A, particularly if the earth

conductor is shallow ( $h_2/h_1 = 0.75$ ). Here, its “pure” edge anomaly according to model B.L.2 remains virtually unchanged after the ocean has been included in the solution (model B.L.1/L.2). This is to be expected, because the inductive coupling between half plane 1 and the whole plane corresponding to model B.L.1 has now been replaced by the stronger coupling between half planes 1 and 2. This in turn leads to a pronounced attenuation of the anomaly associated with the ocean, such that it has almost faded away near the edge of the earth conductor (see particularly Fig. 11c). If the edges of half planes 1 and 2 are very close ( $L/h_1 = 0.5$ ), additional interactions arise between them (Fig. 11d).

The Schmucker horizontal transfer functions are displayed in the centre panels of Figs. 11a-d, respectively. If linear superposition holds, the ocean anomaly causes a downward shift of the edge anomaly of the earth conductor by the magnitude of the ocean anomaly. The calculated shift (solid line) is always less, and a closer inspection of Figs. 11c-d again shows that for shallow earth conductors ( $h_2/h_1 = 0.75$ ) the anomaly due to the ocean must be strongly attenuated. Deep conductors ( $h_2/h_1 = 0.25$ ) are difficult to detect also on

the basis of their associated horizontal transfer functions, but linear superposition now becomes a better approximation (Figs. 11a and b).

These conclusions are also supported by Figs. 12a-d, which compare the sum of the magnetic fields of models B.L.1 and B.L.2 with the magnetic field of model B.L.1/L.2.

### Rapid Modelling of Geomagnetic Coast Effects

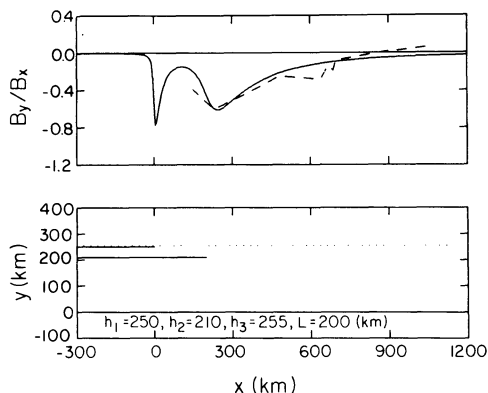
The solutions presented above have primarily been derived to investigate the degree of inductive coupling between two conducting half planes and an underlying whole plane. However, they may also be used for the direct modelling of measured magnetic variations, as long as the observed response is close to the inductive limit. More general modelling techniques do exist, but the following two examples demonstrate that simple configurations consisting of two half planes and a whole plane often suffice for a representation of the fundamental character of the subsurface conductivity structure. As only three model parameters are involved, trial and error modelling is very rapid, and the final configuration can serve as a useful guide when considering more complicated models of the subsurface conductivity distribution.

#### Coast Effect in South-Western Australia

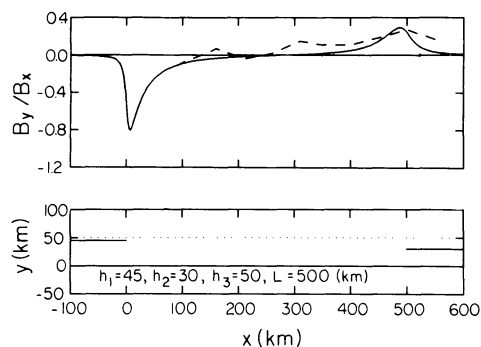
As one example, real Parkinson transfer functions, as measured by Everett and Hyndman (1967) in south-western Australia, have been analyzed. Strictly speaking, the authors regarded their transfer functions as vectors (Parkinson arrows) and decomposed them into components perpendicular to two straight lines, which served as crude representations of the edges of the continental shelves west and south of the survey area.

Figure 13 shows the modelling results for the observed transfer function components perpendicular to the west coast for one-hour periods, by a specific conductor configuration of model B.L.1/L.2. The edge of half plane 1 has been taken to coincide with the edge of the continental shelf. The exact height of the measuring profile above this half plane is only crucial for the behaviour of the model response very close to the singular edge of this half plane, where our model becomes inappropriate and no field observations exist anyway. The most interesting aspect is that a second half plane is required to reconcile the observed attenuation of the coast effect close to the continental margin with the large depth of the conductosphere for one-hour periods far away from the ocean, as established by Lilley et al. (1981). Whether this second conductor actually extends below the real ocean, cannot be inferred from our results because the model ocean has been assumed opaque for electromagnetic fields.

To explain the subdued vertical variation at their westernmost station, Everett and Hyndman (1967) proposed that the Australian shield might terminate along the Darling fault, which separates the sedimentary Perth basin to the west from the shield area to the east. In our model, the non-shield region is represented by half plane 2 at a depth of 45 km below the surface,



**Fig. 13.** *Top:* Measured (dashed) and calculated (solid) Parkinson transfer functions as a function of the distance from the continental margin. *Bottom:* Model conductors (solid) and measuring profile (dotted).  $T=1$  h, south-western Australia (also see text)



**Fig. 14.** *Top:* Measured (dashed) and calculated (solid) Parkinson transfer functions as a function of the distance from the continental margin. *Bottom:* Model conductors (solid) and measuring profile (dotted).  $T=1$  h, eastern United States (also see text)

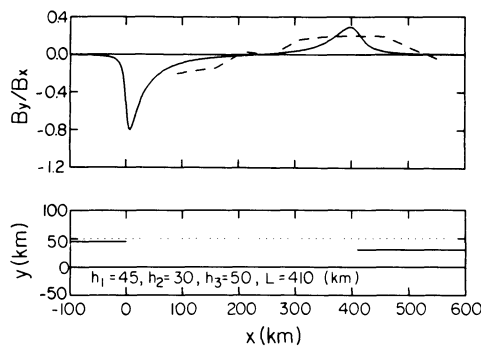


**Fig. 15.** *Top:* Measured (dashed) and calculated (solid) Parkinson transfer functions as a function of the distance from the continental margin. *Bottom:* Model conductors (solid) and measuring profile (dotted).  $T=16$  min, eastern United States (also see text)

whereas the conductosphere is more than 200 km deep. This is similar to the configuration of Fig. 12d, which has been discussed above.

#### Coast Effect in the Eastern United States

As a second example, the coast effect observed by Edwards and Greenhouse (1975) in the eastern United

States is considered. In contrast to Everett and Hyndman (1967), the former interpreted the anomalies quantitatively and concluded that a region of enhanced conductivity lay in the lower crust or uppermost mantle at some distance from the ocean. This conductive zone shows an increase in conductivity with increasing distance from the coast.

The general character of their assumed conductivity distribution together with the smallness of the observed out-of-phase response suggest an explanation of the anomaly by model A.L.1/R.2. Since transfer function estimates for the periods of 16 min and 1 h are available, both data sets have been interpreted. Again, the edge of half plane 1 coincides with the edge of the continental shelf. Comparing Fig. 14 (1 h) with Fig. 15 (16 min), their main difference is that, for the shorter period, the earth conductor (half plane 2) extends closer to the ocean, whereas its depth is not affected at all. This is consistent with the model conductor proposed by Edwards and Greenhouse (1975), which has resistivities close to  $1 \Omega\text{m}$  at some distance from the coast, with a slight rise to about  $20 \Omega\text{m}$  towards the ocean. In contrast with the Australian results, the conductosphere must now be assumed to begin at a shallow depth. In other words, the lower crust or upper mantle are highly conductive in the eastern United States.

Finer details in the observed response cannot be explained by our simple models. Furthermore, other anomalies may require models that are different. The main aspect to be emphasized here is, however, that our fast modelling technique does have the capability of furnishing basic quantitative information on the conductivity distribution in the ground.

### Conclusions and Suggestions for Future Work

It has become obvious that our distinction between cases A and B was not only a matter of mathematical convenience. The conductor configurations corresponding to these two cases also had essentially different response characteristics. This is summarized here.

If we first review the behaviour of model A.L.1/R.2, we realize that its inductive response was almost the sum of the responses of models A.L.1 and A.R.2. This approximation was particularly good if the earth conductor had a large depth ( $h_2/h_1=0.25$ ). If it was shallow ( $h_2/h_1=0.75$ ), the extent of inductive coupling still remained small and only became more significant for  $L/h_1=0.50$ . We therefore call case A the additive case.

For bodies of finite conductivity, additivity should be a still better approximation, because the relative importance of interaction between conductors decreases with decreasing conductivity. And even if the assumption of a two-dimensional conductivity configuration is violated, the basic behaviour ought to be very similar. A problem of current interest is the interpretation of the combined anomaly of a two-dimensional earth conductor extending away from a three-dimensional ocean. Here the ocean anomaly can simply be subtracted and the residual can be interpreted in terms of the earth conductor alone.

Case B was designed to simulate an earth conductor extending towards the ocean. The corresponding model

B.L.1/L.2 incorporates two strongly coupled half planes. Therefore, essentially different response characteristics were to be expected, and the edge effect of the earth conductor was found to be almost unaffected by the ocean. This behaviour was closely followed when the former conductor was shallow ( $h_2/h_1=0.75$ ). It was interpreted as being due to the strong attenuation of the response of the ocean caused by its interaction with the earth conductor. Case B is therefore called the coupled case. This emphasizes the fact that the response of the earth conductor at large distances from the ocean was found to be very nearly identical with the anomaly that it causes in close proximity to this ocean.

If bodies of finite conductivity are considered, the interaction between ocean and earth conductor becomes weaker. But it can be expected that the in-phase portion of the earth conductor anomaly still displays this persistency to a high degree. On the other hand, the out-of-phase portion of the ocean anomaly ought not to be attenuated significantly and is probably superimposed on the out-of-phase portion of the anomaly due to the earth conductor.

If the earth conductor of case B was deeper ( $h_2/h_1=0.25$ ), its edge effect decreased, whereas the ocean effect increased. The latter was explained by the weaker interaction between both conductors and hence the ocean could not be disregarded. Here the main problem is clearly the separation of the minute signature of the earth conductor from the much stronger ocean anomaly. Any further considerations, such as the question of interaction, are only of minor practical importance by comparison.

We may, however, wish to make explicit allowance for the finite conductivity of the ocean. The numerical method of Greenhouse et al. (1973) appears to be a useful way of doing so. It allows the calculation of the total response of a thin sheet of variable conductivity above a perfectly conducting undulating surface, where the whole configuration is two-dimensional. Various shapes can be assumed for these undulations, e.g. combinations of half planes and steps or elliptical bulges. Also, the response of (i) a finitely conducting sheet above a horizontal conductosphere or (ii) an undulated conductosphere alone, can be calculated separately and then superimposed. This again allows the coupling of the thin sheet and the undulating perfect conductor to be investigated. But, the number of free parameters tends to become larger for such a model. This hinders the task of extracting useful general trends from the results.

Another possible extension of our work is to define a useful inverse problem, which is based on the anomalous response, as observed in the vicinity of a coastline. Weidelt (1981) considered configurations without an ocean and constructed extremal models that maximize the depth below the surface of the top of a perfect conductor. In Weidelt's analysis, the measured response at one or two observation points had to be satisfied. The general approach is a problem of constrained maximization of a forward solution, which is based on the Cauchy integral formula. The inclusion of an ocean into Weidelt's approach results in an additional constraint, because the observation points then become

fixed relative to the edge of a perfectly conducting half plane. Nevertheless, if the response at only one observation point is to be satisfied, the solution is straightforward. It leads to a system of equations that must be solved numerically, and which provides an upper limit for the depth of the top of an earth conductor near an ocean.

*Acknowledgements.* This work was funded by a University of Toronto Open Fellowship. Special thanks are due to K. Khan for drafting the figures and to S. Holladay and J. Macnae for providing plotting routines.

## References

- Bailey, R.C.: Electromagnetic induction over the edge of a perfectly conducting ocean: the *H*-polarization case. *Geophys. J. R. Astron. Soc.* **48**, 385–392, 1977
- Bailey, R.C., Edwards, R.N., Garland, G.D., Kurtz, R., Pitcher, D.: Electrical conductivity studies over a tectonically active area in eastern Canada. *J. Geomagn. Geoelectr.* **26**, 125–146, 1974
- Dawson, T.W., Weaver, J.T.: Three-dimensional induction in a non-uniform thin sheet at the surface of a uniformly conducting earth. *Geophys. J. R. Astron. Soc.* **59**, 445–462, 1979
- Dosso, H.W.: A review of analogue model studies of the coast effect. *Phys. Earth Planet. Inter.* **7**, 294–302, 1973
- Edwards, R.N., Greenhouse, J.P.: Geomagnetic variations in the eastern United States: evidence for a highly conducting lower crust? *Science* **188**, 726–728, 1975
- Everett, J.E., Hyndman, R.D.: Geomagnetic variations and electrical conductivity structure in south-western Australia. *Phys. Earth Planet. Inter.* **1**, 24–34, 1967
- Greenhouse, J.P., Parker, R.L., White, A.: Modelling geomagnetic variations in or near an ocean using a generalized image technique. *Geophys. J. R. Astron. Soc.* **32**, 325–338, 1973
- Honkura, Y.: Electrical conductivity anomalies in the earth. *Geophys. Surv.* **3**, 225–253, 1978
- Hyndman, R.D., Hyndman, D.W.: Water saturation and high electrical conductivity in the lower continental crust. *Earth Planet. Sci. Lett.* **4**, 427–432, 1968
- Koppenfels, W.v., Stallmann, F.: *Praxis der konformen Abbildung.* Grundlehren Math. Wiss., Vol. 100. Berlin: Springer 1959
- Lilley, F.E.M., Woods, D.V., Sloane, M.N.: Electrical conductivity from Australian magnetometer arrays using spatial gradient data. *Phys. Earth Planet. Inter.* **25**, 202–209, 1981
- Lines, L.R., Ainslie, B.A., Jones, F.W.: Investigation of the coastal effect by three numerical models. *J. Geomagn. Geoelectr.* **25**, 63–73, 1973
- Morse, P.M., Feshbach, H.: *Methods of theoretical physics*, 2 vols. New York: McGraw-Hill 1953
- Parkinson, W.D.: Directions of rapid geomagnetic fluctuations. *Geophys. J. R. Astron. Soc.* **2**, 1–14, 1959
- Price, A.T.: A note on the interpretation of magnetic variations and magnetotelluric data. *J. Geomagn. Geoelectr.* **15**, 241–248, 1964
- Rikitake, T.: *Electromagnetism and the earth's interior.* Amsterdam: Elsevier 1966
- Schmucker, U.: Anomalies of geomagnetic variations in the southwestern United States. *J. Geomagn. Geoelectr.* **15**, 193–221, 1964
- Schmucker, U.: Anomalies of geomagnetic variations in the southwestern United States. *Bull. Scripps. Inst. Oceanogr.* **13**, 1–165, 1970a
- Schmucker, U.: An introduction to induction anomalies. *J. Geomagn. Geoelectr.* **22**, 9–33, 1970b
- Schmucker, U., Forbush, S.E., Hartmann, O., Giesecke, A.A. jr., Casaverde, M., Castillo, J., Salgueiro, R., del Pozo, S.: Electrical conductivity anomaly under the Andes. *Carnegie Inst. Washington Yearbook* **65**, 11–28, 1966
- Vasseur, G., Weidelt, P.: Bimodal electromagnetic induction in non-uniform thin sheets with application to the northern Pyrenean induction anomaly. *Geophys. J. R. Astron. Soc.* **51**, 669–690, 1977
- Weidelt, P.: The inverse problem of geomagnetic induction. *Z. Geophys.* **38**, 257–289, 1972
- Weidelt, P.: Extremal models for electromagnetic induction in two-dimensional perfect conductors. *J. Geophys.* **49**, 217–225, 1981
- Wolf, D.: Inductive coupling between idealized conductors and its significance for the geomagnetic coast effect. M. Sc. thesis, Univ. Toronto, 1982a
- Wolf, D.: Comment on “Geomagnetic depth sounding by induction arrow representation: A review” by G.P. Gregori and L.J. Lanzerotti. *Rev. Geophys. Space Phys.* **20**, 519–521, 1982b

Received July 6, 1982; Revised October 6, 1982;  
Accepted November 2, 1982

# VHF Radar Observations of Wind Velocities at the Arecibo Observatory

J. Röttger<sup>1</sup>\*, P. Czechowsky<sup>2</sup>, R. Rüster<sup>2</sup>, and G. Schmidt<sup>2</sup>

<sup>1</sup> EISCAT Scientific Association, 981 27 Kiruna, Sweden

<sup>2</sup> Max-Planck-Institut für Aeronomie, 3411 Katlenburg-Lindau, Federal Republic of Germany

**Abstract.** Further measurements carried out in December 1980 and January 1981 with the SOUSY-VHF-Radar at the Arecibo Observatory in Puerto Rico are presented. An example of mesospheric turbulence echoes recorded during a solar flare is described, and it is concluded that the echo detectability strongly depends on the background electron density profile. The resulting limitations to measure winds in the mesosphere are outlined. Average profiles of zonal and meridional wind velocities indicate signatures of the diurnal tide in the height region 60–80 km. A long-period oscillation of 6 days, found in the zonal but not in the meridional winds in the mesosphere, can presumably be explained by a Kelvin wave.

**Key words:** Mesosphere – Stratosphere – Troposphere – Tides – Planetary waves – Winds – VHF radar

## Introduction

The SOUSY-VHF-Radar was operated with the Arecibo Observatory antenna dish during a common project “Radar Studies of the Middle Atmosphere at 50 and 430 MHz” of the Max-Planck-Institut für Aeronomie and the Arecibo Observatory/National Astronomy and Ionosphere Centre. Four campaigns of several weeks duration were carried out in 1980 and 1981 at the Arecibo Observatory (18.3° N, 66.8° W) in Puerto Rico. First results obtained in April/May 1980 with a low-power VHF radar transmitter (4 kW), and a description of the equipment were published by Röttger et al. (1981). During a campaign in December 1980/January 1981 a higher power transmitter was used as well as an upgraded computer control was partly applied. The transmitter was operated at 30 kW pulse peak power and 4% duty cycle. Using the Arecibo dish, the antenna gain was 40 dB. This yielded an average power aperture product of  $5 \cdot 10^7 \text{ W m}^2$ . Some longer term measurements were carried out in order to investigate tides and planetary waves in the lower and middle atmosphere. In this paper some typical results are selected and briefly described, such as indications of the diurnal tide and signatures of a Kelvin wave in the mesosphere.

## General Signal Characteristics

### *Power Profiles and Interference*

The altitude range of reliable VHF radar echoes normally covered the upper troposphere and lower stratosphere (8–25 km) and the mesosphere between about 60 and 85 km. At ranges larger than about 20 km strong scatter from ocean surface waves (sea-clutter) occurred which normally extended to ranges of 50–60 km. Occasionally sea-clutter was also observed out to ranges of 100 km when tropospheric ducting caused propagation beyond the horizon. The sea-clutter sometimes complicates the evaluation of signals from the middle stratosphere and mesosphere, whereas ground-clutter is a minor problem. Man-made interference occasionally was strong in the morning hours (09–12 AST) when ionospheric propagation from the US mainland was possible (Röttger, 1980).

### *Variation of Stratospheric and Mesospheric Echoes*

It is known that stratospheric echoes are due to turbulence causing refractivity changes by temperature variations, but mesospheric echoes are additionally strongly influenced by the electron density profile of the ionospheric D region (e.g. Ecklund and Balsley, 1981) and exhibit typical seasonal variations (Czechowsky et al., 1979). The latter echoes therefore are only observed during daylight hours, which complicates for instance the analysis of tidal variations. Another limitation exists since the turbulence occurs in layers, which often confines the radar echoes to rather thin regions of several 100 m vertical extent, although layers as thick as several kilometers were also observed. However, it never was found that evaluable echoes were observed through the entire altitude region between 60 and 85 km for the given power aperture product  $5 \cdot 10^7 \text{ W m}^2$ . Additionally the echoes indicate quite some temporal variation.

The layered structure of intermittent turbulence as well as the varying electron density profile do not allow the determination of high resolution (<1 km) wind profiles throughout the entire mesosphere. To illustrate the evident temporal and spatial variation, a contour plot of signal strength is presented in Fig. 1. It is recognized that strong signals were almost continuously observed in the low altitudes up to some 20 km. Two stronger layers occurred at about 14 km and 17–18 km where the upper tropospheric winds showed the strongest shear. Some spurious contour lines in Fig. 1 at ranges between 20 and 50 km are due

\* On leave from Max-Planck-Institut für Aeronomie, 3411 Katlenburg-Lindau, Federal Republic of Germany

5 JAN 1981

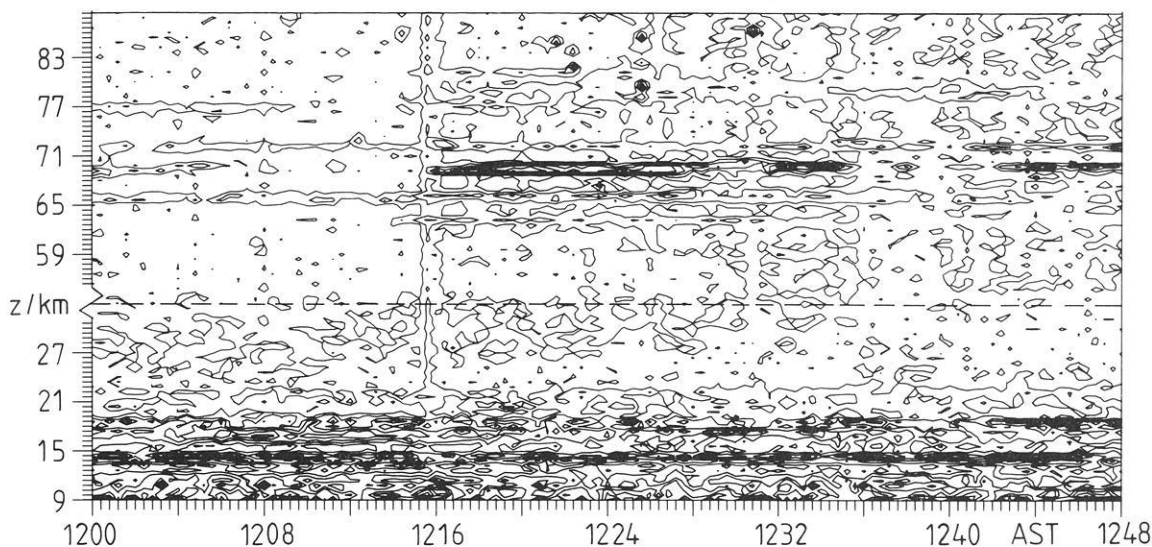


**Fig. 1.** Contour plot of received power (signal+noise) as function of height  $z$  and time (AST=Atlantic Standard Time). The power difference between the contour lines is 2 dB. Because atmospheric signals were not received in the height range 33–53 km, this range is suppressed in the plot. Measurements were carried out with peak power of 30 kW and antenna beam pointing at a zenith angle of  $2.7^\circ$ .

to sea-clutter signals. In the mesosphere four separated regions of turbulence scatter were detected after 1200 AST between 65 and 78 km altitude. At 1215 AST a noise burst was observed, followed by an abrupt increase of signal strength of turbulence scatter. The noise burst was due to enhanced solar radio emission during an  $H_\alpha$  solar flare (Solar-Geophysical Data Prompt Reports, 1981). The enhanced noise level must have been picked up through an antenna sidelobe pointing to the sun. The simultaneously increased flux of UV and X-ray radiation also resulted in an enhancement of the D region electron density which caused sudden increase of turbulence scatter strength by some ten dB. Simultaneous incoherent scatter observations with the 430-MHz radar showed an increase of the mean D region electron density by a factor of 5–8 (personal communication from J. Mathews and M. Sulzer, 1981). However, even the abnormally high electron density still did not yield a continuous power profile of turbulence scatter. The reason is that the mesosphere was not totally turbulent, but the turbulence was confined to intermittent layers. Because of lack of scatter from “non-turbulent” regions, continuous, high-resolution wind profiles cannot be obtained with a VHF radar with a given power-aperture product of  $5 \cdot 10^7 \text{ W m}^2$ . These observations also show that a sudden increase or even moderate variation of signal strength cannot at all be attributed to an increase of turbulence strength, but rather an enhancement of electron density or electron density gradient.

### Wind Observations

To obtain indications on tidal and planetary wave variations, a longer observation period evidently is necessary to smooth the short-term fluctuations. A long-term operation was performed at the Arecibo Observatory from 10 December 1980 until 18 January 1981. Since the observatory schedule did not allow continuous radar operation during such a long time period, two hours were only allotted

almost every day around noon hours. Continuous runs were carried out during a couple of days only.

Although the VHF radar observations do not yield continuous wind profiles during 24 h a day, they extend the lowest height range which is normally covered by meteor or partial reflection measurements at low latitudes (e.g. Bernard et al., 1981; Vincent and Ball, 1981). Incoherent scatter measurements of velocities in the middle mesosphere need a very high power-aperture product (e.g. Mathews et al., 1981). VHF radar measurements with comparatively low power normally have sufficient signal-to-noise ratios in the height region 65–80 km (occasionally up to 90 km), which is not covered by meteor radars. The lowest heights between 65 and 70 km are mostly not reached by partial reflection measurements. We therefore regard our VHF radar observations as a useful complementary information on winds in these lower heights.

The prevailing wind due to the global circulation, planetary waves, tides as well as gravity waves contribute to the observed wind velocities. It is likely that short-period gravity wave oscillations are smoothed out when averaging the data over 1 h. When measuring at the same time of every day, velocities caused by the tides should be rather similar if their forcing or propagation does not change from day to day. Any variations of the wind velocity, e.g. measured every day around noon time, can therefore be regarded as being due to air motions introduced by planetary waves since the prevailing wind changes at periods much longer than those of planetary waves. Because the forcing and propagation of tides are also influenced by temperature and wind variations due to planetary waves, the day-to-day variations of velocity at a given height level have to be caused anyhow by planetary wave disturbances. The separation of tides from the background wind can either be done by recording the diurnal variation (1), or by averaging many sample profiles taken at a constant time to deduce the vertical profile of tidal winds. We essentially report here results obtained with the latter approach (2), the analysis

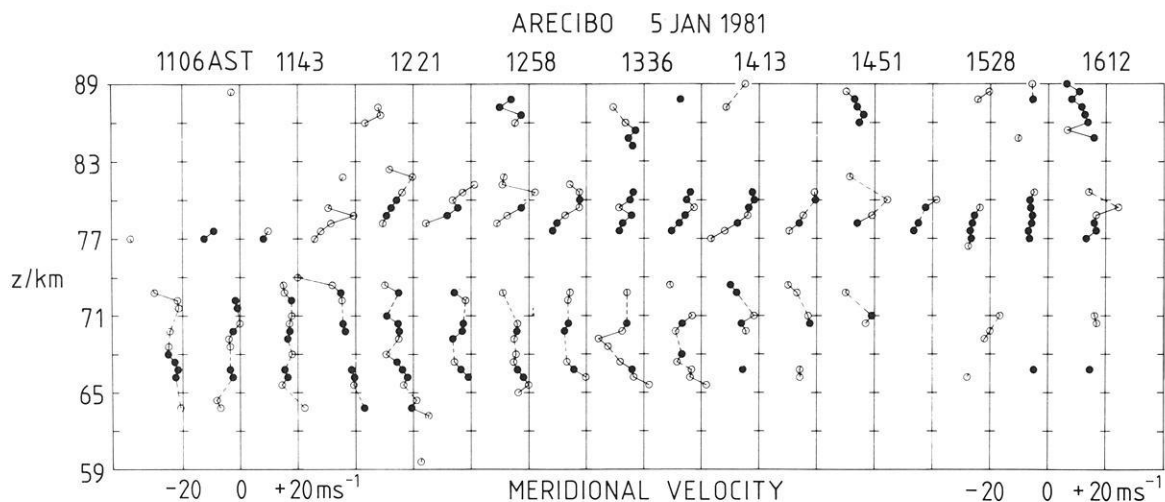


**Fig. 2.** Meridional velocity  $v$ , averaged over 18 min. Open circles denote  $\text{SNR} < 3$  dB, closed circles  $\text{SNR} > 3$  dB. Since SNR is deduced from the spectrum analysis, the reference level is different from that used in Fig. 1

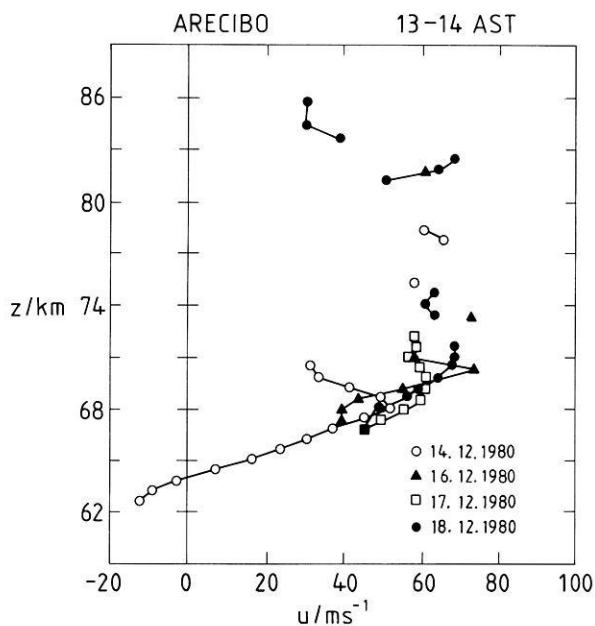


**Fig. 3a.** Zonal velocity  $u$  as function of height  $z$

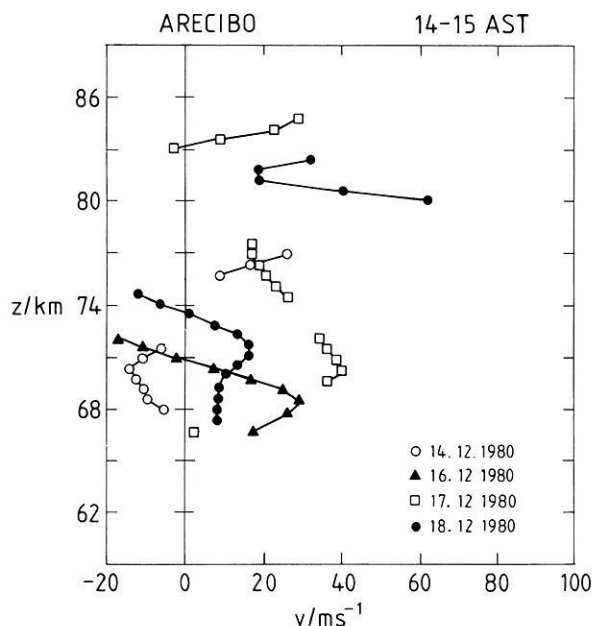


**Fig. 3b.** Meridional velocity  $v$  as function of height  $z$

of continuous radar operations to obtain diurnal variations (1) is still in progress.

#### Search for Tidal Variations

Horizontal velocities were determined from the Doppler spectra if the signal-to-noise ratio (SNR) exceeded a sufficient level. The velocity data were averaged over time intervals of 18 min or longer. An example of height profiles of the meridional velocity in the mesosphere is presented in Fig. 2. It shows an average southward wind component of about  $10 \text{ m s}^{-1}$ , decreasing to zero velocity around 65 km altitude. The velocity variability from profile to profile is most likely caused by non-properly smoothed gravity wave oscillations which often had a substantial velocity amplitude of several  $\text{m s}^{-1}$ . During the course of the day the average wind profiles indicate quite a per-

sistency, and tidal wind variations cannot readily be recognized.

During the observations in December 1980 and January 1981 two dominating regions of echoes existed: region 1 between 65 and 73 km, and region 2 between 77 and 82 km, which are also found in the longer-term statistical analysis (ref. Fig. 4). The lower boundary of region 1 increased in height during the afternoon hours, which presumably was due to the diurnal variation of electron density. The upper boundary of region 1 as well as the lower boundary of region 2 kept the same altitude, whereas the upper boundary of region 2 had a tendency of downward progression. Some sporadic echoes were also detected in the upper height region between 85 and 90 km. Turbulence layers generated by wind shear due to the dominating diurnal tide should move downwards by several kilometers during 5 h. Since there is no clear indication on this expectation, it must be

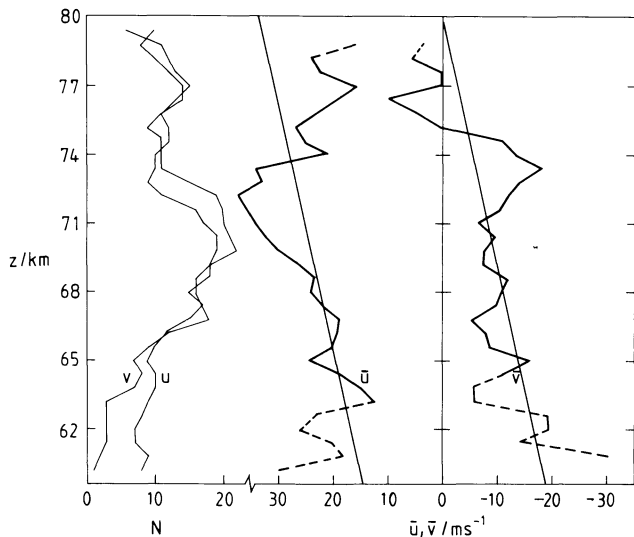


**Fig. 4.** Average zonal ( $\bar{u}$ ) and meridional ( $\bar{v}$ ) velocity components measured between 13 and 15 AST on 32 days during the December 1980/January 1981 campaign. The straight lines indicate the supposed mean background wind profile. Dashed parts of the velocity curves indicate marginal significance. On the left-hand side the height distribution of the number  $N$  of days (out of the 32 days of radar operation) is shown when evaluable echoes were detected

assumed that other factors such as electron density gradients, lapse rate changes due to the tide or planetary waves, or gravity waves superimposed on tidal or planetary wave shear also play a role in generating these echo structures.

In Figs. 3a and 3b zonal and meridional velocities are shown for four consecutive days in December 1980. These diagrams show velocities deduced from hourly averages of Doppler spectra; the antenna pointed at  $5^\circ$  zenith angle. The zonal velocity was obtained from 13–14 AST and the meridional from 14–15 AST. During these times sufficient signal power was mostly found in the two height regions around  $z = 70$  km and 78 km, which was mentioned earlier. The zonal velocity  $u$  had peak values of  $70 \text{ m s}^{-1}$  around  $z = 70$  km and exhibited strong shears of about  $0.01 \text{ s}^{-1}$  below 70 km. The day-to-day variation of the zonal component was smaller than that of the meridional component. The latter one changed from southerly to northerly direction within one day. It is assumed that the consistent westerly velocity  $u$  is due to a pronounced prevailing wind, on which tidal and planetary wave disturbances were superimposed. This assumption can be checked by the following evaluations.

When averaging height profiles of wind velocities over several weeks, one expects to smooth out variations due to transient planetary waves. The averaged height profiles should consist of a superposition of the prevailing wind and tidal variations if all the observations are performed during the same time of the day, and it can be assumed that stationary planetary waves have a small amplitude. A result of average wind profiles, obtained for the period 10 December 1980 to 18 January 1981, is shown in Fig. 4. This period of 40 days appears to be sufficiently longer than typical periods of observed waves which were at about 6 days and 20 days. It therefore can be assumed that the averaging over 40 days attenuated these planetary wave oscillations. The height profiles of average velocity in Fig. 4

indicate a quasi-wavelike pattern superimposed on a steady change of background wind with height. This wavelike pattern has a vertical wavelength of about 12 km and indicates that the velocity vector superimposed on the background wind rotated clockwise with increasing height. The amplitude of the wave increased from about  $5 \text{ m s}^{-1}$  at 66 km to  $8 \text{ m s}^{-1}$  at 72 km and  $10 \text{ m s}^{-1}$  at 78 km. These values are slightly smaller than tidal amplitudes in these height regions, measured by Groves (1975) with grenade experiments at  $5.9^\circ \text{ S}$ . We presume that our observations are consistent with the propagating diurnal tide, but more detailed investigations of these data have to be carried out. Our presumption, however, is supported by continuous measurements during four days in November 1981 which clearly indicate a diurnal variation. These observations, which simultaneously were carried out with measurements by Aso and colleagues at the Jicamarca Observatory in Peru on the opposite side of the equator, and at other locations of the globe, will be described elsewhere. Incoherent scatter observations also showed the diurnal tide over Arecibo (e.g. Mathews, 1976; Fukuyama, 1981).

On the left-hand side of Fig. 4 also the number  $N$  of days is plotted at which the received echo power exceeded a given level sufficient for estimating velocity data. One again surmises the two echo maxima around 70 km and 78 km. It is not discernible that these regions coincide with regions of maximum wind shear, which supports our earlier suggestion that other factors, such as electron density or temperature variations or shears by gravity waves, have to be regarded as well to explain the mesospheric radar echoes.

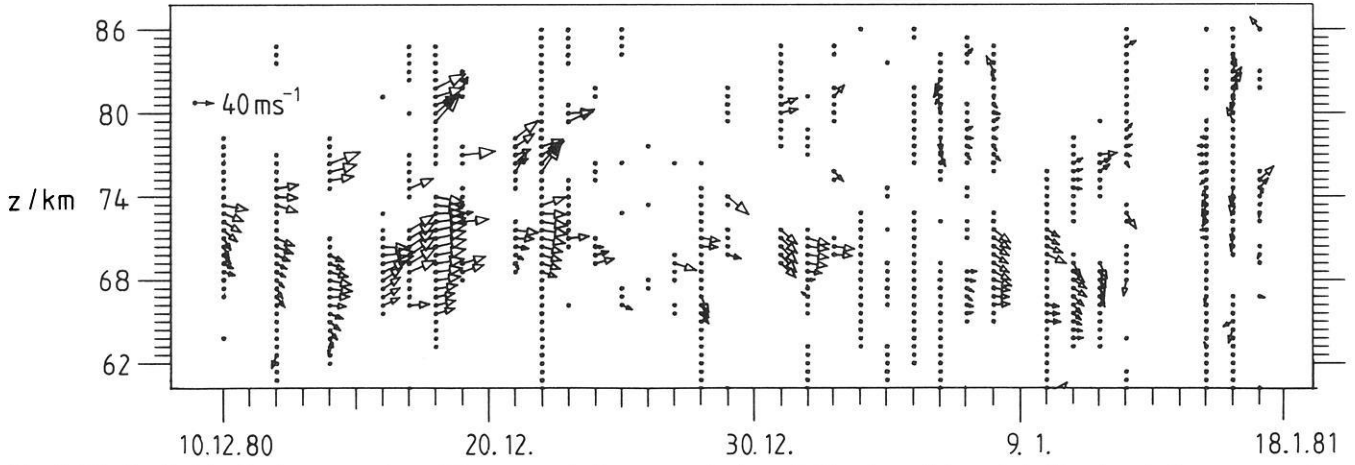
Our analyses of the tidal structure were performed under the assumption that the prevailing wind, i.e. the meanflow due to global circulation, changed linearly with height and can be described by the straight lines in Fig. 4. This may not generally be justified (e.g. Groves, 1980), but it is the only approach we can take since continuous wind observations during 24 h a day during the full campaign could not be achieved at all.

Fig. 5 shows that the prevailing wind in the mesosphere had a rather persistent component to the east. The arrows in this diagram represent speed and direction of the 2-hour averages of the mesospheric winds. At some heights and times only one wind component could be deduced because of too low signal-to-noise ratios or restricted radar operation. These instances are identified by single dots in Fig. 5. It is seen that the westerly winds were strongest during the first part but seem to reverse towards the end of the campaign. The day-to-day variability indicates some oscillating pattern over periods of several days (particularly during the first part of the campaign). The echo minimum around 74 km seems to change slightly its height during the observation period, which will be discussed further in subsequent reports.

#### *Search for Planetary Waves (Tropical Wave Disturbances)*

To obtain a clearer picture of the day-to-day variations depicted in the previous section we have plotted in Fig. 6 the time series of velocity deviations  $u'$  and  $v'$  from the mean velocities  $\bar{u}$  and  $\bar{v}$ . The profiles of mean velocities, which are averages over the entire campaign from 10 December 1980 to 18 January 1981, are plotted in Fig. 7. Since it was not possible to operate the radar on every day be-

ARECIBO (13-15 AST)



**Fig. 5.** Wind velocities in the mesosphere. The arrows indicate magnitude and direction of the wind. The dots indicate cases where radar signals were sufficiently strong, but only one velocity component could be determined

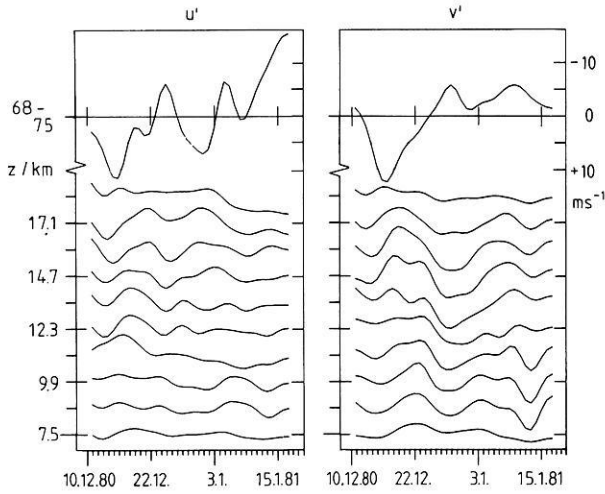


**Fig. 6.** Deviations  $u'$  and  $v'$  from the average zonal ( $\bar{u}$ ) and meridional ( $\bar{v}$ ) velocities (see Fig. 7). Missing days were linearly interpolated, and the time series were filtered with a 3-point Hamming filter

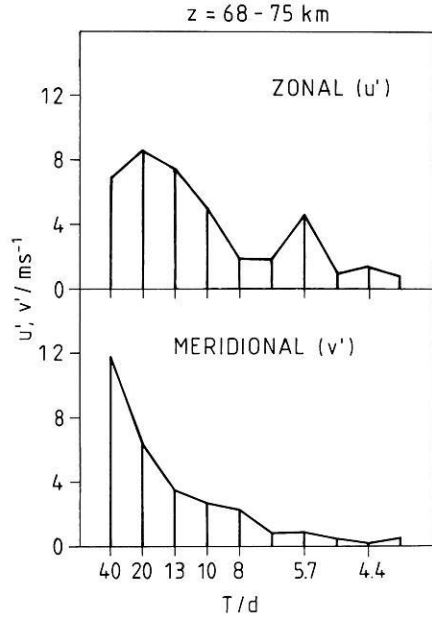


**Fig. 8.** Amplitude spectrum of linearly detrended zonal  $u'$ , and meridional wind component  $v'$  for the mesospheric height range 68-75 km

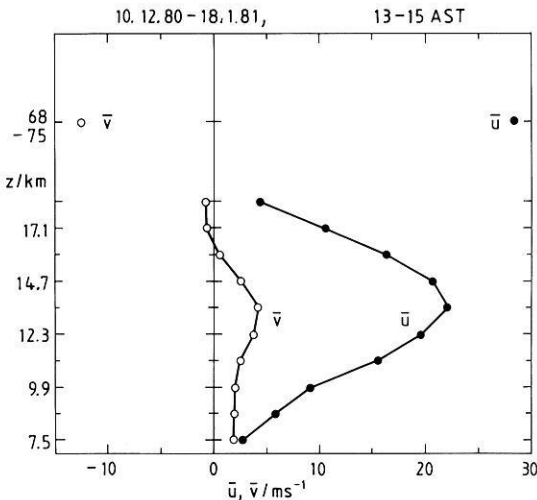


**Fig. 7.** Average velocities  $\bar{u}$  and  $\bar{v}$  measured between 13 and 15 AST in the period 10 December 1980 to 18 January 1981

cause of restrictions due to the observatory schedule, a continuous time series of velocities was not achieved. The interruptions, however, were not longer than 2 days, and these gaps were filled by linear interpolation, followed by smoothing the data series with a 3-point Hamming filter. This procedure is adequate when investigating time changes which are longer than 3-4 days. The mesospheric velocities still had some gaps because of insufficient SNR (Chap. 2.b) and therefore were height averaged over 68-75 km, which is roughly the centre height range from which mesospheric echoes were received. Tropospheric velocities, which could be deduced up to heights around the tropopause, are also included in Fig. 6 to search for tropical disturbances in the lower atmosphere. The average velocities have pronounced maxima in the troposphere around  $z=13.5$  km, which are due to the subtropical jetstream. The velocity deviations

$u'$  and  $v'$  show some quasi-wavelike disturbances with periods between 5 and 20 days. These, however, are mostly confined to height ranges of a couple of kilometers, i.e. they do not appear to propagate vertically. The spectral analysis of the zonal ( $u'$ ) and meridional ( $v'$ ) component does not indicate significant amplitudes at the same period over more than a few kilometers altitude range.

In the mesosphere the zonal component has a significant maximum of  $4 \text{ m s}^{-1}$  amplitude at a period of about 6 days, as can clearly be seen in the spectra shown in Fig. 8. This period of 6 days was also found by earlier meteor radar observations in Puerto Rico (Massebeuf et al., 1981). The 6-days period may point to mixed Rossby gravity waves. However, this oscillation is not at all found in the meridional component, which is a signature of a Kelvin wave (e.g. Wallace, 1973). On the other hand, a 6-days period is not a typical feature of a Kelvin wave. A longer period, such as 15–20 days, is more typical for Kelvin waves, and one may assume that this period is also present in the observed zonal component (see Fig. 8). Hirota (1978) suggested that tropical wave disturbances, such as Kelvin waves, can propagate into the mesosphere where they supply westerly momentum to the zonal mean flow. It cannot be concluded from our presented preliminary observations if the wave disturbances we observed had propagated from the lower atmosphere to the mesosphere. Although the energy source of tropical wave disturbances lies in the troposphere, they most prominently can be detected in the stratosphere. Since our depicted VHF radar observations do not yet cover the stratosphere (due to moderate radar power and sea-clutter problems), analyses of radiosonde data of stratospheric winds have to be included for following investigations. Oscillations with 5–6 and 12–18 days period are also prominent in the stratosphere and mesosphere at middle latitudes and could well generate wind oscillations with small meridional amplitudes at low latitudes (Madden, 1979). We consequently cannot clearly decide from our single-location observations which type of wave we had observed.

## Summary

We have described some features of VHF radar observations which were carried out at the Arecibo Observatory during December 1980 and January 1981. We conclude from our preliminary data interpretation that mesospheric signals are strongly controlled by the background electron density profile. This evidence leads to some limitations for continuous recordings of turbulence and winds in the mesosphere. During daylight hours mesospheric winds could essentially be determined in the height range between 65 and 80 km. Average profiles measured during a nearly 6-weeks campaign from 10 December 1980 until 18 January 1981 indicate velocity variations due to the diurnal tide. Wind oscillations with a period of 6 days showing a typical feature of a Kelvin wave, namely a negligible meridional velocity component, are found in the mesospheric wind profiles.

*Acknowledgements.* We thank the staffs of the Arecibo Observatory and of the laboratory of the Max-Planck-Institut für Aeronomie for constant and efficient cooperation. The National Astronomy and Ionosphere Centre, Arecibo Observatory, is operated by Cornell University under contract with the U.S. National Science Foundation.

## References

- Bernard, R., Fellous J.L., Massebeuf, M., Glass, M.: Simultaneous meteor radar observations at Monpazier (France,  $44^\circ \text{ N}$ ) and Punta Borinquen (Puerto Rico,  $18^\circ \text{ N}$ ). I – Latitudinal variations of atmospheric tides. *J. Atmos. Terr. Phys.*, **43**, 525–533, 1981
- Czechowsky, P., Ruster, R., Schmidt, G.: Variations of mesospheric structures in different seasons. *Geophys. Res. Lett.*, **6**, 459–462, 1979
- Ecklund, W.L., Balsley, B.B.: Long-term observations of the arctic mesosphere with the MST radar at Poker Flat, Alaska. *J. Geophys. Res.*, **86**, 7775–7780, 1981
- Fukuyama, K.: Incoherent scatter radar observations of wavelike structures in the mesosphere over Arecibo. *J. Geophys. Res.*, **86**, 9152–9158, 1981
- Groves, G.V.: Calculated and observed 24-hourly oscillations of the upper atmosphere at  $5.9^\circ \text{ S}$  latitude. *J. British Interplanetary Soc.*, **28**, 127–133, 1975
- Groves, G.V.: Seasonal and diurnal variations of middle atmosphere winds. *Phil. Trans. R. Soc. Lond., A*, **296**, 19–40, 1980
- Hirota, I.: Equatorial waves in the upper stratosphere and mesosphere in relation to the semiannual oscillation of the zonal wind. *J. Atmos. Sci.*, **35**, 714–722, 1978
- Madden, R.A.: Observation of large-scale traveling Rossby waves. *Rev. Geophys. Space Phys.*, **17**, 1935–1949, 1979
- Massebeuf, M., Bernard, R., Fellous, J.L., Glass, M.: Simultaneous meteor radar observations at Monpazier (France,  $44^\circ \text{ N}$ ) and Punta Borinquen (Puerto Rico,  $18^\circ \text{ N}$ ). II – Mean zonal wind and long period waves. *J. Atmos. Terr. Phys.*, **43**, 535–542, 1981
- Mathews, J.D.: Measurements of the diurnal tides in the 80- to 100-km altitude range at Arecibo. *J. Geophys. Res.*, **81**, 4671–4677, 1976
- Mathews, J.D., Sulzer, M.P., Tepley, C.A., Bernard, R., Fellous, J.L., Glass, M., Massebeuf, M., Ganguly, S., Harper, R.M., Behnke, R.A., Walker, J.C.G.: A comparison between Thomson scatter and meteor radar wind measurements in the 65–105 km altitude region at Arecibo. *Planet. Space Sci.*, **29**, 341–348, 1981
- Röttger, J.: Utilization of the lower VHF band for radar experiments at the Arecibo Observatory. Report MPAE-T-00-80-01, Max-Planck-Institut für Aeronomie, Katlenburg-Lindau, Federal Republik of Germany, 1980
- Röttger, J., Czechowsky, P., Schmidt, G.: First low-power VHF radar observations of tropospheric, stratospheric and mesospheric winds and turbulence at the Arecibo Observatory. *J. Atmos. Terr. Phys.*, **43**, 789–800, 1981
- Solar-Geophysical Data Prompt Reports: Data Reports of February 1981, January 1981 & Late Data. No. 439, Part I, p. 129, publ. by NOAA/ERL, Boulder, Colorado, USA, 1981
- Vincent, R.A., Ball, S.M.: Mesospheric winds at low- and midlatitudes in the southern hemisphere. *J. Geophys. Res.*, **86**, 9156–9169, 1981
- Wallace, J.M.: General circulation of the tropical lower stratosphere. *Rev. Geophys. Space Phys.*, **11**, 191–222, 1973

Received July 1, 1982; Revised version November 11, 1982

Accepted November 12, 1982

# Spatial Variations of Ionospheric Conductivity and Radar Auroral Amplitude in the Eastward Electrojet Region During Pre-Substorm Conditions

M.V. Uspensky<sup>1</sup>, R.J. Pellinen<sup>2</sup>, W. Baumjohann<sup>3</sup>, G.V. Starkov<sup>1</sup>, E. Nielsen<sup>4</sup>, G. Sofko<sup>4, 5</sup>, and K.U. Kaila<sup>2</sup>

<sup>1</sup> Polar Geophysical Institute, Vladimirskaia 17, 183023 Murmansk, USSR

<sup>2</sup> Finnish Meteorological Institute, Division of Geomagnetism, Box 503, SF-00101 Helsinki 10, Finland

<sup>3</sup> Institut für Geophysik der Universität Münster, Corrensstr. 24, D-4400 Münster, Federal Republic of Germany

<sup>4</sup> Max-Planck Institut für Aeronomie, Postfach 20, D-3411 Katlenburg-Lindau 3, Federal Republic of Germany

<sup>5</sup> Institute of Space and Atmospheric Studies, University of Saskatchewan, Saskatoon, Sask. S7N 0W0, Canada

**Abstract.** The dependence of auroral backscatter amplitude on different ionospheric parameters (conductivity, current density, electric field) is studied by means of data recorded by STARE (Scandinavian Twin Auroral Radar Experiment), the two-dimensional Scandinavian Magnetometer Array (SMA), and auroral all-sky cameras. The observations were made on 16 March 1978 during pre-substorm conditions in the region of the eastward polar electrojet. The paper shows that in this event the auroral backscatter amplitudes in the 140 MHz frequency band were controlled mainly by spatial variations in the electron density or conductivity inside the back-scatter volume. To a certain extent also a linear relationship between backscatter amplitude and ionospheric current density was found but it is regarded as a special case of a more general relationship between electron density and backscatter amplitude. A stable discontinuity in the Hall conductivity over the most equatorward auroral arc was deduced from the data: On the equatorward side the conductivity was 3–5 times higher than on the nearby poleward side. Our conclusions are discussed in the light of some previously published results on the same subject.

**Key words:** Radar aurora – Eastward electrojet – Substorm growth phase – Hall conductivity – Backscatter amplitude

## Introduction

During recent years the possibilities for ionospheric diagnostics by means of auroral radars have been improved considerably. A linear relationship between radar auroral amplitude and horizontal ionospheric current density was first found by Greenwald et al. (1973) and later confirmed by Greenwald et al. (1975), Siren et al. (1977), Baumjohann et al. (1978) and Mareschal et al. (1979). By means of Doppler techniques, radars have been used to record radial and two-dimensional horizontal ionospheric electric fields (see Greenwald et al., 1978; Cahill et al., 1978; Greenwald, 1979 and references therein). By investigating the different types of auroral backscatter much has been inferred on currents associated with auroras, different phases of magnetic storms or substorm activations, and the spatial location of radar auroral activity (Greenwald et al., 1973, 1975;

Unwin and Keys, 1975; Tsunoda et al., 1974, 1976a, b; Tsunoda and Presnell, 1976; Uspensky, 1977; Kustov et al., 1979).

Powerful new tools like STARE (Scandinavian Twin Auroral Radar Experiment, Greenwald et al., 1978) have facilitated simultaneous temporal and spatial studies of electric fields. There are still several open questions in this field but at present the key problem seems to be to resolve the exact nature of factors affecting the amplitude of radar aurora. This is not a simple problem: the radar auroral amplitude depends on the aspect angle, frequency band (Chestnut 1968; Pyatsi, 1974) and on the azimuth angle between the line-of-sight and the mean irregularity drift velocity (André, 1980).

The data presented in this paper were obtained during a substorm growth phase in the evening sector of 16 March 1978. We have found that there exists a distinct “jump” in the Hall conductivity across the most equatorward discrete auroral arc. In some cases the conductivity “jump” is separated from the auroral arc by a gap in diffuse luminosity on the equatorward side of the arc. The picture that we obtain by means of auroral radars seems to be in agreement with the morphology of diffuse auroral luminosity (Lui and Anger, 1973; Lui et al., 1973; Lui et al., 1977; Val’chuk et al., 1979).

According to our findings the 140 MHz backscatter amplitude may not always be linearly related to the ionospheric current density. Instead, in our case a better linear relation appears to exist between the backscatter amplitude and the mean electron density in the backscatter volume. This is especially valid for electric fields exceeding 1.5–2 times the threshold value for irregularity excitation.

## Experimental Description

This paper is based on ground-based data obtained during the “Auroral Breakup Campaign (ABC)” in 1978 at a number of Scandinavian and Soviet (Kola peninsula) stations (Fig. 1). Auroras were recorded by all-sky cameras at Kilpisjärvi (KIL), Kevo (KEV), Muonio (MUO), and Ivalo (IVA) in Finland and at Loparskaya (LOP) in the USSR. The dashed line in Fig. 1 marks the border of the field of view at 75° zenith angle at 100 km height for all cameras.

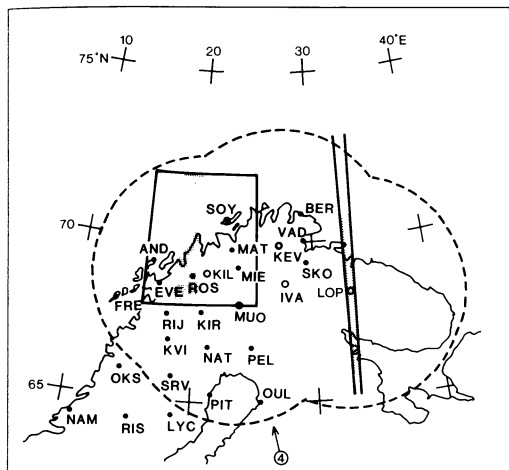


**Fig. 1.** Map of Northern Scandinavia and the Kola peninsula showing the geographical coverage by the STARE and Essoyla radars and the location of other instruments. The dashed line gives the field of view of the four all-sky cameras at 100 km for 15° elevation angle, KIL – Kilpisjärvi, MUO – Muonio, KEV – Kevo, FMI, Finland and LOP – Loparskaya, PGI, USSR. The near rectangular area on the left hand side is the STARE field of view and on the right hand side is the Essoyla 93 MHz antenna beam. The black points give the sites of the SMA magnetometers used in this study

The nearly rectangular region on the left hand side in Fig. 1 is the area covered by STARE measurements of irregularity drift velocities (Greenwald et al., 1978). The measurements are made in the 140 MHz band. The grey vertical strip inside the STARE region is the longitudinal interval of integration for the latitude-time pictures used in the present study (cf. Fig. 4). The intensity data are not corrected for range, antenna radiation pattern and aspect angle. If we do not take into account the aspect angles (for 110 km height in the vertical strip in Fig. 1 they are in the interval 89–91°), the correction factor,  $D^{-3}$  ( $D$  is the slant range), increases with increasing latitude. Inside the vertical strip it is 1.5 dB per 100 km, approximately.

The narrow beam on the right hand side is the antenna lobe of the 93 MHz Essoyla radar, the grey area denoting the highest sensitivity range interval of the radar. It uses a line cable antenna (Balsley and Ecklund, 1972) with the beam directed towards Loparskaya. The azimuthal width of the antenna lobe is around 1.5°. The temporal and spatial resolutions for the radars are 20 s and about 20 × 20 km for the STARE system and 2–5 s and 3 × 25 km for the Essoyla radar.

The irregularity drift velocity vectors were obtained from the Doppler shifts of the radar auroral backscatter recorded simultaneously by the STARE radars in Norway and Finland. The directions and magnitudes of the vectors were calculated by assuming that there exists the so-called “cosine-dependence” (Greenwald, 1979) of the Doppler shift magnitude on the angle between the mean irregularity drift direction and the radar wave vector  $k$ . Sudan et al. (1973), for example, have presented some theoretical evidence that the irregularity drift velocity is equal to the electron drift velocity,  $v_e$ , and hence the drift vectors are oppositely directed to the Hall component of the ionospheric current. Simultaneous STARE and in situ rocket measurements of the ionospheric electric field (Cahill et al., 1978)

tend to confirm this relationship. This implies that the ionospheric electric field,  $E$ , can be determined from the radar measurements, because in the E-layer  $E = -v_e \times B$  holds, where  $B$  is the geomagnetic field vector.

The black dots in Fig. 1 indicate the sites of the Scandinavian Magnetometer Array (SMA) stations used in this study. Most of the stations are located along roughly parallel north-south profiles. The spacing between magnetometers along these profiles and between the profiles themselves varies from 100 to 150 km. All magnetometers observe the magnetic field with a temporal resolution of 10 s. A detailed description of the SMA stations used in the present study has been given by Küppers et al. (1979).

## Observations

On the evening of 16 March 1978 at about 1830 UT a substorm onset was observed at the Scandinavian and Kola peninsula stations. Details of the substorm have been described earlier by Kustov et al. (1979) and Starkov et al. (1979), who observed that the substorm began at 1827 UT to the east of the area under observation. The sharp substorm initiation was preceded by a continuous joint equatorward motion of discrete auroral arcs and radar aurora. During the entire period intense radar aurora was located on the equatorward side of the most equatorward arc of the discrete auroral oval. The whole equatorward shift was about 2.5° in latitude. The equatorward motion began at 1756 UT and continued for about 30 min with a mean speed of about 150 ms<sup>-1</sup>. The period prior to the substorm onset was relatively quiet, resembling an interval between two moderate substorms.

The SMA observations (displayed in Fig. 2 in the equivalent current arrow representation) show that between about 1800 and 1830 UT an eastward electrojet was flowing over Scandinavia. The latitudinal center of the current was located over Kiruna (67.8° N) at the beginning of this interval and about 150 km south of Kiruna at 1824 UT. Hence, the equatorward speed of the current density maximum (about 90 ms<sup>-1</sup>) was less than that of the most equatorward discrete arc. Moreover, throughout the whole interval the current density was higher to the south of the arc which was located north of Kiruna.

The coordinate system indicated in the upper left corners of the diagrams in Fig. 2 has been introduced by Küppers et al. (1979) and has been named the Kiruna system. It is a Cartesian system obtained by a stereographic projection of the globe onto a tangential plane centred at Kiruna, Sweden (67.8° N, 20.4° E). The  $y_{KI}$  axis of the system, whose origin is situated at Kiruna, has been chosen as the tangent to the projection of the revised corrected geomagnetic latitude circle (Gustafsson, 1970) through Kiruna (64.8° N). The  $x_{KI}$  axis points approximately 12° west from geographic north at Kiruna.

During the period of equatorward expansion the most equatorward arc was located for an unusually long period within the STARE field-of-view. The equatorward movement of the auroral arc was observed simultaneously in both the Finnish and the Soviet sectors. The observations of aurora and radar aurora are shown in Fig. 3 in a geographical coordinate system. The solid and dashed curves indicate the location of the lower border of the auroral arc. The intensity of radar aurora on the STARE system is given by a grey scale. The radar auroras recorded by

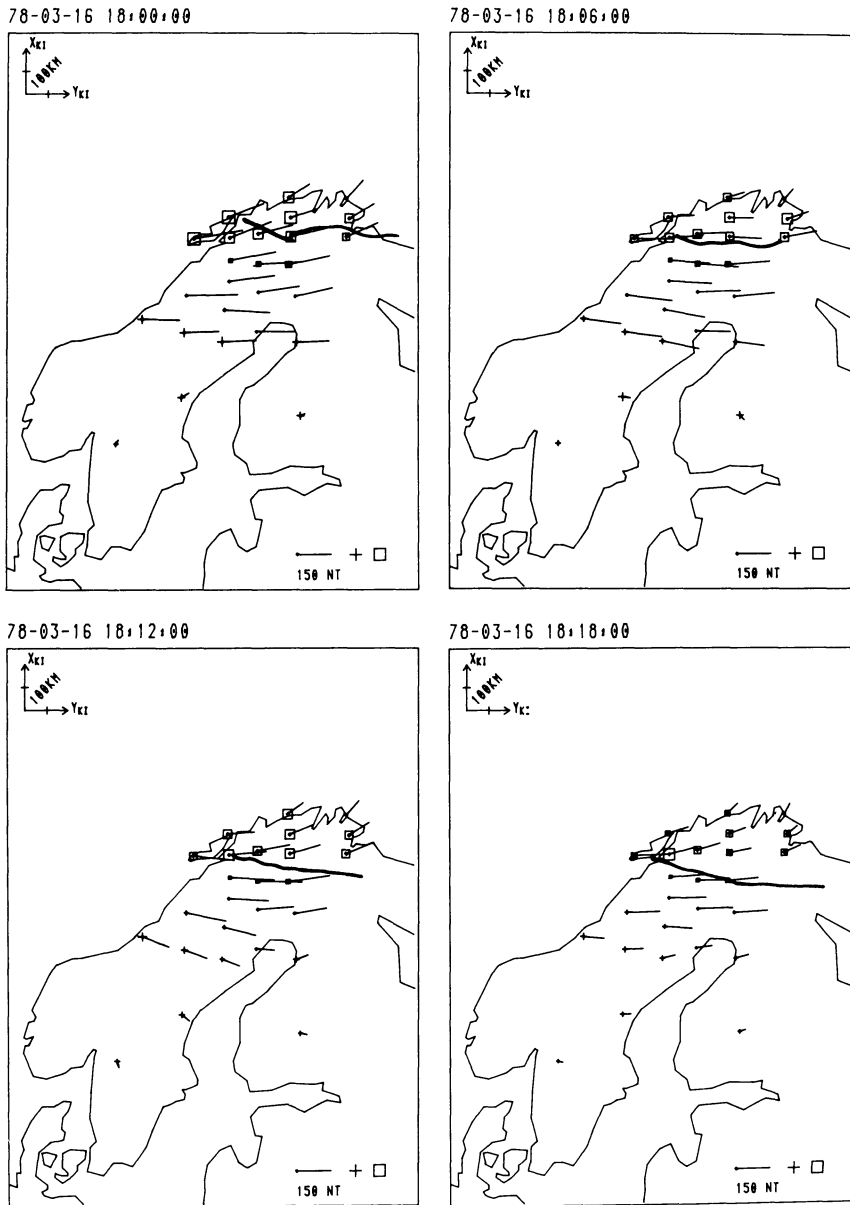


**Fig. 2.** Spatial distribution of equivalent current vectors on the ground for each 6 min between 1800 and 1818 UT. The axes in the upper left corners define the Kiruna system (see text). Squares and crosses denote negative and positive  $Z$  components, respectively. The heavy line indicates the location of the lower border of the most equatorward auroral arc

the STARE and Essoyla radars move equatorward simultaneously. The figure shows that the Essoyla radar aurora is bordered by optical aurora on the poleward side while the STARE system (Finnish radar) detected radar aurora on both sides of the arc. From the STARE frame an amplitude difference of 10–15 dB can be seen between the equatorward and poleward radar aurora, with more intense radar aurora equatorward of the arc. Since the Essoyla radar is not as sensitive as the STARE radars, the observed amplitude difference in the STARE data may be sufficient to explain the absence of radar aurora poleward of the arc in the Soviet data.

Figure 4 shows latitude-time diagrams of the STARE electric field data and radar auroral amplitudes recorded in Norway (N) and in Finland (F). The solid curves show the arc locations. The time interval of main interest to us is bounded by two arrows at 1800 and 1824 UT. In this period one observes an equatorward motion prior to sub-storm activation. As in the case of Fig. 3 above, the arc shown and discussed is the most equatorward arc that was

observed. There are other arcs poleward of this arc that move approximately in accordance with it. Equatorward of the most equatorward arc, the northward electric field is sufficiently strong (25–35 mV/m) to exceed the threshold for excitation of the plasma waves which produce the radar back-scatter. Poleward thereof, there are somewhat higher electric field values. The east-west component of the electric field (not shown) is considerably less than the northward one, and remains at approximately the same strength on both the equatorward and poleward sides of the arc. The latitudinal electric field distribution shown in the top panel of Fig. 4 is in remarkable contrast to the radar auroral amplitude distribution shown both in the lower panels of Fig. 4 and in Fig. 3. Indeed, the radar aurora is more intense equatorward of the arc than on the poleward side, while the electric field magnitude behaves in the opposite way (higher values on the poleward side than on the equatorward side; the direction remains approximately unchanged between both sides of the arc).

It is known that the ionospheric irregularities are excited

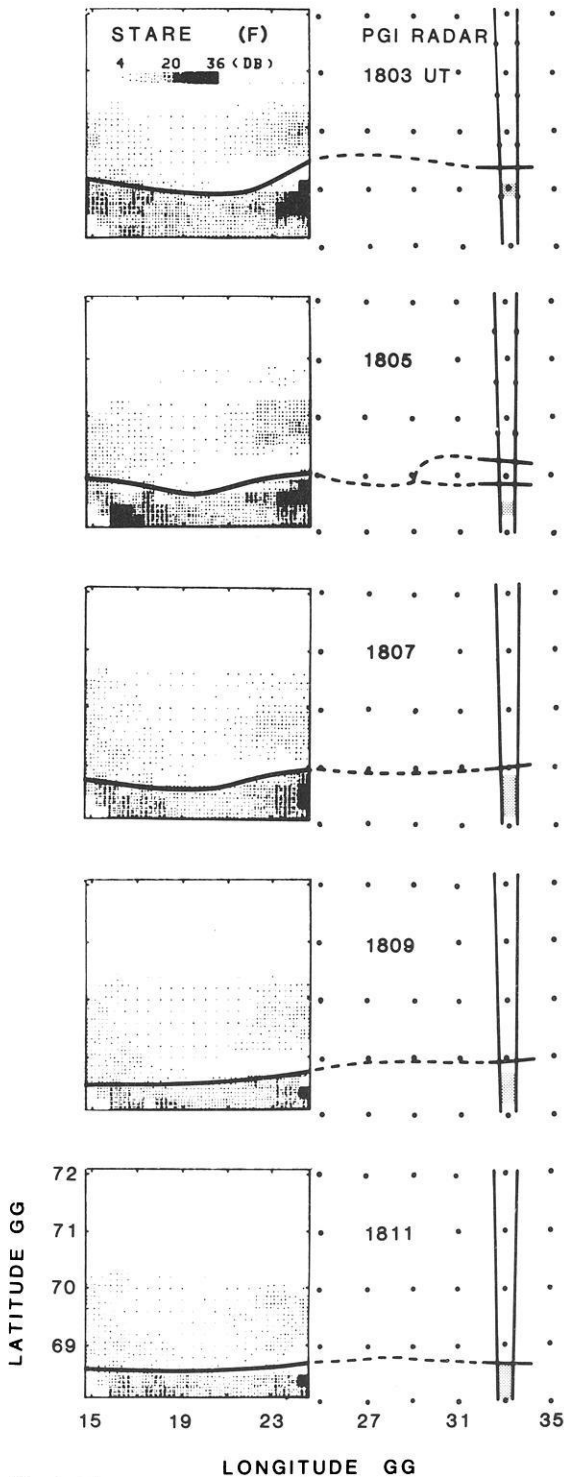


Fig. 3. The most equatorward auroral arc and radar aurora observed over Northern Scandinavia and the Kola peninsula simultaneously. The radar auroral amplitude is shown in grey scale, the heavy line and heavy dashed line denote the arc location

if the electric field exceeds a threshold value which depends on the radar frequency and is typically between 15 and 30 mV/m (Tsunoda and Presnell, 1976; Siren et al., 1977; Moorcroft, 1979; Cahill et al., 1978). In the top panel of Fig. 4 the radar aurora begins to disappear where the electric field is between 15 and 20 mV/m, in agreement with earlier STARE measurements.

Using the linear relationship between radar auroral amplitude and current density observed in several experiments (Greenwald et al., 1973; Greenwald et al., 1975; Siren et al., 1977; Baumjohann et al., 1978; Mareschal et al., 1979), we may conclude that the 10–15 dB amplitude variation across the arc implies an eastward current density on the poleward side of the arc that is 3–5 times less than that on the equatorward side. This is in quantitative agreement with Fig. 2. Since the electric field is greater in the poleward region, the current density change would be due to a conductivity difference of more than a factor of 3–5 on the two sides of the arc. This conclusion differs from that drawn by Greenwald et al. (1975) and Greenwald (1979) who considered the linear relationship of current density and radar aurora amplitude to be a consequence of electric field variations.

### Quantitative Comparison between Height-Integrated Hall Current Density, Northward Electric Field, Height-Integrated Hall Conductivity and Backscatter Amplitude

The rather constant eastward direction of the equivalent current arrows in Fig. 2 and the rather constant direction of the electric field observed by STARE suggests that it is possible to apply methods of two-dimensional potential theory for computing the external part of the northward magnetic field distribution along the  $x_{KI}$  axis at ionospheric heights. This has been done earlier by Mersmann et al. (1979) and the method was later improved by Baumjohann et al. (1979) and Sulzbacher et al. (1980). Two-dimensionality in this respect means that all quantities are independent of one coordinate which in our case turns out to be  $y_{KI}$ .

In Fig. 5 we display latitude profiles along the  $x_{KI}$  axis of the  $A$  (parallel  $x_{KI}$ ) and  $Z$  (vertical) components of the magnetic disturbances observed along SMA profile 4 at 1800, 1806, 1812, and 1818 UT, i.e. each 6 min throughout the interval of interest. The profiles indeed show that the maximum  $A$  component (about 200 nT) is located well south of the most equatorward discrete auroral arc.

Field separation and subsequent upward continuation is done by first Fourier analysing the  $A$  and  $Z$  latitude profiles displayed in Fig. 5, then combining  $A$  and  $jZ$  Fourier transforms ( $j$  imaginary unit), and afterwards multiplying the resultant Fourier coefficients with  $e^{zh}$  ( $h$  is the assumed height of the base of the ionospheric current layer). A subsequent Fourier synthesis yields the external magnetic north-south component  $V$  just below the ionospheric current layer. We have chosen  $h = 120$  km according to the average height distribution of eastward electrojets (Kamide and Brekke, 1977).

In Fig. 6 we display the resultant  $V$  profiles at 120 km height. The above-mentioned relation between the northward magnetic disturbance maximum and the discrete auroral arc becomes even clearer. Since the electric field is northward directed, the northward external  $V$  components must be caused by an ionospheric eastward flowing Hall current. Since the vertical thickness of the Hall current that flows along the  $y_{KI}$  axis is small as compared to its latitudinal extent, the eastward electrojet may be described by a surface current density distribution  $J_y(x_{KI})$ . This quantity is related to the height-continued external magnetic component  $V(x_{KI})$  by multiplying it with  $2/\mu_0$ .

The eastward height-integrated Hall current density  $J_y$

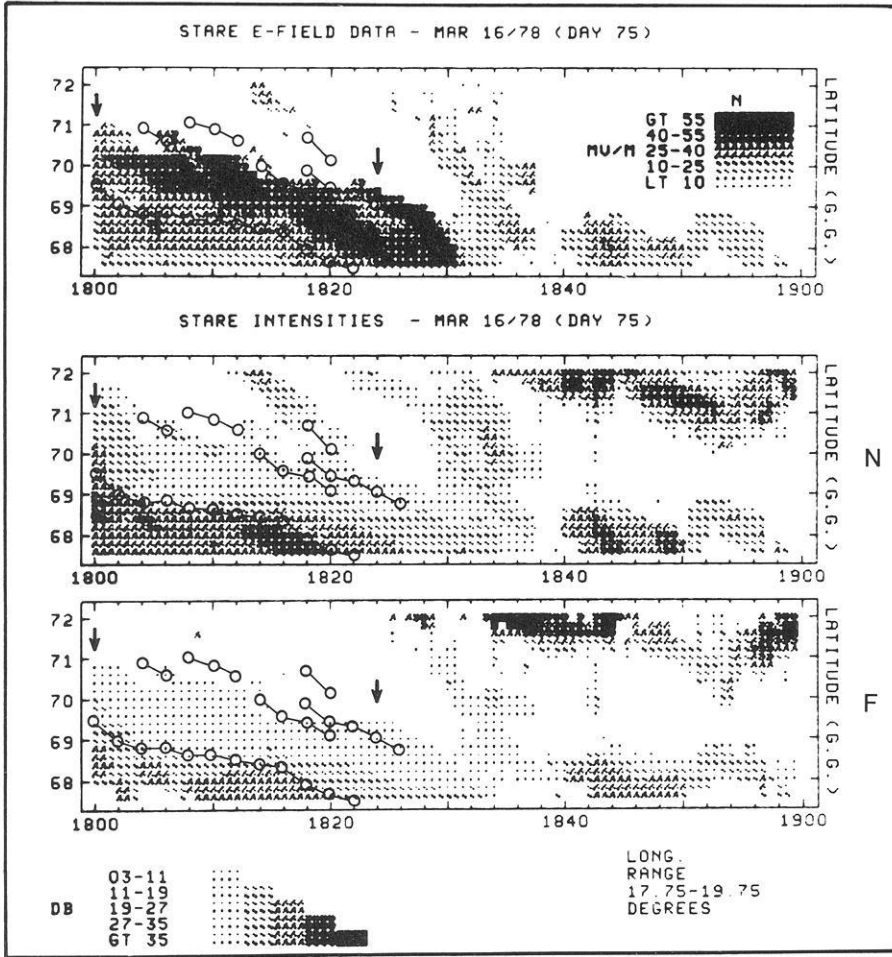


**Fig. 4.** The STARE latitude-time plots of the northward electric field (top panel) and the backscatter intensities (amplitudes) registered by Norwegian (N) and Finnish (F) radars (middle and bottom panels). The plots are averages of the STARE data over the longitude range 17.75–19.75° shown in Figure 1 by the vertical strip in the STARE plot. The heavy lines with open circles give the locations of discrete auroral arcs. The arrows define the interval of main interest in our study

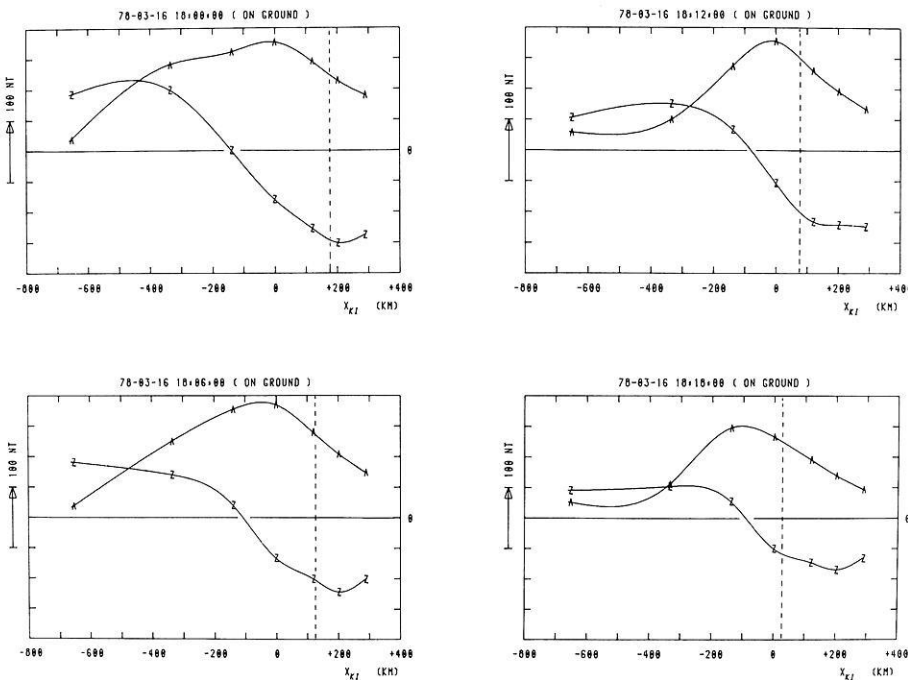


**Fig. 5.** Latitudinal profiles of the magnetic horizontal components parallel to the  $x_{KI}$  axis ( $A$ ) and of the vertical components ( $Z$ ) observed at 1800, 1806, 1812 and 1818 UT on profile 4 of the SMA. The letters denote the  $A$  and  $Z$  profiles and simultaneously give the observed values. The dashed vertical lines give the positions of the most equatorward discrete auroral arc

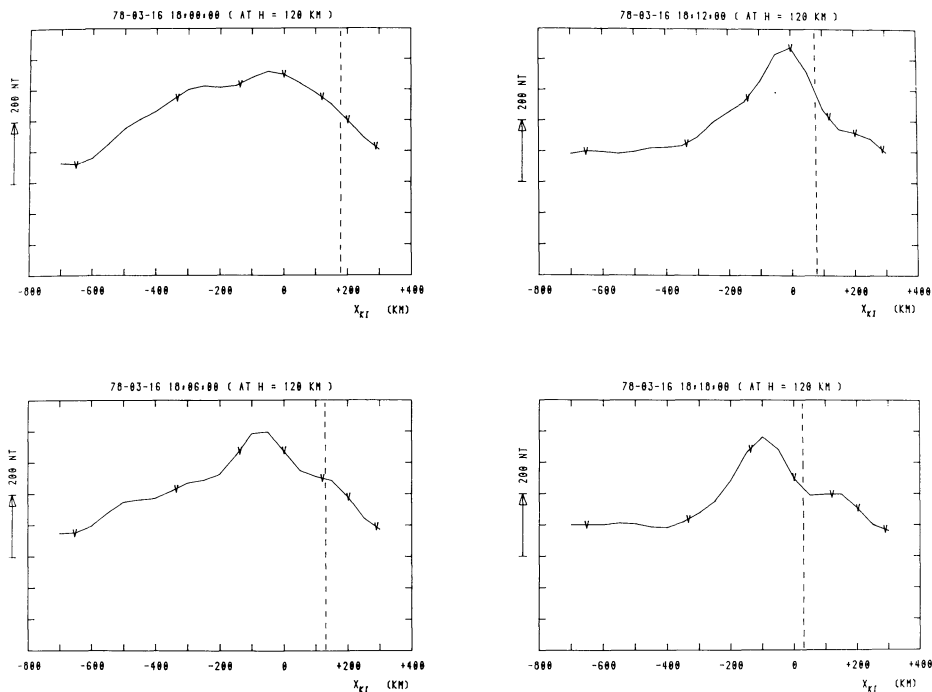


Fig. 6. Latitudinal profiles of the external magnetic horizontal components parallel to the  $x_{KI}$  axis ( $V$ ) at 120 km height; otherwise as Fig. 5

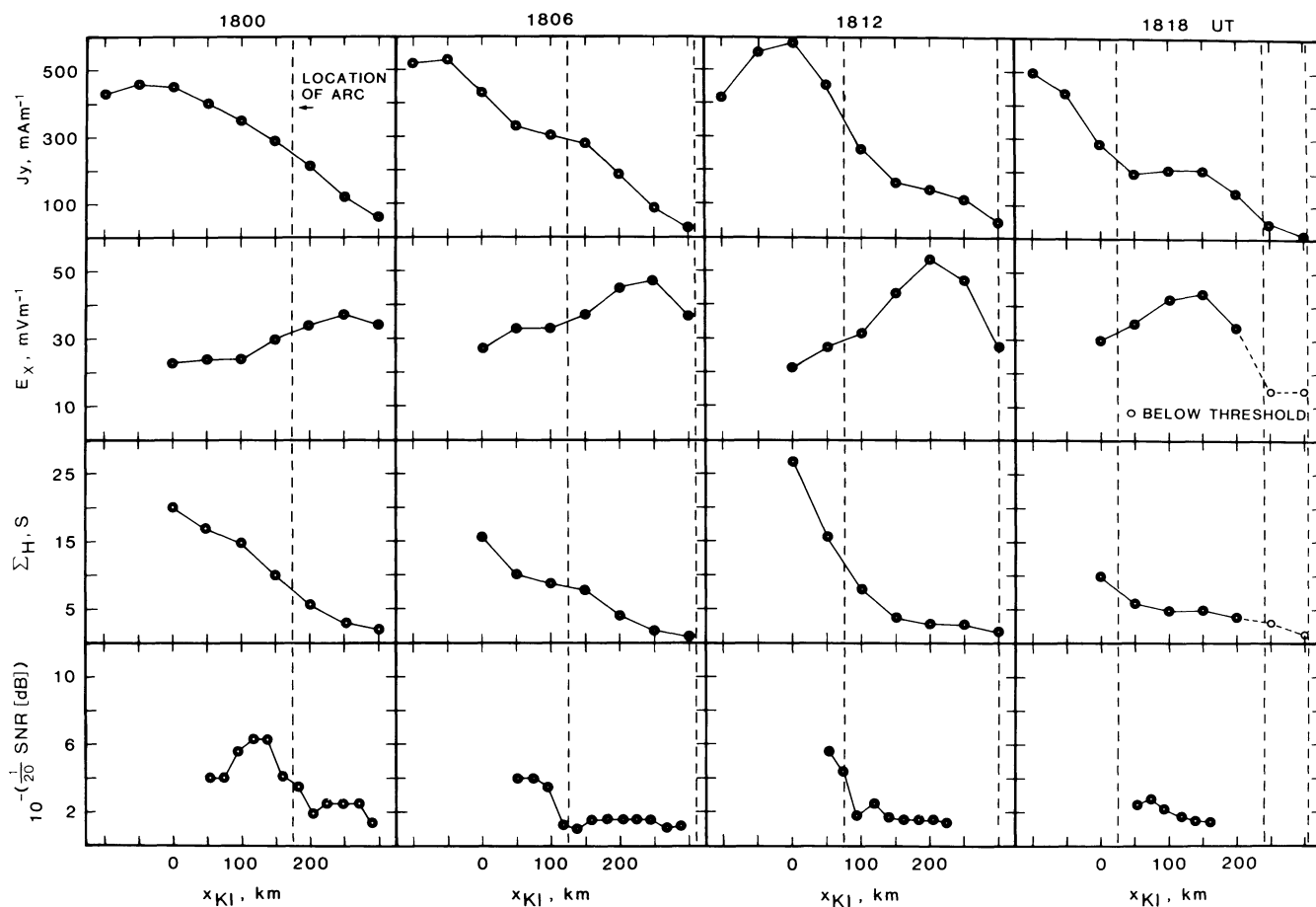


Fig. 7. Latitudinal profiles of the eastward height-integrated Hall current density perpendicular to the  $x_{KI}$  axis ( $J_y$ , upper panel), of the (northward) electric field component parallel to the  $x_{KI}$  axis ( $E_x$ , upper middle panel), of the height-integrated Hall conductivity ( $\Sigma_H$ , lower middle panel), and of the backscatter amplitude ( $1/\sqrt{\sigma_v}$ , lower panel) for 1800, 1806, 1812, and 1818 UT. The dashed vertical lines give the positions of the discrete auroral arcs

(parallel  $y_{KI}$ ) around the discrete arc is displayed in Fig. 7 together with the northward electric field component  $E_x$  (parallel  $x_{KI}$ ), the height-integrated Hall conductivity ( $\Sigma_H = J_y/E_x$ ) and the backscatter amplitude  $\sqrt{\sigma_v}$ , which is here defined as  $10^{-\text{SNR}}[\text{dB}]/20$ . The mean backscatter amplitude values were taken along a strip which runs approximately parallel with the  $x_{KI}$ -axis and where these values were smallest, i.e. where the azimuth angles  $\theta$  between the line-of-sight of the radar and the mean irregularity drift velocity vectors are around  $90^\circ$ . The longitudinal range of the strip was two degrees.

Figure 7 exhibits clearly an anticorrelation between electric field and Hall conductivity, and electric field and radar auroral amplitude, respectively. Such a feature for the eastward electrojet has recently been mentioned by Baumjohann et al. (1980). The Hall conductivity and radar amplitude profiles seem to be well correlated. As here the Hall conductivity (compared to the  $E$ -field) is a dominating factor, a similar type of correlation can, in principle, be found between radar amplitude and current density.

### Discussion

Our event shows that the current density and radar amplitude profiles in the evening sector are more closely related to the conductivity profile than to the northward electric field profile. In this context, the following facts may be mentioned:

*a* The dependence of the radar amplitude on the conductivity follows directly from the equation for the radar volume cross-section since the height-integrated Hall conductivity is approximately linearly related to the  $E_s$ -layer electron density. If we exclude those terms of the equation that are not essential for our discussion, then (see Booker, 1956; Flood, 1967)

$$\sigma_v \sim N^2 \cdot \langle \Delta N/N \rangle^2 \cdot F(\psi, \theta), \quad (1)$$

where  $\Delta N/N$  is the fractional variation in the mean electron density  $N$ , and the term on the right hand side is a function of aspect angle and azimuth angle anisotropies. Hence, Equation (1) shows that the radar amplitude,  $\sqrt{\sigma_v}$ , is proportional as well to the fractional variation in the mean electron density as also to the electron density itself.

*b* Keskinen et al. (1979) studied numerically the nonlinear evolution of large-scale type II irregularities and found the existence of a direct proportionality between electric field values and  $\langle \Delta N/N \rangle^2 >^{1/2}$  (mean effective magnitude of the fractional variation in mean electron density). In their case the radar backscatter amplitude and ionospheric current density are both controlled by the electric field values, i.e. the electron density seemed to be a factor of minor importance for the fractional density variations.

We believe that the analysis of our data in Fig. 4 clearly shows that the linear backscatter amplitude – current density relationship here is mainly due to conductivity, i.e. electron density, changes (point *a*), since our results show a clear correlation between  $\sqrt{\sigma_v}$  and  $\Sigma_H$ , while between  $\sqrt{\sigma_v}$  and  $E$  a clear anticorrelation prevails. The latter apparently has its cause in the well known anticorrelation between conductivity and electric fields (e.g. Baumjohann et al., 1980).

Since the influence of the mean electron density on the backscatter amplitudes is obvious from Equation (1) and can easily be seen in Fig. 4 and if we furthermore assume

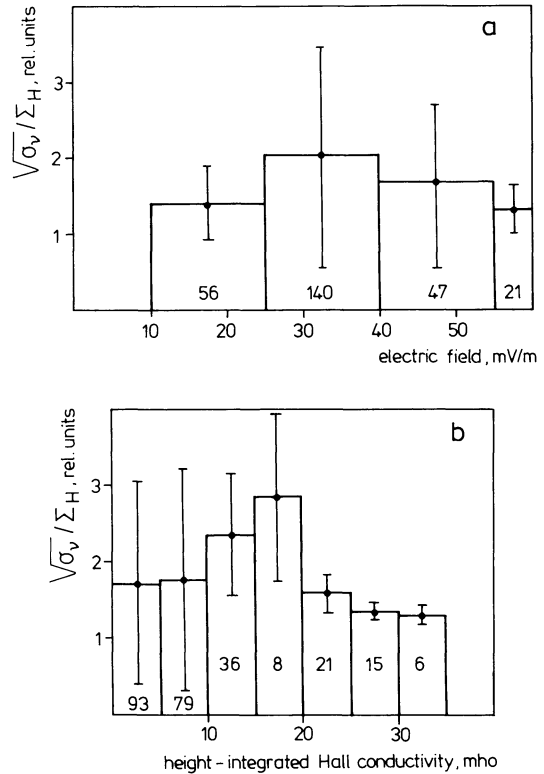


**Fig. 8a and b.** STARE backscatter amplitudes (from the Norway radar) normalized by the height-integrated Hall conductivities (electron densities) as functions of *a* electric field amplitude and *b* Hall conductivity. The bars show standard deviations and the numbers in the histogram boxes give the number of cases for the respective range of values. The backscatter amplitudes are corrected for aspect angle and slant range dependence

that  $F(\psi, \theta)$  in Equation (1) is approximately constant in our case, it remains to be checked if and how the fractional density variations are dependent on the electric field and/or the mean electron density. Since  $\langle \Delta N/N \rangle^2 >^{1/2}$  is proportional to  $\sqrt{\sigma_v}/N$  (if  $F(\psi, \theta) = \text{const.}$ ) and since  $N$  is roughly proportional to  $\Sigma_H$  we have calculated  $\sqrt{\sigma_v}/\Sigma_H$  for all samples recorded by the radar in Norway between 1800 and 1814 UT and plotted these values in the form of histograms versus electric field amplitude (Fig. 8a) and height-integrated Hall conductivity (Fig. 8b) –  $\Sigma_H$  was calculated in the same way as for Fig. 4. Fig. 8 shows rather clearly that there is at least no simple relationship between the fractional electron density variations and electric field or electron density in our case and thus the present result does not support the findings of Keskinen et al. (1979).

Our experimental results lead us to the following conclusions. If the electric field  $E(t, r)$  is constant, but the electron density varies, then  $\sqrt{\sigma_v} \sim N \sim \Sigma_H \sim I_H$ . This is in agreement with the linear relationship between the radar amplitude and current density found earlier by many authors (Greenwald et al., 1973; 1975; Siren et al., 1977; Baumjohann et al., 1978; Mareschal et al., 1979). However, if the electron density is constant but the electric field varies we have no reason to expect a linear relationship between the radar amplitude and the ionospheric current density. As a result of our analysis and experimental findings we consider the earlier experimentally found linear relationship between the radar auroral amplitude and the ionospheric current density as a special case of a more common linear relationship

of the radar auroral amplitude and the mean electron density in the backscattering region.

It is not realistic to look for an inverse relationship between the backscatter amplitude and the electric field everywhere in experimental data. In the 140 MHz frequency band the radar amplitude is determined mainly by the electron density in the echo region while for lower frequencies, e.g. 50 MHz band, the relationship may be more complicated. This may explain the differences between the present conclusions and the earlier suggested electric field dependence (Greenwald et al., 1973; 1975) which was based on radar auroral data in the 50 MHz band.

Tsunoda et al. (1976b) have suggested that in the evening sector the location of the poleward border of the 398 MHz diffuse radar aurora depends on the particle precipitation pattern. They also noted that beyond the poleward boundary of the diffuse radar aurora echoes disappeared in spite of strong electric field in this region. The authors suggested that the electron density must be very low polewards of the boundary of diffuse radar aurora. In this work we have found a similar type of meridional electron density profile, Fig. 7.

The existence of a distinct poleward boundary of diffuse radar aurora was reported by Balsley et al. (1973), Greenwald et al. (1973), (1975), Tsunoda et al. (1974), (1976a, b), Kustov et al. (1979). Our findings allow us to consider the poleward boundary of the evening diffuse radar aurora as a persistent meridional pattern in the electron density. Indeed, in the event discussed the comparison of the electric field meridional profile with the upward continued magnetic field profile (Fig. 7) allows us to conclude confidently that the reduction in amplitude of radar aurora northward of the arc, i.e. the evening radar-aurora/aurora interface, is a result of a lower ionospheric Hall conductivity poleward of the arc as compared to the Hall conductivity equatorward of the arc.

## Summary

*a* During the time prior to a substorm onset the height-integrated Hall conductivity has a distinct jump across the most equatorward auroral arc in the evening sector of the discrete auroral oval. In the event studied the conductivity decreases by a factor of 3–5 in going from the equatorward side of the arc to its poleward side.

*b* We find that the radar auroral amplitude changes proportionally to the changes in mean electron density and Hall conductivity in the regions poleward and equatorward of the arc. This occurs in regions where the *E*-field shows only minor changes.

*c* The abrupt decrease of the mean electron density on the poleward side of the most equatorward arc is the main cause of the distinct decrease in radar aurora backscatter amplitude poleward of this auroral arc.

*d* The analysis of electric fields and currents in the present event shows that there is a linear or nearly linear relationship between the 140 MHz radar amplitude ( $\sqrt{\sigma_v}$ ) and the mean electron density (*N*) (conductivity) in the backscattering region provided that the electric field values are somewhat higher than the threshold values needed for irregularity excitation.

*e* Our results suggest that the earlier experimentally found linear relationship between the radar amplitude and the ionospheric current density is a special case of the more

common relationship between the radar amplitude and the mean electron density in the backscattering region.

*Acknowledgements.* The STARE radars are operated by the Max-Planck-Institut für Aeronomie in co-operation with ELAB and the Norwegian Technical University in Trondheim and the Finnish Meteorological Institute in Helsinki. The SMA observations are made in cooperation with numerous Scandinavian institutions. We wish to thank all co-authors and all institutions and persons acknowledged in the paper by Küppers et al. (1979) for their help in obtaining the Scandinavian Magnetometer Array data.

We are greatly indebted to members of the PGI radar group G.S. Stepanov, V.M. Tolotskin and A.V. Kustov, who were involved in collecting the PGI radar data. We thank Professors M.I. Pudovkin and J. Untiedt for their kind assistance and recommendations and R. Greenwald, A.G. Yahnin and B. Inhester for useful discussions on an earlier version of the manuscript. We also wish to thank Mrs. N.I. Lomakina, E.E. Mikhailova, and N.B. Preobrazhenskaya for their assistance in the preparation of the paper.

This work was financially supported by the Deutsche Forschungsgemeinschaft (W.B.), the Max-Planck-Gesellschaft (R.P., G.S.), the Sohlberg Committee of the Finnish Scientific Society (R.P.), the Academy of Finland (K.K.), and the Finnish-Soviet committee on co-operation in science and technology (M.U., R.P., G.V.S., and K.K.).

## References

- André, D.: Radarmessungen von Plasmawellen in der polaren Ionosphäre. Dissertation Math.-Naturwiss. Fak., Georg-August-Universität, Göttingen, 1980
- Balsley, B.B., Ecklund, W.L.: A portable coaxial collinear antenna. *I.E.E.E. Ant. Prop.* **20**, 513–516, 1972
- Balsley, B.B., Ecklund, W.L., Greenwald, R.A.: VHF Doppler spectra of radar echoes associated with a visual auroral form: observation and implications. *J. Geophys. Res.* **78**, 1681–1687, 1973
- Baumjohann, W., Greenwald, R.A., Küppers, F.: Joint magnetometer array and radar backscatter observations of auroral currents in Northern Scandinavia. *J. Geophys.* **44**, 373–383, 1978
- Baumjohann, W., Sulzbacher, H., Potemra, T.A.: Joint magnetic observations of small-scale structures in a westward electrojet with Triad and the Scandinavian Magnetometer Array. In: *Proceeding of the International Workshop on Selected Topics of Magnetospheric Physics*, Japanese IMS Committee, ed., pp. 49–52, Tokyo, 1979
- Baumjohann, W., Untiedt, J., Greenwald, R.A.: Joint two-dimensional observations of ground magnetic and ionospheric electric fields associated with auroral zone currents. 1. Three-dimensional current flows associated with a substorm-intensified eastward electrojet. *J. Geophys. Res.* **85**, 1963–1978, 1980
- Booker, H.G.: A theory of scattering by nonisotropic irregularities with application to the radar reflections from the aurora. *J. Atmos. Terr. Phys.* **8**, 204–221, 1956
- Cahill, L.J. Jr., Greenwald, R.A., Nielsen, E.: Auroral radar and rocket double-probe observations of the electric field across the Harang discontinuity. *Geophys. Res. Lett.* **5**, 687–690, 1978
- Chestnut, W.: Low frequency waves and irregularities in the auroral ionosphere as determined by radar measurements. In: *Low frequency waves and irregularities in the ionosphere*, N. D'Angelo, ed., pp. 173–191. Dordrecht: D. Reidel 1968
- Flood, F.A.: A brief review of auroral backscatter theory. In: *Aurora and Airglow*, B.M. McCormack, ed., pp. 563–571. New York: Reinhold 1967
- Greenwald, R.A., Ecklund, W.L., Balsley, B.B.: Auroral current, irregularities, and luminosity. *J. Geophys. Res.* **78**, 8193–8203, 1973
- Greenwald, R.A., Ecklund W.L., Balsley, B.B.: Radar observation of auroral electrojet currents. *J. Geophys. Res.* **80**, 3635–3641, 1975

- Greenwald, R.A., Weiss, W., Nielsen, E., Thomson, N.R.: STARE: a new radar auroral backscatter experiment in Northern Scandinavia. *Radio Sci.* **13**, 1021–1039, 1978
- Greenwald, R.A.: Studies of currents and electric fields in the auroral zone ionosphere using radar auroral backscatter. In: *Dynamics of the magnetosphere*, S.-I. Akasofu, ed., pp. 213–248. Dordrecht: D. Reidel 1979
- Gustafsson, G.: A revised corrected geomagnetic coordinate system. *Ark. Geofys.* **5**, 595–617, 1970
- Kamide, Y., Brekke, A.: Altitude of the eastward and westward auroral electrojets. *J. Geophys. Res.* **82**, 2851–2853, 1977
- Keskinen, M.J., Sudan, R.N., Ferch, R.L.: Temporal and spatial power spectrum studies of numerical simulation of type II gradient drift irregularities in the equatorial electrojet. *J. Geophys. Res.* **84**, 1419–1430, 1979
- Küppers, F., Untiedt, J., Baumjohann, W., Lange, K., Jones, A.G.: A two-dimensional magnetometer array for ground-based observations of auroral zone electric currents during the International Magnetospheric Study (IMS). *J. Geophys. Res.* **46**, 423–450, 1979
- Kustov, A.V., Pudovkina, E.V., Starkov, G.V., Stepanov, G.S., Suhoivanenko, P.Ya., Uspensky, M.V.: Aurora and radioaurora observations on Feb. 3 and 8, March 15 and 16, 1978 in the framework “Auroral Breakup Campaign”. In: *Auroral Breakup Experiment*, O.M. Raspopov, ed., pp. 3–21. Apatity, 1979 (in Russian)
- Lui, A.T.Y., Anger, C.D.: A uniform belt of diffuse auroral emission seen by the ISIS-2 scanning photometer. *Planet Space Sci.* **21**, 799–809, 1973
- Lui, A.T.Y., Perreault, P., Akasofu, S.-I., Anger, C.D.: The diffuse aurora. *Planet. Space Sci.* **21**, 857–861, 1973
- Lui, A.T.Y., Venkatesan, D., Anger, C.D., Akasofu, S.-I., Heikkila, W.J., Winningham, J.D., Burrows, J.R.: Simultaneous observations of particle precipitations and auroral emissions by the ISIS-2 satellite in the 19–24 MLT sector. *J. Geophys. Res.* **82**, 2210–2226, 1977
- Mareschal, M., McDiarmid, D.R., McNamara, A.G.: Some properties of diffuse radio aurora at high aspect angles. *J. Geophys. Res.* **84**, 6687–6690, 1979
- Mersmann, U., Baumjohann, W., Küppers, F., Lange, K.: Analysis of an eastward electrojet by means of upward continuation of ground-based magnetometer data. *J. Geophys. Res.* **45**, 281–298, 1979
- Moorcroft, D.R.: Dependence of radioaurora at 389 MHz on electron density and electric field. *Can. J. Phys.* **57**, 687–697, 1979
- Pyatsi, A.Kh.: Auroral radiowave scattering. Radar aurora. In: *High-latitude geophysical phenomena*, B.E. Brunelli, ed., pp. 260–298. Leningrad: Nauka 1974 (in Russian)
- Siren, J.C., Doupnik, J.R., Ecklund, W.L.: A comparison of auroral currents measured by the Chananika radar with 50 MHz backscatter observed from Anchorage. *J. Geophys. Res.* **82**, 3577–3584, 1977
- Starkov, G.V., Raspopov, O.M., Uspensky, M.V.: Pre-breakup fading of radioaurora. In: *Auroral Breakup Experiment*, O.M. Raspopov, ed., pp. 21–38. Apatity, 1979 (in Russian)
- Sudan, R.N., Akinrimisi, J., Farley, D.T.: Generation of small-scale irregularities in the equatorial electrojet. *J. Geophys. Res.* **78**, 240–248, 1973
- Sulzbacher, H., Baumjohann, W., Potemra, T.A.: Coordinated magnetic observations of morning sector auroral zone currents with Triad and the Scandinavian Magnetometer Array: a case study. *J. Geophys. Res.* **48**, 7–17, 1980
- Tsunoda, R.T., Presnell, R.I., Leadabrand, R.L.: Radar auroral echo characteristics as seen by 398 MHz phased array radar operated at Homer, Alaska. *J. Geophys. Res.* **79**, 4709–4724, 1974
- Tsunoda, R.T., Presnell, R.I.: On a threshold electric field associated with the 398-MHz diffuse radar aurora. *J. Geophys. Res.* **81**, 88–96, 1976
- Tsunoda, R.T., Presnell, R.I., Kamide, Y., Akasofu, S.-I.: Relationship of radar aurora, visual aurora and auroral electrojets in the evening sector. *J. Geophys. Res.* **81**, 6005–6015, 1976a
- Tsunoda, R.T., Presnell, R.I., Potemra, T.A.: The spatial relationship between the evening radar aurora and field-aligned current. *J. Geophys. Res.* **81**, 3791–3802, 1976b
- Unwin, R.S., Keys, J.G.: Characteristics of the radio aurora during expansive phase of polar substorms. *J. Atmos. Terr. Phys.* **37**, 55–64, 1975
- Uspensky, M.V.: Luminosity, radar aurora and ionospheric electrojet structure. In: *Structure of magnetic, ionospheric and auroral disturbances*, G.A. Loginov, ed., pp. 3–24. Leningrad: Nauka 1977 (in Russian)
- Val’chuk, T.E., Gal’perin, Yu.I., Crasnier, J., Nikolaenko, L.M., Sauvaud, J.-A., Feldstein, Ya.I.: Diffuse auroral zone. IV The latitude signature of auroral particle precipitations into ionosphere and the plasma sheath structure. *Cosmitsh. Issledovaniya*. XVII, 559–578, 1979 (in Russian)

Received February 8, 1982; Revised version September 22, 1982  
Accepted September 23, 1982

# On the Dependence of Radar Aurora Amplitude on Ionospheric Electron Density

G.V. Starkov<sup>1</sup>, J. Oksman<sup>2</sup>, M.V. Uspensky<sup>1</sup>, and A.V. Kustov<sup>1</sup>

<sup>1</sup> Polar Geophysical Institute, Vladimirskaia 17, 183023 Murmansk, USSR

<sup>2</sup> University of Oulu, Dept. of Electrical Engineering, Linnanmaa, SF-90570 Oulu 57, Finland

**Abstract.** Radar aurora amplitudes have been correlated with mean electron density measurements by means of ionosondes during two geophysically widely different events. A similar, roughly linear relationship was found between the two quantities in both cases. On the other hand, the amplitude seems to be almost independent of the ambient electric field, once it is well above the instability threshold.

**Key words:** Radar aurora amplitude – Electron density.

## Introduction

Greenwald et al. (1973) found a linear relationship between the 50 MHz auroral backscatter amplitude and ionospheric current density in the backscattering region. Subsequent papers (Gray and Ecklund, 1974; Greenwald et al., 1975; Siren et al., 1977; Baumjohann et al., 1978; Mareschal et al., 1979), where an appreciable data set was used, confirmed this linear relationship in general but Greenwald et al. (1975) found that sometimes it breaks down. The reason for such a linear relationship is, on the whole, not clear; Greenwald (1979) has used the findings of Sudan and Keskinen (1979) as an explanation: for rather large-scale gradient-drift irregularities a linear relationship may exist between irregularity amplitudes and the ambient ionospheric electric field. On the other hand, André (1980) found experimentally, for the 140 MHz band, an inverse relationship between radar auroral amplitude and electric field when the latter was well above the instability threshold.

Recently, Starkov et al. (1980) and Uspensky et al. (1982) have suggested that the experimentally found linear relationship between radar amplitude and ionospheric current density, quoted above, is a special case of a more common relationship between radar amplitude and mean electron density in the backscattering region. The present paper aims at checking this result.

We start from the equation for the effective volume cross-section for radar wave backscattering from the ionosphere (Booker, 1956; Flood, 1967; Farley, 1971). The essential part of this equation is:

$$\sigma_v \sim N^2 \langle (\Delta N/N)^2 \rangle F(\psi, \theta) \quad (1)$$

where  $N$  = mean electron density in the backscattering region,  
 $\langle (\Delta N/N)^2 \rangle$  = mean square of relative small-scale spatial

electron density fluctuations,  $\Delta N(2k)$ ,  $k$  = wave vector,  $F(\psi, \theta)$  = normalized aspect angle and azimuth angle anisotropy function (radar aspect angle = angle between the geomagnetic field line and the radio ray; azimuth angle = angle between the mean irregularity drift velocity and the radio ray).

The RHS of Eq. (1) is the three-dimensional spatial power spectrum of the electron density fluctuations. The anisotropy function depends on the geometry of scattering only. If its variation is small (or is constant),  $\sigma_v$  depends mainly on the first two terms, viz.  $N^2$  and  $\langle (\Delta N/N)^2 \rangle$ .

Uspensky et al. (1982) have found in one event a rather weak dependence between the small-scale electron density fluctuations  $\langle \Delta N/N \rangle^{1/2}$  and the  $E$  field above instability threshold and suggest that the radar amplitude is mostly controlled by ionospheric electron density. To answer the question of whether this is more generally the case we study below two events where the electron density could be determined by ionosonde measurements. The auroral radar data are from STARE (Scandinavian Twin Auroral Radar Experiment); we have used results from the Finnish STARE station at Hankasalmi.

## Observations

11 December 1977

This event has been studied in detail by André (1980). The STARE amplitudes, as seen by the Finnish radar, are shown in Fig. 1; these have been taken from André's paper. The data were obtained in a region 100 km × 100 km, with its southern border located about 50 km north of Tromsø. We have included in Fig. 1 the STARE  $E$ -fields; the shaded stripe depicts the  $E$ -field threshold for instability (15–20 mV/m) (Siren et al., 1977; Cahill et al., 1978; Moorcroft, 1979), and we see that the  $E$ -field was well above the threshold during the whole event.

For this event the azimuth angle varies between 100 and 120 degrees. If we assume that the azimuth-dependence of radar amplitude obeys approximately the equation, found from experimental statistics (André, 1980),

$$F(\theta, \psi \approx 0) = 10(1 + \cos 2\theta) \text{ dB} \quad (2)$$

then in the above-mentioned azimuth range the  $F(\theta, \psi)$  variations would be about 4.4 dB or approximately the same as the scatter of radar amplitude values in Fig. 1a, i.e. influence of azimuth angle variations on radar ampli-

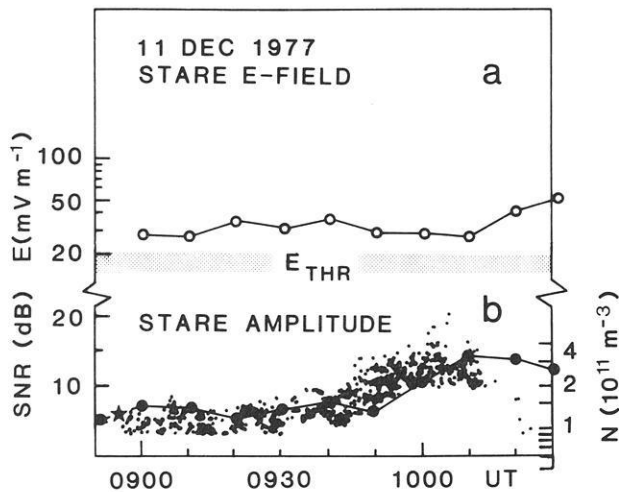


**Fig. 1 a and b.** Data for the event 11 Dec 1977: **a** STARE  $E$  field magnitude, **b** STARE backscatter amplitude from the Finnish radar (scattered small dots), as well as the electron density from the MMK ionosonde (heavy dots) and from the TRO ionosonde (star)

ude in this case would be rather weak; probably it is even smaller than given by Eq. (2), as during rapid variations of the azimuth angle around 0900–0915 and 0935 UT the amplitude changes are rather small.

The influence of the aspect angle anisotropy  $F(\psi, \theta \approx \pi/2)$  is also small because in the limited area in question the aspect angle is small and approximately constant. Thus, in what follows, we can concentrate on the first two terms on the RHS of Eq. (1) only.

Sudan and Keskinen (1979) and Greenwald (1979) have come to the conclusion that the effective mean electron density variations are linearly related to the ionospheric  $E$  field. Our data in Fig. 1 disagree with this conclusion, since there seems rather to be an anticorrelation between the  $E$ -field and radar amplitude variations. Thus it seems to us that, for over-threshold  $E$ -fields, variations in  $N$  and  $\theta$  can explain the main part of radar amplitude variations.

We have checked this assumption by using ionosonde data. The ionosonde in Tromsø (geographic coordinates  $69.7^\circ$  N,  $19.0^\circ$  E) was measuring near the backscatter region ( $70.0$ – $71.0^\circ$  N,  $18.0$ – $20.0^\circ$  E). Unfortunately, only one sounding was made per hour, and at 0955 UT no numerical value for  $f_b E_s$  (a measure of the electron density in the  $E$  region) was obtained due to the lacuna phenomenon (a gap in the ionogram trace). At 0855 UT  $f_b E_s = 3.1$  MHz.

The ionosonde at Murmansk ( $69.0^\circ$  N,  $33.0^\circ$  E) was sounding every 10 min. At 0900 UT Murmansk obtained the value of 3.0 MHz for  $f_b E_s$ , i.e. about the same value as at Tromsø 5 minutes earlier. It seems to us that the  $E_s$  layer had, in this case, about the same density above both stations, and we assume that the same condition prevailed during the next hour.

The electron density values, obtained from ionosonde data, have been added to Fig. 1 (Murmansk = heavy dots, Tromsø = a star). The same logarithmic scale was used for  $N$  as for radar amplitude, the  $N$  curve being shifted along the vertical axis for best possible fit with the intensity.

Radar amplitude and electron density are seen to exhibit fairly similar temporal variations. The increase around 0940 in both curves is particularly conspicuous (though a

time shift of about 5 minutes is seen, possibly caused by the spatial separation of Murmansk from Tromsø area. Approximately the same time shift was seen in the signature of backscatter appearance over Tromsø and Murmansk, as recorded by radars of the Polar Geophysical Institute).

We may conclude that a satisfactory agreement exists during this event between backscatter amplitude and electron density in the backscattering region, irrespective of variations of the electric field, once it is above the instability threshold.

#### 16 March 1978

This event was observed around three months later than the previous one. The technical characteristics of the Finnish radar were approximately the same as before; thus we are able to compare quantitatively the two independent and geophysically different events. (Note that the first event was observed in the morning sector when the ionosphere was sunlit, the second one in the growth phase of a substorm in the premidnight sector.)

The geophysical situation for the 16 March event has been described by Kustov et al. (1979) and Uspensky et al. (1982). The substorm was in the growth phase at 1756–1830 UT. In the STARE viewing area a stable and almost unstructured eastward current flow was observed. The most equatorward auroral arc in this area moved equatorward for an unusually long time. Equatorward of this arc diffuse luminosity existed. The current density on the equatorward side of the arc was 3–5 times higher than on the poleward side. The local breakup over the STARE viewing area occurred at 1833–1835 UT.

In the interval 1755–1830 UT we have data from five ionosondes: Tromsø (TRO), Kiruna (KIR) ( $67.8^\circ$  N,  $20.4^\circ$  E), Sodankylä (SOD) ( $67.4^\circ$  N,  $26.6^\circ$  E) Murmansk (MMK) and Loparskaya (LPY) ( $68.6^\circ$  N,  $33.0^\circ$  E). The TRO and KIR ionosondes were measuring immediately under the STARE viewing area and 30 km south of it, respectively, making one sounding per hour. The SOD ionosonde was located around 70 km east of the eastern border of STARE viewing area and measured once every 30 minutes. The MMK and LPY ionosondes were measuring about 320 km to the east of SOD every 15 minutes.

During the time interval (35 minutes) used here, a homogeneous current flow has been deduced from the SMA (Scandinavian Magnetometer Array) data (Uspensky et al., 1982). The electron density was fairly uniform in the whole longitudinal range of ionosonde measurements. For example, at 1800 UT  $f_b E_s$  was 4.6 MHz at LPY and  $f_o E_s$  4.5 MHz at KIR and 5.3 MHz at SOD. (On the two last stations, no F-layer trace was seen, therefore  $f_b E_s$  could not be scaled,  $f_o E_s$  being the upper limit for  $f_b E_s$ , the lower limit being about 0.7 MHz less.) So, we think that we can project SOD, MMK and LPY ionosondes along the auroral arc into the STARE viewing area.

#### Both Events

In Fig. 2 we show data for both events together. The main aim of the picture is to show the quite satisfactory agreement between the absolute values of the electron densities and the radar aurora amplitudes in the two different sets of data. A dashed line has been added to the figure, depicting an assumed linear dependence between electron density

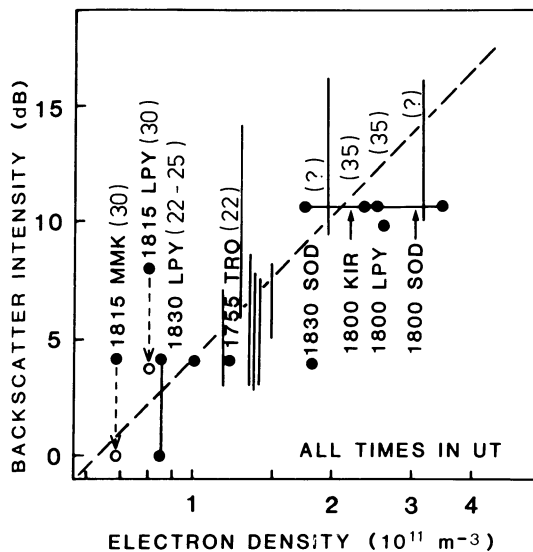


Fig. 2. Backscatter amplitude vs. electron density plot for 11 Dec 1977 and 16 March 1978 data. The scatter ranges of December data are shown by means of thin vertical lines, the March data are shown by means of heavy dots with the time of measurement and the abbreviated name of the ionosonde station. Where necessary, the backscatter amplitude for March data has been corrected for azimuth dependence to correspond to the azimuth angle  $90^\circ$ . The estimated standard deviations for March 16 data are  $\pm 2$  dB in SNR and 10% in  $N$ . The numbers in parantheses give the electric field intensity (in  $\text{mV m}^{-1}$ ) for the respective measurements

and backscatter amplitude. For the location of the March points, the following explanations are necessary:

At 1755 UT  $N$  was  $1.2 \times 10^{11} \text{ m}^{-3}$  at TRO. The backscatter amplitude measured by the Finnish STARE radar just above the ionosonde was 8 dB. The azimuth angle of the mean irregularity drift velocity was  $\theta = 117^\circ$ , thus the azimuth angle correction is 4 dB (Eq. 2) and the corrected value (for  $\theta = 90^\circ$ ) 4 dB.

For LPY  $N$  was  $2.8 \times 10^{11} \text{ m}^{-3}$  at 1800 UT. By projecting LPY parallel to the arc we found a minimum SNR = 8–12 dB. No azimuth correction is necessary in this case, because these values were obtained at about  $\theta = 90^\circ$ . We have plotted the mean of 8 and 12 dB, i.e. 10 dB.

For KIR  $N$  was  $(1.8\text{--}2.5) \times 10^{11} \text{ m}^{-3}$ , and the backscatter SNR = 12 dB for the nearest point to KIR. The azimuth angle there is circa  $75^\circ$ , and the SNR, corrected for azimuth dependence, 10.7 dB. We have estimated the same SNR for SOD, the projection of which lies a little more to the south of the viewing area of STARE than that of KIR; the corresponding  $N = (2.8\text{--}3.5) \times 10^{11} \text{ m}^{-3}$ . We have indicated in Fig. 2 for SOD and KIR the possible ranges of  $N$ , caused by the uncertainty in  $f_p E_s$ , by means of a horizontal bar.

At 1815 UT LPY and MMK were located 50–80 km poleward of the arc. Both ionosondes observed the  $E_s$ -layer electron density to decrease (to  $0.8 \times 10^{11}$  and  $0.7 \times 10^{11} \text{ m}^{-3}$ , respectively). For the MMK ionosonde the projection gives the SNR of 4 dB, for LPY that of 8 dB. The latter value in particular is somewhat higher than expected. We explain these high values as follows:

Around 1813–1814 UT a sudden, short-lived increase in SNR occurred poleward of the arc. This increase was seen by the Finnish STARE radar and also by the Polar Geophysical Institute 46 MHz PPI radar at Essoyla. Also

LPY all-sky data seem to show a short-lived, localized diffuse luminosity in this area around the same time. Thus we conclude that at 1815 UT the possibility of projecting ionospheric data along the arc temporarily breaks down and that the SNR's obtained by projection have to be reduced. We have indicated this fact in Fig. 2 by moving the MMK and LPY values for 1815 UT downward by 4 dB to correspond to SNR-values just before and after the temporary disturbance (4 dB is the gradation in SNR used in our set of data).

At 1830 UT  $N$  was  $1.8 \times 10^{11} \text{ m}^{-3}$  for SOD and  $0.85 \times 10^{11} \text{ m}^{-3}$  for LPY. The minimum SNR value for the SOD projection was 4 dB, that for LPY was smaller because the backscatter disappeared. This is why we have indicated for LPY the SNR interval 0–4 dB.

## Discussion

In the two events studied here the variations of backscatter amplitude can very satisfactorily be explained by variations of electron density in the backscattering region. In addition, as seen in Fig. 2, the two events yield, in spite of the very different geophysical conditions, approximately the same linear dependence between these quantities and a good mutual agreement in absolute values (within the bounds of the long-term stability of radar characteristics). On the other hand, as we have shown here for the 11 December 1977 event and as has been shown by Uspensky et al. (1982) for the 16 March 1978 event, the amplitudes seem to be nearly independent of the  $E$ -field, once it is above the instability threshold.

Uspensky et al. (1982) suggest that the linear relationship found earlier between radar amplitude and ionospheric current density (Greenwald et al., 1973; Greenwald et al., 1975; Siren et al., 1977; Baumjohann et al., 1978; Mareschal et al., 1979) is a special case of the more general relationship between radar amplitude and mean electron density. Our result seems to be in quite satisfactory agreement with this suggestion. It should be noted also that Haldoupis (1981) has suggested that Pi2-variations of radar auroral amplitudes most likely are due to conductivity modifications because the former did not coincide with electric field variations.

The small dependence (or independence) of the backscatter amplitude on the ionospheric  $E$ -field may be a result of nonlinear saturation of the growth of plasma instabilities. Some attempts to develop quasi-linear and non-linear theories which are able to explain a saturation of the Farley-Buneman instability have been made e.g. by Kamenetskaya (1971), Weinstock and Sleeper (1972), Sato (1972, 1976, 1977), Rogister and Jamin (1975), Volosevich and Liperovsky (1979) and Volosevich et al. (1979). A more extensive description of this problem can be found in the recent review by Fejer and Kelley (1980). We do not attempt to discuss the results of these papers in detail here but we conclude that it is difficult to apply quasi-linear mechanisms in our study. As to non-linear theories, Volosevich et al. (1979) have found that for waves with fixed mutual phases a linear  $E$ -field dependence exists, but in the random phase case the question is unresolved (Rogister and Jamin, 1975; Volosevich and Liperovsky, 1979). Thus we conclude that the question of the dependence of spatial electron density variations on the ionospheric  $E$ -field (for irregularities of one-meter scale or shorter) remains open.

It seems to us that possibilities exist to determine, with some accuracy, the ionospheric electron density from auroral backscatter amplitudes, at least in the 140 MHz band. At any rate, our results obtained for aspect angles near  $90^\circ$  and for azimuth angles deviating less than  $30^\circ$  from perpendicularity point in this direction.

*Acknowledgments.* The authors are indebted to Dr. R. Greenwald and Dr. E. Nielsen for STARE data, to Professor E. Leer for TRO ionosonde data, to Dr. T. Turunen for SOD ionosonde data and useful discussions, to Dr. G. Gustafsson for KIR ionosonde data and to Mrs. R. Kukushkina and Mrs. N. Schul'gina for MMK and LPY ionosonde data. This work was financially supported by the Finnish Soviet Committee on cooperation in science and technology (G.S., J.O., M.U.).

## References

- André, D.: Radarmessungen von Plasmawellen in der polaren Ionosphäre. Diss. Georg-August-Universität zu Göttingen, Göttingen, 78 p., 1980
- Baumjohann, W., Greenwald, R.A., Küppers, F.: Joint magnetometer array and radar backscatter observations of auroral currents in Northern Scandinavia. *J. Geophys. Res.* **44**, 373–383, 1978
- Booker, H.G.: A theory of scattering by nonisotropic irregularities with application to the radar reflections from the aurora. *J. Atmos. Terr. Phys.* **8**, 204–221, 1956
- Cahill, L.J. Jr., Greenwald, R.A., Nielsen, E.: Auroral radar and rocket double-probe observations of the electric field across the Harang discontinuity. *Geophys. Res. Lett.* **5**, 687–690, 1978
- Farley, D.T.: Radio wave scattering from the ionosphere. In: *Methods of Experimental Physics, Plasma Physics, part B*, **9**, R.H. Liouberg and H.R. Griem, eds., pp. 135–186. Academic Press 1971
- Flood, W.A.: A brief review of auroral backscatter theory. In: *Aurora and Airglow*, B.M. McCormack, ed., 563–571, New York: Reinhold 1967
- Fejer, B.G., Kelley, M.C.: Ionospheric irregularities. *Rev. Geophys. Space Phys.* **18**, 401–454, 1980
- Gray, A.M., Ecklund, W.L.: The Anchorage Alaska real time auroral radar monitor: System description and some preliminary analyses. NOAA Tech. Rep. EPL 306-AL 9, Nat. Oceanic and Atmos. Admin., Boulder, Colorado, 1974
- Greenwald, R.A., Ecklund, W.L., Balsley, B.B.: Auroral current, irregularities, and luminosity. *J. Geophys. Res.* **78**, 8193–8203, 1973
- Greenwald, R.A., Ecklund, W.L., Balsley, B.B.: Radar observations of auroral electrojet currents. *J. Geophys. Res.* **80**, 3635–3641, 1975
- Greenwald, R.A.: Studies of currents and electric fields in the auroral zone ionosphere using radar auroral backscatter. In: *Dynamics of the magnetosphere*, S.-I. Akasofu, ed., pp. 213–248. Dordrecht: D. Reidel 1979
- Haldoupis, C.: Results based on a correlative study of geomagnetic and radio auroral observations. Report 81–19, 1–16, University of Oslo, 1981
- Kustov, A.V., Pudovkina, E.V., Starkov, G.V., Stepanov, G.S., Suhoivanenko, P.Ya., Uspensky, M.V.: Aurora and radioaurora observations on Feb. 3 and 8, March 15 and 16, 1978 in the framework of the “Auroral Breakup Campaign”. In: *Auroral Breakup Experiment*, O.M. Raspopov, ed., pp. 3–21. Apatity 1979 (in Russian)
- Kamenetskaya, G.Kh.: Quasi-linear theory for the formation of inhomogeneities in the equatorial electrojet. *Geomagn. Aeronomy* **11**, 71–75, 1971
- Mareschal, M., McDiarmid, D.R., McNamara, A.G.: Some properties of diffuse radio aurora at high aspect angles. *J. Geophys. Res.* **84**, 6687–6690, 1979
- Moorcroft, D.R.: Dependence of radioaurora at 398 MHz on electron density and electric field. *Can. J. Phys.* **57**, 687–697, 1979
- Register, A., Jamin, E.: Two-dimensional nonlinear processes associated with “Type 1” irregularities in the equatorial electrojet. *J. Geophys. Res.* **80**, 1820–1828, 1975
- Sato, T.: Stabilization of the two-stream instability in the equatorial electrojet. *Phys. Rev. Lett.* **28**, 732–734, 1972
- Sato, T.: On mechanisms governing the electrojet plasma instabilities. *J. Geophys. Res.* **81**, 539–546, 1976
- Sato, T.: Auroral and equatorial two-stream irregularities: Difference in nonlinear state. *J. Geophys. Res.* **82**, 5195–5200, 1977
- Siren, J.C., Doupnik, J.R., Ecklund, W.L.: A comparison of auroral currents measured by Chatanika radar with 50 MHz backscatter observed from Anchorage. *J. Geophys. Res.* **82**, 3577–3584, 1977
- Starkov, G.V., Uspensky, M.V., Kaila, K.U., Pellinen, R.J., Greenwald, R.A., Nielsen, E., Sofko, G.: Ionospheric conductivity in eastward current flow and radar auroral amplitudes. In: *Auroral substorm structure*, M.V. Uspensky, ed., pp. 126–151. Apatity 1980 (in Russian)
- Sudan, R.N., Keskinen, M.J.: Theory of strongly turbulent two-dimensional convection of low pressure plasma. *Phys. Fluids* **22**, 2305–2314, 1979
- Uspensky, M.V., Pellinen, R.J., Baumjohann, W., Starkov, G.V., Nielsen, E., Sofko, G., Kaila, K.U.: Spatial variations of ionospheric conductivity and radar auroral intensity in the region of eastward electrojet during presubstorm conditions. *J. Geophys.*, in press 1982
- Volosevich, A.V., and Liperovsky, V.A.: On a decay interaction for the Farley-Buneman waves in the polar ionosphere. In: *High latitudinal manifestations of magnetospheric processes*, S.I. Isaev, ed., pp. 39–49. Moscow: Nauka 1979 (in Russian)
- Volosevich, A.V., Livshits, M.A., Liperovsky, V.A.: Nonlinear decay interaction for the instability of Buneman – Farley. *J. Physique* **40**, Supplement N7, 623, 1979
- Weinstock, J., Sleeper, A.M.: Nonlinear saturation of “Type 1” irregularities in the equatorial electrojet. *J. Geophys. Res.* **77**, 3621–3629, 1972

Received February 8, 1982; Revised version September 20, 1982

Accepted September 24, 1982

# A Possibility to Distinguish Between Ionospheric and Magnetospheric Origin of Low Latitude Magnetic Perturbations

I. Papamastorakis<sup>1</sup> and G. Haerendel<sup>2</sup>

<sup>1</sup> University of Crete, Iraklion, Greece

<sup>2</sup> Max-Planck-Institut für Physik und Astrophysik, Institut für extraterrestrische Physik, 8046 Garching, Federal Republic of Germany

**Abstract.** The ratio of  $\Delta Z$  and  $\Delta H$  for short period magnetic variations as observed at the Southern Indian station Annamalaiagar can be used to distinguish contributions from primary currents flowing in the ionosphere from those flowing in the magnetosphere. The signature of an ionospheric source is  $\Delta Z=0$ . Correlation coefficients for  $\Delta Z$  and  $\Delta H$  are given for Annamalaiagar and Trivandrum for pure perturbations of either kind. They can be used to separate the source fields in mixed ionospheric/magnetospheric events. The quality of such a separation is demonstrated and examples of simple applications both to individual events and statistical material are given.

**Key words:** Annamalaiagar – Trivandrum – Coast effect – Sources of magnetic variations

## Introduction

The separation of geomagnetic perturbations observed on the ground into external and internal contributions has been a subject of great interest since the pioneering work of Gauss (1839) and Schuster (1889). They recognized that the magnetic variations were due to externally flowing currents with contributions from earth currents induced by the former. The non-uniform distribution of electrical conductivity in the outer layers of the crust, i.e. in and under the oceans and under the continents, creates quite complex paths of the induced earth currents and leads to characteristic responses of the horizontal and vertical components of the variation field. Far inland, the vertical component is normally small, except near conductivity anomalies or close to concentrations of the primary currents, like the auroral or equatorial electrojets. However, as one approaches a coast, one finds an increasing value of the vertical ( $Z$ -) component. The variation vector tends to lie in a plane that is inclined with respect to the horizontal. Wiese (1962) and Parkinson (1964) studied the orientation of this plane, whose normal vector points towards the better conductor and thus indicates where the induced earth currents tend to be concentrated. Much work on this effect has been done subsequently by various authors. A recent review has been given by Parkinson and Jones (1979).

Beyond separating the external and internal contributions to the magnetic variations observed on the ground, it is desirable to further distinguish for the external sources between currents located in the *ionosphere* and in the higher

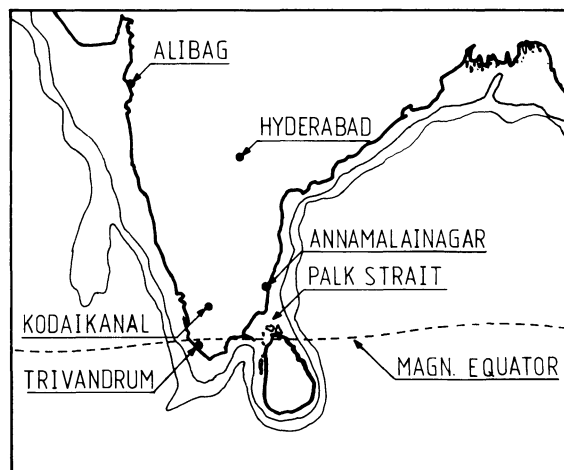


Fig. 1. Location of magnetic observatories in Southern India

*magnetosphere*. This is obviously possible with the aid of low orbiting satellites. In particular, the identification of field-aligned currents has been achieved by Zmuda et al. (1970) and Iijima and Potemra (1976) with data from polar orbiting satellites. A rich literature emerged from this technique.

In spite of the availability and great significance of such satellite data, there remains much interest in possibilities of separating magnetospheric from ionospheric contributions to the primary fields from the study of ground-based measurements alone. For high latitudes this has been undertaken by Hughes and Rostoker (1979) and Baumjohann et al. (1980) by using essentially the latitudinal profile of the  $D$ -component across the auroral oval.

Even with data from only one ground station a separation of the ionospheric and magnetospheric contributions may be successfully achieved. This possibility arises near the geomagnetic equator where the ionospheric current is heavily concentrated in the so-called Equatorial Electrojet (EEJ), in contrast to a much smoother latitudinal profile of any magnetospheric current. The distribution of eddy currents in the highly conducting oceans and ocean floors is affected by the latitudinal distribution of the primary currents and consequently leads to different ratios of the vertical and horizontal variation fields near the coastline. Papamastorakis and Haerendel (1974) noticed that the South Indian station Annamalaiagar (Fig. 1) happens to

be in a position where pure ionospheric currents of short periods ( $\approx 1$  h) lead to zero response in the  $Z$ -component, whereas magnetospheric currents create non-vanishing values of  $Z$ .

Various aspects of this effect formed the subject of the thesis of Papamastorakis (1975). Its essential results will be summarized in this and two accompanying papers. The present paper will elaborate the effect on the basis of observed short-period variations. After giving a quantitative description of the separation method, we will demonstrate the applicability of the method both to complex individual perturbations and to statistical material of SSC-type variations. Paper II (Papamastorakis and Haerendel, 1983) deals with an analogue model simulating the effect and lending credibility to our interpretation. A third paper will concentrate on actual geophysical applications, namely the separation of the ionospheric and magnetospheric currents for perturbations of the storm sudden commencement (SSC) and DP2 types.

### Anomalous Coast Effect at Annamalainagar

The coast effect consists generally of an amplification of the  $Z$ -component of magnetic variations over the value expected from the primary current. It is, however, possible to find locations where for certain types of variations the  $Z$ -component shows zero response. This is observed at Annamalainagar. Figures 2 and 3 show two examples in comparison with the readings at Trivandrum. One notices that even great excursions of  $H$  with periods of the order of 1 h are not accompanied by similarly structured excursions of  $Z$ . This applies mainly to daytime perturbations. At night, the behaviour is completely different. Every little ex-

cursion, even with amplitudes as low as  $2\gamma$  in  $H$ , are clearly seen in  $Z$ . Further, during daytime, by looking first at the  $Z$ -component one is able to find many (normally smaller) perturbations that also appear in  $H$ , but the dominant structure of daytime variations is without counterpart in  $Z$ . At Trivandrum, the situation is quite uniform,  $Z$  and  $H$  are exhibiting a classical coast effect.

The behavior of the  $Z$ -component observed at Annamalainagar is not unique. Kodaikanal is very similar, as can be seen in Fig. 3. However, a small excursion in  $Z$  is noticeable for those perturbations that are characterized by  $\Delta Z = 0$  at Annamalainagar. Furthermore, the measurement of  $Z$  is less sensitive at Kodaikanal. Therefore, we will concentrate on the magnetograms obtained at Annamalainagar, but keep in mind that the interpretation of the effect must allow for its existence at other locations.

Both Annamalainagar and Kodaikanal show a positive ratio  $\Delta Z/\Delta H$  for those perturbations which appear in  $Z$ . If  $\Delta Z$  were just the field caused by an inhomogeneous distribution of the primary current, one should expect negative values of  $\Delta Z/\Delta H$  for a station north of the dip equator ( $Z > 0$  downward,  $H > 0$  northward), since the ionospheric currents are concentrated in the equatorial electrojet. According to Untiedt's (1967) model of the equatorial electrojet  $\Delta Z/\Delta H$  of the primary current at these stations would be  $-0.56$  and  $-0.37$ , respectively. The actual disappearance of  $\Delta Z$  for a certain class of perturbations can only be attributed to a cancellation of the fields contributed by the primary and the induced currents. The location of the null in  $\Delta Z$  can depend not only on the morphology of the good conductors such as ocean, sub-ocean floor, and crustal anomalies, but also on the distribution of the primary currents. Ionospheric currents must necessarily concen-

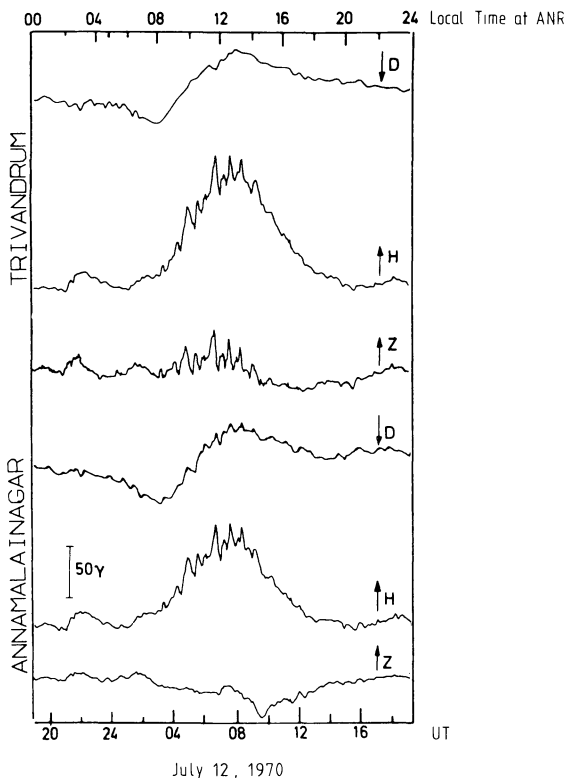


Fig. 2.  $H$ -,  $D$ -, and  $Z$ -components of the magnetic field for 12 July 1970, at Annamalainagar and Trivandrum

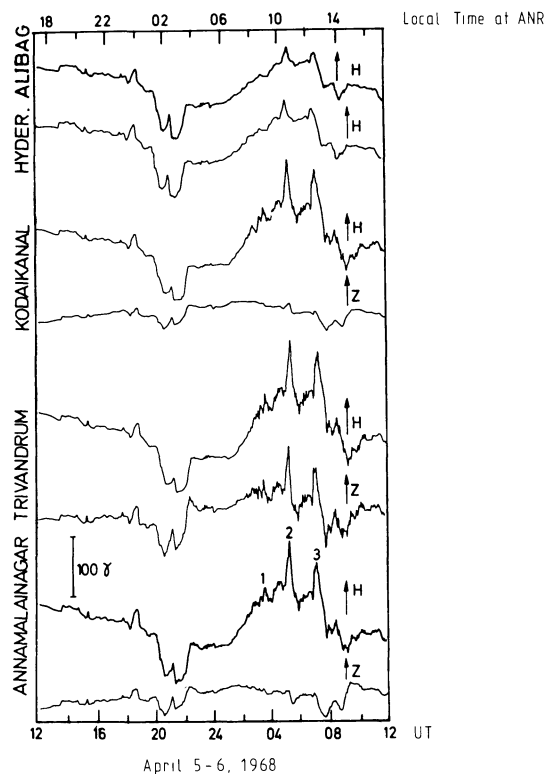


Fig. 3.  $H$ - and  $Z$ -components for 5 Indian magnetic observatories on 5-6 April 1968

trate along the equator, within a few degrees of latitude, because of the high Cowling conductivity. Magnetospheric currents should be much more uniformly distributed in latitude, wherever they may flow. However, for the latter we also except a symmetry with respect to the equator. Hence, there is little chance to attribute the vanishing  $\Delta Z$  to a latitudinal shift of the primary current. But we can understand why one type of primary current may lead to  $\Delta Z=0$  at certain stations, while another one does not. Annamalaiagar and Kodaikanal just happen to fall close to the lines  $\Delta Z=0$  for short-term fluctuations in the ionospheric currents which tend to be small at night.

Before we proceed with interpreting this effect we should comment on the tricky question of the baseline from which the short-term fluctuations (periods  $\sim 1$  hour) are measured. An interesting controversy on this subject had arisen 10 years ago between Matsushita and Balsley (1972, 1973) and Nishida (1973) in the context of DP-2 type perturbations. Short-term excursions like those appearing between 08 and 16 LT in Figs. 2 and 3 could either be enhancements of a quiet time current or transient decreases of its intensity. Often, the latter appears to be the case as witnessed by electric field measurements with the Jicamarca radar (Gonzalez et al., 1979). However, since we had no independent means of judging which point of view may be applicable to an individual perturbation we chose the baseline of daytime fluctuations such that  $\Delta H$  is positive, i.e. in Nishida's sense. At Trivandrum this implies also  $\Delta Z > 0$ . For the quantity of main interest,  $\Delta Z/\Delta H$ , this does not make much of a difference, except for the period that is attributed to the perturbation. For instance, if we had chosen the zero level of  $H$  and  $Z$  on the example shown in Fig. 3 in a way that it would meet the peaks designated 1, 2, 3 in  $H_{ANR}$ , the perturbations would appear as negative with almost 2 hours period. With our choice of baseline they would be classified as positive with 0.5 hours period. But the ratio  $\Delta Z/\Delta H$  would be roughly the same. (Later in this paper we will recognize that the situation in this particular example was even more complex in that two different primary currents exhibited fluctuations of different type with considerable phase shift.) Although the physical interpretation of the perturbation depends on the choice of the zero level, for a discussion of the induction effects it is irrelevant as long as we refer to the same type of primary current and choose the zero lines for  $H$  and  $Z$  in a consistent fashion. Of course, in general we chose the zero lines in a way that the field after subtraction of the so-defined perturbation appeared to vary much more smoothly. For typical night-time perturbations this means that  $\Delta H$  was also frequently negative.

We return to the explanation of the two classes of magnetic variations at Annamalaiagar (and Kodaikanal), one with  $\Delta Z=0$  and the other with  $\Delta Z/\Delta H > 0$ . Papamastorakis and Haerendel (1974) suggested that this was a consequence of the latitudinal distribution of the primary current in combination with the configuration of the (highly conductive) ocean in the Indian sector. The induction at any given site cannot be considered as a local effect when the configuration is as irregular as here. Price (1964) drew attention to so-called *channeled currents* which are induced at some distance from the station under consideration, but whose effect is felt there, because the shape of the conductor leads to formation of eddy currents. The currents induced in the Bay of Bengal by the overhead equatorial electrojet

are partially interrupted by the tip of Southern India and Sri Lanka as well as on the eastern side by the Malay Peninsula. Hence a substantial fraction of those currents can only close by being channeled up the east coast of India and southward again in the eastern half of the Bay. Somewhere north of Sri Lanka, the induced currents become divided into a vortex located in the Bay of Bengal and a contribution flowing around the tip of Southern India, partially through the Palk Strait between Sri Lanka and India. This was demonstrated with the help of an analogue model of Papamastorakis (1975), which will be presented in Paper II. Later confirmation of the flow through the Palk Strait was given by Nityananda et al. (1977), Rajaram et al. (1979), and Thakur et al. (1981). Where the currents flow northward along the coast, they create an upward (negative) component of the secondary field which enhances the primary vertical component of positive excursions of the electrojet. On the other hand, they create a downward (positive)  $Z$ -component where they are directed southward. Annamalaiagar just happens to lie at a point where the negative primary  $Z$ -field is exactly balanced by the induced secondary field. However, this cancellation applies only to primary currents flowing in the ionosphere which are necessarily concentrated within  $\pm 3^\circ$  from the dip equator.

The different effect of magnetospheric currents arises from their nearly uniform distribution over at least  $\pm 10^\circ$  of latitude, i.e. over the whole extent of the Bay of Bengal. Accordingly, the currents induced in this conductor by temporal fluctuations of magnetospheric currents should have a quite different pattern. The current eddy in the northern bay should be smaller. Therefore, Annamalaiagar would come more strongly under the influence of currents forced southward along the coast. A positive (negative)  $Z$ -component is expected for positive (negative)  $\Delta H$  not only because of the changed pattern of the induced currents, but also because  $\Delta Z$  of the primary current should be reduced.

Of course, Annamalaiagar is not the only site where this effect exists. Similar points should be found at the west coast of India well north of Trivandrum, at the coasts of Sri Lanka, Somalia, and the Malay Peninsula. Indeed, we noticed already the similarity of Kodaikanal and Annamalaiagar. Kodaikanal is about 130 km inland from the point on India's west coast where we would expect  $\Delta Z=0$  for ionospheric perturbations (see Paper II). But without more detailed measurements of the variation of  $\Delta Z$  along a normal to the coast we cannot be sure whether the induced currents which lead to a cancellation of the primary  $\Delta Z$  are actually flowing in the ocean, or whether, in addition, there are conductivity anomalies in the subcontinent which play a greater role.

The interpretation given above is supported by the diurnal behavior of the two classes of perturbations. The  $\Delta Z=0$  variations of typically 1 h period (or less) are found exclusively during daytime when the ionospheric conductivity is high and the electrojet concentration of the currents is known to exist. *At night*, practically all short period perturbations visible in  $H$  also appear in  $Z$  at Annamalaiagar. The concentration of the ionospheric current to  $\pm 3^\circ$  latitude still exists at night, but the conductivity is one or two orders of magnitude lower than at midday, whereas the electric fields are of equal magnitude to those during daytime (Kamiyama, 1965; Woodman, 1972; Balsley, 1973). Hence the contribution of ionospheric currents would be almost insignificant at night. Most of the pertur-

bations should be of magnetospheric origin. *During the day* the situation is different. Both ionosphere and magnetosphere contribute. Hence, we observe mixed classes, for which a finite value of  $\Delta Z$  is found, but with a ratio  $\Delta Z/\Delta H$  well below that observed at night. The virtue of this different response to the different primary currents is that any given short period fluctuation of  $H$  and  $Z$  observed at Annamalainagar can be immediately decomposed into an ionospheric and a magnetospheric contribution without the aid of any other observation. The reason is that the response of the induced currents to primary fields of a given period is linear, so that the effect of simultaneous perturbations of two different current sources would be simply superposed. In order to obtain a quantitative tool for this decomposition, we will now proceed with a statistical analysis of perturbations observed at Annamalainagar and, for comparison, also at Trivandrum.

### Statistical Analysis of Magnetic Variations Observed at Annamalainagar and Trivandrum

Figure 4 shows an excellent correlation between the vertical and horizontal components of 17 randomly selected nocturnal events. Since we find in all cases (as well at Trivandrum) that  $\Delta Z$  and  $\Delta H$  have the same sign, we work with positive quantities only in our statistical analysis. Instead of  $\Delta H$  we calculate the full horizontal variation

$$|\Delta \mathbf{H}| = \sqrt{(\Delta H)^2 + (H_0 \cdot \Delta D)^2}. \quad (1)$$

It turns out that  $\Delta D$  and  $\Delta H$  are strongly correlated, i.e. the direction of polarization of the horizontal component is rather stable. At Annamalainagar we find:

$$H_0 \cdot \Delta D = \begin{cases} -0.33 \pm 0.015 \\ -0.24 \pm 0.012 \end{cases} \cdot \Delta H \quad (2)$$

for nocturnal perturbations of  $\sim 1$ -h period and for daytime perturbations with  $\Delta Z = 0$ , respectively (see Papamastorakis, 1975). At Trivandrum  $\Delta D$  is generally much smaller. Accordingly, the difference between  $|\Delta \mathbf{H}|$  and  $\Delta H$  is at most 5% and can be neglected. For this reason and because of the need of using different types of indices we will henceforward abbreviate  $|\Delta \mathbf{H}|$  by  $\Delta H$ .

The correlations between the vertical and horizontal components which we want to corroborate depend, of course, on frequency. A more careful study should proceed via Fourier analysis of the three orthogonal components of the perturbation vector. We have simplified the task in

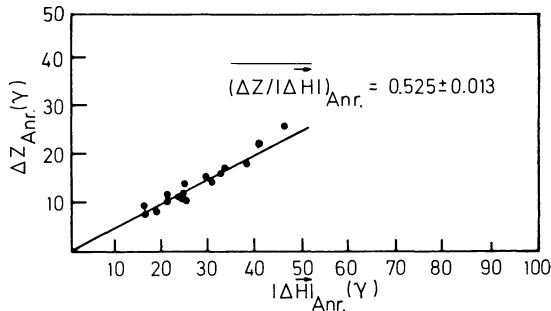


**Fig. 4.** Correlation between the magnitudes of  $\Delta Z$  and  $\Delta H$  for 17 randomly selected nocturnal variations at Annamalainagar.  $|\Delta \mathbf{H}| \simeq \Delta H$

two respects, (1) by selecting individual perturbations of approximately similar duration (e.g.  $\sim 1$  h) and reading their overall amplitudes irrespective of their fine structure, and (2) by considering the correlation of two quantities only,  $\Delta Z$  and  $\Delta H$ . The rather stable polarization of  $\Delta H$ , as expressed in Equation 2, justifies the second point and shows that little additional scatter should be introduced into the values of  $\Delta Z/\Delta H$  thereby. The first simplification is somewhat unsatisfactory, but appears to be appropriate for a first exploration of the effect.

The average ratio,  $\langle \Delta Z/\Delta H \rangle$ , turns out to be  $0.525 \pm 0.013$  at Annamalainagar. It is found to depend very little on the period for  $P \lesssim 1$  h. However, for periods much longer than 1 h, like the daily variation of the Sq-current,  $\Delta Z$  looks completely different.

We can now use the established ratio

$$m_{ANR} = \langle \Delta Z/\Delta H \rangle_{ANR} \quad (3)$$

for nighttime, i.e. *magnetospheric* perturbations, in order to decompose any observed value  $\Delta H$  of sufficiently short period into its magnetospheric and ionospheric components,  $\Delta H^m$  and  $\Delta H^i$ , by

$$\left( \frac{\Delta H^i}{\Delta H^m} \right)_{ANR} = \frac{m}{\left( \frac{\Delta Z}{\Delta H} \right)_{ANR}} - 1. \quad (4)$$

At least, on a statistical basis this equation should be applicable. It is a special case ( $i_{ANR} = 0$ ) of the more general relation:

$$\frac{\Delta H^i}{\Delta H^m} = - \frac{m - \frac{\Delta Z}{\Delta H}}{i - \frac{\Delta Z}{\Delta H}}, \quad (5)$$

with

$$i = \left\langle \frac{\Delta Z}{\Delta H} \right\rangle, \quad (6)$$

for pure ionospheric perturbations. At Trivandrum,  $i$  has a finite value and Equation 5 applies.

Figures 5a and b show the corresponding ratios for Trivandrum. One finds:

$$m_{TRV} = 1.21 \pm 0.026, \\ i_{TRV} = 0.95 \pm 0.017.$$

Our first observation is the large value of  $i_{TRV}$ . If  $\Delta Z$  were only due to the inhomogeneity of the primary current, we should have  $i_{TRV} \approx +0.1$ , as can be seen from Untiedt's (1967) model of the electrojet. Equally,  $m_{TRV}$  should nearly vanish. The actual values are a clear signature of the classical coast effect. Furthermore,  $m_{TRV}$  is substantially larger than  $m_{ANR}$ . This is due to the fact that Annamalainagar is not too far from the line of  $\Delta Z = 0$ , even for magnetospheric perturbations. According to the results obtained by use of an analogue model (Paper II), the null of  $\Delta Z$  should be found  $\approx 150$  km to the north of Annamalainagar.

All data selected for the determination of the latter coefficient represent perturbations during daytime with  $\Delta Z = 0$  at Annamalainagar. Without this tool to recognize pure

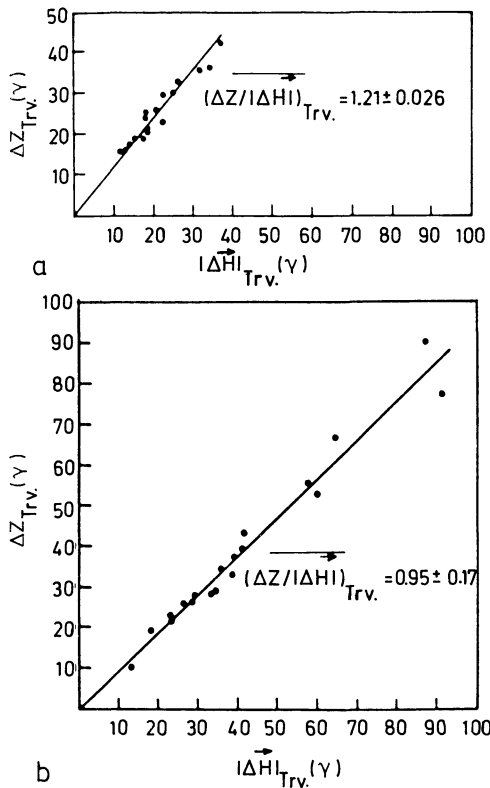


**Fig. 5a and b.** Correlation between the magnitudes of  $\Delta Z$  and  $\Delta H$  at Trivandrum, **a** for the nocturnal variations of Figure 4, **b** for daytime variations with  $\frac{\Delta Z}{\Delta H} = 0$  at Annamalainagar

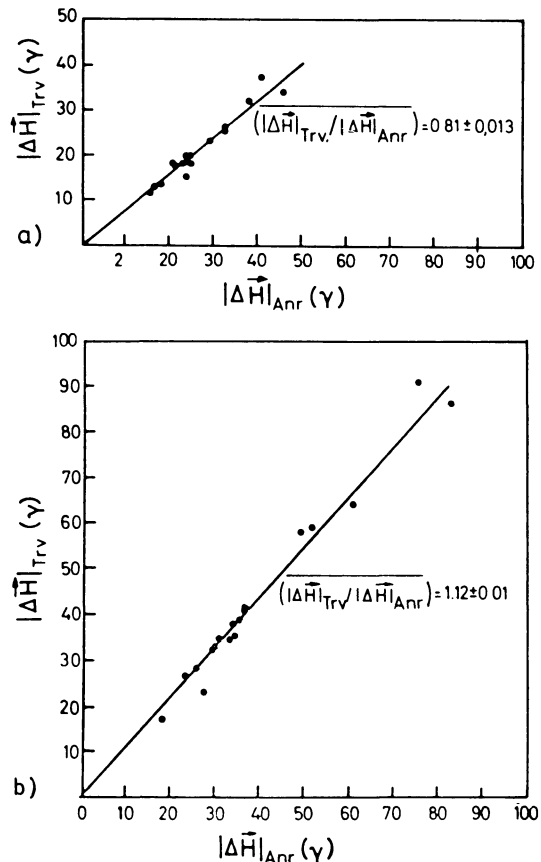


**Fig. 6a and b.** Correlation of the magnitudes of  $\Delta H_{TRV}$  and  $\Delta H_{ANR}$ , **a** for nocturnal variations, **b** for daytime variations with  $\frac{\Delta Z}{\Delta H}_{ANR} = 0$

ionospheric perturbations, this selection would have been much more difficult.

It is interesting to compare the  $H$ -components at Annamalainagar and Trivandrum for the two classes of variations. This is done in Figs. 6a and b. As one should expect from our interpretation of the origin of the anomalous coast effect at Annamalainagar these ratios are not the same for magnetospheric and ionospheric perturbations:

$$h^m = \left\langle \frac{\Delta H_{TRV}}{\Delta H_{ANR}} \right\rangle_m = 0.81 \pm 0.013, \quad (7a)$$

$$h^i = \left\langle \frac{\Delta H_{TRV}}{\Delta H_{ANR}} \right\rangle_i = 1.12 \pm 0.01. \quad (7b)$$

The finding that  $h^i > 1$  reflects the greater proximity of Trivandrum to the center of the electrojet. The primary current alone would yield  $h^i = 1.28$  as can be read from Untiedt's (1967) model. The reason for the actually smaller value of  $h^i$  must lie in a relatively greater contribution of the induced earth currents to the total horizontal perturbation at Annamalainagar. If this is so,  $h^m < h^i$  is no surprise, since the primary field of the wider magnetospheric current should change very little between Trivandrum and Annamalainagar. One of the reasons for the relatively strong induction effect at Annamalainagar may be the channeling of current through the Palk Strait (Fig. 1), as discussed in Paper II.

There is no easy way to determine what fraction of any observed value of  $\Delta H$  is due to the primary and what fraction is due to the induced currents. Above the ocean, well away from the coast, the contribution of the latter almost equals the primary field if the periods are sufficiently short. Near the coast,  $\Delta H_{ind}$  decreases, because of magnetic diffusion through the poorly conducting continent (see Paper II).

It must be mentioned that we find a slight dependence of  $m_{TRV}$  on the period which is not observed at Annamalainagar. The above value applies to periods of  $\approx 1$  h. For 5–10 min fluctuations, as observed in SSCs, we determine  $m_{TRV} = 1.31 \pm 0.018$ .

### Separation into Magnetospheric and Ionospheric Contributions

The observation of a completely different response of the  $Z$ -component at Annamalainagar to magnetospheric and ionospheric primary currents suggests a useful application. Any mixed event should show a  $\Delta Z / \Delta H$  smaller than for pure magnetospheric currents, thus allowing us to deduce the ratio of the respective  $H$ -components by applying Equation 1. We must, however, realize that  $m_{ANR}$  was determined as a statistical average. In any particular event the true value may differ from the statistical average. Furthermore,

there may be some dependence on period, although none was obvious for events between 10 min and 1 h. The reason for this is that the skin depth for any period shorter than 1 h is small compared with the relevant linear dimension  $L_{eff}$ , which is the geometric mean of ocean depth and scale-length of the primary current (see Paper II). So, the geometric behavior of the fields should be quite similar. This has been verified by solving the induction problem for the case of an alternating band current above an infinite, plane ocean. This leads to the conclusion that for the scale-lengths of the ionospheric and magnetospheric source fields the effects of the induction currents at the ocean surface are nearly independent of the period for periods less than about 1 h and ocean depths of more than 2 km.

Let us now check whether any perturbation of less than  $\approx 2$  h duration with complex temporal structure can be evaluated by applying Equation 4 to the instantaneous readings of  $\Delta Z$  and  $\Delta H$  with constant value of  $m$ . We choose one example of a nighttime and hence pure magnetospheric perturbation, namely the period from 20–22 UT on April 5, 1968 (see Fig. 3). Figure 7a is an enlarged plot of the  $H$ - and  $Z$ -components at Annamalainagar with our choice of baseline from which we reckon  $\Delta H$  and  $\Delta Z$  of the perturbation. Figure 7b contains the development of the ratio  $\Delta Z/\Delta H$ . It is not as constant as one would like it to be, and its average value of 0.45 differs from the statistical result for the amplitudes of 1 h perturbations ( $m = 0.525$ ). For a pure magnetospheric event this deviation and the lack of constancy of  $\Delta Z/\Delta H$  may not look so bad. However, small changes of  $\Delta Z/\Delta H$  can produce large changes of  $\Delta H^i/\Delta H^m$  in Equations 4 when applied in the same fashion to a mixed ionospheric-magnetospheric event. This must be borne in mind, and attention should be focussed on the gross structure of the thus separated contributions of ionospheric and magnetospheric origin rather than on the actual values of  $\Delta H^i$  and  $\Delta H^m$ . They may contain substantial errors.

Figure 8 contains an application to an arbitrary mixed event. It was taken from April 6, 1968 (see Fig. 3). Using the dashed baselines and a constant value of  $m = \Delta Z/\Delta H$  for magnetospheric perturbations, we can determine  $\Delta H^m = m\Delta Z$ . The observed readings of  $\Delta H$  are the sum of  $\Delta H^m$  and  $\Delta H^i$ . Hence:

$$\Delta H^i = \Delta H_o - \frac{\Delta Z_{obs}}{m} \quad (8)$$

The choice of baseline from which the short-term variations are counted may be questioned as well as the applicability of the statistical value  $m = 0.525$  in Equation 8 on an instantaneous basis. However, the minima in  $Z$  around 10:30, 12:40 and 13:50 LT indicate clearly the presence of enhanced magnetospheric westward currents which lower the total value of  $H$ . A correction for these magnetospheric contributions results in the dotted line in Fig. 8. We see now that the minima in  $Z$ , i.e. the maxima of the magnetospheric (probably ring-) current, are closely associated with relative maxima of the ionospheric current, which precede by about 15 min (6 min for the event at 13:50 LT). We must bear in mind, however, that the dotted trace of the  $H$ -component in Fig. 8 can only be interpreted in terms of the ionospheric current if the baseline is known. A long-term depression of  $H$  (period  $\gg 1$  h) due to enhanced ring-current (a magnetic storm was in progress) would not be

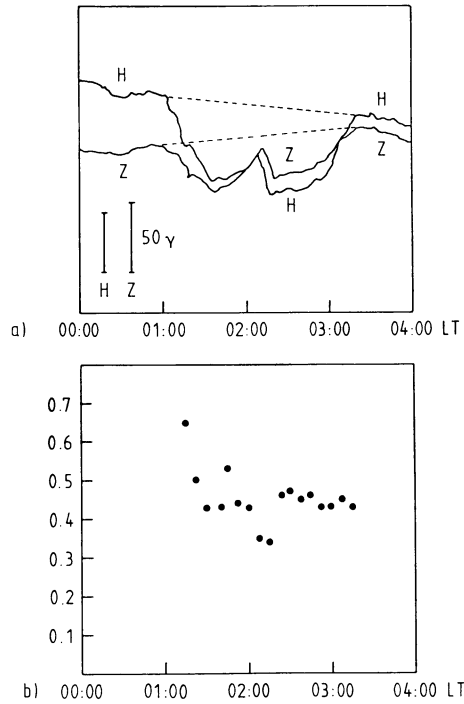


Fig. 7. a Enlarged plot of the  $H$ - and  $Z$ -components of the negative nocturnal variation shown in Fig. 3 (5 April 1968), b ratio  $\Delta Z/\Delta H$  for this variation

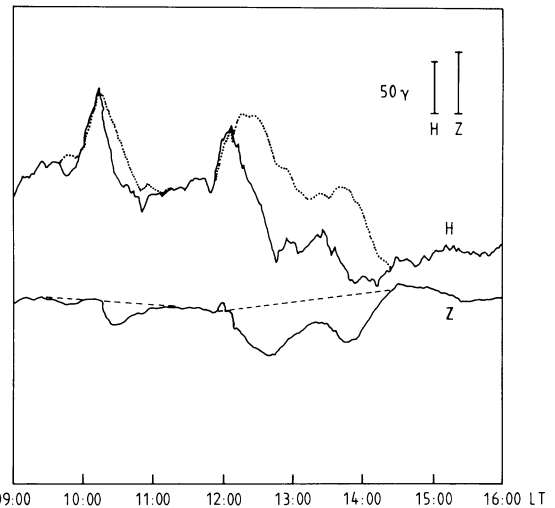


Fig. 8. Determination of the ionospheric part (dotted line) of mixed event observed at Annamalainagar (6 April 1968)

recognized in  $Z$  and would have to be assessed by some other means. By comparing the day under consideration, as shown in Fig. 3, with a less perturbed day as selected for Fig. 2 one gets the impression that the short-term maxima of  $H$  on April 6 (Fig. 8) are true enhancements over the Sq-level. The typical amplitude of the Sq variation at Annamalainagar is  $\approx 100 \gamma$  in  $H$ , whereas the maxima on April 6 over a baseline conjectured to lie close to or even below the trace of  $H$  after 15:00 LT, is of the order of  $150 \gamma$ . Here we will not dwell on the magnetospheric significance of this result, but use it merely as a demonstration of the usefulness of the anomalous coast effect at Annamalainagar.

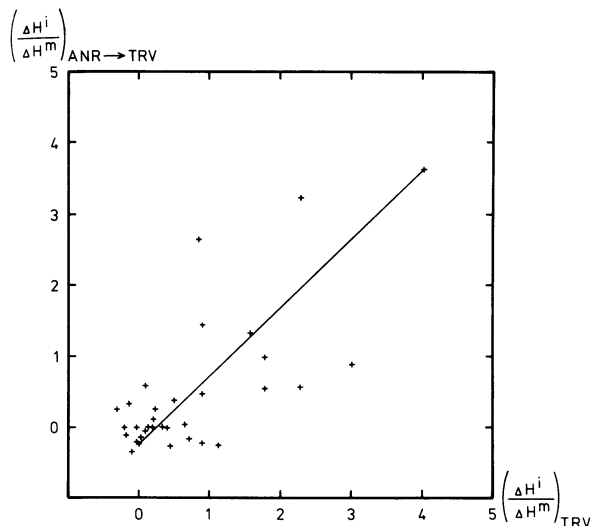


Fig. 9. Correlation between observed ratios  $\frac{\Delta H^i}{\Delta H^m}$  at Trivandrum and those calculated by means of Equation 8 from  $\frac{\Delta H^i}{\Delta H^m}$  as observed at Annamalainagar for 33 SSC events

Whereas the time-dependent separations of  $\Delta H^m$  and  $\Delta H^i$  for one particular event have to be regarded with some caution, statistical applications appear to be more appropriate. We will investigate the consistency of Equations 4, 5 and 7 by comparing the resulting values of  $\frac{\Delta H^i}{\Delta H^m}$  as deduced for Trivandrum in two different ways, by the local measurements on the one hand, and by a transfer of the readings at Annamalainagar to Trivandrum by use of the statistical ratios  $h^m$  and  $h^i$ . The latter is given by:

$$\left(\frac{\Delta H^i}{\Delta H^m}\right)_{ANR \rightarrow TRV} = \frac{h^i}{h^m} \left(\frac{\Delta H^i}{\Delta H^m}\right)_{ANR} \quad (9)$$

with  $h^i/h^m = 1.38$  and  $(\frac{\Delta H^i}{\Delta H^m})_{ANR}$  from Equation 4. In a scatter plot of this ratio determined from Equations 9 and 4 respectively, we expect to find a good correlation if our determinations of  $m$ ,  $i$ ,  $h^m$ ,  $h^i$  for pure magnetospheric or ionospheric events are also applicable to superpositions of the two.

We selected 33 SSC events from 1968, 1969 and 1970. The result is shown in Fig. 9. In view of the fact large values of  $\frac{\Delta H^i}{\Delta H^m}$  are caused by small differences of  $\Delta Z/\Delta H$  from the statistical average and must be regarded as rather inaccurate, the agreement of both methods is not bad. The r.m.s. ratio is  $0.9 \pm 0.03$ . As a geophysical result we learn from Fig. 9 that the ionospheric currents (and hence the electric fields) are clearly affected by sudden commencements. In a later paper we will deal with this subject in more detail, in particular with the local time dependence of the ionospheric response.

## Summary

In this paper we have discussed the origin of the absence of a perturbed  $Z$ -component at the Southern Indian station Annamalainagar for fluctuations of a primary current flowing in the ionosphere. This is contrary to the sensitive response found for currents flowing in the magnetosphere.

This behavior of  $Z$  was attributed in the first case to a cancellation of the contributions of the ionospheric current and the induced earth current (mainly in the waters of the Bay of Bengal). Because of the greater homogeneity of a magnetospheric current, the primary  $\Delta Z$  is small and the contribution of the induced currents appears in the  $Z$ -component. A difference in size of the induced current eddies in the Bay of Bengal may add to the difference in behavior of  $Z$ .

The statistical relations between  $\Delta Z$  and  $\Delta H$  for pure ionospheric and magnetospheric perturbations of no more than 1 h duration have been evaluated for Trivandrum and Annamalainagar, and the ratios of  $\Delta H$  at both stations for both types of perturbations have been established. These coefficients enable us to separate the ionospheric and magnetospheric contributions to any arbitrary short-term variation  $\Delta H$  and thus analyze the ionospheric response to any magnetospheric perturbation. The applicability and potential usefulness have been demonstrated with a few examples.

These findings have been reported by Papamastorakis and Haerendel (1974) and form part of the thesis of the first author (Papamastorakis, 1975). Meanwhile, the discovered effect has found considerable interest and stimulated further investigations (Nityananda et al., 1977; Rajaram et al., 1979; Thakur et al., 1981) so that it appears still useful to present the original material at this late date.

## References

- Baumjohann, W., Untiedt, J., Greenwald, R.A.: Joint two-dimensional observations of ground magnetic and ionospheric electric fields associated with auroral zone currents. 1. Three-dimensional current flows associated with a substorm-intensified eastward electrojet. *J. Geophys. Res.* **85**, 1963–1978, 1980
- Balsley, B.B.: Electric fields in the equatorial ionosphere: A review of techniques and measurements. *J. Atmos. Terr. Phys.* **35**, 1035–1044, 1973
- Gauss, C.F.: Allgemeine Theorie des Erdmagnetismus, Resultate aus den Beobachtungen des magnetischen Vereins im Jahre 1838, 1–57, 1839
- Gonzalez, C.A., Kelley, M.C., Fejer, B.C., Vickrey, J.F., Woodman, R.F.: Equatorial electric fields during magnetically disturbed conditions. 2. Implications of simultaneous auroral and equatorial measurements. *J. Geophys. Res.* **84**, 5803–5812, 1979
- Hughes, T.J., Rostoker, G.A.: A comprehensive model current system for high-latitude magnetic activity. I. The steady-state system. *Geophys. J. R. Astron. Soc.* **58**, 525, 1979
- Iijima, T., Potemra, T.T.: The amplitude distribution of field-aligned currents at northern high latitudes observed by Triad. *J. Geophys. Res.* **81**, 2165–2174, 1976
- Kamiyama, H.: Nocturnal electrical conductivity of the equatorial ionosphere. *Rep. Ionosph. Space Res., Japan* **19**, 359–363, 1965
- Matsushita, S., Balsley, B.B.: A question of DP-2. *Planet. Space Sci.* **20**, 1259–1267, 1972
- Matsushita, S., Balsley, B.B.: Comments on Nishida's reply. *Planet. Space Sci.* **21**, 1260–1261, 1973
- Nishida, A.: Reply to "A question of DP-2" by S. Matsushita and B.B. Balsley". *Planet. Space Sci.* **21**, 1255–1259, 1973
- Nityananda, N., Agrawal, A.K., Singh, B.P.: Induction at short periods in the horizontal variations in the Indian peninsula. *Phys. Earth Planet. Int.* **15**, 5–9, 1977
- Papamastorakis, I.: Eine Möglichkeit zur Unterscheidung von magnetosphärischen und ionosphärischen Magnetfeldstörungen in der Nähe des magnetischen Äquators: Ph.D. Thesis, Max-Planck-Institut, Germany, MPI-PAE/Extraterr. 111, 1975
- Papamastorakis, I., Haerendel, G.: A possibility to separate iono-

- spheric and magnetospheric origins of magnetic perturbations in South India. *EOS, Trans. Amer. Geophys. Union* **55**, 229, 1974
- Papamastorakis, I., Haerendel, G.: An analogue model of the geomagnetic induction in the South Indian Ocean. *J. Geophys.* **51**, this issue, 1983
- Parkinson, W.D.: Conductivity anomalies in Australia and the ocean effect. *J. Geomagn. Geoelectr.* **15**, 222–226, 1964
- Parkinson, W.D., Jones, E.W.: The geomagnetic coast effect. *Rev. Geophys. Spac. Phys.* **17**, 1999–2015, 1979
- Price, A.T.: Note on the interpretation of magnetic variations. *J. Geomagn. Geoelectr.* **15**, 241–248, 1964
- Rajaram, M., Singh, B.P., Nityananda, N., Agrawal, A.K.: Effect of the presence of a conducting channel between India and Sri Lanka Island on the features of the equatorial electrojet. *Geophys. J. R. Astron. Soc.* **56**, 127–138, 1979
- Schuster, A.: The diurnal variation of terrestrial magnetism. *Philos. Trans. Roy. Soc., London A* **180**, 467–518, 1889
- Thakur, N.K., Mahabde, M.V., Arora, B.R., Singh, B.P., Srivastava, B.J., Prasad, S.N.: Anomalies in geomagnetic variations on peninsular India near Palk Street. *Geophys. Res. Lett.* **8**, 947–950, 1981
- Untiedt, J.: A model of the equatorial electrojet involving meridional currents. *J. Geophys. Res.* **72**, 5799–5810, 1967
- Wiese, H.: Geomagnetische Tiefentellurik. *Geophys. Pura Appl.* **52**, 83–103, 1962
- Woodman, R.F.: East-west ionospheric drifts at the magnetic equator. *Space Res.* **12**, 969–974, 1972
- Zmuda, A.J., Armstrong, J.C., Heuring, F.T.: Characteristics of transverse magnetic disturbances observed at 1100 km in the auroral oval. *J. Geophys. Res.* **75**, 4757–4762, 1970

Received April 1, 1982; Revised version August 4 and October 13, 1982

Accepted October 29, 1982

# An Analogue Model of the Geomagnetic Induction in the South Indian Ocean

I. Papamastorakis<sup>1</sup> and G. Haerendel<sup>2</sup>

<sup>1</sup> University of Crete, Iraklion, Greece

<sup>2</sup> Max-Planck-Institut für Physik und Astrophysik, Institut für extraterrestrische Physik, 8046 Garching, Federal Republic of Germany

**Abstract.** The role of currents induced in the Bay of Bengal and the Arabian Sea in the response of the  $Z$ - and  $H$ -components of geomagnetic variations is investigated. Particular attention is paid to the measurements at Annamalainagar at the East coast of Southern India. First, induction arrows are derived which suggest that currents channeled through the Palk Strait between India and Sri Lanka are essential for the observed coast effect. It is shown to be plausible that these currents flow in conductivity enhancements under the shallow waters of the Palk Strait. An analogue model of the ocean water around India has been used to measure the impact of different primary currents and of the presence or absence of the conducting channel of the Palk Strait on the geomagnetic coast effect. The results support the hypothesis expressed in an accompanying paper that primary currents in the ionosphere give rise to responses in  $\Delta Z$  and  $\Delta H$  that are different from those of currents flowing in the magnetosphere. Thus the general location of the source current can be distinguished by the readings at just one station like Annamalainagar.

**Key words:** Annamalainagar – Palk Strait – Geomagnetic coast effect – Induction arrows – Analogue model

## Introduction

Near coastlines it is typically observed that geomagnetic variation fields possess an abnormally large vertical component. This is ascribed to the strong conductivity gradients between the sea-water (and the material underneath) and the continental crust. The magnetic field created by time-varying external currents cannot penetrate the regions of higher conductivity (ocean and suboceanic crust) readily. Depending on the thickness of the high conductivity region and the dimensions of the external current, the time required for the magnetic field to diffuse through the better conductor will range from several minutes to several hours. Hence, near coastlines one observes a dependence of the ratio of vertical and horizontal perturbations,  $\Delta Z/\Delta H$ , on the period. Short-term variations related to geomagnetic bays (substorms) at high latitudes or storm sudden commencements show an entirely different behavior of  $\Delta Z/\Delta H$  than the daily variation of the Sq-current system. The whole effect is referred to as the *geomagnetic coast effect* (Parkinson, 1962). A recent review was given by Parkinson and Jones (1979).

Offprint requests to: G. Haerendel

A special situation exists at the geomagnetic observatory at Annamalainagar in Southern India. The  $Z$ -component of short-term variations shows completely different responses at night and during the day. This was noticed by Papamastorakis and Haerendel (1974) and formed the subject of the thesis by the first author (Papamastorakis, 1975) of the present work. The explanation of the different responses was given in terms of the latitudinal profile of the primary currents and the resulting differences in the morphology of the currents induced in the ocean. A method was derived to distinguish between ionospheric and magnetospheric sources of the variations based on the ratio of  $\Delta Z$  and  $\Delta H$  at Annamalainagar. This has been described in an accompanying paper (Papamastorakis and Haerendel, 1983; referred to as Paper I).

An *analogue model* of the highly conducting Indian ocean was constructed in order to check the hypothesis concerning the role of the morphology of the primary currents. For the primary currents two different conductors were chosen. A narrow one following the magnetic dip equator was intended to resemble the ionospheric current system with its concentration towards the equator, the equatorial electrojet. A significantly broader band conductor was chosen to resemble current sources in the magnetosphere with little latitudinal variation. The results obtained with this model, in particular  $\Delta Z$  and  $\Delta H$  measured along the coastlines, form the main subject of this paper.

Before turning to the analogue model we will inspect some actual measurements with regard to the orientation of the conductor carrying the induced currents near Annamalainagar. We apply the method of deriving induction arrows after Wiese (1962), Parkinson (1962) and Untiedt (1964). The subject of particular interest is the role of the shallow Palk Strait between Southern India and Sri Lanka. The induced fields at Annamalainagar would look quite different depending on whether a substantial amount of the induced current is channeled through the Palk Strait or not. This subject has received much attention recently (Nityananda et al., 1977; Rajaram et al., 1979; Takeda and Maeda, 1979; Thakur et al., 1981).

## Induction Arrows

Far from the coast, from conductivity anomalies, or strong concentrations of the primary current, the magnetic variation field is horizontal. In approaching the coast an increasing  $Z$ -component is noted. This means that the variation field lies in a plane with increasing slope, the “preferred plane”. The vector normal to this plane, or better, its hori-

zontal component points away from the better conductor. There are different ways to demonstrate this fact in graphical terms (Wiese, 1962; Parkinson, 1962; Untiedt, 1964). In the following, we shall apply two of these methods for magnetic variations observed at Annamalainagar.

Figure 1 shows two arbitrarily selected nighttime perturbations of about 1-h duration. Following Untiedt (1964) we plot the hodograph of the horizontal perturbation vector ( $\Delta H$ ,  $\Delta D$ ) for these two events separately and connect points of equal value of  $\Delta Z$  by straight lines. The induction arrow  $\vec{C}_u$  is normal to these lines and points towards higher  $\Delta Z$ . Its length is proportional to the distance between two straight lines for constant  $\Delta Z$ . Both events give rather similar results. The induction arrow points to  $57^\circ$  and  $63^\circ$ , respectively, west from north. The better conductor should be located in the opposite direction, i.e. approximately  $30^\circ$  south of east. This is shown in Fig. 2. A straight line perpendicular to the two arrows runs parallel to the channel between Southern India and Sri Lanka, the Palk Strait, thus implying that the currents induced in the ocean water are channeled through the Palk Strait in spite of the shallowness of the water ( $<30$  m).

It should be noted that the determination of induction arrows after Untiedt (1964) leads to great uncertainties concerning the true orientation of the better conductor if the plane of polarization of the selected magnetic perturbation is nearly constant. There is a strong tendency for such behavior in the short-term variations at Annamalainagar, irrespective of time of day.

Before further discussing this subject, we apply another method. Figure 3 contains the ratios  $\Delta H/\Delta Z$  plotted against  $\Delta D/\Delta Z$  for 43 SSC events in 1968–1970 observed at Annamalainagar. The periods are typically 5–10 min, and the maximum of the amplitudes has been chosen. No selection according to time of day has been applied. Wiese's (1962) method for finding the induction arrow consists of fitting the data by a straight line and determining the vector normal to it. The result differs significantly from the former determination of the induction arrow (Fig. 2). The reason is to be sought in the fact that daytime events have also been included in Fig. 3, with relatively small values of  $\Delta Z$ . The nighttime values alone cluster between 1.5 and 2.0 for  $\Delta H/\Delta Z$  and do not allow a good definition of a straight line. On the other hand, their distribution does not exhibit any clear cut relation to the two induction arrows of Fig. 2.

It was demonstrated in Paper I that pure ionospheric perturbations cause practically zero  $\Delta Z$  at Annamalainagar. This is the consequence of a superposition of contributions of equal magnitude but opposite sign from the primary ionospheric current and the induced earth current at this location. The latter flows predominantly in the ocean water of the Bay of Bengal, but the sub-ocean floor may contribute significantly, in particular in the shallow water near the coast. The shape of the Bay of Bengal leads to the formation of a large current eddy whose size depends on the distribution of the primary current. We will discuss this subject in detail later in this paper, but refer here to Fig. 9 which shows the induced current vortex for a primary current concentrated at the equator. If the primary current is flowing in the magnetosphere, it should be much more homogeneous in latitude and consequently cause a smaller primary  $\Delta Z$ . Secondly, the current vortex in the Bay of Bengal would have a different size. It should be shifted northward. Therefore, it is qualitatively clear why such pri-

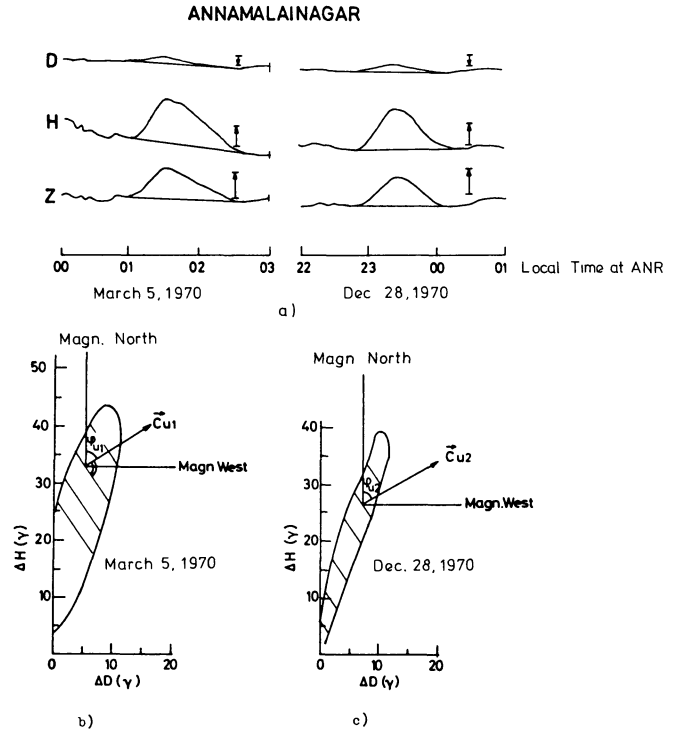


Fig. 1. a Two arbitrary nighttime perturbations at ANR. b Construction of the induction arrows  $\vec{C}_u$  after Untiedt (1964)

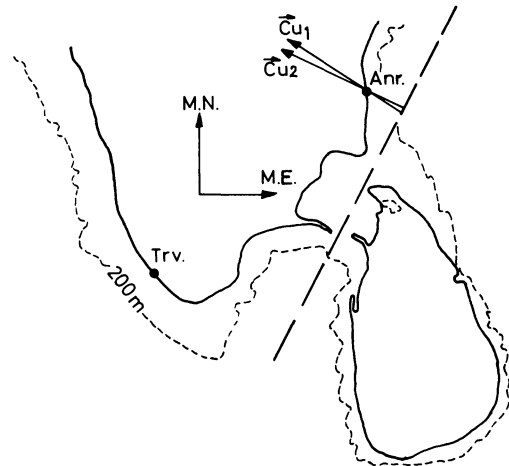


Fig. 2. Induction arrows from Fig. 1 shown in a map. The dashed line indicates the direction of preferred flow of the induction currents. Channeling through the Palk Strait is suggested

mary perturbation currents cause a finite  $\Delta Z$  at the location of Annamalainagar and why its sign (positively correlated with  $\Delta H$ ) is that expected from induced currents flowing southward towards the Palk Strait.

We return now to Fig. 3 which was derived from SSC events. As shown in Paper I they are composed of contributions from primary perturbation currents flowing both in ionosphere and magnetosphere. Hence,  $\Delta Z \neq 0$  for all events, but  $\Delta Z$  becomes relatively small during the middle of the day. The determination of the induction arrow,  $C$ , according to Wiese suffers from the same deficiency as that according to Untiedt, but more seriously. It lies in the fact that the polarization plane of the primary perturbation

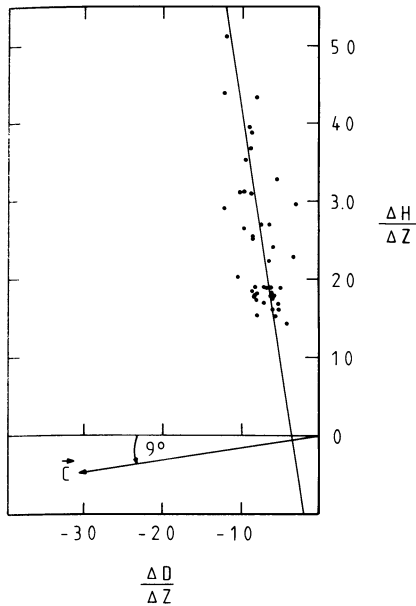


Fig. 3. Construction of an induction arrow,  $\vec{C}$  from a large number of SSC events following Wiese (1962).

vector varies very little in the course of the day, and deviates not much from the direction of the coast line. Hence, the straight line fitting the data of Fig. 3 shows essentially the direction of polarization of the primary field. Therefore, we should have higher confidence in the induction arrows derived in Fig. 1, which imply a channeling of induced current through the Palk Strait.

The suggestion that the Palk Strait carries a significant amount of the induced current has attracted much attention. It is interesting that Nityananda et al. (1977) derived significantly different induction vectors for SSC than those shown in Fig. 2, namely between  $32.5^\circ$  and  $42.5^\circ$  west of north. They corrected the readings of  $\Delta H$  and  $\Delta D$  at Annamalaiagar by subtracting those of Kodaikanal as a normal station. Furthermore, they used only nighttime data. However, the induction vector was not determined by following the method of Wiese (1962), but by taking the mean direction of the so corrected horizontal variations directly. Hence the discrepancy between this work and the present paper is not surprising.

Takeda and Maeda (1979) modeled numerically the induction effect in the ocean water around Southern India and concluded that currents channeled through the Palk Strait play the dominant role for the magnetic variations from SSCs and Bays. Their model includes a finite conductivity for the land. Comparison of the results of this model with observations indicated a spreading of the induced currents into the land mass.

Thakur et al. (1981) investigated the effect with an array of magnetometers spread over Southern India. They concluded that current channeling does indeed exist in the Palk Strait, but that it is difficult to envisage the current as being concentrated in the shallow water of the Strait. It should flow predominantly in the deeper crust or even in the upper mantle.

These results are quite consistent with the induction arrows presented here and with the analogue model results of the present work.

## General Considerations

The geomagnetic coast effect is a typical example of the diffusion of magnetic field through a conductor of finite width and complex shape. The diffusion equation is:

$$\frac{\partial B}{\partial t} = D_m \nabla^2 B \quad (1)$$

with  $D_m$  being the magnetic diffusivity defined as

$$D_m = (\mu \mu_0 \sigma)^{-1} \quad (2)$$

$\mu$  is the magnetic permeability and  $\sigma$  the electrical conductivity. We will set  $\mu = 1$ .

A time-scale,  $\tau_0$ , for diffusion through a conductor of thickness,  $d$ , is readily obtained from Equation 2:

$$\tau_0 = \frac{d^2}{D_m} = \mu_0 \sigma d^2 = \left(\frac{d}{\lambda_s}\right)^2 \frac{2}{\omega} \quad (3)$$

$\lambda_s = \left(\frac{\mu_0 \sigma}{2}\right)^{-1/2}$  is the skin depth and  $\omega$  the frequency.

The diffusion time  $\tau_0$  is, however, not relevant for our problem in which the linear dimensions  $L$  of the primary current exceed by far the thickness  $d$  of the conductor (ocean) through which the magnetic diffusion is considered. From the theory of Price (Price, 1967), we can derive a characteristic time-scale,  $\tau_1$ , for the case  $d \ll \lambda_s$  in the thin sheet approximation:

$$\tau_1 = \frac{2dL}{\pi \lambda_s^2 \omega} \quad (4)$$

$L$  should be interpreted either as the width or twice the height of the primary current above the conductor (ocean), whatever is the greater number. A measure of the relative diffusion time is  $\alpha = \omega \tau_1$ . A convenient numerical expression is obtained if we take for the conductivity of ocean water the standard value (e.g. Parkinson and Jones, 1979),  $\sigma = 4 \Omega^{-1} \text{m}^{-1}$ , and measure  $d$  in units of  $10^3$  m,  $L$  in units of  $10^5$  m, and the period  $P$  in units of 1 h:

$$\alpha = \omega \tau_1 = 0.28 \frac{d_3 L_5}{P_h} \quad (5)$$

For  $\alpha \gg 1$ , the diffusion time  $\tau_1$  is long compared with the characteristic period of the magnetic variation considered.

In analyzing the induction fields in Southern India it is revealing to consider the value of the parameter  $\alpha$  for typical periods and different ocean depths. The ocean reaches a depth of more than 2,000 m typically within 100–150 km from the coast of Southern India, except near Sri Lanka. Since the distance of a station like Annamalaiagar or Trivandrum from the 2,000 m line is less than the width of the primary current, we should get relevant answers concerning the existence of secondary magnetic perturbations at these stations when evaluating Equation 5 with  $d \cong 2,000$  m ( $d_3 = 2$ ). We consider the equatorial electrojet as the primary current and adopt a value of 650 km ( $L_5 = 6.5$ ) for its equivalent width (cf. Untiedt 1967). We choose three different periods,  $P = 16$  h, 1 h, and 0.1 h in characterizing the Sq-, bay- and SSC-type magnetic variations, respectively. In Table 1 we compare the values of  $\alpha$  for  $d_3 = 2$  with those for an ocean depth of 20 m ( $d_3 = 0.02$ ) which is characteristic for the Palk Strait.

We see that  $\alpha$  substantially exceeds unity for periods of 1 h or less and ocean depths exceeding 2,000 m. For

**Table 1.**  $\alpha$ -Parameter (Eq. 5) for Various Periods and Ocean Depths

$d_3$	$P_h$	$\alpha$
2.0	16	0.23
	1.0	3.7
	0.1	37
0.02	16	$2.3 \cdot 10^{-3}$
	1.0	0.04
	0.1	0.37

such perturbations the ocean has still a high magnetic shielding capability. Hence the secondary magnetic variation fields at nearby stations should be appreciable. This is not so for the daily  $S_q$ -variations. Therefore, it is no surprise to see that for  $S_q$  the response of  $\Delta Z$  at Annamalaiagar is quite different from that of short-term ionospheric perturbations, for which  $\Delta Z$  happens to vanish as discussed in Paper I. Actually for  $S_q$ -variations,  $\Delta Z < 0$  and largely reflects the primary field. On the other hand, as far as the ratio of  $\Delta Z/\Delta H$  is concerned, there should be little dependence on the period, as long as  $\alpha \gg 1$ . From this point of view, SSC's and 1-h variations should behave rather similarly. This is consistent with our findings in Paper I.

For ocean depths of 20 m (Palk Strait),  $\alpha \ll 1$  even for periods of a few minutes. The magnetic field diffuses through such a thin layer with a time-scale of 2 min. When applied to a channel like the Palk Strait, this time-scale is even shorter because of the channel's limited horizontal extent. The evaluation of the magnetic perturbations for bay-type events would not show any sign of induction in the Palk Strait, if the ocean water were the sole conductor. Even SSC's should cause only a weak coast effect. However, current channeling can modify such a conclusion appreciably, as shown, for instance, by Nienaber et al. (1979) in a study of current channeling in the Vancouver Island region by means of an analogue model. Unfortunately, quantitative comparison with this work is difficult, because two essential parameters are different from ours. The primary field is more homogeneous and the depth of the channel is a factor of 10 higher than in our case. Another way of assessing the importance of current channeling is to compare the overall resistance of the Palk Strait (water only) with that of a path of equal width around Sri Lanka. It is at least by a factor of 20 higher for the case where the skin depth exceeds the depth of the ocean. It is hard to conceive that such a channel would alter the current pattern in the ocean appreciably. Therefore, we are led to the conclusion that the sub-ocean floor plays an important role in channeling the current through the Palk Strait (Papamastorakis, 1975). The same conclusion was reached by Takeda and Maeda (1979) and Thakur et al. (1981). Obviously, the electrical conductivity of this part of the crust must be enhanced. The geophysical significance of this conclusion is not the subject of this paper (cf. Nityananda and Jayakumar, 1981).

### Analogue Model

The motivation behind the work summarized in this and the following sections was a *qualitative* study of the geomagnetic coast effect in Southern India (Papamastorakis, 1975).

In particular, it was intended to determine the location of the nulls in the vertical component of the total variation field and their displacements when switching from a primary current concentrated within  $\pm 3^\circ$  of the dip equator to a much wider one. Furthermore, the ratios of  $\Delta Z/\Delta H$  along the coastline are subjects of this study, since they can be readily compared with the values actually observed. Finally, the gross shape of the current vortices induced in the Bay of Bengal and the Arabian Sea could be conveniently determined with the help of the analogue model.

From the diffusion equation and in particular, the dimensionless diffusion parameter,  $\alpha$  (Eq. 5), it is obvious how an analogue model has to be scaled. If the scaling of the linear dimensions of the model (index  $m$ ) and the natural (index  $n$ ) situations are chosen and the material, i.e. the electrical conductivity,  $\sigma_m$ , of the analogue model has been selected, we have the following relation between the periods of the natural and the model variations of the magnetic field:

$$P_m = \frac{\sigma_m d_m L_m}{\sigma_n d_n L_n} P_n \quad (6)$$

for  $\mu_m = \mu_n$ .

A model ocean has been cut from a copper plate of 0.8 mm thickness. This was meant to represent a uniform ocean depth of 4,000 m. Hence, the linear scaling factor for the thickness as well as for the horizontal dimensions of the ocean was  $5 \cdot 10^6$ . The profile of the (plane) ocean was tailored after the actual coastline, rather than following a contour of constant depth. A cylindrical map projection was chosen. The Palk Strait was included in the first model, as if it had the same depth. This was done in view of the above conclusion that the conductor is to be found in the subocean floor in this area. For comparison, we investigated a second model in which the Palk Strait was cut out of the ocean profile. In a further modification of this model, the Palk Strait was represented by a thin copper foil bridging the cutout and corresponding to a conducting layer of 40 m of ocean water.

The equatorial electrojet was represented by a steel band of 13 cm width ( $\cong 650$  km) and 3 mm thickness ( $\cong 15$  km) at a height of 2.2 cm ( $\cong 110$  km). The total model which is shown in Fig. 4a had a size of  $2 \text{ m} \times 1 \text{ m}$ .

The magnetospheric current source was simulated by a steel band of 40 cm width ( $\cong 19^\circ$  of latitude) at a height of 15.5 cm. A picture of the model with the broad primary current is shown in Fig. 4b.

The choice of materials for ocean and primary currents was on the one hand dictated by simple practical considerations, like the ability to cut a complex profile. More important was the aspect that there should be a significant ratio between the height-integrated conductivities of ocean and primary current conductors, in order to keep mutual induction effects from "ocean" to primary conductor low. In the real world the ratio of the integrated conductivities of ocean and source region is of the order of 50. The corresponding ratio for the model is 13.

The conductivity  $\sigma_n$  of ocean water is  $4 \Omega^{-1} \text{m}^{-1}$ ; that of copper is  $\sigma_m = 6 \cdot 10^7 \Omega^{-1} \text{m}^{-1}$ . The natural and model permeabilities,  $\mu$ , are essentially unity. Hence we obtain from Equation 6 the following relationship between the natural and model periods:

$$P_m = 6 \cdot 10^{-7} P_n \quad (7)$$

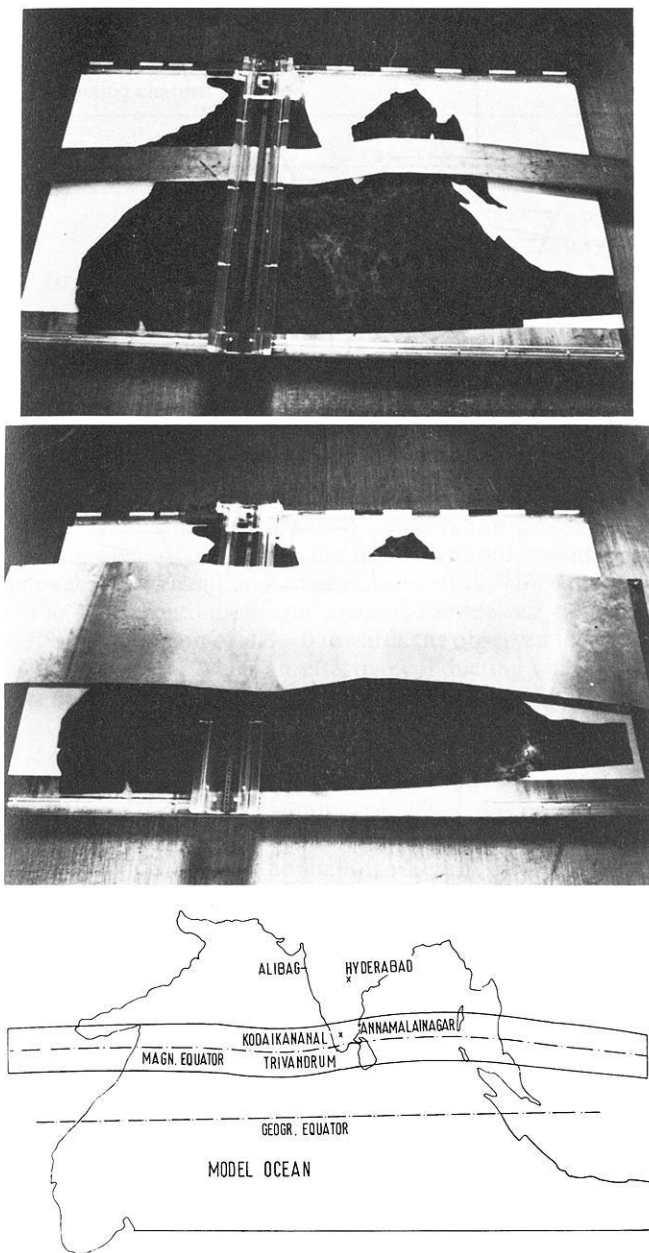


**Fig. 4a-c.** Photographs and map of the analogue model, **a** with narrow current band representing the equatorial electrojet, **b** with broad band representing a current in the magnetosphere, **c** map corresponding to **a**. The model ocean has a constant thickness of 0.8 mm ( $\cong 4,000$  m depth). The overall dimensions are 1 m  $\times$  2 m

A natural period of 1 h is scaled down to  $2.16 \cdot 10^{-3}$  s ( $\cong 465$  Hz). This is the frequency with which the primary current was generated. Its amplitude was 7.5 A. Special care was taken with the feeds to the primary generator. They were physically separated from the model as much as possible. Furthermore, helical winding of the wires to the diagnostic probe was employed. Several tests consisting of displacements of instruments, wires, etc. showed that mutual inductions in the various conductors surrounding the model could be kept so low that the perturbation on the measured fields did not exceed 2%.

The magnetic field probe consisted of a small coil of 1.5 mm inner diameter and 1.5 mm length with 100 wind-

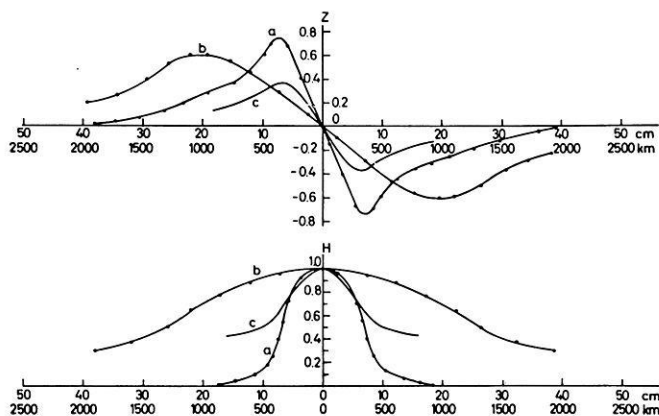


**Fig. 5a-c.** Z and H components of three different primary currents as function of distance from the equator, **a** for narrow model current, **b** for broad model current, **c** for electrojet according to Untiedt (1967)

ings. Each component of the magnetic field was measured with a special probe mounted in X, Y and Z directions. The voltage induced in the probes ranged from 1–100 V. The magnitude as well as the phase relative to the primary current was measured. The total error in the measurements ranged from 2–5%, partially caused by inaccurate reading, partially due to errors in the phase of the signal ( $\pm 5^\circ$ ). Near the “coastline”, where the magnetic field has strong gradients, errors of a few percent were introduced by the finite size of the probe. The positioning of the probe had an accuracy of 0.5 mm ( $\cong 2.5$  km).

### Results Obtained with the Analogue Model

Before we discuss the measurements obtained with the full model, we should compare the applied primary magnetic fields with those of the equatorial electrojet. This is shown in Fig. 5, giving the latitudinal profiles of H and Z at ocean level normalized to  $H=1$  at  $0^\circ$  magnetic latitude. Curves **a** and **b** represent the fields of the narrow and broad primary currents of the analogue model, respectively, whereas curves **c** were taken from Untiedt's (1967) theoretical model of the equatorial electrojet. The measurements were carried out in the absence of the copper plate representing the ocean. The profiles of our narrow primary current (**a**) and Untiedt's electrojet model (**c**) resemble each other quite closely and differ much from the broad-band model (**b**). However, the main simplification which we applied in the analogue model, namely to completely neglect the currents flowing outside about  $\pm 3^\circ$  magnetic latitude, shows up as a decay of the H-component at higher latitudes which does not exist in Untiedt's more realistic model of the equatorial current concentration. Equally, the vertical component of our model reaches unrealistically high amplitudes. These differences should be borne in mind when interpreting the coast effect of the analogue model.

In the light of the findings described in Paper I, we were mostly interested in the differences of the coast effect introduced by different degrees of homogeneity of the latitudinal distribution of the primary currents. However, we wanted to do this with a sufficiently realistic model of the conductivity distribution at the earth's surface. Therefore, we concentrated initially on the role of the channeling of

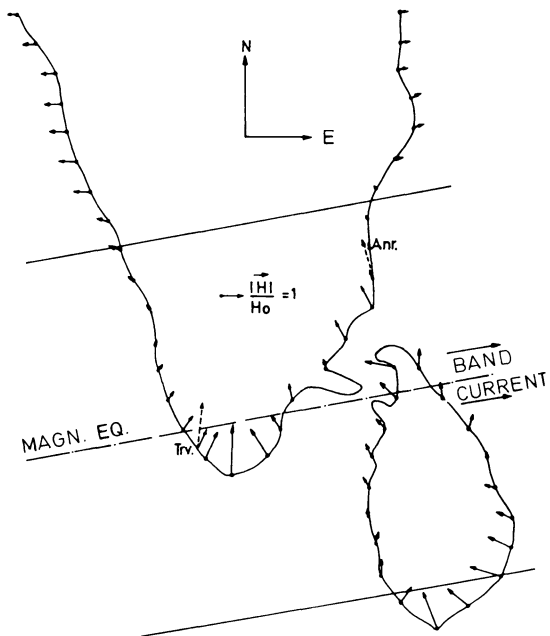
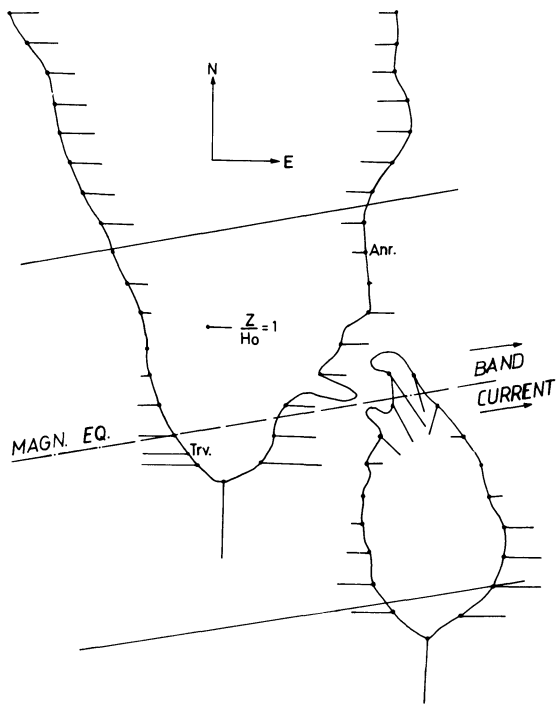


**Fig. 6a and b.** Normalized  $Z$  and  $H$  components measured with the analogue model along the coast of Southern India for variations of  $2.16 \cdot 10^{-3}$  s period. The solid lines parallel to the magnetic equator show the boundaries of the applied primary current. A conducting channel exists between India and Sri Lanka. **a** Bars extending into the ocean indicate  $\Delta Z < 0$ , bars extending inland indicate  $\Delta Z > 0$ . **b** The arrows represent the induced horizontal component only. The dashed arrows at TRV and ANR show the total perturbation field

currents through the Palk Strait. Figures 6a and 7a show, for comparison, the vertical components of the total field with and without the Palk Strait for the narrow primary current representing the daytime situation. The field is normalized to the primary  $H$ -component ( $H_0$ ) at ocean level underneath the electrojet axis in the absence of the model

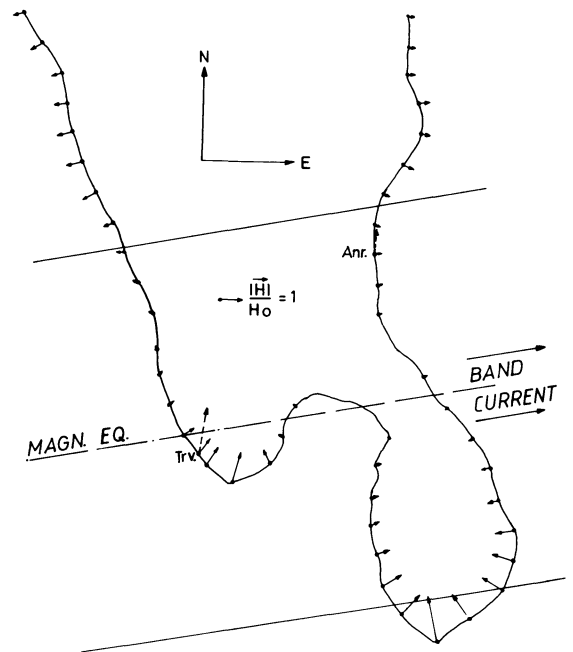
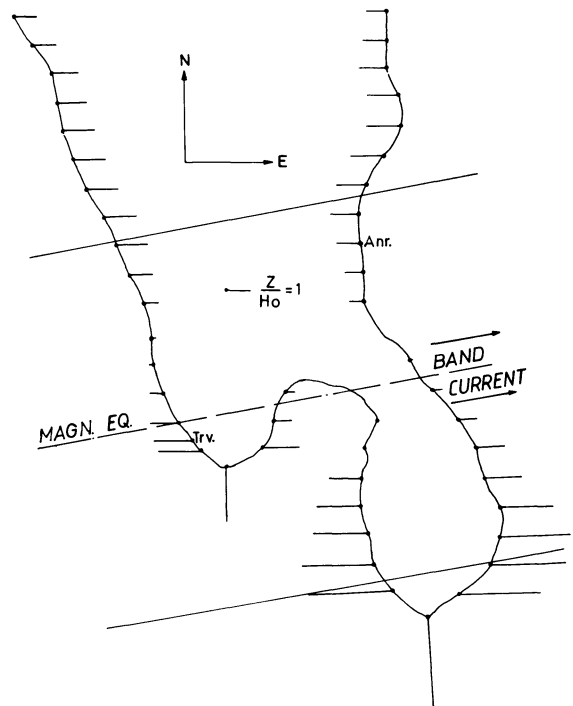


**Fig. 7a and b.** Same as Fig. 6 without a conducting channel at the Palk Strait. **a**  $Z$ -component, **b** induced part of  $H$ -component

ocean plate. Positive values of  $\Delta Z$  are indicated by bars pointing from coast to ocean; negative  $\Delta Z$  by bars pointing inland. Measurements were made every 1 cm ( $\cong 50$  km) along the coast. Figures 6b and 7b show the induced part of the  $H$ -component only, using the same normalization. Only at ANR and TRV do we show the total  $H$ -component.

The most significant differences naturally appear in the Palk Strait and over Sri Lanka. Attention should be given to the position of  $\Delta Z = 0$  on the east coast. The zero appears 3 cm south of ANR in the model without Palk Strait corresponding to 150 km and only 0.8 cm ( $\cong 40$  km) south of

**Table 2.** Some ratios of magnetic variations with  $\Delta Z=0$  at Annamalaiagar, *a* from magnetograms, *b* from analogue model, primary field only, *c* from analogue model, total field, with Palk Strait as conducting channel

Ratio	Station	<i>a</i>	<i>b</i>	<i>c</i>
$\Delta Z/\Delta H$	ANR	0	-0.63 <sup>a</sup>	0 <sup>a</sup>
	TRV	+0.95	+0.1	+0.92
	KOD	+0.1	-0.43	-0.19
$\Delta D/\Delta H$	ANR	-0.24	-0.18 <sup>a</sup>	-0.26 <sup>a</sup>
	TRV	+0.05	-0.11	+0.2
$\Delta H_{TRV}/\Delta H_{ANR}$	-	+1.12	+1.08	+1.30

<sup>a</sup> reading at 0.8 cm south of ANR point

ANR in the presence of a conducting channel. Recent measurements of Thakur et al. (1981) in the Palk Strait at Adiramapattinam (their station D4) confirm the presence of a strong positive  $\Delta Z$  where the model without conducting channel gives essentially a zero value (Fig. 7b). In spite of the simplifications of our analogue model we take the shift of the position of  $\Delta Z=0$  towards the observed location on the east coast when an effective conducting channel is introduced as strong evidence for its existence. On the west coast the Palk Strait channel has little effect. The values of  $\Delta Z$  and  $\Delta H$  at Trivandrum and further north are essentially unchanged. Here, the position of  $\Delta Z=0$  moved by only 0.4 cm ( $\approx 20$  km) southward when the conducting channel was removed.

The model in which the shallow water of the Palk Strait was represented by a thin foil bridging the gap in the model ocean plate did not yield induced fields near Annamalaiagar that were noticeably different from those obtained by the model without Palk Strait. Channeling in the shallow water only is obviously insignificant.

A better quantitative judgement of the validity of the analogue model can be obtained by comparing the ratios  $\Delta Z/\Delta H$ ,  $\Delta D/\Delta H$  for various stations and the ratio  $\Delta H_{TRV}/\Delta H_{ANR}$  as found from pure ionospheric perturbations (i.e.  $\Delta Z=0$  at ANR) with the readings of the analogue model. This is done in Table 2. Instead of taking the measurements at a point corresponding to the geographic location of Annamalaiagar, we took them at the equivalent location of the analogue model, namely where  $\Delta Z=0$  in the model (i.e. 0.8 cm south). This is indicated by an asterisk.

The comparison of columns *b* and *c* shows clearly the importance of the induction fields for  $\Delta Z$  and  $\Delta D$ . Furthermore, it is seen that the observed values at ANR and TRV are reasonably well reproduced by the model. The positive value of  $\Delta Z/\Delta H$  at Kodaikanal is not quite obtained by the model, but the induction fields drift  $\Delta Z$  in the right direction. This may be taken as an indication of a conductivity gradient in the crust underneath the Indian subcontinent (compare Murty and Swamy, 1978). If the model ocean had been tailored to follow the contour of 2,000 m depth,  $\Delta Z/\Delta H$  would have been much closer to the primary field value (column *b*). The ratio of  $\Delta H_{TRV}/\Delta H_{ANR}$  is mainly determined by the primary fields. The induction fields make the agreement slightly worse.

The next step is the comparison of the variations caused by narrow and broad primary currents. Figure 8 shows the  $Z$ -component for the latter in the presence of a conducting channel. This is to be compared with Fig. 6. We see a dis-

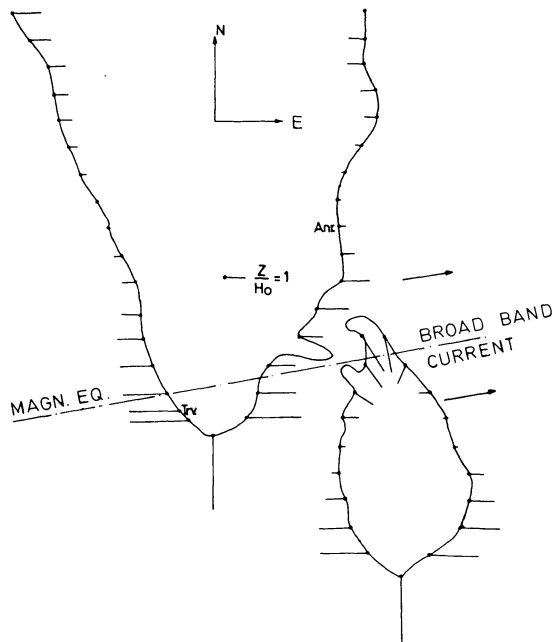


**Fig. 8.**  $Z$ -component for a broad primary current in a model with conducting channel at the Palk Strait

placement of the  $\Delta Z=0$  positions by 2.3 cm ( $\approx 115$  km) northward on the east coast and even by 4 cm  $\approx 200$  km on the west coast. This shift is the main point to note. It confirms the hypothesis expressed by Papamastorakis and Haerendel (1974) (see Paper I) that the appearance of a positive  $\Delta Z/\Delta H$  at ANR is a consequence of the wider latitudinal extent of primary currents flowing in the magnetosphere. The sign of the model  $Z$ -component is as observed, only its magnitude is somewhat lower than the actual value ( $\approx 60\%$ ). This is likely to be due to the limitations of the truncated model ocean, the flat earth model, and other unexplored subtleties such as sub-surface conductivity structure. On the other hand, a small but noticeable increase of  $\Delta Z/\Delta H$  between narrow and broad primary currents as actually observed for TRV (from 0.95 to 1.21, see Paper I) is also found with this model.

In order to obtain an idea of the distribution of the currents induced in the Arabian Sea and the Bay of Bengal we measured the electric field on the bottom side of the copper plate representing the ocean. This was done by voltage measurements between two fine steel spikes separated by 1 cm which were pressed into the copper plate. The induced current density is proportional to the electric field which was found to be essentially in phase with the primary current. The measurable shift was ranged between  $10^\circ$  and  $20^\circ$  in the sense that the electric field was leading the primary current. The flow lines of the electric current (perpendicular to the equipotentials) are shown in Fig. 9 for a narrow primary current. Although the model extended well below the lower rim of this figure (compare Fig. 4) the results become increasingly unreliable for southern latitudes because of the artificial cutoff of the conductor. The main features to observe are the two current vortices in the Arabian Sea and the Bay of Bengal and the channeling of current through the Palk Strait. As indicated by the shift of the locations of  $\Delta Z=0$ , the southern extent of the vortices shrink by 100–200 km when a broad primary current is applied.

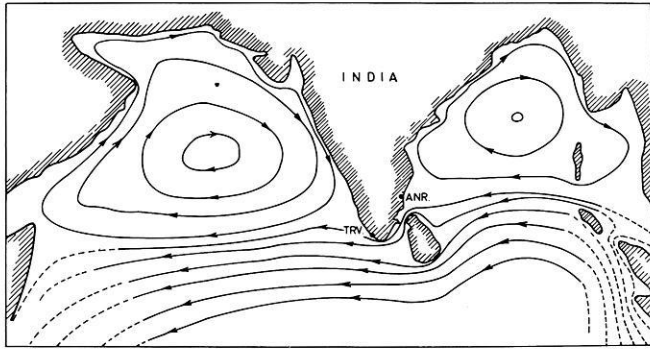


**Fig. 9.** Current flow lines as deduced from electric potential measurements at the bottom of the model ocean with conducting channel and for the narrow primary source current. The southern contours have been omitted because of edge effects

As a final step we studied the possible influence of a zone of increased conductivity at great depth underneath the continents as discussed by many researchers (e.g. Parkinson and Jones, 1979; Chan et al., 1981). To this end we placed a 3 mm thick copper plate at 6 cm ( $\approx 300$  km) underneath the surface level. As expected we observed a reduction of the coast effect on  $\Delta Z$  ( $\approx 25\%$  at TRV) but no qualitative change of the described results.

### Summary

We investigated essentially two questions concerning the geomagnetic coast effect in Southern India, the influence of a concentration of the primary current to a region of a few degrees width around the equator as compared with a broad profile in latitude, and the influence of a conducting channel through the Palk Strait on the readings of  $\Delta Z$  and  $\Delta H$  at the east coast, in particular. Induction arrows derived from magnetic perturbations seen at Annamalainagar as well as the measurements with the analogue model favor the existence of a conducting channel. It is argued that the currents rather than being concentrated in the shallow seawater flow predominantly in a layer of highly conducting material under the ocean floor. Such conductivity enhancements in the subocean crust have been postulated by many researchers. Careful studies with magnetometers on either side of the Palk Strait extending into India and Sri Lanka, in particular studies of the dependence of  $\Delta Z/\Delta H$  on period would be needed to derive more quantitative conclusions on the spatial extent of the conductivity enhancements. This is outside the scope of this paper.

Our main aim was to support conclusions described in Paper I on the separability of primary current sources in ionosphere and magnetosphere. The analogue model gives this support. It shows that the points of  $\Delta Z=0$  at the crust are at substantially different locations for narrow or wide primary currents. This is mainly a consequence of the difference in the magnitude of the primary  $\Delta Z$ , on which the secondary  $\Delta Z$  of the induced currents is superposed. The latter currents are forming vortices in the Bay of Bengal and the Arabian Sea whose sizes shrink with increasing width of the primary current. Zero secondary  $\Delta Z$  is found where the southern edge of the vortex meets the coastline. Our model with narrow primary current gives a location of the zero at the east coast almost precisely where it is actually observed, namely close to Annamalainagar. For

broad primary currents,  $\Delta Z/\Delta H$  is found to be positive at this station, in accordance with the observations.

This paper complements Paper I which deals with the observations of geomagnetic variations. Taken together we are now provided with a tool allowing us to separate ionospheric and magnetospheric origins of any short-period magnetic variation in the Asian sector. In a further publication we will apply this tool to bay-type and SSC-type magnetic perturbations and to the question of penetration of electric fields to low latitudes.

### References

- Chan, E., Dosso, H.W., Nienaber, W.: An analogue model study of electromagnetic induction in the Queen Charlotte Islands region. *J. Geomagn. Geoelectr.* **33**, 587–606, 1981
- Murty, A.V.S., Swamy, G.N.: A possible crust-mantle configuration near Trivandrum deduced from Indian geomagnetic data. *Phys. Earth Planet. Int.* **17**, 82–88, 1978
- Nienaber, W., Dosso, H.W., Law, L.K., Jones, F.W., Ramaswamy, V.: Electromagnetic induction in the Vancouver Island region. *J. Geomagn. Geoelectr.* **31**, 599–613, 1979
- Nityananda, N., Agrawal, A.K., Singh, B.P.: Induction at short periods in the horizontal variations in the Indian peninsula. *Phys. Earth Planet. Int.* **15**, 5–9, 1977
- Nityananda, N., Jayakumar, D.: Proposed relation between anomalous geomagnetic variations and the tectonic history of South India. *Phys. Earth Planet. Int.* **27**, 223–228, 1981
- Papamastorakis, I., Haerendel, G.: A possibility to separate ionospheric and magnetospheric origins of magnetic perturbations in South India. *EOS, Trans. Amer. Geophys. Union* **55**, 229, 1974
- Papamastorakis, I.: Eine Möglichkeit zur Unterscheidung von magnetosphärischen und ionosphärischen Magnetfeldstörungen in der Nähe des magnetischen Äquators, Ph. D. Thesis, Max-Planck-Institut, MPI-PAE/Extraterr. 111, 1975
- Papamastorakis, I., Haerendel, G.: A possibility to distinguish between ionospheric and magnetospheric origin of low latitude magnetic perturbations. *J. Geophys.* **51**, this issue, 1983
- Parkinson, W.D.: The influence of continents and oceans on geomagnetic variations. *Geophys. J. R. Astron. Soc.* **6**, 441–449, 1962
- Parkinson, W.D., Jones, F.W.: The geomagnetic coast effect. *Rev. Geophys. Space Phys.* **17**, 1999–2015, 1979
- Price, A.T.: Electromagnetic induction within the earth. In: *Physics of geomagnetic phenomena*, Vol. I, S. Matsushita and W.H. Campbell, eds. pp. 235–298. New York, London: Academic Press 1967
- Rajaram, M., Singh, B.P., Nityananda, N., Agrawal, A.K.: Effect of the presence of conducting channel between India and Sri Lanka Island on the features of the equatorial electrojet. *Geophys. J. R. Astron. Soc.* **56**, 127–138, 1979
- Thakur, N.K., Mahashabde, M.V., Arova, B.R., Singh, B.P., Srivastava, B.J., Prasad, S.W.: Anomalies in geomagnetic variations on peninsular India near Palk Strait. *Geophys. Res. Lett.* **8**, 947–950, 1981
- Takeda, M., Maeda, H.: Effect of the coastline configuration of South Indian and Sri Lanka Regions on the induced field at short period. *J. Geophys.* **45**, 209–218, 1979
- Untiedt, J.: Über den linearen Zusammenhang zwischen den Komponenten erdmagnetischer Variationen und seine Bedeutung für die erdmagnetische Tiefensondierung, *Nachr. Akad. Wiss. Göttingen, Math. Phys. Kl.* **1**, 1–24, 1964
- Untiedt, J.: Equatorial electrojet with meridional currents, *J. Geophys. Res.* **72**, 5799–5810, 1967
- Wiese, H.: Geomagnetische Tiefentellurik, *Geophys. Pura Appl.* **52**, 83–103, 1962

Received April 1, 1982; Revised August 4 and October 13, 1982  
Accepted October 29, 1982

## *Book Review*

**Wang, Herbert F. and Anderson, Mary P.: Introduction to Groundwater Modeling.** Finite Difference and Finite Element Methods. X + 237 pp., W.H. Freeman and Company, San Francisco, 1982. The authors' goal is "to enable readers to solve groundwater flow problems with the digital computer ... developed with the aim of conveying a full understanding of the steps leading to the short sample computer programs included as part of the text" This goal was realized throughout the book in a very good manner.

The book is divided into eight chapters. The first gives the basic physics of groundwater flow. It is a short description of the governing equations without any complications. The second chapter introduces Finite Difference models in general and especially solving Laplace's equation for steady-state flow. The chapter leads to a five-point star FD-approximation computer program solved by the iterative Gauss-Seidel method. The third chapter considers sources and sinks through the use of Poisson's equation including also the development of the equations for an unconfined aquifer with Dupuit assumptions. In the fourth chapter the authors present explicit and implicit FD solving methods for the transient (unsteady) flow. The fifth chapter points out other solution methods than the iterative methods used in the foregoing chapters. Presented are e.g. the short Thomas algorithm and the Alternating Direction Implicit method. The sixth chapter introduces the Finite Element method for the steady-state problem. Galerkin's method with triangular elements is used to develop the matrix equation. In the seventh chapter the transient (unsteady) flow is solved using the FE-method with rectangular elements for space and the FD-method for time. The eighth chapter is a short

introduction to the physical concepts of advective-dispersive transport and leads to the FE-example of solute dispersion in uniform flow field. The appendix consists of short notes on anisotropy and tensors, variational method, isoparametric quadrilateral elements and analogies.

In my view this book is not only a good introduction to numerical groundwater modeling but also to Finite Difference- and Finite Element-methods in general. It can readily be understood by all newcomers to numerical methods requiring only basic mathematical techniques. The presentation of short FORTRAN-computer programs for almost every problem of the context is a great advantage of the book. The reader has a tool for solving his own problem much easier than from theory-books. The book is completed by several notes and problems to the reader after every chapter reinforcing the principles presented in the foregoing chapter. Because of the aim of the book some simplifications of the mathematical theory of the Finite Difference- and Finite Element-method had to be made. But it is quite difficult to draw the line between exactness and application. To me, especially the validity of the numerical methods seems to have been neglected. More attention should be drawn to these problems than two little notes and a problem to the reader.

I think this book should be recommended to all, students as well as professionals, who want to be introduced to numerical groundwater modeling. This book is as good as a complete and very detailed university course.

**Nikolaus Klever**



# Investigations of the Internal Geomagnetic Field by Means of a Global Model of the Earth's Crust

J. Meyer<sup>1</sup>, J.-H. Hufen<sup>1</sup>, M. Siebert<sup>1</sup>, and A. Hahn<sup>2</sup>

<sup>1</sup> Institut für Geophysik der Universität Göttingen, Herzberger Landstr. 180, 3400 Göttingen, Federal Republic of Germany

<sup>2</sup> Niedersächsisches Landesamt für Bodenforschung, Stilleweg 2, 3000 Hannover 51, Federal Republic of Germany

**Abstract.** A global model of the Earth's crust has been constructed of two-layer blocks of  $2^\circ \times 2^\circ$  dimension, with thickness and susceptibility selected from a ten-step classification of the various crustal types. Considering induced magnetization only, the magnetic effect of each block has been approximated by a single dipole in the middle of the block, directed parallel to the field for a given main field model (32 400 dipoles altogether). The magnetic field of this global model of the crust has been calculated for an altitude of 450 km, appropriate for a comparison with anomaly fields from satellite surveys. From field values at  $1^\circ \times 1^\circ$  grid points, model anomaly charts for the X, Y, Z-components and for the total intensity can be plotted. The underlying crustal parameters have been prepared for modification towards adjusting the model field to the final Magsat anomaly field. The aim is to construct a truly realistic model of the whole Earth's crust.

Based on a global distribution of the Z-component of the model field a spherical harmonic analysis has been made by a direct integral method, up to degree and order 35. The energy density spectrum of the magnetic field, apart from the lowest degree terms, resembles a "white" spectrum in which the level nearly meets that obtained for the crustal part of an actual field model (from  $n=15$  to 29), except for a factor of less than 3. A supplemental evaluation of the core part of the observed spectrum indicates a source depth of some 100 km below the surface of the Earth's core, supported by a similar result for the secular variation of the core field.

**Key words:** Internal geomagnetic field – Crustal magnetization – Global crustal model – Spherical harmonic analysis – Energy density spectrum – Spatial spectrum of secular variation – Magsat

## Introduction

During the past two decades artificial Earth satellites have proved to be one of the most powerful tools in geosciences. The Magnetic Field Satellite (Magsat) conceived by NASA in cooperation with the U.S. Geological Survey and flown from 30 October 1979 to 11 June

1980 in a nearly polar, sun-synchronous orbit was designed to provide the first global survey of the Earth's magnetic field since the POGO-series (POGO 1, 2, 3 = OGO 2, 4, 6) of 1965–1971, and the very first vector survey at all. One of the main purposes of Magsat was a specific study of the large and intermediate-scale magnetic anomalies of lithospheric origin that had already been revealed by the POGO measurements (Regan et al., 1975). An example is the famous Bangui anomaly in Central Africa. Accordingly, the satellite was operated at particularly low altitudes providing data roughly between 570 and 190 km. A comprehensive description of Magsat including technical details can be found in a special volume of the John Hopkins APL Technical Digest (Gilbert, 1980). A brief overview has been given by Langel (1979) and by Mobley et al. (1980). Preliminary results of data evaluation have been set forth in a special issue of Geophysical Research Letters (Langel, 1982).

If the internal part of the geomagnetic field is understood as the sum of the *main field*  $B_c$  originating in the Earth's core and the crustal field or *crustal anomalies*  $B_a$  due to the irregularly distributed rock magnetization, then the crustal anomalies are obtained from the measured whole field  $B_w$  by subtracting both the core field  $B_c$  and the external part  $B_e$  resulting from ionospheric and magnetospheric currents,

$$B_a = B_w - B_c - B_e \quad (1)$$

where  $B$  stands for either the vector field or one of the cartesian field components. A minor field constituent in connection with internal electric currents induced by time variations of  $B_e$  will here be reckoned as part of the latter, as being proportional to it and lastly related to a primarily external origin. The appearance of a substantial  $B_e$  can be avoided or at least kept small by several means: by a satellite orbit continually near the dawn-dusk plane to evade considerable influence of the  $S_q$  daily variations; by evaluation of data from magnetically quiet days only; and by rejection of vector data from higher latitudes where field-aligned currents distort the field. Also, the homogeneous, i.e., the first-order part of the magnetospheric field can be determined and subtracted to some extent. Residuals of an incompletely eliminated external part, of course, restrict the accuracy of the anomalies derived. For simplicity,

however, it will be assumed that by a preceding evaluation of the raw data the external part has been fully removed. Thus  $B_e$  will be ignored in the following.

The core field  $B_c$  within global or regional investigations is usually represented by a worldwide field model derived from spherical harmonic analysis of the whole field and including all terms up to a certain maximum order and degree  $n$ . Cain (1975; 1976), Langel et al. (1980a; b), and Langel and Estes (1982) suggest a maximum  $n$  of 13 for an appropriate core field model. The anomaly charts defined and constructed in this manner simply display the distribution of the higher order terms of the whole field.

The real objective of mapping such anomaly charts is to interpret them in terms of large-scale geological and geophysical characteristics of the crust, in connection with similar studies of gravity anomalies, seismological findings, and regional geothermics, hence ultimately to facilitate future resource exploration strategy. Procedures like this are known as inversion. An example is the equivalent source technique applied, e.g., by Mayhew (1979; 1982a), Mayhew et al. (1980), and von Frese et al. (1981). Based on the measured anomaly chart as described above, they determine a uniform assemblage of source dipoles, for a limited surface section of a spherical earth, through a least-squares fit of the respective magnetic fields. The dipole coverage is then reduced further to a corresponding geographical distribution of magnetization in a crust of constant thickness (40 km). The direction of the surface dipoles or the magnetization is mostly chosen to be that of the main field at the same location, indicating that merely induced magnetization is considered. The existing results as well as their geophysical interpretation have already led to interesting aspects, mentioning only the attempts towards Curie isotherm mapping (Mayhew, 1982b).

An essential deficiency of this method is the uncertainty about the underlying anomaly charts. It can be taken for sure that the field model subtracted from the measured field in place of the true core field also comprises a non-vanishing crustal part of global or continental extent which thence is missing in the anomaly field and its equivalent source distribution. For the present investigations we have, therefore, raised the question of what the whole magnetic field of a given crustal model or, more strictly, a global magnetization model of the Earth's crust actually looks like without involving other sources. The calculated model field will be compared with and adjusted to the Magsat anomaly field as far as possible, on a global or regional scale, by modifying the underlying crustal parameters. The final aim is to construct a truly realistic model of the Earth's crust. Its significance lies in the fact that it renders possible not only a quantitative separation of core and crustal parts of the internal field but, along with this, also an improvement of the satellite anomaly charts towards inclusion of the lacking lower order terms.

### The Global Crust Model

For any global model of the Earth's crust the reliability desired must be balanced against the computation labour required. A discrete source representation of the crustal field must be spaced at intervals dense enough

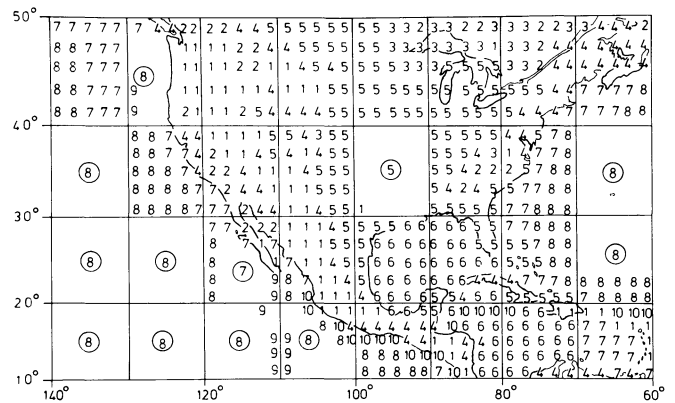


**Fig. 1.** Distribution of crustal types for North and Central America. Encircled numbers indicate the same type of crust for a large area

to secure that single sources will not be resolved as such. Since the comparison of the measured and the computed fields will be done for satellite altitudes, it is sufficient to subdivide the whole crust into segments of  $2^\circ \times 2^\circ$  dimension (16 200 altogether). Each of these segments is characterized by the predominant type of crust in a ten-step classification. For the first group of models discussed here the classification is based merely on geological considerations, as demonstrated in Fig. 1 by the section for North America. The key for this classification is as follows:

- (1) Basic rocks: basalt, diabase, amphibolite, serpentinite;
- (2) Acid rocks: granite, gneiss, acid volcanic;
- (3) Continental shields: Precambrian metamorphic rocks (except areas attributed to type (1) or (2));
- (4) Deformation zones: large fault systems, orogenic belts of Paleozoic or Mesozoic era including minor occurrences of basic, acid, and metamorphic rocks;
- (5) Platform sediments: undisturbed sediments with great thickness;
- (6) Shallow seas with high rates of deposition;
- (7) Continental shelves and slopes: up to 5 km water depth;
- (8) Oceanic crust: water depth of more than 5 km;
- (9) Midoceanic ridges;
- (10) Oceanic trenches.

Admittedly, such a ten-step classification can illustrate the complex nature of the real crust only roughly. And it must be emphasized that it is neither suited nor intended for modeling regional or even local anomalies. The model in all its parts ought to be seen definitely under global aspects. Also, it is still rather provisional in many respects, serving primarily to develop the software and to test the method as a whole. For instance, possible Curie isotherm effects (leading, for example, to a reduced thickness of the magnetized layer under young mountain ranges) have not been taken into account as yet. They will be considered when regionally adjusting the model more to reality, together with other crustal properties not incorporated with a merely geological description. What we are striving for is a usable magnetization model of the Earth's crust.

For the model treated here each of the above ten

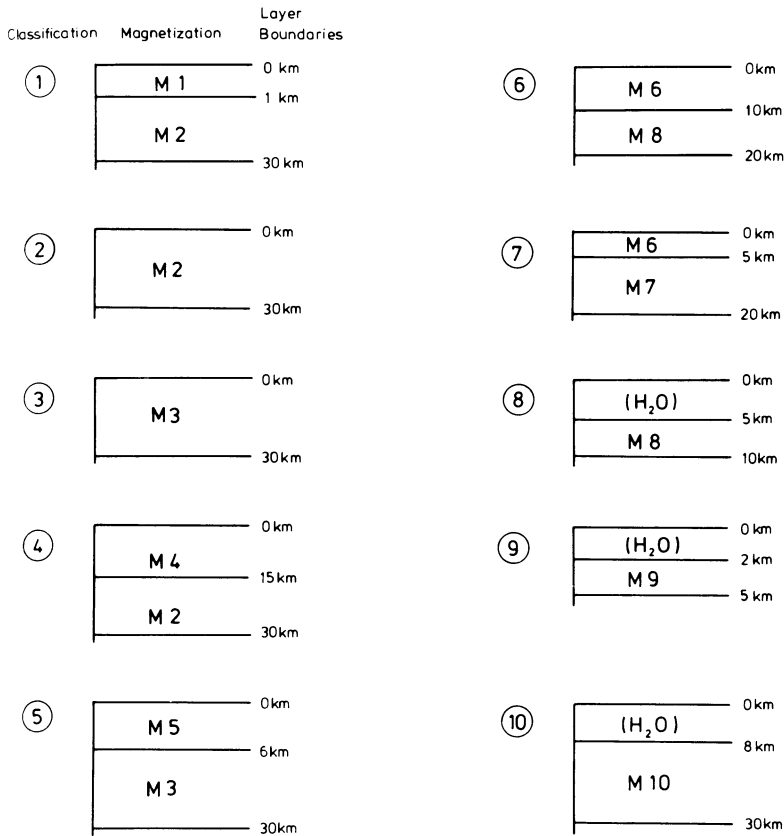


**Fig. 2.** Magnetization models of the ten types of crust (crustal model CRST-D-07-11);  $M_1$ ,  $M_2$ , etc. indicate specific values of magnetization

types of crust has been ascribed a two-layer magnetization model with, in general, different depths of layer boundaries. Thus every crustal segment consists of two blocks, each with a uniform magnetization  $M$  allowing a choice of 20 different values. Both thickness and magnetization are vanishing for some upper layers or equal for others (see Fig. 2). However, with regard to an easy modification of all parameters the two-grade classification of depth-structure and magnetization has been kept throughout the computation program. Actually, instead of the magnetization  $M$ , corresponding values of susceptibility  $\chi$  are presumed from which the latitude-dependent induced magnetization is then calculated. The values of  $\chi$  are in turn derived from magnetization estimates for middle latitudes (inducing field of 50 000 nT) as shown in Table 1 (cf. Landolt-Börnstein, 1982). In other words, the given susceptibility values are such that, for an inducing field of 50 000 nT, these magnetizations come out. The earth itself is regarded as spherical, and the topography has been neglected.

Each of the uniformly magnetized crustal blocks is now substituted by a single dipole at the center of the block having the coordinates  $r'$ ,  $\theta'$ ,  $\lambda'$  (spherical coordinate system with conventional notation). Its scalar magnetic moments  $m$  is

$$m(r', \theta', \lambda') = M\tau = \chi\tau F_c \quad (2)$$

where  $\tau$  is the block volume (varying with colatitude  $\theta'$ , upper surface depth  $r'_2$ , and block thickness  $d$ ),

$$\tau = \frac{\pi}{135} \sin 1^\circ \sin \theta' (3r'_2{}^2 d - 3r'_2 d^2 + d^3), \quad (3)$$

**Table 1.** Magnetization estimates and corresponding susceptibility of the crustal blocks for an inducing field of 50 000 nT

Magnetization Type	Magnetization value [A/m]	Susceptibility [SI-System]
$M_1$	2.0	$5.027 \times 10^{-2}$
$M_2$	0.7	$1.759 \times 10^{-2}$
$M_3$	1.5	$3.770 \times 10^{-2}$
$M_4$	0.5	$1.257 \times 10^{-2}$
$M_5$	0.0	0.0
$M_6$	0.0	0.0
$M_7$	0.7	$1.759 \times 10^{-2}$
$M_8$	1.3	$3.267 \times 10^{-2}$
$M_9$	1.3	$3.267 \times 10^{-2}$
$M_{10}$	0.2	$0.503 \times 10^{-2}$

and  $F_c$  is the total intensity of the inducing main field which here is represented provisionally by the IGRF 1965. The direction of the block dipole is considered to be that of the main field at the position of the dipole, i.e., at block center according to the restriction on induced magnetization. The ambiguity mentioned above of the field model regarding its significance as a mere core field is of less importance in this connection. Nevertheless, the IGRF 1965 will later be replaced in the program by an improved core field model. The main field elements at block center are obtained from an existing subroutine program (Cain et al., 1968). The three components of the block dipole moment are then calculated in the same manner as the components of the main field itself ( $I$ =inclination,  $D$ =declination at

dipole location):

$$\begin{aligned} m_r &= -m \sin I, \\ m_\theta &= -m \cos I \cos D, \\ m_\lambda &= +m \cos I \sin D. \end{aligned} \quad (4)$$

### Magnetic Field of the Crustal Model

Although the actual computation program does not pursue the following description in all details, the model field calculation on the whole can be divided into three sections. The first section comprises the calculation of the main field elements  $I$ ,  $D$ , and  $F_c$  at block center, and of the block volume  $\tau$  for each of the 32 400 crustal blocks and, based upon that, the computation of the magnetic moment  $m$  and its vector components for every single block, according to Eqs. (2)–(4). Any later modification of the global crustal model is done in this first section.

In the second section the magnetic field  $\mathbf{B}$  of the global crust model is computed for a fixed external point  $P(r, \theta, \lambda)$ . For simplicity and to save computation time, only those crustal dipoles within a limited geocentric angular distance around  $P$  are taken into account. By various test runs it turned out that in most respects a circle of  $30^\circ$  already yields sufficient accuracy for the succeeding plots of isolines. The results shown in Figures 3–12 have been obtained with a circle of  $70^\circ$ .

Let  $m(r', \theta', \lambda')$  be the magnetic moment of any crustal dipole within this circle. Its contribution to the magnetic potential, i.e., the potential of magnetic induction at  $P$  is (in SI-formulation)

$$\begin{aligned} V(r, \theta, \lambda) &= -\frac{\mu_0}{4\pi} \mathbf{m} \cdot \text{grad}(1/l) = \frac{\mu_0}{4\pi} \frac{\mathbf{m} \cdot \mathbf{l}}{l^3} \\ &= \frac{\mu_0}{4\pi} \frac{ml \cos(\mathbf{m}, \mathbf{l})}{l^3}, \end{aligned} \quad (5)$$

where  $\mathbf{l}$  is the vector distance between the positions of  $\mathbf{m}$  and  $P$  and  $\mu_0$  the permeability of vacuum. The potential of  $\mathbf{m}$  is calculated by adding the respective parts from the three dipole components,

$$\begin{aligned} V(r, \theta, \lambda) &= \frac{\mu_0}{4\pi} (\mathbf{m}_r + \mathbf{m}_\theta + \mathbf{m}_\lambda) \cdot \frac{\mathbf{l}}{l^3} \\ &= \frac{\mu_0}{4\pi} [m_r l \cos(\mathbf{m}_r, \mathbf{l}) + m_\theta l \cos(\mathbf{m}_\theta, \mathbf{l}) \\ &\quad + m_\lambda l \cos(\mathbf{m}_\lambda, \mathbf{l})] / l^3, \end{aligned} \quad (6)$$

where the direction cosines can be expressed by the known coordinates of  $\mathbf{m}$  and  $P$  (primed and unprimed coordinates, respectively):

$$V = (\mu_0/4\pi) [m_r(r a - r') - m_\theta r b + m_\lambda r c] / l^3 \quad (7)$$

with

$$\begin{aligned} l &= (r^2 + r'^2 - 2r r' a)^{1/2}, \\ a &= \cos \theta \cos \theta' + \sin \theta \sin \theta' \cos(\lambda - \lambda'), \\ b &= \cos \theta \sin \theta' - \sin \theta \cos \theta' \cos(\lambda - \lambda'), \\ c &= \sin \theta \sin(\lambda - \lambda'). \end{aligned} \quad (8)$$

As concerns the single dipole field, the algorithm is

similar to the one used by Mayhew (1979) for his equivalent source technique.

The magnetic induction  $\mathbf{B}$  at  $P$  is

$$\begin{aligned} \mathbf{B} &\equiv (B_r, B_\theta, B_\lambda) = -\text{grad } V \\ &= \left( -\frac{\partial V}{\partial r}, -\frac{\partial V}{r \partial \theta}, -\frac{\partial V}{r \sin \theta \partial \lambda} \right), \end{aligned} \quad (9)$$

where the components come from the partial derivatives of Eq. (7):

$$\begin{aligned} \frac{\partial V}{\partial r} &= \frac{\mu_0}{4\pi} \left\{ m_r \left[ a \left( \frac{1}{l^3} + 3r \frac{r' a - r}{l^5} \right) - 3r' \frac{r' a - r}{l^5} \right] \right. \\ &\quad + m_\theta \left[ -b \left( \frac{1}{l^3} + 3r \frac{r' a - r}{l^5} \right) \right] \\ &\quad \left. + m_\lambda \left[ c \left( \frac{1}{l^3} + 3r \frac{r' a - r}{l^5} \right) \right] \right\}, \end{aligned} \quad (10a)$$

$$\begin{aligned} \frac{\partial V}{r \partial \theta} &= \frac{\mu_0}{4\pi} \left\{ m_r \left[ \left( \frac{1}{l^3} + 3r \frac{r' a - r}{l^5} \right) (-\sin \theta \cos \theta' \right. \right. \\ &\quad \left. \left. + \cos \theta \sin \theta' \cos(\lambda - \lambda')) \right] \right. \\ &\quad + m_\theta \left[ -\frac{1}{l^3} (-\sin \theta \sin \theta' - \cos \theta \cos \theta' \cos(\lambda - \lambda')) \right. \\ &\quad \left. - 3b \frac{r r'}{l^5} (-\sin \theta \cos \theta' + \cos \theta \sin \theta' \cos(\lambda - \lambda')) \right] \\ &\quad + m_\lambda \left[ \frac{1}{l^3} \cos \theta \sin(\lambda - \lambda') \right. \\ &\quad \left. + 3c \frac{r r'}{l^5} (-\sin \theta \cos \theta' + \cos \theta \sin \theta' \cos(\lambda - \lambda')) \right] \left. \right\}, \end{aligned} \quad (10b)$$

$$\begin{aligned} \frac{\partial V}{r \sin \theta \partial \lambda} &= \frac{\mu_0}{4\pi} \left\{ m_r \left[ -\left( \frac{1}{l^3} + 3r \frac{r' a - r}{l^5} \right) \sin \theta' \sin(\lambda - \lambda') \right] \right. \\ &\quad + m_\theta \left[ -\frac{1}{l^3} \cos \theta' \sin(\lambda - \lambda') \right. \\ &\quad \left. + 3b \frac{r r'}{l^5} \sin \theta' \sin(\lambda - \lambda') \right] \\ &\quad \left. + m_\lambda \left[ \frac{1}{l^3} \cos(\lambda - \lambda') - 3c \frac{r r'}{l^5} \sin \theta' \sin(\lambda - \lambda') \right] \right\}. \end{aligned} \quad (10c)$$

The cartesian components  $X$ ,  $Y$ ,  $Z$  defined as usual (positive north-, east-, or downwards, respectively) are then

$$\begin{aligned} X &= -B_\theta \\ Y &= +B_\lambda \\ Z &= -B_r. \end{aligned} \quad (11)$$

The total field  $B$  follows from their root sum square:

$$B = (X^2 + Y^2 + Z^2)^{1/2}. \quad (12)$$

Summing up the computed field components  $X$ ,  $Y$ ,  $Z$  of all crustal dipoles involved, i.e., within the circular range considered, yields the magnetic field components

for the whole crust model at  $P$ . The corresponding total field again follows from Eq. (12).

If the components of the core field (suffix  $c$ ; here represented again provisionally by the IGRF 1965) are added to those of the crust model field, one gets the components of the whole internal field (suffix  $i$ ) at  $P$ ,

$$\begin{aligned} X_i &= X + X_c, \\ Y_i &= Y + Y_c, \end{aligned} \quad (13)$$

$$Z_i = Z + Z_c,$$

with the respective total fields

$$B_c = (X_c^2 + Y_c^2 + Z_c^2)^{1/2}, \quad (14a)$$

$$B_i = (X_i^2 + Y_i^2 + Z_i^2)^{1/2}. \quad (14b)$$

The scalar difference between  $B_i$  and  $B_c$  may be regarded as *model anomaly*  $B_a$  of the total field at that point:

$$B_a = B_i - B_c. \quad (15)$$

The model anomaly of any single field component is the model field component itself, as follows from Eqs. (13), and thus need not be treated separately.

In the third section the magnetic field quantities  $X$ ,  $Y$ ,  $Z$ ,  $B$ , and  $B_a$  of the global crust model are computed for a  $1^\circ \times 1^\circ$  net of grid-points at a provisional altitude of 450 km. The results for the whole Earth are stored, and a special plot-program delineates isomagnetic charts of the crust model field as well as model-isoanomalous charts of the total field, for any given region.

Figure 3 shows the isodynamic chart of the  $Z$ -component for North and Central America as an example. The numbers attached to the isolines give directly the numerical value of  $Z$  in units of nanotesla, the solid lines indicating positive and the dashed lines negative values. The lines are drawn at intervals of 1 nT ranging from  $-4$  nT to  $+9$  nT in this specific region. However, the single values are of less importance. What actually is important is the general pattern of the isolines in comparison with the large-scale crustal structure and the satellite anomaly chart. For instance, the Gulf of Mexico, the Caribbean Sea, and the Western Atlantic Ocean are clearly reflected as negative foci, whereas positive values are predominant throughout the United States and the isles of the Greater Antilles. The isoanomalous lines of the total field,  $B_a$ , ranging from  $-3$  to  $+8$  nT (Fig. 4) have a quite similar pattern, except for the foci which lie slightly more southward. Corresponding large-scale features are visible in the isoline structure of  $Z$  and  $B_a$  for Europe (Figs. 5 and 6), although the whole distribution, as expected, appears to be more complex. Again the continent is distinguished by positive values, whereas negative values prevail over oceanic crust including the Mediterranean and surrounding area.

The provisional global Magsat anomaly map derived by Langel (1981) (see also Langel et al., 1982a, b; Coles et al., 1982) shows comparable characteristics only partly. As to North America, the particulars mentioned above can in general be well recognized. On the other hand, the satellite map contains a number of real anomalies which are not or not as clearly reflected in

the crustal model field. Vice versa, the continental margins which in the crustal model field are so remarkably pronounced are hardly visible in the satellite map.

An extensive comparison of both charts requires consideration of the following aspects. (1) The field derived from Magsat data and the crustal model field must be compatible with respect to their spherical harmonic constituents (spatial spectrum). (2) Both elements of the global model, namely, the geological classification of the crustal blocks and the magnetization values associated with the crustal types involved, probably need a careful revision in regard to more reality and on grounds of the Magsat anomaly distribution. (3) One has to envisage the existence of anomalies which on principle cannot be described by a global model of the crust based merely on present geological knowledge and estimates of Curie isotherm variations. Anomalies of this type would have to be regarded as particular events to be studied by separate investigations. (4) The Magsat anomaly map might still contain uncertainties due to a possibly incomplete elimination of ionospheric contributions.

At the time being only aspect (1) has been treated further. As mentioned already, the satellite anomaly map is intrinsically truncated by subtracting a main field model of maximum degree and order 13 obtained from spherical harmonic analysis of the whole internal field, thereby also cutting off the lower order terms of the crustal part. The crustal model field, however, displays the whole spatial spectrum of crustal anomalies. The significance of the truncation of the satellite anomaly field can easily be demonstrated with the crustal model field by subtracting all terms up to  $n=13$  and comparing the result with the original, non-truncated field. Figure 7 shows the truncated crustal  $Z$ -distribution and Fig. 8 the truncated  $B_a$ -distribution for North and Central America; Figs. 9 and 10 give the same for Europe. The considerable change of structure, as compared with the non-truncated distributions (Figs. 3-6), is immediately obvious. Besides the finding that positive and negative foci thus appear more balanced in distribution and magnitude (ranging, e.g., from  $-4$  nT to  $+4$  nT for  $B_a$  in Fig. 8), it seems as if there would be also a somewhat higher resolution, induced simply by the lack of the lower-order terms, i.e., the absence of constituents of continental scale. In this way the general character of the truncated model-isoanomalous maps in fact resembles that of the satellite anomaly maps visibly better. The strong accentuation of the continental margins has almost vanished. And quite new features have appeared as, e.g., the focus of negative values for  $Z$  and  $B_a$  west to southwest of the Great Lakes to be noticed also in the satellite maps.

The improvement of compatibility for the "truncated" model charts is also visible for the section comprising Europe and the Mediterranean, concerning both  $Z$  and  $B_a$  (Figs. 9, 10). The focus of positive values north of the Black Sea obviously corresponds to the southern part of the positive anomaly in the satellite map. (The anomaly of Kursk observed at  $51^\circ$  E,  $36^\circ$  E is apparently one of the above mentioned particular events with sources not reflected in the geological classification of the crust). This positive anomaly stretches with a small saddle to the positive cell in Greece and

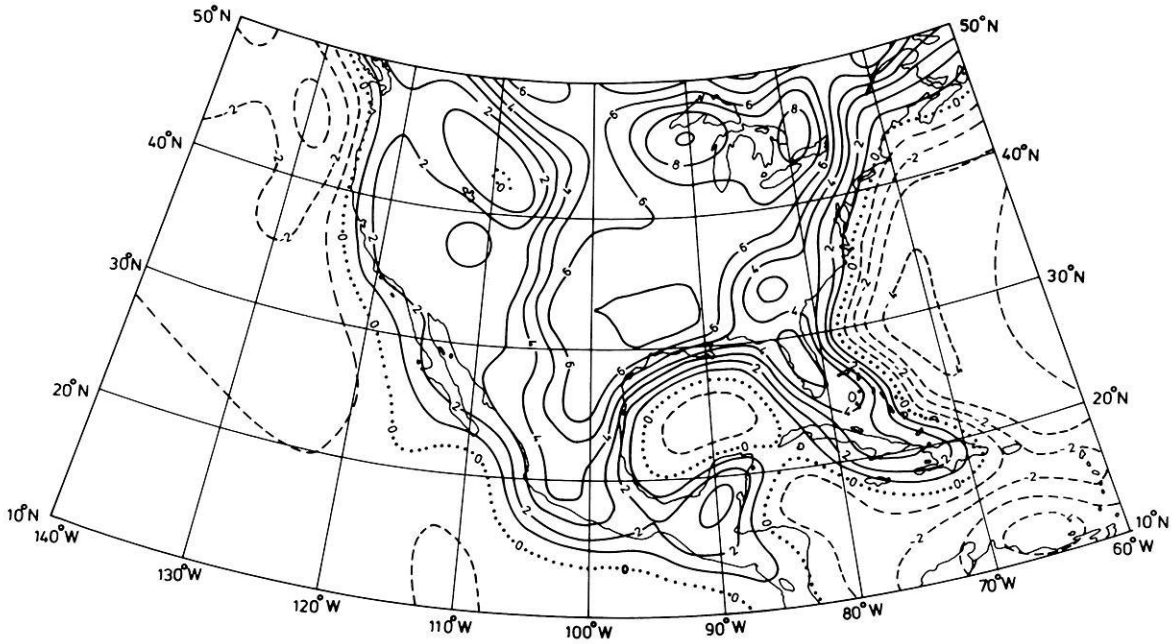


**Fig. 3.** Model-isodynamic chart of the Z-component for North and Central America (crustal model CRST-D-07-11). Units are nanotesla

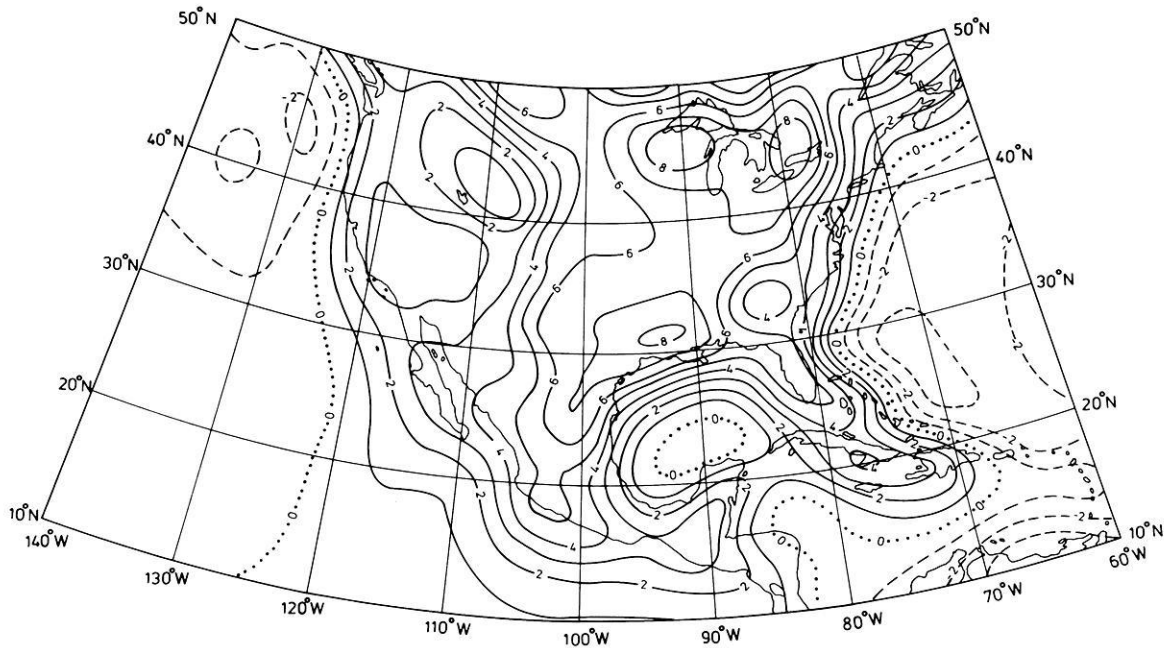


**Fig. 4.** Model-isoanomalous chart of the total field,  $B_a$ , for North and Central America (crustal model CRST-D-07-11). Units are nanotesla

the Aegean Sea. The strong positive focus in the crustal model field for Southern Scandinavia, lightly connected with the focus north of the Black Sea, relates well to a broad band of positive values in the satellite map. Also the negative focus near the Gulf of Finland can be recognized in both charts. On the other hand, the negative anomaly in Central Europe, extending from the North Sea to the Balkans, which is clearly evident in the satellite map can only partially be realized in the crustal model field, superimposed by other elements. Altogether, the correspondence of Figs. 9 and 10 to the

satellite map is poorest for the south-western section of the charts. However, when judging the present results of the crustal model field, it should again be called to mind that the whole model is based solely on a limited number of crustal types associated with certain magnetization estimates, and that no effort for an adjustment of the model field to the satellite maps has been made as yet. The model field distribution shown in Figs. 7–10 thus may be regarded as a first attempt at a real interpretation of the satellite anomalies.

Figures 11 and 12 illustrate the sum of the cut-off

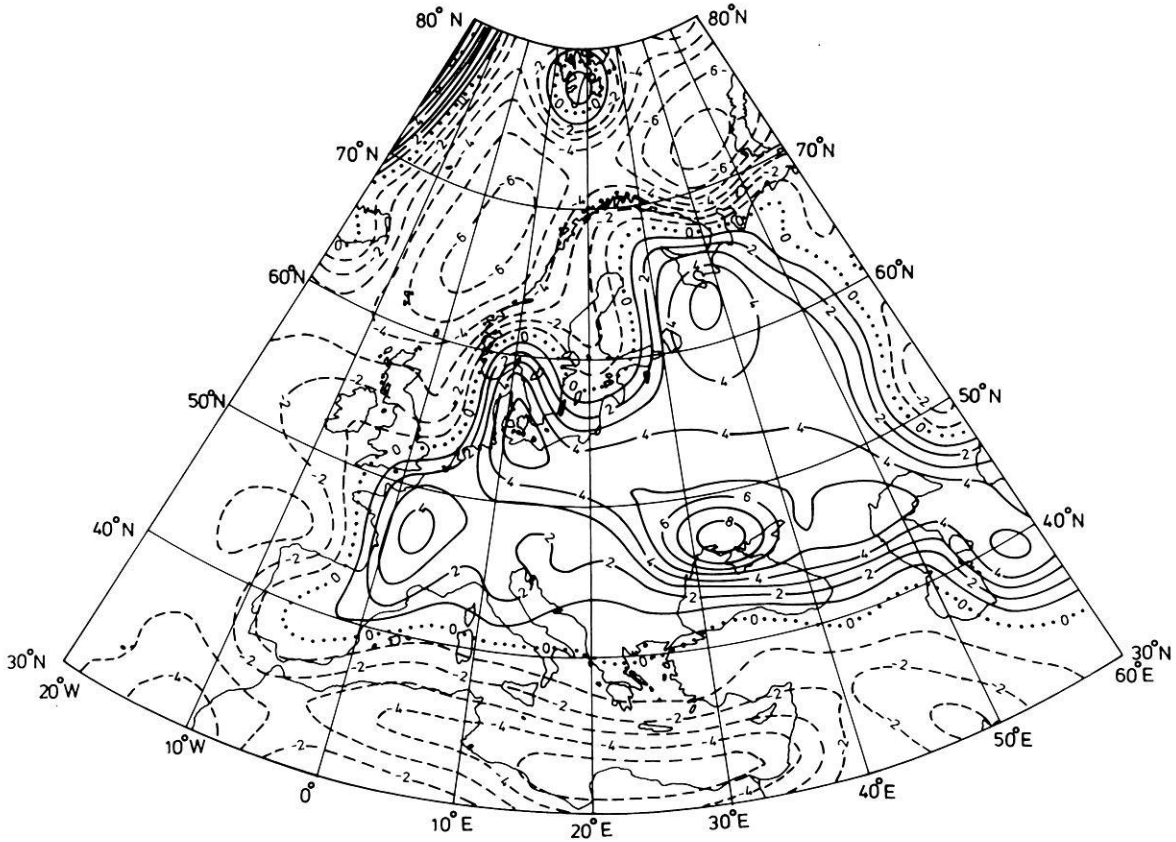


Fig. 5. Model-isodynamic chart of the Z-component for Europe and surrounding area

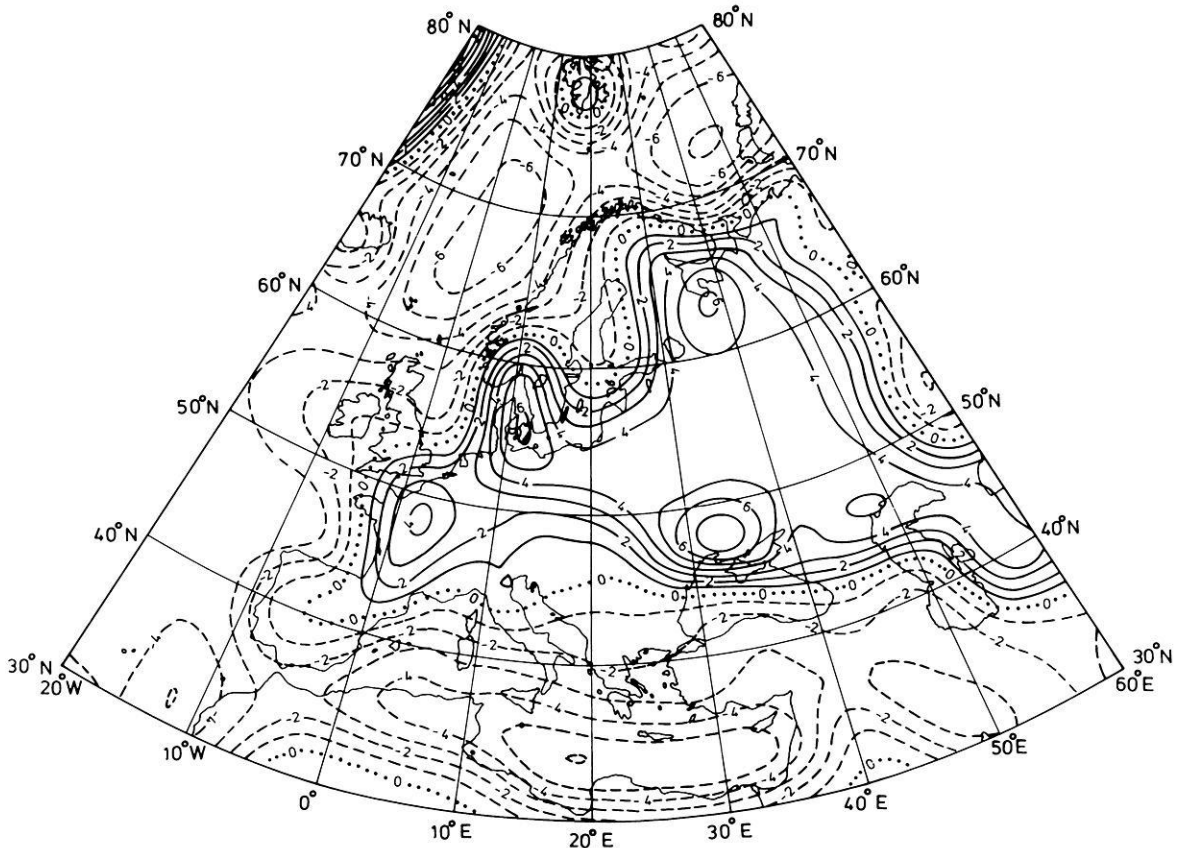


Fig. 6. Model-isoanomalous chart of the total field,  $B_a$ , for Europe and surrounding area

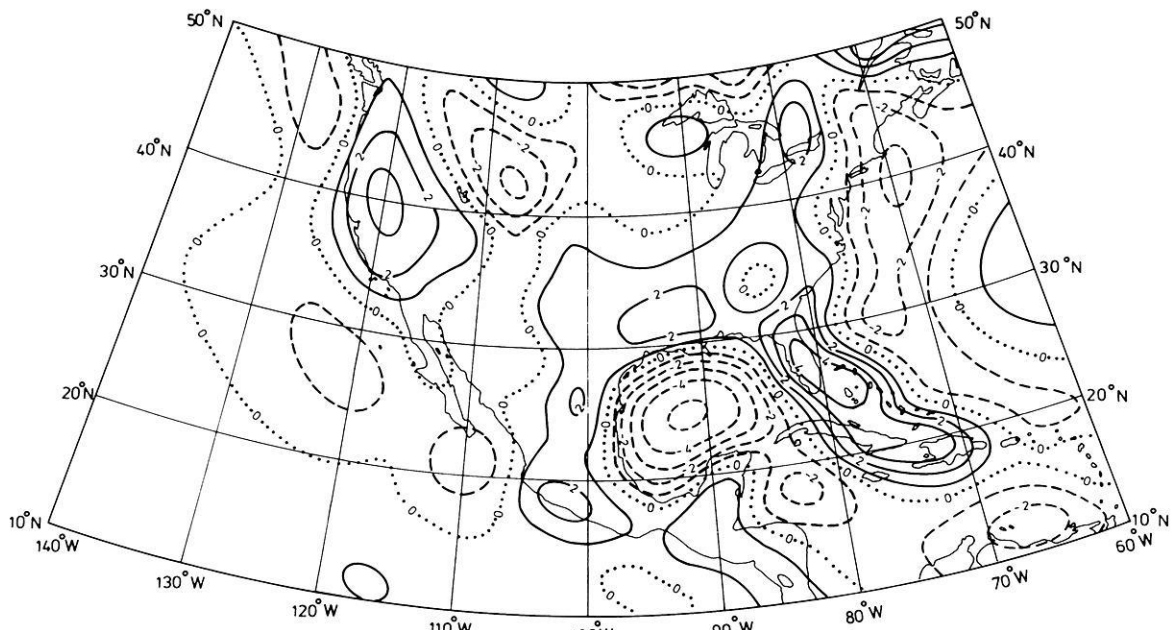


Fig. 7. Truncated model-distribution of  $Z$  for North and Central America, i.e., same as Fig. 3 except all terms from  $n=1$  to 13

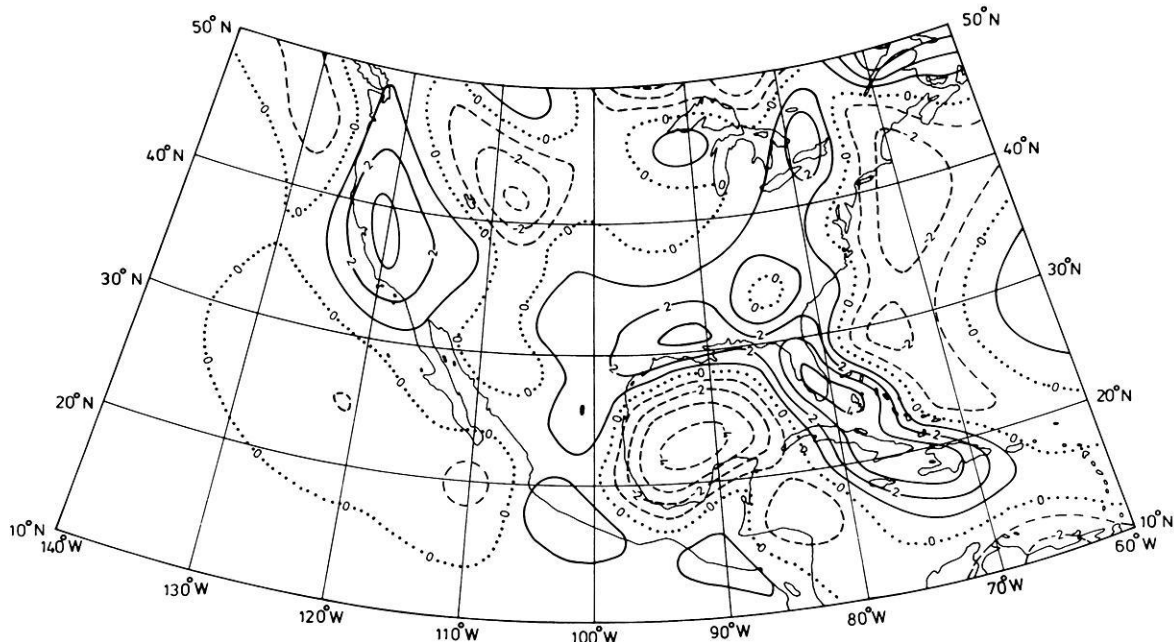


Fig. 8. Truncated model-distribution of  $B_a$  for North and Central America, i.e., same as Fig. 4 except all terms from  $n=1$  to 13

terms from  $n=1$  to 13 for the  $Z$  and  $B_a$  model distributions within a section including North America, the North Atlantic, and Europe. Note that the magnitude of the contours rises to the same order as for the truncated model-isoanomalous charts (Figs. 7–10), namely +7 nT in North America and +6 nT in Europe. This accounts for the predominance of positive values for the whole model field over the continental areas (Figs. 3–6), and for the considerable alteration including change of sign if this field part is subtracted. The structure of the low-order part clearly follows the large-scale composition of the crust, elucidating the predominance of continental margins in the whole crustal model field. For comparison see the low-order spherical harmonic

model of crustal thickness derived from seismological measurements (Soller et al., 1981). The results about magnitude and structure of the cut-off part accentuate the importance of taking this constituent into account for any isodynamic chart intended to display the whole crustal field. Future investigations will have to be made aiming at an inclusion of the lacking lower-order terms, for instance by a truly realistic global model of crustal magnetization.

#### Energy Density Spectrum

As has already been pointed out, a comparison of our crustal model field with the satellite anomaly field

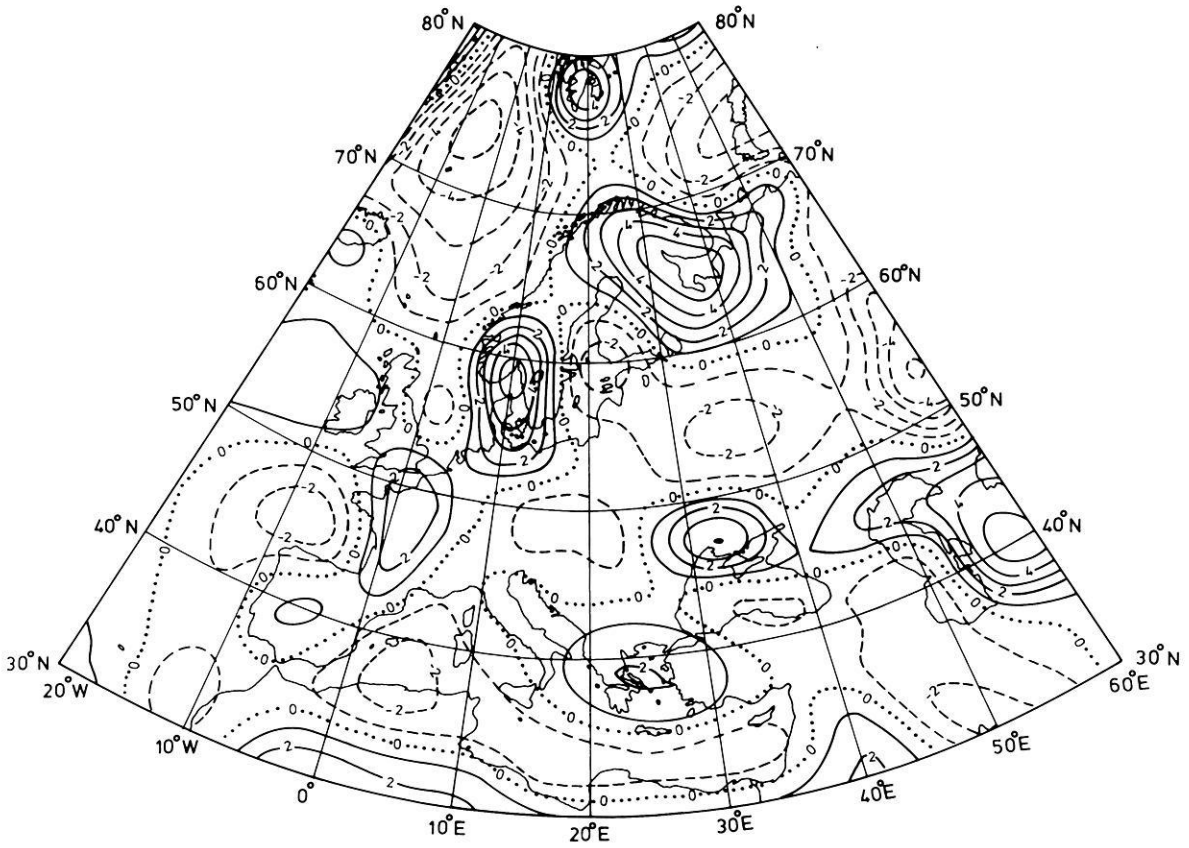


Fig. 9. Truncated model-distribution of  $Z$  for Europe and surrounding area, i.e., same as Fig. 5 except all terms from  $n=1$  to 13

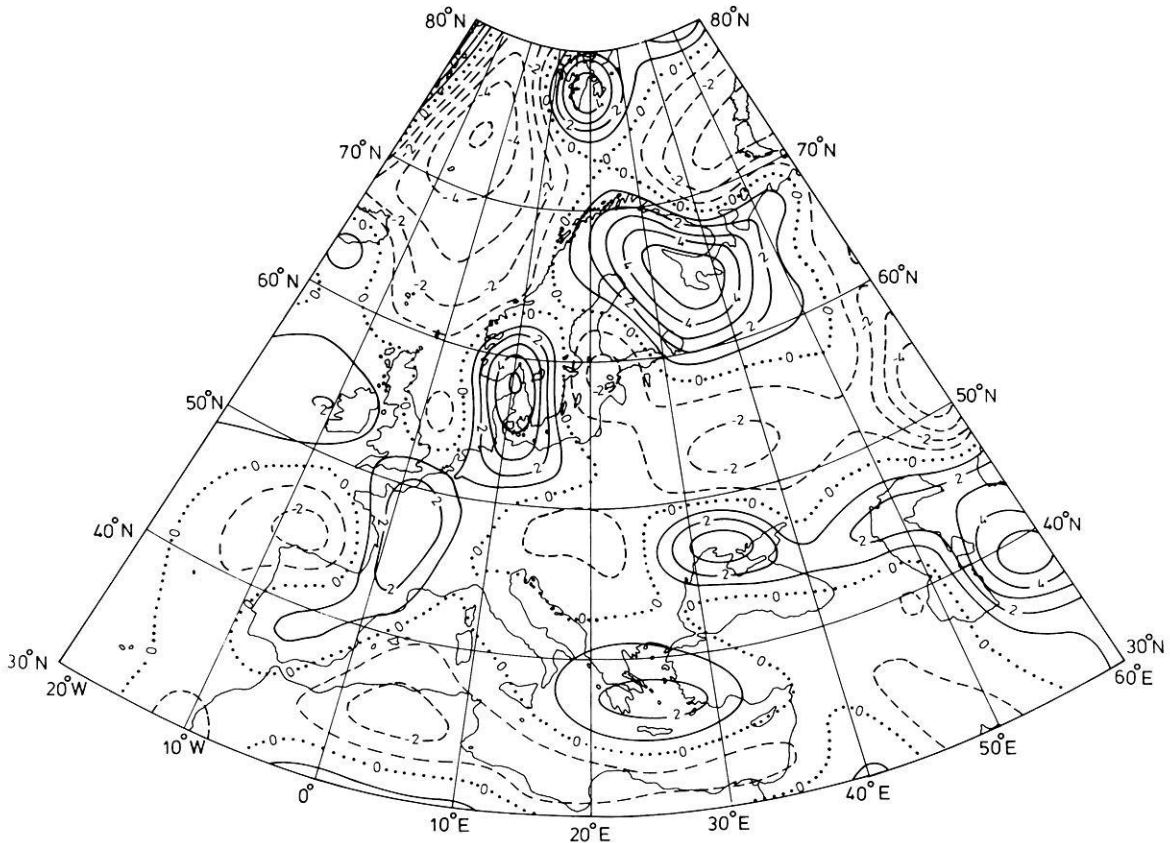


Fig. 10. Truncated model-distribution of  $B_a$  for Europe and surrounding area, i.e., same as Fig. 6 except all terms from  $n=1$  to 13

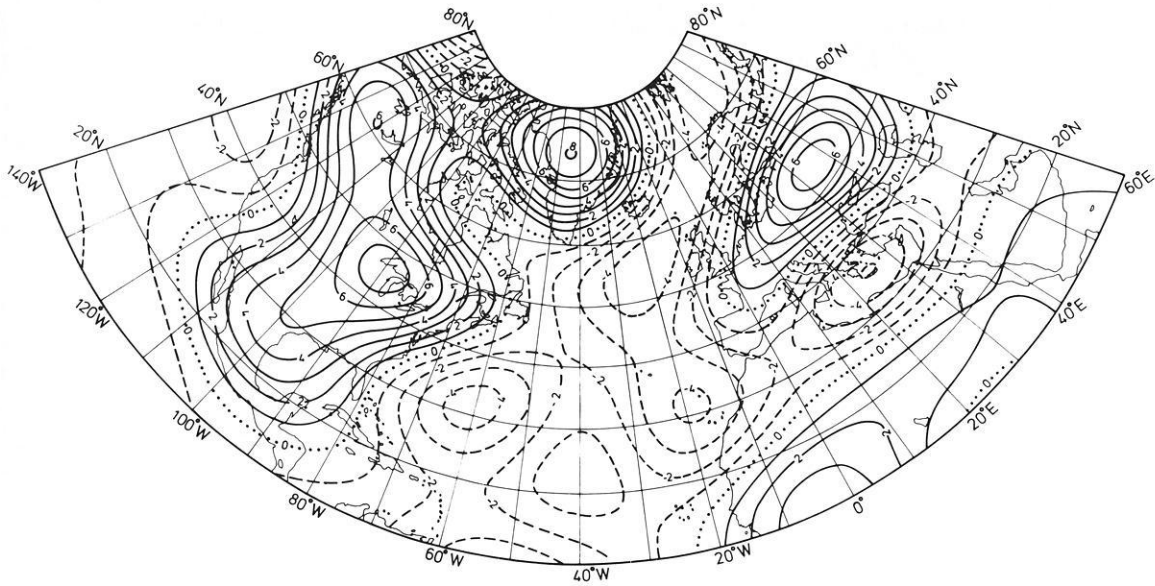


Fig. 11. Model field part of  $Z$  from  $n=1$  to 13 for a section covering the area of Figs. 3 and 5

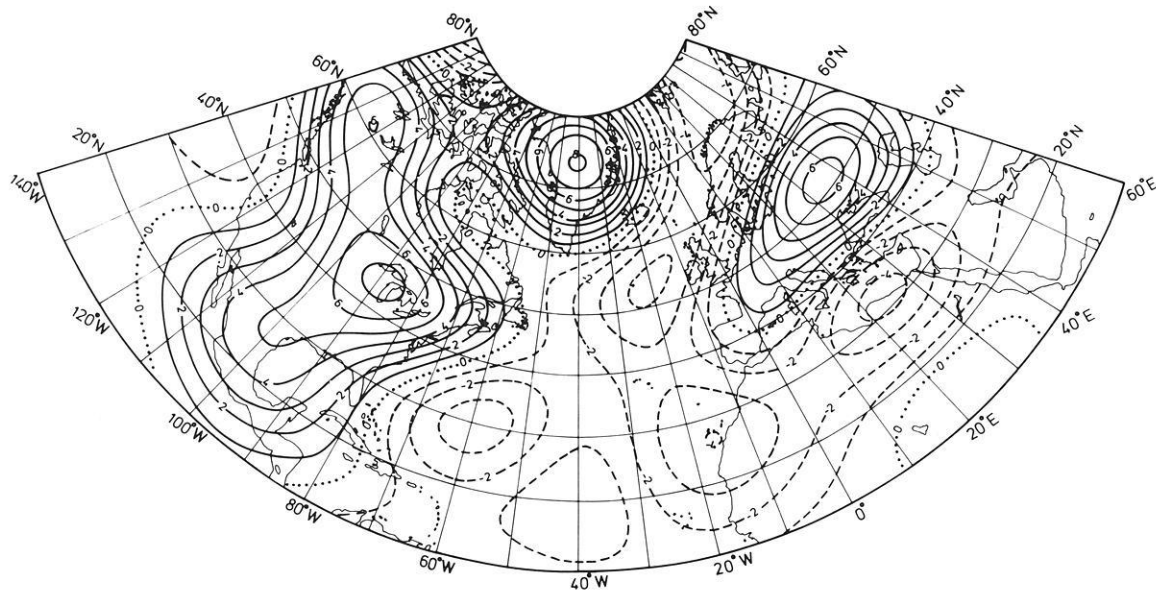


Fig. 12. Model anomaly part of  $B_a$  from  $n=1$  to 13 for the same section as in Fig. 11

should preferably be done under global aspects, even though the model field may be accommodated to the truncation of the latter. A method which accentuates certain global characteristics of a potential field is the classical spherical harmonic analysis. The magnetic field  $\mathbf{B}$  at an altitude of 450 km is expressed by an expansion of its potential  $V$  into a series of associated Legendre functions,

$$V = R_E \sum_{n=1}^{\infty} \sum_{m=0}^n \left( \frac{R_E}{r} \right)^{n+1} (g_n^m \cos m\lambda + h_n^m \sin m\lambda) P_n^m(\theta) \quad (16)$$

where  $R_E = 6371.2$  km is the Earth's radius, and  $r = R_E + 450$  km. The  $P_n^m(\theta)$ , by convention, are the Schmidt quasi-normalized functions. The Gaussian coefficients  $g_n^m$  and  $h_n^m$  decisive for the field distribution are usually

determined from the measurements by an extensive least-squares method. Since, however, the crustal model field has been calculated to a high accuracy for the  $1^\circ \times 1^\circ$  net of grid-points covering the whole Earth, and since further, per definition, there is no external part, the calculation here was made directly by a twofold numerical integration based solely on the  $Z$ -component:

$$\begin{aligned} \begin{Bmatrix} g_n^m \\ h_n^m \end{Bmatrix} &= -\frac{2n+1}{4\pi(n+1)} \left( \frac{r}{R_E} \right)^{n+2} \int_0^\pi \int_0^{2\pi} Z(\theta, \lambda) P_n^m(\theta) \\ &\quad \times \begin{Bmatrix} \cos m\lambda \\ \sin m\lambda \end{Bmatrix} \sin \theta d\theta d\lambda \\ &\quad (n=1, 2, \dots; m=0, 1, \dots, n). \end{aligned} \quad (17)$$

With  $r$  specified as indicated above the coefficients  $g_n^m, h_n^m$  all refer to the surface of a spherical earth. But they can easily be reduced to any other concentric reference sphere with radius  $R_c$  (outside the sources) by a mere reduction factor of  $(R_E/R_c)^{n+2}$ .

The actual computation (cf. Chapman and Bartels, 1940) begins with a Fourier analysis along circles of constant colatitude  $\theta$ , at  $1^\circ$ -intervals, yielding the Fourier coefficients

$$\left\{ \begin{array}{l} a_m(\theta) \\ b_m(\theta) \end{array} \right\} = \frac{1}{\delta_m \pi} \int_0^{2\pi} Z(\theta, \lambda) \left\{ \begin{array}{l} \cos m\lambda \\ \sin m\lambda \end{array} \right\} d\lambda \quad (18)$$

$$(m=0, 1, \dots)$$

with

$$\delta_m = \begin{cases} 2 & \text{for } m=0 \\ 1 & \text{for } m \geq 1. \end{cases}$$

From these the  $g_n^m, h_n^m$  can be obtained by a simple quadrature:

$$\left\{ \begin{array}{l} g_n^m \\ h_n^m \end{array} \right\} = -\delta_m \frac{2n+1}{4(n+1)} \left( \frac{r}{R_E} \right)^{n+2} \int_0^\pi \left\{ \begin{array}{l} a_m(\theta) \\ b_m(\theta) \end{array} \right\} P_n^m(\theta) \sin \theta d\theta$$

$$(n=1, 2, \dots; m=0, 1, \dots, n).$$

In both cases the integration is done numerically.

For the crustal model field the Gaussian coefficients were calculated up to degree and order 35 (1295 coefficients altogether). The  $2n+1$  coefficients of the same degree  $n$  were then reduced to a single quantity  $W$  through their summed squares:

$$W(n) = (n+1) \sum_{m=0}^n [(g_n^m)^2 + (h_n^m)^2]. \quad (20)$$

Physically, this quantity measures the energy density of the particular field constituent averaged over the whole Earth, except for a factor of  $1/2\mu_0$  (Mauersberger, 1956; Lucke, 1957; both reviewed by Kautzleben, 1963; see also Lowes, 1966). The function  $W(n)$  thus can be regarded as the spatial spectrum of the mean energy density of the magnetic field. It is in many respects an appropriate measure for a global comparison of the crustal model field and the observed field.

### Spatial Spectrum of the Crustal Field

Figure 13 shows in the upper diagram the spatial energy density spectrum of the crustal model field considered. Apart from the lowest two degrees it resembles a "white" spectrum on a level of nearly  $10^1$  (nT)<sup>2</sup>. Of course, in view of a finite total energy amount the spectrum cannot really be white throughout. For some very high  $n$  it must drop off to zero. Yet for illustration the term "white spectrum" has been retained for any horizontal section of the spectrum.

The diagram beneath gives to the same scale the corresponding spectrum of the observed internal magnetic field or, more strictly, of a particular field model

(M051782) developed by J.C. Cain of the U.S. Geological Survey. It is based on a selected magnetically quiet sample of Magsat data and extends up to the degree of 29. As is readily apparent, the spectrum is split into two quasi-linear sections where the right one, from about  $n=15$  on, again resembles a "white" spectrum on a level which lies very close to that of the crust model field spectrum, being only slightly higher by a factor of less than 3. This finding not only identifies the horizontal section of the internal field spectrum clearly as a part of predominantly crustal origin. It justifies at the same time in a certain measure the assumptions made about the global crust model on the whole. Moreover, since the induced crustal field is essentially the result of the large-scale characteristics of the crust irrespective of the inducing core field structure (Runcorn, 1975), the equipartition of energy with regard to sum-square surface harmonic distributions of different degrees implies that there is obviously no world-wide, significant harmonic constituent prevailing in the global magnetization structure of both the crustal model and the real crust.

### Main Field Analysis

The left-hand section in the lower diagram of Fig. 13, up to about  $n=12$ , must surely be attributed to deeper sources, i.e., to the core part of the internal magnetic field. (The two terms of degree 13 and 14 are the transition terms). From the spatial spectrum of the crustal model field it is certainly evident that these terms still include a non-vanishing part of crustal origin. But the crustal constituent is in all cases small compared with the real core field part. This already renders feasible a particular core field analysis by a coarse separation of the core and crustal parts of the internal field spectrum.

The dipole part ( $n=1$ ) clearly stands above the general trend of spectral terms, requiring conclusively a separate treatment with a source mechanism probably involving major parts of the whole core. The following evaluation, therefore, is confined to the terms from  $n=2$  to 12 where a quasi-linear decrease is to be noticed. Owing to the fact that the ratio of the radii in Eq. (17) is involved with a specific power of  $n$ , any linear decrease of spectral terms in the semi-logarithmic diagram of Fig. 13 strictly accords with a "white" spectrum at a certain depth beneath the Earth's surface, determined by the reduction factor which compensates the slope of the spectrum. If one assumes that this depth is in a way indicative of the depth of a corresponding source layer – analogous to what has been found to be true for the crustal field – then one can easily estimate the respective source layer depth. The line drawn in the lower left corner of the diagram shows the theoretical slope for a white spectrum at the surface of the Earth's core, i.e.,  $-2 \log(6371/3471) = -0.5275$ , involving the ratio of the radii of Earth and core. It fits the inclined spectrum section already pretty well. The line actually drawn through the point distribution is the calculated regression line which has only an insignificantly steeper slope indicating a slightly greater source depth of 162 km beneath the surface of the Earth's core.

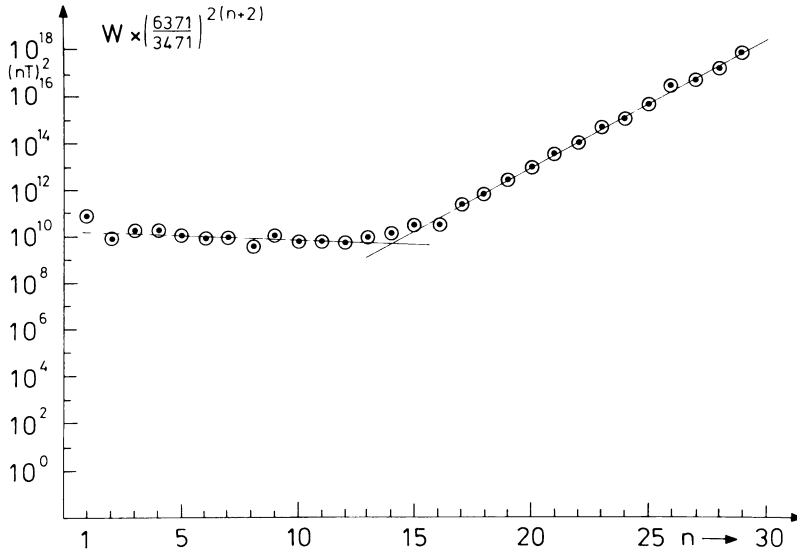
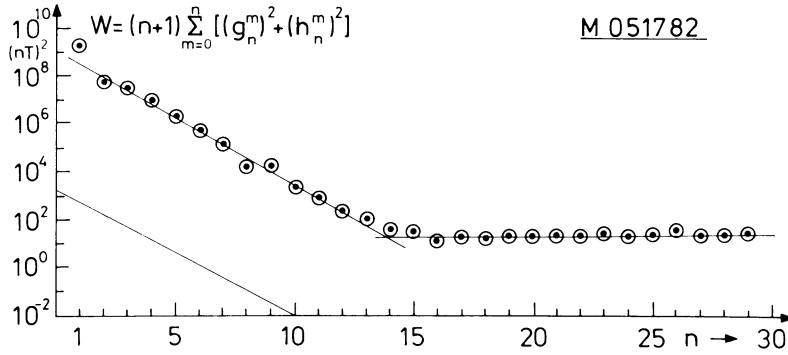
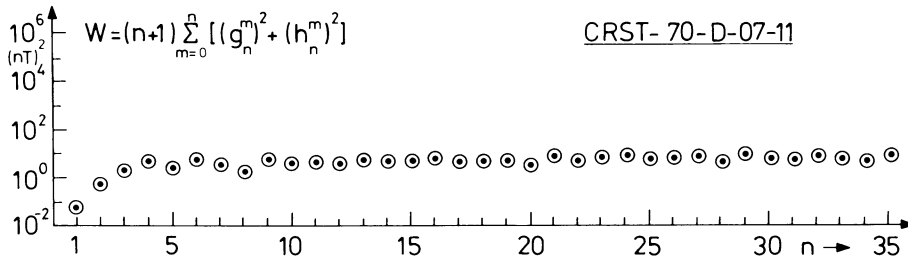


**Fig. 13.** Spatial energy density spectrum of the crustal model field (above) and the observed internal field (below).  $W$  is the total mean square contribution of magnetic induction by all harmonics of degree  $n$

**Fig. 14.** Spectrum of the internal field (same as in Fig. 13, lower diagram) reduced to the surface of the Earth's core

**Table 2.** Results of effective source layer depth

Field model	Author	Epoch	Depth beneath core surface of a "white" spectrum ( $n=2 \dots 12$ )
M051780	J.C. Cain	1980.0	(162 ± 48) km
U061380	J.C. Cain	1965.0	(115 ± 54) km
U041580	J.C. Cain	1965.0	(150 ± 57) km
M050580	J.C. Cain	1980.0	(142 ± 48) km
M061581	J.C. Cain	1980.0	(153 ± 49) km
MGST 6/80	R.A. Langel	1979.85	(163 ± 48) km
Mean			(147 ± 50) km

To better recognize the deviation from a white spectrum at the core surface we have reduced the spectral function  $W(n)$  to exactly this level of reference, simply through multiplying  $W(n)$  by a factor of

$(6371/3471)^{2(n+2)}$  (Fig. 14). A white spectrum at this level would per definition appear as a strictly horizontal section. In fact, the slight decrease to be noticed for the spectral terms from  $n=2$  to 12, perceptible also for the regression line, again corresponds to an effective source layer depth of 162 km beneath the reference level. The step increase of the right-hand spectrum section is of merely formal character. It shows only how an equivalent source field spectrum at the surface of the Earth's core would have to be conceived in order to produce the white spectrum of the crustal field part observed at the Earth's surface.

Analyses like this have been done for six recent field models. The results about the source layer depth are made up in Table 2. The particular standard error is derived from the deviations of the spectral terms from the regression line. Its average of  $\pm 50$  km gives an impression of how the calculated source depth varies on account of the secular variation and, in ad-

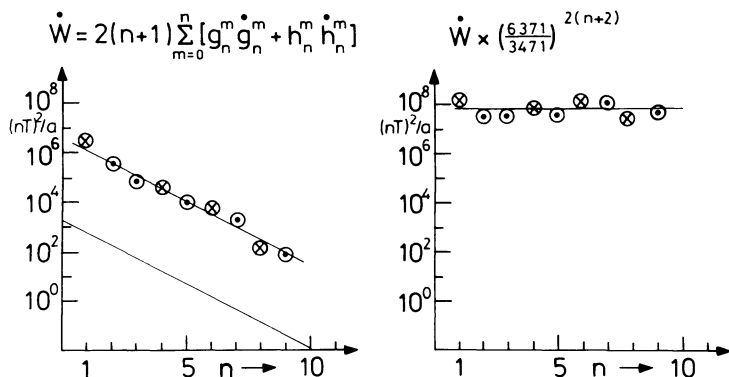


**Fig. 15.** Spatial energy density spectrum of the observed secular variation, referring to the surface of the earth (left) or reduced to the surface of the Earth's core (right).  $\dot{W}$  is the first time-derivative of the spectral function  $W$

dition, may indicate the order of thickness of the source layer. The actual scattering of the five depth values about the average depth of 147 km, however, is notably smaller ( $\pm 16$  km only), indicating that the underlying field models cannot be considered as statistically independent. Besides the fact that in part the same raw data have been utilized, even completely different field models within a time-span of one or two decades would not yet reflect the full range of secular variation. Thus the de facto scattering of the source layer depth primarily expresses magnetic survey and data reduction deficiencies. Anyway, the finding that the calculated source depth clearly lies within the uppermost layer of the core provides substantial evidence for its physical significance.

The same evaluation has been made for the energy density spectrum of the secular variation, i.e., for the time-derivative of the spectral function  $W(n)$ :

$$\dot{W} = 2(n+1) \sum_{m=0}^n [g_n^m \dot{g}_n^m + h_n^m \dot{h}_n^m]. \quad (21)$$

For a model based on pre-Magsat data (U041580) and developed again by J.C. Cain, there is sufficient accuracy up to a degree of 9 (Fig. 15). The regression line here indicates an effective source depth of 66 km beneath the surface of the earth's core, rather well in accordance with the result for the main field model itself, within the  $3\sigma$ -limit of random deviations. However, differing from the spectrum for the field model the term  $n = 1$ , i.e., the dipole term can now be fully included. It no longer deviates significantly from the regression line. This signifies that the secular variation of the dipole field is predominantly due to that part of the field which most likely originates in a relatively thin surface layer of the Earth's core and which, by its quasi-white spectrum there, contributes also to the observed dipole field (by approximately 15–20%).

The other terms of the secular variation spectrum, besides their specific magnitude, come out with an almost alternating sign. (The encircled dots denote positive rates, i.e., increase of field energy, the crosses negative rates or decrease of field energy). Hence, a white spectrum at the surface of the earth's core – the reduced spectrum is shown in the right-hand diagram of Fig. 15 – means that the energy of the magnetic field at that depth is well-balanced. The secular variation does not lead to a change of the gross amount of magnetic energy there. It rather represents a change of field structure in connection with structural changes in the

specific source layer, i.e., the surface layer of the earth's core. Seemingly contradictory statements regarding the observable field at the earth's surface have to be understood through the non-uniform radial decrease of the different spectral terms, especially by the relatively enlarged effect of the dipole term.

### Conclusions

The forward calculation of the crustal magnetic field by means of a global model of the Earth's crust turns out to be an effective instrument for the study of crustal magnetization. It accentuates global aspects and is especially more capable of revealing universal components than the repeatedly applied inversion method of equivalent sources. The present state of the model, although based on rather simplifying assumptions, has already led to satisfactory results regarding magnitude, structure, and spatial spectrum of the model field. If the field is truncated at the same spherical harmonic level as the satellite anomaly map, a number of positive and negative foci in both charts are clearly correlated. Besides, the model field makes it possible to demonstrate for the first time the potential failure of the truncation to properly represent the total crustal field.

Remaining inconsistencies indicate that much effort must be expended to improve the model for universal agreement. But it should be kept in mind that also the available Magsat anomaly map is still highly preliminary. Notwithstanding, there are probably several anomalies in the satellite map which definitely cannot be reproduced in any crustal model field of global extent. These anomalies certainly provide additional information beyond our present knowledge of the Earth's crust. The model field finally constructed thus may serve as an appropriate reference field for the truly anomalous part of the crustal field.

Whatever particulars a comparison of the crustal model field and Magsat measurements may further reveal, the present results on spatial spectra definitely signify a tripartition of the internal geomagnetic field (except for the local anomalies):

- (1) a relatively stable dipole part originating probably in the deeper core or in the core as a whole;
- (2) a part from a relatively thin surface layer of the core, (including, amongst others, a further dipole constituent), with structural changes that causes the secular variation of the observed field,
- (3) a part from the Earth's crust attributed to magnetic minerals.

The revealed separation of the core field into a universal dipole and a more complex surface field part resembles to some extent the main field representation by a centered dipole and an assemblage of additional radial dipoles at a constant geocentric distance inside the core as suggested by Alldredge and Hurwitz (1964); see also Alldredge and Stearns (1969) and Stearns and Alldredge (1973). Indeed, if the surface field part is due to a comparatively thin current sheet involving various loops and whirls, the first-order magnetic field of such a current distribution is a set of radial dipoles equidistant from the Earth's center. Although this may in effect concern merely the *description* of the core field, the results about the core field energy spectrum must certainly be considered for any true theory of the core field generation.

*Acknowledgements.* Thanks are due to Dipl.-Min. B. Bode for assistance in setting up the global crust classification. We are grateful to Dr. P.D. Lowman Jr. for suggestions towards regional improvements for North and South America. The continuous cooperation of Dr. J.C. Cain of the U.S. Geological Survey and Dr. R.A. Langel of the NASA Goddard Space Flight Center is highly acknowledged. This work was supported by the Deutsche Forschungsgemeinschaft.

## References

- Allredge, L.R., Hurwitz, L.: Radial dipoles as the sources of the Earth's main magnetic field. *J. Geophys. Res.* **69**, 2631–2640, 1964
- Allredge, L.R., Stearns, C.O.: Dipole model of the sources of the Earth's magnetic field and secular change. *J. Geophys. Res.* **74**, 6583–6593, 1969
- Cain, J.C.: Structure and secular change of the geomagnetic field. *Rev. Geophys. Space Phys.* **13**, No. 3, 203–206, 1975
- Cain, J.C.: Introductory remarks, Abstract. EOS, Trans. Am. Geophys. Union **57**, 907, 1976
- Cain, J.C., Hendricks, S., Daniels, W.E., Jensen, D.C.: Computation of the main geomagnetic field from spherical harmonic expansions. Data User's Note NSSDC 68-11. Greenbelt: NASA-Goddard Space Flight Center 1968
- Chapman, S., Bartels, J.: *Geomagnetism*, Vol. 2, Chap. XVII. Oxford: Clarendon Press 1940
- Coles, R.L., Haines, G.V., Jansen van Beek, G., Nandi, A., Walker, J.K.: Magnetic anomaly maps from 40°N to 83°N derived from Magsat satellite data. *Geophys. Res. Lett.* **9**, 281–284, 1982
- Frese, R.R.B. von, Hinze, W.J., Braile, L.W.: Spherical Earth gravity and magnetic anomaly analysis by equivalent point source inversion. *Earth Planet. Sci. Lett.* **53**, 69–83, 1981
- Gilbert, M.B. (manag. ed.): *The Magsat issue*. John Hopkins University, Applied Physics Laboratory, Technical Digest **1**, No. 3, 1980
- Kautzleben, H.: Die analytische Darstellung des geomagnetischen Hauptfeldes und der Säkularvariation. *Abh. Geomagn. Inst. Potsdam*, **32**, pp. 62–66. Berlin: Akademie-Verlag 1963
- Landolt-Börnstein: Numerical data and functional relationships in science and technology, Vol. V/1b. Physical properties of rocks, G. Angenheister, ed.; Berlin, Heidelberg, New York: Springer 1982
- Langel, R.A.: Near-Earth satellite magnetic field measurements: A prelude to Magsat. EOS, Trans. Am. Geophys. Union **60**, 667–668, 1979
- Langel, R.A.: Global magnetic anomaly map from Magsat, Paper presented at the 4th IAGA Scientific Assembly, Edinburgh, Aug. 3–15, 1981, Abstract published in IAGA Bull. **45**, p. 105 f., 1981
- Langel, R.A.: The magnetic Earth as seen from Magsat, Initial results. *Geophys. Res. Lett.* **9**, 239–242, 1982
- Langel, R.A., Coles, R.L., Mayhew, M.A.: Comparisons of magnetic anomalies of lithospheric origin measured by satellite and airborne magnetometers over western Canada. *Can. J. Earth Sci.* **17**, 876–887, 1980a
- Langel, R.A., Estes, R.H., Mead, G.D., Fabiano, E.B., Lancaster, E.R.: Initial geomagnetic field model from Magsat vector data. *Geophys. Res. Lett.* **7**, 793–796, 1980b
- Langel, R.A., Estes, R.H.: A geomagnetic field spectrum. *Geophys. Res. Lett.* **9**, 250–253, 1982
- Langel, R.A., Phillips, J.D., Horner, R.J.: Initial scalar magnetic anomaly map from Magsat. *Geophys. Res. Lett.* **9**, 269–272, 1982a
- Langel, R.A., Schnetzler, C.C., Phillips, J.D., Horner, R.J.: Initial vector magnetic anomaly map from Magsat. *Geophys. Res. Lett.* **9**, 273–276, 1982b
- Lowes, F.J.: Mean-square values on sphere of spherical harmonic vector fields. *J. Geophys. Res.* **71**, 2179, 1966
- Lucke, O.: Über Mittelwerte von Energiedichten der Kraftfelder. *Wiss. Z. Päd. Hochschule Potsdam, Math.-Nat. Reihe* **3**, 39–46, 1957
- Mauersberger, P.: Das Mittel der Energiedichte des geomagnetischen Hauptfeldes an der Erdoberfläche und seine säkulare Änderung. *Gerlands Beitr. Geophys.* **65**, 207–215, 1956
- Mayhew, M.A.: Inversion of satellite magnetic anomaly data. *J. Geophys.* **45**, 119–128, 1979
- Mayhew, M.A.: An equivalent layer magnetization model for the United States derived from satellite-altitude magnetic anomalies. *J. Geophys. Res.* **87**, 4837–4845, 1982a
- Mayhew, M.A.: Application of satellite magnetic anomaly data to Curie isotherm mapping. *J. Geophys. Res.* **87**, 4846–4854, 1982b
- Mayhew, M.A., Johnson, B.D., Langel, R.A.: An equivalent source model of the satellite-altitude magnetic anomaly field over Australia. *Earth Planet. Sci. Lett.* **51**, 189–198, 1980
- Mobley, F.F., Eckard, L.D., Fountain, G.H., Ousley, G.W.: Magsat – A new satellite to survey the Earth's magnetic field. *IEEE Transactions on Magnetics*, Vol. MAG-16, No. 5, Sept. 1980
- Regan, R.D., Cain, J.C., Davis, W.M.: A global magnetic anomaly map. *J. Geophys. Res.* **80**, 794–802, 1975
- Runcorn, S.K.: On the interpretation of lunar magnetism. *Phys. Earth Planet. Int.* **10**, 327–335, 1975
- Soller, D.R., Ray, R.D., Brown, R.D.: A global crustal thickness map. McLean, Va.: Phoenix Corporation 1981
- Stearns, C.O., Alldredge, L.R.: Models of the sources of the Earth's magnetic field. In: *Methods in computational physics*, Vol. 13, pp. 61–92. New York, London: Academic Press 1973

Received July 22, 1982; Accepted January 28, 1983

# A Palaeointensity Method for Use with Highly Oxidised Basalts, and Application to Some Permian Volcanics

W.E. Senanayake and M.W. McElhinny

Research School of Earth Sciences, Australian National University, Canberra ACT, Australia

**Abstract.** A palaeointensity technique is proposed for use with basalts that have undergone high temperature oxidation and whose magnetic minerals are in their most advanced oxidation state. In such basalts the main magnetic mineral is haematite, although there is usually a minor constituent of magnetite present. Because magnetite is a very much stronger magnetic mineral, typically the total remanence of these basalts is derived about equally from each mineral. Such a two-mineral assemblage is quite unsuitable for use in the Thelliers' method. However they are well distinguished by their coercive force spectrum. Therefore a modification to Shaw's method enables palaeo-intensities to be determined separately for each mineral. The low alternating field demagnetization spectrum ( $\leq 150$  mT) provides the palaeointensity for the magnetite fraction and high field alternating field demagnetization ( $\geq 500$  mT) the palaeointensity from the haematite fraction. Agreement between these values provides a powerful consistency check.

Application of this technique to samples of the Permian Exeter traps (U.K.) and the Esterel volcanics (France) shows that it can be used with success. The Exeter traps yield a mean VDM of  $6.11 \pm 1.12 \times 10^{22}$  Am<sup>2</sup> and the Esterel volcanics a mean of  $4.03 \pm 1.43 \times 10^{22}$  Am<sup>2</sup>. These values are higher than have previously been suggested for the Permian dipole moment. Standard deviations of the VDMs are 42.9% and 40.6% respectively. This suggests that fluctuations in dipole intensity are the main source of scatter as has been observed in VDMs for the past 5 million years.

**Key words:** Geomagnetic palaeointensity – Permian volcanics – Two-component remanence.

## Introduction

It is well known that the determination of palaeointensity is much more difficult and much less reliable than that of palaeodirection. So that, apart from work in archaeomagnetism, there has been little effort in determining the variation of the magnitude of the earth's dipole moment on the geological time-scale. The main

reasons for this are that the procedures are usually very time-consuming and even then it is not guaranteed that a reliable result will be forthcoming. As a result many attempts have been made to circumvent the classical Thelliers' method (Thellier and Thellier, 1959) with varying degrees of success. The main problem is that heating samples to a temperature above the Curie point (total TRM methods) or successive heatings (Thelliers' method) may cause alteration to the magnetic mineralogy. In Thelliers' method the alteration can be monitored and use made of results prior to the alteration occurring. In total TRM methods, such as Shaw (1974), comparison of coercive force spectra before and after heating is used to monitor whether or not alteration has occurred. We have extended Shaw's method for use in special cases so that an additional consistency check is obtained.

In this paper we consider only the problem of determining palaeointensities from basaltic rocks. We propose a method that makes use only of highly oxidised basalts (Class 5 of Watkins and Haggerty, 1967 or Class 5 and 6 of Haggerty, 1976). The high temperature oxidation in these basalts took place during initial cooling and at temperatures above the Curie temperatures of magnetite and haematite. There are two advantages in using rocks in this oxidation state. First, as the magnetic minerals are in their most advanced oxidation state, further heating should not cause further oxidation. Second, the main magnetic mineral in these basalts is haematite, but there will always be a minor constituent of magnetite present. Because magnetite has saturation magnetization about 200 times that of haematite, its presence in a ratio  $\sim 1/200$  times that of haematite will contribute equal magnetizations from the two minerals to the total TRM. Furthermore magnetite and haematite have very different coercive force spectra. In special cases the coercive force of magnetite may extend up to about 0.3 T (Evans and McElhinny, 1969) whereas that of haematite probably extends up to 2.5 T (Rimbert, 1959). Thus it may be possible to determine separate palaeointensities for the low coercivity region (from magnetite) and the high coercivity region (from haematite) using Shaw's method. This would serve as an additional consistency check. Agreement between palaeointensities determined for each mineral fraction would lend much weight to the results obtained.

## The New Method

### Background

Fundamental to any palaeointensity technique is the relationship (Nagata, 1943) relating the NRM ( $J_n$ ) of a rock sample with the TRM ( $J_i$ ) induced in a known magnetic field.

$$\frac{J_n}{J_i} = \frac{F_a}{F_l} \quad (1)$$

where  $F_a$  and  $F_l$  are the palaeointensity and the laboratory field respectively. The application of this relationship to palaeointensity determinations is hampered by:

- (1) the acquisition of secondary components of magnetization since formation of the rock;
- (2) the decay of the primary components of magnetization; and
- (3) chemical changes that occur during the laboratory heating.

To overcome the first two problems, alternating field (AF) demagnetization has been used to isolate the more stable components of NRM (Van Zijl et al., 1962; Smith, 1967a; McElhinny and Evans, 1968; Doell and Smith, 1969). Sometimes thermal demagnetization (Smith, 1967a) is used, but this then reduces to a form of Thelliers' method, because there will be no consistency between successive temperature intervals until the secondary components are eliminated. The comparison of successive temperature intervals or coercive force intervals then modifies Eq. (1) to:

$$\frac{J_n(T_1, T_2)}{J_i(T_1, T_2)} = \frac{F_a}{F_l} \quad (2)$$

or

$$\frac{J_n(\tilde{H}_1, \tilde{H}_2)}{J_i(\tilde{H}_1, \tilde{H}_2)} = \frac{F_a}{F_l}$$

where  $(T_1, T_2)$  and  $(\tilde{H}_1, \tilde{H}_2)$  describe the blocking temperature interval and range of alternating magnetic field respectively.

Although the Thelliers' method will detect the point at which chemical changes occur on heating, the alternating field methods require heating to the Curie temperature and chemical changes can only be detected by comparison of the coercive force spectrum before and after heating. Various attempts to minimize chemical alteration have been attempted. Tanguy (1975) tried rapid heating in a preheated furnace, Khodair and Coe (1975) used a vacuum and Kono and Tanaka (1977) used a reducing atmosphere of nitrogen or argon gas. None of these has been particularly successful.

The Thelliers' method (Thellier and Thellier, 1959) and modified versions (Coe, 1967a; Kono and Ueno, 1977; Domen, 1977) has been applied to young basaltic rocks and palaeointensities have been determined using the low to intermediate temperature ranges (e.g. Coe, 1967a; Coe and Grommé, 1973; Coe et al., 1978; Champion, 1980). The problem is the long time required for step-wise heatings and the interpretation of

non-ideal behaviour of the NRM-PTRM relationships or Arai diagrams (Arai, 1963; Nagata et al., 1963) as has been discussed by Coe (1967b) and Levi (1975). Also the Thelliers' method is unsuitable for rocks possessing thermally discrete components (i.e. the blocking temperatures are not well distributed) where all the magnetization is acquired on cooling through a relatively narrow temperature range (McElhinny and Evans, 1968).

The method described by Shaw (1974) compares coercive force spectra of NRM and TRM and also compares the coercive force spectra of ARM before and after a single heating to the Curie temperature to demonstrate the absence of alteration or to identify a coercivity region which has not been affected by this alteration. Kono (1977, 1978) applied Shaw's method to volcanic rocks up to 34 m.y. in age and observed that only a few samples satisfied the 'ideal' conditions set out by Shaw (1974). He concluded that a reliable palaeointensity could be determined, even though the ideal condition was not satisfied, by introducing an appropriate correction term.

We now extend Shaw's method to highly oxidized basalts containing magnetite and haematite with different coercive force spectra.

### Procedure

- (1) The NRM of the specimen is progressively demagnetized in alternating magnetic fields up to some maximum peak field  $\tilde{H}_m$ . The demagnetized NRM is measured at each step.
- (2) An ARM (ARM1) is given to the specimen by applying an alternating field ( $\tilde{H}_m$ ) whose amplitude is reduced to zero in the presence of a steady magnetic field of 0.05 mT. The ARM1 is then progressively demagnetized as in (1).
- (3) An IRM (IRM1) is given to the specimen in increasing steps up to fields of about 2.2 T. The magnetization is measured after each step.
- (4) The specimen is given a TRM in a field of about 0.05 mT and it then progressively demagnetized as in (1).
- (5) An ARM (ARM2) is given to the specimen as in (2) and then progressively demagnetized as in (1).
- (6) An IRM (IRM2) is given to the specimen in increasing steps as in (3).

### Low Coercivity Spectrum

A palaeointensity value for the magnetite fraction may be determined as in Shaw's method using only the low coercivity region ( $0 \leq \tilde{H} \leq 150$  mT) of NRM, TRM and ARM. A comparison is then made of NRM and TRM and ARM1 and ARM2 in this range of demagnetizing fields. The following conditions need to be satisfied to obtain a palaeointensity value.

(a) The magnetite fraction must be sufficient to produce a significant contribution to the total NRM.

(b) At least a part of the low coercivity region must be unaffected by secondary magnetic components or the decay of NRM.

At any alternating field  $\tilde{H}$  up to the maximum available  $\tilde{H}_m$ , the magnetization will be made up of two components, one due to magnetite and the other due to haematite, so that

$$J_n(\tilde{H}) = J_{mn}(\tilde{H}) + J_{hn}(\tilde{H}), \quad (3)$$

$$J_t(\tilde{H}) = J_{mt}(\tilde{H}) + J_{ht}(\tilde{H}) \quad (4)$$

where  $J_{mn}(\tilde{H})$  and  $J_{mt}(\tilde{H})$  are the contributions from magnetite and  $J_{hn}(\tilde{H})$  and  $J_{ht}(\tilde{H})$  are the contributions from haematite. From Eq. (2) then

$$\frac{J_{mn}(\tilde{H}) + J_{hn}(\tilde{H})}{J_{mt}(\tilde{H}) + J_{ht}(\tilde{H})} = \frac{F_a}{F_t}. \quad (5)$$

We now assume that in the range  $0 \leq \tilde{H} \leq 100$  mT the contribution to the total coercive force spectrum from haematite is very much less than that from magnetite. Then  $J_{hn}(\tilde{H})$  and  $J_{ht}(\tilde{H})$  may be considered as constants and

$$J_{mn}(\tilde{H}) = \frac{F_a}{F_t} J_{mt}(\tilde{H}) + \text{constant}; \quad 0 \leq \tilde{H} \leq 100 \text{ mT}. \quad (6)$$

This expression describes a linear relationship between NRM and TRM with slope  $F_a/F_t$  providing that the magnetic mineralogy in this coercivity region has not been altered. These alterations may be investigated by comparing ARM1 with ARM2 in the range  $0 \leq \tilde{H} \leq 100$  mT (Shaw, 1974; Kono, 1977; 1978). If it is assumed that the change in TRM (or NRM) capacity is the same as the change in ARM capacity, then the gradient of the best fitting line of ARM1 against ARM2 may be used as a correction term for alterations (Kono, 1978). If the NRM-TRM and ARM1-ARM2 plots show linear relationships with slopes  $m_1$  and  $m_2$  respectively in the coercivity range corresponding to  $0 \leq \tilde{H} \leq 100$  mT, then

$$F_a(m) = \frac{m_1}{m_2} F_t. \quad (7)$$

### High Coercivity Spectrum

Suppose the coercivity spectrum of magnetite is completely eliminated at  $\tilde{H}_e$ , where  $0 \leq \tilde{H}_e \leq \tilde{H}_m$ . Then at any alternating field  $\tilde{H}$  in the range  $\tilde{H}_e \leq \tilde{H} \leq \tilde{H}_m$  only the haematite component remains and Eqs. (3) and (4) become:

$$\frac{J_n(\tilde{H})}{J_t(\tilde{H})} = \frac{J_{hn}(\tilde{H})}{J_{ht}(\tilde{H})} \quad \tilde{H}_e \leq \tilde{H} \leq \tilde{H}_m. \quad (8)$$

Haematite becomes saturated in fields of about 2.5 T, so it is not a practical proposition to attempt the comparison of ARMs, since alternating fields of this magnitude are difficult to produce. To detect changes in the haematite fraction before and after heating an IRM technique has therefore been used (Carmichael, 1967). For the present study a maximum D.C. field of 2.2 T was available and this is sufficiently close to that required to saturate haematite. As the final step before heating and after heating (steps 3 and 6), the IRM acquired by the specimen is measured in increasing steps.

Suppose the magnetite grains are saturated at some steady D.C. field  $H_0$  ( $0 \leq H_0 \leq 2.2$  T). Then the IRM spectrum for fields greater than  $H_0$  is due entirely to haematite. At any field  $H$  in this range ( $H_0 \leq H \leq 2.2$  T) the IRMs before and after heating can be written as:

$$\begin{aligned} I_1(H) &= M_1 + h_1 \\ I_2(H) &= M_2 + h_2 \end{aligned} \quad H_0 \leq H \leq 2.2 \text{ T} \quad (9)$$

where  $M_1$  and  $M_2$  are the saturation IRMs of magnetite,  $h_1$  and  $h_2$  are the IRMs of haematite before and after heating (subscripts 1 and 2 respectively).

If the magnetization of haematite has been altered by a factor  $k_2$  after heating ( $k_2 \sim h_1/h_2$ )

$$\frac{I_1(H) - M_1}{I_2(H) - M_2} = k_2 \quad H_0 \leq H \leq 2.2 \text{ T}$$

and

$$I_1(H) = k_2 I_2(H) + (M_1 - k_2 M_2). \quad (10)$$

This represents a straight line with slope  $k_2$  which may be determined from a plot of IRM1 versus IRM2. This is analogous to the ARM1-ARM2 plot in the low coercivity range. If the NRM-TRM relationship is linear with slope  $k_1$  from Eq. (8) in the range  $\tilde{H}_e \leq \tilde{H} \leq \tilde{H}_m$ , then from Eq. (1)

$$F_a(h) = \frac{k_1}{k_2} F_t. \quad (11)$$

The complete procedure is illustrated in Fig. 1. The overall requirement is that  $F_a(m) = F_a(h)$ . So that even though the method has to rely on corrections for any alterations that occur, their justification ultimately is that the two independently determined values of the palaeointensity agree. This adds an extra dimension to the point made by Kono (1978) that such "corrected" NRM-TRM slopes may still give correct palaeointensities in certain cases. Senanayake et al. (1982) have demonstrated that, for oxidised rocks, the correction factor proposed by Kono (1978) always produces palaeointensity values in agreement with that determined by the Thellier's method.

### High Field A.F. Demagnetization Apparatus

Because of the requirement that high alternating fields be used to obtain at least part of the coercivity spectrum of haematite beyond that of magnetite, a new high field device has had to be constructed. Basically it is a very much larger version of that described by McElhinny (1966) and currently in use in the laboratory at the Australian National University (A.N.U.).

The solenoid is wound with bicalex covered rectangular cross-section copper wire of size 3.14 mm  $\times$  1.26 mm. The bicalex cover adds a further 0.11 mm to each dimension, and the cross-section is equivalent to 13 SWG, making it possible to pass about 20 A through it without any special cooling arrangement. The solenoid has 6940 turns, has internal diameter 9 cm with 78 turns per layer for 89 layers, giving a length of 25.7 cm and external diameter of 34.7 cm. A thin sheet of mylar (thickness 0.008 cm), capable of with-

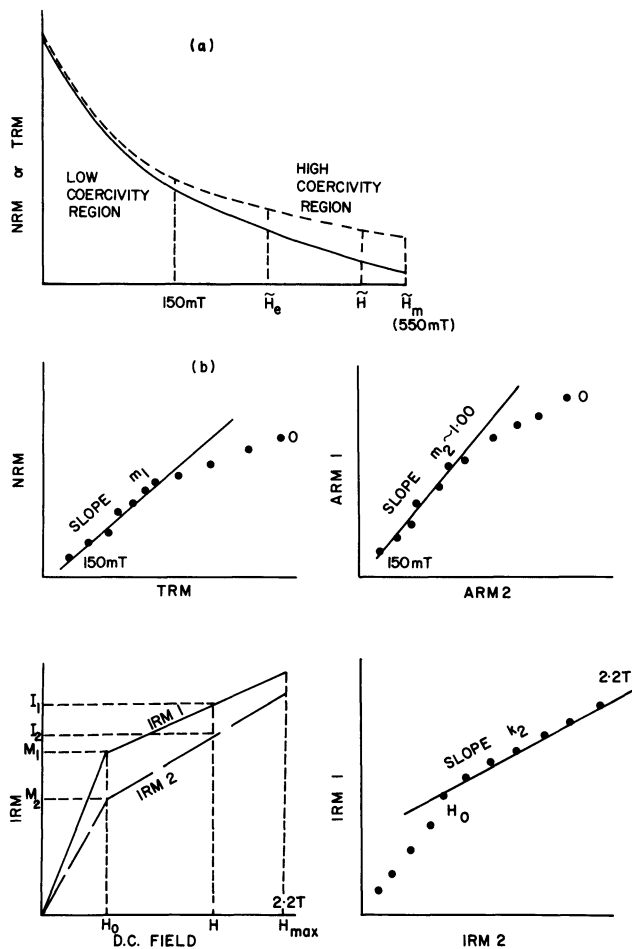


**Fig. 1a-c.** Illustration of the new palaeointensity technique. **a** Comparison of A.F. demagnetization of NRM and TRM. The magnetite fraction predominates in the low coercivity region in fields  $< 150$  mT. The haematite fraction predominates in the high coercivity region above some field  $H_e$  representing the highest coercivity of magnetite; **b** The low coercivity palaeointensity compares NRM and TRM up to fields of 150 mT, and ARM1 and ARM2 before and after heating to the Curie temperature. This corresponds to Shaw's (1974) method as extended by Senanayake and McElhinny (1982); **c** Comparison of the acquisition of IRM before (IRM1) and after (IRM2) heating. Above  $H_0$  the magnetite grains are saturated. The slope  $k_2$  of the IRM1-IRM2 plot at fields  $> H_0$  determines the factor by which the magnetization of haematite has been altered on heating

standing a voltage difference of about 5,000 V was glued between each layer with Araldite 'D', a good electrical insulator. The solenoid weighs about 160 kg, has a D.C. resistance of 21.5 ohms and produces a peak alternating field of 36.6 mT/A (rms) as determined by the output of a small search coil placed at the centre of the solenoid.

The demagnetizing solenoid is connected in series with a bank of capacitors (60 kV oil filled) of 2.65  $\mu$ F to form a series resonance circuit at 50 Hz. The tuned circuit has a  $Q$  factor of about 40 and the apparatus produces peak fields up to 0.55 T under normal conditions with a supply voltage of 485 V (rms). A further 17% increase in the maximum peak field can be obtained using the overvoltage connections on the supply variac. Smooth raising and lowering of the current in

the solenoid is achieved using a motor driven variac which is supplied from second variac connected between two phases of the normal three phase supply giving a source of 415 volts. Because of dangers produced by the high voltage magnification across the solenoid and the capacitors, they are all located behind earthed wire screens.

During trial runs some A.F. demagnetization experiments carried out using the system showed that some spurious magnetization was induced in specimens. Investigation showed that this was not an ARM or RRM but was related to the automatic switching off of the A.C. power through the circuit. The switching gave rise to a very short term high amplitude uni-directional spike through the solenoid. The effect of this would be similar to a lightning effect producing an IRM component. It is apparently due to the capacitors discharging some accumulated charge through the solenoid. To overcome this the A.C. power through the solenoid is never switched off but maintained near zero. The specimen is removed from the coil with the tumbling mechanism still operating.

## Application to Some Permian Volcanics

### Sample Descriptions

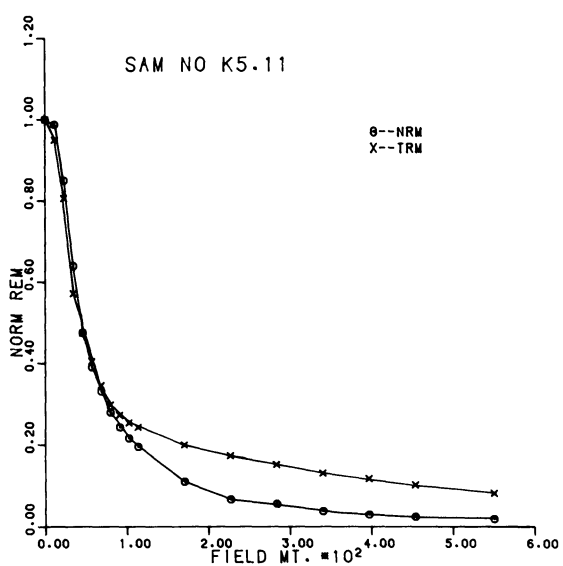
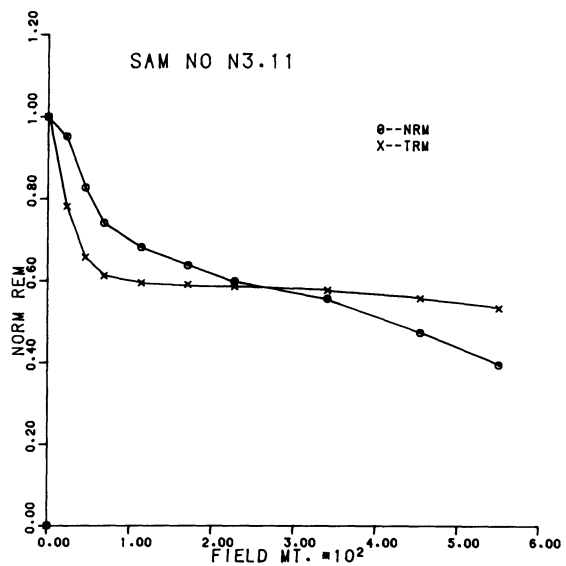
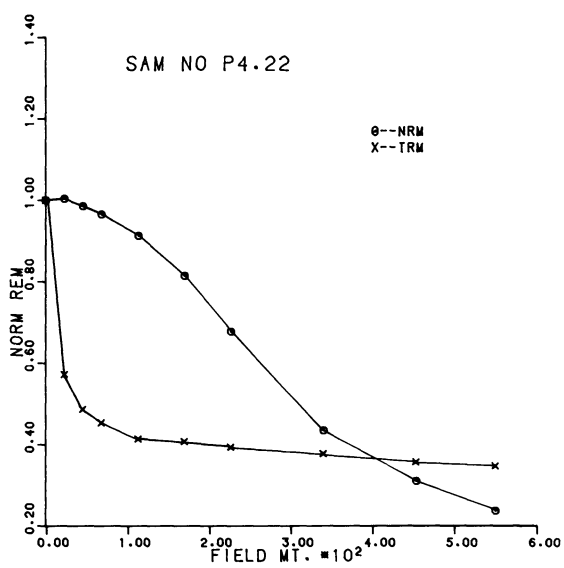
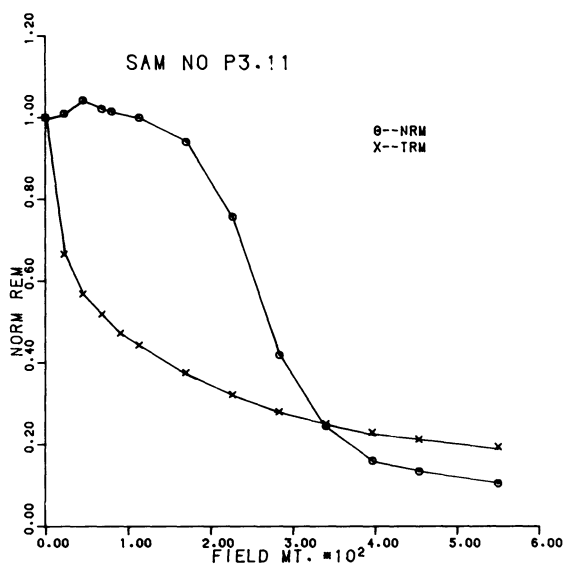
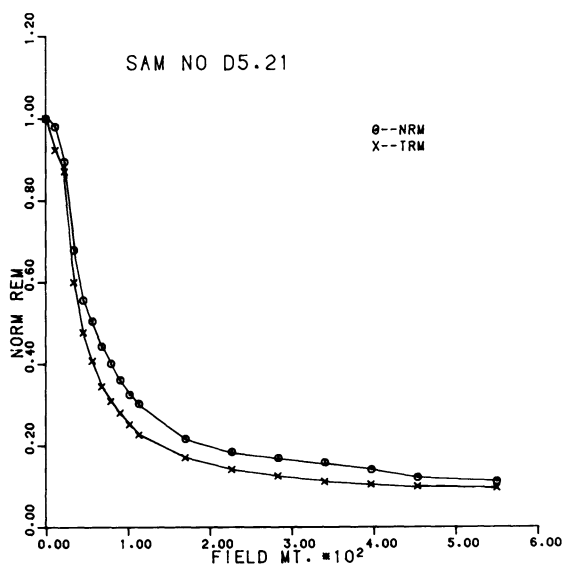
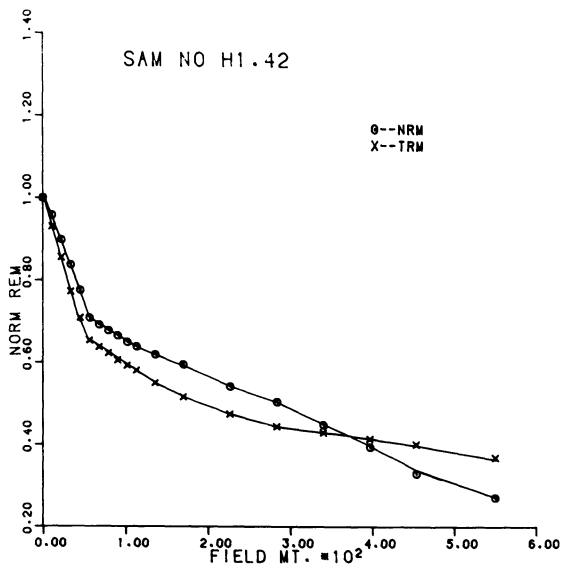
Some very oxidized basalts have been collected from the Exeter traps in England and the Esterel volcanics in southern France, both of Permian age. The A.F. demagnetization characteristics of many of these volcanics described by Zijdeveld (1967; 1975) made it clear that, because they were so resistant to high alternating fields, they were of the type required for the palaeointensity technique.

Previous work on the Exeter traps has been carried out by Creer (1957) and Zijdeveld (1967), and descriptions of the localities and geology are adequately described by them. A K-Ar age of  $279 \pm 6$  m.y. has been determined by Miller et al. (1962). The detailed A.F. demagnetization experiments of Zijdeveld (1967) showed that there were 'soft' (low coercivity) and 'hard' (high coercivity) components present in these rocks, but that these had the same palaeodirection, presumed to be primary. This clearly suggests the two mineral magnetite-haematite system required for the palaeointensity method. Zijdeveld (1967) reports a mean palaeodirection of  $D = 198^\circ$ ,  $I = -25^\circ$  for these rocks. Twenty-four unoriented blocks were collected from quarries in the Exeter traps at Dunchideock (D), Killerton (K), Heazville (H), Duns Moor (N) and Pocombe (P).

Zijdeveld (1975) has carried out very extensive work on the Esterel volcanics of southern France. Descriptions of the geology and sampling localities have been given by him in some detail. The volcanics are of Late Permian age. Nine specimens from six sites having the most suitable magnetic characteristics were kindly provided by Dr. Zijdeveld from his collection. All these specimens had not been treated either thermally or by alternating fields.

### Experimental Results

The procedure outlined above was applied to 32 specimens from the Exeter traps and the 9 specimens from the Esterel volcanics. Preliminary investigations had al-



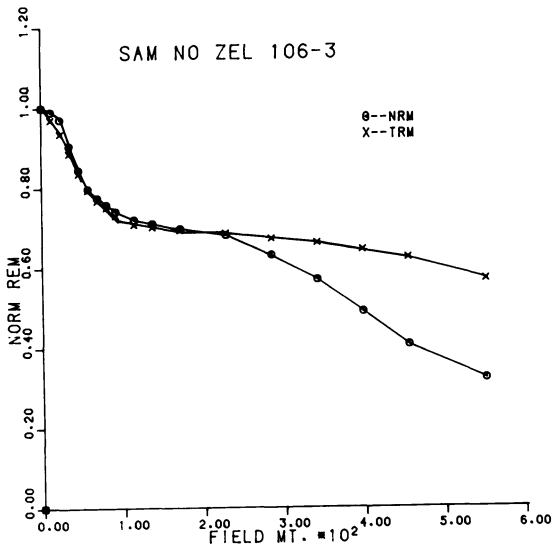
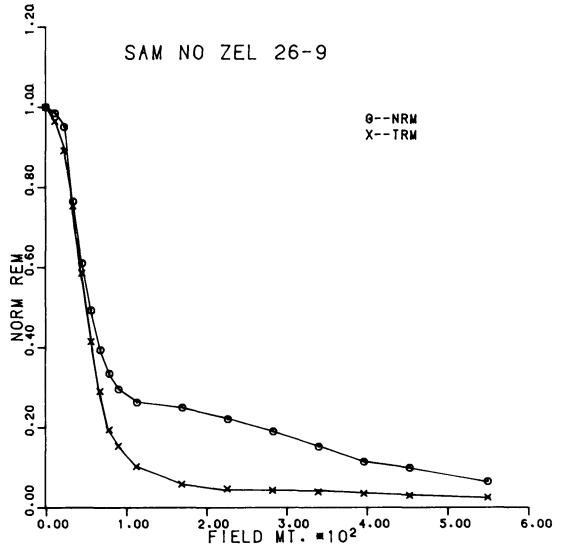
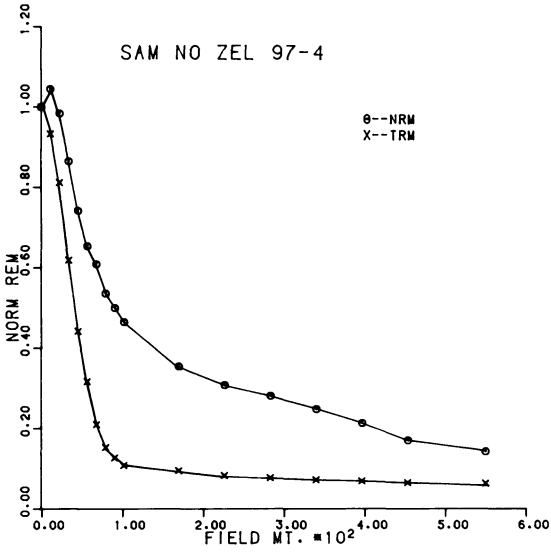
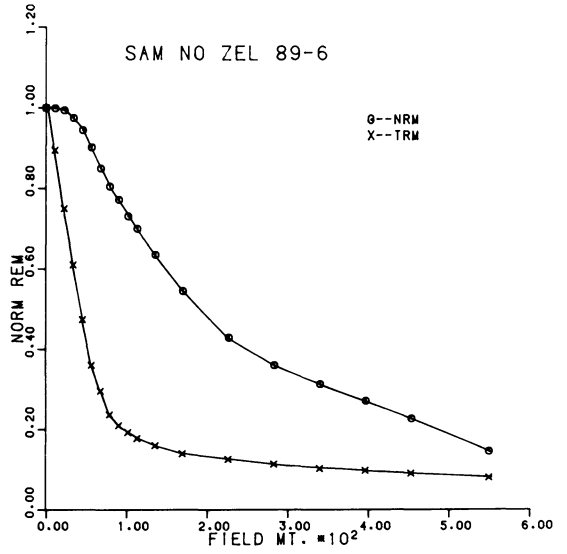
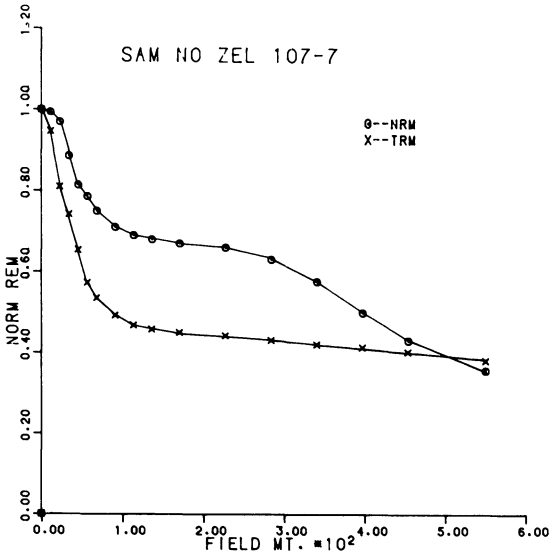


**Fig. 2a and b.** Comparison of A.F. demagnetization curves of NRM and TRM for samples of **a** Exeter traps, **b** Esterel volcanics



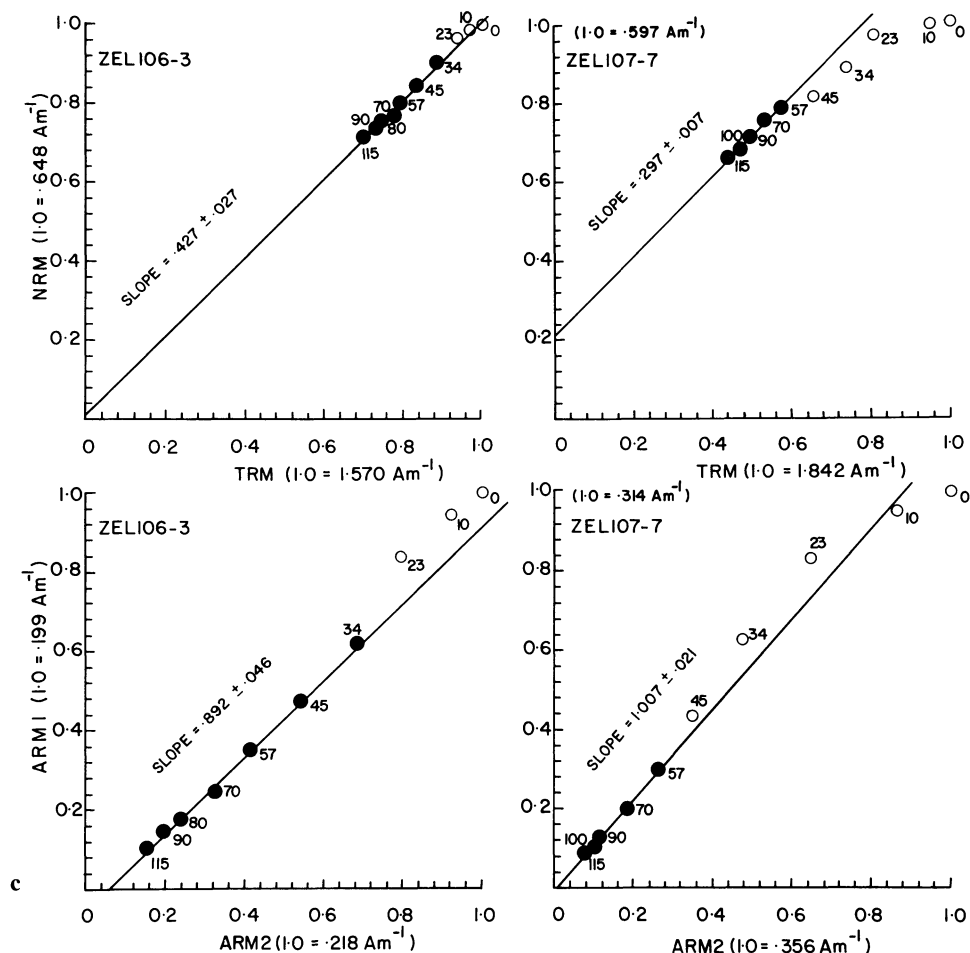


**Fig. 3a-c.** NRM-TRM and ARM1-ARM2 plots at various alternating fields (indicated in mT at each point) for **a** and **b** samples of the Exeter traps, and **c** samples of the Esterel volcanics. Solid points are those used to determine the slope of the line

ready been made of 43 specimens from the Exeter traps using peak alternating fields up to 200 mT (the previous limit available at A.N.U.). These results confirmed the viability of the technique and the complete procedure using peak fields up to 550 mT was then applied to a further 32 specimens the results from which are reported here.

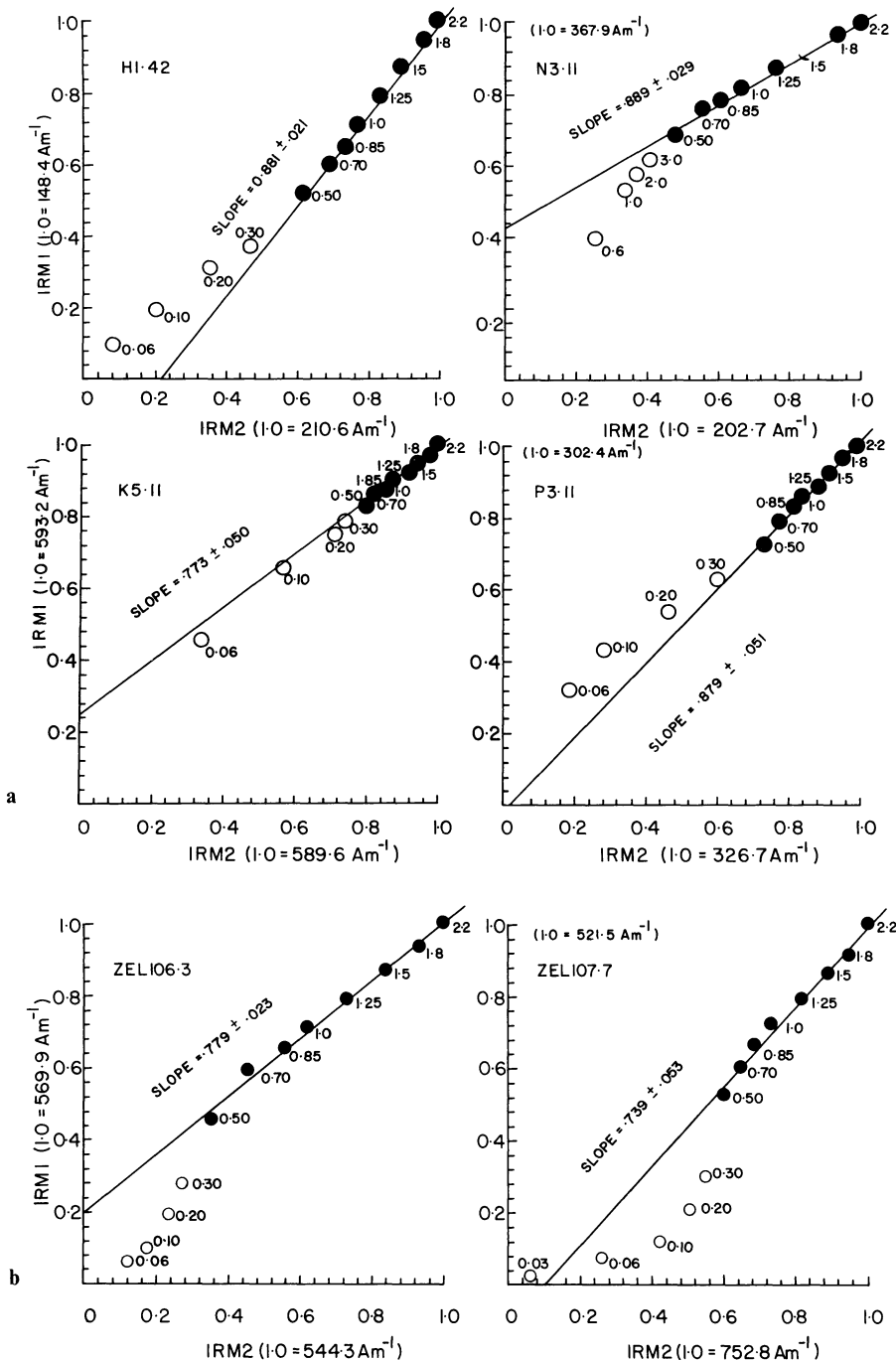
Figure 2 shows normalized A.F. demagnetization. Curves of NRM and TRM for samples from each of the sites collected (Fig. 2a, Exeter traps; Fig. 2b, Esterel volcanics). The curves show the range of responses that are typical of these very oxidized basalts. In the Exeter traps, samples from localities D, H, and K show close correspondence between NRM and TRM whereas for locality P there is little agreement at the low coercivity end, the curves only beginning to merge above about 300 mT. On the other hand the Esterel volcanics show intermediate type responses to the demagnetization of NRM and TRM. Generally the TRM demagnetization is much steeper at low fields than the NRM.

Figure 3 compares plots of NRM versus TRM with ARM1 versus ARM2. The least squares slope in each case is measured over that range of alternating fields where there is a linear segment at higher fields. Standard errors are given for the slopes in each case. In virtually all cases the slopes of ARM1 versus ARM2 are close to the values 1.0 required for an ideal Shaw

palaeointensity, but in most cases they can be shown to be significantly different from 1.0 at the 95 percent confidence level. Thus some correction has to be made following Eq. (8). As Kono (1978) points out this assumes that the change in the coercivity spectrum of NRM has followed that of ARM.

Figure 4 now compares the magnetization curves of IRM1 versus IRM2 up to the maximum D.C. field available of 2.2 T. Generally speaking the data at high magnetizing fields greater than 0.5 T showed linear relationships. However in all cases the slopes in this region were significantly less than one, the only exception being results from sample P4 (Table 1). This indicates that there has been an increase in the amount of haematite present after heating in virtually every case. The slope of the IRM1-IRM2 plot between 0.5 and 2.2 T provides the appropriate correction factor to take account of this as given in Eq. (12). Because the IRM plots suggest that only haematite is involved at fields greater than about 500 mT, we have used the maximum peak alternating field of 550 mT only to determine the NRM/TRM ratio for the haematite high coercivity component. This involves the ratio of two measurements on the magnetometer, each of which is measured with about 5% accuracy. Therefore an accuracy of 7% is assumed for this ratio.

Tables 1 and 2 list the overall results for the two



**Fig. 4a and b.** IRM1-IRM2 plots at various D.C. fields (indicated in T at each point) for samples of **a** Exeter traps, and **b** Esterel volcanics. The solid points are those used to determine the slope of the line

formations. The errors quoted are always standard errors and are similar for both the low and high coercivity determinations of palaeointensity, averaging about 10% (Fig. 5). The results for the two parts of the coercivity spectrum are not systematically higher or lower by either method, nor are the two values ever significantly different at the 95% confidence level. This encourages us to believe the method is a viable one, enabling the extension of Shaw's method to highly oxidized rocks. The results also provide further indication that the ARM correction method of Kono (1978) is a viable one. However they should not be taken to suggest that the IRM acquisition correction method by itself is always necessarily a viable one, and can be used in isolation.

### Permian Dipole Moment

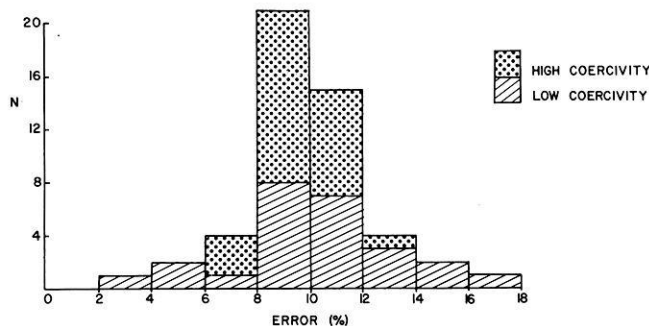
For each of the samples listed in Tables 1 and 2 a Virtual Dipole Moment (VDM) has been calculated using the observed values of inclination at each locality given by Zijdeveld (1967, 1975). The conversion of palaeointensity to VDM follows the proposal of Smith (1967a), who pointed out that this enabled the effects of dipole wobble to be eliminated when an average VDM is calculated. It is not clear at each of the localities in the Exeter traps whether or not more than one flow has been sampled. Certainly, the variation within each locality suggests this to be the case. Therefore in the Exeter traps all 21 values of VDM have been averaged to give a mean value of  $6.11 \pm 1.12 \times 10^{22} \text{ Am}^2$  where the

**Table 1.** Palaeointensity values from the Exeter trap basalt samples. ( $F_1$ ,  $P_1$  = palaeointensity and VDM from low coercivity region;  $F_2$ ,  $P_2$  = palaeointensity and VDM from high coercivity region; VDM = Virtual Dipole Moment). Errors quoted are standard errors

Sample Number	Low Coercivity				High Coercivity				
	Slope of ARM1-ARM2	Slope of NRM-TRM	$F_1$ ( $\mu\text{T}$ )	$P_1$ ( $10^{22}$ Am $^2$ )	Slope of IRM1-IRM2	$\left(\frac{\text{NRM}}{\text{TRM}}\right)_{550}$	$F_2$ ( $\mu\text{T}$ )	$P_2$ ( $10^{22}$ Am $^2$ )	VDM ( $10^{22}$ Am $^2$ )
	K1.41	1.289 ± 0.060	0.612 ± 0.081	28.15 ± 3.95	6.77 ± 0.95	0.742 ± 0.051	0.375	29.97 ± 2.94	7.21 ± 0.71
K2.31	1.224 ± 0.109	0.556 ± 0.047	26.95 ± 3.30	6.48 ± 0.80	0.739 ± 0.047	0.367	29.45 ± 2.79	7.09 ± 0.67	6.79
K3.12	1.181 ± 0.076	0.581 ± 0.034	29.19 ± 2.54	7.03 ± 0.61	0.751 ± 0.046	0.448	35.37 ± 3.29	8.51 ± 0.80	7.77
K4.32	1.230 ± 0.038	1.020 ± 0.024	49.19 ± 1.92	11.84 ± 0.46	0.698 ± 0.055	0.542	46.06 ± 4.81	11.09 ± 1.54	11.47
K4.43	1.219 ± 0.043	0.976 ± 0.031	47.49 ± 2.27	11.42 ± 0.55	0.722 ± 0.062	0.574	47.14 ± 5.12	11.34 ± 1.23	11.38
K5.11	1.246 ± 0.106	0.717 ± 0.069	34.13 ± 4.39	8.21 ± 1.06	0.773 ± 0.050	0.389	29.84 ± 2.81	7.18 ± 0.67	7.70
K5.72	1.198 ± 0.082	0.753 ± 0.052	37.27 ± 3.62	8.97 ± 0.87	0.741 ± 0.041	0.398	31.85 ± 2.84	7.66 ± 0.068	8.01
K6.12	1.168 ± 0.113	0.726 ± 0.052	36.86 ± 4.43	8.87 ± 1.07	0.695 ± 0.037	0.416	35.49 ± 3.12	8.54 ± 0.75	8.71
K6.31	1.189 ± 0.086	0.761 ± 0.061	37.96 ± 4.09	9.31 ± 0.98	0.670 ± 0.047	0.437	38.68 ± 3.83	9.31 ± 0.92	8.97
D1.13	0.891 ± 0.060	0.403 ± 0.019	26.82 ± 2.20	6.45 ± 0.53	0.739 ± 0.048	0.328	26.35 ± 2.52	6.34 ± 0.60	6.40
D1.31	0.914 ± 0.056	0.425 ± 0.028	27.57 ± 2.48	6.63 ± 0.60	0.771 ± 0.052	0.334	25.68 ± 2.50	6.18 ± 0.60	6.41
D3.41	0.828 ± 0.073	0.278 ± 0.018	19.91 ± 2.16	4.79 ± 0.52	0.716 ± 0.067	0.196	16.23 ± 1.90	3.90 ± 0.46	4.35
D4.13	0.880 ± 0.053	0.213 ± 0.025	14.35 ± 1.88	3.45 ± 0.45	0.685 ± 0.037	0.216	18.70 ± 1.65	4.50 ± 0.40	3.98
D5.21	0.940 ± 0.056	0.289 ± 0.026	18.25 ± 1.97	4.39 ± 0.47	0.703 ± 0.058	0.230	19.40 ± 2.09	4.67 ± 0.50	4.53
D5.41	0.932 ± 0.043	0.272 ± 0.028	17.31 ± 1.95	4.16 ± 0.46	0.732 ± 0.060	0.245	19.84 ± 2.14	4.77 ± 0.51	4.47
H1.42	1.110 ± 0.020	0.334 ± 0.027	17.84 ± 1.48	4.29 ± 0.36	0.881 ± 0.021	0.285	19.28 ± 1.42	4.64 ± 0.34	4.47
H2.51	1.083 ± 0.051	0.382 ± 0.024	20.92 ± 1.64	5.03 ± 0.40	0.860 ± 0.041	0.295	20.34 ± 1.72	4.89 ± 0.41	4.96
H2.22	1.067 ± 0.069	0.356 ± 0.031	19.80 ± 2.15	4.76 ± 0.52	0.881 ± 0.039	0.292	19.65 ± 1.63	4.73 ± 0.39	4.75
H3.41					0.831 ± 0.065	0.278	19.83 ± 2.08	4.77 ± 0.50	4.77
H4.51					0.998 ± 0.044	0.305	18.19 ± 1.50	4.38 ± 0.36	4.38
H4.12					0.978 ± 0.041	0.308	18.68 ± 1.53	4.50 ± 0.37	4.50
N1.11					0.898 ± 0.046	0.195	12.87 ± 1.11	3.10 ± 0.27	3.10
N3.11					0.889 ± 0.030	0.162	10.81 ± 0.84	2.61 ± 0.20	2.61
N3.21					0.872 ± 0.041	0.140	9.52 ± 0.80	2.29 ± 0.19	2.29
N4.42					0.891 ± 0.052	0.106	7.06 ± 0.64	1.71 ± 0.15	1.71
P1.21					0.792 ± 0.038	0.330	24.70 ± 2.10	5.94 ± 0.51	5.94
P1.11					0.801 ± 0.045	0.324	23.99 ± 2.15	5.77 ± 0.52	5.77
P2.21					0.828 ± 0.061	0.453	32.41 ± 3.29	7.80 ± 0.79	7.80
P3.11					0.879 ± 0.051	0.572	38.58 ± 3.51	9.28 ± 0.84	9.28
P3.21					0.858 ± 0.056	0.535	36.98 ± 3.54	8.90 ± 0.85	8.90
P4.22					0.974 ± 0.066	0.738	44.93 ± 4.38	10.81 ± 1.05	10.81
P4.41					0.982 ± 0.059	0.721	43.54 ± 4.02	10.48 ± 0.96	10.48

**Table 2.** Palaeointensity values from the Esterel volcanics. (I\* = palaeoinclination obtained from Zijdeveld, 1975). The other symbols are as in Table 1.

Sample Number	I*	Low Coercivity			High Coercivity			$F_2$ ( $\mu$ T)	$P_2$ ( $10^{22}$ Am $^2$ )	VDM ( $10^{22}$ Am $^2$ )
		Slope of ARM1-ARM2	Slope of NRM-TRM	$F_1$ ( $\mu$ T)	$P_1$ ( $10^{22}$ Am $^2$ )	Slope of IRM1-IRM2	$(\frac{NRM}{TRM})_{550}$			
ZEL 106-3	-29.5°	0.892 ± 0.046	0.427 ± 0.027	28.39 ± 2.31	6.64 ± 0.54	0.779 ± 0.023	0.324	5.77 ± 0.44	6.21	
ZEL 106-4	-29.5°	0.907 ± 0.065	0.473 ± 0.036	30.92 ± 3.23	7.23 ± 0.76	0.789 ± 0.047	0.311	5.40 ± 0.50	6.32	
ZEL 107-7	-29.5°	1.007 ± 0.020	0.297 ± 0.006	17.49 ± 0.50	4.09 ± 0.12	0.739 ± 0.053	0.232	4.35 ± 0.44	4.22	
ZEL 107-11	-29.5°	0.978 ± 0.53	0.316 ± 0.019	19.16 ± 1.55	4.49 ± 0.36	0.758 ± 0.070	0.258	4.72 ± 0.55	4.61	
ZEL 26-9	-19.5°	0.939 ± 0.019	0.106 ± 0.003	6.70 ± 0.24	1.68 ± 0.07	-	-	-	1.68	
ZEL 89-6	-25.0°	1.060 ± 0.091	0.235 ± 0.039	13.15 ± 2.44	3.17 ± 0.59	0.642 ± 0.053	0.210	4.68 ± 0.51	3.93	
ZEL 97-2	-21.5°	1.120 ± 0.077	0.252 ± 0.028	13.34 ± 1.74	3.27 ± 0.43	0.812 ± 0.053	0.257	4.61 ± 0.44	3.95	
ZEL 97-4	-21.5°	1.176 ± 0.061	0.268 ± 0.037	13.51 ± 1.99	3.32 ± 0.49	0.829 ± 0.041	0.241	4.23 ± 0.36	3.78	
ZEL 22-5	-	Non-Linear	Non-Linear	-	-	-	-	-	-	

**Fig. 5.** Histogram of the standard errors for each palaeointensity determination using the high coercivity or low coercivity fraction

error quoted is the 95% confidence limit. The standard deviation is  $2.62 \times 10^{22}$  Am $^2$  which is 42.9% of the mean. This is typical of the scatter observed in VDMs over the last 5 million years (McFadden and McElhinny, 1982) and again suggests that fluctuations in dipole intensity are the main source of this scatter.

In the Esterel volcanics the five sites yield a mean VDM of  $4.03 \pm 1.43 \times 10^{22}$  Am $^2$  with error given at the 95% confidence level. The standard deviation is  $1.64 \times 10^{22}$  Am $^2$  which is 40.6% of the mean. The mean VDM is significantly different from that for the Exeter traps, but this may not be very significant because archaeomagnetic data suggest wide variations in dipole moment over times of  $<10^5$  years (McElhinny and Senanayake, 1982). The data from these two formations is probably inadequate to provide a good mean dipole moment for the Permian. However, both values are somewhat higher than those predicted from previous palaeointensity data for the Phanerozoic (Smith, 1967b; McElhinny, 1973).

*Acknowledgements.* Sampling of the Exeter traps was carried out with the assistance of Dr. N. Hamilton, University of Southampton. We gratefully acknowledge his assistance. Our thanks are due also to Dr. J.D.A. Zijdeveld, University of Utrecht who provided suitable samples from his collection of the Esterel volcanics. The high field alternating field demagnetizer was constructed with the assistance of D.J. Edwards, M. Laybutt and P.J. Morrison. We gratefully acknowledge their assistance.

## References

- Arai, Y.: Secular variation in the intensity of the past geomagnetic field. M.S. Thesis, University of Tokyo, Tokyo, Japan, 1963
- Carmichael, C.M.: An outline of the intensity of the paleomagnetic field of the earth. *Earth Planet. Sci. Lett.* **3**, 351-354, 1967
- Champion, D.E.: Holocene geomagnetic secular variation in the western United States: Implications for the global geomagnetic field. U.S. Geol. Surv. Rept., Open File Series, No. 80-824, 314 pp., 1980
- Coe, R.S.: Paleointensity of the earth's magnetic field determined from Tertiary and Quaternary rocks. *J. Geophys. Res.* **72**, 3247-3262, 1967a
- Coe, R.S.: The determination of Paleointensities of the earth's magnetic field with emphasis on mechanisms which could

- cause non-ideal behaviour in Thellier's method. *J. Geomagn. Geoelectr.* **19**, 157-179, 1967b
- Coe, R.S., Grommé, C.S.: A comparison of three methods of determining geomagnetic paleointensities. *J. Geomagn. Geoelectr.* **25**, 415-435, 1973
- Coe, R.S., Grommé, C.S., Mankinen, E.A.: Geomagnetic paleointensities from radiocarbon-dated lava flows on Hawaii and the question of the Pacific nondipole low. *J. Geophys. Res.* **83**, 1740-1755, 1978
- Creer, K.M.: The natural remanent magnetization of certain stable rocks from Great Britain. *Phil. Trans. Roy. Soc. London, Ser. A*, **250**, 111-129, 1957
- Doell, R.R., Smith, P.J.: On the use of magnetic cleaning in paleointensity studies. *J. Geomagn. Geoelectr.* **21**, 579-594, 1969
- Domen, H.: A single heating method of paleomagnetic field intensity determination applied to old roof tiles and rocks. *Phys. Earth Planet. Int.* **13**, 315-318, 1977
- Evans, M.E., McElhinny, M.W.: An investigation of the origin of stable remanence in magnetite-bearing igneous rocks. *J. Geomagn. Geoelectr.* **21**, 757-773, 1969
- Haggerty, S.E.: Oxidation of opaque mineral oxides in basalts, in *Oxide Minerals (Short Course Notes)*, D. Rumble, ed. Mineralogical Soc. Amer. **3**, pp. 1-100, 1976
- Khodair, A.A., Coe, R.S.: Determination of geomagnetic field intensity in vacuum. *Geophys. J.R. Astron. Soc.* **42**, 107-115, 1975
- Kono, M.: Reliability of palaeointensity methods using alternating field demagnetization and anhysteretic remanence. *Rock Mag. Palaeogeophys.* **4**, 22-28, 1977
- Kono, M.: Reliability of palaeointensity methods using alternating field demagnetization and anhysteretic remanence. *Geophys. J.R. Astron. Soc.* **54**, 241-261, 1978
- Kono, M., Tanaka, H.: Influence of partial pressure of oxygen on thermoremanent magnetization of basalts. *Phys. Earth Planet. Int.* **13**, 276-288, 1977
- Kono, M., Ueno, N.: Palaeointensity determination by a modified Thellier method. *Phys. Earth Planet. Int.* **13**, 305-314, 1977
- Levi, S.: Comparison of two methods of performing the Thellier experiment. *J. Geomagn. Geoelectr.* **27**, 245-255, 1975
- McElhinny, M.W.: An improved method for demagnetizing rocks in alternating magnetic fields. *Geophys. J.R. Astron. Soc.* **10**, 369-374, 1966
- McElhinny, M.W.: *Palaeomagnetism and Plate Tectonics*, Cambridge University Press, London, 1973
- McElhinny, M.W., Evans, M.E.: An investigation of the strength of the geomagnetic field in the early Precambrian. *Phys. Earth Planet. Int.* **1**, 485-497, 1968
- McElhinny, M.W., Senanayake, W.E.: Variations in the Geomagnetic Dipole 1: The past 50,000 years. *J. Geomagn. Geoelectr.* **34**, 39-51, 1982
- McFadden, P.L., McElhinny, M.W.: Variations in the Geomagnetic Dipole 2: Statistical analysis of VDMs for the past 5 Million Years. *J. Geomagn. Geoelectr.* **34**, 163-189, 1982
- Miller, J.A., Shibata, K., Monono, M.: The potassium-argon age of the lava of Killerto Park, near Exeter, Geophys. J.R. Astron. Soc. **6**, 304-396, 1962
- Nagata, T.: The natural remanent magnetism of volcanic rocks and its relation to geomagnetic phenomena. *Bull. Earthquake Res. Inst.* **21**, 1-196, 1943
- Nagata, T., Arai, Y., Momose, K.: Secular variation of the geomagnetic total force during the last 5,000 years. *J. Geophys. Res.* **68**, 5277-5281, 1963
- Rimbert, F.: Contribution a l'étude de l'action de champs alternatifs sur les aimantations remanentes des roches, applications géophysiques. *Rev. Inst. Franc. Petrole et Ann. Combustibles Liquides* **14**, 17-15 and 123-155, 1959
- Senanayake, W.E., McElhinny, M.W., McFadden, P.L.: Comparison between the Thellier's and Shaw's palaeointensity methods using basalts less than 5 Million Years old. *J. Geomagn. Geoelectr.* **34**, 141-161, 1982
- Shaw, J.: A new method of determining the magnitude of the Palaeomagnetic field. *Geophys. J.R. Astron. Soc.* **39**, 133-141, 1974
- Smith, P.J.: The intensity of the Tertiary geomagnetic field. *Geophys. J.R. Astron. Soc.* **12**, 239-258, 1967a
- Smith, P.J.: Intensity of the ancient geomagnetic field: A review and analysis. *Geophys. J.R. Astron. Soc.* **12**, 321-362, 1967b
- Tanguy, J.C.: Intensity of the geomagnetic field from recent Italian lavas using anew palaeointensity method. *Earth Planet. Sci. Lett.* **27**, 314-320, 1975
- Thellier, E., Thellier, O.: Sur l'intensité du champ magnetique terrestre dans le passé historique et géologique. *Ann. Geophys.* **15**, 285-376, 1959
- Van Zijl, J.S.V., Graham, K.W.T., Hales, A.L.: The palaeomagnetism of the Stormberg lavas of South Africa, 1 and 2. *Geophys. J. Astron. Soc.* **7**, 23-39 and 169-182, 1962
- Watkins, N.D., Haggerty, S.E.: Primary oxidation variation and petrogenesis in a single lava. *Contrib. Mineral. Petrol.* **15**, 251-271, 1967
- Zijderveld, J.D.A.: The natural magnetizations of the Exeter volcanic traps (Permian, Europe). *Tectonophysics* **4**, 121-153, 1967
- Zijderveld, J.D.A.: *Palaeomagnetism of the Esterel rocks*, Ph. D. Thesis, State University of Utrecht, 1975

Received May 17, 1982; Revised version October 28, 1982

Accepted November 18, 1982

# Comparison of Errors in Local and Reference Estimates of the Magnetotelluric Impedance Tensor

P. Kröger, H.J. Micheel, and R. Elsner

Institut für Nachrichtentechnik der Technischen Universität, Schleinitzstr. 23, D-3300 Braunschweig, Federal Republic of Germany

**Abstract.** The estimation of the magnetotelluric impedance tensor by a regression analysis from locally measured electromagnetic surface fields includes a bias-error, if both the electric and the magnetic field are degraded by additive noise. The remote reference method developed by Gamble et al. (1979a) avoids this bias-error. The errors of the traditional local estimation and the remaining error in the reference estimation are compared. It is shown that for some different types of noise the standard deviation of the reference estimate may be as large as the bias-error of the local estimate. However in order to get a consistent reference estimate, and in order to take full advantage of this method, generally much more data have to be recorded and analysed if using the reference estimation instead of local estimation.

**Key words:** Coherent noise – Noise reduction – Error analysis – Bias-error – Variance – Magnetotellurics

## Introduction

The magnetotelluric impedance tensor  $[Z]$  relates the horizontal electric field  $\mathbf{E}$  to the horizontal magnetic field  $\mathbf{H}$  at the Earth's surface in the frequency domain

$$\mathbf{E}(\omega) = Z(\omega) \cdot \mathbf{H}(\omega), \quad (1)$$

with angular frequency  $\omega = 2\pi/T$ .  $T$  denotes the period of interest. Written in components Eq. (1) gives

$$\begin{bmatrix} E_x \\ E_y \end{bmatrix} = \begin{bmatrix} Z_{xx} & Z_{xy} \\ Z_{yx} & Z_{yy} \end{bmatrix} \cdot \begin{bmatrix} H_x \\ H_y \end{bmatrix}. \quad (1a)$$

All values are dependent on the angular frequency  $\omega$ , and on the resistivity distribution of the Earth in the vicinity of the recording location.

In order to find the unknown resistivity distribution below the Earth's surface, first the elements of the impedance tensor are calculated from the measured values of the electromagnetic field. Then data interpretation can be undertaken in several ways, for example, by inversion procedures or model fitting.

Generally the magnetotelluric method including the interpretation of the impedance tensor requires the

measured fields  $\mathbf{E}$  and  $\mathbf{H}$  to be homogeneously induced, because otherwise the elements of the impedance tensor are not only dependent on the resistivity distribution but on the primary source field distribution as well. A homogeneously induced field is the total field at the Earth's surface, if the inducing primary field is homogeneous. This condition is valid for natural fields in middle geomagnetic latitudes up to periods of about 1,000 s (Wait, 1954; Rikitake, 1966; Madden and Nelson, 1964).

Magnetotelluric measurements are degraded by equipment noise, but often much more by artificial and man made noise. This noise in general, results in an erroneous impedance tensor. In order to reduce this error influence, the impedance tensor is estimated from a lot of measurements of the electromagnetic field. Normally a regression analysis is used (Swift, 1967; Rankin and Reddy, 1969). Starting point of this method is the postulated regression model, for example

$$\mathbf{E}_i = [Z] \mathbf{H}_i + \delta \mathbf{H}_i, \quad (i = 1 \dots M) \quad (2)$$

with a noise term  $\delta \mathbf{E}_i$  in the measured electric field data  $\mathbf{E}_i$ . Correlating the *output* data  $\mathbf{E}_i$  of the regression model with the *input* data  $\mathbf{H}_i$  gives the estimate.

$$[\hat{Z}]_L = \begin{bmatrix} \hat{Z}_{xxL} & \hat{Z}_{xyL} \\ \hat{Z}_{yxL} & \hat{Z}_{yyL} \end{bmatrix} = [C_{EH}] \cdot [P_{HH}]^{-1} \quad (3a)$$

where  $[C_{EH}]$  is the estimated crosspower matrix and  $[P_{HH}]$  is the estimated autopower matrix of the measured data  $\mathbf{E}_i$  and  $\mathbf{H}_i$ . Exchanging the input and output data in the regression model leads to another estimate of the impedance tensor

$$[Z]'_L = [P_{EE}] \cdot [C_{EH}]^{-1}. \quad (3b)$$

In the following  $[\hat{Z}]_L$  and  $[\hat{Z}]'_L$  are called the *local estimates of the impedance tensor* because they are calculated from measured data of only *one* location.

Inherent in the local regression models is the assumption that the input data is free of noise. Only in this case the local estimates are bias-free estimates of the impedance tensor, and with a large number of samples  $[\hat{Z}]_L$  and  $[\hat{Z}]'_L$  tend towards the "true" impedance tensor  $[Z]$ . In practice this assumption often is violated. Noise in the input data causes at least an error in the estimated autopower matrices  $[P_{HH}]$  and  $[P_{EE}]$ . Different authors have shown that in

this case the estimates are biased downward and upward respectively, if Eq. (3b) is used, compared with the true value (e.g. Sims et al., 1971). Moreover, if the noise in the input data is coherent with the noise in the output data, an error also occurs in the estimated crosspower matrix  $[C_{EH}]$ . In this situation the values of the bias-errors in the local estimates of the impedance tensor cannot be seen immediately. One of the aims of this paper is to describe this type of error (see below).

Several methods have been presented to reduce the bias in the local estimates of the impedance tensor (Sims et al., 1971; Kao and Rankin, 1977; Gundel, 1977). All these estimates are based on local measurements of the electromagnetic field. To obtain a reduction of the bias-error, these methods require the components of noise in the estimate to be incoherent. Otherwise a separation of homogeneously induced data and noise by a local measurement is impossible (Goubau et al., 1978).

A definite improvement in the reduction of the bias-error, even in the case of coherent noise, was obtained by the so-called reference magnetotellurics, developed by Goubou et al. (1978). A detailed description of this method can be found in Gamble et al. (1979a). In this method the impedance tensor at a measuring station is estimated by using reference data  $\mathbf{R}_i$ , which are recorded synchronously at a remote station, the reference station. Normally a magnetic reference is used. The *reference estimate*  $[\hat{\mathbf{Z}}]_R$  of the impedance tensor is obtained by the correlation of data from the measuring station and the reference station.

$$[\hat{\mathbf{Z}}]_R = \begin{bmatrix} \hat{\mathbf{Z}}_{xxR} & \hat{\mathbf{Z}}_{xyR} \\ \hat{\mathbf{Z}}_{yxR} & \hat{\mathbf{Z}}_{yyR} \end{bmatrix} = [C_{ER}] \cdot [C_{HR}]^{-1}. \quad (4)$$

This estimate only contains crosspowers between data from the measuring station and the reference station. Provided the noise at the measuring station is incoherent with the noise at the reference station the reference estimate Eq. (4) is bias-free. In practice this condition is satisfied by a sufficiently large distance between the measuring and reference station, usually some tens of km. This condition should not be confused with coherency between local noise in the electric and magnetic channels at the measuring station, which is permitted in the remote reference method. Indeed the reference method theoretically leads to a bias-free estimate, but there is some practical expense in comparison with the local method, which should be mentioned. First, more measurement equipment is needed. Also measuring and reference data have to be recorded synchronously within certain bounds. This either requires very stable time bases in both sets of equipment, or a telemetry connection for synchronising. In each case the sampling at both stations has to be done automatically. Foremost, in the last few years automatically recording MT-equipment has been developed which enables synchronous recording in the period range below 1,000 s.

Besides the differences in cost of equipment there is a second main difference between the local and the reference method. The reference method requires measuring of two more data channels, which may also suffer interference. Due to this additional noise it is to be ex-

pected that the reference estimate has a larger associated variance than that of the local estimates, provided the same quantity of data is used.

The increase of measurement equipment, the demand for automatic recording and the possible increased amount of data required seem to be the reasons why the reference method has not, up to now, been used as the standard method in MT surveys, although its advantage in avoiding bias errors is obvious. In particular, the quantity of data necessary to obtain a consistent estimate is as yet an unsolved quantity. Also it is not yet known how large the bias-errors in the local estimates for different kinds of noise are. In the literature there are derivations of the bias-errors only for the case of incoherent noise at the measuring station (e.g. Sims et al., 1971). Furthermore, the question arises of how large the bias-error is in practice. This paper will illustrate one example, which shows that for locations with coherent noise only the reference method is suitable for increasing the estimation accuracy in MT soundings.

By comparing the errors in both the local and the reference estimates of the impedance tensor this paper will help to answer the above mentioned questions. First, the value of the bias-error in one of the local estimates in the case of different kinds of noise shall be evaluated theoretically. The variance of the reference estimate in these cases will be derived. Secondly the analysis of real MT data will show which kind of noise in practice has to be expected and how large the bias-error and the variances are.

### Definition of Signal and Noise

The MT-method requires homogeneously induced fields, which in the following are called the signal. Therefore noise is that part in the measured data  $\mathbf{E}_i$  and  $\mathbf{H}_i$ , which either is not induced or not homogeneously induced.

The first group, the non-induced part, is noise measurable in the magnetic and electric channels. The noise measurements in these channels are independent from each other, i.e. *incoherent*. Examples are the noise of the measurement equipment, activity caused by moving vehicles, or mechanical vibration of the sensors.

The second group comprises noise caused by inhomogeneously induced fields. Physically these are the man made electromagnetic fields of electrical power lines or industrial areas. A simple model of such a field is given by Kröger (1981). In contrast to the first group, the noise in the electrical field is related to that in the magnetic channels, i.e. the noise is *coherent*.

Signal and noise are always generated by different sources and therefore the signal is not coherent with the noise.

### Definition of Different Types of Noise

The measured data  $\mathbf{E}_i$  and  $\mathbf{H}_i$  are composed of the signals  $\mathbf{E}_{si}$ ,  $\mathbf{H}_{si}$  and the noise  $\mathbf{E}_{ni}$ ,  $\mathbf{H}_{ni}$ .

$$\begin{aligned} \mathbf{E}_i &= \mathbf{E}_{si} + \mathbf{E}_{ni} \\ \mathbf{H}_i &= \mathbf{H}_{si} + \mathbf{H}_{ni}. \end{aligned} \quad (5)$$

**Table 1.** Definition of the types of noise distinguished by their coherency characteristics

Type	Definition	COH	$[\hat{Z}]_L$ biased by:
1	incoherent	$\text{COH}(\mathbf{E}_n, \mathbf{H}_n) = 0$ $\text{COH}(H_{xn}, H_{yn}) = 0$	autopowers of $\mathbf{H}_n$
2	input-coherent	$\text{COH}(\mathbf{E}_n, \mathbf{H}_n) = 0$ $\text{COH}(H_{xn}, H_{yn}) \neq 0$	autopowers of $\mathbf{H}_n$ crosspowers of $H_{xn}$ and $H_{yn}$
3	multiple-coherent	$\text{COH}(\mathbf{E}_n, \mathbf{H}_n) \neq 0$ $\text{COH}(H_{xn}, H_{yn}) \neq 0$	autopowers of $\mathbf{H}_n$ crosspowers of $H_{xn}$ and $H_{yn}$ crosspowers of $\mathbf{E}_n$ and $\mathbf{H}_n$

The “true” tensor  $[\mathbf{Z}]$  relates the signals

$$\mathbf{E}_{si} = [\mathbf{Z}] \cdot \mathbf{H}_{si}. \quad (6)$$

Due to this relation in the following  $[\mathbf{Z}]$  is called the *signal impedance*.

Concerning the different influence on the bias-error, the noise has to be distinguished by its coherency characteristic. Possible types of noise are summarized in Table 1.

1. The noise components  $\mathbf{E}_n$  and  $\mathbf{H}_n$  are incoherent and furthermore the input components  $H_{xn}$ ,  $H_{yn}$  are incoherent. This type shall be referred to as *incoherent noise*.

2. The noise components  $\mathbf{E}_n$  and  $\mathbf{H}_n$  are incoherent but the input components of the noise  $H_{xn}$ ,  $H_{yn}$  are coherent. This type is called an *input-coherent noise*.

3. The noise  $\mathbf{E}_n$  is coherent with the noise  $\mathbf{H}_n$  and furthermore  $H_{xn}$  and  $H_{yn}$  are coherent. This type shall be referred to as *multiple-coherent noise*.

### Bias Error in the Local Estimate of the Impedance Tensor

A general two dimensional error analysis for each case of different types of noise in Table 1 is given by Kröger (1981). For simplification and demonstration of the main effects on bias and variance only, the absolute values of the diagonal elements  $Z_{xx}$ ,  $Z_{yy}$ , in the tensor  $[\mathbf{Z}]$  are assumed to be negligible small in comparison with the off-diagonal elements  $Z_{xy}$ ,  $Z_{yx}$ . In practice, this is a good approximation for many existing conductivity distributions. In this case the local estimates may be reduced to one-dimensional estimates (Scheelke, 1972). Also for simplification in the following we want to restrict ourselves to the demonstration of the bias (and variance) for one of the local estimates, i.e.  $[\hat{Z}]_L$ , Eq. (3a). The reader may easily transfer the results if  $[\hat{Z}]_L$ , Eq. (3b) instead of  $[\hat{Z}]_L$  is used. For example, the one-dimensional local estimate for the element  $Z_{xy}$  is given by

$$\hat{Z}_{xyL} = \frac{\sum_i E_{xi} H_{yi}^*}{\sum_i |H_{yi}|^2} \quad \left( \sum_i = \sum_{i=1}^M \right), \quad (7)$$

where  $H_{yi}^*$  is the complex conjugate of  $H_{yi}$ .

In this estimate noise of type 2 has no bias influence and that of type 3 simply reduces to coherent noise. This is not very restrictive, because, as shown by Kröger (1981), the multiple coherent noise usually will have much more error influence than the input coherent noise.

The estimate of the bias error  $\Delta Z_{xy}$  in the local estimate  $\hat{Z}_{xyL}$  is defined by

$$\Delta \hat{Z}_{xy} = \langle \hat{Z}_{xyL} \rangle - Z_{xy} \quad (8)$$

where  $\langle \rangle$  denotes the ensemble average and  $Z_{xy}$  is the signal impedance (true but unknown value). In the following error analysis stationarity of signals and noise is always assumed. For a sufficiently large number  $M$  of samples in Eq. (7) the variance of  $\hat{Z}_{xyL}$  becomes small compared with the bias of  $\hat{Z}_{xyL}$  (see next section) and  $\langle \hat{Z}_{xyL} \rangle$  may be approximated by

$$\langle \hat{Z}_{xyL} \rangle \simeq \hat{Z}_{xyL}. \quad (9)$$

Separating the measured data into signals and noise and considering incoherency between them, Eq. (7) leads to

$$\hat{Z}_{xyL} = \frac{\sum_i E_{xsi} H_{ysi}^* + \sum_i E_{xni} H_{yni}^*}{\sum_i |H_{ysi}|^2 + \sum_i |H_{yni}|^2}. \quad (10)$$

The signals are related by  $E_{xsi} = Z_{xy} \cdot H_{ysi}$ . For the noise a regression model may be set up and described by

$$E_{xni} = Z_{xyN} H_{yni} + \delta \delta E_{xi}. \quad (11)$$

Here, in the case of coherent noise  $Z_{xyN}$  is a well defined function and shall be called the *interference impedance*.  $\delta \delta E_{xi}$  is the incoherent (with  $H_{yni}$ ) part of the noise  $E_{xni}$ . Assuming known noise,  $Z_{xyN}$  can be estimated in accordance with Eq. (7)

$$\text{as } \hat{Z}_{xyN} = \frac{\sum_i E_{xni} H_{yni}^*}{\sum_i |H_{yni}|^2}. \quad (12)$$

Inserting the signal impedance  $Z_{xy}$  and the interference impedance  $\hat{Z}_{xyN}$ , given by Eq. (12), into Eq. (10) yields

$$\hat{Z}_{xyL} = \frac{Z_{xy} \hat{S}_{Hy} + \hat{Z}_{xyN} \hat{N}_{Hy}}{\hat{S}_{Hy} + \hat{N}_{Hy}}, \quad (13)$$

where the following abbreviations were used:

$$\begin{aligned} \hat{S}_{Hy} &= \sum_i |H_{ysi}|^2: \text{estimated signal power in } H_y, \\ \hat{N}_{Hy} &= \sum_i |H_{yni}|^2: \text{estimated noise power in } H_y. \end{aligned} \quad (13a)$$

With Eqs. (8), (9) and (13) the bias-error is

$$\Delta \hat{Z}_{xy} \simeq \hat{Z}_{xyL} - Z_{xy} = \frac{1}{1 + \left( \frac{\hat{S}}{\hat{N}} \right)_{Hy}} \cdot (\hat{Z}_{xyN} - Z_{xy}). \quad (14)$$

$\left( \frac{\hat{S}}{\hat{N}} \right)_{Hy}$  is the estimated signal-to-noise-ratio  $\hat{S}_{Hy}/\hat{N}_{Hy}$ . A

similar result may be derived for the estimated bias-error  $\Delta\hat{Z}_{yx}$  in the element  $\hat{Z}_{yxL}$ .

The bias-error depends on the noise parameters: signal-to-noise ratio and interference impedance. The difference between the interference impedance and the signal impedance is determined by the inhomogeneity of the source field of the noise. For example, in the near region of such a noise source the interference impedance due to the high inhomogeneity is very different from the signal impedance (absolute and phase value) as shown by Kröger (1981). With a low signal-to-noise ratio the bias-error may be much larger than the signal impedance, that means the local estimate  $\hat{Z}_{xyL}$  is “unusable” for modelling. If the distance between the location of measurement and the source increases, the inhomogeneity of the inducing field decreases. This means the interference impedance tends towards the signal impedance and the resulting bias-error becomes smaller. For a sufficient large distance from a coherent source of noise you will get the far field solution which is equivalent to the homogenous inducing (natural) field and  $\hat{Z}_{xyN}$  becomes equal to  $Z_{xy}$ . If there is no other type of noise, then the bias-error is zero.

If the noise is incoherent (type 1), according to Eq. (12),  $\hat{Z}_{xyN}$  is zero and Eq. (14) leads to the well known expression for the bias-error (Sims et al., 1971)

$$\Delta\hat{Z}_{xy} \simeq -\frac{1}{1 + \left(\frac{S}{N}\right)_{Hy}} \cdot Z_{xy}. \quad (15)$$

For incoherent noise the phase of the relative bias-error  $\Delta\hat{Z}_{xy}/Z_{xy}$  is  $180^\circ$  and therefore the local estimate  $\hat{Z}_{xyL}$  is downward biased compared with the signal impedance  $Z_{xy}$ .

For coherent noise the phase in Eq. (14) depends on the interference and signal impedance and, in this case,  $\hat{Z}_{xyL}$  may be upward biased (see also practical results below).

In contrast to the local estimate  $[\hat{Z}]_L$ , the reference estimate  $[\hat{Z}]_R$  does not depend on the autopowers and the crosspowers of the locally measured data and therefore it is not biased, provided the noise at the measuring station and that at the reference station is incoherent.

### Variance of the Estimates of the Impedance Tensor

For the different types of noise the variances of the local and reference estimate shall be compared. Again, for simplification, it is assumed  $|Z_{xx}|, |Z_{yy}| \ll |Z_{xy}|, |Z_{yx}|$ .

The estimated variance of the local estimate, for example, is given by Bendat and Piersol (1971). For the element  $\hat{Z}_{xyL}$  it is approximately

$$V\hat{A}R\{\hat{Z}_{xyL}\} \simeq \frac{1}{M} \cdot \frac{\sum_i |\delta E_{xi}|^2}{\sum_i |H_{yi}|^2}, \quad (16)$$

where  $\delta E_{xi}$  is the residuum

$$\delta E_{xi} = E_{xi} - \hat{Z}_{xyL} \cdot H_{yi} \quad (17)$$

and  $M$  is the number of samples in the regression analysis.

With Eqs. (17) and (7), Eq. (16) transforms into

$$V\hat{A}R\{\hat{Z}_{xyL}\} \simeq \frac{1}{M} \cdot \left[ \frac{\sum_i |E_{xi}|^2}{\sum_i |H_{yi}|^2} - |\hat{Z}_{xyL}|^2 \right]. \quad (18)$$

The total power in the electric channel,  $\sum_i |E_{xi}|^2$ , can be decomposed into the signal power  $\hat{S}_{Ex}$ , the noise  $\hat{N}_{ExC}$ , (which is totally coherent to the noise power  $\hat{N}_{Hy}$ ) and the noise power  $\hat{N}_{ExU}$  (which is totally incoherent to  $\hat{N}_{Hy}$ )

$$\sum_i |E_{xi}|^2 = \hat{S}_{ExC} + \hat{N}_{ExU} + \hat{N}_{ExC}. \quad (19)$$

In Appendix A1 it is shown how the expression for the variance in Eq. (18) by use of this decomposition becomes

$$V\hat{A}R\{\hat{Z}_{xyL}\} \simeq \frac{1}{M} \cdot \frac{1}{1 + \left(\frac{N}{S}\right)_{Hy}} \cdot \left[ \left(\frac{N_U}{S}\right)_{Ex} \cdot |Z_{xy}|^2 + \frac{1}{1 + \left(\frac{S}{N}\right)_{Hy}} \cdot |\hat{Z}_{xyN} - Z_{xy}|^2 \right]. \quad (20)$$

A similar expression may be derived for the element  $\hat{Z}_{yxL}$ . The variance of the local estimate depends on the already defined noise parameters  $\left(\frac{S}{N}\right)_{Hy}$  and  $\hat{Z}_{xyN}$  and on the signal-to-noise ratio  $\left(\frac{S}{N_U}\right)_{Ex}$  in the electric channel.  $N_U$  is the incoherent part of the noise power in  $E_x$ .

A general expression for the variance of the reference estimate was given by Gamble et al. (1979b). The expressed variance is dependent on the crosspowers of the measured data. For the aims of this paper, namely comparing bias and variance, the variance shall be given by its dependency of the above noise parameters. This is done by Kröger (1981). With  $|Z_{xx}|, |Z_{yy}| \ll |Z_{xy}|, |Z_{yx}|$ , the variance for  $\hat{Z}_{xyR}$  is

$$V\hat{A}R\{Z_{xyR}\} \simeq \frac{1}{M} \cdot \frac{1}{|\hat{K}_{yy}|^2 \cdot \sum_i |R_{yi}|^2} [\hat{N}_{ExU} + |\hat{Z}_{xyN} - Z_{xy}|^2 \cdot \hat{N}_{Hy}] \quad (21)$$

$$\text{with } |\hat{K}_{yy}|^2 = \frac{\hat{S}_{Hy}/\hat{S}_{Ry}}{\left[1 + \left(\frac{N}{S}\right)_{Ry}\right]^2}. \quad (21a)$$

$\hat{S}_{Ry}$  is the estimated signal and  $\left(\frac{S}{N}\right)_{Ry}$  the estimated signal-to-noise ratio at the reference station. In Appendix A2 it is shown that Eq. (21) can be transformed into

$$V\hat{A}R\{\hat{Z}_{xyR}\} \simeq \frac{1}{M} \cdot \left[ 1 + \left(\frac{N}{S}\right)_{Ry} \right] \cdot \left[ \left(\frac{N_U}{S}\right)_{Ex} \cdot |Z_{xy}|^2 + \left(\frac{N}{S}\right)_{Hy} \cdot |\hat{Z}_{xyN} - Z_{xy}|^2 \right]. \quad (22)$$

Besides the noise parameters at the measuring station the signal-to-noise ratio at the reference station appears in Eq. (22) and, as will be shown in the following, the variance of the reference estimate increases compared with the variance of the local estimate.

In Table 2 the ratio of the two variance expressions of Eq. (20) and Eq. (22) is given for the limits of the signal-to-noise ratios  $\left(\frac{S}{N}\right)_{Hy}$  and  $\left(\frac{S}{N_U}\right)_{Ex}$  and for the interference impedance  $\hat{Z}_{xyN}$ . This table points out that, due to the finite signal-to-noise ratio at the reference station, the reference estimate always has a larger variance than the local estimate. If the reference method is used, the reference station should be chosen as free of noise as possible because then the variance ratio becomes smallest for fixed noise parameters at the measuring station. Only in the case of large signal-to-noise ratios at the measuring and at the reference station do both methods give nearly the same variance.

The reference method becomes very important in the case of low signal-to-noise ratios at the measuring station  $\left(\frac{S}{N}\right)_{Hy} \ll 1$ . In this case the local estimation

leads to unusable results because of its large bias-error. But, as shown in Table 2, in just this case is  $V\hat{A}R\{\hat{Z}_{xyR}\} \gg V\hat{A}R\{\hat{Z}_{xyL}\}$ . With totally coherent noise (case a) a very consistent local estimate  $\hat{Z}_{xyL}$  is obtained, which of course is wrong. The reference method in this case needs much more data to get an estimate with as low a variance. The large bias-error or  $\hat{Z}_{xyL}$  is exchanged for a large variance of  $\hat{Z}_{xyR}$ .

Also in the case of totally incoherent noise and a low  $\left(\frac{S}{N}\right)_{Hy}$  (case b) is  $V\hat{A}R\{\hat{Z}_{xyR}\} \gg \{Z_{xyL}\}$  and therefore even for this type of noise the reference method needs much more data.

### Separation of Signal and Noise

An analysis of magnetotelluric data will show how large the noise parameters can be. In order to determine these parameters the signal and the noise at the measuring station have to be estimated. Gamble et al. (1979b) describe a method for estimating signal and noise power, based on two assumptions:

1. The noise at the measuring station is incoherent with the noise at the reference station.
2. The noise at the measuring station is incoherent.

Condition 1 can be satisfied by a sufficiently large distance between the two stations. However, it is easy to understand that the second assumption can be violated especially for measurements in industrialized areas, for example in central Europe. Our own experiences verify this (see below). Therefore a different method for the separation of signal and noise will be given. This method also uses the magnetic reference  $\mathbf{R}_i$ ; condition 1 has to be valid, but it is not restricted to incoherent noise at the measuring station. Instead of assumption 2 this method requires the reference station to be much less contaminated by noise than the measuring station. The necessity of this restriction will be explained in the following. Methods for choosing such a reference and checking this condition by use of

**Table 2.** Comparison of variances for limits of noise parameters

$\left(\frac{S}{N}\right)_{Hy}$	$\left(\frac{N_U}{S}\right)_{Ex}, \hat{Z}_{xyN}$	$V\hat{A}R\{\hat{Z}_{xyR}\}/V\hat{A}R\{\hat{Z}_{xyL}\}$
$\left(\frac{S}{N}\right)_{Hy} \gg 1$		$1 + \left(\frac{N}{S}\right)_{Ry} > 1$
$\left(\frac{S}{N}\right)_{Hy} \ll 1$	a) totally coherent noise	$\left(\frac{N_U}{S}\right)_{Ex} = 0$ $\left[1 + \left(\frac{N}{S}\right)_{Ry}\right] \cdot \left(\frac{N}{S}\right)_{Hy}^2 \gg 1$
	b) totally incoherent noise	$\left(\frac{N_U}{S}\right)_{Ex} = \left(\frac{N}{S}\right)_{Ex}$ $\left[1 + \left(\frac{N}{S}\right)_{Ry}\right] \cdot \left(\frac{N}{S}\right)_{Hy}$ $\hat{Z}_{xyN} = 0$ $\left(\frac{N}{S}\right)_{Hy} + \left(\frac{N}{S}\right)_{Ex} \gg 1$ $1 + \left(\frac{N}{S}\right)_{Ex}$

a second reference station are described by Kröger (1981).

For separating the signal and the noise in the magnetic field a regression model is set up between magnetic data measured at the measuring and the reference station.

$$\mathbf{H}_i = [\mathbf{K}] \cdot \mathbf{R}_i + \delta \mathbf{H}_i. \quad (23)$$

The transfer-function  $[\mathbf{K}]$  can be estimated similarly to Eq. (3)

$$[\hat{\mathbf{K}}] = \begin{bmatrix} \hat{K}_{xx} & \hat{K}_{xy} \\ \hat{K}_{xy} & \hat{K}_{yy} \end{bmatrix} = [C_{HR}] \cdot [P_{PR}]^{-1}. \quad (24)$$

Once  $[\hat{\mathbf{K}}]$  has been estimated the magnetic field at the measuring station can be predicted as

$$\mathbf{H}_{pi} = [\hat{\mathbf{K}}] \cdot \mathbf{R}_i. \quad (25)$$

Under the conditions that the reference  $\mathbf{R}_i$  is nearly free of noise and the noise at the measuring station is incoherent with the noise at the reference station,  $[\hat{\mathbf{K}}]$  will be estimated without bias-error and, with a sufficiently large number  $M$  of samples, has a low variance.  $[\hat{\mathbf{K}}]$  then describes the linear relationship between the (coherent) signals at the measuring and the reference stations and therefore the predicted  $\mathbf{H}_{pi}$  are nearly the signals at the measuring station

$$\mathbf{H}_{pi} \simeq \mathbf{H}_{si}. \quad (26)$$

The noise in the magnetic data at the measuring station is estimated by the residuals

$$\delta \mathbf{H}_i = \mathbf{H}_i - \mathbf{H}_{pi} \simeq \mathbf{H}_{ni}. \quad (27)$$

Only under the condition of a low interference reference station the separation is exact.

In a second regression model the predicted (signals)

$\mathbf{H}_{pi}$  are linearly related to the electric data  $\mathbf{E}_i$  at the measuring station

$$\mathbf{E}_i = [\mathbf{Z}] \cdot \mathbf{H}_{pi} + \delta \mathbf{E}_i. \quad (28)$$

The estimate of this impedance tensor is

$$[\hat{\mathbf{Z}}]_R = [\mathbf{C}_{EP}] \cdot [\mathbf{P}_{pp}]^{-1}. \quad (29)$$

The reference estimate of the impedance tensor is used to predict signals in the electric data

$$\mathbf{E}_{pi} = [\hat{\mathbf{Z}}]_R \cdot \mathbf{H}_{pi}, \quad (30)$$

which are estimates of the signal at the measuring station and with the above assumption of a reference station nearly free of noise, is

$$\mathbf{E}_{pi} \simeq \mathbf{E}_{si}. \quad (31)$$

The estimated noise in the electric data are the residuals

$$\delta \mathbf{E}_i = \mathbf{E}_i - \mathbf{E}_{pi} \simeq \mathbf{E}_{ni}. \quad (32)$$

The reference method described here gives the signals and the noise at the measuring station and moreover the bias-free reference estimate  $[\hat{\mathbf{Z}}]_R$ .  $[\hat{\mathbf{Z}}]_R$  tends towards the signal impedance  $[\mathbf{Z}]$  if a sufficiently large number of samples is used in the regression. From the isolated signals and noise the noise parameters are estimated. Results are shown in the next section.

It is easy to verify, as shown in Appendix A3, that the elements of  $[\hat{\mathbf{Z}}]_R$  given by Eq. (29) in any case of noise are exactly the same as given by Gamble et al. (1979a). This is because Eq. (4) can be decomposed into a double linear regression analysis given by Eqs. (24) and (29). Therefore the condition of a noise free reference in this method only has to be valid for the decomposition of signals and noise, but not for the estimation of the impedance  $[\hat{\mathbf{Z}}]_R$ .

## Results of Measurements

The magnetotelluric measurements for the recognition of noise and errors have been made in northern Germany between Braunschweig and Uelzen. Figure 1 shows the measurement area. The period range of registrations and data analysis extended from 2.5 s up to 128 s. The measuring station was chosen at ADB5 north of Braunschweig and the reference station at UMM1, approximately 20 km remote from the measuring station. Previous recordings by the authors at more than one reference station have shown that UMM1 has much less noise than ADB5 and therefore it is a suitable reference station for separation of signals and noise at ADB5 (see Kröger, 1981).

For the data analysis we used  $M=521$  synchronously recorded samples with sufficiently large "signal activity" which were transformed into the frequency domain by the usual methods.

The results for the local estimate  $[\hat{\mathbf{Z}}]_L$  and the reference estimate  $[\hat{\mathbf{Z}}]_R$  at ADB5 are given in Fig. 2. It shows for example the absolute value of the element  $\hat{Z}_{xy}$  versus period  $T$ . The bars at each estimated point

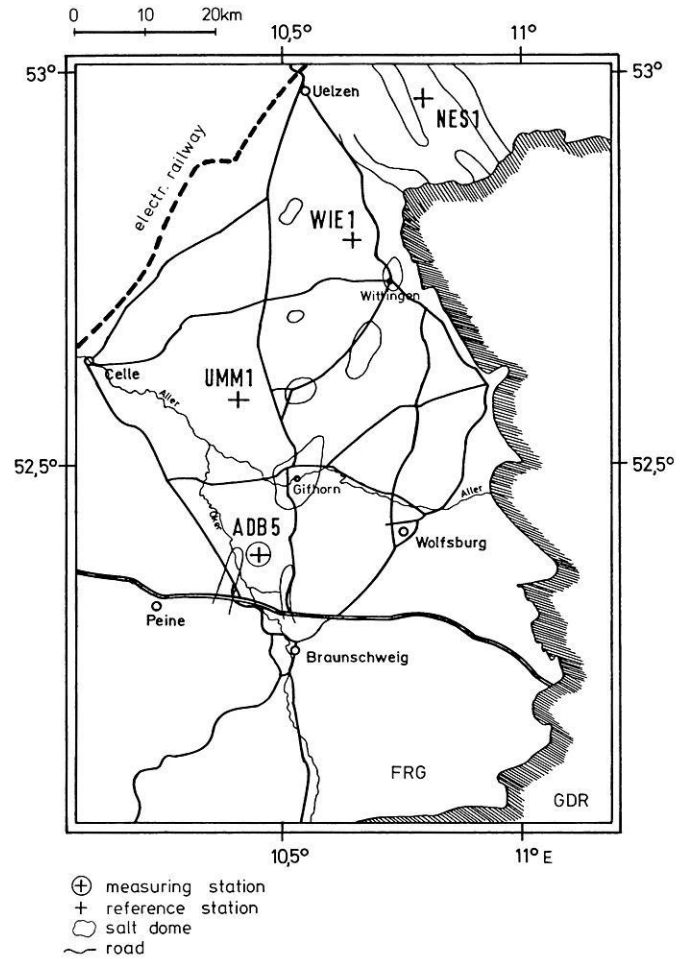


Fig. 1. Map of stations

denote the standard deviation  $\sqrt{\text{VAR}}$ , determined by standard methods (see e.g. Kröger, 1981). For comparison  $|\hat{Z}_{xyL}|$  has been indicated in the drawing of  $|\hat{Z}_{xyR}|$ .

At periods greater than 80 s both estimates are almost equal in amplitude and phase, and both have a very low variance. By comparison with  $\hat{Z}_{xyR}$ , which is assumed to be the signal impedance, there is a large bias-error in the local estimate  $\hat{Z}_{xyL}$  between about 15 s and 50 s. This indicates a large noise contribution at the measuring station. A more exact analysis, which include the phases, shows that this bias-error is nearly as large as the signal impedance (absolute value). Therefore in this period range for this location the local estimate  $\hat{Z}_{xyL}$  is unusable for MT-modelling.  $|\hat{Z}_{xyL}|$  is larger than  $|\hat{Z}_{xyR}|$  which implies that the noise must be coherent.

As expected, in the whole period range the variance of  $\hat{Z}_{xyR}$  is larger than that of  $\hat{Z}_{xyL}$ . This difference can be recognized particularly in the range between 15 s and 50 s where the bias of  $\hat{Z}_{xyL}$  is large (exchange of bias and variance). While  $\hat{Z}_{xyL}$  seems to be estimated "very well", but wrongly,  $\hat{Z}_{xyR}$  needs much more data to get a similar consistent estimate. Although there are a large number of samples in the regression the element  $\hat{Z}_{xyR}$  is badly estimated below about 8 s.

These errors of both estimates can be explained by the magnitude of the noise parameters. Figure 3 shows

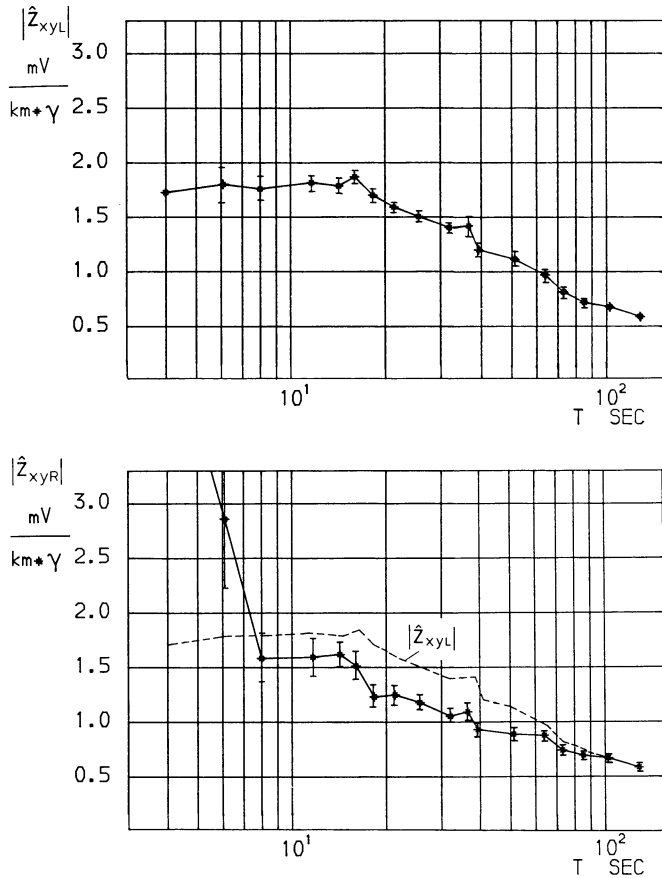


Fig. 2. Absolute value of the local estimate  $\hat{Z}_{xyL}$  and the reference estimate  $\hat{Z}_{xyR}$

the estimated signal-to-noise ratio in the component  $H_y$  versus period. This ratio was calculated from Eq. (26) and Eq. (27) as

$$\left(\frac{S}{N}\right)_{H_y} = \frac{\hat{S}_{H_y}}{\hat{N}_{H_y}} = \frac{\sum_i |H_{ypi}|^2}{\sum_i |\delta H_{yi}|^2}. \quad (33)$$

In the analysed data the estimate of the signal-to-noise ratio is much larger than one above 80 s. Therefore in this range the bias-error in  $\hat{Z}_{xyL}$  is very small. Both methods of estimating the impedance tensor lead to nearly the same results. Below 50 s the signal-to-noise ratio decreases rapidly, and is even much smaller than one below 20 s. This explains a large bias-error in  $\hat{Z}_{xyL}$  and the large variance of  $\hat{Z}_{xyR}$ , below 50 s. Below about 8 s there is hardly any signal power compared to noise power, hence  $\hat{Z}_{xyR}$  is inconsistent (see Fig. 2 and Table 2 with  $\left(\frac{S}{N}\right)_{H_y} \ll 1$ ).

Figure 4 demonstrates that the noise at the measuring station ADB5 is highly coherent especially in the range from 15 s up to 70 s. The figure shows the absolute value of the coherency

$$|\text{COH}(E_{xn}; H_{yn})| \approx \frac{|\sum_i \delta E_{xi} \cdot \delta H_{yi}^*|}{\sqrt{\sum_i |\delta E_{xi}|^2 \cdot \sum_i |\delta H_{yi}|^2}}, \quad (34)$$

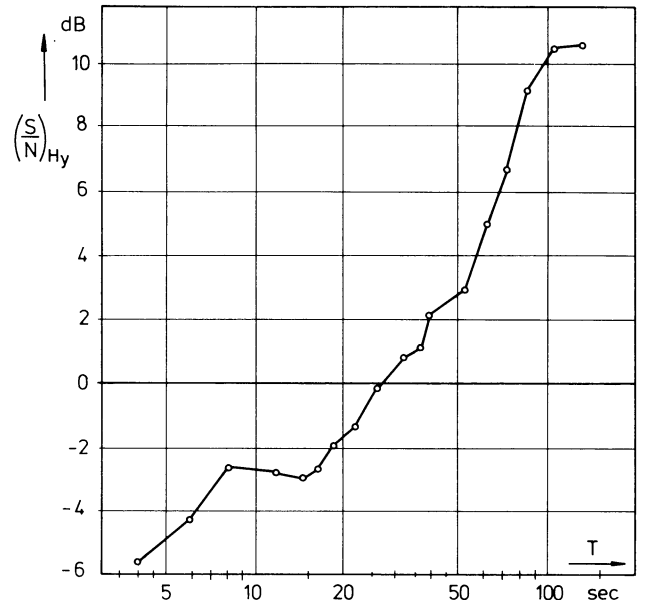


Fig. 3. Estimated signal-to-noise ratio in  $H_y$  at the measuring station ADB5

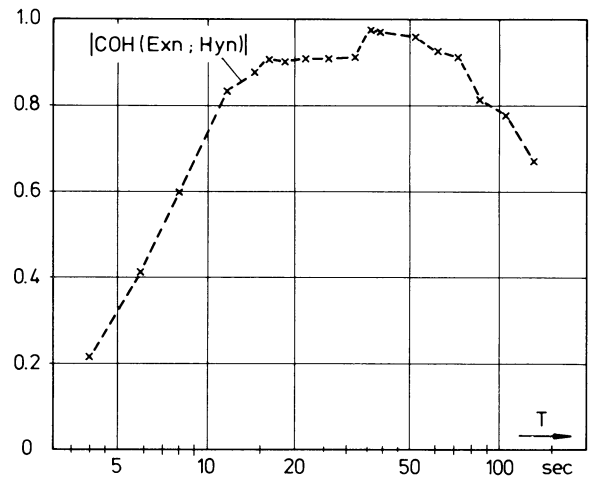


Fig. 4. Coherency function of noise at ADB5

calculated from Eqs. (27) and (32). The high coherency of the noise does not influence the estimates  $\hat{Z}_{xyL}$  and  $\hat{Z}_{xyR}$  very much at periods above 80 s, because the signal-to-noise ratio is sufficiently large here. Most importantly, at the low signal-to-noise ratios below 50 s, there is an influence. Due to this high coherency there is a well defined interference impedance, which actually differs greatly from the signal impedance. This leads to an upward biased local estimate  $\hat{Z}_{xyL}$  and, furthermore, from Table 2, to a large variance of  $\hat{Z}_{xyR}$  below 20 s. On the other hand, due to the high coherency,  $\hat{Z}_{xyL}$  appears to be well defined down to 4 s.

## Summary

Magnetotelluric recordings and data analysis over the last few years have shown that the homogeneously induced signals are very often degraded by artificial noise content, which sometimes causes large errors in the estimates of the impedance tensor.

In this work two methods of estimation, the local and the reference method, are compared with regard to the errors resulting from different types of noise. The main types are: incoherent and coherent noise.

The advantage of the local estimate is based on the fact that only one set of measurement equipment is needed, and that data analysis is relatively simple. But there can be a very large bias-error in the local estimate  $[\hat{Z}]_L$ , if the signal-to-noise ratio of the measured data is very low. Moreover, if the noise is coherent, the bias may be too large for MT-modelling. Measurement results prove that this type of noise exists in practice.

The reference method introduced by Goubau et al., (1978) and Gamble et al. (1979a) yields a bias-free estimate of the impedance tensor  $[\hat{Z}]_R$  if the noise at the measuring station is incoherent with the noise at the reference station. However, due to additionally introduced measurement data  $\mathbf{R}_i$  this method generally requires more data to obtain an estimate as consistent as  $[\hat{Z}]_L$ . Coherent noise between electric and magnetic field at the measuring station, in particular, leads to a large variance of  $[\hat{Z}]_R$  and, therefore, requires a large number of samples for a consistent estimation. The large bias-error of  $[\hat{Z}]_L$  at this type of noise exchanges with a large variance of  $[\hat{Z}]_R$ .

From the results presented the following conclusions may be drawn: Generally the locations of magnetotelluric measurements are primarily fixed by geological aspects and usually there are only a few degrees of freedom in fixing stations. In the industrialized central Europe especially it is unavoidable that measuring stations are used which are very "noisy". The noise cannot be recognized if measurements are done without a reference and if the noise is coherent. Any local estimate of the impedance tensor, in these cases, can be unusable as shown in this paper. To avoid large errors, future magnetotelluric measurements should be made with an additional reference station and the impedance tensor should be estimated using the reference method as advised by Gamble et al. (1979a). The reference station should be chosen as free of noise as possible. This method, in fact, needs more measurement equipment and, depending on the type of noise, possibly much more data but it yields, in any case, more exact estimates of the impedance tensor.

### Appendix A1: Estimated variance of $\hat{Z}_{xyL}$

With Eqs. (13), (18), and (19) follows

$$\text{V}\hat{\text{A}}\text{R}\{\hat{Z}_{xyL}\} \simeq \frac{1}{M} \cdot \left[ \frac{\hat{S}_{Ex} + \hat{N}_{ExC} + \hat{N}_{ExU}}{\hat{S}_{Hy} + \hat{N}_{Hy}} - \frac{|Z_{xy}\hat{S}_{Hy} + \hat{Z}_{xyN}\hat{N}_{Hy}|^2}{(\hat{S}_{Hy} + \hat{N}_{Hy})^2} \right]. \quad (\text{a1})$$

For the signal power and the coherent noise power it is

$$\hat{S}_{Ex} = |Z_{xy}|^2 \hat{S}_{Hy} \quad (\text{a2})$$

$$\hat{N}_{ExC} = |\hat{Z}_{xyN}|^2 \hat{N}_{Hy}. \quad (\text{a3})$$

Equations (a2) and (a3) introduced into Eq. (a1) leads to

$$\text{V}\hat{\text{A}}\text{R}\{\hat{Z}_{xyL}\} \simeq \frac{1}{M} \cdot \frac{1}{1 + \left(\frac{N}{S}\right)_{Hy}} \cdot \left[ \frac{\hat{N}_{ExU}}{\hat{S}_{Hy}} + \frac{1}{1 + \left(\frac{S}{N}\right)_{Hy}} \cdot \left( |Z_{xy}|^2 + |\hat{Z}_{xyN}|^2 - 2 \text{Re}\{Z_{xy} \cdot \hat{Z}_{xyN}^*\} \right) \right]. \quad (\text{a4})$$

Equation (a4) with Eq. (a2) gives

$$\text{V}\hat{\text{A}}\text{R}\{\hat{Z}_{xyL}\} \simeq \frac{1}{M} \frac{1}{1 + \left(\frac{N}{S}\right)_{Hy}} \cdot \left[ \left(\frac{N_u}{S}\right)_{Ex} \cdot |Z_{xy}|^2 + \frac{1}{1 + \left(\frac{S}{N}\right)_{Hy}} \cdot |Z_{xy} - \hat{Z}_{xyN}|^2 \right]. \quad (\text{a5})$$

### Appendix A2: Estimated variance of $\hat{Z}_{xyR}$

In Eq. (21) the total power at the reference station  $\sum_i |R_{yi}|^2$  is separated into signal and noise power (estimated values)

$$\sum_i |R_{yi}|^2 = \hat{S}_{Ry} + \hat{N}_{Ry}. \quad (\text{a6})$$

Then with Eq. (21a)

$$|\hat{K}_{yy}|^2 \cdot \sum_i |R_{yi}|^2 = \hat{S}_{Hy} \cdot \frac{1}{1 + \left(\frac{N}{S}\right)_{Ry}}. \quad (\text{a7})$$

Equation (a7) introduced into Eq. (21) leads to

$$\text{V}\hat{\text{A}}\text{R}\{\hat{Z}_{xyR}\} \simeq \frac{1}{M} \cdot \left[ 1 + \left(\frac{N}{S}\right)_{Ry} \right] \cdot \left[ \frac{\hat{N}_{ExU}}{\hat{S}_{Hy}} + |\hat{Z}_{xyN} - Z_{xy}|^2 \cdot \frac{\hat{N}_{Hy}}{\hat{S}_{Hy}} \right]$$

or with  $\hat{S}_{Ex} = |Z_{xy}|^2 \cdot \hat{S}_{Hy}$

$$\text{V}\hat{\text{A}}\text{R}\{\hat{Z}_{xyR}\} \simeq \frac{1}{M} \cdot \left[ 1 + \left(\frac{N}{S}\right)_{Ry} \right] \cdot \left[ \left(\frac{N_u}{S}\right)_{Ex} \cdot |Z_{xy}|^2 + \left(\frac{N}{S}\right)_{Hy} \cdot |\hat{Z}_{xyN} - Z_{xy}|^2 \right] \quad (\text{a8})$$

### Appendix A3

With Eq. (24) and Eq. (25) it is

$$[C_{EP}] = [C_{ER}] \cdot [\hat{K}]^*{}^T \quad (\text{a9})$$

and

$$\begin{aligned} [P_{PP}] &= [\hat{K}] \cdot [P_{RR}] \cdot [\hat{K}]^*{}^T \\ &= [C_{HR}] \cdot [\hat{K}]^*{}^T, \end{aligned} \quad (\text{a10})$$

where  $[\hat{K}]^*{}^T$  is the Hermitian adjoint matrix of  $[\hat{K}]$ .

Equation (a9) and Eq. (a10) introduced into Eq. (29) gives

$$\begin{aligned} [\hat{Z}]_R &= [C_{ER}] \cdot [\hat{K}]^{*T} \cdot [[C_{HR}] \cdot [\hat{K}]^{*T}]^{-1} \\ &= [C_{ER}] \cdot [C_{HR}]^{-1}. \end{aligned} \quad (\text{a11})$$

## References

- Bendat, J.S., Piersol, A.G.: Random data: Analysis and measurement procedures. New York: John Wiley & Sons, Inc. 1971
- Gamble, T.D., Goubau, W.M., Clarke, J.: Magnetotellurics with a remote magnetic reference. *Geophysics* **44**, 53–68, 1979a
- Gamble, T.D., Goubau, W.M., Clarke, J.: Error analysis for remote reference magnetotellurics. *Geophysics* **44**, 959–968, 1979b
- Goubau, W.M., Gamble, T.D., Clarke, J.: Magnetotelluric data analysis: removal of bias. *Geophysics* **43**, 1157–1166, 1978
- Gundel, A.: Erdmagnetische Induktion in einer dreidimensionalen Salzstruktur. Diss. math.-naturwiss. Fakultät der Universität Göttingen, 1977
- Kao, D.W., Rankin, D.: Enhancement of signal-to-noise-ratio in magnetotelluric data. *Geophysics* **42**, 103–110, 1977
- Kröger, P.: Der Magnetotellurik-Impedanztensor bei lokal gestörten Meßgrößen. Diss. Fakultät für Maschinenbau und Elektrotechnik der TU Braunschweig, 1981
- Madden, T., Nelson, P.: A defence of Cagniard's magnetotelluric method. Geophysics Lab., M.I.T., Cambridge, Mass. 1964
- Rankin, D., Reddy, I.K., A magnetotelluric study of resistivity anisotropy. *Geophysics* **34**, 438–449, 1969
- Rikitake, T.: Electromagnetism and the Earth's interior. Amsterdam: Elsevier Publ. Comp. 1966
- Scheelke, I.: Magnetotellurische Messungen im Rheingraben und ihre Deutung mit zweidimensionalen Modellen. Diss. naturwiss. Fakultät der TU Braunschweig, 1972
- Sims, W.E., Bostick, F.X. Jr., Smith, H.W.: The estimation of the magnetotelluric impedance tensor elements from measured data. *Geophysics* **36**, 938–942, 1971
- Swift, C.M. Jr.: A magnetotelluric investigation of an electrical conductivity anomaly in the south-western United States. Ph. D. thesis, M.I.T., Cambridge, Mass., 1967
- Wait, J.R.: On the relation between telluric currents and the earth's magnetic field. *Geophysics* **19**, 281–289, 1954

Received March 2, 1982; Revised version October 26, 1982  
Accepted January 28, 1983

## Discrete Chorus Emissions Recorded at Nainital

P.N. Khosa, Lalmani, and M.M. Ahmad

Department of Physics, Regional Engineering College, Srinagar Kashmir, India

**Abstract.** Discrete Chorus type emissions recorded in May/June 1970 at our ground based observation station at Nainital (geomagnetic lat.  $19^{\circ}1'N$ ) are presented. It is shown that these emissions are generated in the equatorial plane ( $L \sim 1.2$ ) by cyclotron resonance between the propagating whistler wave and the gyrating electrons.

**Key words:** Whistlers – VLF emissions – Discrete chorus emissions – Absorption band – ELF hiss – Cyclotron resonance – Electron density – Gyration electrons – Growth rate.

### Introduction

The study of whistlers and VLF (Very Low Frequency) emissions at low latitudes dates back to the pioneering work of Japanese scientists. The low latitude whistlers were first recorded at Toyakawa (geomagnetic lat.  $24^{\circ}5'N$ ) (Iwai and Otsu, 1956), and later on, efforts were made to record them at still lower latitudes (Ondoh and Tanaka, 1973; Kotaki et al., 1977). The first successful records of whistlers in India were obtained at Gulmarg (geomagnetic lat.  $24^{\circ}10'N$ ) by Somayajulu et al. (1965). Recording was later carried out at Nainital (geomagnetic lat.  $19^{\circ}1'N$ ) and whistlers with comparatively lower dispersion and reduced rate of occurrence were reported (Lalmani, 1974). Singh et al. (1977) carried out successful recording of low dispersion whistlers at their low latitude ground-based station at Varanasi (geomagnetic lat.  $14^{\circ}55'N$ ) which previously was believed to lie in what was then supposed to be some sort of a low latitude cut-off for whistler waves (Rao et al., 1974). Very low frequency emissions of this type have frequently been observed at the Japanese low latitude ground stations (Nishino and Tanaka, 1960; Ondoh, 1963; Iwai and Tanaka, 1968; Tanaka et al., 1970; Tanaka, 1972). An excellent review of low latitude VLF emissions has been given by Kimura (1967). No successful attempts were made to record the VLF emissions in India. During the course of our analysis of the huge amount of whistler data collected in May/June 1970 at Nainital we have found some excellent records of discrete chorus type emissions which we reproduce here together with their most probable generation mechanism.

### Observations

On 13 May and 8 June 1970, we observed about thirty discrete rising emissions between 2200 and 0315 hours IST

local time. Some of the emissions are shown in Fig. 1. The emissions recorded on May 13, 1970 occurred in the frequency range 2.5–4.5 kHz and 4.5–7 kHz, while emissions on 8 June 1970 occurred in the frequency range 3.5–5.5 kHz. Figure 1 (a) shows a single trace rising emission in the frequency range 2.5–4.5 kHz. Figure 1 (b) shows two rising emissions occurring at the same time in two different frequency ranges 2.5–4.5 kHz and 4.5–7 kHz. Figure 1 (c) shows a single trace rising emission of long duration in the frequency range 3.5–5 kHz. Figure 1 (d) shows two rising emissions with almost similar features as shown in Fig. 1 (b). Figure 1 (e–g) depicts rising emission of long duration in the frequency range 3.5–5.5 kHz recorded on 8 June 1970.

### Discussions

Observed emissions differ markedly in frequency and rate of change of frequency with time from those of the riser whistlers observed earlier at the low latitude ground station of Gulmarg (geomagnetic lat.  $24^{\circ}10'N$ ; Dikshit et al., 1971). Further, because of the presence of a strong absorption band around 2 kHz these emissions could not have been high latitude discrete type chorus emissions propagating to our low latitude station in the Earth-ionosphere wave guide. The possibility that these emissions are generated at high  $L$ -values in the vicinity of the plasmapause and have propagated to our ground station after successive magnetospheric reflections in a manner similar to those of the ELF (Extremely Low Frequency) hiss observed by satellites in the inner zone (Muzzio and Angerami, 1972; Tsurutani et al., 1975) does not seem to be tenable. This is because of the fact that heavy attenuation would make the amplitude of these signals extremely small and so they could not have been detected. At the base of the  $F$ -region ionosphere, the wave normal angles of these waves are such that the downward waves are unlikely to penetrate the lower ionosphere and reach the ground. Wave normals of chorus in the outer magnetosphere have been determined for the first time from data obtained with OGO5 search coil magnetometre by Burton and Holzer (1974).

It is, therefore, believed that these emissions are generated in the equatorial plane in the inner zone radiation belt ( $L \sim 1.2$ ) by the cyclotron resonance between whistler mode waves and the inner zone radiation belt electrons (Rycroft, 1972; Imhof et al., 1973). All such emissions generated at higher  $L$ -values will reach the ground stations corresponding to higher latitudes than that of Nainital and

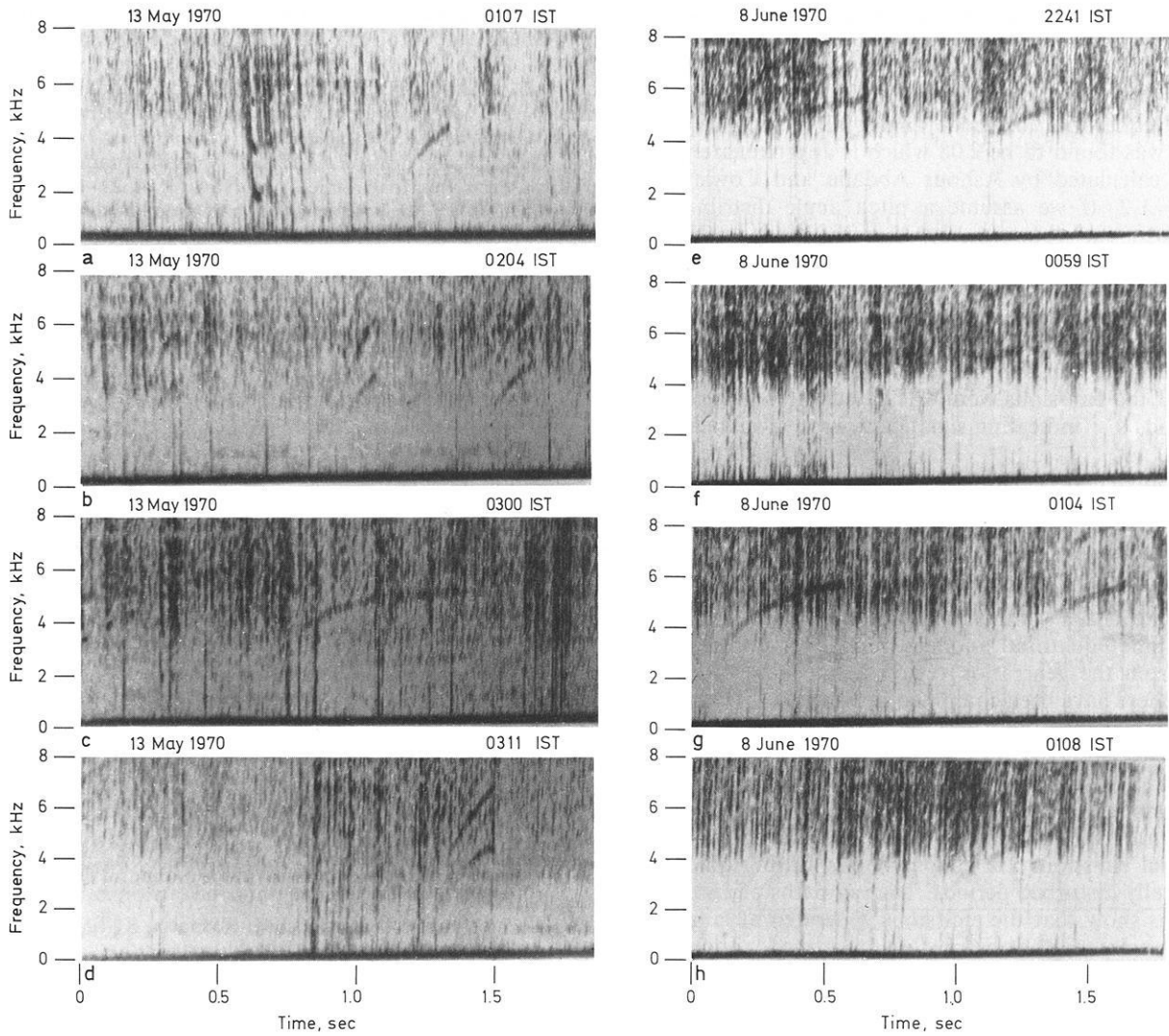


Fig. 1. Sonograms of discrete chorus emissions observed at Nainital

the chances for the generation of these emissions for values of  $L < 1.2$  are small because of the non-availability of such high energy electrons in large numbers. In order to test cyclotron resonance as a possible generation mechanism for these emissions, we have calculated the resonant energy of the high energy interacting electrons and growth rate of the whistler waves at  $L=1.2$  in the equatorial plane. The resonant energies for various frequencies of the emissions were calculated from the expression (Tsurutani et al., 1975)

$$E_{11} = (\gamma_n - 1) m_0 C^2 \quad (1)$$

where  $m_0$  is the rest mass of electron;  $C$ , the velocity of light in vacuum and  $\gamma$  the relativistic factor to be obtained from the relation

$$\gamma_n^2 - 1 \cong \left( \frac{\Omega^-}{\omega_p} \right)^2 \left( \frac{\Omega}{\omega} \right) \left( 1 + \frac{\Omega^+}{\omega} \right). \quad (2)$$

In Eq. (2)  $\Omega^-$  is the electron gyrofrequency,  $\Omega^+$  the proton gyrofrequency,  $\omega_p$  the plasma frequency and  $\omega$  the wave frequency. The plasma frequency  $\omega_p$  was calculated from the ionospheric model of Singh (1976) which yielded an

electron density of  $8.13 \times 10^3$  electrons  $\text{cm}^{-3}$  at  $L=1.2$ . The resonant energies for various frequencies of the emissions were found to be in the range 3–5 MeV. Recently Burton and Holzer (1974) have shown that the chorus is generated by cyclotron resonance with electrons in the approximate energy range 5–150 keV with pitch angle distribution peaked at  $90^\circ$  to  $\mathbf{B}$  and anisotropy greater than a critical value. Further, it has also been shown by Lalmani et al. (1970) that the resonant energies for various frequencies of the emission at  $L=1.2$  are in the MeV range.

The growth rates of these waves was calculated from the expression (2.20) of Kennel and Petschek (1966), which for the case of  $\omega \ll \Omega^-$  reduces to

$$\gamma = \pi \Omega^- \eta A \quad (3)$$

where  $\eta$  is the ratio of the density of energetic electrons to that of thermal electrons and  $A$ , the pitch angle anisotropy. The density of energetic electrons at  $L=1.2$  were taken from the observed intensity versus  $L$ -value curves (energy  $> 1$  MeV) given by Katz (1966) for the inner zone radiation belt. The curve indicated a flux of  $3 \times 10^6$  el  $\cdot \text{cm}^{-2} \text{sr}^{-1}$  at  $L=1.2$  which yielded a density of 3–5 MeV electrons as roughly  $1.26 \times 10^{-3}$  el  $\text{cm}^{-3}$ . The pitch angle anisotropy

$A$  was calculated from the relation (Kennel and Petschek, 1966)

$$A = \frac{1}{2} / \log_e (1/\alpha_0)$$

( $\alpha_0$  being the equatorial loss cone angle, mirror height = 100 km) and was found to be 2.08 which is approximately the same as calculated by Ashour Abdalla and Cowley (1974) at  $L=1.2$ . If we assume a pitch angle distribution of the form  $\sin^m \Phi$  ( $m=4$ , and  $\Phi$  is the pitch angle) and compare the calculated pitch angle versus intensity curve with that of Katz (1966), the two distributions are found to be nearly the same. Thus the value of anisotropy  $A=2.08$  at  $L=1.2$  is justified. By substituting the values of  $\Omega^-$ ,  $\eta$  and  $A$  in Equ. (3), the growth rates for various frequencies of the emissions were calculated and found to be about  $3 \text{ rads s}^{-1}$  indicating significant wave amplification.

Recently Singh (1981) has studied the propagation characteristics; of low latitude VLF emissions with the help of ray tracing computation in the presence of negative horizontal density gradients of the equatorial anomaly. Assuming that the low latitude emissions are generated in the equatorial plane at  $L=1.2$ , the ray paths of these emissions in the quiet time equatorial anomaly model for different frequencies from the generation region to the base of  $F$ -region ionosphere have been computed by Singh (1981) and it has been shown that the waves lie in the transmission cone and can be observed on the ground. Further, Singh (1981) calculated the ray paths of these waves in the equatorial anomaly model which corresponds to disturbed periods and has shown that the propagation characteristics of daytime equatorial emissions are almost similar during quiet and magnetically disturbed periods. The ray paths of night time emissions show that the emissions generated at large wave normal angles may be observed on the ground without any influence of density gradients of the anomaly (Singh 1981). During disturbed periods the night time anomaly extends to a wide latitude range around the equator. This produces negative horizontal density gradients in the ionization at low latitudes (Singh, 1976; Singh et al., 1978). Singh et al. (1978) have shown that the final wave normals of the night time VLF emissions are tilted almost along the downward vertical direction as a result of such horizontal density gradients.

*Acknowledgements.* The authors are grateful to Dr. O.N. Wakhlu for his constant encouragement and keen interest in the work reported here.

## References

- Ashour – Abdalla, M., Cowley, S.W.H.: Wave particle interactions near the geostationary orbit. In: Magnetospheric physics, B.M. Mc. Cormac, (ed.), pp. 241–270. Dordrecht: D. Reidel 1974
- Burton, R.K., Holzer, R.E.: The origin and propagation of chorus in the outer magnetosphere. *J. Geophys. Res.* **79**, 1014–1023, 1974
- Dikshit, S.K., Somayajulu, V.V., Tantry, B.A.P.: Riser whistlers at a ground station at low latitude. *Nature Phys. Sci.* **230**, 115–116, 1971
- Imhof, W.L., Gains, E.E., Reagan, J.B.: Dynamic variations in intensity and energy spectra of electrons in the inner radiation belt. *J. Geophys. Res.* **78**, 4568, 1973
- Iwai, A., Otsu, J.: On the investigation of whistling atmospherics in Japan. *Proc. Res. Inst. Atmos. Nagoya Univ.* **4**, 29–47, 1956
- Iwai, A., Tanaka, Y.: Measurement of polarization, incident angle and direction of VLF emissions. I. *Proc. Res. Atmos. Nagoya Univ.* **15**, 1, 1968
- Katz, L.: Radiation trapped in the earth's magnetic field (ed. Mc. Cormac B.M.) 130, 1966
- Kennel, C.F., Petschek, H.E.: Limit on stably trapped particle fluxes. *J. Geophys. Res.* **71**, 1, 1966
- Kimura, I.: On observations and theories of the VLF emissions. *Planet. Space Sci.* **15**, 1427, 1967
- Kotaki, M., Ondoh, T., Murakami, T., Watanabe, S.: Characteristics of low latitude whistlers as observed at Okinawa, Japan. *J. Radio Res. Lab.* **24**, 117, 1977
- Lalmani: Whistlers and VLF hiss at low latitudes. Ph. D. Thesis, Banaras Hindu University Varanasi, 1974
- Lalmani, Somayajulu, V.V., Tantry, B.A.P.: Very low frequency (VLF) emissions at low latitudes. *Ind. J. Pure Appl. Phys.* **8**, 564, 1970
- Muzzio, J.L., Angerami, J.J.: Ogo 4 observations of extremely low frequency hiss. *J. Geophys. Res.* **77**, 1157, 1972
- Nishino, M., Tanaka, Y.: The observation of VLF emissions at Moshiri. *Rept. Jap. Amt. Res. Exp.* **35**, 37, 1960
- Ondoh, T.: The ionospheric absorption of the VLF emissions at the auroral zone. *J. Geomagn. Geoelectr.* **15**, 90, 1963
- Ondoh, T., Tanaka, Y.: VLF emissions and whistlers observed in Japan for the August 1972 events. *Rept. Uag-28. Part II*, 389, 1973
- Rao, M., Somayajulu, V.V., Dikshit, S.K., Tantry, B.A.P.: Low latitude cut off of whistlers observed on the ground. *J. Geophys. Res.* **79**, 3867, 1974
- Rycroft, M.J.: VLF emissions in the magnetosphere. *Radio Science* **7**, 811, 1972
- Singh, B.: On the ground observation of whistlers at low latitudes. *J. Geophys. Res.* **81**, 2429, 1976
- Singh, B.: A study of whistlers and VLF emissions at low latitudes, Tech. Rept. (R.B.S. College Agra) 1981
- Singh, D.P., Jain, S.K., Singh, B.: Propagation characteristics of VLF hiss observed at low latitude ground stations. *Ann. Geophys.* **34**, 37, 1978
- Singh, R.N., Lalmani, Singh, R.P.: Whistlers recorded at Varanasi. *Nature Phys. Sci.* **266**, 40, 1977
- Somayajulu, V.V., Srivastava, K.M.L., Tantry, B.A.P.: The observation of whistlers at low latitude ground station Gulmarg. *Ind. J. Pure Appl. Phys.* **3**, 405, 1965
- Tanaka, Y., Nishino, M., Iwai, A.: A study of auroral VLF hiss observed at Syowa station, Antarctica. *Proc. Res. Inst. Atmos.* **17**, 43, 1970
- Tanaka, Y.: VLF hiss observed at Syowa station, Antarctica. I. Observation of VLF hiss. *Proc. Res. Inst. Atmos.* **19**, 33, 1972
- Tsurutani, B.T., Smith, E.J., Thorne, R.M.: Electromagnetic hiss and relativistic electron losses in the inner zone. *J. Geophys. Res.* **80**, 600, 1975

Received January 28, 1982; Revised November 22, 1982

Accepted November 23, 1982

# Evidence for Lamination in the Lower Continental Crust Beneath the Black Forest (Southwestern Germany)

N. Deichmann and J. Ansorge

Institute of Geophysics, ETH-Hönggerberg, CH-8093 Zürich, Switzerland

**Abstract.** A 113 km long seismic refraction profile, with an average station spacing of 3 km, was recorded along the eastern margin of the Black Forest (southwestern Germany). Travel-times were modelled by ray-tracing, and amplitudes by a combination of reflectivity and asymptotic ray-theory methods. The resulting upper crustal model is characterized by a strong velocity gradient reaching 6.0 to 6.1 km/s at a depth between 8 and 10 km. Sedimentary reverberations are found to mask possible evidence for a discontinuity or a low-velocity layer in the middle crust, so that the existence of such a structure could not be demonstrated from this data alone. The reflections from the crust-mantle boundary consist of higher-frequency precursors and a lower-frequency main phase, followed by irregular reverberations. While the latter are probably due to multiple reflections and conversions within the sediments, the amplitudes and the frequency selective character of the former is best explained by a transition zone, between 20 and 26 km depth, consisting of a lamina-like sequence of velocity inversions.

**Key words:** Crustal structure – Refraction seismology – Synthetic seismograms – Velocity gradients – Low-velocity zone – Crust-mantle Transition

## Introduction

The seismic refraction profile presented in this paper was recorded along the eastern margin of the Black Forest, southern Germany. It fills a gap between the intensively studied area of the southern Rhinegraben in the west (Mueller et al., 1969; Mueller et al., 1973; Edel et al., 1975; Prodehl et al., 1976), the area of the South German Molasse Basin in the east (Emter, 1971; 1976) and the recently investigated geothermal anomaly in the Suabian Jura, near Urach, to the northeast (Bartelsen et al., 1982; Jentsch et al., 1982).

Using both travel-time and amplitude information, it was possible to investigate the velocity gradient of the upper crystalline basement, the problem of the possible existence of a low-velocity layer in the upper or middle crust and the nature of the crust-mantle transition.

*Offprint requests to:* N. Deichmann

Contribution No. 403, Institute of Geophysics ETH Zürich, Switzerland

## Geological Setting

The data were obtained between 1974 and 1980, along a north-south trending profile, from ten explosions in a single quarry near the town of Sulz am Neckar. As can be seen from the locations of the recording sites in Fig. 1, the first 90 km of this 113 km long line are situated along the edge of the crystalline Black Forest, where it dips beneath the Triassic sediments. Beyond 90 km, the line enters the Swiss Molasse Basin and crosses the eastern end of the Swiss Jura. From borehole data at Sulz and at other locations along the profile compiled in the geological literature

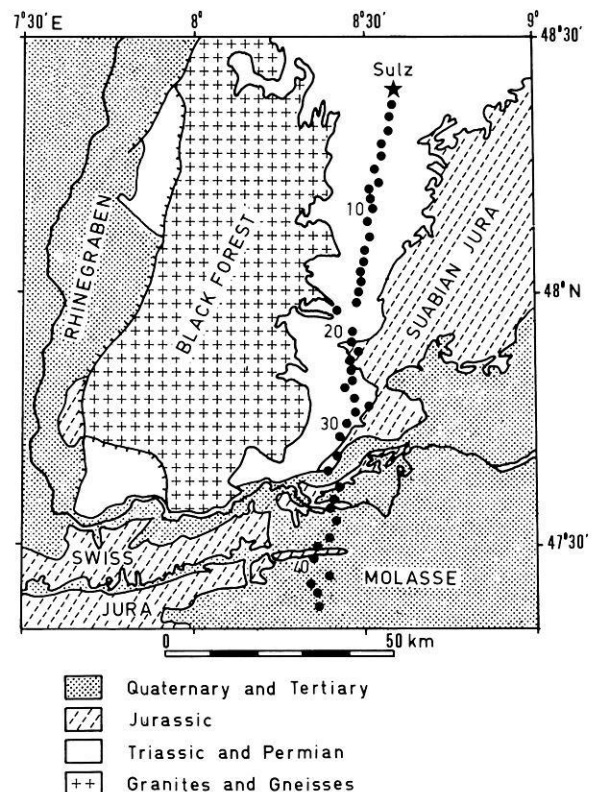


**Fig. 1.** Geological map with shotpoint (star) and station locations (dots) of profile Sulz-south. Stations are numbered consecutively from north to south. Information regarding the crust-mantle transition applies to the range between stations 10 and 20

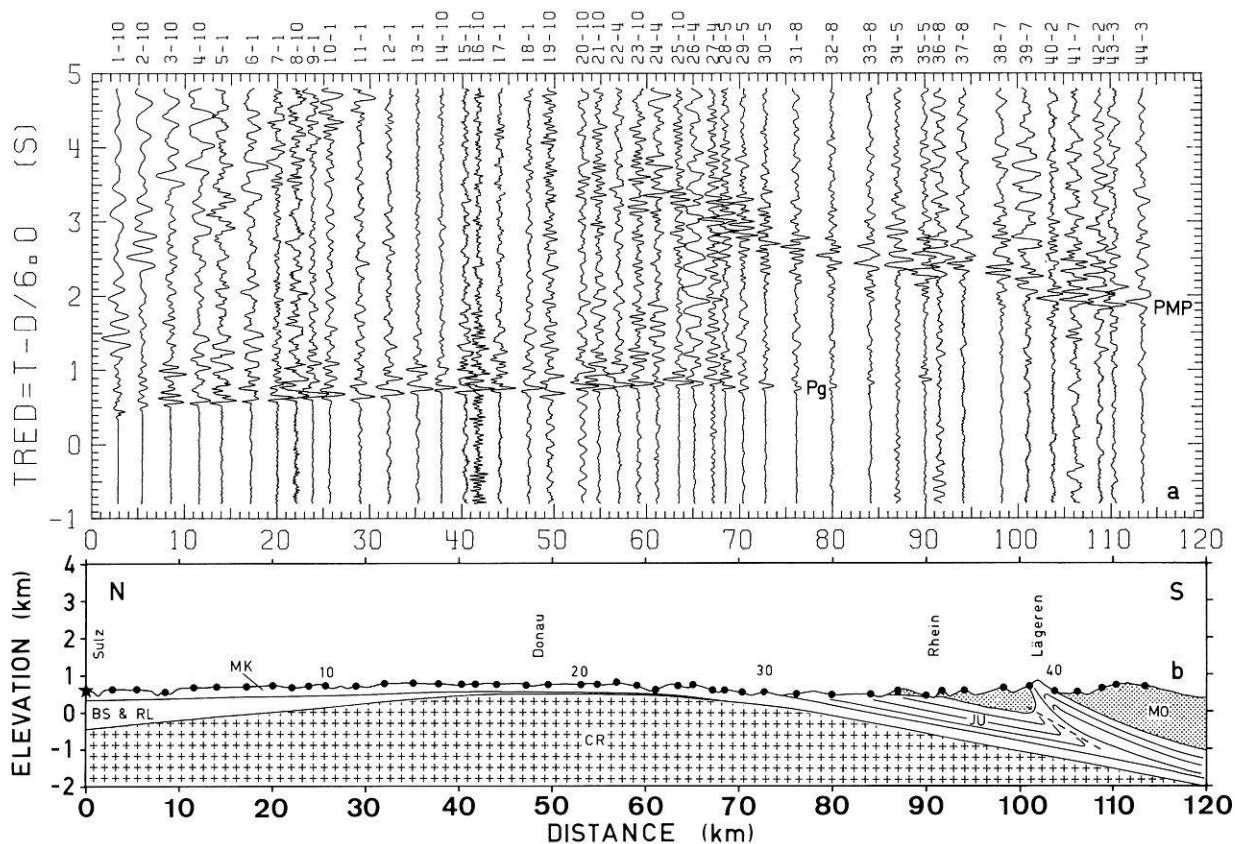


Fig. 2. **a** Trace-normalized, vertical component record section, with 32-Hz anti-aliasing filter. Numbers above each trace indicate station and shot. **b** Topography and geological cross-section along profile Sulz-south. Vertical exaggeration: 4 times. MK-Muschelkalk and Keuper, BS = Buntsandstein, RL = Rotliegendes, MO = Molasse, JU = Jura, CR = Crystalline basement

(Boigk and Schoeneich, 1968; Breyer, 1956; Buechi et al., 1965; Lemcke et al., 1968; Schneider, 1980), it is possible to construct a rough cross-section of the sedimentary structure and of the topography of the crystalline basement (Fig. 2b). Thus the sediment-basement boundary is characterized by an up-dip over the first 40 km and a down-dip beyond about 60 km. In the north, the surficial upper Triassic sediments (Keuper and Muschelkalk) are underlain by a thick wedge of lower Triassic and Permian deposits (Buntsandstein and Rotliegendes). In the south, these Triassic sediments are covered by a layer of Jurassic limestones and by two Molasse basins, which are separated by the Jurassic outcrop of the Laegeren, the easternmost part of the folded Jura mountains.

#### Data Acquisition and Processing

All shots were recorded on FM-magnetic tape instruments of the MARS type (Berckhemer, 1970). Except for three stations with FS-60 seismometers (nos. 5, 6, 7 in Figs. 1 and 2), all instruments were equipped with three-component MARK L-4 seismometers with a natural frequency of 2 Hz. Timing was accomplished by recording the coded DCF radio-transmitted time signal along with the shots. The signals were digitized electronically with a sampling rate of about 400 Hz, using the recorded pilot frequency of the MARS instruments to drive the digitizer. After decoding the time signal, determining the exact sampling rate and removing possible spikes from the seismograms, the signals

were filtered with a digital, zero-phase, 32-Hz low-pass filter, and the sampling rate was reduced to 100 Hz. During plotting of the record sections, an additional recursive, zero-phase band-pass filter could be applied to the data, to enhance various features of the signals. Figure 2a presents the vertical component data, filtered only with the 32-Hz anti-aliasing filter. The amplitudes are trace-normalized, but gain factors, which are calculated for each seismogram by the plot program, allow the determination of absolute ground velocity.

Since the distance range over which individual shots were recorded overlap with each other, amplitudes could be normalized to the same charge size where necessary. Because of poor recordings, some sites were occupied more than once.

#### Upper Crust

The  $P_g$  travel-time and amplitude data have already been presented in the context of a general discussion of amplitude modelling of the  $P_g$ -phase (Banda et al., 1982). In the resulting model (Fig. 4), the crystalline basement is characterized by a zone with a velocity gradient of 0.074 km/s/km between 1 and about 6 km depth, followed by a second zone with a weaker gradient (0.02 km/s/km) down to a depth of about 8 km.

Usually, several models can be made to fit the travel-time data by compensating changes in basement velocities with changes in sediment structure. However, in this case,

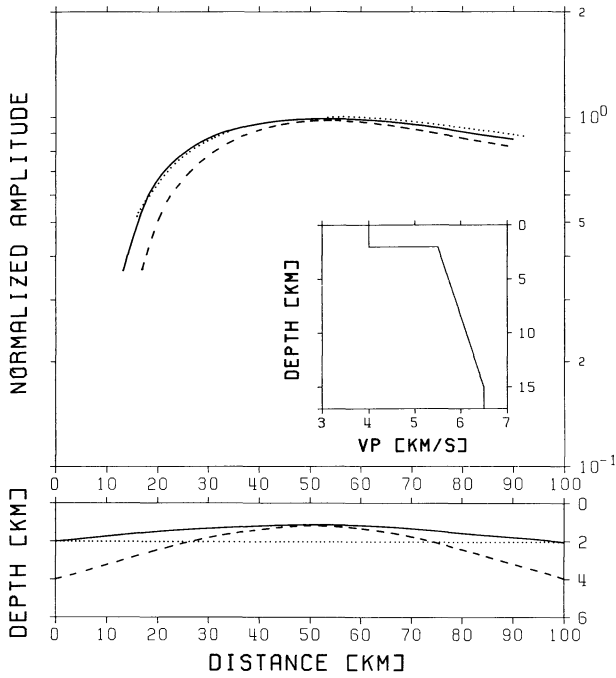


Fig. 3. Ray amplitudes (top) for model PG11, shown in the inset, with three different interface shapes (bottom)

the overall topography of the sediment-basement boundary is fairly well known and for the first 70 km the sediments are less than 1 km thick, so that the travel-time data alone strongly constrains the range of possible velocity gradients in the upper crust. The calculation of additional models showed that reducing the upper gradient to less than 0.06 km/s/km, or increasing it beyond 0.085 km/s/km would no longer be compatible with the measured travel times. Beyond about 70 km, the thickness of the sedimentary layer increases and its velocity is not well known: thus sediment velocities can be varied in order to compensate for travel-time effects due to different velocities in the lower of the two gradient zones mentioned before. As shown by model 3 in Fig. 14 of the paper by Banda et al. (1982), a stronger gradient, extending over a sufficiently large depth range, produces a second amplitude increase beyond about 65 km. From those results it follows that the lower gradient is not greater than 0.04 km/s/km and that the velocity at the bottom of the gradient zone, which is reached at a depth between 8 and 10 km, is less than 6.1 km/s.

The amplitude calculations were performed using the reflectivity method developed by Fuchs (1968) and Fuchs and Müller (1971), as modified by Kind (1978). For computational reasons the models with curved interfaces, derived from the combination of borehole data (Fig. 2b) and ray-trace modelling (Banda et al., 1982), had to be approximated by a flat-layered model. In order to estimate the error introduced into the amplitude calculations by this simplification, several test-models were calculated using program RAY81, written by V. Červený and I. Pšenčík, which, based on asymptotic ray-theory, allows for laterally inhomogeneous models (Červený et al., 1977; Červený, 1979). Figure 3 shows the amplitude-distance curves for the  $P_g$ -phase, computed by this method for a flat-layered model, for a model with interfaces curved like those beneath Sulz (Fig. 2b) and for one with stronger curvature. The

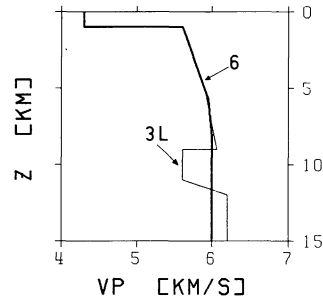


Fig. 4. Velocity-depth models of the upper crust. Model 6 is from Banda et al. (1982) with slightly lower sedimentary velocity. Model 3L corresponds to the synthetic seismograms in Fig. 5b

flat-layered model corresponds to PG11 in the paper by Banda et al. (1982, Fig. 8). The discrepancies between these curves and those calculated with the reflectivity method by Banda et al. are due to the inability of asymptotic ray-theory to account for wave-effects occurring at the top and bottom of the gradient zone. However, asymptotic ray-theory correctly accounts for geometrical spreading, so that the effects of different model geometries on the amplitudes can be compared with each other. The results displayed in Fig. 3 demonstrate that, in the case of the Sulz profile, shooting up-dip over the first 40 km and down-dip beyond about 60 km has only a negligible effect on the amplitudes of the  $P_g$ -phase. Consequently, all the synthetic seismograms discussed below were computed with the reflectivity method.

### Structure of the Middle Crust

Looking at refraction data alone, evidence for a velocity discontinuity or inversion in the upper or middle crust should manifest itself as one or two intermediate reflections between the  $P_g$  and  $PMP$  arrivals. Although some of the records from Sulz contain large amplitudes in this interval, phases are very difficult to correlate over more than a few traces (see Fig. 2). Only in the distance range between 70 and 90 km does there seem to be a coherent arrival at about 0.5 s after the  $P_g$  (Fig. 5a).

In order to explain the travel time of these arrivals, several ray-trace models were calculated, both with a positive velocity discontinuity and with an inversion. A simple positive velocity jump below the gradient zone cannot simultaneously account for the large delay of this phase and for the close distance from the shot. Therefore a low-velocity layer had to be taken into consideration. The most satisfactory fit of the travel time data and of the  $P_g$  amplitudes was obtained with model 3L, which is characterized by a velocity drop from 6.06 to 5.6 km/s at a depth of 9 km and a gradual increase to 6.2 km/s between 11 and 12 km (Fig. 4). The synthetic seismograms corresponding to model 3L, in the distance range between 65 and 95 km, are displayed in Fig. 5b. A comparison of the amplitudes of the reflection from the bottom of the low-velocity layer (denoted by  $PcP$ ), relative to those of the  $P_g$ , between data and synthetics shows a significant discrepancy. While in the calculated seismograms the amplitude ratios of  $PcP$  to  $P_g$  reaches a value greater than 2 at a distance of 85 km, in the data the maximum is about 1, and occurs at distances as short as 76 km.

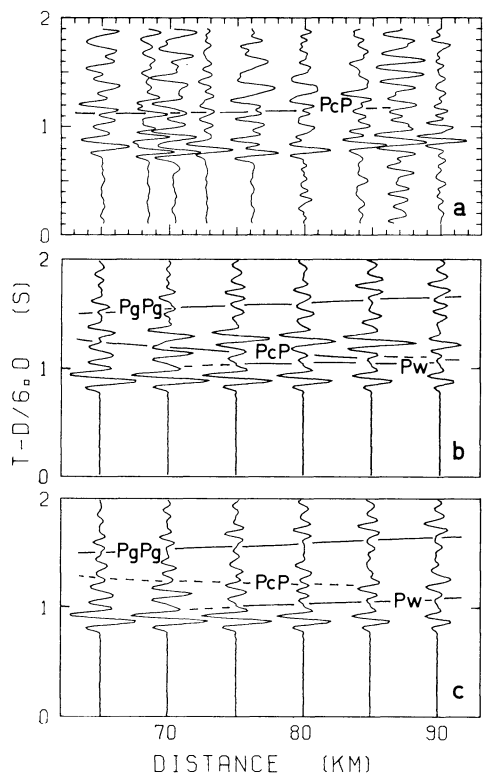


**Fig. 5.** **a** Vertical component records, trace normalized, 4–16 Hz band-pass filtered, showing possible reflections from the lower edge of an upper-crustal low-velocity layer (*PcP*). **b** Synthetic records for model 3L (Fig. 4) with  $Q=100$  for the sediments and 500 for the rest of the crust. **c** Synthetic records for model 3L (Fig. 4) with  $Q=50$  and  $V_p=5.4$  km/s in the low-velocity zone. *PgPg*: *Pg* phase reflected once at the surface. *PcP*: reflection from the bottom of the low-velocity layer. *Pw*: interference head-wave, or “Whispering gallery phase” (see Červený et al., 1977). The amplitudes of the synthetic records are multiplied by distance and correspond to ground velocity

Changes in the gradient at the base of the inversion or a decrease of the velocity inside the channel will not simultaneously reduce the amplitudes of the *PcP* phase and move the maximum to shorter distances (Braile and Smith, 1975; Müller and Mueller, 1979). Braile (1977) showed that lowering the  $Q$ -value in the channel will significantly decrease the amplitudes of the *PcP* reflection. The synthetic seismograms presented so far were all calculated with a constant  $Q$  of 500 for the crystalline crust underlying a sedimentary layer with  $Q$  equal to 100. The seismograms shown in Fig. 5c correspond to a model similar to the previous one, except for the velocity and  $Q$ -value of the inversion zone, which were lowered to 5.4 km/s and 50, respectively. Under these conditions, the *PcP* reflection is so weak that it cannot be distinguished from the multiple reflections and conversions of the *Pg* phase within and beneath the sediments. Though other more realistic  $Q$ -values in the range between 50 and 500 are likely to be compatible with the observations, the data is not judged to be distinctive enough to allow a simultaneous determination of both velocity and  $Q$  structure in the middle crust. Indeed Banda et al. (1982) showed a synthetic seismogram example for a model without any discontinuity or inversion beneath the upper crustal gradient zone, in which the multiply reflected and converted phases within the sedimentary layer

produce amplitudes similar to those observed here (see also Fig. 9). Accurate modelling would also require a better knowledge of  $Q$  in the sediments: anelastic attenuation is likely to influence the strength of the sedimentary reverberations as well.

Though the synthetic seismograms contain reflections from the upper boundary of the low-velocity layer, which closely follow the *Pg*-arrivals between 35 and 55 km (not shown here), they are also masked by sedimentary effects. Similarly, the reverberations observed in the data at these distances (Fig. 2a) do not exhibit the character of a distinct arrival, so that they cannot be relied upon for a unique interpretation.

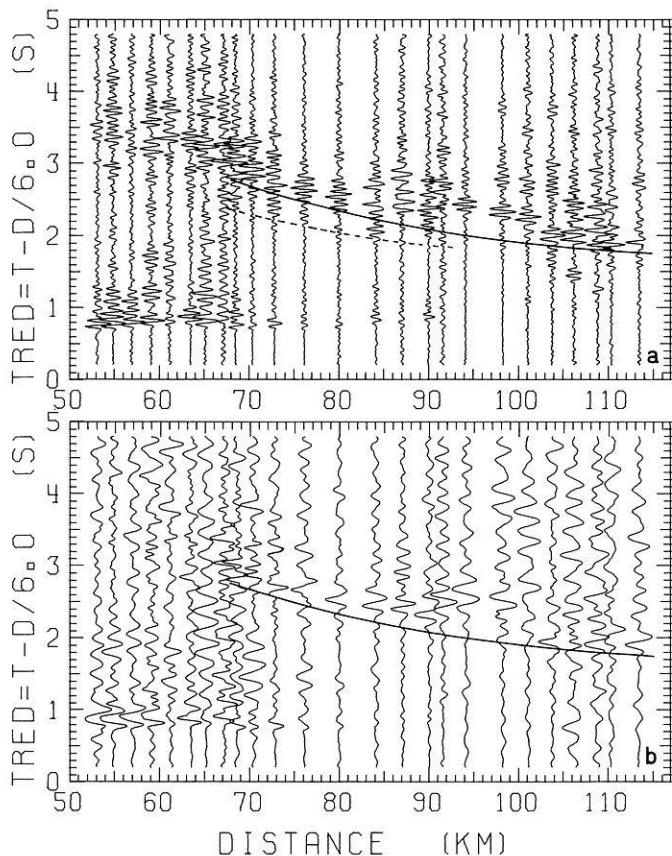
Thus, based on the evidence from this data alone, it is not possible to conclusively resolve the problem of the possible existence of a low velocity layer in the middle crust below the Sulz profile. Resorting, therefore, to the criterion which favours the simpler of those models that are not in conflict with the data, further calculations were performed assuming a constant velocity of 6.0 km/s for the middle crust (model 6 in Fig. 4).

### Crust-Mantle Transition

While the *Pg*-phase is quite impulsive, the *PMP* has a fairly well correlated precursor, and is followed by a coda of irregular reverberations. Moreover, the *PMP*-precursor appears to be frequency dependent: it is enhanced in the high-pass record section, while it is only faintly visible in the low-pass section (see Fig. 6). In fact, spectral analysis shows that the main signal energy lies in the frequency range between 2 and 16 Hz. However, the spectrum of the *Pg*-phase peaks around 8 Hz, while the reflection from the crust-mantle boundary often contains a maximum around 4 Hz and another one around 10 Hz. Since two different shots were recorded in the distance range in which the *PMP* and its precursor are observed, it is very unlikely that this signal character is merely a source effect. Thus the structure of the lower crust appears to be selective with regard to the frequency of the seismic signals returned from it.

Davydova (1972) classified possible crust-mantle transitions into three different types: first order discontinuities, transition zones with smoothly or stepwise increasing velocities, and transition zones consisting of lamina-like velocity inversions. Her conclusions indicate that a detailed analysis of the frequency dependent dynamic properties of the reflected wave field can provide criteria for distinguishing between the different types (see also Davydova et al., 1972).

In the course of studying the wave field generated by various models of the crust-mantle transition (Moho) with the aid of synthetic seismograms, Fuchs (1970) showed how a laminated upper mantle structure could produce a ringing signal following the main reflection, which is quite similar to that observed on some of the records in Fig. 6a. An alternative explanation for these reverberations is illustrated by the synthetic seismograms in Fig. 7. In this case the phases following the main *PMP* reflection are entirely due to multiple reflections and conversions of the *PMP* within the sedimentary layer both beneath the shotpoint and the receivers. Assuming a sedimentary layer which is thinner than the 2 km chosen for this example and whose thickness is not constant over the entire profile, the individual arrivals will merge and interfere with each other, thus producing an irregular pattern of vibrations, similar to those observed



**Figs. 6a and b.** Trace normalized, vertical component record sections with **a** 10–24 Hz band-pass filter and **b** 5 Hz low-pass filter. Continuous travel-time curves correspond to the wide-angle reflections from the crust-mantle transition of the models in Fig. 9, calculated with a ray-trace program (Gebrande, 1976) taking into account the curved sediment-basement boundary shown in Fig. 2. The dashed curve indicates the *PMP*-precursor (*PrP*)

in the data. This shows that reverberations from an upper mantle lamellation will be at least partially masked by this sedimentary effect. Additional upper crustal discontinuities will of course increase these interference phenomena even further. Since the length of the profile is insufficient to detect a first arrival refracted from the upper mantle (*Pn*), the data cannot contribute anything to the knowledge of the structure below the Moho. Thus, following the reasoning of Edell et al. (1975), a constant upper mantle velocity of 8.0 km/s was adopted for further calculations.

Fuchs (1970) as well as Braile and Smith (1975) presented several synthetic record sections for various models of the Moho. From a comparison with these, it is obvious that the Sulz data cannot be modelled with a simple first order velocity discontinuity at the Moho, but that some kind of transition zone must be introduced in the lower crust. Figure 8 shows portions of synthetic record sections computed for various kinds of transitions. As shown by Fuchs (1968), the behaviour of a velocity gradient can be approximated by a stack of thin layers with stepwise increasing velocities. If, however, these layers are not thin enough relative to the wavelength of the incident signal, and if the velocity contrast between each layer is too strong, they will generate individual reflections. The faint precursors in the first seismograms of model 2 in Fig. 8 are due to subcritical reflections from the individual layers, while the large amplitude phase corresponds to the wide-angle reflection from the velocity jump at the bottom of the transition zone. The amplitude of the precursors relative to the main phase will increase as the number of steps in the gradient zone is decreased, but, at the same time, the reverberation-like character observed in the data is lost. This is illustrated by models 5 and 9 in Fig. 8. By extending the gradient zone all the way to the mantle without a larger velocity jump at the Moho, as in model 10, the individual velocity jumps are more pronounced than in model 2, which increases the amplitude of the reverberations. The velocity

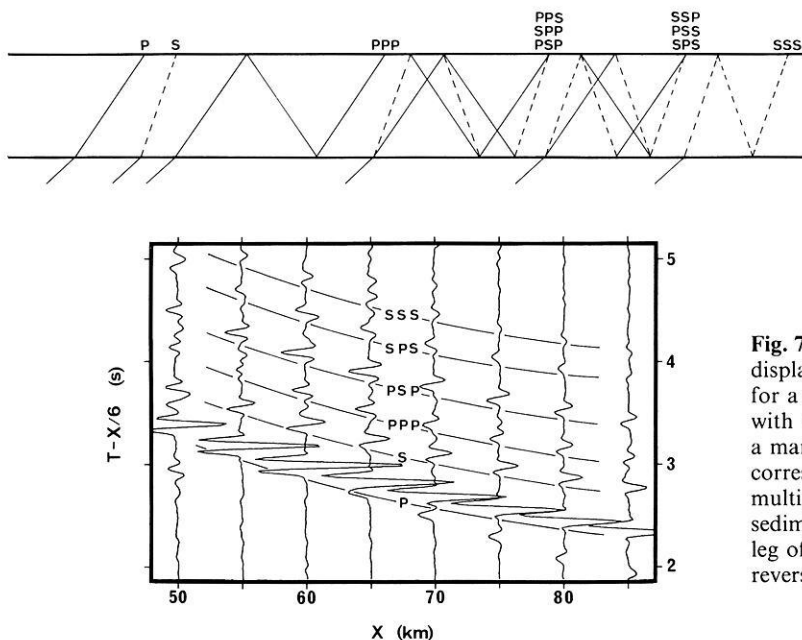


**Fig. 7.** Synthetic seismograms (vertical) component, ground displacement, amplitudes multiplied by distance) calculated for a model consisting of a 2 km thick sedimentary layer, with  $V_p = 4.5$  km/s, over a basement with  $V_p = 6.0$  km/s and a mantle with  $V_p = 8.0$  km/s at 23 km depth. The first phase corresponds to *PMP*, while all subsequent arrivals are multiple reflections and conversions of the *PMP* within the sediments. Each letter of the phase identification denotes one leg of the ray-paths in the sedimentary layer. Note the phase reversals of the reflections at the surface

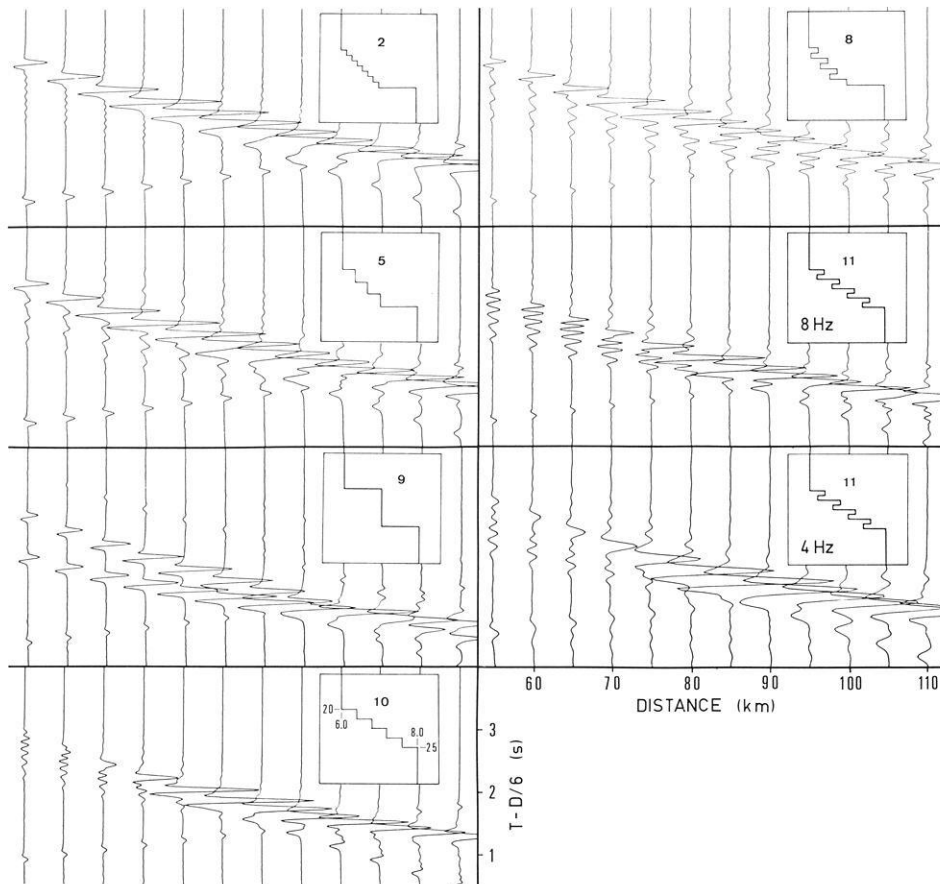


Fig. 8. Synthetic seismograms (vertical component, ground displacement, amplitudes multiplied by distance) for various models of the lower crust. The transition zone extends from a depth of 20 to 25 km, and the velocity increases from 6.0 to 8.0 km/s in all models. The phase with an apparent velocity of 5.5 km/s, visible in the lower part of each quadrant, is a numerical effect corresponding to the lower limit of the phase-velocity window used in the reflectivity program

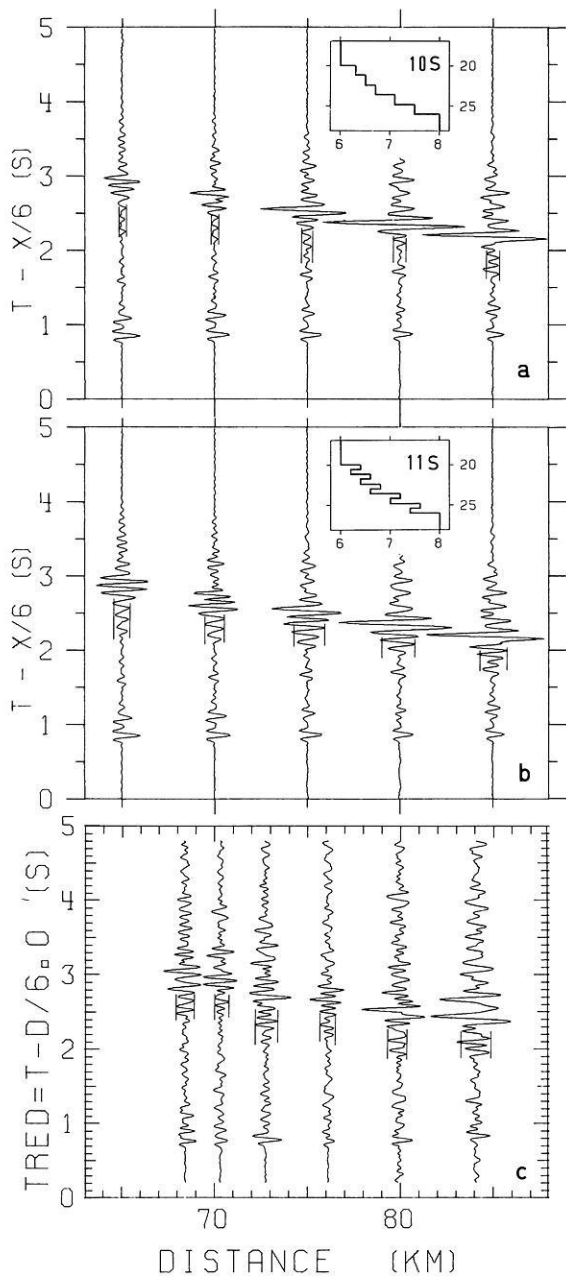
contrast and consequently also the precursor amplitudes will be even larger if the individual steps include velocity inversions.

Reflections from a transition zone consisting of a series of lamellae with alternating high and low velocities have been investigated theoretically by Fuchs (1968; 1969; 1970), who demonstrated the dependance of the signal character both on frequency and angle of incidence. In order to account for high-frequency precursors before the lower-frequency *PMP* phase observed along a seismic refraction profile in France, Fuchs and Schulz (1976) proposed a model of the crust-mantle transition consisting of a thin high-velocity lamella over a zone of strong velocity gradient. However, in these cases, the large velocity discontinuity at the top of the transition zone would produce precursor amplitudes larger than observed under Sulz. A structure in which the velocity of the lamellae increases with depth will produce reverberations whose amplitudes increase more gradually. This is illustrated by models 8 and 11 in Fig. 8. The amplitude of the precursor relative to the main reflection depends on the size of the individual velocity jumps. The synthetic seismograms, corresponding to model 11, were also calculated for a signal with a dominant frequency of 4 Hz instead of 8 Hz (Fig. 8). A comparison of the two record sections shows a frequency dependent behaviour similar to that observed in the low- and high-pass filtered record sections in Fig. 6. At lower frequencies, the precursors, corresponding to subcritical reflections from the lamellae, are significantly attenuated, and the whole transition zone appears more like a smooth gradient, producing

a single strong phase whose amplitude decreases rapidly towards shorter distances. A similar frequency dependent behaviour will of course also be produced by a step-model without inversions, such as model 10 in Fig. 8 (see Fuchs, 1968). On the basis of the preceding discussion, we must conclude that the crust-mantle boundary beneath Sulz is a transition zone several kms thick, and that it does not consist of a smooth gradient, but of a series of velocity jumps or even of a series of lamina-like inversions.

In order to fit the Sulz *PMP*-travel-time data as well as the amplitudes, the linear velocity increase from one step or lamella to the next in models 10 or 11 had to be modified. The data requires a thicker transition zone with velocities increasing slowly at the top and more rapidly below. This resulted in the models 10s and 11s, presented in Figs. 9a and b, together with the corresponding synthetic seismograms. For comparison, the recorded seismograms in the same distance range are reproduced in Fig. 9c.

A qualitative comparison alone already indicates that the recorded signal is better matched by the lamella-structure. Only the most significant part of the record section is shown: beyond about 85 km, the precursors interfere with the emerging *Pn* phase, while at distances shorter than 68 km, they are masked by strong signal generated noise (see Figs. 2 and 6). Some records at the shorter distances lack a clearly defined *PMP*-arrival, so that for a quantitative evaluation not all amplitudes could be measured. While both the *PMP* amplitude-distance curves and the *Pg* to *PMP* amplitude ratios of the step- and of the lamella-model fit the data equally well, the *PrP* to *PMP* amplitude ratios



**Figs. 9a and b** Synthetic seismograms (vertical component, ground velocity, dominant frequency 8 Hz) for the crust-mantle transitions shown in the insets. Upper crustal model used corresponds to model 6 in Fig. 4 (see Table 1). Note the phases between  $Pg$  and  $PMP$ -precursors, caused by multiples and conversions of  $Pg$  within and beneath the sediments. **c.** Vertical component records, 4–16 Hz band-pass filtered. Vertical lines indicate amplitude of precursors as plotted in Fig. 11. Amplitudes of synthetics and data are scaled by multiplying with distance

allow one to distinguish between the two models (Figs. 10 and 11). In the distance range over which the precursors are clearly identifiable, the lamella-model fits the data very well, while the step-model deviates by about a factor of 3. Since errors due to faulty instrument gains or to differences in local site responses have no effect on the amplitude ratios this deviation can be regarded as significant. From this it follows that, of the models discussed here, a laminated crust-mantle transition explains the observations best.

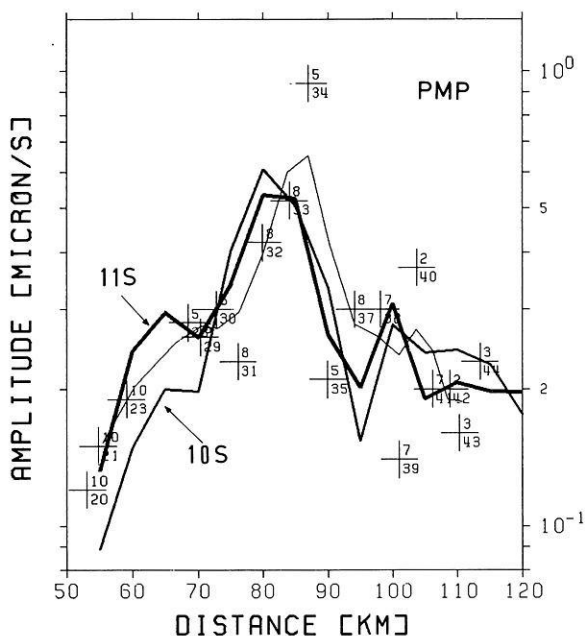


**Fig. 10.** Maximum amplitudes of  $PMP$  main phase (crosses with shot number above and station number below) from 4–16 Hz band-pass filtered records. Thin curve corresponds to smoothed data. Thick curves correspond to the step- (10S) and lamella-model (11S) in Fig. 9

We have also investigated two of the models consisting of a series of step-like gradients proposed by Edel et al. (1975) for the southern Black Forest: while the travel times can be made to fit the Sulz data quite accurately, the amplitudes of the  $PMP$  and its precursor do not match the observations sufficiently well. Indeed, it is likely that a quantitative amplitude interpretation of Edel's data might reveal that the  $PMP$ -precursors visible in some of his record sections are more adequately explained by some kind of lamination similar to that proposed here.

## Conclusions

This study is the result of a combined interpretation of travel-times and amplitudes. For the computation of synthetic seismograms, the reflectivity method has proven to be a very powerful tool. For models with only slight lateral variations, its limitation to flat homogeneous layers is not serious and is amply compensated by its ability to correctly simulate the wave nature of seismic signals. However, computational techniques based on asymptotic ray-theory, which allow for lateral heterogeneities, are a valuable tool for estimating the effect of the flat-layer approximation.

The influence of the frequency content of the source on the ability to resolve finer structural details has already been pointed out by others (see Spudich and Orcutt, 1980, for an excellent review of computational techniques and interpretational pitfalls), but is all too often forgotten when comparing results from different investigations, in particular from sea- and land-shots.

A further important and often neglected consideration to be taken into account when interpreting the deeper crustal structure is the influence of the sediments or surficial weathered layer. Small variations in sedimentary structure or velocity can produce significant travel-time effects, while

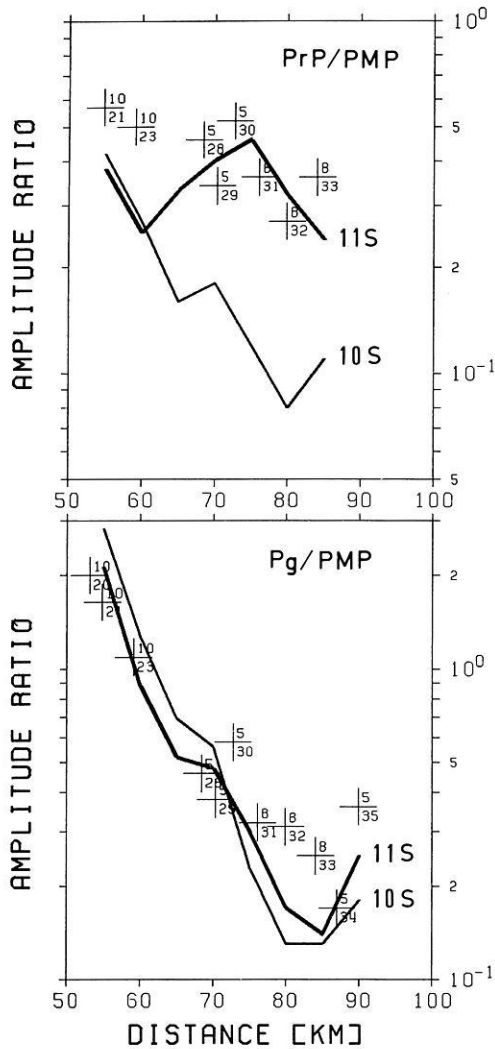


Fig. 11. Amplitude ratio of *PMP*-precursor (*PrP*) to *PMP* main phase (top) and amplitude ratio of *Pg* to *PMP* (bottom). Crosses correspond to data (shot numbers above, station numbers below). Continuous curves correspond to the step- (10S) and the lamella-model (11S) in Fig. 9

multiple reverberations and *P-S* conversions between the top of the basement and the Earth's surface can mask phases from deeper discontinuities. For example, without independent information from borehole data about the dip of the sediment-basement boundary under Sulz, the travel-time interpretation would have resulted in a significantly different velocity gradient in the upper crust, and it would have been difficult to achieve an agreement with the amplitude data. A more accurate knowledge of the sedimentary structure at the southern end of the Sulz-profile would put stronger constraints on the lower part of the upper crustal gradient as well as on the shape of the velocity increase in the transition zone above the Moho. For accurate synthetic seismogram modelling, it would furthermore be desirable to obtain reliable *Q*-values for the sediments.

Figure 12 shows the complete velocity-depth model proposed for the crustal structure along the eastern margin of the southern Black Forest (see also Table 1). Its main features are a strong gradient in the upper crust and a crust-mantle transition zone composed of a series of lamella-shaped velocity inversions.

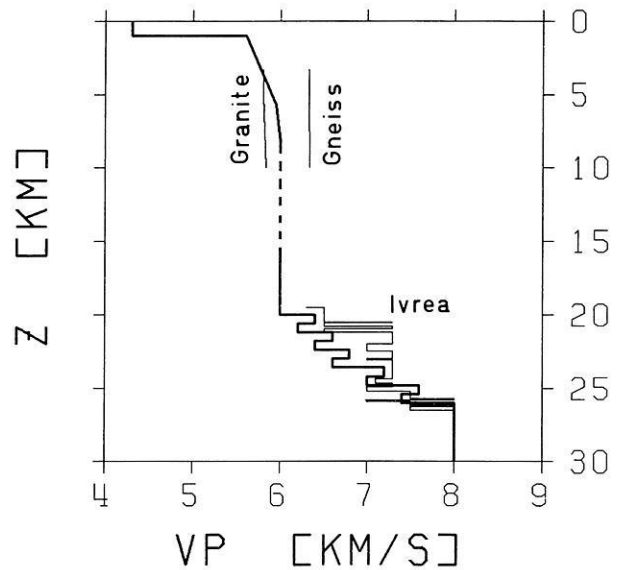


Fig. 12. Velocity-depth model for SULZ 11S with results of laboratory measurements by Kern and Richter (1981) and velocity profile through the Ivrea body, after Hale and Thompson (1982)

Table 1. Parameters of model SULZ 11S

Lower limit of layer (km)	Layer thickness (km)	$V_p$ (km/s)	Number of layers	Gradient (km/s/km)
1.0	1.0	4.3	2	0.0
5.7	4.7	5.6 -5.95	7	0.074
8.2	2.5	5.95-6.0	4	0.02
20.0	11.8	6.0	2	0.0
20.6	0.6	6.4	1	0.0
21.2	0.6	6.2	1	0.0
21.8	0.6	6.6	1	0.0
22.4	0.6	6.4	1	0.0
23.0	0.6	6.8	1	0.0
23.6	0.6	6.6	1	0.0
24.2	0.6	7.2	1	0.0
24.8	0.6	7.0	1	0.0
25.4	0.6	7.6	1	0.0
26.0	0.6	7.4	1	0.0
30.0	4.0	8.0	1	0.0

Unambiguous evidence for or against a discontinuity or low-velocity zone in the middle crust could not be found from this data alone. However, it is possible that near-vertical reflection data would reveal additional structure at depths of 10–12 km: in the Rhinegraben, echoes with a travel-time of about 4 s have been interpreted as reflections from the top of a low-velocity layer in this depth range (Mueller et al., 1969; 1973), which could extend to the east below the Black Forest.

The upper crustal gradient is exceptionally well constrained by information about the basement topography (boreholes) and by travel-time as well as amplitude data. From the geological setting (Fig. 1), it is to be expected that the granites and gneisses of the Black Forest extend to greater depths below the Sulz profile. For comparison, the top part of two velocity-depth curves from laboratory measurements by Kern and Richter (1981) for a granite and a gneiss sample, assuming a geotherm corresponding

to a warm continental crust (Theilen and Meissner, 1979) are included in Fig. 12. Only the lower part of the gradient zone, below a depth of about 5 km, is similar to these measurements. They were performed on dry and unfractured samples. The much stronger gradient found in the uppermost part of the crust could imply that fractures and water content, including pore pressure, have to be taken into account when interpreting the elastic parameters of the basement, even at depths down to about 5 km (Nur and Simmons, 1969; Mueller, 1977).

The evidence for the lamination in the lower crust is based on a quantitative comparison of the amplitudes of the *PMP* and its precursors with those of theoretical seismograms. It also correctly accounts for the observed travel-times and for the frequency dependent nature of the reflections from the crust-mantle transition. In addition the Moho-depth of 26 km, corresponding to the distance range between 30 and 50 km from the shot point, agrees perfectly with the results extrapolated from the Rhinegraben by Edel et al. (1975).

Several other authors have postulated a laminated crust-mantle transition zone before, based partly on near-vertical reflection data (Meissner, 1967; 1973; Fuchs, 1969; Clowes and Kanasevich, 1970; Davydova, 1972; Bartelsen et al., 1982). The present study provides additional independent evidence for the existence of such a structure. As presented here, it corresponds closely to a laminated Conrad discontinuity extending all the way to the Moho, in analogy to the high-velocity tooth in the lower crust, discussed by Mueller (1977).

While the vertical extent of the transition zone and the general velocity increase with depth is directly supported by the data, the regularity of the lamella thickness and the strength of the inversions is largely an arbitrary artifact. Whether an existing lamella-structure is seen or not is in part a function of the wavelength of the recorded signals, which in turn puts certain constraints on the average thickness of the individual lamellae. However, the real structure is probably much less regular than suggested by this model. Moreover, nothing can be said about the lateral extent of such a structure.

Hale and Thompson (1982) review a number of seismic reflection lines which show evidence of lamination in the lower continental crust, and note that such a structure seems to be relatively discontinuous. In addition, taking the lithologic sequence of the Ivrea-Verbano zone (northern Italy) as a model of the lower crust, they computed a synthetic vertical incidence reflection seismogram, which shows striking similarities to recorded ones. For comparison, this model has been superimposed on the Sulz-model in Fig. 12. Though the two models differ in detail, the laminated sequence of high- and low-velocity layers is common to both.

*Acknowledgements.* This project was possible thanks to D. Emter (Schiltach) who advised us of the quarry blasts and recorded the shot-times. His helpful suggestions regarding the sedimentary structure in the northern part of the profile are also gratefully acknowledged. E. Banda, H. Scriba and L.W. Braile contributed with numerous helpful discussions. M. Grieder's maintenance and improvements of the recording instruments were essential to the success of the measurements. Thanks are due to D. Gajewski, B. Guggisberg and V. Červený for advice on computing the ray-theoretical amplitudes. St. Mueller critically read the manuscript and added several suggestions for improvement.

## References

- Banda, E., Deichmann, N., Braile, L.W., Ansorge, J.: Amplitude study of the *Pg* phase. *J. Geophys.*, **51**, 153–164, 1982
- Bartelsen, H., Lueschen, E., Krey, Th., Meissner, R., Schmolli, H., Walter, Ch.: The combined seismic reflection-refraction investigation of the Urach geothermal anomaly. In: *The Urach Geothermal Project*, pp. 247–262. Stuttgart: Schweizerbart 1982
- Berckhemer, H.: MARS66 – a magnetic tape recording equipment for deep seismic sounding. *Z. Geophys.* **36**, 501–518, 1970
- Boigk, H., Schoeneich, H.: Die Tiefenlage der Permbasis im nördlichen Teil des Oberrheingrabens. In: *Graben Problems*, J.H. Illies and St. Mueller (eds.), pp. 45–55. Stuttgart: Schweizerbart 1968
- Braile, L.W., Smith, R.B.: Guide to the interpretation of crustal refraction profiles. *Geophys. J. R. Astron. Soc.* **40**, 145–176, 1975
- Braile, L.W.: Interpretation of crustal velocity gradients and Q structure using amplitude-corrected seismograms. In: *The earth's crust*, *Am. Geophys. Union Mon.* **20**, 427–439, 1977
- Breyer, F.: Ergebnisse seismischer Messungen auf der süddeutschen Grossscholle besonders in Hinblick auf die Oberfläche des Varistikums. *Z. d. Dt. Geol. Ges.* **108**, 21–36, 1956
- Büchi, U.P., Lemcke, K., Wiener, G., Zimdars, J.: Geologische Ergebnisse der Erdölexploration auf das Mesozoikum im Untergrund des schweizerischen Molassebeckens. *Bull. Ver. Schweiz. Petrol.-Geol. u. -Ing.* **32**, 82, 7–38, 1965
- Červený, V.: Ray Theoretical seismograms for laterally inhomogeneous structures. *J. Geophys.* **46**, 335–342, 1979
- Červený, V., Molotkov, I.A., Pšenčík, I.: *Ray method in seismology*. Prague: Charles University Press 1977
- Clowes, R.M., Kanasevich, E.R.: Seismic attenuation and the nature of reflecting horizons within the crust. *J. Geophys. Res.* **75**, 6693–6705, 1970
- Davydova, N.I.: Possibilities of the DSS technique in studying properties of deep-seated seismic interfaces. In: *Seismic properties of the Mohorovicic discontinuity*, Davydova, N.I., ed.: pp 4–22. Moscow: Izdatel'stvo Nauka 1972. English translation from: National Technical Information Service, U. S. Dept. of Commerce, Springfield, Va, 1975
- Davydova, N.I., Kosminskaya, I.P., Kapustian, N.K., Michota, G.G.: Models of the earth's crust and M-boundary. *Z. Geophys.* **38**, 369–393, 1972
- Edel, J.B., Fuchs, K., Gelbke, C., Prodehl, C.: Deep structure of the Southern Rhinegraben area from seismic refraction investigations. *J. Geophys.* **51**, 333–356, 1975
- Emter, D.: *Ergebnisse seismischer Untersuchungen der Erdkruste und des obersten Erdmantels in Südwestdeutschland*. Diss. Univ. Karlsruhe, 1971
- Emter, D.: Seismic results from Southwestern Germany. In: *Exploration seismology in Central Europe*, P. Giese, C. Prodehl, A. Stein, eds.: pp. 283–289. Berlin, Heidelberg, New York: Springer 1976
- Fuchs, K.: Das Reflexions- und Transmissionsvermögen eines geschichteten Mediums mit beliebiger Tiefenverteilung der elastischen Moduln und der Dichte für schrägen Einfall ebener Wellen. *Z. Geophys.* **34**, 389–413, 1968
- Fuchs, K.: On the properties of deep crustal reflectors. *Z. Geophys.* **35**, 133–149, 1969
- Fuchs, K.: On the determination of velocity depth distributions of elastic waves from the dynamic characteristics of the reflected wave field. *Z. Geophys.* **36**, 531–548, 1970
- Fuchs, F., Müller, G.: Computation of synthetic seismograms with the reflectivity method and comparison with observations. *Geophys. J. R. Astron. Soc.* **23**, 417–433, 1971
- Fuchs, K., Schulz, K.: Tunneling of low-frequency waves through the subcrustal lithosphere. *J. Geophys.* **42**, 175–190, 1976
- Gebrande, H.: A seismic-ray tracing method for two-dimensional inhomogeneous media. In: *Explosion seismology in Central Europe*, P. Giese, C. Prodehl, A. Stein, eds.: pp. 162–167. Berlin, Heidelberg, New York: Springer 1976

- Hale, L.D., Thompson, G.A.: The seismic reflection character of the continental mohorovicic discontinuity. *J. Geophys. Res.* **87**, 4625–4635, 1982
- Jentsch, M., Bamford, D., Emter, D., Prodehl, C.: A seismic-refraction investigation of the basement structure in the Urach geothermal anomaly, Southern Germany. In: *The Urach Geothermal Project*, pp. 231–245. Stuttgart: Schweizerbart 1982
- Kern, H., Richter, A.: Temperature derivatives of compressional and shear wave velocities in crustal and mantle rocks at 6 kbar confining pressure. *J. Geophys.* **49**, 47–56, 1981
- Kind, R.: The reflectivity method for a buried source. *J. Geophys.* **44**, 603–612, 1978
- Lemcke, K., Buechi, U.P., Wiener, G.: Einige Ergebnisse der Erd-ölexploration auf die mittelländische Molasse der Zentralschweiz. *Bull. Ver. Schweiz. Petrol.-Geol. u. -Ing.* **35**, 87, 15–34, 1968
- Lohr, J.: Die seismischen Geschwindigkeiten in der Ostschweiz. *Bull. Ver. Schweiz. Petrol.-Geol. u. -Ing.* **34**, 85, 29–38, 1967
- Lohr, J.: Die seismischen Geschwindigkeiten der jüngeren Molasse im Ostschweizerischen und Deutschen Alpenvorland. *Geophys. Prosp.* **17**, 111–125, 1969
- Meissner, R.: Exploring deep interfaces by seismic wide angle measurements. *Geophys. Prosp.* **15**, 598–617, 1967
- Meissner, R.: The 'Moho' as a transition zone. *Geophys. Surveys* **1**, 195–216, 1973
- Mueller, S.: A new model of the continental crust. In: *The Earth's crust*, Geophysical Monograph 20, pp. 289–317. Washington, D.C.: Am. Geophys. Union 1977
- Mueller, S., Peterschmitt, E., Fuchs, K., Ansorge, J.: Crustal structure beneath the Rhinegraben from seismic refraction and reflection measurements. *Tectonophys.* **8**, 529–542, 1969
- Mueller, S., Peterschmitt, E., Fuchs, K., Emter, D., Ansorge, J.: Crustal structure of the Rhinegraben area. *Tectonophys.* **20**, 381–391, 1973
- Müller, G., Mueller, S.: Travel-time and amplitude interpretation of crustal phases on the refraction profile Delta-W, Utah. *Bull. Seismol. Soc. Am.* **69**, 1121–1132, 1979
- Nur, A., Simmons, G.: The effect of saturation on velocity in low porosity rocks. *Earth Planet. Sci. Lett.* **7**, 183–193, 1969
- Prodehl, C., Ansorge, J., Edel, J.B., Emter, D., Fuchs, K., Mueller, S., Peterschmitt, E.: Explosion-seismology research in the Central and Southern Rhinegraben – A case history. In: *Explosion seismology in Central Europe*, P. Giese, C. Prodehl, A. Stein, eds.: pp. 313–328. Berlin, Heidelberg, New York: Springer 1976
- Schneider, T.R.: Geologische Beilage, Sondiergesuche an die Gemeinden Weiach und Bachs, ZH, NSG11, NSG12. Baden: NAGRA 1980
- Spudich, P., Orcutt, J.: A new look at the seismic velocity structure of the oceanic crust. *Rev. Geophys. Space Phys.* **18**, 3, 627–645, 1980
- Theilen, F., Meissner, R.: A comparison of crustal and upper mantle features in Fennoscandia and the Rhenisch shield, two areas of recent uplift. *Tectonophys.* **61**, 227–242, 1979

Received September 29, 1982; Revised version December 8, 1982

Accepted December 13, 1982

## FENNOLOGRA Recordings at NORSAR\*

R.F. Mereu<sup>1</sup>, S. Mykkeltveit<sup>2</sup>, and E.S. Husebye<sup>2</sup>

<sup>1</sup> University of Western Ontario, London, Ontario, Canada, N6A 587

<sup>2</sup> NNTF/NORSAR, Post Box 51, N-2007 Kjeller, Norway

**Abstract.** During August 1979 a number of major shots belonging to the FENNOLOGRA deep seismic sounding experiment across Scandinavia were recorded at NORSAR. The 42 sensors of the NORSAR array enabled us to examine both in-line and off-line features of the seismic signals as the wavefronts swept across the seven subarrays. A least squares analysis of the first arrival data indicate that the upper mantle velocities under NORSAR are azimuth dependent and vary from 8–9 km/s laterally. The data can also be used to infer approximate crustal thicknesses beneath shot points within 700 km.

A detailed analysis of the coda following the first arrival onsets was made using various velocity filters and correlation detectors to determine if any deterministic multiple arrivals arising from sharp large-scale regional vertical velocity gradients in the upper 300 km of the mantle were present. No later arrivals which were coherent beyond a few kilometers were found. We take this to indicate that scattering particularly in the source and receiver regions is of major importance in the generation of the seismic coda.

**Key words:** Deep seismic sounding – NORSAR array – FENNOLOGRA experiment – Crustal thickness – Crustal heterogeneity – Scandinavia – scattering

### Introduction

During the month of August 1979 a major long-range seismic profile called the FENNOLOGRA experiment was carried out across Scandinavia. Charges ranging in size from 700–8,000 kg of TNT were fired at locations shown in Fig. 1, where also the main line deployment of mobile seismic stations is shown. Technical details of this experiment in terms of shot point information, etc., have been given by Ansgore (1981). In this paper the results obtained from analysis of recordings made at the NORSAR array are presented.

Most of the major shots (i.e., B, C, D, E, F, H, and I in Scandinavia, PU1 in Poland and PU3 in the USSR) were well recorded by the short-period sensors of

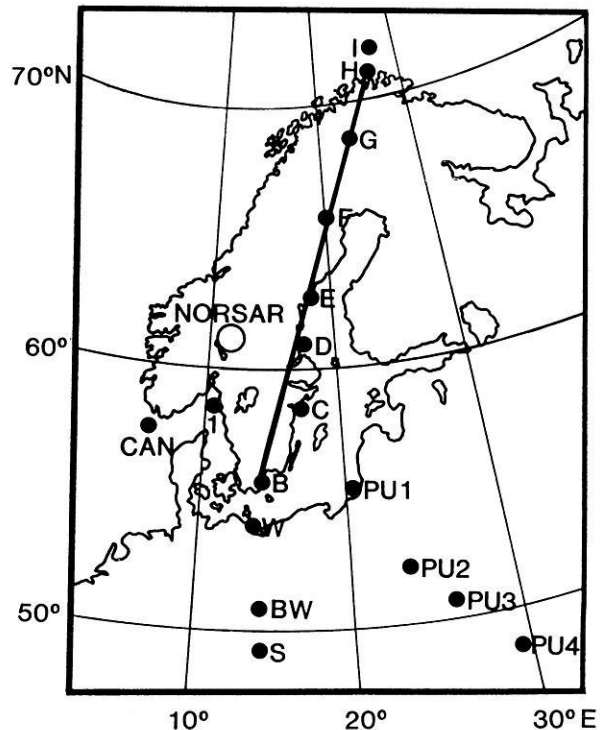


**Fig. 1.** Station and shot-point locations for the FENNOLOGRA long range experiment. Also shown is a shot-point belonging to the CANOBE experiment (CAN, Cassell et al., 1983), the location of a presumed explosion (1) in the sea about 260 km due south of NORSAR as well as the location of the NORSAR array

NORSAR. Shots at G, W, BW, S, PU2 and PU4 were not detected. In order to improve the azimuthal coverage, the recordings from one of the CANOBE (CAN) shots of July 1980 (Cassell et al. in press, 1983) were also included in this study. Altogether the NORSAR records presented here cover the distance and azimuth ranges shown in Table 1. The configuration of the 7 subarrays and 42 short-period sensors making up the NORSAR array at the time of the FENNOLOGRA experiment is shown in Fig. 2.

In most seismic experiments where portable instruments are deployed, off-line coverage is not obtained. In this experiment the two-dimensional areal extent of the whole NORSAR array has enabled us to examine both the in-line and off-line features of the seismic signals as the wavefronts

\* NORSAR Contribution No. 322

Offprint requests to: R.F. Mereu

**Table 1.** Shot point data and apparent velocities

Shot	Distance range (km)	Azimuth <sup>a</sup> range (km)	Apparent <i>Pg</i> velocity (km/s)	Apparent <i>Pn</i> velocity (km/s)
D2	315– 375	87– 97	$6.53 \pm 0.64$	$8.65 \pm 0.13$
E1	360– 420	63– 69	$6.28 \pm 0.38$	$8.50 \pm 0.37$
C1	415– 485	122–130	$7.31 \pm 0.28$	$8.06 \pm 0.27$
CAN	453– 515	219–225	$6.63 \pm 0.22$	$8.08 \pm 0.14$
B3	585– 665	149–155	6.28–0.14	$8.38 \pm 0.24$
F1	630– 695	34– 41		$8.18 \pm 0.31$
PU11	895– 972	136–141		$8.38 \pm 0.20$
H1	1,335–1,396	20– 22		$8.14 \pm 0.19$
I1	1,335–1,396	20– 22		$8.99 \pm 0.99$
Complete set	315–1,396	20–225	$6.36 \pm 0.02$	$8.31 \pm 0.01$

<sup>a</sup> The azimuth values are from NORSAR to the sources

**Table 2.** Delay times and crustal thicknesses

Shot	Distance to array center <i>x</i> (km)	Travel time to array center <i>t</i> (s)	Delay time <i>t</i> – <i>x</i> /8.1 (s)	Azimuth (degrees)
CAN	456.7	62.5	6.1	220.0
B3	616.2	83.1	7.0	150.0
C1	451.5	64.3	8.6	123.0
D2	364.0	53.3	8.4	87.6
E1	414.3	60.1	9.0	62.3
F1	690.8	94.3	9.0	37.0

from different azimuths swept across each of the subarrays. Because of the large number of widely spaced azimuths which were used, this experiment can be described as a large-scale fan-type one for assessing propagation characteristics from a perspective generally different from that of conventional in-line refraction profiles.

## Data Analysis and Results

### Record Sections

Record sections with normalized traces for each of the shot points are presented in Fig. 3a–i. The sections are arranged in order of increasing shot-point distances. The first arrivals on all the traces, hereafter referred to as *Pn*, are upper mantle waves, as the minimum recording distance was 316 km. The large, easily identifiable second arrival wave-trains seen on shots D2, E1, C1, CAN, and B3 are crustal *Pg* waves. More emergent *Pg* arrivals are seen for F1. *Pg* is observed to 700 km, and is not detected on record sections PU11, H1 and I1 (distances beyond 900 km). It must be emphasized that the symbol *Pg* as used in this paper represents the guided body wave which travels through the crust. It does not represent the refracted wave from the basement layer which is normally observed to distances up to 100 km.

### Apparent Velocities and Crustal Thicknesses

Least squares apparent velocity determinations from first arrival onsets of both *Pn* and *Pg* waves are listed in Table 1.

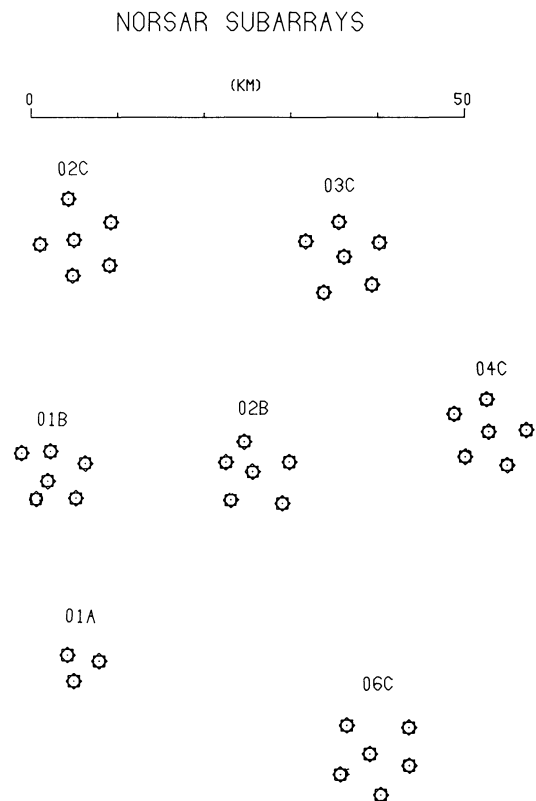


**Fig. 2.** The seven subarrays of the NORSAR array at the time of the FENNOLOGRA experiment. During the CAN shot, a six-element mini-array termed NORESS of diameter less than 2 km was in operation, substituting the 01B channels. NORESS is located within subarray 06C and further information is given by Mykkeltveit and Ringdal (1981)

When all of the arrivals were used together, i.e., the entire distance ranges over which the phases are observed, apparent velocities of  $6.36 \pm 0.02$  and  $8.31 \pm 0.01$  km/s were found for these waves. Since there is a positive velocity gradient in the upper mantle, the *Pn* velocity just below the Moho is probably closer to 8.1 km/s, with 8.31 km/s representing an average velocity 'sampled' by rays penetrating to depths large enough to reach distances up to 1,400 km. It is interesting to note from the standard errors given that the apparent velocities for the data sets from each of the shot-points are very poorly determined and are scattered about in the 8.0–9.0 km/s range for *Pn*. Figure 4 shows a reduced travel time plot for all the arrival time data. Clearly the poor determinations of apparent velocity stem from the fact that the observational points are scattered about in clusters with little evidence of alignment within each set. This scatter of points indicates that the energy must have passed through laterally varying structures before reaching the stations.

Another very significant observation of the points of Fig. 4 is the fact that the clusters of points for *Pg* from each of the shots all tend to line up along a straight line indicating that the average nature (with the exception of thickness) of the crust sampled by the *Pg* waves does not depend on azimuth. It is well known that the *Pg* wave is a sort of guided crustal wave trapped between the surface and the large velocity gradient in the lower crust. Mereu et al. (1977) observed an à echelon pattern in the *Pg* waves

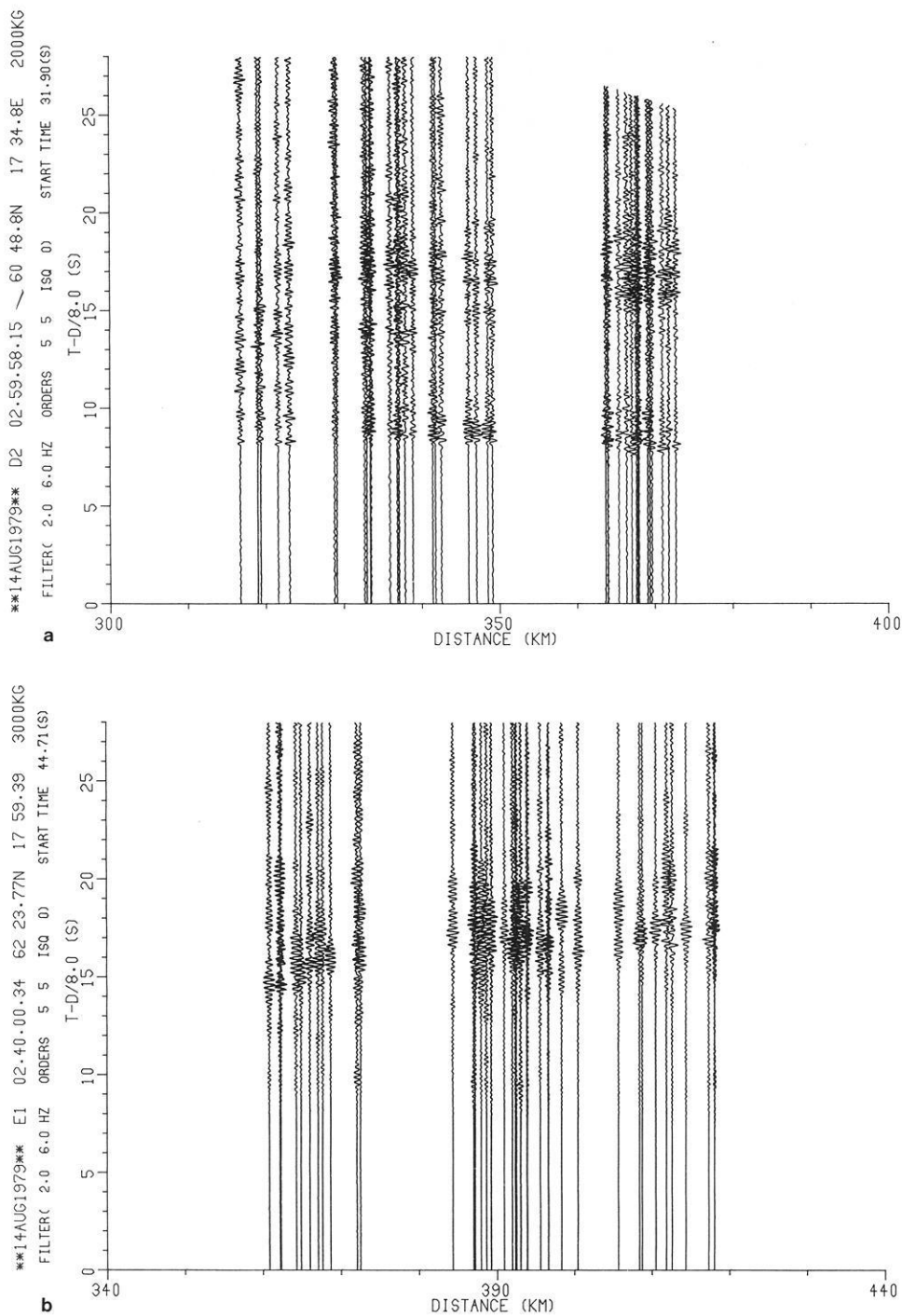


**Fig. 3a-i.** Seismic record sections. **a** for shot D2; **b** for shot E1; **c** for shot C1; **d** for shot CAN; **e** for shot B3; **f** for shot F1; **g** for shot PU11; **h** for shot H1; **i** for shot I1.

with short segments of these waves having relatively high apparent velocities of 6.6–6.9 km/s, while the overall apparent velocities were only 6.2 km/s. Our observations exhibit similar features. Despite the fact that the overall apparent velocity is 6.36 km/s, there are segments such as in the CAN section and in the C1 section with apparent velocities well over 6.50 km/s.

The clusters of points for the  $P_n$  waves are much more scattered than those of  $P_g$ . The reason for this is probably that the thickness of the crust, which significantly affects the travel times of the  $P_n$  waves, does depend on shot point locations. This is clearly seen if one compares the records

of the C1 shot of Fig. 3c with the CAN shot of Fig. 3d. Both shots were at approximately the same distance from the array, but the  $(P_g - P_n)$  times for the CAN shot are 2–3 s larger than the  $(P_g - P_n)$  times for the C1 shot. This is a clear indication that the Moho under shot-point C is much deeper than the Moho under the CAN shot.

Further comparisons on the variation of crustal thickness with azimuth were obtained from a simple delay time analysis of the observations. The CAN shot is associated with a profile line running right into the NORSAR array (Cassell et al., in press 1983), and the thickness of the crust is found to be 28 km beneath this shot point. Now, adopt-

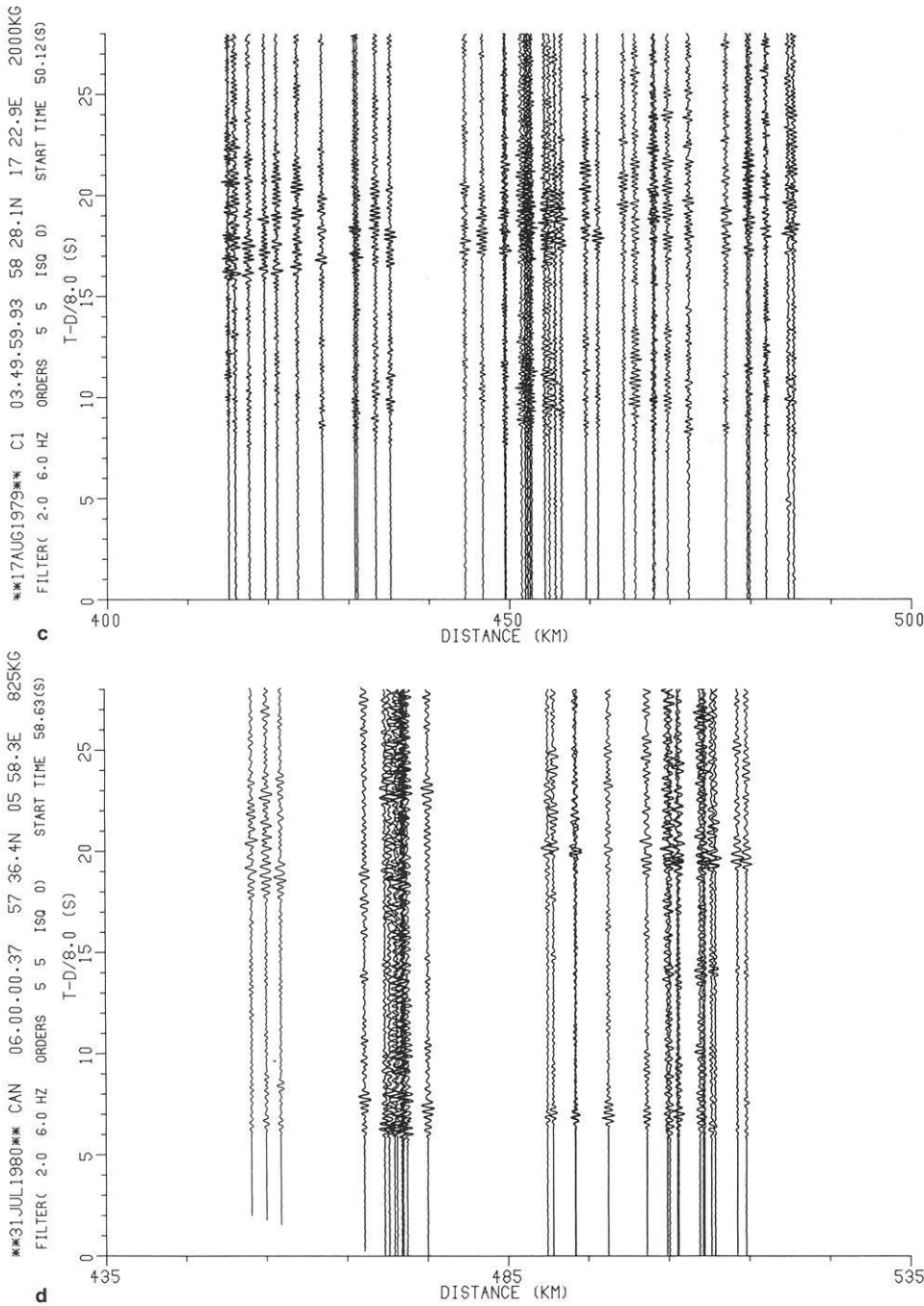


Fig. 3c-d

ing the simplified assumption that the average crustal velocity beneath all shot-points as well as average upper mantle velocity for all propagation paths (shorter than 700 km) are equal, delay time differences arise from variable Moho depths beneath the shot-points. For a fairly wide range of upper mantle velocities, a delay time difference of 1 s corresponds to a variation in Moho depth of about 10 km. 'Calibrating' against the known CAN shot Moho depth of 28 km gives crustal thicknesses of 37, 53, 51, 57 and 57 km for shot-points B, C, D, E and F, respectively. Uncertainties of these estimates are mainly tied to possible lateral variations in the  $P_n$  velocity. Variations in average  $P_n$  velocity for paths to NORSAR by as much as 0.1 km/s would contribute about 5 km to the Moho depth estimates for these shot-points.

### Signal Correlation

In order to obtain the fine structure of the upper mantle it is necessary to identify and position fairly precisely later arrival branches also. A detailed analysis of the coda following the first arrival onsets was therefore undertaken using various velocity filters, envelope analysis, and correlation detectors to determine if any deterministic multiple arrivals arising from large scale regional velocity gradients were present in the upper mantle. No later arrivals, however, were found that were coherent beyond a few kilometers. The lack of coherency in most of the traces is obvious from the records in Fig. 3a-i. Some idea of the correlation distance which was observed can be seen in Fig. 5, which illustrates the normalized individual traces of the CAN shot.

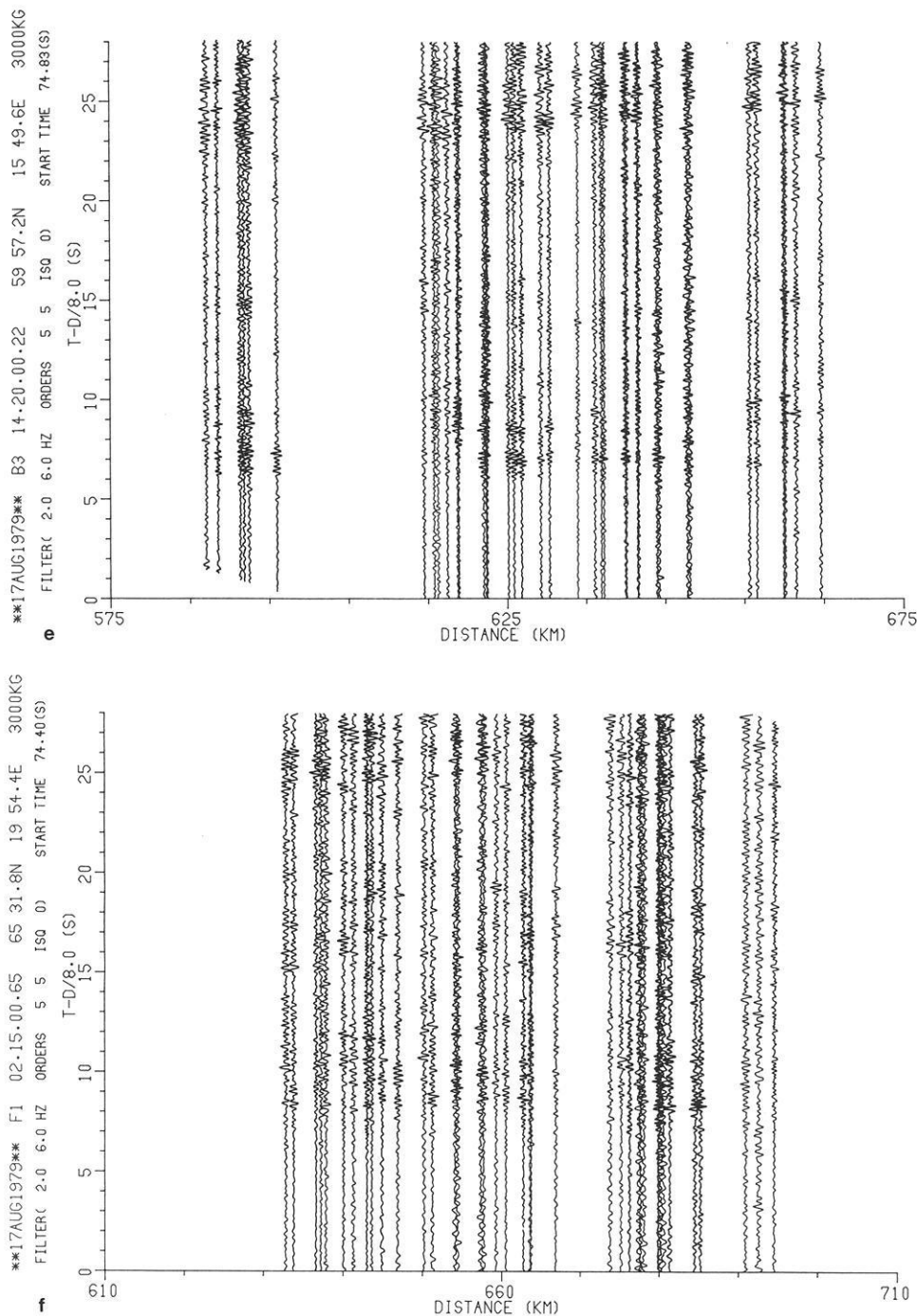


Fig. 3e-f

This figure shows that the signals correlated very well at the new NORESS subarray where the station spacing was less than 2 km, but once the distances increased beyond 2 km as was the case for the other subarrays, the correlations rapidly disappeared.

#### Amplitude Variations

The normalizing factors used for each trace in Fig. 5 are given under the column labelled AMP. An examination of the numbers in this column shows that large amplitude variations by as much as a factor of 5 are observed within one subarray. Compare for example trace 06C00 (AMP=1034) with trace 06CO4 (AMP=249). These two stations were only a few kilometers apart. Similar large scale ampli-

tude variations were observed for the other shots. Another example is shown in Fig. 6, where the unnormalized traces of subarrays 01B and 02B for shot H1 are plotted in a record sections with an expanded distance scale. The weak amplitudes at station 01B04, the very large amplitudes at station 02B02 and the double pulse at station 02B03 all suggest that lateral structures beneath the arrays are focusing and defocusing the energy as well as creating multipath effects. Comparisons of the amplitudes observed at each subarray for different azimuths confirmed, as was expected, that the amplitude and attenuation effects were also very strongly dependent on azimuth. This dependency is illustrated in Fig. 7 which shows areal views of how the amplitudes fluctuate from station to station for two different

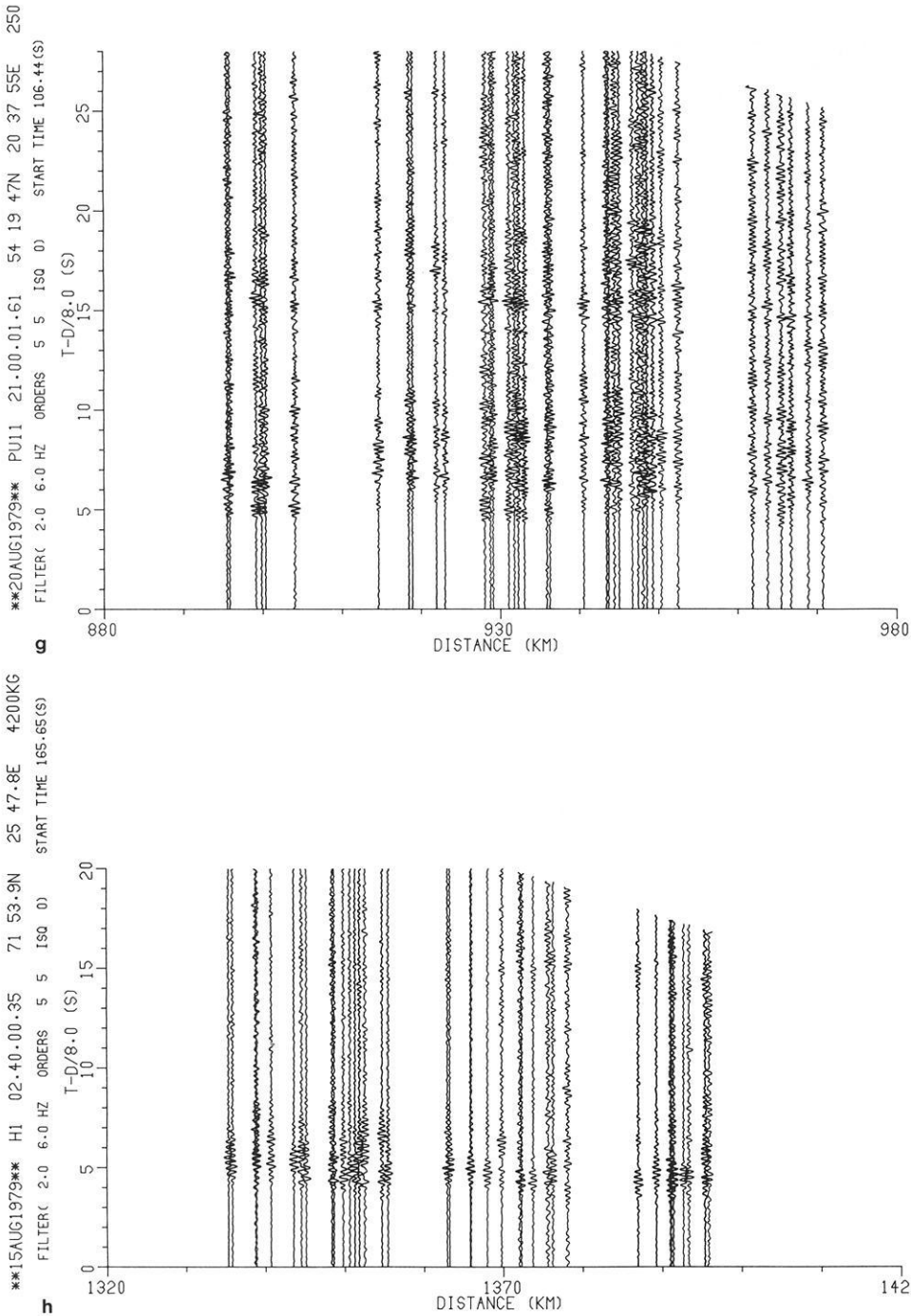


Fig. 3g-h

shots. In this figure the sizes of the various points plotted are directly proportional to the average amplitude measured over a 4 window after the onset of the arrival. The measurements were made on the envelopes of the signals. Similar amplitude fluctuations were observed for the other shots.

The amplitude data for the  $P_n$  waves were also compared with the corresponding data for the  $P_g$  waves. Figure 8 shows that rather distinct correlations exist for B3, C1 and F1, implying that local effects are amplifying and attenuating both waves together. In other cases such as CAN and E1 this relationship is lacking. The relative amplitudes of  $P_n$  and  $P_g$  for shot E1 is rather anomalous with the  $P_g$  amplitude being much larger than  $P_n$ . A comparison of Fig. 3a-c) shows that the distance range of shot E1 over-

laps the ranges for shot points D2 and C1. The latter two shots have approximately the same relative amplitude for  $P_g$  and  $P_n$ . The effect is thus clearly an azimuthal effect. It should also be noted that the source function for E1 tended to have a ringing appearance which differed significantly from all the other observations. A spectrum of E1 showed a very narrow peak at 3 Hz.

#### Apparent $P_n$ Dispersion

Another interesting observation may be noted in Table 1 which shows that there is a large difference in the apparent velocity of the first arrivals for H1 (8.14 km/s) from that of I1 (8.99 km/s). This seemed very puzzling at first as the

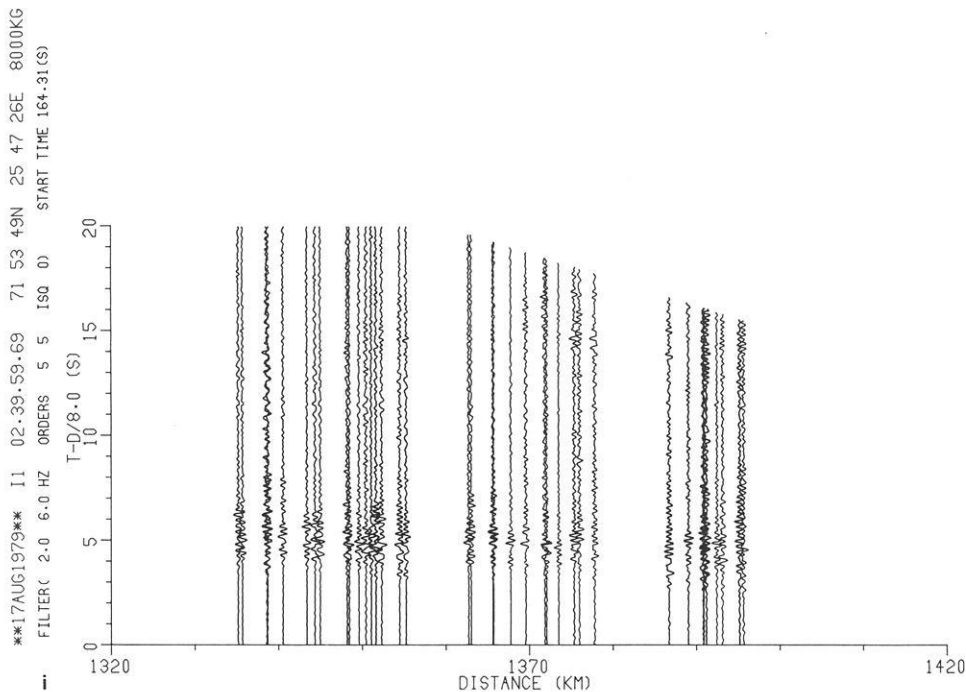
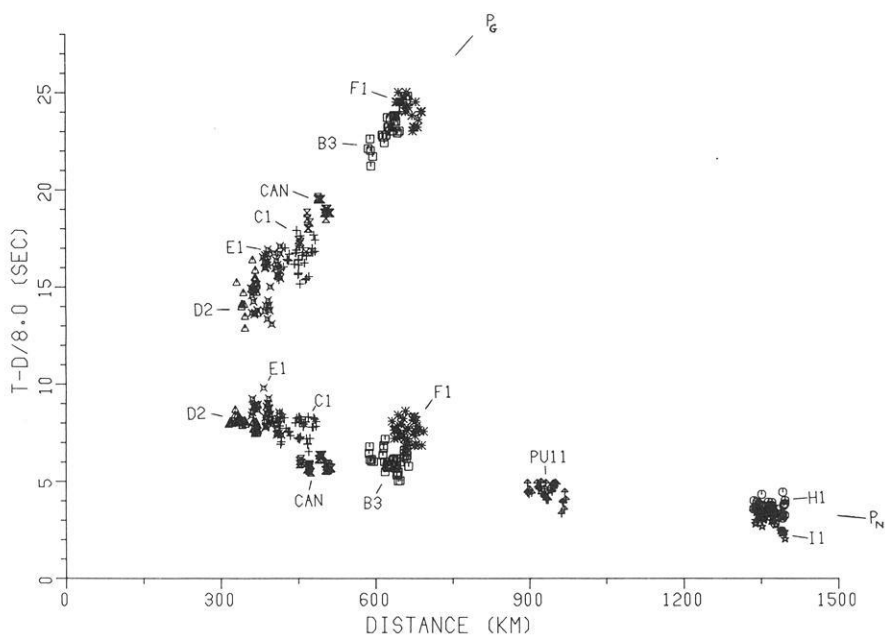


Fig. 3i



**Fig. 4.** Reduced travel time plot of all first onsets of crustal  $P_g$  waves and upper mantle  $P$  waves. A different symbol is used for arrivals from each shot point

two shot points were only a few hundred meters apart meaning that the travel paths were practically identical. A closer examination of this problem revealed that this effect arose because the spectrum of I1 had a much larger low frequency 2 Hz component compared to that of H1. The spectra of the 02B00 traces for these two shots are shown in Fig. 9a and b. There is no doubt that the difference in the spectral content is related to their respective charge sizes. A closer examination of the record sections showed that the higher apparent velocity for I1 came from the fact that dispersion had taken place with the lower frequency components arriving at the array about a second earlier than the high frequency components. The amplitudes of the 2 Hz waves from the H1 shot were not large enough

to be detected and hence their first arrivals were later than those of I1. It thus appears that the low frequency waves have formed a shorter time path or were scattered less than the high frequency components. The dispersion referred to here is an apparent dispersion and not the true dispersion associated with anelasticity.

#### Beamforming and Further Processing

A search of the record sections was made using conventional beamforming and adaptive processing methods to determine if any later arrival time branches could be identified in the mantle coda. A typical example is shown in Fig. 10. This figure illustrates how beams formed from the traces

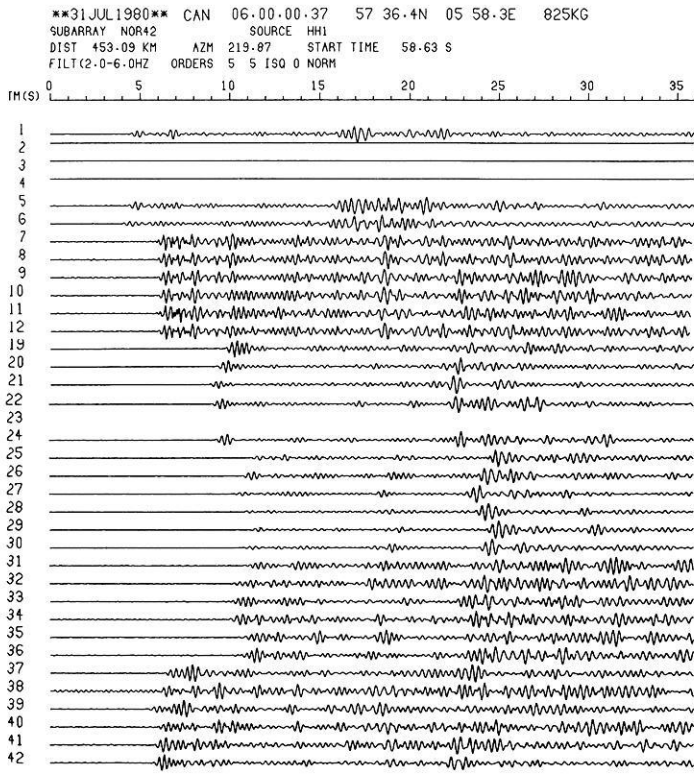


Fig. 5. Seismic traces from the CAN shot. Note: The coherency of the signals across the closely spaced NORESS stations and how this coherency is destroyed for the other subarrays

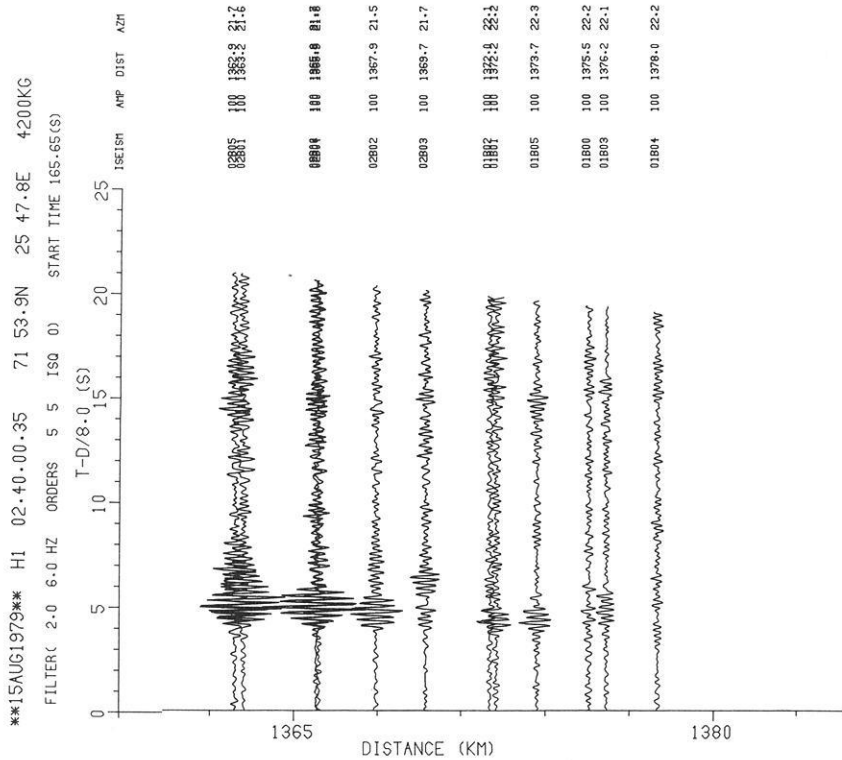


Fig. 6. Unnormalized record section for subarray 01B and 02B of the H1 shot

from 3 subarrays 1B, 2B and 2C change as beamforming velocities are varied from 7.6–9.6 km/s. No velocity creates a well-defined peak in the beam amplitudes, furthermore, because of large spatial aliasing effects in the coda noise, even the  $P_g$  amplitudes were not attenuated when high apparent velocities such as 9 km/s were attempted.  $N$ th root beamforming methods and adaptive processing methods

both gave spurious results. All of these techniques are effective only for low frequency coherent signals which are characteristic of long distant teleseisms. The FENNOLORA signals have a dominant frequency of over 4 Hz and are thus much more sensitive to small-scale lateral inhomogeneities. These quickly contaminate the wavefront with the obvious effect of lost coherency.

PN AMPLITUDE PATTERNS FOR SOURCE B3

SOURCE AZIMUTH 149.6

PN AMPLITUDE PATTERNS FOR SOURCE I1

SOURCE AZIMUTH 21.8

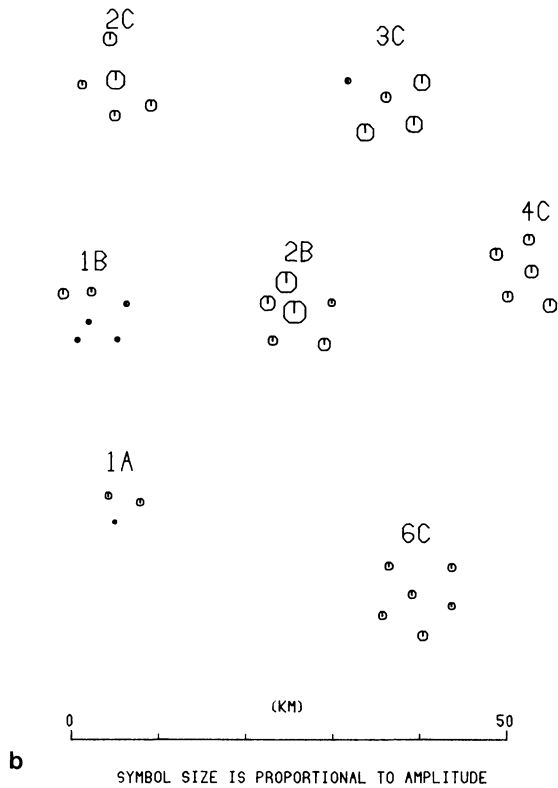
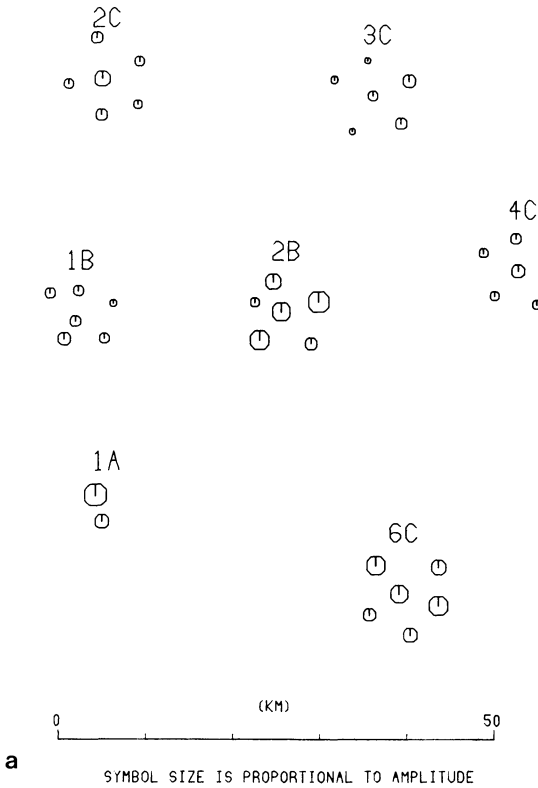
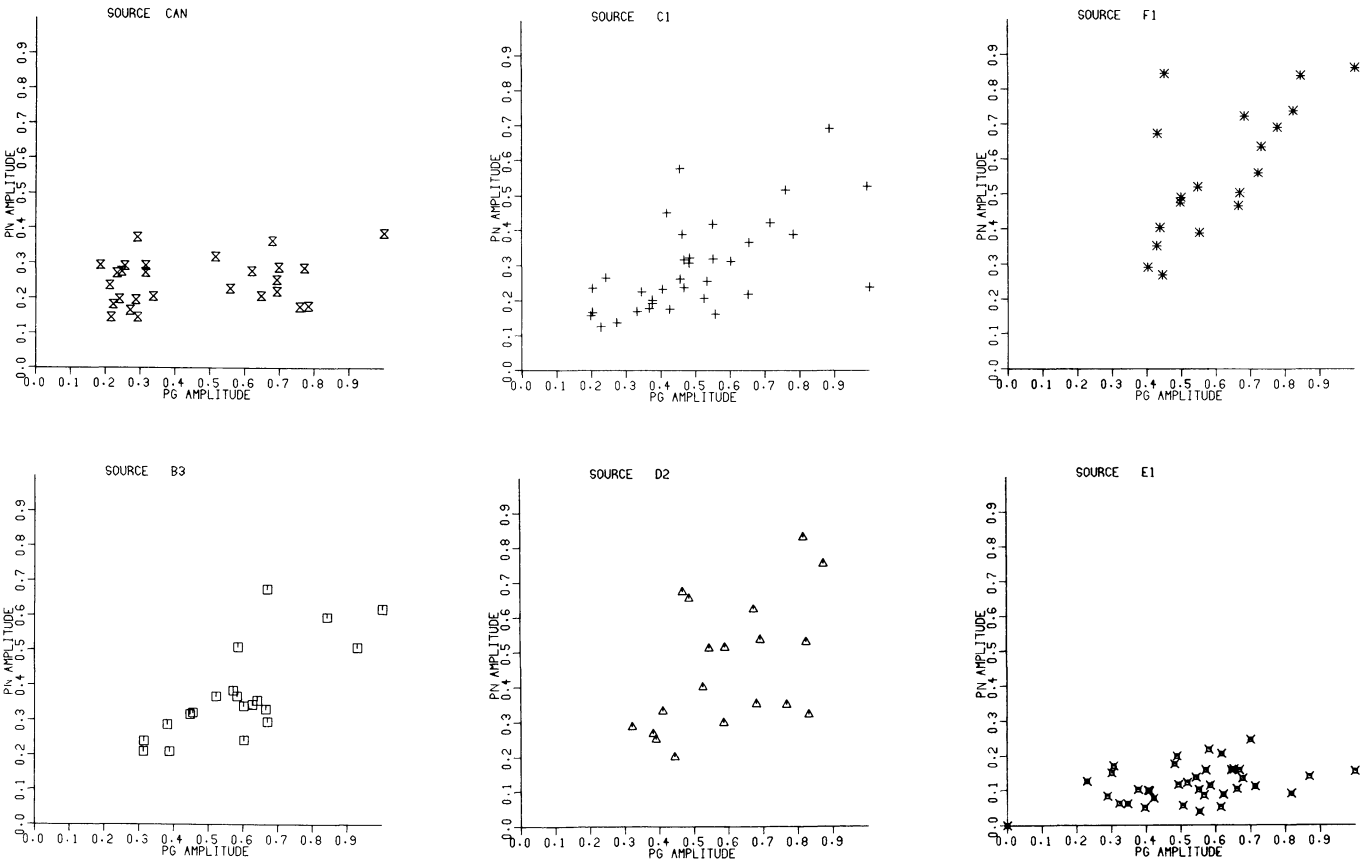
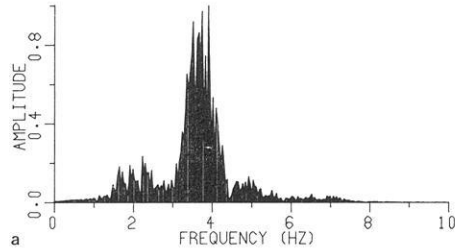
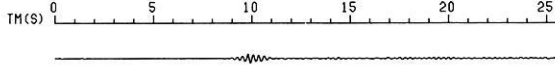


Fig. 7 a and b. Observed amplitude patterns for two shots



\*\*15AUG1979\*\* H1 02:40:00.35 71 53.9N 25 47.8E 4200KG  
 SUBARRAY NOR42 SOURCE H1  
 DIST 1395.83 KM AZM 21.76 START TIME 165.65 S  
 FILTERED DATA



\*\*17AUG1979\*\* I1 02:39:59.69 71 53 49N 25 47 26E  
 SUBARRAY NOR42 SOURCE I1  
 DIST 1395.64 KM AZM 21.76 START TIME 164.31 S  
 FILTERED DATA

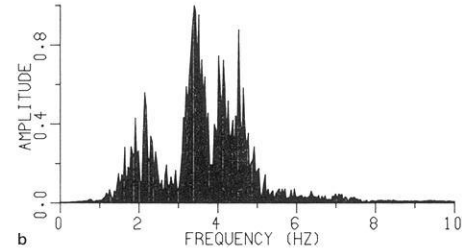
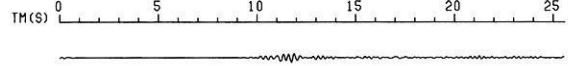
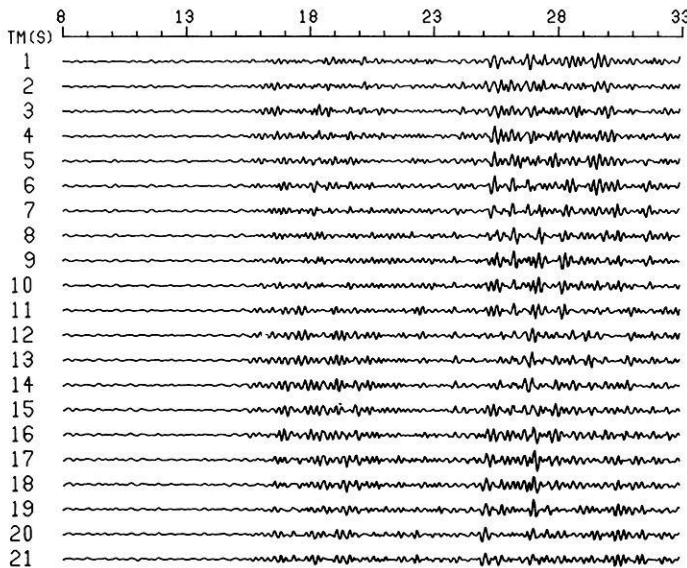


Fig. 9 a and b. Signal spectra of a the H1 shot observed at station 02B00, b the I1 shot observed at station 02B00

\*\*17AUG1979\*\* C1 03:49:59.93 58 28.1N 17 22.9E 2000KG  
 SUBARRAY 1B2B2C SOURCE C1  
 DIST 468.01 KM AZM 124.67 START TIME 50.12 S  
 BEAMS FORMED USING ROOT = 1.0



	AMP	VEL
BEAM	.24	7.6
BEAM	.19	7.7
BEAM	.20	7.8
BEAM	.30	7.9
BEAM	.27	8.0
BEAM	.29	8.1
BEAM	.21	8.2
BEAM	.25	8.3
BEAM	.28	8.4
BEAM	.26	8.5
BEAM	.24	8.6
BEAM	.22	8.7
BEAM	.26	8.8
BEAM	.22	8.9
BEAM	.22	9.0
BEAM	.24	9.1
BEAM	.30	9.2
BEAM	.26	9.3
BEAM	.31	9.4
BEAM	.22	9.5
BEAM	.20	9.6

Fig. 10. Set of beams formed from traces of three subarrays (01B, 02B and 02C) for shot C1. Amp = normalizing amplitude used to normalize the traces. Vel = apparent velocity used in creating the beams

In order to get around the spatial aliasing problem and the incoherency problem, beams were also formed using envelopes of the traces. Figure 11 shows that this method is not sensitive enough to variations in apparent velocity to yield useful information.

## Discussion

In long range seismic experiments numerous arrivals or energy bursts are observable in the recordings and the FENNOLORA seismograms in Fig. 3 are no exception in this respect. However, only two *P* phases can be identified with confidence, namely, the first-arriving *P<sub>n</sub>* wave and *P<sub>g</sub>*, the latter out to a range of 700 km. Traditionally, there has been a tendency among many controlled-source seismologists to associate secondary arrivals with multi-layered crust and upper mantle models. Others have in general been

opposed to the multilayering models on the grounds of lack of objective phase identification criteria and the non-uniqueness in association of the various arrivals. The validity of these objections has been demonstrated with the now widespread use of seismogram synthesis as an analysis tool in the interpretation of refraction data. In particular, multi-layered models often do not account properly for the observed amplitude distributions. We think that many features of the NORSAR FENNOLORA records and specifically the absence of clear secondary mantle arrivals can be attributed to wave scattering effects of small-scale heterogeneities particularly in the crust both at the source and receiver sides. The effect of such inhomogeneities on the amplitudes is often much more pronounced than the amplitude effects caused by possible regional discontinuities or velocity gradients. Travel time fluctuations as well as amplitude fluctuations lead to difficulties in measuring accurate apparent

\*\*17AUG1979\*\* C1 03.49.59.93 58 28.1N 17 22.9E 2000KG  
 SUBARRAY NOR42 SOURCE C1  
 DIST 452.76 KM AZM 122.54 START TIME 50.12 S  
 BEAMS FORMED USING ROOT = 1.0

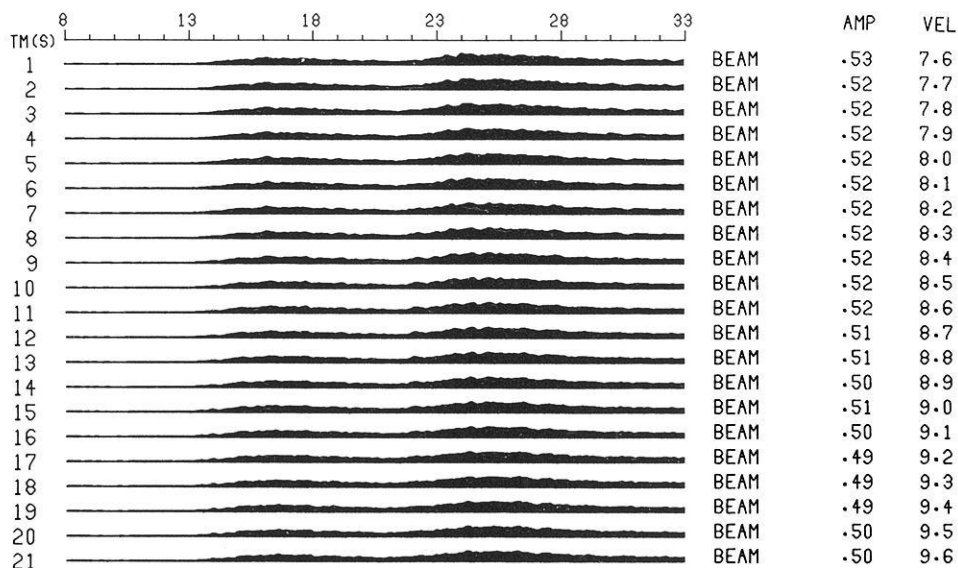


**Fig. 11.** Set of beams formed from the envelopes of all the traces of the NORSAR array for shot C1. Amp = normalizing amplitude used to normalize the traces. Vel = apparent velocity used in creating the beams

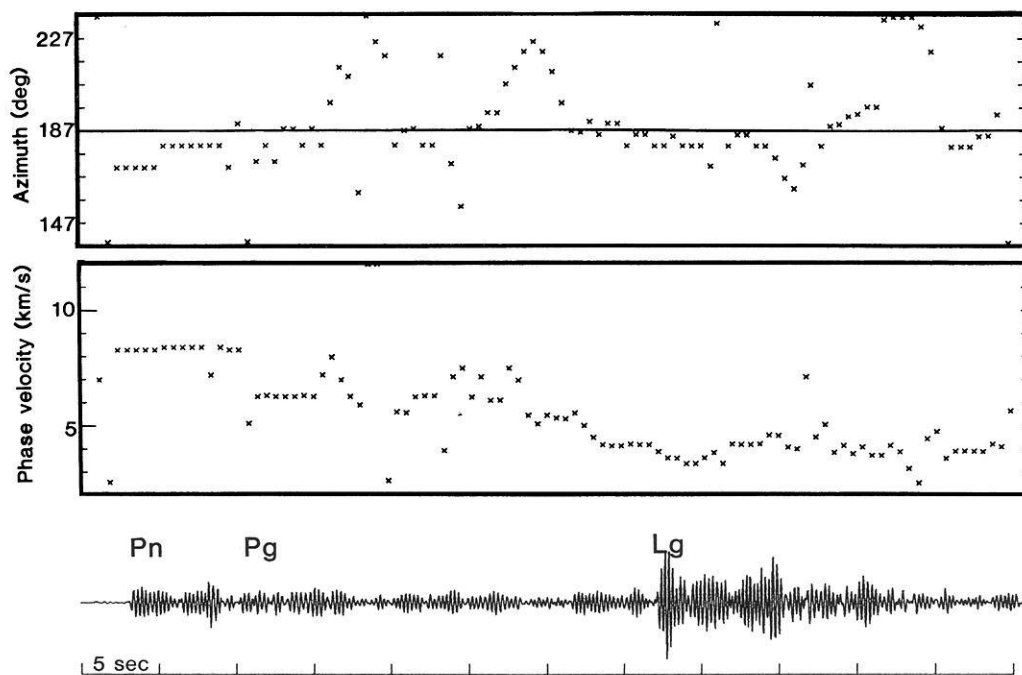


**Fig. 12.** Results from a sliding window frequency-wavenumber analysis of NORESS data from a presumed explosion in the sea at a distance of 260 km, direction south. At the time of this explosion NORESS had 12 sensors (data is shown for one of these) all within an area of 2 km diameter. Frequency-wavenumber analysis results in terms of phase velocity and azimuth for frequencies corresponding to the peak power are plotted for data window lengths of 2.5 s each, with time shifts of 0.6 s. The line in the azimuth diagram shows the azimuth according to the epicenter solution by the Scandinavian network of seismic stations. The uncertainty of this solution in terms of azimuth from NORESS may be as large as 5–10 degrees

velocities over a short distance even in cases where onset times are well defined. Mereu and Ojo (1981) showed, using numerical models of random media, that it is possible to have breaks in the travel time curves even though there may not be a discontinuity associated with that break. Their study showed why deep seismic reflection experiments give

a different picture of the crust and upper mantle than the long-range refraction experiments.

Now, in case of the NORESS array, with sensor interspacings of the order of 125–2,000 m, even high frequency signals ( $\sim 4$  Hz) are coherent. We therefore took the opportunity to demonstrate in practice our comments on the im-

portance of scattering in the crust by subjecting an event, a presumed explosion in the Kattegat (Fig. 1) with features rather similar to a number of FENNOLOGA recordings at NORSAR, to frequency-wavenumber analysis. The outcome of this analysis in terms of phase velocities and azimuths is shown in Fig. 12. The *Pn* wave train results imply that the various ray paths are mainly in the source-receiver plane. The *Pg* phase exhibits quite different features. This wave has been subject to strong scattering resulting in a rather weak, diffuse onset, while the relatively energetic coda appears to be made up of *Pg*-type of waves possibly reflected from the western 'wedge' of the Oslo Graben (in view of the azimuth variations). The coda of the *Lg* wave apparently also consists of significant scattering contributions.

Because of lack of correlation and presumed predominance by scattered waves we were unable as demonstrated in previous sections to utilize techniques like beamforming, envelope beamforming or adaptive processing methods for decomposing the wavetrains in phase velocity/azimuth units and thus facilitate the phase identification of even energetic arrivals. This does not preclude the existence of discontinuities in the upper mantle, but suggests that such contributions are rather insignificant in comparison to scattering arrivals. Indeed, the existence of a rather complex lithosphere beneath the NORSAR array has been repeatedly demonstrated in several studies based on a variety of approaches like random (Chernov) media modelling (Dahle et al., 1975; Berteussen et al., 1975), deterministic modelling on the basis of time and amplitude inversions (Aki et al., 1977; Christoffersson and Husebye, 1979; Haddon and Husebye, 1978) and inversion based on holographic principles (Troitskiy et al., 1981).

We have previously labelled the large difference in *Pn* phase velocities as observed from shots H1 and I1 a dispersion phenomenon. A plausible explanation is that the *Pn* path is slightly frequency dependent due to velocity gradients or heterogeneities beneath Moho. From the work of Mereu and Ojo (1981) it is not unreasonable to assume that lower frequencies which do not 'see' small-scale heterogeneities, form shorter propagation paths than higher frequencies.

Rough approximations of crustal thicknesses beneath the individual shot points can be inferred from the data at hand. Our estimate of the Moho depth beneath shot point B seems reasonable when comparison is made with previous studies (e.g., Bungum et al., 1980), while crustal thicknesses derived for C, D, E and F appear a bit excessive. In order to reduce these values to the more 'acceptable' range 41–47 km, it is necessary to infer a difference in upper mantle average velocities for paths to NORSAR by as much as 0.2 km/s between the CAN and B shots on one side and C, D, E and F on the other. Such variations are, however, larger than we would expect for the ray paths in question (Husebye and Hovland, 1982), indicating that our data point to larger Moho depths than hitherto conceived of for these areas of Sweden. We can only await the results from the FENNOLOGA line for full assessment of the usefulness of NORSAR's FENNOLOGA recordings in this respect.

## Conclusion

Our concept of a rather simple Fennoscandian crustal/upper mantle structure is not invalidated by NORSAR's recordings of the FENNOLOGA shots. We find that short wavelength heterogeneities both at source and receiver ends contribute significantly to the observed seismogram complexities and tend to 'mask' the effects of possible large-scale regional gradients. We recommend long range profiling layouts to be supplemented with small arrays to check the extent of lateral heterogeneities.

*Acknowledgements.* The authors would like to thank the technical and secretarial staffs both at NORSAR and at the University of Western Ontario for their valuable assistance while conducting this research.

This research project was financed by an NTFN/NORSAR Fellowship and the Natural Sciences and Engineering Research Council of Canada (NSERC) grant no. 1793.

## References

- Aki, K., Christoffersson, A., Husebye, E.S.: Determination of the three-dimensional seismic structure of the lithosphere. *J. Geophys. Res.* **82**, 277–296, 1977
- Ansorge, J.: Fennoscandia long-range project 1979 (FENNOLOGA), first results, Working Group of European Seismological Commission. Presented at the 21st General Assembly of IASPEI, London, Ontario, July 1981
- Berteussen, K.-A., Christoffersson, A., Husebye, E.S., Dahle, A.: Wave scattering theory in analysis of P wave anomalies at NORSAR and LASA. *Geophys. J. R. Astron. Soc.* **42**, 403–417, 1975
- Bungum, H., Pirhonen, S.E., Husebye, E.S.: Crustal thicknesses in Fennoscandia. *Geophys. J. R. Astron. Soc.* **63**, 759–774, 1980
- Cassell, B.R., Mykkeltveit, S., Kanestrøm, R., Husebye, E.S.: A North Sea-Southern Norway seismic crustal profile. *Geophys. J. R. Astron. Soc.* **72**, in press 1983
- Christoffersson, A., Husebye, E.S.: On 3-D inversion of P-wave time residuals: option for geological modeling. *J. Geophys. Res.* **84**, 6168–6176, 1979
- Dahle, A., Husebye, E.S., Berteussen, K.-A., Christofferson, A.: Wave scattering effects and seismic velocity measurements. In: *Exploitation of Seismograph Networks*, K.G. Beauchamp, ed., Holland: Noordhoff-Leiden 1975
- Haddon, R.A.W., Husebye, E.S.: Joint interpretation of P wave time and amplitude anomalies in terms of lithospheric heterogeneities. *Geophys. J. R. Astron. Soc.* **55**, 19–43, 1978
- Husebye, E.S., Hovland, J.: On upper mantle seismic heterogeneities beneath Fennoscandia. *Tectonophysics* **90**, 1–17, 1982
- Mereu, R.F., Majumdar, S.B., White, R.E.: Moho topography under the highest ranges of the Canadian Rockies. *Can. J. Earth Sci.* **14**, 196–208, 1977
- Mereu, R.F., Ojo, S.B.: The scattering of seismic waves through a crust and upper mantle with lateral and vertical inhomogeneities. *Phys. Earth Planet. Inter.* **26**, 233–240, 1981
- Mykkeltveit, S., Ringdal, F.: Phase identification and event location at regional distance using small-aperture array data. In: *Identification of Seismic Sources – Earthquake or Underground Explosion*, E.S. Husebye and S. Mykkeltveit, eds. Dordrecht: D. Reidel Publ. Co. 1981
- Troitskiy, P., Husebye, E.S., Nikolaev, A.: Lithospheric studies based on holographic principles. *Nature* **294**, 618–623, 1981

Received August 27, 1982; Revised version January 31, 1983  
Accepted February 1, 1983

# Earth's Flattening Effect on the Tidal Forcing Field\*

H. Wilhelm

Geophysikalisches Institut, Hertzstr. 16, D-7500 Karlsruhe, Federal Republic of Germany

**Abstract.** A small part of the tidal forcing field whose contribution is omitted in the conventional spherical harmonic development of the tidal potential is caused by the flattening of the earth. It is a homogeneous tidal field of magnitude of about 1 ngal superposed on the commonly known tidal forcing field. The conventional tidal forcing field can be completely described by the spatial variation of the gravity field of the tide-generating body within the space occupied by the earth. The advantage of this description is that any reference to the Earth's motion with respect to the tide-generating body (called revolution without rotation) can be avoided.

**Key words:** Ellipticity of the earth - Tidal forces - Earth tides

## Introduction

Some decades ago Jung (1955) pointed out that the tidal forcing field of the Moon contains a small part which is not included in the conventional derivation of this field. Bartels (1957) noted this point but did not consider it in detail. Recently Wahr (1979; 1981) insisted again on the existence of this part, surely without knowing Jung's paper. A reconsideration of Jung's article showed that some modifications have to be introduced and that a clarification is needed.

## Tidal Forcing Field

In every spatially extended physical system upon which an inhomogeneous forcing field is acting, relative forces are induced resulting from the inhomogeneity of the forcing field in the space occupied by the system. For example the Moon, for simplicity regarded as a point mass, exerts a corresponding inhomogeneous gravitational field on the Earth. Introducing an inertial coordinate system with origin  $S$  at the unaccelerated common centre of mass, this gravitational field shall be described by  $\mathbf{g}_M(\tilde{\mathbf{r}})$  where  $\tilde{\mathbf{r}}$  is the position vector. The difference between the gravitational field at an arbitrary point  $P(\tilde{\mathbf{r}})$  and the centre of mass  $O(\tilde{\mathbf{r}}_0)$  of

the earth is a relative gravitational field resulting from subtraction of the constant field  $\mathbf{g}_H = \mathbf{g}_M(\tilde{\mathbf{r}}_0)$  from the spatially varying field  $\mathbf{g}_M(\tilde{\mathbf{r}})$

$$\mathbf{b}_d(\tilde{\mathbf{r}}) = \mathbf{g}_M(\tilde{\mathbf{r}}) - \mathbf{g}_M(\tilde{\mathbf{r}}_0) = \mathbf{g}_M(\tilde{\mathbf{r}}) - \mathbf{g}_H. \quad (1)$$

It can be computed from a potential  $V_d(\tilde{\mathbf{r}})$

$$\mathbf{b}_d(\tilde{\mathbf{r}}) = \nabla V_d \quad (2)$$

with

$$V_d(\tilde{\mathbf{r}}) = V(\tilde{\mathbf{r}}) - V_H(\tilde{\mathbf{r}}), \quad (3)$$

where

$$\mathbf{g}_M(\tilde{\mathbf{r}}) = \nabla V \quad (4)$$

and

$$V_H(\tilde{\mathbf{r}}) = \tilde{\mathbf{r}} \cdot \mathbf{g}_M(\tilde{\mathbf{r}}_0) + C_0. \quad (5)$$

$V(\tilde{\mathbf{r}})$  is the lunar gravitational potential,  $V_H(\tilde{\mathbf{r}})$  the potential of the homogeneous field  $\mathbf{g}_H$  which has to be subtracted in Eq.(1), and  $C_0$  is a free constant which will be given a suitable value by Eq. (9).

These fields can also be expressed in a geocentric spherical coordinate system  $(r, \psi, \gamma)$  with its origin at the Earth's centre of mass  $O$  and its axis pointing to the Moon, see Figs. 1a, 2. In this system  $P$  is characterized by its radius vector  $\mathbf{r}$  and the fields given by the Eqs. (1)-(5) can be calculated by the conventional development of  $V(\mathbf{r})$  in spherical harmonics (Bartels, 1957)

$$V(\mathbf{r}) = V(r, \psi) = \frac{GM_L}{c} \sum_{n=0}^{\infty} \left(\frac{r}{c}\right)^n P_n(\cos \psi), \quad (6)$$

where  $G$  is the gravitational constant,  $M_L$  the lunar mass,  $c$  the distance between the centres of mass of the Earth and the Moon. Introducing the unit vector  $\hat{\mathbf{s}}$  pointing from  $O$  to the Moon (Fig. 1b) and regarding

$$\tilde{\mathbf{r}} = \tilde{\mathbf{r}}_0 + \mathbf{r} \quad (7)$$

$$\begin{aligned} V_H(\tilde{\mathbf{r}}) &= \frac{GM_L}{c^2} \hat{\mathbf{s}} \cdot \tilde{\mathbf{r}} + C_0 \\ &= \frac{GM_L}{c^2} (r \cos \psi - \tilde{r}_0) + C_0, \end{aligned} \quad (8)$$

so that for

\* Contribution No. 250, Geophysikalisches Institut, Universität Karlsruhe

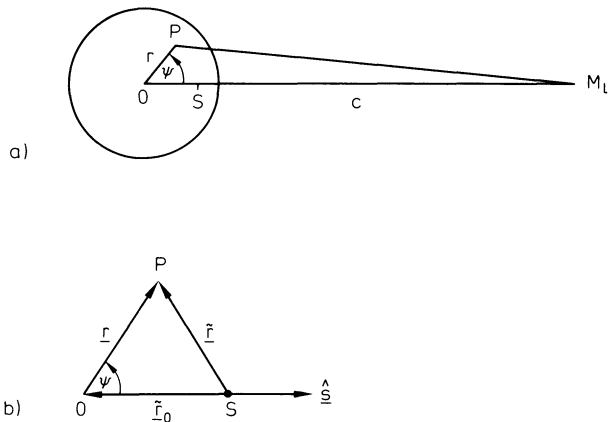


**Fig. 1.** **a** Spherical coordinate system  $r, \psi$  centred with respect to the axis  $OM_L$ ,  $O$  centre of mass of the earth,  $S$  common centre of mass of earth and moon;  $M_L$  lunar mass;  $c$  distance  $OM_L$ . **b** Radius vector  $\tilde{\mathbf{r}}$  and  $\mathbf{r}$  of  $P$  in the inertial system with origin  $S$  and the geocentric system with origin  $O$  respectively;  $\tilde{\mathbf{r}}_0$  radius vector of  $O$  in the inertial system;  $\hat{\mathbf{s}}$  unit vector in direction  $OM_L$

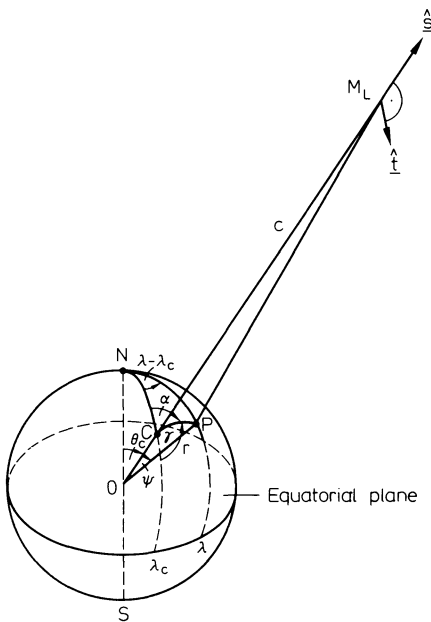


**Fig. 2.** Spherical coordinates  $r, \psi, \gamma$  of a mass point of the earth at  $P$  in the system centred with respect to the axis  $OM_L$  and corresponding coordinates  $r, \theta, \lambda$  and  $c, \theta_c, \lambda_c$  of  $P$  and lunar mass  $M_L$  with respect to a geocentric coordinate system with NS-axis,  $\alpha$  coazimuth of  $\gamma$ . Unit vectors  $\hat{\mathbf{s}}$  and  $\hat{\mathbf{t}}$  designate  $r$ - and  $\theta$ -direction at the moon's place  $\mathbf{r}=\mathbf{c}$  or at the corresponding surface point  $C$  respectively

$$C_0 = \frac{GM_L}{c^2}(\tilde{\mathbf{r}}_0 + c) \quad (9)$$

$$V_d(r, \psi) = V(r, \psi) - V_H(r, \psi) = \frac{GM_L}{c} \sum_{n=2}^{\infty} \left(\frac{r}{c}\right)^n P_n(\cos \psi). \quad (10)$$

This potential is known as the forcing tidal potential of the Moon and has been derived here without reference to the Earth's orbital motion, known as "revolution without rotation", and without any assumptions about

its physical properties such as density, rigidity or elasticity.

However, the difference in the gravitational field of the moon between a point  $P$  of the earth and its centre of mass  $O$  is *not* the lunar tidal forcing field. As initially mentioned, tidal forces are acting with respect to the centre of mass of a physical system which is exposed to an inhomogeneous forcing field generating an acceleration of the centre of mass in an inertial frame. The subtraction of this orbital acceleration from the forcing field yields the relative forces, i.e. the tidal forcing field, in the accelerated system associated with the centre of mass. Hence, the tidal forcing field is the vector difference between the gravitational field of the tide-generating body at the observation point and the orbital acceleration of the Earth's centre of mass with respect to the unaccelerated common centre of mass of the Earth and the tide-generating body, i.e. with respect to the inertial frame. In the inertial system with origin  $S$  the lunar tidal forcing field  $\mathbf{b}(\tilde{\mathbf{r}})$  is therefore

$$\mathbf{b}(\tilde{\mathbf{r}}) = \mathbf{g}_M(\tilde{\mathbf{r}}) - \mathbf{g}_0 \quad (11)$$

where

$$\mathbf{g}_0 = \frac{1}{M_E} \int \rho_E(\tilde{\mathbf{r}}) \mathbf{g}_M(\tilde{\mathbf{r}}) d^3 \tilde{\mathbf{r}}$$

is the orbital acceleration of the Earth's centre of mass in the Earth-Moon system relative to  $S$ ,  $M_E$  is the mass of the earth and  $\rho_E(\tilde{\mathbf{r}})$  the density of the Earth at  $\tilde{\mathbf{r}}$ . The lunar tidal forcing field therefore by definition does not contribute to the orbital motion of the Earth with respect to the Moon which is completely determined by  $\mathbf{g}_0$ . If the Earth were rigid no relative accelerations with respect to its centre of mass could occur in response to the tidal forcing field and the orbital motion of the Earth would remain unchanged. However, the response of the Earth to the tidal forcing field actually has an influence on  $\mathbf{g}_0$  and therefore on the orbital motion of the Earth. For example the dissipation of ocean tide energy is a major factor for orbital variation in the Earth-Moon system. But also the elastic response has, at least in principle, an effect on the orbital acceleration of the Earth by its flattening effect.

The two fields  $\mathbf{b}_d(\tilde{\mathbf{r}})$  and  $\mathbf{b}(\tilde{\mathbf{r}})$  given by Eqs. (1) and (11) are identical only if

$$\mathbf{g}_0 = \mathbf{g}_M(\tilde{\mathbf{r}}_0). \quad (12)$$

It will be shown that this relation would be valid if the Earth were spherically symmetric.

The acceleration  $\mathbf{g}_0$  of the Earth's centre of mass is given by

$$\mathbf{g}_0 = -\frac{M_L}{M_E} \mathbf{g}_E(\mathbf{c}) \quad (13)$$

where  $\mathbf{g}_E(\mathbf{c})$  is the gravitational field of the Earth at the place  $\mathbf{r}=\mathbf{c}$  of the moon which is assumed to be a point mass.

The gravitational field of the Earth is known from measurements of orbits of artificial satellites and can be expressed by its gravitational potential  $U(\mathbf{r})$

$$\mathbf{g}_E(\mathbf{r}) = \nabla U. \quad (14)$$

Neglecting longitude dependent terms in  $U(\mathbf{r})$  (Heiskanen and Moritz, 1967)

$$U(r, \theta) = \frac{GM_E}{r} \left[ 1 - \sum_{n=2}^{\infty} J_n \left( \frac{a}{r} \right)^n P_n(\cos \theta) \right] \quad (15)$$

where  $(r, \theta, \lambda)$  is a geocentric spherical coordinate system centred with respect to the Earth's axis of main inertia, the constant  $a$  is the Earth's equatorial radius and  $J_n$  are the coefficients of the expansion in spherical harmonics.

At the position of the Moon ( $r=c$ ,  $\theta=\theta_c$ ) the gravitational field of the Earth is

$$\begin{aligned} \mathbf{g}_E(\mathbf{c}) &= \nabla U|_{r=c, \theta=\theta_c} \\ &= -\frac{GM_E}{c^2} \left\{ \left[ 1 - \sum_{n=2}^{\infty} (n+1) J_n \left( \frac{a}{c} \right)^n P_n(\cos \theta_c) \right] \hat{\mathbf{s}} \right. \\ &\quad \left. + \sum_{n=2}^{\infty} J_n \left( \frac{a}{c} \right)^n \frac{dP_n}{d\theta} \Big|_{\theta=\theta_c} \hat{\mathbf{t}} \right\} \quad (16) \end{aligned}$$

where  $\theta_c$  is the lunar colatitude and  $\hat{\mathbf{s}}$  and  $\hat{\mathbf{t}}$  are the unit vectors in  $r$ - and  $\theta$ -direction at  $r=c$ ,  $\theta=\theta_c$ . Figure 2 shows the geometric configuration.

The first part  $-\frac{GM_E}{c^2} \hat{\mathbf{s}}$  is the gravitational field of a spherically symmetric Earth of the same mass  $M_E$  acting at the position of the Moon. The rest is contributed by the non-radially symmetric part of the Earth's mass distribution.

If all coefficients  $J_n$  disappear

$$J_n = 0, \quad n=2, 3, 4, \dots \quad (17)$$

$$\mathbf{g}_E(\mathbf{c}) = -\frac{GM_E}{c^2} \hat{\mathbf{s}} \quad (18)$$

and with (13)

$$\mathbf{g}_0 = \frac{GM_L}{c^2} \hat{\mathbf{s}} = \mathbf{g}_M(\tilde{\mathbf{r}}_0). \quad (19)$$

Hence, only if the Earth were spherically symmetric would the acceleration of its centre of mass be equal to the gravitational field acting at its centre of mass. Actually, because of the flattening of the Earth  $\mathbf{g}_0 \neq \mathbf{g}_M(\tilde{\mathbf{r}}_0)$ . Therefore, the two fields (1) and (11) are not identical.

The tidal field (11) can be split into two parts from which the effect of the flattening becomes obvious:

$$\begin{aligned} \mathbf{b}(\tilde{\mathbf{r}}) &= \mathbf{g}_M(\tilde{\mathbf{r}}) - \mathbf{g}_0 = \mathbf{g}_M(\tilde{\mathbf{r}}) - \mathbf{g}_M(\tilde{\mathbf{r}}_0) + \mathbf{g}_M(\tilde{\mathbf{r}}_0) - \mathbf{g}_0 \\ &= \mathbf{b}_d(\tilde{\mathbf{r}}) + \mathbf{b}(\tilde{\mathbf{r}}_0) = \mathbf{b}_d(\tilde{\mathbf{r}}) + \mathbf{b}_H. \quad (20) \end{aligned}$$

The first part  $\mathbf{b}_d(\tilde{\mathbf{r}})$  is the relative gravitational field introduced by Eq. (1) which by Eq. (10) represents the conventional tidal forcing field whereas the second part is the specific tidal force at the Earth's centre of mass  $\tilde{\mathbf{r}} = \tilde{\mathbf{r}}_0$  which is non-vanishing for a flattened Earth. To the conventional tidal forcing field  $\mathbf{b}_d(\tilde{\mathbf{r}})$  is added the homogeneous field  $\mathbf{b}_H = \mathbf{b}(\tilde{\mathbf{r}}_0)$  if the flattening of the Earth is taken into account.

From (2), (11), and (16) it follows for the tidal forcing field expressed in geocentric coordinates

$$\begin{aligned} \mathbf{b}(\mathbf{r}) &= \frac{GM_L}{c} \nabla \sum_{n=2}^{\infty} \left( \frac{r}{c} \right)^n P_n(\cos \psi) \\ &\quad + \frac{GM_L}{c^2} \sum_{n=2}^{\infty} J_n \left( \frac{a}{c} \right)^n \\ &\quad \cdot \left\{ (n+1) P_n(\cos \theta_c) \hat{\mathbf{s}} - \frac{dP_n}{d\theta} \Big|_{\theta=\theta_c} \hat{\mathbf{t}} \right\}. \quad (21) \end{aligned}$$

The first expression is the usual tidal forcing field which really is the relative gravitational field (1) and which is completely independent of the physical properties of the Earth. The second part is the expression for  $\mathbf{b}_H$ . It depends on the density distribution of the Earth and vanishes if this density distribution is spherically symmetric. From (21) it is evident that the flattening of the Earth makes a contribution to the tidal forcing field of the Moon. The physical explanation for this effect is given by Eq. (16). The gravitational field of the Earth acting on the Moon depends on the aspherical part of the density distribution of the Earth and by the action-reaction principle the acceleration of the Earth's centre of mass  $\mathbf{g}_0$  also depends on this part of the Earth's density distribution. Since  $\mathbf{g}_0$  is involved in the tidal forcing field this field, too, must depend on the mass distribution of the Earth. A corresponding contribution from the Earth's flattening to the solar tidal forcing field is smaller by  $(M_s/M_L) \cdot (c/c_s)^4 \sim 10^{-3}$  where  $M_s$  is the solar mass and  $c_s$  is 1 AU.

From (13) and (16)

$$\begin{aligned} \mathbf{g}_0 &= \frac{GM_L}{c^2} \left\{ \hat{\mathbf{s}} - \sum_{n=2}^{\infty} \left( \frac{a}{c} \right)^n J_n \right. \\ &\quad \left. \cdot \left[ (n+1) P_n(\cos \theta_c) \hat{\mathbf{s}} - \frac{dP_n}{d\theta} \Big|_{\theta=\theta_c} \hat{\mathbf{t}} \right] \right\}. \quad (22) \end{aligned}$$

Hence, the motion of the Earth is disturbed by its nonspherical mass distribution. These disturbances are however small compared to the gravitational disturbances caused by the sun (Kaula, 1968, p. 176) resulting from the change of the gravitational field of the sun by the variation of the distance between the geo-lunar mass centre  $S$  and the sun. This effect is of the order of  $2GM_s a/c_s^3$  which is about  $c/(aJ_2) \sim 6 \cdot 10^4$  times greater than the aspherical mass distribution effect in (22) for  $n=2$ . Therefore the effect of the Earth's aspherical mass distribution is not revealed in orbital motion, but it shows up in precession and nutation.

For the development of the tidal potential  $\hat{\mathbf{s}} \cdot \mathbf{r}$  and  $\hat{\mathbf{t}} \cdot \mathbf{r}$  have to be calculated. From Fig. 2 follows:

$$\begin{aligned} \hat{\mathbf{s}} \cdot \mathbf{r} &= r \cos \psi \\ \hat{\mathbf{t}} \cdot \mathbf{r} &= -r \sin \psi \cos \alpha. \quad (23) \end{aligned}$$

Following from (10) and (20) the complete expression for the tidal forcing potential is given by

$$\begin{aligned} V(r, \psi) &= V_d(r, \psi) + \mathbf{r} \cdot \mathbf{b}_H \\ &= \frac{GM_L}{c} \left\{ \sum_{n=2}^{\infty} \left( \frac{r}{c} \right)^n P_n(\cos \psi) + \frac{r}{c} \sum_{n=2}^{\infty} J_n \left( \frac{a}{c} \right)^n \right. \\ &\quad \cdot \left[ (n+1) P_n(\cos \theta_c) \cos \psi \right. \\ &\quad \left. \left. + \frac{dP_n}{d\theta} \Big|_{\theta=\theta_c} \sin \psi \cos \alpha \right] \right\}. \quad (24) \end{aligned}$$

The last sum of (24) is caused by the non-spherical mass distribution of the Earth and relates to the homogeneous field  $\mathbf{b}_H$  in (20) whereas the first part is the usual tidal forcing potential.

With

$$\cos \theta = \cos \theta_c \cos \psi + \sin \theta_c \sin \psi \cos \alpha \quad (25)$$

$$\cos \psi = \cos \theta \cos \theta_c + \sin \theta \sin \theta_c \cos(\lambda - \lambda_c) \quad (26)$$

$$\begin{aligned} P_n(\cos \psi) &= P_n(\cos \theta) P_n(\cos \theta_c) \\ &+ 2 \sum_{m=1}^n \frac{(n-m)!}{(n+m)!} P_n^m(\cos \theta) P_n^m(\cos \theta_c) \\ &\cdot \cos m(\lambda - \lambda_c) \end{aligned} \quad (27)$$

where  $P_n^m(\cos \theta)$  are the associated Legendre polynomials, Eq. (24) can be expressed in geocentric coordinates  $r, \theta, \lambda$

$$\begin{aligned} V(r, \theta, \lambda) &= \frac{GM_L}{c} \sum_{n=2}^{\infty} \left(\frac{r}{c}\right)^n \\ &\cdot \left\{ P_n(\cos \theta) P_n(\cos \theta_c) + 2 \sum_{m=1}^n \frac{(n-m)!}{(n+m)!} \right. \\ &\cdot \left. P_n^m(\cos \theta) P_n^m(\cos \theta_c) \cdot \cos m(\lambda - \lambda_c) \right\} \\ &+ \frac{GM_L}{c} \frac{r}{c} \sum_{n=2}^{\infty} J_n \left(\frac{a}{c}\right)^n \\ &\cdot \left\{ (n+1) P_n(\cos \theta_c) [\cos \theta \cos \theta_c \right. \\ &+ \sin \theta \sin \theta_c \cos(\lambda - \lambda_c)] + \left. \frac{dP_n(\cos \theta)}{d\theta} \right|_{\theta=\theta_c} \\ &\cdot [\cos \theta \sin \theta_c - \sin \theta \cos \theta_c \cos(\lambda - \lambda_c)] \left. \right\}. \end{aligned} \quad (28)$$

By introducing Cartesian coordinates it can be verified that the second sum in (28) determined by the coefficients  $J_n$  represents the potential of the homogeneous field  $\mathbf{b}_H$ .

## Numerical Results

For the determination of the flattening effect on the tidal forcing field only the term  $n=2$  will be considered in (16) because  $J_n/J_2 \lesssim 10^{-2}$  for  $n > 2$  (Kaula, 1968). With

$$\mathbf{g}_M(\tilde{\mathbf{r}}_0) = \frac{GM_L}{c^2} \hat{\mathbf{s}} \quad (29)$$

$$\begin{aligned} \mathbf{b}_H &= \mathbf{g}_M(\tilde{\mathbf{r}}_0) - \mathbf{g}_0 = \frac{GM_L}{c^2} \hat{\mathbf{s}} + \frac{M_L}{M_E} \mathbf{g}_E(\mathbf{c}) \\ &= \frac{GM_L}{c^2} \left(\frac{a}{c}\right)^2 \frac{3}{2} J_2 [(3 \cos^2 \theta_c - 1) \hat{\mathbf{s}} + \sin 2\theta_c \hat{\mathbf{t}}]. \end{aligned} \quad (30)$$

The corresponding term in the tidal potential is given by Eq. (24)

$$\begin{aligned} \mathbf{r} \cdot \mathbf{b}_H &= \frac{GM_L}{c} \left(\frac{a}{c}\right)^2 \frac{r}{c} \frac{3}{2} J_2 \\ &\cdot [(3 \cos^2 \theta_c - 1) \cos \psi - \sin 2\theta_c \sin \psi \cos \alpha]. \end{aligned} \quad (31)$$

With  $a/c = 0.016593$ ,  $M_E/M_L = 81.30$ , and  $GM_E$ ,  $a$  and  $J_2$  from the IAG 1980 system of constants (Müller, 1980)

$$\frac{3}{2} \frac{GM_L}{c} \left(\frac{a}{c}\right)^3 J_2 = 9.462 \cdot 10^{-5} \text{ m}^2/\text{s}^2. \quad (32)$$

This is about 10% of the  $n=4$  term of the normal tidal potential

$$\frac{GM_L}{c} \left(\frac{a}{c}\right)^4 = 9.688 \cdot 10^{-4} \text{ m}^2/\text{s}^2. \quad (33)$$

The magnitude of the corresponding force per unit mass given by Eq. (30) is

$$\frac{3}{2} \frac{GM_L}{c^2} \left(\frac{a}{c}\right)^2 J_2 = 1.48 \cdot 10^{-11} \text{ m/s}^2 \approx 1 \text{ ngal} \quad (34)$$

that is about 3% of the magnitude of the vertical force per unit mass for  $n=4$

$$4 \frac{GM_L}{c^2} \left(\frac{a}{c}\right)^3 = 62.3 \text{ ngal}. \quad (35)$$

The first part of the homogeneous field  $\mathbf{b}_H$  in (30)

$$\mathbf{b}_s = \frac{3}{2} J_2 \frac{GM_L}{c^2} \left(\frac{a}{c}\right)^2 (3 \cos^2 \theta_c - 1) \hat{\mathbf{s}} \quad (36)$$

always points away from the Moon since  $\cos^2 \theta_c < \frac{1}{3}$  for all possible values of the lunar declination  $\delta_c = \frac{\pi}{2} - \theta_c$ . The second part

$$\mathbf{b}_t = \frac{3}{2} J_2 \frac{GM_L}{c^2} \left(\frac{a}{c}\right)^2 \sin 2\theta_c \hat{\mathbf{t}} \quad (37)$$

changes its sign for  $\theta_c = \frac{\pi}{2}$  i.e., when the Moon is in the equatorial plane of the Earth. As  $\mathbf{b}_H$  is a homogeneous field it represents a constant tidal forcing field acting simultaneously on the whole Earth at a specific time  $t$ . It is of course varying with time.

The periodicities can be determined from the corresponding part of the potential expressed in geocentric coordinates. From the Eqs. (28) and (31) this is

$$\begin{aligned} \mathbf{r} \cdot \mathbf{b}_H &= \frac{GM_L}{c} \left(\frac{a}{c}\right)^2 \frac{r}{c} \frac{3}{2} J_2 \{ (3 \cos^2 \theta_c - 1) (\cos \theta \cos \theta_c \\ &+ \sin \theta \sin \theta_c \cos(\lambda - \lambda_c)) \\ &- \sin 2\theta_c [\cos \theta \sin \theta_c - \sin \theta \cos \theta_c \cos(\lambda - \lambda_c)] \}. \end{aligned} \quad (38)$$

The time variations are caused by the variations of  $c$ ,  $\theta_c$  and  $\lambda_c$  in Eq. (38). The major inherent periodicities are lunar-daily from  $\cos(\lambda - \lambda_c)$ , lunar-third-monthly from the products of  $\cos \theta_c$  and  $\sin \theta_c$  with  $\cos^2 \theta_c$  and  $\sin 2\theta_c$ , and monthly from  $c^{-4}$ ,  $\cos \theta_c$  and  $\sin \theta_c$ .

At present it appears hopeless to search for the described effect in the tidal gravity records because it

has an amplitude of only about 1 ngal. It should however be noticed that a homogeneous tidal field may raise deformations in a radially stratified Earth and especially a forced tidal motion of the central core of the Earth into an eccentric position, and it might be suspected that this effect could have significant dynamical consequences. This suspicion must however be discarded because the displacement will be of the order of  $1\ \mu\text{m}$  as can be shown by considering the balance between the homogeneous tidal and the repelling gravitational force acting on a solid inner core in a fluid outer core with constant but different densities and an assumed density difference of  $2\ \text{g/cm}^3$ .

*Acknowledgements.* I am grateful to Professor M. Siebert, Professor K. Fuchs and Dr. W. Zürn helpful comments.

## References

- Bartels, J.: Gezeitenkräfte, Handb. d. Physik **48**, Geophys. 2, 734-744. Berlin: Springer 1957
- Jung, K.: Über die Darstellung der Gezeitenkräfte, Gerlands Beitr. Geophys. **64**, 278-283, 1955
- Heiskanen, W., Moritz, H.: Physical geodesy. San Francisco: Freeman 1967
- Kaula, W.M.: Introduction to planetary physics. New York: Wiley & Sons, 1968
- Müller, I.I.: Bulletin Géodésique, Vol. **54**, No. 3, Paris, 1980
- Wahr, J.M.: The tidal motions of a rotating, elliptical, elastic and oceanless earth, Ph.D. Thesis, University of Colorado, USA, 1979
- Wahr, J.M.: Body tides on an elliptical, rotating, elastic and oceanless earth, Geophys. J.R. Astron. Soc. **64**, 677-703, 1981

Received August 30, 1982; Revised version December 7, 1982  
Accepted December 7, 1982

# Some Results of Calibration Factor Determination of LaCoste and Romberg Gravity Meters (Model D)

H.-J. Götze<sup>1</sup> and B. Meurers<sup>2</sup>

<sup>1</sup> Institut für Geophysik der Technischen Universität Clausthal, Postfach 230, D-3392 Clausthal-Zellerfeld, Federal Republic of Germany

<sup>2</sup> Institut für Meteorologie und Geophysik der Universität Wien, Hohe Warte 38, A-1190 Wien, Austria

**Abstract.** Contrary to the manufacturer's manual we observe a non-linearity of the calibration-factors of the D-8 and D-9 LCR gravity meters. By measuring on two local calibration-lines ( $\Delta g_1 = 27$  mgal and  $\Delta g_2 = 41$  mgal) and in various ranges of the measuring screw, we were able to prove the effects of non-linearity by experiments. The calculation of calibration factor functions is outlined and the quality of the approximation-model could be verified in terms of measurements on parts of the European Calibration line (ECL). The results show, that the effects of non-linearity have to be considered with regard to high precision gravity measurements. By using the calibration factor as given by the manufacturer; errors up to 0.08 mgal will be observed.

**Key words:** Nonlinearity of gravity meters – Calibration factors – Calibration factor function – Accuracy of readings – LaCoste and Romberg gravity meter (Model D)

## Introduction

LaCoste and Romberg model D gravity meters have a resolution in the  $\mu\text{gal}$  range, and at present they belong to the most sensitive field gravity meters in the world. The instruments D-8 and D-9 described here are used for both gravity and vertical gradient measurements in the Eastern Alps mainly (Götze et al. 1979; Steinhauser et al., 1980). Because of the elevation differences of several measuring points in this region it is necessary to measure in various reset ranges of the gravity meters with a range of approximately 200 mgal<sup>1</sup> (corresponding to 2,000 turns of the measuring screw) only.

The instruments D-8 and D-9 were calibrated quickly and easily by comparison of measurements with corresponding gravity differences  $\Delta g$  on calibration lines (sections of the European calibration line ECL). The following sections of the ECL were used:

D-8 gravity meter: Torfhaus G – Bad Harzburg G,  
 $\Delta g = 84.15$  mgal

D-9 gravity meter: Kufstein N – Stafflach X,  
 $\Delta g = 224.71$  mgal.

<sup>1</sup> 1 mgal =  $10^{-5}$  ms<sup>-2</sup>

The calibration factors of LCR-D gravity meters are stated to be constant in the whole measuring range by the manufacturer. Different ranges of counter units had to be used during the calibrations, which have been performed on the calibration lines mentioned above during the last ten years, because of frequent reset displacements. Thereby systematic differences from the expected values of the corresponding gravity differences could be observed, which amounted to six counter units at the most corresponding to a gravity difference of 0.06 mgal. They were interpreted qualitatively as non-linearities of the calibration factors. Observations of this kind have been described by other authors too (e.g. Wenzel, pers. comm. 1973; Steinhauser, 1978; Torge and Kannieser, 1980) and initiated an examination of the systematic effects concerning the LCR-D gravity meters mentioned above. This is particularly true for the experiments of Lambert et al. (1979).

The existing measuring results clearly show, that deviations from the expected values of gravity differences on calibration lines are not due to measuring errors, but a functional relation exists between the gravity differences (calculated by using a constant calibration factor) and the mean readings. Figure 1 shows the measured gravity differences on the calibration line Torfhaus G – Bad Harzburg G as a function of the mean position of the measuring screw for the gravity meter D-8. The gravity differences decrease with increasing mean positions of the measuring screw and deviate from the "true" value up to the amount of 0.08 mgal.

In case of the LCR D-9 the differences between the readings at the final points of a local calibration line in Vienna increase with the mean position of the measuring screw almost linearly (Steinhauser, 1978).

A significant nonlinearity of the measuring screw depending upon the reset screw position was also found in case of other LCR Model D gravity meters (Torge and Kannieser, 1980; Dragert et al., 1981; Lambert and Liard, 1981).

## Measurements and Nonlinearity Determination

The gravity differences on the sections of the ECL described above are too large for a reliable determination of the effects of non-linearity. Local calibration lines had to be used or to be installed for this purpose.

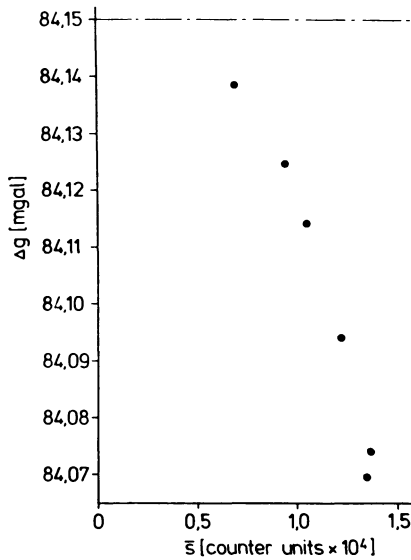


Fig. 1. Relationship between measured gravity differences and the mean measuring position, plotted for the LCR-gravity meter D-8; calibration line: Torfhaus G – Bad Harzburg G

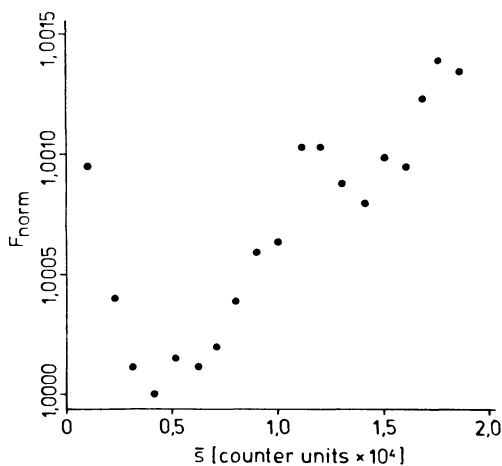


Fig. 2. Normalized calibration factor function  $F_{Norm}$  for the D-8 gravity meter on the local calibration line Clausthal – Osterode

### Local Calibration Lines and Experimental Results

The following criteria are decisive for the selection of local calibration lines:

- Sufficient gravity differences for a reliable proof of non-linearity effects. Starting from a reproducibility of 0.02 mgal of relative measurements the gravity difference of the local calibration line should amount to 30 mgal approximately. This relation corresponds to observations mentioned above, which show variations of 0.06 mgal at gravity differences of 84 mgal. Gravity differences larger than 30 mgal should not be used, as the extrema of the calibration factor function could not be resolved because of the integral effect of the measurements.

- Low noise at the gravity stations and sufficient short-term stability to ensure reliable repetitions of the measurements.

- Short time intervals between the readings at the ends

of the calibration lines to guarantee a favourable drift behaviour of the gravity meters.

For the examination of the LCR D-8 a local calibration line was installed between Clausthal and Osterode, meeting the requirements mentioned above. The gravity difference amounts to 27 mgal. On this calibration line the gravity difference was measured at 19 consecutive positions of the reset screw in the available measuring range of 200 mgal approximately. At the ends of the calibration line measurements were carried out 4 or 5 times in each reset position to guarantee reliable results; all readings were corrected with respect to instrumental drift. The time intervals between the readings at the ends of the line amounted to 10–12 min only. Figure 2 shows the results of 19 single measurements in normalized form, where the ratio defined by

$$F_{Norm} = d_m / d_i \quad (1)$$

$d_m$  = maximal value of the differences  
between the readings  
 $d_i$  = difference between the readings  
for  $i = 1, \dots, 19$

is represented as a function of the mean readings  $\bar{s}_i$  ( $i = 1 \dots, 19$ ). Figure 2 evidently shows that the gravity difference of 27 mgal is sufficient to resolve local extrema of the calibration factor function. In Figure 1 a corresponding trend, at best, is shown because of the limited resolution there.

The existing calibration line between Vienna Hohe Warte and Kahlenberg with a gravity difference of 41 mgal approximately was used for the examination of the instrument D-9 again. In addition to a better resolution by using further reset positions the temporal reproducibility of the nonlinearity effects should be tested. The end points of the calibration line were measured 3 or 4 times at each reset position; all readings were evaluated taking into account the tidal gravity variations and instrumental drift. The measurements were repeated at three reset positions. The time interval between the measurements at the end points of the calibration line was of the order of 20–25 min. The measuring results of 1979 and 1976 are shown in Fig. 3, also in normalized form. The temporal variation of the sensitivity of the LCR D-9, which was determined by yearly measurements on the profile section of the ECL between Kufstein N and Stafflach X using the same reset screw position every time, was considered here accordingly. The measurements of 1979 confirm the earlier results. This fact shows temporal stability of the observed effects. In the upper range of counter units a modification of the calibration factor function determined in 1976 has to be made, as the measurements of 1976 did not yield reliable information about the uppermost range.

### Numerical Calculations

The determination of the calibration factor  $Caf(r)$  as a function of the readout value ( $r$ ) may be outlined with regard to the fact that the true gravity difference is (still) unknown on local calibration lines. Let  $\Delta g$  be the unknown gravity difference between the end points of the calibration line with the readings  $s_1$  and  $s_2$ , we have

$$\Delta g = \int_{s_1}^{s_2} Caf(r) dr. \quad (2)$$

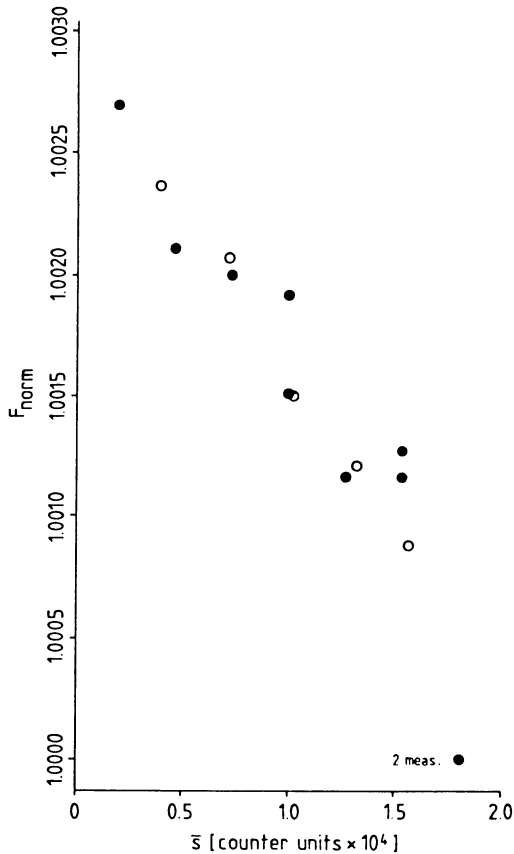


**Fig. 3.** Normalized calibration factor function  $F_{Norm}$  for the D-9 gravity meter on the local calibration line in Vienna: ○ 1976 measurements; ● 1979 measurements

Is the reading  $s_1$  close to  $s_2$ , the  $\Delta g$  of gravity becomes

$$\Delta g = Caf(\bar{r}) \cdot d, \quad (3)$$

with  $d = s_2 - s_1$  and  $\bar{r} = \frac{1}{2}(s_2 + s_1)$

after application of Newton's interpolation formula to solve the integral of Eq. (2). We now introduce  $F_{Norm}$ , the normalization factor of Eq. (1). Substituting this factor into Eq. (3) for the calibration factor function due to different readings  $\bar{r}_i$  we obtain

$$Caf(\bar{r}_i) = F_{Norm}(\bar{r}_i) \cdot Caf(\bar{r}_m) \quad (4)$$

with  $i$ =index of the mean reading at various reset screw positions and  $m$ =index of the mean reading with maximal difference  $d$ ,

because the product in Eq. (3) is a constant defined by  $\Delta \tilde{g}$ . Considering  $Caf(\bar{r}_m) = \text{const}$ , we get from Eqs. (2) and (4) and according to a well-known  $\Delta \tilde{g}$  from the observed differences on a calibration line:

$$Caf(\bar{r}_m) = \Delta \tilde{g} \left[ \int_{s_1}^{s_2} F_{Norm}(\bar{r}) d\bar{r} \right]^{-1}. \quad (5)$$

The calibration factor function  $Caf(r)$  is determined after selecting a suitable approximating function to satisfy the discrete values of  $F_{Norm}(\bar{r})$ . This function can be found by least squares fitting or applying spline algorithms. We take a Tschebyscheff polynomial of degree up to 5.

The calibration factor functions of the gravity meters D-8 and D-9 are calculated independently of each other

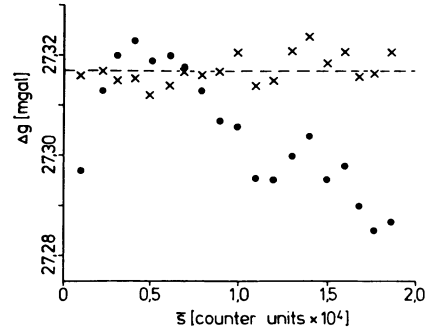


**Fig. 4.** Representation of measured gravity differences  $\Delta g$  as a function of the mean measuring screw position (D-8 meter) on the local line: ● calculated with constant calibration factor; × calculated with calibration factor function

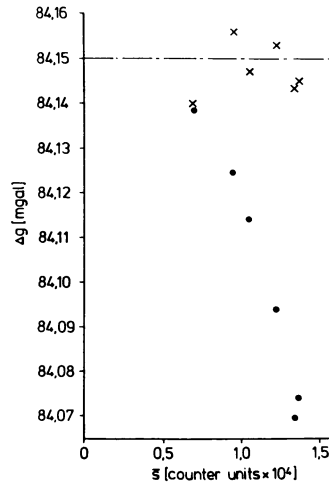


**Fig. 5.** Representation of measured gravity differences  $\Delta g$  related to the mean measuring screw position on the calibration line Torfhaus – Bad Harzburg (D-8 meter): ● calculated with constant calibration factor; × calculated with calibration factor function

by utilizing the gravity differences  $\Delta \tilde{g}$  mentioned at the beginning. They are also used to reinterpret the observations of the calibration lines (see also Fig. 5).

## Discussions

We are able to prove the quality of the calculated calibration factor functions of the last section by comparing the evaluations of those with a linear factor and those with a non-linear factor. In Figures 4 and 5 this comparison is presented with regard to the investigations of the D-8 gravity meter. First of all Fig. 4 shows calculation results with respect to various calibration factors on the local calibration line between Clausthal and Osterode. The observed differences of gravity are plotted as a function of the mean measuring screw position. It is evident that the reinterpretation with the function  $Caf(r)$  provides gravity differences, which deviate statistically from the mean value. In contrast, the interpretation with a fixed calibration factor clearly depends on the superposition of the measured results by a trend-function. The mean of the local gravity difference on the calibration line is

$$\Delta g = 27.317 \pm 0.004 \text{ mgal.}$$

The calculation of gravity differences on the ECL-section Torfhaus – Bad Harzburg demonstrates a significant improvement of the expected gravity differences in the same way: no systematic relationship with the mean measuring screw position is observed any longer. Thus, the calculated calibration factor satisfies real conditions in the gravity meter (see Fig. 5).

We have to emphasize that the nonlinearity can be determined by the method described only for a small reset range. Therefore the question of whether the observed nonlinearities are caused by mechanical defects of the measuring screw or by faults in the spring is unresolved. This question can not be answered before the investigations are repeated on other calibration lines and in different reset ranges of the gravity meter. To check and possibly improve the calculated calibration factor functions of the two gravity-meters D-8 and D-9, more test measurements are planned on local calibration lines in Vienna and Clausthal.

*Acknowledgements.* The authors wish to thank G. Lang for the realization of the measurements on the Clausthal calibration line and W. Große-Brauckmann for his helpful critical comments on this paper.

## References

- Dragert, H., Lambert, A., Liard, J.: Repeated precise gravity measurements on Vancouver Island, British Columbia. *J. Geophys. Res.* **86**, 6097–6106, 1981
- Götze, H.J., Rosenbach, O., Schöler, W.: Gravimetrische Untersuchungen in den östlichen Zentralalpen. *Geol. Rundsch.* **68**, 61–82, 1979
- Lambert, A., Liard, J., Dragert, H.: Canadian precise gravity networks for crustal movement studies: An instrumental evaluation. *Tectonophys.* **52**, 87–96, 1979
- Lambert, A., Liard, J.: Nonlinearities in LaCoste Romberg Model D gravimeters determined by the “Cloudcroft Junior” method. *Bull. D’Information of the Bureau Gravimetrique International*, **49**, Toulouse 1981
- Steinhauser, P.: Scale factor determination of a LaCoste and Romberg gravimeter Model D. *J. Geophys.* **44**, 395–396, 1978
- Steinhauser, P., Seiberl, W., Zych, D., Ruess, D.: Bestimmung des Bouguer-Schwerefeldes der Karawanken und der Sattnitz. *Mitt. Österr. Geol. Ges.* **71/72**, 299–306, 1980
- Torge, W., Kanngieser, E.: Periodic calibration errors of LaCoste-Romberg Model G and D gravity meters. *Veröff. d. DGK, Reihe B, Heft Nr.* **252**, 81–94, 1980

Received July 21, 1982; Revised version November 17, 1982  
Accepted December 2, 1982

*Short Communication***Ocean Tides and Periodic Variations  
of the Earth's Rotation**

H.-R. Baader, P. Brosche, and W. Hövel

Sternwarte der Universität Bonn, Auf dem Hügel 71, 5300 Bonn 1, Federal Republic of Germany

**Abstract.** We consider the periodic acceleration of the Earth's rotation rate caused by the oceanic  $M_2$ -tide and the corresponding cumulative effect in universal time UT1. The necessary information stems from a hydrodynamical model of the world's oceans. The time variations of the contributions to the relative angular momentum balance and of the solid Earth's center-of-mass are provided. As for the theoretical aspects, two hypotheses are examined: the 'quasi-isolated-Earth'-hypothesis, which is basic for the derivation of the  $\Delta\omega$ - and  $\Delta UT1$ -effects, is acceptable at least as a first-order approximation, whereas the idea of 'locked oceans' is not. The main result is a  $\Delta UT1$ -contribution with a total range of 0.05 ms, thus nearly detectable by means of modern observational techniques: this effect essentially originates from the tidal currents.

**Key words:** Earth's rotation –  $M_2$ -tide – Angular momentum balance of the oceans

**Introduction**

The "classical" effects of precession and nutation have been understood for a long time. They are a result of the reaction of a non-spherical rigid Earth exposed to the action of tidal torques from the Moon and the Sun. Later on, elastic deformations of the solid Earth were also taken into account. Recently, Yoder et al. (1981) re-studied the periodic tidal variations of the Earth's rotation rate and thereby, for the first time, estimated "the effect of fluid core and ocean tides on the dynamical motion of the Earth". They argued on the basis of two assumptions:

- Oceans act as if locked to the mantle;
- External torques are negligible, i.e., the Earth is an isolated system in a tidal period.

Because of the second assumption the whole Earth's angular momentum  $P_z = C\omega_z$  is conserved, and hence by means of the resulting relation:

$$\frac{\Delta\omega_z}{\omega_z} = -\frac{\Delta C}{C} \quad (1)$$

changes in  $\omega$  and in universal time UT are derivable from variations of  $C$  ( $C$ : polar moment of inertia,  $\omega_z$ : angular velocity of the whole Earth, the rotation vector is fixed

to the  $z$ -coordinate – as a permanent simplifying assumption hereafter).

The purpose of this note is to examine the above assumptions and to provide a more realistic view plus the corresponding estimates for the oceanic  $M_2$ -tide. Some aspects of the topic were already mentioned briefly by Brosche (1982).

Our main interest is dedicated to the secular influence of the oceanic tides on the Earth's rotation. Therefore, we regard the solid Earth only in a most rough and simple way, i.e. as a *rigid* sphere, except for its equilibrium tide response reducing the tangential forces of the ocean model by the Love factor  $\gamma = 1 + k - h = 0.69$ . The world's oceans in contrast are considered in detail (e.g. including shelf seas): our work is based on a modified version of Zahel's (1970) nonlinear  $4^\circ \times 4^\circ$ -HN-model (see also Brosche and Hoevel, 1982), mainly applied to the  $M_2$ -tide. The model output allows *direct* access to all angular momentum and moment of inertia quantities in their dependence on the tidal phase  $\tau = \sigma t$  ( $\sigma$ : angular velocity of the  $M_2$ -tide). Of course, any theoretical model of a partial oceanic tide provides for this information, at least in principle, but it seems unusual to publish the velocities too.

**Comments on Zahel's Model**

First we would like to comment on the apparently outstanding Zahel-model values for the  $M_2$ -tide given in a recent comparative compilation of certain characteristic parameters of diverse ocean models (Yoder et al., 1981). They seem unrepresentative to the authors of this paper, who are working with original and modified versions of the Zahel-model. One reason is that the  $M_2$ -effect on UT1 quoted in Table 4 of Yoder et al. (1981) is approximately twenty-six times greater than our corresponding  $\Delta UT1$ -amplitude of  $\sim 0.008$  ms (see Eq. 6). Also their harmonic coefficients  $h_{22}$  (Table 3) differ considerably from the values listed in Table 6.4 of Lambeck (1980), which show fair agreement with our findings. Our main argument against the reliability of that spherical harmonic analysis of Zahel's model is the very poor mass conservation (evident in the huge values of  $h_{00}$  in Table 3), whereas we find an excellent fulfillment of this essential constraint: the relative error in the water elevation is  $\frac{\Delta\zeta}{\zeta} \sim 10^{-13}$ , i.e. the defects of the mass balance would induce modifications of this order of magnitude. Furthermore, the reported "coordinate offsets of the

**Table 1.** Amplitudes of the  $M_2$ -variations of the solid Earth's center-of-mass ( $\delta\mathbf{S} = \mathbf{A} \cos \sigma t + \mathbf{B} \sin \sigma t$ ) relative to its time-average position (or also to the center-of-mass of the whole Earth) in  $10^{-3}$  m. From the origin the  $z$ -axis parallels the rotation vector, the  $x$ - and  $y$ -axes point towards the Greenwich meridian and  $90^\circ$  E, respectively

Component of vector $\delta\mathbf{S}$	A	B
$\delta x$	-1.5	3.6
$\delta y$	2.8	3.9
$\delta z$	-3.7	1.5

**Table 2.** Typical contributions (amplitudes) to the relative polar angular momentum balance of the world's oceans during an  $M_2$ -period (units:  $10^{21}$  kg  $m^2$   $s^{-2}$ ). The storage term results from the net effect of the other torques quoted. (Incidentally the Coriolis torque will counteract the changes in the moment of inertia in later context; the contribution of the pressure gradient force dominates the ocean-solid Earth interaction)

Torque due to	Order of magnitude
Tidal potential force (= oceanic-lunar interchange)	0.3
(Its period average = secular value)	$4.4 \times 10^{-5}$
Pressure gradient force	2.0
Coriolis force	0.8
Lateral eddy viscosity	$10^{-2}$
Bottom friction	$2 \times 10^{-3}$
Storage (= time variation of angular momentum)	3.0

center-of-mass of mantle" (i.e. of mantle-plus-core relative to the position of the whole Earth's barycenter, according to their calculation; see Tables 3 and 5) are also too high compared to our  $10^{-3}$  m-order results for the modified Zahel-model in Table 1.

### The Mechanical Isolation Hypothesis

As is shown by Table 2, with its estimates of the contributions to the oceanic angular momentum balance, the neglect of the angular momentum transfer to the Moon via the tidal potential forces (listed in the first line) is a first-order approximation during an  $M_2$ -period (Baader, 1982). In particular, the first two figures are remarkable because of the fact that we cannot infer a negligible role of the potential force term during the period (mainly due to the 'undisturbed' ocean depth) from its very small time average (effect of the 'disturbed' water elevation).

On the other hand, this periodic transfer of angular momentum between the water and the Moon is only a part of the total interchange between the Earth and its satellite. From the fact that the geoid has tesseral undulations which are one order of magnitude smaller than the depth of the oceans (Gaposchkin, 1974) we now conclude that the total periodic change of the Earth's angular momentum is correspondingly smaller than the value in the first line of Table 2. We therefore accept the quasi-isolation hypothesis of the Earth at least in the sense indicated above.

In principle we should have listed a term depending

on the total time derivative of  $\omega$  in Table 2. During an  $M_2$ -period  $\dot{\omega}$  is of the order  $10^{-17}$   $s^{-2}$ ; its contribution to the oceanic angular momentum balance consequently is of the order  $10^{17}-10^{18}$  kg  $m^2$   $s^{-2}$  and thus of relative order  $10^{-3}-10^{-4}$  (as can easily be estimated by means of the isolation hypothesis via Eq. (5) or by means of the solid Earth's angular momentum balance). Its effect is therefore neglected, as usually.

### The Influence of the Tidal Currents

From the different mechanisms changing the oceanic angular momentum we shall now go on to discuss the manifestations of its contents. We then have to consider the time variability of only two kinds of oceanic quantities:

- the variation of the inertia tensor  $\theta$  due to changing water elevations,
- the relative water motion (in the terrestrial frame) corresponding to a relative angular momentum  $P_r$ .

Therefore the total oceanic angular momentum is no longer

$$P_z = \theta_{zz} \omega \quad (2)$$

( $z$ -component only;  $\theta_{zz}$  is the oceanic part of  $C$ )

$$\text{but } P_z = \theta_{zz} \omega + P_{rz} = P_{\theta z} + P_{rz}, \quad (3)$$

(Lambeck, 1980; Munk and MacDonald, 1960).

The idea of 'locked oceans' means that the  $P_{\theta z}$  contribution should dominate. If for the moment we regard only the time dependent parts and out of these, the overwhelming harmonic ones (see also Baader, 1982), we obtain

$$\begin{aligned} P_{\theta z}(\tau) &= 6.93 \sin(\tau + 41.4^\circ) \quad 10^{24} \text{ kg m}^2 \text{ s}^{-1} \\ P_{rz}(\tau) &= 24.6 \sin(\tau - 189.5^\circ) \quad 10^{24} \text{ kg m}^2 \text{ s}^{-1} \\ \text{hence} \\ P_z(\tau) &= 20.93 \sin(\tau - 204.39^\circ) \quad 10^{24} \text{ kg m}^2 \text{ s}^{-1}. \end{aligned}$$

It can be seen that the amplitude of  $P_{rz}$  is larger than that of  $P_{\theta z}$  by a factor 3 and that the phase angles are completely different. Therefore we conclude that the hypothesis of 'locked' oceans is not justified and should be discarded - at least for the  $M_2$ -tide, as Yoder et al. (1981) were already inclined to do. Nevertheless it is possible that loading and self-attraction lead to a slightly stronger coupling to the solid Earth.

Our  $P_{rz}$  corresponds to a typical zonal relative velocity of the oceans  $u = 4 \times 10^{-3}$  m  $s^{-1}$ , (which may be converted to a differential rotation of the order  $\omega_{rOC} = u/R \sim 6.3 \times 10^{-10}$   $s^{-1}$ ; subscript  $OC$  for ocean,  $R$ . Earth's radius).

### The Effects in $\omega$ and UT

In what follows our line of reasoning very much resembles that of previous treatments of the atmospheric aspect of the topic (Hide et al., 1980). If we assume a rigid solid Earth ( $SE$ ), the change of its angular momentum will be

$$\Delta P_{SE} = -\Delta P_{OC}, \quad (4)$$

because of the conservation in the whole  $SE-OC$  system (i.e. neglecting the atmosphere). Consequently

$$\Delta \omega_{SE} = \Delta P_{SE} / \theta_{SE} = -\Delta P_{OC} / \theta_{SE}. \quad (5)$$

By means of (5) we relate the changes of the oceanic quantities  $P_{\theta z}$ ,  $P_{rz}$ ,  $P_z$  to the changes in  $\omega$  (dropping the subscript

$SE$  because  $\omega$  is the same for the oceans in our definition of relative motions). We use  $\theta_{SE} = 0.804 \times 10^{38} \text{ kg m}^2$  (Lambeck, 1980). If one considers a decoupled mantle only, then  $\theta_{\text{mantle}} = 0.71 \times 10^{38} \text{ kg m}^2$ , and the following values should be raised by a factor of 1.13.

$$\begin{aligned} \Delta\omega &= 8.62 \sin(\tau - 138.6^\circ) \quad 10^{-14} \text{ s}^{-1} \text{ due to the moment} \\ &\text{of inertia only,} \\ &= 30.60 \sin(\tau - 9.5^\circ) \quad 10^{-14} \text{ s}^{-1} \text{ due to relative} \\ &\text{motions only,} \\ &= 26.03 \sin(\tau - 24.39^\circ) \quad 10^{-14} \text{ s}^{-1} \text{ due to the com-} \\ &\text{bined effect.} \end{aligned}$$

A time integration leads to the change in UT1:

$$\Delta\text{UT1} = \int \frac{86400}{2\pi} s \Delta\omega dt \quad (6)$$

$$\begin{aligned} \Delta\text{UT1} &= 0.008 \text{ ms} \sin(\tau + 131.4^\circ) \quad \text{due to the moment of} \\ &\text{inertia, only,} \\ &= 0.030 \text{ ms} \sin(\tau - 99.5^\circ) \quad \text{due to relative} \\ &\text{motions only,} \\ &= 0.025 \text{ ms} \sin(\tau + 245.61^\circ) \quad \text{totally.} \end{aligned}$$

It should be noted that the total range of 0.05 ms runs close to the measurement accuracy of Very Long Baseline Interferometry and Lunar Laser Ranging. In the case of fortnightly tides the  $\Delta\text{UT1}$ -effect is presumably even more important.

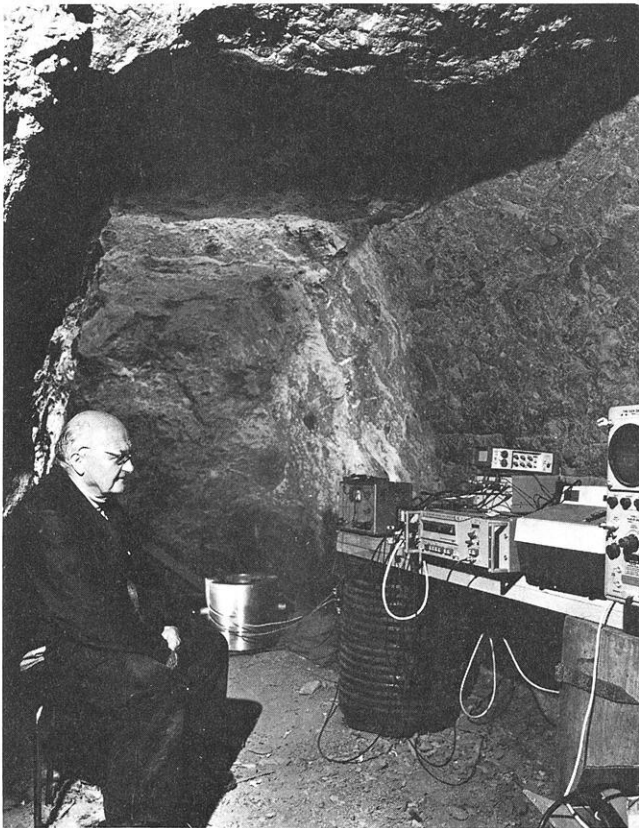
## References

- Baader, H.-R.: Balance problems in tidal computations. In: Tidal Friction and the Earth's Rotation, P. Brosche, J. Sündermann, eds., pp. 122–164. Berlin, Heidelberg, New York: Springer, 1982
- Brosche, P.: Oceanic tides and the rotation of the Earth. In: Sun and Planetary System, W. Fricke, G. Teleki, eds.: pp. 179–184. Dordrecht: D. Reidel Publ. Comp. 1982
- Brosche, P., Hövel, W.: Tidal friction for times around the present. In: Tidal Friction and the Earth's Rotation, P. Brosche, J. Sündermann, eds.: pp 175–182. Berlin: Springer, 1982
- Gaposchkin, E.H.: Earth's gravity field to the eighteenth degree and geocentric coordinates for 104 stations from satellite and terrestrial data. *J. Geophys. Res.* **79**, 5377–5411, 1974
- Hide, R., Birch, N.T., Morrison, L.V., Shea, D.J., White, A.A.: Atmospheric angular momentum fluctuations and changes in the length of the day. *Nature* **286**, 114–117, 1980
- Lambeck, K.: The Earth's variable rotation: geophysical causes and consequences. London: Cambridge University Press 1980
- Munk, W.H., MacDonald, G.J.F. The rotation of the Earth, a geophysical discussion. London: Cambridge University Press 1960
- Yoder, C.F., Williams, J.G., Parke, M.E.: Tidal variations of Earth rotation. *J. Geophys. Res.* **86**, 881–891, 1981
- Zahel, W.: Die Reproduktion gezeitenbedingter Bewegungsvorgänge im Weltozean mittels des hydrodynamisch-numerischen Verfahrens. Mitt. Institut für Meereskunde, 17, University of Hamburg 1970

Received September 1, 1982; Revised version November 16, 1982  
Accepted November 26, 1982

*In Memoriam***Anton Graf****(1901–1981)**

Im September 1981, wenige Monate nach Vollendung seines 80. Lebensjahres verstarb Prof. Dr.-Ing. Anton Graf, langjähriges Mitglied der Deutschen Geophysikalischen Gesellschaft. Mit ihm ist ein ungemein vielseitiger und unermüdlich tätiger Forscher und akademischer Lehrer dahingegangen.



Anton Graf wurde am 26. Mai 1901 in Holzkirchen (Niederbayern) als neuntes von zehn Kindern des Oberlehrers Ludwig Graf und seiner Ehefrau Josefa geboren. Seine Ausbildung und sein beruflicher Werdegang sind durch folgende Stationen gekennzeichnet:

- 1907–1914 Volksschule in Holzkirchen; vorgesehen war eine anschließende Ausbildung als Buchdrucker
- 1914–1923 Realschule und Humanistisches Gymnasium in Straubing; Abitur
- 1923–1927 TH München – Studienfach „Technische Physik“; Dipl.-Physiker
- 1927–1928 Fa. Hartmann und Braun, Frankfurt/M.; Laborphysiker
- 1928–1932 Fa. Piepmeyer und Co., Kassel; Geophysiker

- 1932 Promotion zum Dr.-Ing., TH Berlin-Charlottenburg
- 1933–1945 Fa. Askania-Werke, Berlin-Friedenau; Leiter der geophysikalischen Abteilung
- ab 1946 – O.v. Miller-Polytechnikum, München; Dozent für Experimentalphysik und Feinmeßtechnik
- Universität und Technische Hochschule, München; Lehraufträge „Angewandte Geophysik“
- Freier Mitarbeiter bei Askania-Werke, Berlin
- 1953 Habilitation, TH München
- 1959 apl. Professor, TH München

Diese kurze Aufzählung der Stationen zeigt bereits, daß es sich dabei nicht um den Standardweg für ein spezifisches Berufsbild handelt, sondern daß dahinter auch starke persönliche Komponenten verborgen sein müssen. Das wahre Ausmaß an Individualität und Kreativität des Wissenschaftlers Anton Graf ist wohl am besten über eine Synopsis seiner Arbeiten und Erfolge erkennbar:

*Der Theoretiker und Praktiker der Angewandten Geophysik.* Bei der Fa. Piepmeyer wurden A. Graf Entwicklungsaufgaben auf dem Gebiet der Geoelektrik übertragen. Er verbesserte die induktiven Methoden und erprobte sie mit gutem Erfolg an Kupfer- und Bleierzvorkommen in Südspanien und Chile. – Hierzu ist als Hauptergebnis seine Dissertation zu nennen:

„Theoretische Grundlagen der Ringsendemethode“ (Beitr. z. Angew. Geoph. 4, 1–76, 1934)

Diese Abhandlung weist den Verfasser als hohen Können sowohl der Physik als auch der Mathematik aus, der auch die zugehörigen numerischen Berechnungen durchführt, um seine Ergebnisse für die Praxis anwendungsreif zu machen.

Eine spätere Fortsetzung dieser Arbeitsrichtung bildet die Habilitationsschrift:

„Über die Möglichkeit der Aufsuchung von Grund- und Salzwasserhorizonten vermittels induktiver geoelektrischer Methoden“

A. Graf beschäftigte sich mit der Theorie nicht um ihrer selbst willen, sondern als richtungsweisende Grundlage für die praktische Anwendung; umgekehrt regte ihn jede Aufgabe der Praxis zwangsläufig zu tieferer theoretischer Durchdringung an.

*Der Konstrukteur geophysikalischer Instrumente.* Die Hauptverdienste und die größten Erfolge des Wissenschaftlers Anton Graf liegen auf dem Gebiet des Instrumentenbaus, auf dem er seit seinem Eintritt in die Askania-Werke nahezu 45 Jahre lang intensiv tätig war. Kennzeichnend für seine individuelle Arbeitsweise war seine Fähigkeit, Neuentwicklungen zu konzipieren und von der Konstruktion bis zur Fertigungsreife zu führen; selbstverständlich wurden dabei sämtliche theoretischen und experimentellen Grundlagen mit größter Sorgfalt analysiert, insbesondere mögliche Störeinflüsse wohl durchdacht und Maßnahmen zu ihrer Beseitigung getroffen.

Die von A. Graf geschaffenen Geräte sind Meßinstrumente höchster Präzision, alle genial im Konzept wie in der Ausführung und bahnbrechend für die geophysikalische Meßtechnik. Sie sind ein Spiegel der Fähigkeiten ihres Schöpfers: Hohe physikalisch-mathematische Begabung, Phantasie und Erfindungsreichtum sowie beweglicher und kritischer Verstand, glücklich ergänzt durch Geschicklichkeit und Ausdauer in der Experimentierkunst.

Die eindrucksvollsten Leistungen des Konstrukteurs Anton Graf sind manifestiert in den nachstehend aufgeführten geophysikalischen Instrumenten, die jedes für sich weltweite Publizität und Anerkennung gefunden haben:

- Askania-Gravimeter, „großes“ Gerät, ca. 1937/38
- Askania-Gravimeter, „kleines“ Gerät, ca. 1941/42
- Askania-Mikrobarometer, für barometrische Höhenmessung, ca. 1950
- Askania-Seegravimeter, ab ca. 1956
- Askania Bohrloch-Vertikalpendel, ab ca. 1962

Viele dieser Geräte werden noch heute im In- und Ausland benutzt.

Das bei den Askania-Werken durch die Tätigkeit von A. Graf entstandene Geophysikalische Geräteprogramm wurde Mitte der 70er Jahre von der Fa. Siemens auf die Fa. Bodenseewerke Geosystem, Überlingen, übertragen. Für die vom Bodenseewerk vorgenommene grundlegende Modernisierung und Weiterentwicklung war A. Graf stets zu ausführlicher Beratung bereit, um aus dem reichen Schatz seiner Erfahrungen wertvolle Anregungen zu geben.

Eine derartig vielseitige und erfolgreiche Tätigkeit findet zwangsläufig ihren entsprechenden publizistischen Niederschlag; hierzu ist summarisch zu verzeichnen:

- ca. 50–60 Publikationen, darunter 2 Bücher
- ca. 30 Patente im In- und Ausland
- unzählige Vorträge auf Tagungen wissenschaftlicher Gesellschaften, bei Universitäten usw., in Europa und in Übersee, insbesondere in USA und Japan

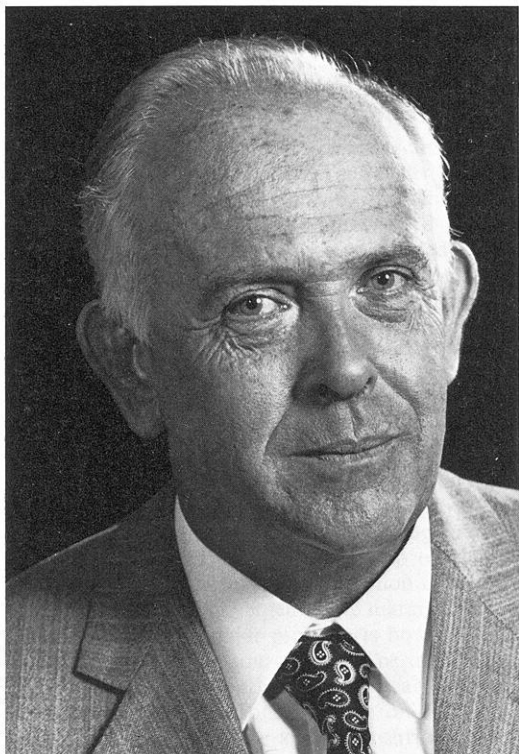
Das aus der bisherigen Übersicht der Erfolge erkennbare Bild des Wissenschaftlers wäre nur recht unvollständig, wenn man die dahinter stehende Persönlichkeit nicht berücksichtigen würde: Als Mensch war er gekennzeichnet durch großen Charme und ausgesprochene Bescheidenheit. Diese Wesenszüge waren in ihm so tief verwurzelt, daß sie niemals irgendwie angetastet werden konnten, sei es durch die erreichten großen Erfolge oder durch die dafür erhaltene Anerkennung.

Anton Graf war bis in seine letzten Lebensjahre dem geophysikalischen Instrumentenbau eng verbunden. Er arbeitete an verschiedenen, auch von der Deutschen Forschungsgemeinschaft geförderten Entwicklungsvorhaben. Das diesem Nachruf beigegebene Bild, das einem DFG-Bericht vom November 1976 zum Forschungsvorhaben „Modernisierung des Pendelapparates“ entstammt, zeigt einen Meßplatz in einem Stollen des Salzbergwerks Berchtesgaden, an dem die Neuentwicklung (unten links in der Bildmitte) auf Herz und Nieren geprüft wird. Vor der Apparatur als aufmerksamer Beobachter, erkennbar in tiefer Konzentration und geduldiger Ausdauer, mit seinen leidenschaftlich geliebten Instrumenten gewissermaßen stille Zwiesprache haltend:

#### **Anton Graf**

Dem verstorbenen, hochgeachteten Kollegen werden die Deutsche Geophysikalische Gesellschaft sowie alle seine Freunde im In- und Ausland ein ehrendes Gedenken bewahren.

O. Rosenbach W. Gauthier

*In Memoriam***Jürgen Henning Illies****March 14, 1924 – August 2, 1982**

The International Committee for the Lithosphere mourns the loss of Henning Illies, member of its bureau and secretary of its former steering committee. He was courageously fighting a serious illness and was engaged in research work up to the last moment.

He studied at the universities of Halle and Hamburg where he received his Ph.D. in 1948 and the *venia legendi* for Geology and Palaeontology in 1951. In 1953 he entered the field of his future research when he became a lecturer at the University of Freiburg in the Rhinegraben. In 1958, after a two years stay at the University of Valdivia/Chile, he accepted a call to the University of Karlsruhe where he was appointed full professor and director of the Geological Institute in 1963. Soon he perceived the vicinity of Karlsruhe as a key-region for the understanding of graben tectonics which fascinated him so much that he declined several offers from other universities. At his initiative a very close cooperation developed with colleagues from Geophysics,

Geodesy, Rock Mechanics and Petrology leading to several major joint ventures, which, because of their design, became known as the Karlsruhe model for research projects in geosciences. He introduced in-situ stress measurements as a means of better understanding the causes of recent tectonics in Southwestern Germany.

To grasp graben formation not only as a local phenomenon but as a worldwide tectonic element, he travelled for comparative studies in East Africa, the Jordan graben, lake Baikal, Malta and the Rio Grande Rift as well as the Basin and Range Province. In addition to numerous scientific papers this research was documented in the trilogy: *Graben Problems* (1970, with St. Müller), *Approaches to Taphrogenesis* (1974, with K. Fuchs) and *Mechanism of Graben Formation* (1981). A growing number of symposia and meetings on continental rifts were organized by him in and nearby Karlsruhe.

Henning Illies was engaged in various scientific societies. The German Quaternary Society appointed him as council member from 1960–1965. For the Upper-Rhenisch geological Society he served as president (1964–71) and vice-president (1972–77). For the Geologische Vereinigung (Geological Society) he was appointed member of the board (1974–77) and vice-president since 1978. In 1973 he accepted a call to become member of the Deutsche Akademie der Naturforscher Leopoldina in Halle. In 1978 he became a Fellow of the Geological Society of America. The German Geological Society granted him the Hans-Stille-Medal in 1981.

Henning Illies served actively on various international committees. During the International Geodynamics Project he was the representative of the Federal Republic of Germany and, at the same time a member of Working Group 4 (Geodynamics of continental and oceanic rifts). In 1976 he was appointed a member of the Working Group "Interpretation" by the International Commission on Recent Crustal Movements.

A climax in his international involvement was certainly the leading role he played in the initiation of the new International Lithosphere Project. Under the chairmanship of Carl Kisslinger and Henning Illies the joint IUGG and IUGS Task Group prepared a document which was adopted after thorough discussions, by the two Unions and finally also by ICSU. In January 1981 the new Inter-Union Commission on the Lithosphere was born and Henning Illies served as one of the five bureau-members until his end.

His death is not only felt in international science but also greatly in the Federal Republic of Germany. In 1972 he became chairman of the National Committee for the Geodynamics Project, in 1975 he was appointed as a member of the Senate Commission for Geoscience of the German Research Society. From 1976 to 1982 he served as coordinator of the major priority research program "Vertical movements and their causes exemplified by the Rhenish Shield", sponsored by the German Research Society.

Henning Illies is survived by his wife Gisela who shares his enthusiasm for geology. Nearly 120 publications by

Henning and 15 by Gisela Illies are the result of this partnership in research.

In 1979 a serious illness befell Henning Illies. A critical operation caused severe impediment which he fought with tremendous courage and energy, even after it became evident that there were only months, weeks, or days left.

All those who have worked closely with Henning Illies will miss his enthusiasm, his encyclopaedic knowledge, his critical mind, the refreshing humour with which he mastered many difficult situations, and, especially, the ability with which he led and encouraged people, freely sharing his ideas. We will miss Henning Illies. Karl Fuchs

## Book Reviews

**Gill, J.: Orogenic Andesites and Plate Tectonics, Minerals and Rocks.** Springer, Berlin Heidelberg New York, 390 pp., 1981.

Almost all volcanic activity on Earth is confined to plate margins. The largest volume of volcanic rock is produced at accreting margins at ocean ridges. Most volcanoes are located at convergent plate margins where lithosphere is subducted into the mantle. These volcanoes are arranged in long narrow chains that parallel the ocean trenches which mark the downward bending of the lithosphere. A major constituent rock type erupted from these volcanoes is Andesite which is chemically and petrologically different from basalts, the major rock extruded at ocean ridges. Conversely, Andesites are primarily associated with convergent plate boundaries. According to Gill, the term Andesite was introduced by the German geologist Leopold von Buch to distinguish from the European trachytes the rocks brought to Germany from the Andes by Alexander von Humboldt. Gill defines Andesites as hypersthene – normative volcanic rocks with 53–63% silica. Orogenic Andesites are defined as a subset characterized by low titanium and potassium. Ironically, von Buch's rock (which is no longer available) would stand a good chance to fail Gill's criteria of being Andesite.

Interpretation of data with the help of plate tectonic theory led to the suggestion that the production of Andesites (and other rocks that erupt at convergent plate margins) is linked to the subduction process. A major problem is how enough heat could be generated to melt the source rock. The descending lithosphere is more of a heat sink rather than a heat source. A heat source frequently cited is frictional heating on the fault zone between the subducting lithosphere and the overriding mantle. A detailed understanding of the peculiarities of Andesites is vital to any assessment of geophysical models of its magma generation. Moreover, Andesites are similar in composition to the continental crust and may be important agents of continental growth. Also, andesitic magma are likely sources of ore deposits.

Gill compiled and critically synthesized an overwhelming amount of chemical, petrographical, and geophysical data on Andesites in chapters 1–7 which he calls the core of his book. These chapters (annotating more than 1100 references) provide an enormous source of information for everybody interested in the subject. Chapter 1 deals with the difficulties of defining Andesites and arrives at the above cited definition. Chapter 2 discusses the occurrence of Andesites in different plate tectonic environments. Chapter 3 reviews the geophysical characteristics of subduction zones, while chapter 4 summarizes the physical characteristics of Andesite magma. Chapter 5 gives a detailed discussion of major and trace element chemistry, chapter 6 a description of the mineralogy of Andesites, while chapter 7 discusses the variations in magma composition in time and along and across volcanic arcs. Chapters 8–12 are more interpretive (and also more speculative). They discuss the role of the subducted crust, the overlying mantle wedge, the crust underlying Andesite volcanoes, and the process of basalt differentiation in Andesite genesis. These chapters pave the way to

Gill's conclusion that "differentiation of basalt by crystal fractionation of anhydrous minerals at low pressure is the most frequent and most fundamental process of orogenic Andesite genesis". The link to subduction is not direct but occurs through the formation of the primary melt. Whether one is willing or not to agree to all the conclusions (this reviewer is not quite satisfied with Gill's evaluation of the shear heating process and magma ascent theories), this book is an outstanding source of information and provides a stimulating discussion. The book is highly recommended for all geoscience libraries.

**T. Spohn**

*National Research Council. Geophysics Study Committee:*

Continental Tectonics ser.: Studies in Geophysics. National Academy of Sciences, Washington, D.C., 197 pp., 1980 (Off. Publ. Nat. Acad. Sci., 2101 Constitution Ave., N.W. Washington, D.C. 20418 USA)

'Continental Tectonics' is something between an internal study group report to a science decision making agency and a book for the scientific public or it is both things in one. It was written in 16 individual papers by the members of a Panel on Continental Tectonics chaired by B.C. Burchfield (MIT), J.E. Oliver (Cornell), and L.T. Silver (Caltech), "to provide assessments from the scientific community to aid policymakers in decisions on societal problems that involve geophysics. An important part of such an assessment is an evaluation of the adequacy of present ... knowledge ...". "This study ... was motivated by ... problems ... involving natural hazards .... The thesis of this report is that more reliable scientific input to the decisions ... can be provided only with a much improved basic understanding of continental tectonics". "The study was developed through meetings ... and presentation of papers in preliminary form at the American Geophysical Union meeting in Miami in April 1978 ... the authors had the benefit of discussion ... as well as the comments of several scientific referees". "They provide examples of our current basic geophysical knowledge of the architecture and processes on the continents. They also pose many of the fundamental questions and uncertainties that require additional research. The essays allude to several practical applications ...".

These quotations from the Preface give a good impression of the character and intention of the report. It begins with an "Overview and Recommendations", followed by a "Summary" of "Plate Tectonics and the Continents: A Review" by B.C. Burchfield and "Problems of Pre-Mesozoic Continental Evolution" by L.T. Silver. The second chapter is on "Plate Boundary Tectonics" covering "Complexities of Modern and Ancient Subduction Systems" (W.B. Hamilton); "Intracontinental Rifts and Aulacogens" (K. Burke), and "Evolution of Outer Highs on Divergent Continental Margins" (M.A. Schuepbach and P.R. Vail). Chapter III

on "Intraplate Tectonics" contains four papers: "Tectonics of Noncollisional Regimes – The Modern Andes and the Mesozoic Cordilleran Orogeny..." (B.C. Burchfield); "Models for Midcontinent Tectonics" (W.J. Hinze, L.W. Braile, G.R. Keller, E.G. Lidiak); "Problems of Intraplate Extensional Tectonics, Western U.S." (G.A. Davis); "Geophysical and Geological Characteristics of the Crust of the Basin and Range Province" (G.P. Eaton). Chapter IV on "Characterization of Continental Crust": "Seismic Exploration of the Continental Basement" (J.E. Oliver); "Exploration of the Continental Crust Using Aeromagnetic Data" (I. Zietz); "Chemistry of the Lower Crust: Inferences from Magmas and Xenoliths" (R.W. Kay, S. Mahlburg Kay); and "Geochemical Evolution of the Continental Crust" (G.N. Hanson). Finally the fifth chapter concentrates on "Continental Evolution": "Cenozoic Volcanism in the Western United States: Implications for Continental Tectonics" (P.W. Lipman); "The Shape of North America during the Precambrian" (W.R. Muehlberger); and "An Outline

of the Tectonic Characteristics of China" (T.K. Huang: essentially a reprint from *Eclogae Geol. Helv.*, **71**, 611–635, 1978).

The above demonstrates the broad spectrum of the earth sciences covered in the report. This series of "Studies in Geophysics" covers geophysics in the widest possible sense, it is a good example of a truly interdisciplinary approach, not a mere profession of interdisciplinarity.

The papers represent the state of the art and define topical questions. Much is to be learned from them, particularly about North American geology.

I feel every report to an administrative body should be written in a similar fashion as this one was, i.e. publishable to the scientific public, clearly written, somewhat tutorial, stimulating. Other kinds of reports should not be written at all. I recommend "Continental Tectonics" to those who are interested in doing research on continental tectonics and to those who request earth scientists to write reports.

**W.R. Jacoby**

## Preface

The present special issue of Journal of Geophysics comprises articles which are based on papers given at the recent European Geophysical Society symposium on "Plasma and Energetic Particles in the Magnetosphere", EGS Meeting, 23–27 August 1982, Leeds, UK.

The symposium was held at a time when a wealth of data from a number of spacecraft devoted to the study of the magnetosphere (HEOS, GEOS, ISEE, PROGNOZ) had been sufficiently digested to draw a more comprehensive picture of the dynamical processes acting within the magnetosphere. Improved instrumentation allowed identification of the ion species contributing to the cold and hot magnetospheric plasma. It seems to become increasingly clear that ions heavier than hydrogen cannot always be treated as minor tracer ions, but often dominate the plasma population and may play an important role in the wave-particle interaction. The ionosphere and the solar wind plasma both seem to be the source of the plasma in the magnetosphere. Recent results from Dynamics Explorer indicate that ionospheric ion beams flow out from the polar caps

and may be as important a source of the tail-lobe plasma as the polar wind. High temporal resolution and simultaneous observation on two or more spacecraft at different positions (e.g. ISEE-1 and -2) in the magnetosphere allowed the separation of temporal and spatial structures necessary to study various boundary phenomena in the magnetosphere.

In order to summarize the present knowledge of the magnetospheric dynamics the major part of the symposium was devoted to invited speakers.

The special issue follows basically the order of the symposium. Unfortunately, not all papers materialized. Nevertheless, this issue will give a good overview of the present knowledge of the physics of the magnetosphere, useful to the interested scientific community.

The Journal Editor thanks all the referees for their efforts and support.

D. Hovestadt  
J. Untiedt

## Review Article

## Global Pattern of Auroral Ion Precipitation: A Review of the Results from the AUREOLE-1 and AUREOLE-2 Satellites

J. Crasnier<sup>1</sup>, J.A. Sauvaud<sup>1</sup>, F. Cambou<sup>1</sup>, V.A. Gladyshev<sup>2</sup>, R.A. Kovrazhkin<sup>2</sup> and Yu.I. Galperin<sup>2</sup>

<sup>1</sup> Centre d'Etude Spatiale des Rayonnements, CNRS-Toulouse University, BP 4346 – 31029 Toulouse Cédex, France

<sup>2</sup> Space Research Institute (I.K.I.), USSR Academy of Sciences, 117810 Moscow, USSR

**Abstract.** The ion measurements (0.2–30 keV) made on-board the AUREOLE-1 and 2 polar orbiting satellites are reviewed in order to construct a synthetic global pattern of the auroral ion precipitation. The more prominent features of the picture obtained can be summarized as follow: (1) A narrowly localized zone of the near-noon direct penetration of magnetosheath protons in the dayside cusp, located *inside* the dayside auroral oval. (2) A low energy ion precipitation ( $E < 3$  keV) at the polar border of the nightside auroral oval occurring during periods of very quiet magnetic conditions and after storm recovery. (3) A continuous and homogeneous band of proton aurora all along the auroral oval due to adiabatic drift of plasmashet protons ( $E > 1-3$  keV) in the magnetosphere, accompanied by their pitch angle scattering above the diffuse auroral zone. (4) The presence in diffuse aurora of a less regular but denser soft ion component ( $E < 1-3$  keV) in the precipitation spectra. (5) A morning sector, substorm-related, low energy proton (ion) precipitation dispersive structure at auroral and sub-auroral latitudes due to the differential eastward drift of particles after substorm injection (with the lowest energy part presumably of ionospheric origin).

This global pattern is discussed in the context of the distribution of the various plasma domains in the outer magnetosphere.

**Key words:** Auroral ion precipitation – Polar cusp – Acceleration – Convection

### Introduction

Studies of the so-called “proton aurora” have constituted a typical aim of auroral investigations over the last few decades (Chamberlain, 1961; Eather, 1967; Vallance Jones, 1974). Although there are far fewer experimental results on the ion than on the electron component of auroral pre-

cipitation, direct measurements of the precipitating energetic protons responsible for the proton aurora were made before the ARCAD project from several near-earth polar satellites: ESRO-1 (Hultqvist, 1973; 1979), INJUN-5 (Frank and Ackerson, 1971; Frank, 1975), ISIS (Heikkila, 1972), COSMOS-261 and COSMOS-348 (Kovrazhkin, 1976).

It became clear from these results that the flux of precipitating auroral protons rarely exceeds  $10^7$  particles ( $\text{cm}^2 \cdot \text{s} \cdot \text{sr} \cdot \text{keV}^{-1}$ ) and that their average energy is of the order of 10–30 keV in the evening sector of the proton auroral band during substorms. During magnetically quiet periods the sensitivity and spectral range of the spectrometers used on these satellites were not adequate to study much less intense proton precipitation.

The French-Soviet ARCAD experiments, launched aboard the polar satellites AUREOLE-1 and 2, were designed to allow the study of these quiet-time low ion fluxes. Nevertheless, they revealed (and for the first time analysed in detail) the prominent features of the auroral ion precipitation:

- A narrowly localized zone for the near-noon direct penetration of magnetosheath protons in the dayside cusp.
- A continuous and homogeneous band of proton aurora all along the auroral oval ( $E > 1-3$  keV) due to adiabatic drift of plasmashet protons in the magnetosphere. Also, for the diffuse aurora, an additional soft ion component  $< 1$  keV in the precipitation spectra observed at all local times,
- A low-energy ion precipitation ( $E < 3$  keV) at the polar border of the nightside auroral oval.
- A morning sector low-energy ion precipitation at auroral and sub-auroral latitudes due to the differential eastward drift of particles after a substorm injection.

In this paper the essential characteristics of these regions will be reviewed in the context of the distribution of the various hot plasma domains in the outer magnetosphere.

### Dayside Polar Cusp

The shape of the region at the ionospheric projection of the magnetosheath plasma penetration into the magneto-

Based on a paper given at the Symposium on Plasma and Energetic Particles in the Magnetosphere, EGS Meeting, 23–27 August 1982, Leeds, U.K.

Offprint requests to: J. Crasnier

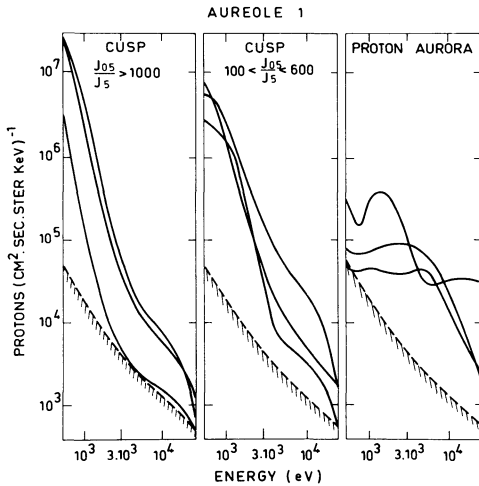


Fig. 1. Typical proton energy spectra at the dayside cusp and at the dayside auroral oval near magnetic noon

sphere was first considered as a more or less homogeneous band along the dayside auroral oval  $08 \text{ h} \lesssim \text{MLT} \lesssim 16 \text{ h}$  with a latitudinal width of several degrees (Winningham, 1970; Heikkila et al., 1972; Vasyliunas, 1974). This has led to the widely adopted concept of a free penetration of magnetosheath plasma through an ever present cleft-like magnetic field branching structure extending from the dawn side to the dusk side, through noon. An initial analysis of the ARCAD results appeared to contradict this proposed pattern (Gladyshev et al., 1974). The shape of the polar

cusps has been studied extensively from the ARCAD experiment by using nearly simultaneous, sequential oblique crossings on the same polar pass. The proton precipitations were categorized by their spectra. The magnetosheath-like spectra were defined according to the following criteria: the ratio  $\alpha$  of the differential flux at 0.5 keV to that at 5 keV is greater than 100; the hot proton density  $N_p$  is higher than  $1\text{--}3 \text{ cm}^{-3}$ . It was assumed that such high densities of energetic particles at the dayside can be reached only in the magnetic flux tubes that are (or recently were) directly connected to the magnetosheath and filled with solar wind plasma. Spectra with lower values of  $\alpha$  and  $N_p$  were considered as plasmasheet-like (Fig. 1) and were actually observed in all local time sectors along the auroral oval.

These soft protons with the magnetosheath-like spectra were found only near the magnetic noon meridian in a narrowly localized zone lying at auroral latitudes (Figs. 2 and 3) poleward of the so-called "sharp trapping boundary" (Cambou and Galperin, 1974a, b, 1982; Gladyshev et al., 1974; Sauvaud et al., 1980; Muliarchik et al., 1982). It turned out that this region can be non stationary (intermittent), and that this localisation indicates a funnel pattern of the cusp region at the magnetopause in contradiction to the longitudinally extended cleft inferred by other experimenters (Sauvaud et al., 1980).

Furthermore, it was recently shown (Muliarchik et al., 1982) by the analysis of simultaneous measurements of protons and electrons from the ARCAD experiment that the above mentioned near-noon area of soft protons with temperatures and fluxes similar to those in the magnetosheath

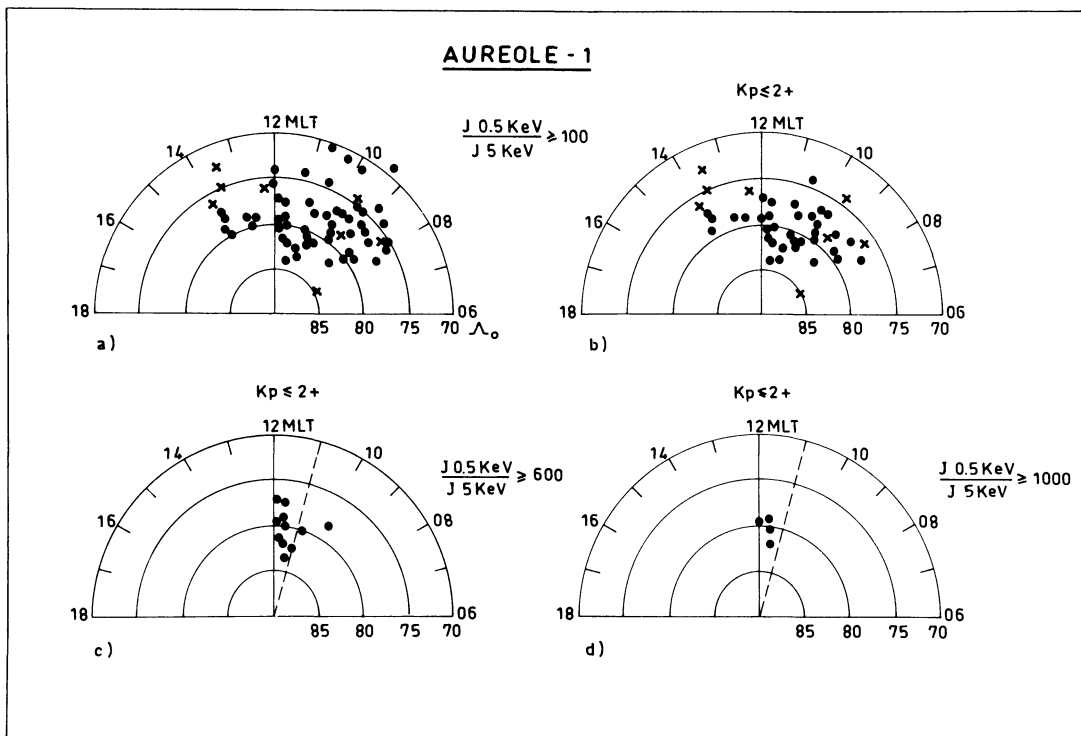
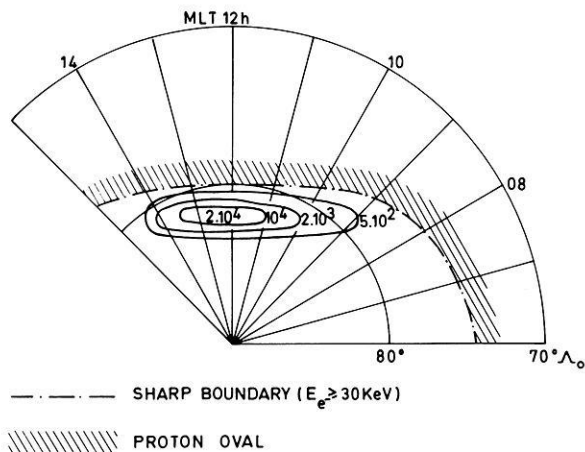
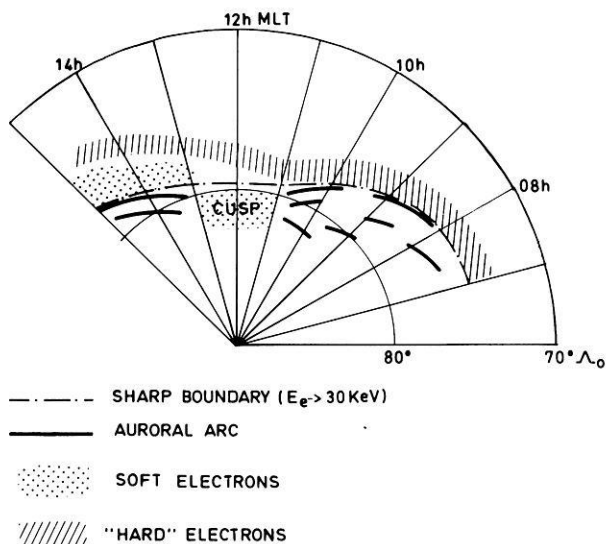


Fig. 2a-d. Polar  $A_0$  - MLT plots of the positions of the maximum 0.5 keV proton fluxes in the polar cusp with a spectral ratio  $\alpha$  equal to or higher than 100 ( $\alpha = (dJ/dE)_{0.5 \text{ keV}} / (dJ/dE)_{5.0 \text{ keV}}$ ) for a all passes and b quiet period passes  $Kp \lesssim 2_+$ , for c quiet period passes with a spectral ratio  $\alpha > 600$ , and for d quiet period passes with a spectral ratio  $\alpha > 1000$ . Secondary maxima are shown by crosses if their intensity is not less than a half of the principal maximum of the pass and if they are not adjacent to the principal maximum (from Sauvaud et al. 1980)



**Fig. 3.** Isocontours of the 0.5 keV proton fluxes at the dayside cusp in the summer hemisphere. The position of the sharp boundary ( $A_s$ ) defined as a sharp drop in the flux of the energetic electrons ( $E \geq 30$  keV), is indicated by a dot-dashed line. The hatched region corresponds to the band of the higher energy protons drifting inside the trapping zone (from Muliarchik et al., 1982)



**Fig. 4.** View of electron precipitation at the dayside auroral oval. (from Muliarchik et al. 1982)

is situated just inside the dayside part of the discrete auroral oval (Fig. 4) and just coincides in position with the analogous zone of soft electrons recently found by Meng (1981). It also coincides with the so-called "gap" in the discrete auroral arcs found in this same noon region (Ismail et al., 1977; Dandekar and Pike, 1978; Reiff et al., 1978; Meng, 1981).

In contrast to these "cusp protons", significantly harder "plasma-sheet-like" proton spectra (usually with an additional maximum at keV energies) were invariably observed on every oval crossing equatorward of the trapping boundary.

### Quiet Auroral Precipitation

During quiet times the proton auroral band must be regarded as practically continuous in local time (Crasnier

et al., 1974). The energy spectra of precipitating protons in sequential local time sectors change gradually in shape (Galperin et al., 1976a), and the spectral forms have been found to be rather similar to those observed in the same local time sectors from ATS-5 at geostationary orbit (De Forest and McIlwain, 1971).

The "plamsasheet-like" spectra, usually with additional maxima at several keV for particles precipitating in the noon and postnoon sectors, were observed in the region of the diffuse electron aurora, that is, equatorward of the trapping boundary on the dayside, at the  $L$ -shells of stable trapping. It was concluded (Galperin et al., 1976a), that the origin of these harder protons is the adiabatic particle drift around the earth. Their drift paths can be traced from a "source" region situated, according to the E3-M2 model, in the nightside plasmasheet up to the region of pitch-angle scattering and precipitation at the dayside. The strong reduction of proton fluxes for energies higher than 15–20 keV, observed in the late morning sector, can be explained as due to the loss at the magnetopause of such protons drifting from the nightside towards the dayside along the E3-M2 drift paths.

The scattering processes were not identified, but some inferences on their characteristics and localisation have been made. First of all, the similarity between the high energy part ( $E \geq 1-3$  keV) of the precipitating and equatorial (Maxwellian-like) proton (ion) energy spectra along the proton auroral band suggests that there is no very significant energy diffusion inherent in this spectral component in the scattering process and also that there is no significant field-aligned electric potential drop in this region (Galperin et al., 1976a). (For the lower energy part of the energy spectrum the situation is much more complex). Secondly, the scattering takes place in dayside  $L$ -shells where stable trapping of hard electrons and protons is maintained. According to the recent data taken close to the magnetopause (Williams et al., 1979; Williams, 1980), this region can be identified with the Low Latitude Boundary Layer (LLBL), or even with the region earthward from it on the dayside. The conventional auroral oval on the dayside, as well as on the nightside, is defined by discrete auroral arcs and lies along and poleward of the "sharp trapping boundary",  $A_c$  (McDiarmid and Burrows, 1968). It lies at least partly, however, on the closed magnetic field lines. Hence the proton auroral band, both on the nightside and on the dayside, lies on closed, adiabatically drifting, field tubes (within the so-called diffuse auroral zone) bordering, on the equatorial side, the conventional auroral oval and discrete arcs (Feldstein and Starkov, 1967). Thirdly, the shape of the proton (ion) precipitation spectrum in the proton auroral band normally consists of two distinct populations. The higher energy population, which mainly carries the energy flux, varies in a systematic manner along the proton auroral band. The lower energy part of the spectrum ( $E \lesssim 1-3$  keV) is less regular but usually carries the main density of hot ions in magnetospheric field tubes above the proton auroral band, that is in the same range of latitudes as the diffuse auroral zone.

The latitudinal variation of the precipitating proton spectra across the nightside proton auroral band reflects variations of the proton characteristics in the magnetospheric equatorial region. By field line tracing of the position of the AUREOLE satellite to the equatorial plane with the magnetospheric models of Mead-Fairfield MF-73 Q

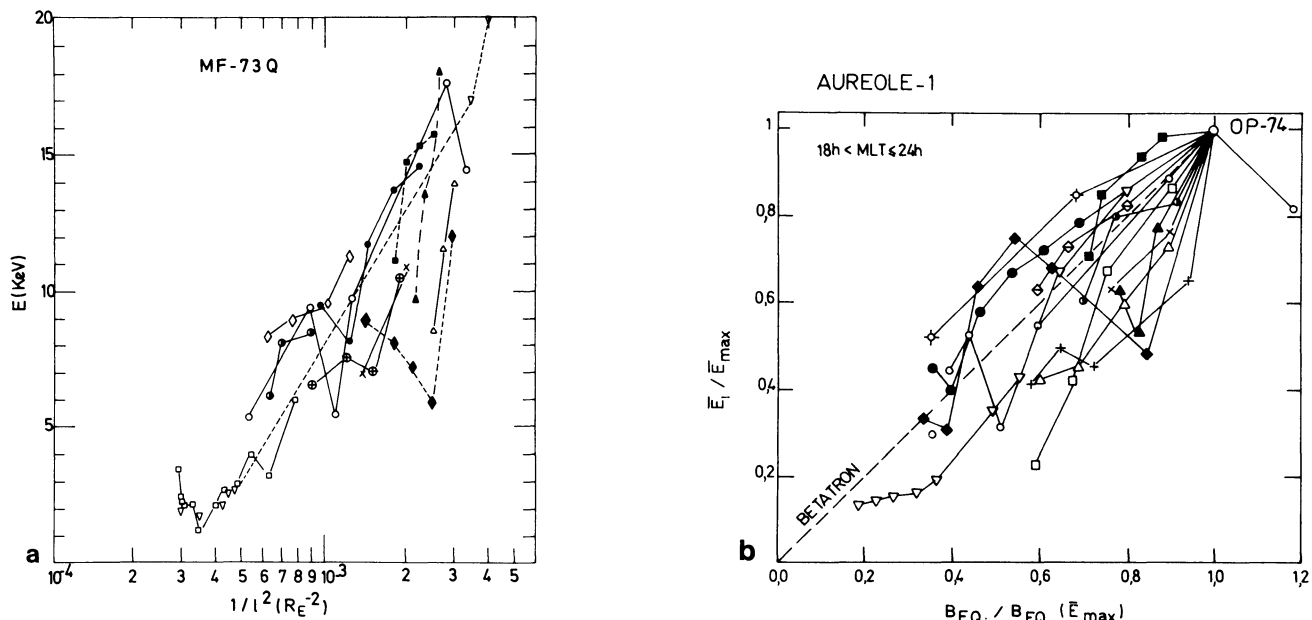


**Fig. 5a, b.** Correlation of the auroral proton (0.4–30 keV) average energy  $\bar{E}$ , with the magnetospheric field tube characteristics of the models OP-74 and MF-73 Q for the evening and midnight sectors. **a** Correlation with  $l^{-2}$  ( $l$  equals field tube length in earth radii  $R_E$ ). **b** Correlation with  $B_{eq}$  (equatorial magnetic field); for each pass the average energy  $\bar{E}$  has been normalized to its maximum value  $\bar{E}_{max}$  and  $B_{eq}$  has been normalized to the respective value  $B_{eq}(\bar{E}_{max})$ . (from Galperin et al., 1978)

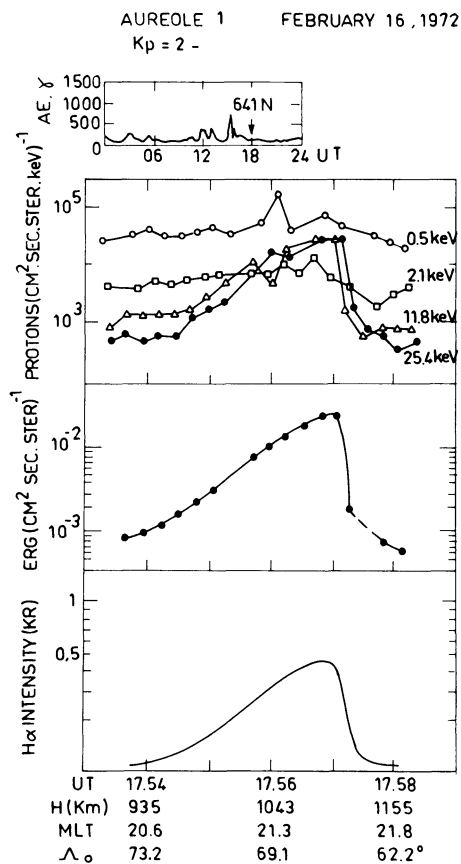


**Fig. 6.** Example of a coordinated observation between low-energy ions (0.5–25 keV) measured on board AUREOLE-2 and  $H_\alpha$  intensity measured from the Loparskaya station. The AE index variation, the ion differential flux, the ion integral energy flux and the  $H_\alpha$  intensity for the pass 641 N on 16 February 1972 are illustrated

(Mead and Fairfield, 1975) and of Olson and Pfizter OF-74 (Olson and Pfizter, 1974), it was possible to compare the average ion energy  $\bar{E}$  (or Maxwellian temperature) variation across the band with the variation of the equatorial magnetic field  $B_{eq}$ , and with the variation of the length of the satellite field line  $l$ . During the particle's earthward drift inside the plasmashet a proportionality is expected between the perpendicular particle energy component  $E_\perp$ , and  $B_{eq}$  (betatron and acceleration) and a similar relation is expected between the particle's parallel energy  $E_\parallel$  and  $l^{-2}$  (Fermi acceleration).

The comparisons made using the ARCAD observational data (Galperin et al., 1978) have shown that both such proportionalities are equally consistent (within experimental scatter) with the observed variations of the proton energy spectra across the nightside part of the proton auroral band (Fig. 5a, b). It was concluded that during quiet times the observed particle drift in the plasmashet is indeed adiabatic, but it is still impossible to discriminate between betatron (near equatorial drift until the moment of precipitation) and Fermi acceleration (gradual lowering of mirror points for particles with low equatorial pitch angles) or a combination of the two, as the dominant process.

It must be stressed that the ARCAD spectrometers did not make a mass selection. Therefore, it is not possible to decide directly if the analyzed particles are protons or other ions. For this reason simultaneous coordinated observations of the Balmer auroral emissions from the Loparskaya station near Murmansk were correlated with ion differential flux and integral energy flux measurements from AUREOLE-1 passes above this region (Bolunova et al., 1982). From photometric ground-based observations the extent of the  $H_\alpha$  intensity along the magnetic meridian was measured. For the case illustrated by Fig. 6 the low-latitude border of the proton auroral band was seen from the Lo-

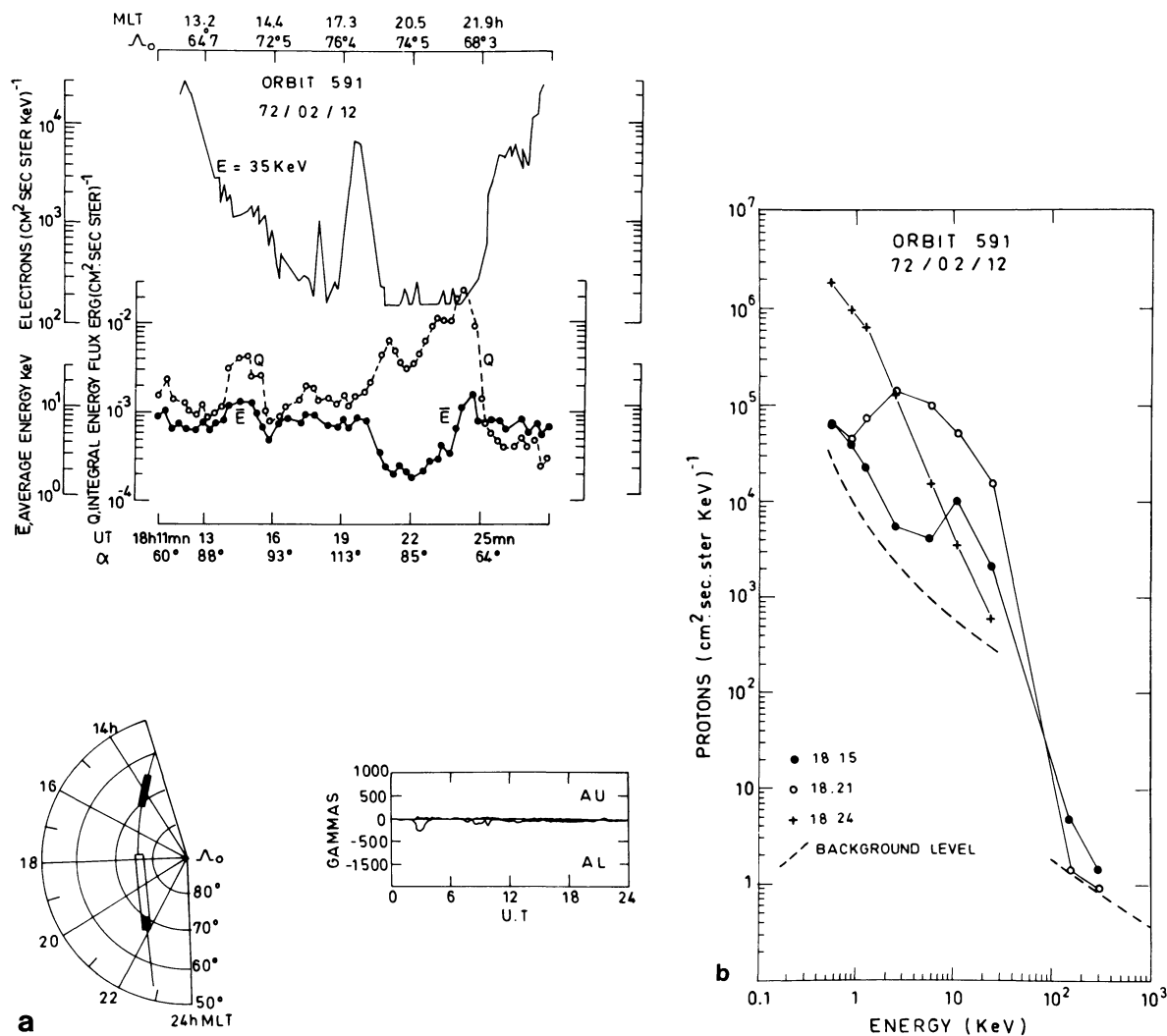


**Fig. 7a and b.** Example of soft ion precipitation on the polar side ( $A_0 \approx 75^\circ$ ) of the auroral oval during very quiet magnetic conditions. **a** In the upper part of the figure the flux of high energy electrons ( $E = 35 \text{ keV}$ ), the auroral proton (0.4–30 keV) average energy  $\bar{E}$ , and their integral energy flux  $Q$ , are plotted as a function of universal time. The pitch angle  $\alpha$  of the detected particles, the magnetic local time MLT and the invariant latitude  $A_0$  of the satellite are also indicated. The low energy ion precipitation is detected between approximately 18:20 and 18:23 UT. In the lower part of the figure the AU and AL indices and the satellite trajectory in a  $A_0$  – MLT polar plot are illustrated. **b** Three typical energy spectra. The points and circles indicate auroral proton energy spectra while the crosses are for a typical spectra of soft ion precipitation

parskaya station and its position coincided very well with the equatorial boundary of the ion precipitation measured simultaneously from AUREOLE-1. In other cases during more disturbed conditions the proton auroral band filled the sky from the horizon at Loparskaya, and the satellite data also show an extended proton auroral band above this region with its low latitude border at lower subauroral latitudes. The intensities of Balmer emissions and of particles assumed to be protons were in reasonable agreement in both of these cases showing that protons constitute more than 50% of the precipitating ions (Ponomarev, 1976).

### Polar Low-Energy Precipitation

Sometimes during periods of very low global magnetic activity, i.e. low convection electric field, very soft proton (ion) precipitation extended more poleward than the normal

proton auroral band through the auroral oval and even further poleward into the polar cap (Cambou et al., 1975; Galperin et al., 1978). An example of this type of precipitation is shown in Fig. 7a. Between 18:20 and 18:23 UT ( $70^\circ \lesssim A_0 \lesssim 75^\circ$ ,  $18:00 \lesssim \text{MLT} \lesssim 21:00$ ), AUREOLE-1 detected a low energy ( $\bar{E} \approx 3 \text{ keV}$ ) precipitation beyond the trapping boundary for 35 keV electrons, while an auroral precipitation ( $E > 10 \text{ keV}$ ) was observed inside this boundary. The typical energy spectrum of this precipitation is compared to two spectra characteristic of auroral-type ion precipitation in Fig. 7b. It has already been noted that a closed field-line region during such quiet periods, usually characterized by strong positive  $B_z$  (IMF), can extend far into the polar cap (McDiarmid et al., 1980) while the average characteristics of plasmasheet particles are similar to those of magnetosheath particles (Akasofu, 1977); these reconfigurations of the magnetospheric tail during such specific conditions with  $B_z > 0$  must therefore be reflected

## AUREOLE 1 - ORBIT 714 - FEBRUARY 22, 1974

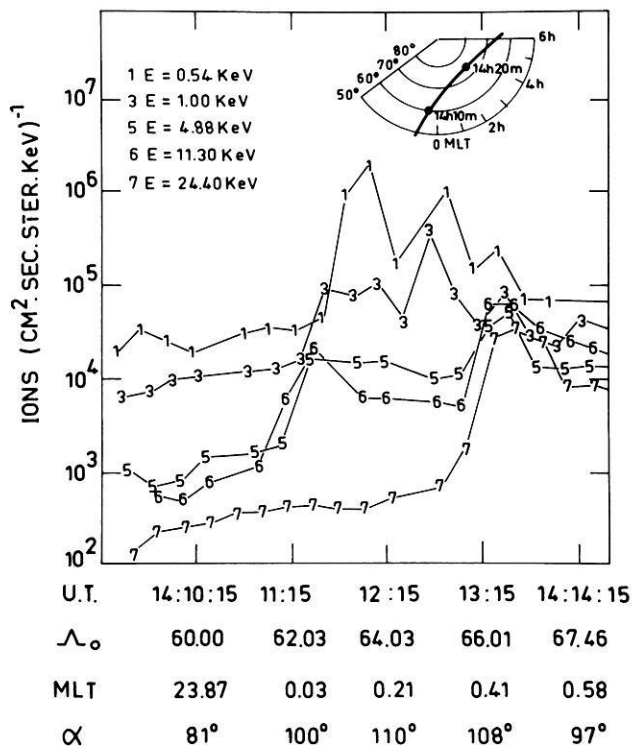


Fig. 8. Ion differential energy flux for 5 energy levels. The AUREOLE-1 satellite orbit is illustrated in the upper part of the figure on a  $A_0$ -MLT polar plot. The invariant latitude ( $A_0$ ), the magnetic local time (MLT) of the satellite, and the pitch-angle  $\alpha$  of the detected ions are also indicated. The morning subauroral precipitation of low energy ions is recognizable between approximately 14:11:15 and 14:12:45 UT. (From Sauvaud et al., 1981)

somehow in the precipitating particle spectra and location. More sensitive ion detectors are needed in future experiments for detailed investigations of these interesting phenomena during intervals of  $B_z > 0$ .

## Substorm-Related Flux Variations

One of the significant new findings from the AUREOLE-1 data base was that in the post-midnight and early morning sectors a peculiar structure with energy separation in the latitudinal profile of ions was found at the equatorial edge of the proton precipitation band from one to several hours after a substorm. Fig. 8 shows a measurement taken near 24:00 MLT, for which a precipitation zone at subauroral latitudes appears, and for which 24.4 keV ion fluxes are absent. In general, the average energy of precipitated particles decreases later in the morning sector. This dispersive pattern was observed on several occasions at low energies, making it possible to establish typical characteristics of this morning-side substorm injection phenomena (Sauvaud et al., 1981). This appears to be somewhat related to the previously discovered (Smith and Hoffman, 1974) evening energetic proton "nose" events resulting from substorm ion energisation/injection near midnight followed by westward gradient and curvature drift.

Here, for low energy ions in the morning subauroral sector, the eastward  $E_{cor} \times B$  drift dominated in accordance with the E3-M2 electric field model (Fig. 9). Trajectory tracing calculations have confirmed that the substorm timings, according to ground-based data, were consistent with the positions of the observed eastward-drifting dispersive structure of low-energy ions injected at midnight during a substorm (presumed, without definite proof, to be protons, as they were measured by an electrostatic analyser which selects particles only according to their  $E/Q$  ratio.

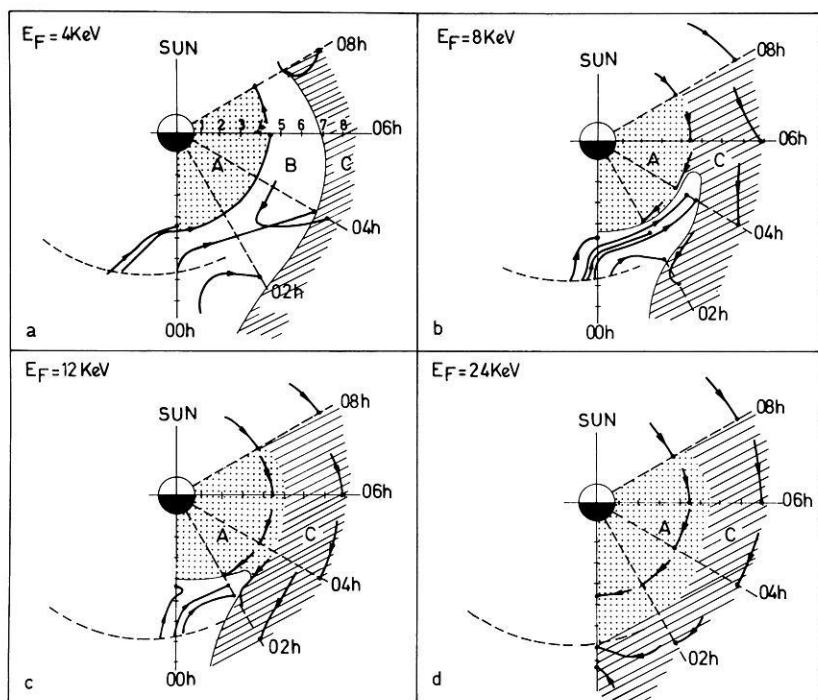


Fig. 9. Results of the calculations of ion trajectories (E3-M2 model) in the equatorial plane of the magnetosphere for 4 final energies (4, 8, 12, and 24 keV) assuming a pitch-angle of  $90^\circ$ . The dashed line indicates the "injection boundary" position ( $Kp=1$ ). Zone A is the trapping region, zone B is accessible to particles drifting eastward from the injection boundary. Zone C is accessible to particles drifting westward, from the injection boundary, around the Earth. (From Sauvaud et al., 1981)

## Discussion

The global pattern of ion precipitation presented in this paper leads to a tentative classification as a function of its origin and of the physical mechanisms responsible for its main characteristics. The picture constructed can be used as a reference for future observations related to ion precipitation and acceleration. However, it has strong limitations, especially due to the instrument performance which does not allow a mass analysis. Furthermore, it is evident that a detailed analysis of the precipitating regions would require simultaneous plasma, energetic particle, wave, magnetic and electric field measurements. These will be the main goals for more advanced future experiments in order to find an unifying pattern for the hot particle structure, field-aligned currents and convection in these complex and important regions of the near-Earth magnetosphere.

On the other hand, it must be stressed that one of the most important results deduced from AUREOLE-1 is that the ion energy spectra of precipitation in the diffuse aurora, which extend several degrees equatorward of the classical auroral oval defined from observations of auroral arcs, show two components. A suprathermal component from several 10's of eV to 3 keV and a more energetic component ( $E \geq 3$  keV), which had been proven to be of magnetospheric origin and adiabatically accelerated during the ions' drift toward the earth. The origin of the suprathermal component ( $E \lesssim 1-3$  keV) which is also detected in the equatorial plane (Balsiger et al., 1980) remains unclear. It seems however reasonable to propose that a direct connection exists between this suprathermal ion population and the dense secondary electron produced by the plasmashet electron precipitation in the diffuse auroral zone (Evans and Moore, 1979). Indeed, this high number densities ( $> 1-3 \text{ cm}^{-3}$ ) found for this secondary electron population of ionospheric origin well above the night-side diffuse auroral zone evidently implies equal ion densities. Such high ion densities can be supplied by the ionosphere in the "source cone" and released into the magnetospheric field tube together with secondary electrons (Cambou and Galperin, 1982). It is possible to suggest that thermal protons from the upper ionosphere probably constitute the main part of this outward flowing ion population, but other ionospheric constituents, presumably  $\text{He}^+$  and  $\text{O}^+$ , may participate in this additional ionospheric source above the diffuse auroral zone. This hypothesis must be directly verified by simultaneous measurements of the velocity distribution functions of the electrons and of the main ionospheric ions in a wide energy range in order to taken into account the "background" ionospheric plasma as well as the accelerated particles. This kind of study is one of the main goals of the new ARCAD-3 experiment.

*Acknowledgements.* This research was carried out as part of the Franco-Soviet space program. The authors would like to thank the people in charge of various organizations who have made this cooperative effort possible, particularly the Centre National d'Etudes Spatiales and Intercosmos. Extensive magnetic data have been provided by the World Data Center in Colorado. The data recorded aboard AUREOLE-1 and 2 satellites were treated through the help of J.L. Bessis and D. Monchy of the C.N.E.S. and V.M. Pokras, I.G. Khatkevitch and L.M. Nicolaenko of the IKIAN.

## References

- Akasofu, S.I.: Physics of magnetospheric substorms. Dordrecht-Holland, Boston-USA: D. Reidel Publ. Co. 1977
- Balsiger, H., Eberhardt, P., Geiss, J., Young, D.T.: Magnetic storm injection of 0.9–16 keV/e solar and terrestrial ions into the high-altitude magnetosphere, *J. Geophys. Res.* **85**, 1645–1662, 1980
- Bolunova, A.D., Kovrazhkin, R.A., Crasnier, J., Mouala, K., Sauvau, J.A., Totunova, G.F., Fedorova, N.I.: Diffuse auroral zone, Part V, Coordinated measurements of precipitating proton energy spectra and of optical hydrogen line emissions. *Losmich. Issled. (Cosmic Research)* **19**, 919–929, 1982
- Cambou, F., Galperin, Yu.I.: Overall results from the ARCAD experiment aboard the satellite AUREOLE. Proceedings of the International Symposium on Solar-Terrestrial Physics, jointly sponsored by the IAU, IUGG, IUAP, URSI, COSPAR and SCOSTEP, Sao Paulo, Brazil, **2**, 396–411, 1974a
- Cambou, F., Galperin, Yu.I.: Résultats d'ensemble obtenus grâce à l'expérience ARCAD à bord du satellite AUREOLE. *Ann. Géophys.* **30**, 9–19, 1974b
- Cambou, F., Galperin, Yu.I.: Main results of the joint French-Soviet space project ARCAD-1 and ARCAD-2 for magnetospheric, auroral and ionospheric physics. *Ann. Géophys.* **38**, 87–110, 1982
- Cambou, F., Sauvau, J.A., Crasnier, J.: Low-energy proton precipitation in invariant high-latitude regions. Paper presented at IAGA, Grenoble, France, 1975
- Chamberlain, J.W.: Physics of the aurora and airglow. New-York and London: Academic Press 1961
- Crasnier, J., Sauvau, J.A., Galperin, Yu.I., Kovrazhkin, R.A., Ponomarev, Yu.N.: Measures in situ à bord du satellite AUREOLE des protons auroraux durant des périodes magnétiques calmes. *Ann. Géophys.* **30**, 357–367, 1974
- Dandekar, B.S., Pike, C.P.: The midday, discrete auroral gap. *J. Geophys. Res.* **83**, 4227–4236, 1978
- De Forest, S.E., McIlwain, C.E.: Plasma clouds in the magnetosphere. *J. Geophys. Res.* **76**, 3587–3612, 1971
- Eather, R.H.: Auroral proton precipitation and hydrogen emission. *Rev. Geophys.* **5**, 207–284, 1967
- Evans, D., Moore, T.E.: Precipitating electrons associated with the diffuse aurora: Evidence for electrons of atmospheric origin in the plasmashet. *J. Geophys. Res.* **84**, 6451–6457, 1979
- Frank, L.A., Ackerson, K.L.: Observations of charged particle precipitation into the auroral zone. *J. Geophys. Res.* **76**, 3612–3643, 1971
- Frank, L.A.: Magnetospheric and auroral plasma: a short survey of progress. *Rev. Geophys. Space Phys.* **13**, 974–989, 1975
- Feldstein, Y.I., Starkov, G.V.: Dynamics of auroral belt and polar geomagnetic disturbances. *Planet. Space Sci.* **15**, 209–230, 1967
- Galperin, Yu.I., Kovrazhkin, R.A., Ponomarev, Yu.N., Crasnier, J., Sauvau, J.A.: Pitch-angle distribution of auroral protons. *Ann. Géophys.* **32**, 109–115, 1976a
- Galperin, Yu.I., Jorjio, N.V., Kovrazhkin, R.A., Cambou, F., Sauvau, J.A., Crasnier, J.: On the origin of auroral protons at the dayside auroral oval. *Ann. Géophys.* **32**, 117–129, 1976b
- Galperin, Yu.I., Gladyshev, V.A., Jorjio, N.V., Kovrazhkin, R.A., Sinitsin, V.M., Cambou, F., Sauvau, J.A., Crasnier, J.: Adiabatic acceleration induced by convection in the plasmashet. *J. Geophys. Res.* **83**, 2567–2573, 1978
- Gladyshev, V.A., Jorjio, N.V., Shuiskaya, F.K., Crasnier, J., Sauvau, J.A.: Détermination de la position du cornet polaire à l'aide de mesures de particules de basse énergie effectuées à bord du satellite AUREOLE. *Ann. Géophys.* **30**, 301–308, 1974
- Heikkila, W.J.: Penetration of particles into the polar cap and auroral regions. In: Critical problems of magnetospheric physics. Proceedings of the symposium jointly sponsored by COSPAR/URSI/IAGA, Madrid 1972, E.R. Dyer, ed. Publ. by the IUCSTP Secretariat c/o National Academy of Sciences, Washington D.C., 1972

- Heikkila, W.J., Winningham, J.D., Eather, R.H., Akasofu, S.I.: Auroral emissions and particle precipitation in the noon sector. *J. Geophys. Res.* **77**, 4100–4115, 1972
- Hultqvist, B.: Rocket and satellite observations of energetic particle precipitation in relation to optical aurora. Review paper presented at IAGA, Kyoto, Japan, 1973.
- Hultqvist, B.: The hot ion component of the magnetospheric plasma and some relations to the electron component observation and physical implication. *Space Sci. Rev.* **23**, 581–675, 1979
- Ismail, S., Wallis, D.D., Cogger, L.L.: Characteristics of polar cap sun-aligned arcs. *J. Geophys. Res.* **82**, 4741–4749, 1977
- Kovrazhkin, R.A.: Auroral proton precipitation structure. *Kosmich. Issled. (Cosmic Research)* **14**, 53–63, 1976
- McDiarmid, I.B., Burrows, J.R.: Local time asymmetries of the high-latitude boundary of the outer radiation zone for the different electron energies. *Can. J. Phys.* **46**, 49–55, 1968
- McDiarmid, I.B., Burrows, J.R., Wilson, M.D.: Comparison of magnetic field perturbations and solar electron profiles in the polar cap. *J. Geophys. Res.* **85**, 1163–1170, 1980
- Mead, G.D., Fairfield, D.H.: A quantitative magnetospheric model derived from spacecraft magnetometer data. *J. Geophys. Res.* **80**, 523–534, 1975
- Meng, C.I.: Electron precipitation in the midday auroral oval. *J. Geophys. Res.* **86**, 2149–2174, 1981
- Muliarchik, T.M., Feldstein, Y.I., Galperin, Yu.I., Gladyshev, V.A., Nikolaenko, L.M., Sauvaud, J.A., Crasnier, J.: Two dimensional structure of proton and electron precipitation throughout the dayside auroral oval as inferred from their energy spectra. *Kosmich. Issled. (Cosmic Research)* **20**, 244–263, 1982
- Olson, W.P., Pfizter, K.A.: A quantitative model of the magnetospheric field. *J. Geophys. Res.* **79**, 3739–3748, 1974
- Ponomarev, Yu.N.: Precipitation in the upper atmosphere of directional and monoenergetic proton beams. *Geomagn. Aeron.* **14**, 144–148, 1976
- Reiff, P.H., Burch, J.L., Heelis, R.A.: Dayside auroral arcs and convection. *Geophys. Res. Lett.* **5**, 391–394, 1978
- Sauvaud, J.A., Galperin, Yu.I., Gladyshev, V.A., Kuzmin, A.K., Muliarchik, T.M., Crasnier, J.: Spatial inhomogeneity of magnetosheath proton precipitation along the dayside cusp from the ARCAD experiment. *J. Geophys. Res.* **85**, 5105–5112, 1980
- Sauvaud, J.A., Crasnier, J., Mouala, K., Kovrazhkin, R.A., Jorjio, N.V.: Morning sector ion precipitation following substorm injections. *J. Geophys. Res.* **86**, 3430–3438, 1981
- Smith, P.H., Hoffman, R.A.: Direct observations in the dusk hours of the characteristics of the storm time ring current particles during the beginning of magnetic storms. *J. Geophys. Res.* **79**, 966–971, 1974
- Vallance Jones, A.: *Aurora. Dordrecht-Holland, Boston-USA: D. Reidel Publ. Co.* 1974
- Vasyliunas, V.M.: Magnetospheric cleft symposium. *EOS Trans AGU* **55**, 60–66, 1974
- Williams, D.J., Fritz, T.A., Wilken, B., Keppler, E.: An energetic particle perspective of the magnetosphere. *J. Geophys. Res.* **84**, 6385–6396, 1979
- Williams, D.J.: Magnetopause characteristics at 0840–1040 hours local time. *J. Geophys. Res.* **85**, 3387–3395, 1980
- Winningham, J.D.: Penetration of magnetosheath plasma to low altitudes through the dayside magnetospheric cusp. Ph. D., Teyas, AM University, 1970

Received November 22, 1982; Revised January 31, 1983

Accepted February 22, 1983

# A Technique for Studying Density Gradients and Motions of Plasmaspheric Irregularities\*

D. Jones

British Antarctic Survey, NERC, Madingley Road, Cambridge CB3 0ET, U.K.

**Abstract.** Terrestrial myriametric radiation (TMR) is received by spacecraft in the magnetospheric cavity beyond the plasmasphere. There is now general agreement that the radiation emanates mainly from the plasmopause and a technique is under development which allows information on the source regions to be extracted. The method is based on the theory that the radiation has passed through a radio window, this being one mechanism for producing TMR which is receiving considerable attention at present. With accurate direction-finding measurements in which wave polarisation effects must be considered, it is shown how the radial and local-time positions of the TMR sources can possibly be determined, thereby allowing the tracking of plasmopause irregularities and regions of detached plasma which move around from the night side. If additional information is available such as an estimate from banded emissions of the source gyro-frequency, it is shown how it may also be possible to determine the latitudinal positions of sources.

**Key words:** Terrestrial myriametric radiation – Non-thermal continuum – Remote sensing – Plasmopause – Radio window – Direction finding – Wave polarisation

## Introduction

Terrestrial myriametric radiation (TMR), also called non-thermal continuum, is electromagnetic radiation in the frequency range 10–100 kHz (Gurnett, 1975). Its free-space wavelength is of the order of  $10^4$  m; hence the adoption of the term myriametric (Jones, 1980).

There is evidence that TMR is produced in the left-hand ordinary ( $L$ - $O$ ) mode (Gurnett and Shaw, 1973; Jones, 1980; Okuda et al. 1982; Kurth, 1982) although Etcheto et al. (1982) have reported the observation of what appears to be a predominantly right-hand extraordinary ( $R$ - $X$ ) continuum event on the ISEE spacecraft.

It is becoming well established that the main source of TMR lies in upper hybrid waves at the plasmopause, with a possible secondary source at the morning magneto-sheath. Gurnett (1975) noted the close association between continuum radiation and intense bands of electrostatic

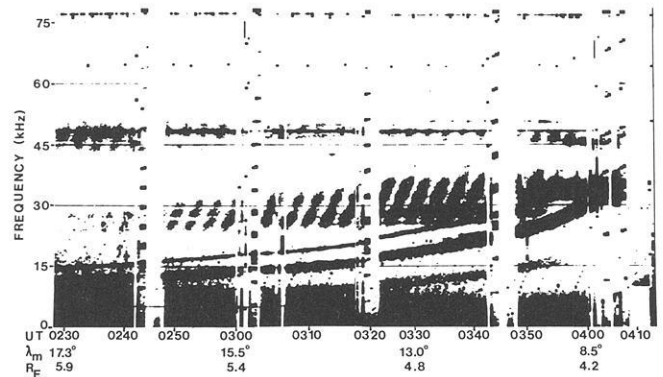


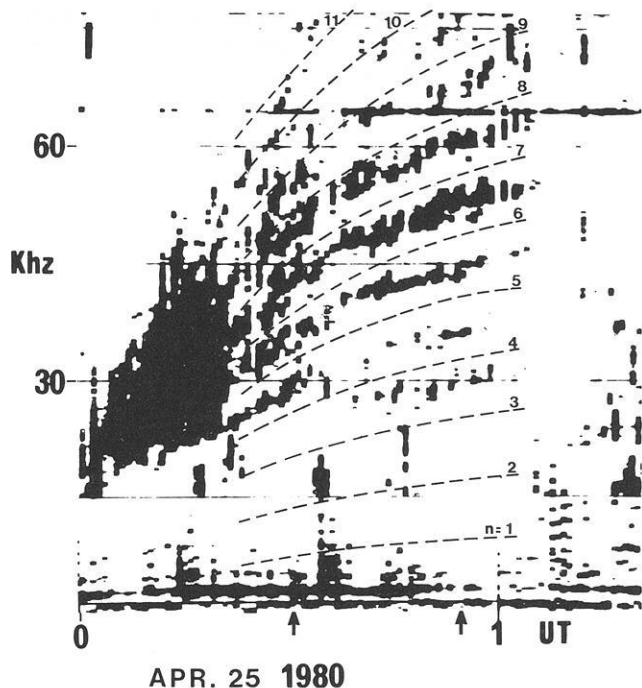
**Fig. 1.** Wave spectrogram from GEOS 1 showing spin-modulated TMR observed on 4 March 1978

noise observed near the electron plasma frequency at the plasmopause. Kurth et al. (1979a; b) showed an example of intense upper hybrid waves near  $4.3R_E$  at 5–6 h LT that were apparently causing emission in the TMR frequency band. Further evidence that the two types of emission are intimately linked has been presented by Jones (1980; 1981a; b; 1982), Kurth et al. (1981) and Kurth (1982). Since the most intense electrostatic emissions, at least during relatively quiet geomagnetic conditions, appear to be very tightly confined to the geomagnetic equator (Gough et al., 1979), it has been reasonable to suppose initially that the most intense TMR, such as that which can be observed by spacecraft at relatively large distances from a plasmopause source, also emanates from the magnetic equatorial plane.

Two examples of TMR recorded by the wave experiment (Jones, 1978) on the GEOS 1 and 2 spacecraft are shown in Figs. 1 and 2 respectively. These examples were selected to illustrate the different types of TMR which can be observed. Many other examples have appeared in the literature which further illustrate the wide variety of TMR which can exist (Kurth et al., 1981; Jones, 1982; Gough, 1982; Kurth, 1982; Etcheto et al., 1982).

In Fig. 1, the striated emissions seen in two relatively wide bands are TMR, the stronger straddling  $\sim 30$  kHz and the weaker lying just above 45 kHz. The narrow line at  $\sim 48$  kHz is instrumental and should be ignored. The striations are indicative of spin-modulation of the wave electric field received by the 40 m tip-to-tip dipole antenna and lead to the conclusion that the source region is relatively compact. The inclination of the striations is due to the

\* Based on a paper given at the Symposium on Plasma and Energetic Particles in the Magnetosphere, EGS Meeting, 23–27 August 1982, Leeds, U.K.



APR. 25 1980

Fig. 2. Wave spectrogram from GEOS 2 showing multi-banded TMR observed on 25 April 1980. The arrows on the ordinate are at 0033 UT and 0057 UT (see text)

beat between the sweep period (22s) of the on-board frequency analyser and the spin period (6s) of the spacecraft. It is clear that the spin modulation contains information on the direction of the source. In the past, source directions have been determined from the spin modulation without any consideration being given to the effect of wave polarisation (Gurnett, 1975; Kurth et al., 1981; Gough, 1982; Etcheto et al., 1982), but it has been shown that this approach can introduce large errors (Lecacheux et al., 1979; Manning and Fainberg, 1980; Jones, 1982).

Attention is drawn to other characteristics of TMR visible in Fig. 1. The frequency and bandwidth of the lower band varies as the spacecraft moves, whereas for the upper band the parameters remain fairly constant. The spin modulation of the lower band varies between unity (no spin modulation) and a figure of  $\sim 4$ , depending on the time and on the frequency. Thus, since it is the power that is being displayed in the Figure, the electric field modulation lies between 1 and 2.

The manner in which the various items of information contained in Fig. 1 can be used for remote sensing of the plasmopause requires a brief discussion of what has been proposed as a source mechanism of TMR. This is given in the next section and is followed by a detailed discussion of possible source positions of the TMR shown in Figs. 1 and 2. The main thrust of the paper is firstly to draw attention to the problems of direction-finding and secondly to show how the work of Jones (1982), which assumed sources confined to the magnetic equatorial plane, can be generalised to allow remote sensing of non-equatorial sources.

### TMR Generation Mechanism

Barbosa (1982) has recently presented a good review of the characteristics of TMR and has considered the three

leading theories which have been proposed for its production. The synchrotron mechanism proposed by Frankel (1973) apparently falls short of the required power level by a factor of  $10^2$ – $10^3$ . The linear theory of Jones (1976a; b) which invokes UHR/ $Z$  mode to  $L$ – $O$  mode conversion is also too inefficient by a factor of  $10^2$ , although Barbosa adds that if some efficiency-saving mechanism can be found, this theory could achieve a paramount position and be universally accepted. The third theory, non-linear wave-coupling suggested by Melrose (1981), can achieve the required efficiency, but, again according to Barbosa, it lacks credibility because of the ad hoc nature of its assumptions and the lack of observations of the requisite ingredients (low frequency waves cospatial with upper hybrid noise). Lembege and Jones (1982) have considered the ray paths relevant to the linear theory and have suggested an efficiency-saving mechanism. On the basis of this, and of Barbosa's comments, it is suggested that the linear theory and its possible implications for remote sensing of TMR sources deserves a more thorough investigation.

Following the observation by Gurnett (1975) that continuum radiation seemed to be closely associated with intense bands of electrostatic noise observed near the electron plasma frequency at the plasmopause, Jones (1976a) provided the first theory relating the continuum to upper hybrid waves. This is the linear theory which invoked the generation of  $Z$ -mode waves by the Cerenkov mechanism, and the subsequent propagation of the waves in a density gradient so as to access a radio window which exists where the wave frequency equals the plasma frequency  $f_{pe}$ .  $Z$ -mode waves have since been observed in the generation regions of TMR (Jones, 1982; Kurth, 1982) and the Cerenkov mechanism is undoubtedly the source of some continuum. However, the observation of more intense, banded TMR, whose frequency spacing satisfies the relation  $f \approx (n + \frac{1}{2})f_{ce} \approx f_{UHR}$  where  $f_{ce}$  is the electron cyclotron frequency and  $f_{UHR} = (f_{pe}^2 + f_{ce}^2)^{\frac{1}{2}}$ , has led to the conclusion that electrostatic upper-hybrid waves play the most important role. Since these electrostatic waves lie on the same dispersion branch as the  $Z$ -mode radiation (Oya, 1971), it was suggested by Jones (1980) that their propagation in the density gradient at the plasmopause will naturally convert them into  $Z$ -mode waves, with mode conversion to the  $L$ – $O$  mode again occurring at the radio window. In parallel, it was becoming evident that the most intense electrostatic (e.s.) emissions were located at the magnetic equator (Gough et al., 1979) and this would allow the best access by energy in the e.s. waves to the radio window via the  $Z$ -mode. Lembege and Jones (1982) have shown detailed ray paths of the electrostatic and electromagnetic waves at the magnetic equatorial plasmopause and have commented on the characteristics required of the source e.s. waves if the window theory is to be sufficiently efficient. Their suggestion requires additional observations and theoretical work, which are beyond the scope of this present paper, but a brief summary of the proposal will be given here since, as stated by Barbosa, this factor is crucial if the linear theory is to be elevated to a paramount position.

Figure 3 is a three-dimensional representation which endeavours to portray simultaneously both refractive index space and 'real' space. The elements of the latter are the magnetic field vector  $B_0$ , the magnetic equator lying perpendicular to  $B_0$ , and the plasmopause shown as the cross-hatched surface which, for clarity, has been limited to one



concerning the e.s. instability and these also require a separate investigation. Observations are needed of unambiguous sources of TMR in which the gyrotropy or otherwise of the e.s. waves can be further tested; preliminary results indicate that the waves are indeed non-gyrotropic (W. Kurth, private communication). In parallel, it is necessary to consider the theory of the convective instabilities in a density gradient in order to determine which  $k$ -vectors will tend to grow preferentially.

## Remote Sensing

### Sources in Magnetic Equatorial Plane

Details of how the window theory allows TMR to be used for remote sensing of the plasmopause if one assumes that the sources are confined to within  $\pm 1^\circ$  in latitude have been reported previously (Jones, 1981b; 1982) and only a very brief summary will be given here. The confinement of the intense e.s. waves to the magnetic equatorial plane is most apparent during quiet magnetic conditions, such as those which correspond to Fig. 1. In such cases, knowing the magnetic coordinates of the spacecraft and assuming the radiation propagates in the magnetospheric cavity from the source to the spacecraft at the angle  $\alpha = \arctan(f_{ce}/f_{pe})^{1/2}$  with respect to the equatorial plane, it is possible to determine the loci of possible sources in the magnetic equatorial plane. Given additional information, such as the direction of arrival of the radiation, one may then pinpoint the position of the source in radial distance and in local time. Two interpretations of Fig. 1 will be considered. In the first it is assumed that the TMR source lies in a direction radially inwards from the spacecraft; in the second that the source lies nearly perpendicular to that direction. These two extremes will serve to illustrate the importance of determining the azimuth from which the radiation is arriving at the spacecraft. In the former case one can, in theory, determine the density profile in the source region, whereas in the latter it is shown how it may also be possible to detect motion of the source region.

If it is assumed that the source of the TMR in Fig. 1 lies radially inwards from the satellite, the plasma frequency profile obtained by remote sensing is shown in Fig. 4 (see Jones, 1982). The frequency change with time of the lower TMR band in Fig. 1 is due to the spacecraft's orbit being such that it encounters beams of different frequencies as it moves. In contrast, the upper frequency band in Fig. 1 is relatively stationary indicating that GEOS 1 remained within the beam during the time shown. Examples of the TMR ray paths for this event are given in Fig. 8 of Jones (1982).

Gough (1982) has published the directions of electric field minima detected by the spinning dipole on GEOS-1 for this event and these are found to lie within  $20^\circ$  of the radial direction. At first sight, this seems to imply that the source was indeed approximately radially inwards from the satellite. Unfortunately, however, Gough did not consider the effects of wave polarisation on his measurements and hence, as Jones (1982) has shown, the difference between the spin modulation nulls and the direction of the source may differ by up to  $\pi/2$  if the radiation is in the  $L-O$  mode. At this stage, therefore, it is of interest not to limit the discussion to the radial direction, but to discuss the more general case which is depicted in Fig. 5.

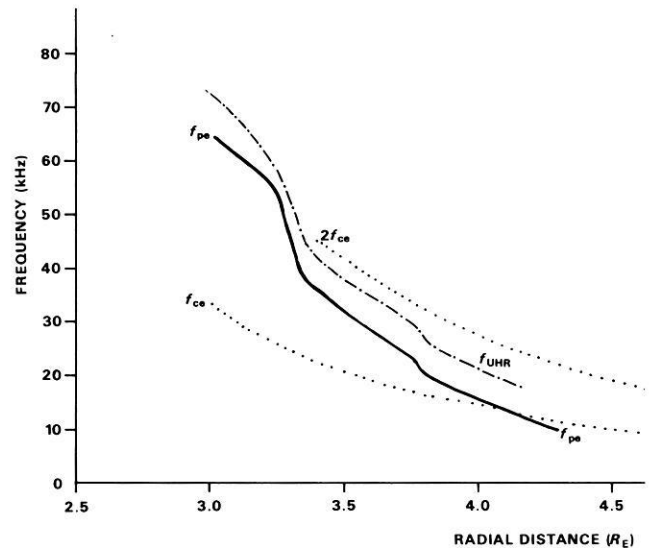


Fig. 4. Plasma frequency profile obtained from the spectrogram in Fig. 1 by remote sensing, assuming that the TMR emanates from a source located at the magnetic equatorial plane radially inwards from the satellite

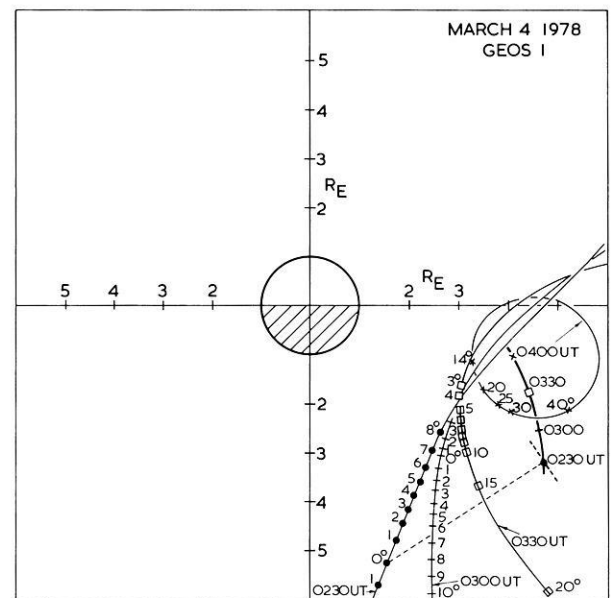


Fig. 5. The thick line represents the portion of the GEOS 1 orbit during which the spectrogram in Fig. 1 was recorded. Positions of the spacecraft at 0230, 0300, 0330 and 0400 UT are indicated by the different symbols. Source loci of 27 kHz TMR for each of these four positions are shown. Along these loci are marked the angle between the perpendicular to the magnetic field vector at the satellite and the satellite-source line. The short dashed line through the satellite position at 0230 UT represents the direction of the minimum wave electric field detected by the spinning spacecraft

Figure 5 shows the positions of GEOS 1 at half-hourly intervals during the observation of the TMR shown in Fig. 1. Also shown are the corresponding loci in the magnetic equatorial plane of possible sources of 27 kHz TMR, which is a frequency visible to the satellite from 0230 UT until just after 0350 UT. On the loci are marked the angle between the ray direction and the plane perpendicular to

the magnetic field direction at the satellite, assuming a dipole magnetic field model. This angle is of the utmost importance when considering the spin modulation and the latter's use in direction-finding. For example, if at 0230 UT the source of TMR lies at the point marked  $0^\circ$  on the corresponding source locus, then at the satellite, the wave normal direction, assuming it to be parallel to the ray direction, is perpendicular to the magnetic field and thus the wave's electric field will be nearly linearly polarised along the magnetic field. Since the spacecraft spin axis is not parallel to the magnetic field, the dipole antenna will therefore observe a null when it makes the largest angle with  $B_0$ , and in general this bears no relation to the direction of the source. It is interesting to note that the direction of the null obtained at 0230 UT by Gough (1982) makes exactly an angle of  $\pi/2$  with the direction of the " $0^\circ$  source" at 0230 UT. This would, therefore, be compatible with a source of 27 kHz TMR at  $5.5R_E$ , 0100 LT at 0230 UT, if the projection of the magnetic field direction on the spin plane of GEOS 1 makes an angle of  $\sim 20^\circ$  with the radial direction at that time. Similar arguments may be made at the other times shown since the angles over most of the loci, except for those at 0400 UT when the radiation is not observed at 27 kHz, are of the order of  $10^\circ$  or less, implying that the electric vector at GEOS would be quite highly elliptically polarised nearly parallel to  $B_0$  for any source position. It should also be noted that the magnitude of the maximum electric field of the TMR detected on GEOS will be an underestimate of the wave electric field.

It is of interest, therefore, to consider the other extreme where it is assumed that the true directions of the TMR sources, at least for the lower frequency band in Fig. 1, are perpendicular to those determined by Gough (1982). One may then plot their positions at the different times as shown in Fig. 6. Where possible, i.e. at 0300 and 0330 UT, the sources of a lower frequency, 25 kHz, and a higher frequency, 32 kHz, are shown. At 0230 UT only TMR having a frequency of  $\sim 25$  kHz is observed, whereas at 0400 UT only frequencies in the vicinity of  $\sim 32$  kHz are recorded. Figure 6 thus shows how sources rotating around from the night side at a speed greater than that of corotation with the Earth could, in theory, produce the TMR appearing in Fig. 1. The average supercorotation component is found to be approximately 3 km/s which is compatible with the plasma flow speeds computed from measurements made from the GEOS DC electric field experiment in the post-midnight sector (A. Pedersen, private communication), and also in agreement with the values derived by Lemaire and Kowolowski (1981). Clearly, however, before one can attach significance to the motions determined from Fig. 6 one must be able to determine the azimuth of the source.

It is unfortunate that the GEOS magnetometer was malfunctioning over a period including that shown in Fig. 1. It may be possible, however, that other experiments on the spacecraft could yield the information necessary to determine accurately the direction of the magnetic field at this time, and this possibility is being explored at present. Without such information it seems impossible to determine where, between the two extremes considered, the sources actually lie. The importance of obtaining an accurate field direction whenever direction finding measurements are made is emphasised by the example shown in Fig. 7, which shows the effects of wave polarisation on the depth of spin

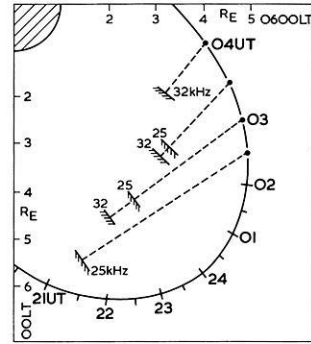


Fig. 6. Source positions of 25 kHz and 32 kHz TMR corresponding to the four times considered in Fig. 5, and assuming the sources are perpendicular to the directions of the null wave electric field detected on GEOS

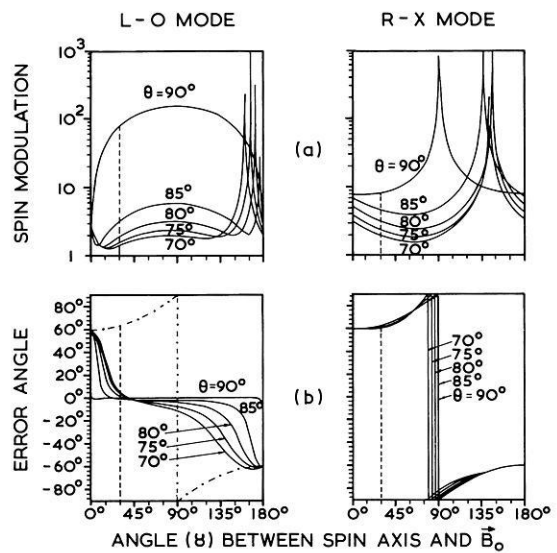


Fig. 7. **a** Depth of spin modulation of  $L-O$  and  $R-X$  waves as a function of  $\gamma$  (see text) for wave normal angles of  $70^\circ$ – $90^\circ$ . **b** Direction of wave electric field null compared with direction of  $k$  vector in spin plane (---) as a function of  $\gamma$  for wave normal angles  $70^\circ$ – $90^\circ$

modulation and on the direction of the minimum electric field detected. The wave normal  $k$  and spacecraft spin axis make angles  $\theta$  and  $\gamma$  respectively with  $B_0$  and the azimuth of the spin axis from the  $k-B_0$  plane is assumed to be  $30^\circ$ .

The wave frequency is taken to be 30 kHz and the plasma and gyro-frequencies are set at 15 kHz and 6.5 kHz respectively, corresponding approximately to conditions at 0320 UT in Fig. 1. The five curves in each frame correspond to angles  $\theta$  of  $70^\circ$  to  $90^\circ$  in  $5^\circ$  steps as labelled. The frames on the left of Fig. 7 relate to the  $L-O$  mode and those on the right to the  $R-X$  mode. The general case, in which a range of  $\gamma$ ,  $\theta$ ,  $\phi$ ,  $f$ ,  $f_{pe}$  and  $f_{ce}$  are considered will be reported separately.

The parameters considered in Fig. 7 are the depth of spin modulation and the difference between the antenna direction when it observes minimum electric field (full lines) and the direction of the projection of  $k$  in the spin plane (dash-dot line). On the basis of a magnetic field model, for illustrative purposes, the angle  $\gamma$  corresponding to Fig. 1 can be assumed to be  $\sim 30^\circ$ . Thus, the depth of spin modu-

lation for the  $L$ - $O$  waves is  $\lesssim 2$  except for wave normal angles  $\theta$  between  $80^\circ$  and  $90^\circ$ , when the spin modulation can become very large. The difference between the direction of the modulation null and that of the projection of  $k$  in the spin plane, which will be called the "error angle", is seen to be  $\sim 60^\circ$  for all wave normal angles  $\theta \geq 70^\circ$ . The parameters of the  $R$ - $X$  mode are shown on the right merely for comparison. Until accurate values of  $\gamma$  and  $\Phi$  corresponding to Fig. 1 are available, no concrete conclusions can be drawn, but the results serve to emphasise the very large errors in source directions which could arise unless wave polarisation is considered.

In summary, therefore, it has been shown that the TMR event reproduced in Fig. 1 may contain more information on the positions and movement of sources than was previously believed. Two interpretations of the data have been considered, one in which it is assumed that the source lies radially inward from the spacecraft and the other where the source is nearly perpendicular to that direction. In the latter case, the remarkable possibility of observing plasmaspheric irregularities or cold plasma islands (Chappel, 1974) moving around from the night side has been demonstrated. When accurate magnetic field measurements become available it is believed that, in conjunction with DF measurements and information on the depth of spin-modulation, the technique of remote sensing considered here will allow a better understanding of the plasmopause and of the convection of associated irregularities.

#### *TMR Sources not Restricted to Magnetic Equatorial Plane*

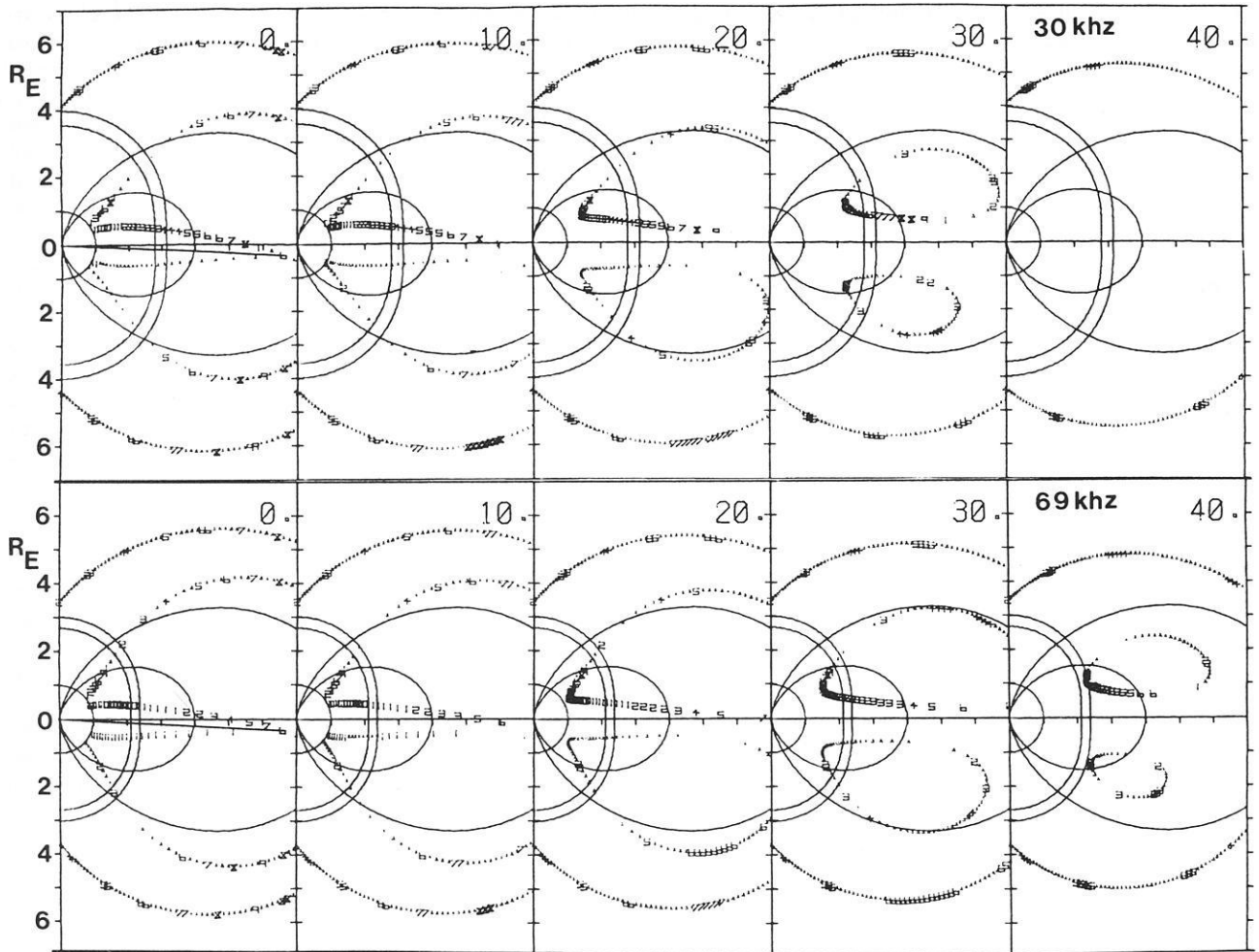
The previous section dealt with the case of TMR sources restricted to the magnetic equatorial plane, as would be expected, for example, under quiet geomagnetic conditions. When magnetic activity increases, the intense electrostatic waves believed to be responsible for TMR are no longer rigidly confined to the magnetic equator (Gough et al., 1979) and the remote sensing technique must therefore be extended to accommodate such cases.

Figure 2 is an example of a short-lived continuum event recorded during 00–01 UT on 25 April 1980 by the GEOS-2 spacecraft which is in geostationary orbit at  $6.6R_E$ . The event is characterised by an intense emission appearing at  $\sim 20$  kHz at  $\sim 00$  UT which spreads in frequency upwards so as to cover the band 25–45 kHz by 0020 UT. The emission then splits into four or five discrete bands whose frequency and frequency separation increase as time progresses, the event coming to an abrupt end at  $\sim 01$  UT. The frequency spacing between bands is estimated to be  $\sim 6.5$  kHz at 0033 UT and  $\sim 8$  kHz at 0057 UT. The spacing in such events as this have been related to the electron cyclotron frequency  $f_{ce}$  at the source (Kurth et al., 1981; Gough, 1982; Kurth, 1982). At the plasmopause, the plasma frequency and hence the upper hybrid frequency  $f_{UHR}$  may increase rapidly compared to the electron cyclotron frequency, so that  $f_{UHR}$  may cross several gyro-harmonic bands in a short distance. The most intense electrostatic emissions occur where  $f_{UHR} \approx (n + \frac{1}{2})f_{ce}$  and hence it is natural to expect the resultant TMR to be similarly banded. Thus, from Fig. 2 it is possible to deduce the value of  $f_{ce}$  at the source from the spacing between the emission frequency bands and hence to obtain the  $f_{ce}$  harmonic lines as drawn. Since Fig. 2 was recorded during a period of

moderate magnetic activity ( $K=4$  at Kiruna, which is located near the foot of the GEOS 2 field line) it is probable that the TMR sources were not restricted in this case to the magnetic equatorial plane.

The remote sensing technique has now been generalised to include non-equatorial sources (Jones, Gapper and Herring, private communication). It is still assumed that the plasma density gradient is perpendicular to the magnetic field vector, but the restriction that the TMR source must lie at the equator has been removed. Thus, the source locus is no longer a line in the equatorial plane but a three-dimensional surface in space, certain longitudinal cuts of which, for example, are given in Fig. 8. The upper five frames in this Figure correspond to a wave frequency  $f$  of 30 kHz, whereas the lower frames are for  $f=69$  kHz, these being chosen to represent approximately the lowest and highest frequency bands at  $\sim 01$  UT in Fig. 2. Concentrating on the first frame, two dipole field lines are shown for reference, one at  $L=4$  and the other at  $L=8.5$ . At the time when Fig. 2 was recorded the electron gyrofrequency at the spacecraft was found to be  $\sim 1.65$  kHz (B. Higel, private communication). The position of GEOS 2 is represented by the radius vector to  $6.6R_E$  at  $-3^\circ$  latitude. The two quasi-elliptical lines are the contours of  $f=1.4f_{ce}$  and  $f=2f_{ce}$ , and will not be considered further in the present paper. The lines of symbols in the first frame are the loci of possible sources of 30 kHz TMR which would be visible to GEOS 2 assuming the TMR emanates from field-aligned plasma density enhancements via the radio window. The symbols are coded so that the angle between the wave  $k$ -vector and  $B_0$  at the spacecraft is known. On the original computer plots the symbols are colour-coded to allow one to distinguish between  $5^\circ$  and  $50^\circ$  for example, both of which appear as the symbol 5 in Fig. 8. The first frame is for loci in the same meridian plane as the spacecraft ( $\delta=0^\circ$ ) and the other frames show loci at  $10^\circ$  longitude steps away from this meridian plane, the maximum longitude difference considered in the present example being  $\delta=40^\circ$ . It is seen that no low-latitude sources of 30 kHz TMR within  $7R_E$  are visible to GEOS-2 when  $\delta=40^\circ$ ; the low-latitude sources of 69 kHz TMR disappear from view before  $\delta$  reaches  $50^\circ$ .

Concentrating on source loci in the same meridian plane as the satellite and initially on sources in the Northern hemisphere, i.e. in the hemisphere opposite to that of the satellite, Fig. 9a shows the variation in  $f_{ce}$  as a function of latitude for sources corresponding to the frequency bands in Fig. 2. At 0033 UT, the bands are observed to be at frequencies of 30, 36.5, 43 and 49.5 kHz, yielding a frequency spacing of 6.5 kHz. Assuming the latter to be the source gyrofrequency, the emissions are seen from Fig. 9a to emanate from magnetic latitudes covering  $2.54$ – $3.63^\circ$ , i.e. at a latitude of  $\sim 6^\circ$  with respect to the latitude of the satellite. The corresponding radial distance of the sources, which is shown in Fig. 9b, lies at  $4.18R_E$ . At 0057 UT, the bands have frequencies of 30, 36.5, 45, 53, 61 and 69 kHz indicating a source  $f_{ce} \approx 8$  kHz. Thus from Fig. 9a, the latitude range of the sources at this time is  $2.63^\circ$ – $4.56^\circ$  and, from Fig. 9b, the sources lie at  $3.9R_E$ . Hence, the effect of the magnetic substorm which occurred just after 00 UT on April 25 1980 is to cause the plasmopause to move to a smaller radial distance, and the average speed of motion is found from Fig. 9b to be 1.24 km/s. This is more clearly illustrated in Fig. 10 which shows the positions of the plas-



**Fig. 8a and b.** Loci of TMR sources visible to a geostationary spacecraft at  $-3^\circ$  magnetic latitude. The upper **a** and lower **b** sets of frames are for frequencies of 30 and 69 kHz respectively. The first frame in each set is for the meridian plane through the satellite; the satellite position is shown by the line of length  $6.6R_E$  at  $-3^\circ$ . The other frames are for loci in meridian planes at  $10^\circ$ – $40^\circ$  longitudes relative to that of the spacecraft. The symbols on the loci are coded to yield the direction of the wave normal with respect to the magnetic field at the spacecraft (see text)

mapause at the two times considered, with a sketch of the most intense TMR at  $f \approx (n + \frac{1}{2})f_{ce}$  being beamed away into the magnetospheric cavity, the beaming angles with respect to the magnetic field being given by  $\arctan(f/f_{ce})^{\frac{1}{2}}$  (see Jones, 1982).

A number of other important conclusions can be drawn from Figs. 9 and 10. It can be deduced from Fig. 9 that the TMR wave-normal at the spacecraft makes an angle of  $\sim 85^\circ$  with  $B_0$  for  $f = 30$  kHz and  $\sim 88^\circ$  for  $f = 69$  kHz. Thus the wave electric field will be quite highly elliptically polarised along  $B_0$  and it is again of the utmost importance to know the spacecraft orientation with respect to  $B_0$  if one is to arrive at meaningful source directions from spinning dipole DF measurements. An added complication in the present example, where the spacecraft is near to local midnight, may be the relatively rapid temporal and spatial variation of the local magnetic field direction due to magnetic activity. This could result in a change in the position of the electric field nulls detected by the dipole antenna, even if the source remains fixed relative to the spacecraft. This will to some extent also affect the remote sensing which, at present, is based on the assumption of a dipole

magnetic field. In the present example, the magnetic latitude of GEOS-2 is assumed to be  $-3^\circ$  as is shown in Fig. 8, but clearly the exact latitude of the spacecraft when the magnetic field is changing is unknown. Had the latitude been assumed to be  $0^\circ$ , the difference between the latitude of the sources and the satellite latitude is found to be reduced by  $\sim 1.3^\circ$  from the  $6^\circ$  deduced from Fig. 9. However, the radial positions at 0033 and 0057 UT of the sources are both decreased by  $\sim 0.68R_E$ , thereby resulting in the same value for the speed of inward motion of the plasmopause.

The constancy of the frequency separation with frequency in Fig. 2 implies that the plasmopause is very steep, the gradient being far larger than the value obtained from Fig. 4 corresponding to the event in Fig. 1. Such a large density gradient has the effect of greatly increasing the window dimensions compared to those computed by Jones (1982). This will, in turn, render the TMR beam wider and hence the remote sensing technique less accurate; this is an effect which will be the subject of further study.

Sources in the same hemisphere as the satellite and those out of the satellite's meridian plane (see Fig. 8) show very

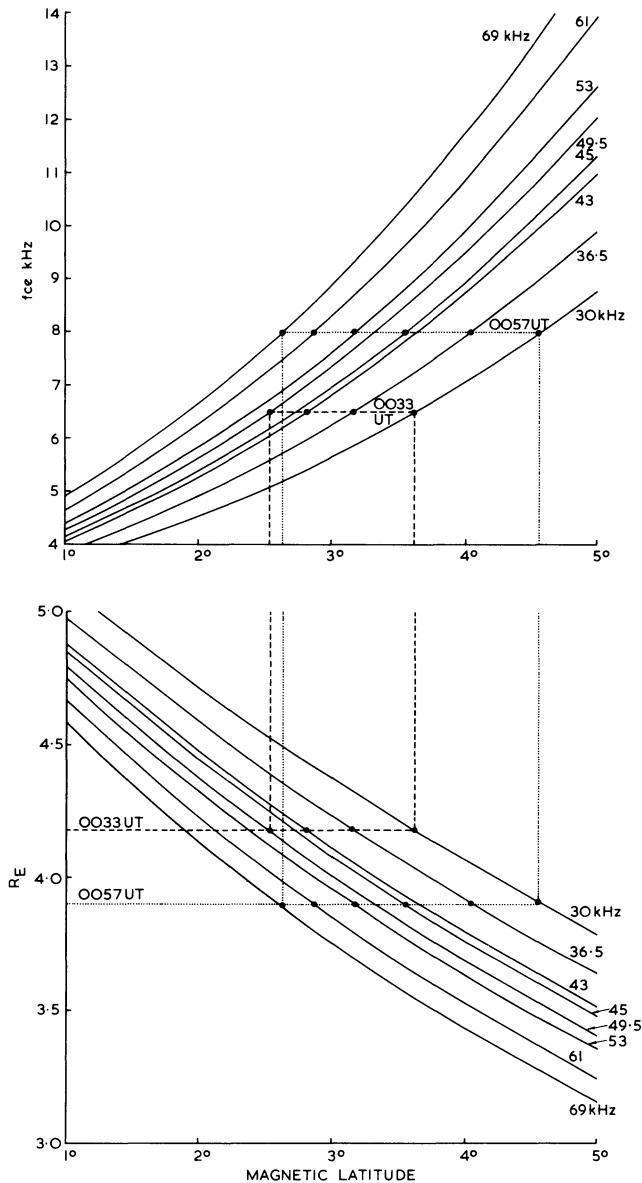


**Fig. 9.** The upper frame shows the variation of the source gyrofrequency  $f_{ce}$  as a function of latitude for the Northern equatorial sources derived from computations similar to those shown in Fig. 8. The TMR frequencies (30–69 kHz) are taken at two times, 0033 UT and 0057 UT, from Fig. 2. The spacings between the TMR bands are taken as indicative of the source  $f_{ce}=6.5$  kHz and 8.0 kHz respectively. The lower frame shows the variation of the source radial distance as a function of latitude corresponding to the upper frame

similar characteristics to those discussed above. Clearly the gyrofrequency spacing restricts the source radial distance to quite strict limits if latitudes  $\lesssim 10^\circ$  only are considered and hence the speed of inward motion of the plasmopause is close to 1.24 km/s in all cases. However, the angle between the magnetic field and the  $k$ -vector at the spacecraft does change, but is within  $10^\circ$  of being perpendicular except when the longitude difference between source and spacecraft is  $\gtrsim 30^\circ$ , i.e. close to the limit of observation.

In conclusion, it has been demonstrated that it may be possible to obtain both the radial distance and latitude of the sources of TMR which exhibit harmonic structure

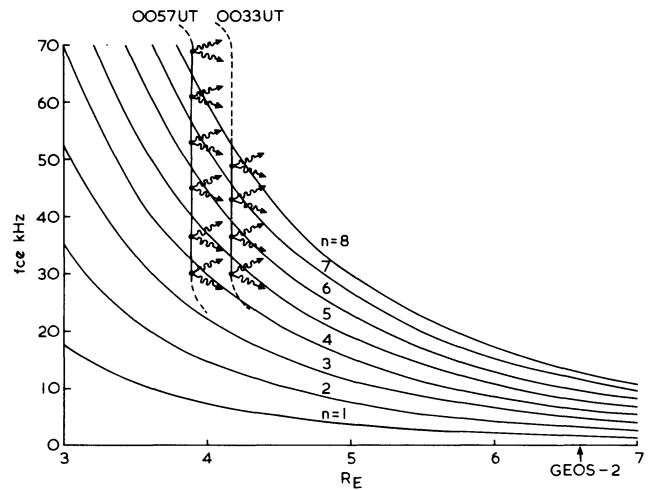


**Fig. 10.** Variation of the gyrofrequency  $f_{ce}$  fundamental ( $n=1$ ) and its harmonics ( $n=2$  to 8) as a function of radial distance. The lines labelled 0033 UT and 0057 UT indicate the positions of the plasmopause at the two times. The sources of the banded TMR are as shown.

of the form shown in Fig. 2. The broadband nature of the event shown prior to 0020 UT may indicate that another mechanism, such as the Cerenkov production of  $Z$ -mode waves, may be operating in parallel with the  $(n+\frac{1}{2})f_{ce}$  e.s. instability during this period. The abrupt termination of the event at 0.1 UT could be due to a number of effects, such as a switching off of the source instability, the movement of the TMR source from the vicinity of the spacecraft meridian plane, or the swinging of the TMR beams away from the spacecraft by a change in the direction of the density gradient at the source.

## Discussion

The technique of remote sensing of the plasmopause and its associated irregularities by TMR is still very much in its infancy and it is clear that a number of problems remain to be solved.

The first problem concerns the TMR emission mechanism itself. Although the linear theory outlined here appears to be the favoured candidate at present, it requires an independent confirmation by some means or other. This could come from measurements of the wave-distribution function of the UHR source waves as is being done by Kurth (private communication). If the  $k$ -vectors are found to be clustered in the plane containing the density gradient and magnetic field vectors, this would, as Barbosa (1982) puts it, “elevate the linear theory to a paramount position”. Indeed, the non-gyrotropy of the waves may provide a means of determining the direction of the density gradient vector which is a very difficult parameter to measure. Alternatively, or in parallel, the convective behaviour of the e.s. instability in the sort of density gradients encountered at the plasmopause needs to be investigated theoretically. It should be added that it is becoming evident that the density gradient does indeed play a crucial role in the conversion mechanism and/or in the basic instability relevant to the type of planetary emissions considered here (Kurth et al., 1981; Gurnett et al., 1981). The gradients observed by Kurth (1982) and inferred from Fig. 10 in the present paper are far greater

than those used in the window calculations of Jones (1982) with the result that the window dimensions are expected to be considerably larger; full-wave calculations are underway to investigate this. It may also be possible to test the window theory by using two spacecraft such as ISEE-1 and 2 which are not too far apart. If the TMR is beamed as predicted by the window theory, dual spacecraft measurements could obtain valuable information on the beamwidth. Etcheto et al. (1982) have endeavoured to investigate this effect using GEOS-1 located at  $6.9R_E$ ,  $23^\circ$  magnetic latitude, 6.26 magnetic local time (MLT) and ISEE-1 at  $8.7R_E$ ,  $-4.2^\circ$  magnetic latitude, 8.03 MLT. TMR with similar spectra were observed on both spacecraft and this was taken as evidence of no beaming. Surprisingly, however, the wave intensities were greater on ISEE which was at the larger radial distance, and this seems to be more compatible with a magnetosheath source, in which case the beam characteristics cannot be as easily defined since the source magnetic field and density gradient orientations are not well-known. It should also be added that the direction-finding measurements of Etcheto et al. (1982) which indicated a plasmaspheric source were made without considering wave-polarisation effects.

The remote sensing technique at present assumes a dipole magnetic field for the Earth. It is believed that this is sufficiently accurate for plasmaspheric sources under quiet geomagnetic conditions, in which case it may also be sufficient to assume that the source e.s. waves are confined to the magnetic equatorial plane. Under geomagnetically active conditions, however, especially on the night-side, it may be necessary to introduce a more complicated magnetic field model if one requires more exact source locations.

The importance of taking wave polarisation effects into account when performing DF measurements cannot be over-stressed. When accurate magnetic field measurements for GEOS-1 and 2 do become available it should be possible to pinpoint the sources in radial distance, local time and possibly in latitude and hence to track their motion, thereby obtained valuable information on plasma convection in the magnetosphere.

*Acknowledgements.* Valuable discussions with K.G. Budden, J. Etcheto, P. Christiansen, G. Gapper, E. Gershuny, P. Gough, B. Higel, W. Kurth, B. Lembege, A. Pedersen, M. Rycroft and R. Stoneham are gratefully acknowledged, and R.M. Laws is thanked for his encouragement and support.

## References

- Barbosa, D.D.: Low-level VLF and LF radio emissions observed at Earth and Jupiter. *Rev. Geophys. Space Phys.* **20**, 316, 1982
- Budden, K.G.: *Radio waves in the Ionosphere*, Cambridge Univ. Press, 1961
- Budden, K.G.: The theory of radio windows in the ionosphere and magnetosphere. *J. Atmos. Terr. Phys.* **42**, 287, 1980
- Chappel, C.R.: Detached plasma regions in the magnetosphere. *J. Geophys. Res.* **79**, 1861, 1974
- Etcheto, J., Christiansen, P.J., Gough, M.P., Trotignon, J.G.: Terrestrial continuum radiation observations with GEOS-1 and ISEE-1. *Geophys. Res. Lett.* **9**, 1239–1242, 1982
- Frankel, M.S.: LF radio noise from the Earth's magnetosphere. *Radio Sci.* **8**, 991, 1973
- Gough, M.P.: Non-thermal continuum emissions associated with electron injections: remote plasmopause sounding. *Planet. Space Sci.* **30**, 657, 1982
- Gough, M.P., Christiansen, P.J., Martelli, G., Gershuny, E.J.: Interaction of electrostatic waves with warm electrons at the geomagnetic equator. *Nature* **279**, 515, 1979
- Gurnett, D.A.: The Earth as a radio source: the non-thermal continuum. *J. Geophys. Res.* **80**, 2751, 1975
- Gurnett, D.A., Shaw, R.R.: Electromagnetic radiation trapped in the magnetosphere above the plasma frequency. *J. Geophys. Res.* **78**, 8136, 1973
- Gurnett, D.A., Kurth, W.S., Scarf, F.L.: Narrowband electromagnetic emissions from Saturn's magnetosphere. *Nature*, **292**, 733, 1981
- Jones, D.: Mode coupling of Cerenkov radiation as a source of noise above the plasma frequency. In: *Proceedings of the 10th Eslab. Symposium, Vienna (1975)*, p. 281. Hingham, Mass.: D. Reidel 1976a
- Jones, D.: Source of terrestrial non-thermal radiation. *Nature* **260**, 686, 1976b
- Jones, D.: Introduction to the S-300 wave experiment on board GEOS. *Space Sci. Rev.* **22**, 327, 1978
- Jones, D.: Latitudinal beaming of planetary radio emissions. *Nature* **288**, 225, 1980
- Jones, D.: Beaming of terrestrial myriametric radiation. *Adv. Space Res.* **1**, 373, 1981a
- Jones, D.: First remote sensing of the plasmopause by terrestrial myriametric radiation. *Nature* **294**, 728, 1981b
- Jones, D.: Terrestrial myriametric radiation from the Earth's plasmopause. *Planet. Space Sci.* **30**, 399, 1982
- Kurth, W.S.: Detailed observations of the source of terrestrial narrowband electromagnetic radiation. *Geophys. Res. Lett.* **9**, 1341–1344, 1982
- Kurth, W.S., Craven, J.D., Frank, L.A., Gurnett, D.A.: Intense electrostatic waves near the upper hybrid resonance frequency. *J. Geophys. Res.* **84**, 4145, 1979a
- Kurth, W.S., Ashour-Abdalla, M., Frank, L.A., Kennel, C.F., Gurnett, D.A., Sentman, D.D., Burek, B.G.: A comparison of intense electrostatic waves near  $f_{UHR}$  with linear instability theory. *Geophys. Res. Lett.* **6**, 487, 1979b
- Kurth, W.S., Gurnett, D.A., Anderson, R.R.: Escaping non-thermal continuum. *J. Geophys. Res.* **86**, 5519, 1981
- Lecacheux, A., Harvey C.C., Boischot, A.: Source localisation and polarisation determination in low frequency satellite radio astronomy. *Annales Telecomm.* **35**, 253, 1979
- Lemaire, J., Kowolkowski, L.: The role of plasma interchange motion for the formation of a plasmopause. *Planet. Space Sci.* **29**, 469, 1981
- Lembege, B., Jones, D.: Propagation of electrostatic upper-hybrid emission and Z-mode waves at the geomagnetic equatorial plasmopause. *J. Geophys. Res.* **87**, 6187, 1982
- Manning, R., Fainberg, J.: A new method of measuring radio source parameters of a partially polarised distributed source from spacecraft observations. *Space Sci. Instrum.* **5**, 161, 1980
- Melrose, D.B.: A theory for the non-thermal continuum radiation. *J. Geophys. Res.* **86**, 30, 1981
- Okuda, H., Ashour-Abdalla, M., Chance, M.S., Kurth, W.S.: Generation of non-thermal continuum radiation in the magnetosphere. *J. Geophys. Res.* **87**, 10457–10462, 1982
- Oya, H.: Conversion of electrostatic plasma waves into electromagnetic waves: Numerical calculation of the dispersion relation for all wavelengths. *Radio Sci.* **6**, 1131, 1971

Received November 15, 1982; Revised version January 24, 1983  
Accepted March 8, 1983

## Review Article

## Heavy Ion Plasmas in the Outer Magnetosphere\*

D.T. Young

Los Alamos National Laboratory, Los Alamos, New Mexico 87545, USA \*\* and Southwest Research Institute, San Antonio, Texas 78284, USA

**Abstract.** This brief review discusses heavy ions (below 30 keV/Q) in magnetospheric plasmas from two points of view: heavy ions as minor species or “tracers”, and heavy ions as major plasma constituents. At present some 12 species of heavy ions have been detected in concentrations ranging from nearly 100% of the total ion density to  $<10^{-2}\%$ . Tracer ions detected thus far include  $^4\text{He}^{2+}$ ,  $\text{O}^{2+}$ ,  $\text{N}^+$  and  $\text{N}^{2+}$ ; whereas the species  $\text{O}^+$  and  $^4\text{He}^+$  very often appear as major ions, i.e., they make up a large enough fraction of the plasma to significantly alter its dynamical properties. Still other ion species, such as high charge state solar wind oxygen or ionospheric molecular species, may be present in the high altitude magnetosphere but have not yet been detected. Some discussion of future prospects in this field is included.

**Key words:** Ion composition – Magnetosphere – Mass spectrometry

## Introduction

The era of heavy ions (i.e. ions other than  $\text{H}^+$ ) in the Earth's magnetosphere began in 1969 with two events: Axford's paper, given in 1969, suggesting the utility of heavy ions as tracers of magnetospheric plasma origins (Axford, 1970), and the Lockheed group's initial measurements of precipitating heavy ion fluxes in the Earth's upper ionosphere (Shelley et al., 1972). In view of later developments, these two events also serve to establish a useful physical distinction between heavy ions as tracers, and heavy ions as major constituents of magnetospheric plasmas. Over the past decade, ion composition has grown to be a key ingredient in the study of magnetospheric plasma and dynamics. At the present time, an even dozen ion species, including two isotopes, have been identified at energies per charge  $\leq 30$  keV/Q (Fig. 1).

During the 1960's, experiments carried on board sounding rockets succeeded in identifying  $\text{H}^+$  and  $^4\text{He}^{2+}$  ions

\* Based on an invited review paper given at the Symposium on Plasma and Energetic Particles in the Magnetosphere, EGS Meeting, 23–27 August 1982, Leeds, U.K.

\*\* Permanent Address: Los Alamos National Laboratory, Los Alamos, NM 87545, USA

Offprint requests to: D.T. Young

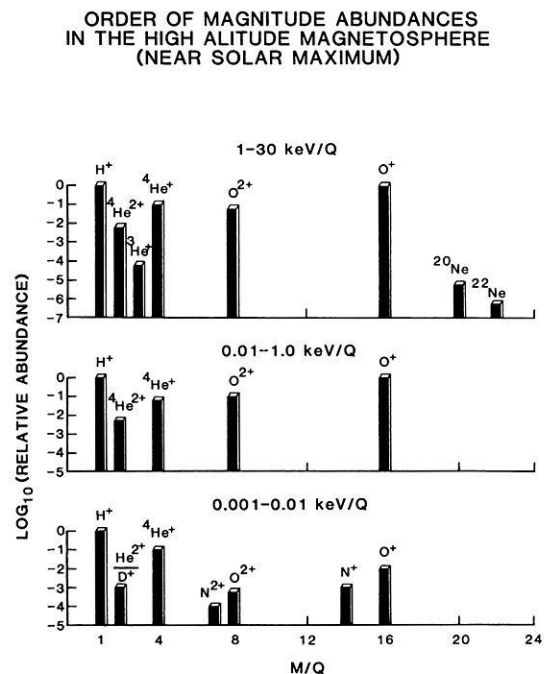


**Fig. 1.** Schematic overview of magnetospheric ion composition in three energy ranges. The two isotopes of neon as well as  $^3\text{He}$ , were detected in foils (Lind et al., 1979) and have not yet been observed by charged particle detectors. They are included here because their abundances suggest a solar wind ion source, which in turn implies that these species entered the magnetosphere as ions.

in auroral fluxes (Reasoner, 1973). This tended to confirm the conventional wisdom of the time which identified the solar wind as the expected source of auroral particles. The only competing source was the polar wind, which could have been distinguished by the presence of  $^4\text{He}^+$  in measurements made at high altitudes (Reasoner, 1973). Solar wind helium could also be traced by its distinctive  $^3\text{He}/^4\text{He}$  ratio (Axford, 1970; Bühler et al., 1976). In the late 1960's, the Lockheed group began flying a series of satellite-borne ion mass spectrometers of the Wien filter type (see the review by Balsiger, in press, for a discussion of instrumentation). These instruments were able to distinguish the major ion species and were responsible for the discovery that large fluxes of  $\text{O}^+$  ions are present in the ring current during geomagnetic storms (Shelley et al., 1972). A second obser-

vational breakthrough (not dealt with in this review) occurred with the detection of kilovolt ions flowing upward out of the auroral regions (Shelley et al., 1976).

In 1970, groups at the University of Bern and the Max-Planck-Institut in Garching began developing the first in a series of focusing mass spectrometers that were optimized for space plasma measurements (Balsiger et al., 1976). This design first saw service on GEOS-1 and has since been flown on GEOS-2, ISEE-1 (Shelley et al., 1978), and DE-1 (Shelley et al., 1981). GEOS provided the first in situ measurements of trapped magnetospheric ions of ionospheric origin, including composition of the ring current up to 17 keV (Geiss et al., 1978; Balsiger et al., 1980). With ISEE-1, composition observations have been extended out to 22  $R_E$  in the magnetotail (Sharp et al., 1981). The Wien filter design also continues to provide important measurements, having been flown on S3-3, PROGNOZ-7 and SCATHA, the latter instrument reaching energies of 32 keV (Johnson et al., in press).

New instrument designs have been proposed for NASA's OPEN mission. They will push magnetic mass spectrometers to still higher energies ( $\sim 40$  keV) and provide better time resolution with complete mass-energy-pitch angle scans once per spacecraft spin period, or  $\approx 3$  s.

Following this abbreviated background survey, we discuss in the remainder of this review the most significant composition observations and a few of the consequences for magnetospheric plasmas. The paper is divided along lines mentioned earlier, namely (1) heavy ions as tracers, and (2) heavy ions as major constituents.

### Heavy Ions as Tracers

The following section presents a list of ion species detected thus far in the high-altitude magnetosphere. Three energy ranges may be distinguished: *energetic* (1–30 keV/ $Q$ , where  $Q$  is the ionization state), *suprathermal* (0.01–1.0 keV/ $Q$ ), and *thermal* (1–10 eV/ $Q$ ). Roughly speaking, five ion species can be detected with good reliability by present day instrumentation. The capability of these detectors is typified by the averaged GEOS-2 spectrum shown in Fig. 2.

#### 1–30 keV/ $Q$ (Energetic Plasmas)

$^4\text{He}^{2+}$ . Detected throughout the magnetosphere, usually at concentrations from a few tenths of a percent to a few percent. Typical differential fluxes near geostationary orbit ( $L \approx 6.6$ ) are 3–30 ions  $(\text{cm}^2 \text{ s sr eV})^{-1}$  (Balsiger et al., 1980).  $^4\text{He}^{2+}$  has been detected (at lower flux levels) out to  $\sim 20 R_E$  in the tail on ISEE-1 (Peterson et al., 1981). Although low-energy  $^4\text{He}^{2+}$  of terrestrial origin has also been detected (see below), at the measured  $^4\text{He}^{2+}$  mean energies of 5–10 keV/ $Q$  and above, we have every reason to believe that the solar wind is the source of  $^4\text{He}^{2+}$ . Several studies have been initiated to trace the temporal signature, and hence the transport, of solar wind  $^4\text{He}^{2+}$  into the magnetosphere (cf. Balsiger et al., in press) thus far without conclusive results. Generally speaking, the densities of  $\text{H}^+$  and  $^4\text{He}^{2+}$  increase with increasing distance from the Earth (Fig. 3) as might be expected of ions whose source region is at the outer boundary of the magnetosphere.

$^3\text{He}^{2+}$ . Because of its very low flux,  $^3\text{He}^{2+}$  has not been detected by satellite-borne mass spectrometers. Instead,  $^3\text{He}$  has been observed using the foil-trapping technique both

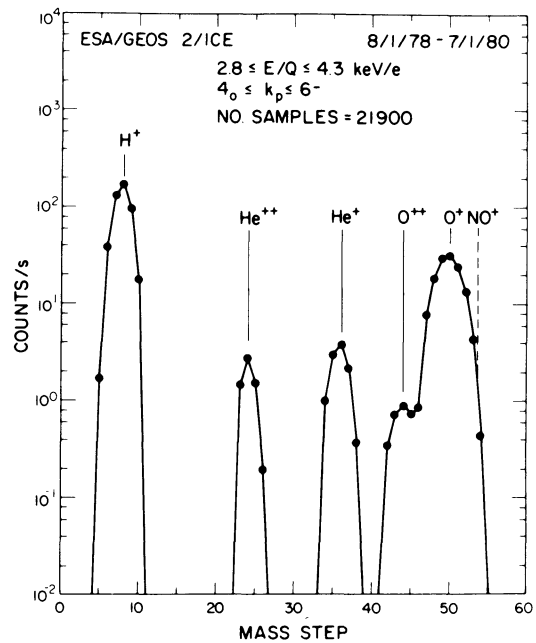


Fig. 2. Integrated mass spectrum based on 11 months of GEOS 2 data. Four energy steps have been summed over and a total of 21,900 samples of 0.1505 s have gone into each data point. The average background subtracted was 6.78 counts/s. The mass step scale extends to 63 but the last 3 steps are not shown. Note that 5 ion species are easily seen and resolved, and also the absence of any 'ghost' or other spurious peaks. If  $\text{NO}^+$  were present it would be located in mass channel 53.5 (dashed line). On the basis of the analysis of the  $\text{O}^+$  peak shape it is estimated that  $\text{NO}^+/\text{O}^+ < 0.03$ . (From Young et al., 1982)

in the aurora (Bühler et al., 1976) and on Skylab at  $L < 4$  (Lind et al., 1979). The Skylab  $^4\text{He}/^3\text{He}$  ratio at  $\sim 30$  keV was found to be  $3,100 \pm 200$ , similar to that of the solar wind ( $2,350 \pm 150$ ), with perhaps a small admixture of terrestrial  $^4\text{He}$ . Based on Skylab results we might expect typical  $^3\text{He}$  fluxes near  $L \approx 6.6$  to be  $10^{-3}$  to  $10^{-2}$  ions  $(\text{cm}^2 \text{ s sr eV})^{-1}$ , well below current state-of-the-art in ion mass spectrometer sensitivity.

$^4\text{He}^+$ . Detected throughout the magnetosphere (Figs. 3 and 4), it is most intense near the inner edge of the ring current (Balsiger et al., 1980; Lennartsson et al., 1981; Lundin et al., 1980) but has also been observed in the subsolar magnetopause boundary layer and magnetosheath (Peterson et al., 1982). Within the magnetosphere it is found that  $^4\text{He}^+$  and  $^4\text{He}^{2+}$  have dissimilar energy spectra, with  $^4\text{He}^{2+}$  having a higher mean energy and  $^4\text{He}^+$  a higher mean density (Balsiger et al., 1980). This suggests that, at least in the 1–15 keV/ $Q$  energy range, the two species are unrelated, i.e.  $^4\text{He}^+$  does not originate from  $^4\text{He}^{2+}$  by charge exchange. Furthermore, long term studies with GEOS (Young et al., 1982) show no correlation of averaged  $^4\text{He}^+$  and  $^4\text{He}^{2+}$  densities, again suggesting independent sources for the two species:  $^4\text{He}^+$  being terrestrial,  $^4\text{He}^{2+}$  being solar.

$^{16}\text{O}^{6+}$ ,  $5^+$ ... Have not been detected by any means, except in the magnetosheath (Geiss et al., 1978), and are expected to be present only at low flux levels (cf. Fig. 2). Typically the relative solar wind  $\text{O}/\text{He}$  elemental abundance ratio is

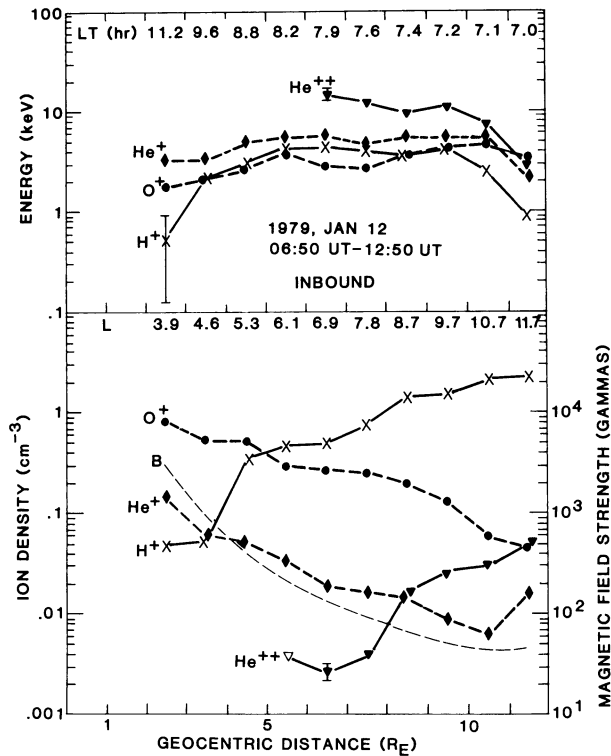


Fig. 3. Characteristic energies (*upper panel*) and number densities (*lower panel*) sampled during a magnetically quiet day, plotted versus the distance of ISEE-1 from the center of the Earth. The local time of each data point is shown at the top of the figure, the corresponding  $L$  parameter (dipole) is shown in the middle. The  $\pm 1\sigma$  uncertainty carried over from the counting statistics is shown as an error bar when larger than the data symbol. The open data symbol on the  $\text{He}^{2+}$  density graph (*bottom*) represents an upper limit. The  $\text{He}^{2+}$  was below background at  $L < 6$  (corresponding to a density of less than a few percent of the total density). The thin dashed curve labelled B (*lower panel*) shows the measured magnetic field with the scale to the right. Qualitatively similar trends in composition during storms has been reported by Balsiger et al. (1980). (From Lennartsson and Sharp, 1982.)

$\sim 0.01$  (Bame et al., in press). In GEOS-type instruments, which are currently the most sensitive,  ${}^4\text{He}^{2+}$  approaches the detection limit for isotropic fluxes except during disturbed periods. Moreover, solar wind oxygen should have roughly four times the total energy of  ${}^4\text{He}^{2+}$ , or about 1.5 times its energy per charge, which places the bulk of it above the  $\sim 20 \text{ keV}/Q$  energy per charge limit of most plasma mass spectrometers. Routine detection of  ${}^{16}\text{O}^{6+}$  would nonetheless be of some interest because it, together with  ${}^4\text{He}^{2+}$ , represents a second solar wind ion species pair (after the  $\text{H}^+ - {}^4\text{He}^{2+}$  pair) on which to base studies of magnetospheric ion transport. The high percentage of terrestrial  $\text{H}^+$  in the magnetosphere greatly detracts from the usefulness of the  $\text{H}^+ - {}^4\text{He}^{2+}$  ion pair as a tracer.

${}^{16}\text{O}^{2+}$ . Detected under disturbed conditions and in long-term averages (Fig. 2) which increase the signal to noise ratio of the data (Young et al., 1982).  $\text{O}^{2+}$  has been detected in magnetotail ion beams (Sharp et al., 1981), and Young et al. report that it, like  $\text{O}^+$ , has a strong solar cycle dependence (see below). At low levels of magnetic activity ( $K_p < 2$ ) the long term  $\text{O}^{2+}/\text{O}^+$  ratio is  $\sim 0.05$  in kilovolt plasmas located near geostationary orbit.

${}^{16}\text{O}^+$ . Detected under nearly all conditions at fractions ranging from a few percent to over 80% of the total density (Figs. 3, 4). Often kilovolt  $\text{O}^+$  is too abundant to be called a tracer (see below) although its presence at any measurable concentration indicates an ionospheric source. The bulk of composition observations have been made near the maximum of the current solar cycle (Fig. 5) and, as a result, some bias undoubtedly affects our present thinking about "average" magnetospheric composition. One example of the consequences of heavy ion enriched plasmas has been suggested by Baker et al. (1982): the presence of  $\text{O}^+$  in the tail plasma sheet may promote growth of the ion tearing mode instability, thereby facilitating the onset of magnetospheric substorms.

${}^{20}\text{Ne}$ ,  ${}^{22}\text{Ne}$ . Lind et al. (1979) report the detection of neon isotopes trapped in Al and Pt foils on the Skylab experiment. Typical measured values of  ${}^{20}\text{Ne}/{}^{22}\text{Ne}$  were 13–20. This is reasonably near the solar wind ratio of 13.7 and rules out a terrestrial source for which the ratio is 9.8. Furthermore, the  ${}^{20}\text{Ne}/{}^3\text{He}$  ratio was found to be 0.1–0.2, again very close to the solar wind value of  $0.23 \pm 0.05$ . Measurement of the neon isotopes demonstrates the power of the foil technique for detecting and identifying rare noble gas ions since typical magnetospheric fluxes would be  $\sim 10^{-4}$  to  $10^{-3} (\text{cm}^2 \text{ sr eV})^{-1}$ .

#### *0.01–1 keV/Q (Suprathermal Plasma)*

There are now considerable data in the literature to show that this category of plasma population exists (Young, 1982). Figure 6, taken from Balsiger et al. (1980), shows several instances of  $< 1 \text{ keV}$  populations found near  $L = 6.6$ . Generally, suprathermal plasmas are found outside the plasmopause with typical densities of  $\sim 0.1\text{--}10 \text{ cm}^{-3}$ . They are characterized by a tendency to exhibit highly anisotropic pitch angle distributions (cf. Horwitz, 1982). These may be field-aligned or pancake (flux maximum at  $90^\circ$  pitch angle) or conical (flux maxima at some pitch angle between  $0^\circ$  and  $90^\circ$  or  $90^\circ$  and  $180^\circ$ ). Composition of this population is both energy and pitch angle dependent, with the field-aligned and conical components dominated by  $\text{O}^+$  and  $\text{H}^+$  and the trapped component characterized very roughly by  $\text{H}^+ > \text{He}^+ > \text{O}^+$  ordering. The reader is directed to recent reviews by Horowitz (1982) and Young (1982) for further details.

${}^4\text{He}^{2+}$ . Detected at concentrations such that  ${}^4\text{He}^{2+}/{}^4\text{He}^+$  is usually below a few percent. Because of its low mean energy and the shape of its energy distribution, it is clear that this component of  ${}^4\text{He}^{2+}$  is of terrestrial origin (Fig. 6). Although acceleration of  ${}^4\text{He}^+$  to suprathermal energy by wave-particle interactions has been observed (see below), similar observations of  ${}^4\text{He}^{2+}$  are problematic due to its low concentration. However, since waves near  $\Omega_{\text{He}^+}$  (the  $\text{He}^+$  cyclotron frequency) are quite intense and exhibit harmonics as well, there is no reason why  ${}^4\text{He}^{2+}$  could not also be accelerated in a manner similar to  ${}^4\text{He}^+$ .

${}^4\text{He}^+$ . Nearly always present in the suprathermal plasma at levels of a few percent to a few tens of percent. Investigation of intense ULF waves near  $\Omega_{\text{He}^+}$  on the GEOS satellites has established that  ${}^4\text{He}^+$  plays a critical role in the generation and amplification of these waves and is in turn heated

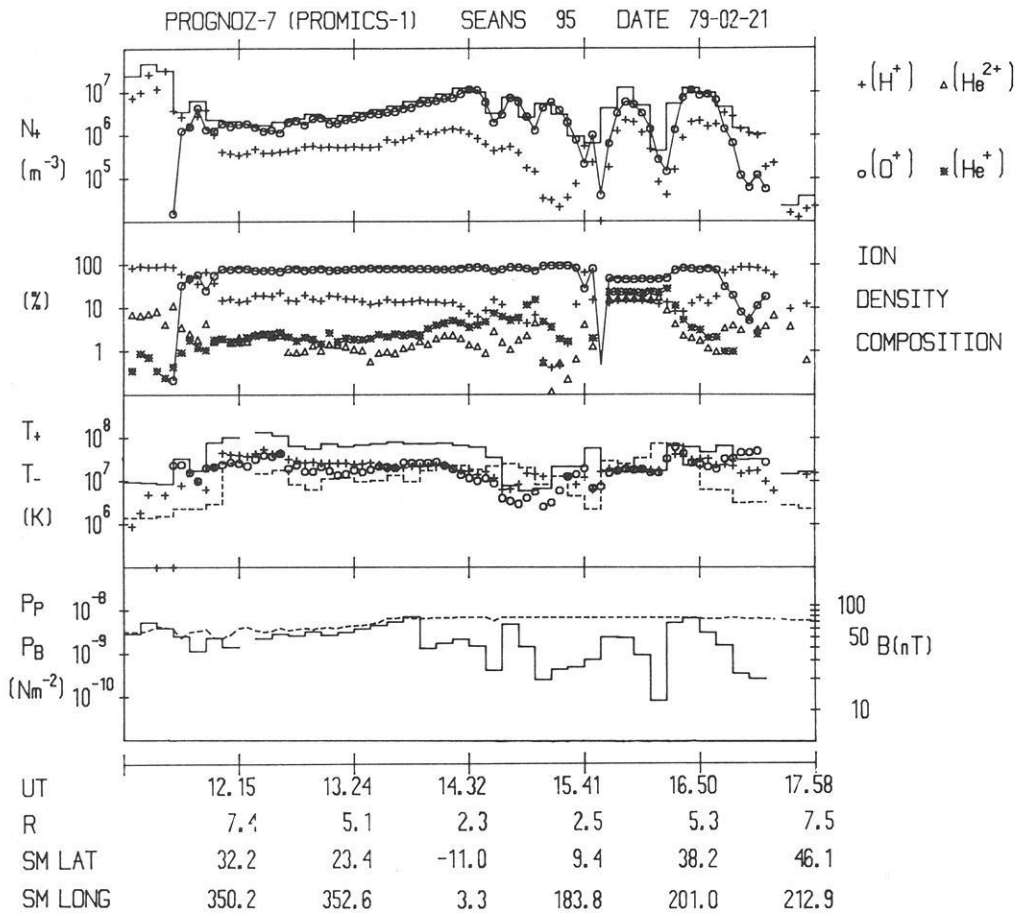


**Fig. 4.** An example of a storm time ring current observed on PROGNOZ, when  $O^+$  ions dominated completely over the entire dayside magnetosphere and also part of the nightside ring current. Between  $\sim 1545$  and  $\sim 1635$  UT, radiation belt MeV electrons produced a background that dominated the detectors. The upper panel shows the ion number density ( $N_+$ ) as deduced from  $E/q$  spectrometers, assuming the ions to be protons (solid line). Plus signs represent the number density of  $H^+$  as deduced from the perpendicularly oriented mass spectrometer assuming isotropy, and circles represent the number density of  $O^+$  derived from the measurements of both the perpendicular mass spectrometer and one pointing  $25^\circ$  from the direction to the sun. The second panel from the top represents the percentages of the four major ion constituents. The third panel shows the temperatures of ions (solid line) and electrons (dashed line) as deduced from  $E/q$  electron and ion spectrometer data fitted to Maxwellians. In the same panel the ‘perpendicular’  $H^+$  (pulses) and  $O^+$  (circles) temperatures have been plotted. The fourth panel contains the magnetic field and flow velocity components in the  $xy$  and  $yz$  solar ecliptic coordinate planes. Flow velocity components represented by solid lines refer to  $H^+$  ions, and dashed lines to  $O^+$  ions. The time and space coordinates (in solar magnetic (SM) coordinates;  $R$  in earth radii) are given along the horizontal axis. (From Hultqvist, 1982.)

by them (Roux, 1982). In this case one cannot consider  $^4He^+$  as a tracer ion, rather it becomes an active ingredient of the plasma as discussed below. The presence of  $^4He^+$  is, however, useful as a tracer of plasmaspheric-like ion composition signatures (Balsiger et al., 1980). The plasmaspheric ordering of composition ( $H^+ > He^+ > O^+$ ), which is the result of either diffusion or polar wind-like flow, can be distinguished from ionospheric ordering ( $H^+, O^+ > He^+$ ), which is usually associated with kilovolt plasmas. A critical issue now under investigation is the extent to which near-equatorial acceleration processes, such as the interaction of  $^4He^+$  with ULF waves, contribute to more energetic plasma populations such as the storm time ring current.

$O^{3+}$ . Has been observed a few times (Fig. 6) in conjunction with high  $He^{2+}$  and  $O^{2+}$  abundances (Balsiger, 1981; Balsiger et al., in press). Its source is thought to be the same as that of  $O^{2+}$  (see below).

$O^{2+}$ . Detected at concentrations of  $O^{2+}/O^+ \sim 0.1$  and higher, although we emphasize that  $O^{2+}$  and  $^4He^{2+}$  are both highly variable. The generally higher  $O^{2+}/O^+$  ratios in comparison to those of  $He^{2+}/He^+$  may be understood largely in terms of production rates for the respective doubly charged ions (Geiss et al., 1978). Transport processes also play an important role in determining these ratios, particularly within the plasmasphere (see below). As ion detectors evolve towards greater sensitivity with future space missions, it should become practical to employ the doubly charged species as diagnostics of magnetospheric wave-particle interactions in a situation analogous to the role of multiply-charged species used to study heavy ion acceleration in the solar wind.

$O^+$ . Commonly detected, particularly in the field-aligned plasma component. For example, Kaye et al. (1981) have argued that because the field-aligned component of so-called ‘zipper’ events is  $O^+$  dominated, these ions are

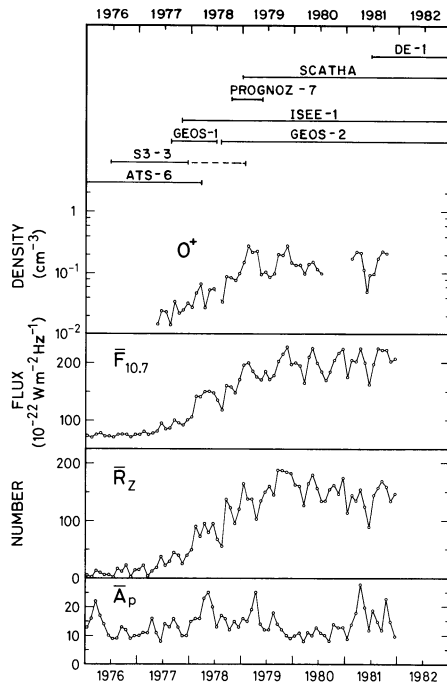


**Fig. 5.** Upper panel shows spacecraft which carried ion composition experiments over the past seven years (ATS-6 carried only solid state detectors sensitive to heavy ions  $\geq 100$  keV/nucleon, all others carried plasma composition and most had solid state experiments as well). The bottom four panels are taken from Young et al. (1982). Upper panel is the density of 1–14 keV  $O^+$  ions measured near geostationary orbit with the GEOS-1 and -2 satellites. The GEOS data are monthly averages restricted to intervals of  $K_p < 20$  in order to remove variations caused by geomagnetic activity. The bottom three panels are monthly averages of (from top to bottom) the 10.7 cm solar radio flux, the Zurich sunspot number, and the global magnetic activity index (these data are taken from J. Geophys. Res.)

being injected directly from the ionosphere into the near-Earth portion of the plasma sheet. There is also some evidence for the existence of ULF waves, and presumably wave-particle interactions as well, near  $\Omega_{O^+}$  (Fraser and McPherron, 1982).

#### 1–10 eV/Q (Thermal Plasma)

Routine ion measurements within the plasmasphere are somewhat problematic for experimental reasons, primarily the limited angular coverage of mass spectrometers. Outside the plasmasphere these difficulties are exacerbated by high positive spacecraft potentials ( $\sim +5$  V) and the nonequilibrium state of the lower density plasma ( $< 10$  cm $^{-3}$ ). Remarks in this section are therefore confined to thermal plasma within the plasmasphere.

$^4He^{2+}$ . Has been detected at concentrations  $\leq 10^{-3}$  relative to total ion density. Typically the  $^4He^{2+}/^4He^+$  ratio is less than a few percent. This points toward an enrichment of  $^4He^{2+}$  relative to  $^4He^+$  in comparison to its ionospheric value. Geiss et al. (1978) have suggested that enrichment is driven by the temperature gradient between the equatorial plane and the ionosphere (roughly several thousand degrees K) through the mechanism of thermal diffusion. This process is discussed in more detail below in connection with  $O^{2+}$ .

$^2D^+$ . Assuming the different plasmaspheric ion species to be in thermal equilibrium, then it is possible to determine whether the  $M/Q=2$  peak is predominantly  $^4He^{2+}$  or  $^2D^+$ . On one occasion, at  $L \approx 3.5$  in the plasmasphere, Geiss et al. (1978) found that the  $M/Q=2$  peak was most likely  $^2D^+$  since this gave the most consistent result for the temperatures of all species (i.e., because of its extra charge, the assumption that  $^4He^{2+}$  was present would have yielded twice the temperature of the other species). Geiss et al. have argued that  $^2D^+$  is the dominant  $M/Q=2$  ion if the abundance of  $M/Q=2$  ions is  $\leq 5 \times 10^{-4}$  that of  $H^+$ , whereas  $^4He^{2+}$  is dominant if the abundance is  $\geq 10^{-3}$  that of  $H^+$ .

$^4He^+$ . Is typically the second most abundant plasmaspheric ion (after  $H^+$ ) with relative concentrations of  $\sim 10\%$ . Earlier studies based on OGO-5 data gave the impression that  $^4He^+$  comprised only  $\sim 1\%$  of the total, a result that may have been due partly to data selection and partly to instrumental effects (see Young, 1979 for discussion of the latter). Modeling efforts are now under way that should aid in our understanding of plasmaspheric  $^4He^+$  which, in this regard, can be treated as a minor ion species (Murphy et al., 1979). What is presently lacking are good synoptic measurements that accurately describe the distribution and dynamic behavior of  $^4He^+$ .

$N^{2+}, N^+$ . Have been observed with the Retarding Ion Mass Spectrometer on DE-1 by Chappell et al. (1982). Both species were seen in the plasmasphere where the  $N^+/O^+$  ratio was  $\sim 0.1$  during one spacecraft orbit, with a corresponding  $N^{2+}/N^+$  value of 0.01 to 0.05. Over the polar cap  $N^+$  was observed at similar concentrations and at altitudes up to  $3 R_E$ . Near the equator at  $L \sim 6.6$ , Young et al. (1977) placed an upper limit of 0.3 on the  $N^+/O^+$  ratio.

The observation of thermal nitrogen ions opens up the question of what percentage of the “oxygen” seen at kilovolt energies is in fact nitrogen. Are we witnessing another example of the situation described previously for protons, in which we will later find that most of the magnetospheric oxygen is in fact nitrogen? From the point of view of ionospheric chemistry one can argue that this cannot be the case since atomic oxygen, the main source of  $O^+$  and  $O^{2+}$  ions, is the dominant neutral constituent over a wide range of altitudes. Secondly, the relative difference in the masses of  $O^+$  and  $N^+$  is small and should not alter plasma behavior even at concentrations above the presently observed  $N^+/O^+$  ratio of  $\sim 0.1$ . Nitrogen may nonetheless play an important observational role, for example as a tracer of the influence of ionospheric chemistry on magnetospheric composition.

$O^{2+}$ . Detected in the plasmasphere in varying concentrations. Of particular interest is the observation that the  $O^{2+}/O^+$  ratio increases with time as the plasmasphere fills following a magnetic disturbance (Geiss et al., 1978). Over a few days  $O^{2+}/O^+$  rises from  $\sim 0.01$  to concentrations  $\geq 0.3$ , the latter being  $\sim 100$  times the value found in the topside ionosphere. Geiss and Young (1981) explain the  $O^{2+}$  enrichment relative to  $O^+$  as being the result of thermal diffusion of the doubly charged ion species in a background gas of singly charged ions. This has been tested by solving the time-dependent diffusion equation between the topside ionosphere ( $\sim 300$  km) and the equatorial plane. Their results show that the temperature gradient between

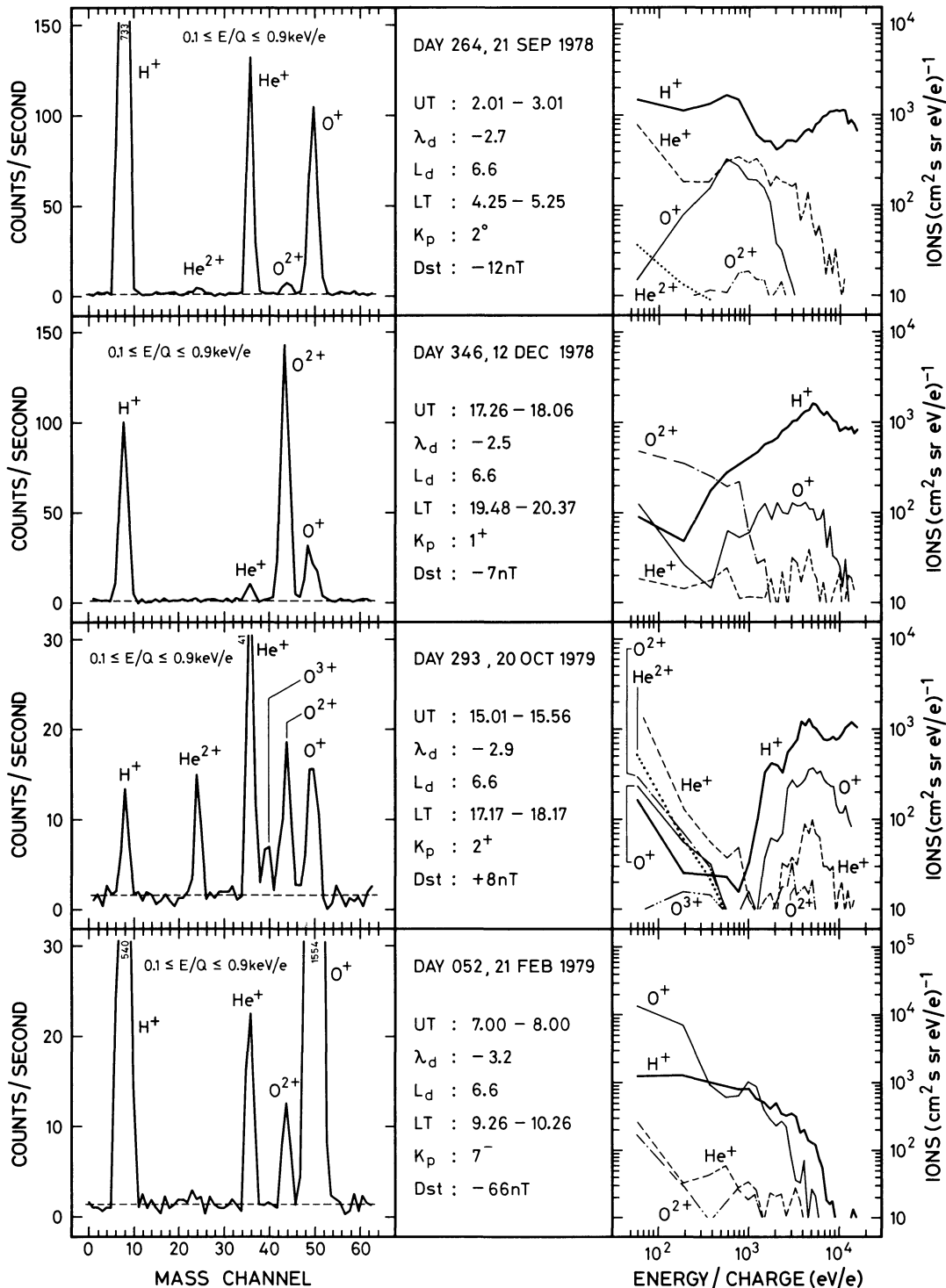


**Fig. 6.** Ions from “plasmaspheric” source (see text). Mass and energy spectra measured at geostationary orbit by the GEOS-2 mass spectrometer. Mass spectra (left) are averaged over the energy per charge range 0.1–0.9 keV/e. Counts per second are proportional to differential flux. Where mass peaks exceed the scale, the corresponding counting rates are given. Energy spectra (right) cover the full range of the mass spectrometer. In all four examples a plasmaspheric source is clearly recognizable by the source specific ions He<sup>+</sup> and/or O<sup>2+</sup>. The O<sup>3+</sup> ion, resulting from further ionization of O<sup>2+</sup>, is clearly recognizable on 20 October 1979; at the same time plasmaspheric He<sup>2+</sup> is exceptionally high (He<sup>2+</sup>/He<sup>+</sup> ≈ 0.3). (From Balsiger, 1981.)

the topside ionosphere ( $T_i = 1,000$  K) and equatorial magnetosphere ( $T_i \geq 5,000$  K) plays an important role in determining the build-up of doubly charged ions (Fig. 7). In this way, O<sup>2+</sup> has served in exemplary fashion as a tracer of transport processes.

O<sup>+</sup>. Detected in the plasmasphere, typically at concentrations of ~0.01 of the total ion density. An interesting point about O<sup>+</sup> is that its very presence in the high altitude plasmasphere is difficult to explain and no models presently exist which include O<sup>+</sup> transport. Geiss and Young (1981)

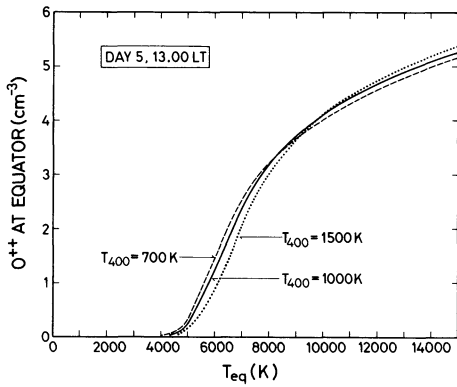


**Fig. 7.** Computed density of  $O^{2+}$  at the  $L=3$  equator as a function of equatorial temperature. Data are for 1,300 LT on the fifth day of plasmasphere filling. The three curves demonstrate that the effect of varying ion temperature at the ionospheric boundary is quite small. Note that the threshold temperature at which thermal diffusion becomes effective is  $\approx 5000$  K for all three curves. (From Geiss and Young, 1981.)

have solved the transport problem only for minor ions, and their models of the major ions  $H^+$  and  $O^+$  were based on observational data.

$NO^+$ ,  $N^{2+}$  ... Not detected. Young et al. (1977) estimated the sum of  $NO^+$ ,  $N_2^+$  and  $O_2^+$  to be less than 10% of the  $O^+$  density. Both chemistry and gravity work against molecular ions escaping into the high altitude plasmasphere,

although this may not always be the case. For example, during the large magnetic storm of August 1972, high concentrations of molecular species were seen at altitudes of 1,400 km by Hoffman et al. (1974).

### Heavy Ions as Major Constituents

A major constituent is one which is sufficiently abundant to alter plasma properties in a significant way. Evidence for two phenomena that fall into this category has been found with data from the GEOS spacecraft: the participation of  $He^+$  ions in the propagation and amplification of ULF waves, and the presence of large quantities of  $O^+$  ions in the magnetosphere. The subject of  $He^+$  in wave-particle interactions is treated in more detail by Roux (1982).

### $He^+$ and Wave-Particle Interactions

Intense, nearly monochromatic ULF waves near  $\Omega_{He^+}$  are often observed on GEOS-1 and 2 and on ATS (Mauk and McPherron, 1980). The free energy source for the waves is the pitch angle anisotropy of energetic protons above  $\sim 20$  keV. When thermal ( $\sim 1$  eV)  $He^+$  ions are present at concentrations  $\geq 0.05$  the waves are destabilized. Although details of the instability are rather complicated (Roux et al., 1982)  $He^+$  may play a further role in the amplification process by creating a laser-like effect in which waves propagating away from the equator are reflected when they reach a value of the magnetic field such that

1 AUG. 1977  
13.25 – 13.54 UT  
7.6 – 7.8  $L_d$   
16.8 – 18.8  $\lambda_d$   
13.49 – 14.03 LT

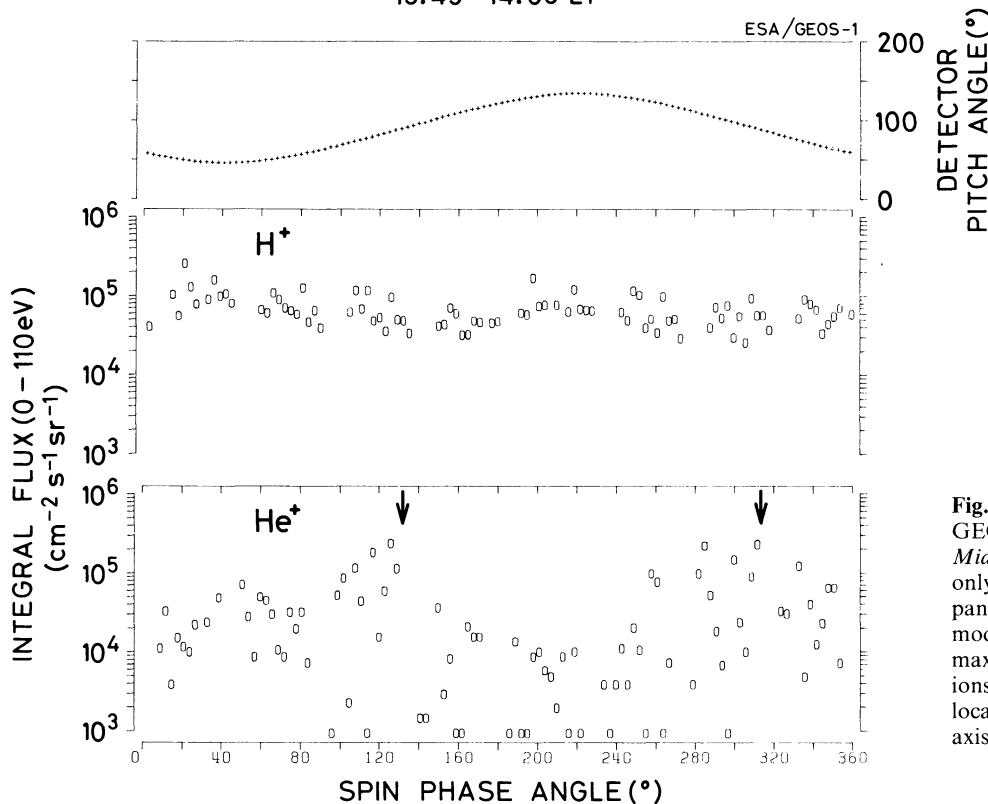


**Fig. 8.** *Top* Pitch angle sampled by the GEOS Ion Composition Experiment. *Middle* The  $H^+$  flux, showing that it is only weakly modulated. On the lower panel the  $He^+$  flux is strongly spin modulated due to ULF waves; it is maximum when  $90^\circ$  pitch angle  $He^+$  ions are sampled. The angle between the local magnetic field and the satellite spin axis is  $44^\circ$ . (From Roux et al., 1982.)

the wave frequency is equal to the local bi-ion hybrid frequency (Young et al. 1981b)

$$f_{bi} = [f_{He^+}] \cdot [(1 + 3\eta)/(1 - 3\eta/4)]^{1/2}$$

where  $\eta$  is the  $He^+$  concentration. Upon reflection the wave again passes through the amplification region and growth is sustained. A final point of interest is that the waves are apparently intense enough to trap cold  $He^+$  ions and accelerate them to energies up to  $\sim 100$  eV (Fig. 7). Roux (1982) has pointed out that this heating represents an effective friction between the hot ( $\geq 20$  keV) protons and cold ( $\sim 1$  eV)  $He^+$ .

The point to be stressed here is that the presence of  $He^+$  in sufficient quantities ( $\geq 5\%$ ) alters plasma characteristics and causes new phenomena to appear. Similar phenomena may also occur near the  $O^+$  gyrofrequency, and ULF waves indeed been observed in this range (Fraser and McPherron, 1982).

### *O<sup>+</sup> and Solar-Cycle Induced Variations in Magnetospheric Composition*

Beginning with GEOS-1 operations in 1977 and continuing with GEOS-2, it has been possible to obtain nearly complete coverage of ion composition in the vicinity of geostationary orbit ( $L \approx 6.6$ ) through the end of 1982. This  $5^{1/2}$  year period brackets the current solar cycle maximum, during which the  $O^+$  content of the equatorial magnetosphere has been observed to increase dramatically (Fig. 2). Detailed analysis of  $3^{1/2}$  years of GEOS data has shown that the abundance of terrestrial heavy ion species ( $O^+$ ,  $O^{2+}$  and  $He^+$ ) increases with increasing solar EUV flux, apparently due to increased scale heights of ions in the upper atmosphere and ionosphere as well as to increased ion production (Young et al., 1981a; 1982). One possible consequence of this phenomenon is a systematic variation in the decay time of the storm ring current due to changes in the proportions of major ion species which are present. A second consequence is suggested by the work of Baker et al. (1982) who find that  $O^+$  has a destabilizing effect on the magnetotail, and the presence of  $O^+$  may facilitate the occurrence of substorms. One might therefore look for a solar cycle dependence in either the frequency or onset characteristics of substorms, based on variations in the abundance of  $O^+$  in the outer magnetosphere.

### **Discussion**

Figure 1 gives a very qualitative overview of typical magnetospheric abundances. The reader should keep in mind, however, that large variations are observed, and in particular that the data refer primarily to a period near solar maximum (cf. Fig. 5).

We have tried to show in this brief resume how our knowledge of magnetospheric heavy ions has expanded both qualitatively and quantitatively in the past 5–10 years. The discovery that heavy ions are major participants in the dynamics of magnetospheric plasmas represents an important qualitative departure from earlier concepts. Likewise the growing number of ion species observed in the magnetosphere is a real quantitative expansion of the ion family, somewhat reminiscent of the proliferation of subatomic particles in the field of nuclear physics with the advent of large accelerators. At this juncture, and with the

planning of the next spacecraft mass spectrometers for the OPEN mission already upon us, we might pause to ask what composition measurements are most important and will lead to real progress in this field.

### *Minor Ions*

One question is whether it is useful to push for routine detection of new and even rarer species, e.g. for solar wind  $O^{6+}$  or  $O^{5+}$  or for ionospheric  $N^+$  or  $NO^+$ . As mentioned above, one can argue that a second, uniquely solar wind species would be most useful if it could be detected together with  $^4He^{2+}$  on a routine basis. This would require  $\sim 100$  times the present sensitivity of GEOS-type instruments. Since the GEOS-type has a geometric factor of  $\sim 10^{-2}$  cm<sup>2</sup> sr, which is already quite large for a plasma analyzer, an order of magnitude increase in this parameter is difficult to achieve without some radical design breakthrough such as mass spectrometers which focus in both azimuthal and polar directions. Increases in detector signal-to-noise ratio also present a feasible avenue for improvement. Thus far only passive shielding has been used and active shielding by anti-coincidence techniques needs to be investigated. Unfortunately, this requires some investment in detector mass and in electronic complexity. At present, 2-dimensional focusing devices, but no methods of active shielding, are being considered for the next generation of plasma instruments being studied for OPEN.

### *Major Ions*

Improvements in this area can and will be made in the future. Emphasis will be placed on obtaining rapid pitch angle-energy measurements of several major ion species simultaneously. The OPEN era should see the development of both mass spectrograph and time-of-flight techniques. The former requires an ion optical design capable of imaging all ion species simultaneously on a microchannel plate detector. These instruments are planned to be imaging in two dimensions, e.g. mass and polar angle. Time-of-flight relies on nearly simultaneous detection of ions of nearly equal energy per charge but different mass according to their time-of-flight over a fixed distance of a few cm. Both techniques are well known in the laboratory although neither has been applied to satellite-borne plasma instruments.

We may conclude by saying that the reign of the "proton" is at an end. Its demise is not regretted, although as a result magnetospheric particle populations have become even more complex than previously imagined.

*Acknowledgements.* The author thanks Hans Balsiger for comments on an early version of the manuscript, and Jean DeField and Rose Mary Bryant for typing. This work was supported by the Swiss National Science Foundation through the University of Bern, by the U.S. Department of Energy, and by the Southwest Research Institute.

### **References**

- Axford, W.I.: On the origin of radiation belt and auroral primary ions. In: *Particles and fields in the Earth's magnetosphere*, by B.M. McCormac, ed.: p. 76. Dordrecht, Holland: D. Reidel 1970
- Baker, D.N., E.W. Hones, Jr., D.T. Young, Birn, J.: The possible role of ionospheric oxygen in the initiation and development of plasma sheet instabilities. *Geophys. Res. Lett.* **9**, 1337, 1982

- Balsiger, H.: Composition of hot ions (0.1–16 keV/e) observed by the GEOS and ISEE mass spectrometers and inferences for the origin and circulation of magnetospheric plasmas. *Adv. Space Res.* Vol. 1, 289, 1981
- Balsiger, H.: Recent developments in ion mass spectrometers in the energy range below 100 keV. *Adv. Space Res.*, in press
- Balsiger, H., P. Eberhardt, J. Geiss, A. Ghielmetti, H.P. Walker, D.T. Young, H. Loidl, Rosenbauer, H.: A satellite-borne ion mass spectrometer for the energy range 0 to 16 keV. *Space Sci. Instrum.* **2**, 499, 1976
- Balsiger, H., P. Eberhardt, J. Geiss, Young, D.T.: Magnetic storm injection of 0.9- to 16-keV/e solar and terrestrial ions into the high-altitude magnetosphere. *J. Geophys. Res.* **85**, 1645, 1980
- Balsiger, H., J. Geiss, Young, D.T.: The composition of thermal and hot ions observed by the GEOS-1 and -2 spacecraft. In: *Energetic ion composition in the Earth's magnetosphere*, R.G. Johnson, ed. Tokyo: Terra Scientific Publishing Co. and Dordrecht, Holland: D. Reidel (in press)
- Bame, S.J., W.C. Feldman, J.T. Gosling, D.T. Young, Zwickl, R.D.: What magnetospheric workers should know about solar wind composition. In: *Energetic ion composition in the Earth's magnetosphere*, R.G. Johnson, ed. Tokyo: Terra Scientific Publishing Co. and Dordrecht, Holland: D. Reidel (in press)
- Bühler, F., W.I. Axford, H.J.A. Chivers, Marti, K.: Helium isotopes in an aurora. *J. Geophys. Res.* **81**, 111, 1976
- Chappell, C.R., R.C. Olsen, J.L. Green, J.F.E. Johnson, Waite, J.H. Jr.: The discovery of nitrogen ions in the Earth's magnetosphere. *Geophys. Res. Lett.* **9**, 937, 1982
- Fraser, B.J., McPherron, R.L.: Pc-2 magnetic pulsation spectra and heavy ion effects at synchronous orbit: ATS 6 results. *J. Geophys. Res.* **87**, 4560, 1982
- Geiss, J., H. Balsiger, P. Eberhardt, H.P. Walker, L. Weber, D.T. Young, Rosenbauer, H.: Dynamics of magnetospheric ion composition as observed by the GEOS mass spectrometer. *Space Sci. Rev.* **22**, 537, 1978
- Geiss, J., Young, D.T.: Production and transport of  $O^{++}$  in the ionosphere and plasmasphere. *J. Geophys. Res.* **86**, 4739, 1981
- Hoffman, J.H., W.H. Dodson, C.R. Lippincott, Hammack, H.D.: Initial ion composition results from the Isis 2 satellite. *J. Geophys. Res.* **79**, 4246, 1974
- Horwitz, J.L.: The ionosphere as a source for magnetospheric ions. *Rev. Geophys. Space Phys.* **20**, 8174, 1982
- Hultqvist, B.: Recent progress in the understanding of the ion composition of the magnetosphere and some major question marks. *Rev. Geophys. Space Phys.* **20**, 589, 1982
- Johnson, R.G., R.J. Strangeway, E.G. Shelley, J.M. Quinn, Kaye, S.M.: Hot plasma composition results from the SCATHA spacecraft. In: *Energetic ion composition in the Earth's magnetosphere*, R.G. Johnson, ed. Tokyo: Terra Scientific Publishing Co. and Dordrecht, Holland: D. Reidel (in press)
- Kaye, S.M., E.G. Shelley, R.D. Sharp, Johnson, R.G.: Ion composition of zipper events. *J. Geophys. Res.* **86**, 3383, 1981
- Lennartsson, W., R.D. Sharp, E.G. Shelley, R.G. Johnson, Balsiger, H.: Ion composition and energy distribution during 10 magnetic storms. *J. Geophys. Res.* **86**, 4628, 1981
- Lennartsson, W., Sharp, R.D. A comparison of the near equatorial ion composition between quiet and disturbed conditions. *J. Geophys. Res.* **87**, 6109, 1982
- Lind, D.L., J. Geiss, Stettler, W.: Solar and terrestrial noble gases in magnetospheric precipitation. *J. Geophys. Res.* **84**, 6345, 1979
- Lundin, R., L.R. Lyons, Pissarenko, N.: Observations of the ring current composition at  $L < 4$ . *Geophys. Res. Lett.* **7**, 425, 1980
- Mauk, B.H., McPherron, R.L.: An experimental test of the electromagnetic ion cyclotron instability within the Earth's magnetosphere. *Phys. Fluids* **23**, 2111, 1980
- Murphy, J.A., G.J. Bailey, Moffett, R.J.: Helium ions in the mid-latitude plasmasphere. *Planet. Space Sci.* **27**, 1441, 1979
- Peterson, W.K., R.D. Sharp, E.G. Shelley, R.G. Johnson, Balsiger, H.: Energetic ion composition of the plasma sheet. *J. Geophys. Res.* **86**, 761, 1981
- Peterson, W.K., E.G. Shelley, G. Haerendel, Paschmann, G.: Energetic ion composition in the subsolar magnetopause and boundary layer. *J. Geophys. Res.* **87**, 2139, 1982
- Reasoner, D.L.: Auroral helium precipitation. *Rev. Geophys. Space Phys.* **11**, 169, 1973
- Roux, A. Anomalous friction between various magnetospheric components through ion cyclotron waves. *EOS, Trans. Am. Geophys. U.* **63**, 1319, 1982
- Roux, A., S. Perraut, J.L. Rauch, C. de Villedary, G. Kremser, A. Korth, Young, D.T.: Wave-particle interactions near  $\Omega_{He^+}$  observed onboard GEOS-1 and -2: 2. Generation of ion cyclotron waves and heating of  $He^+$  ions. *J. Geophys. Res.* **87**, 8174, 1982
- Sharp, R.D., D.L. Carr, W.K. Peterson, Shelley, E.G.: Ion streams in the magnetotail. *J. Geophys. Res.* **86**, 4639, 1981
- Shelley, E.G., R.G. Johnson, Sharp, R.D.: Satellite observations of energetic heavy ions during a geomagnetic storm. *J. Geophys. Res.* **77**, 6104, 1972
- Shelley, E.G., R.G. Johnson, Sharp, R.D.: Satellite observations of an ionospheric acceleration mechanism. *Geophys. Res. Lett.* **3**, 654, 1976
- Shelley, E.G., R.D. Sharp, R.G. Johnson, J. Geiss, P. Eberhardt, H. Balsiger, G. Haerendel, Rosenbauer, H.: Plasma Composition Experiment on ISEE-A. *IEEE Trans. Geosci. Elec.* Vol. **GE-16**, 266, 1978
- Shelley, E.G., Simpson, D.A., T.C. Sanders, E. Hertzberg, H. Balsiger, Ghielmetti, A.: The Energetic Ion Composition Spectrometer (EICS) for the Dynamics Explorer-A. *Space Sci. Instrum.* **5**, 443, 1981
- Young, D.T.: Ion composition measurements in magnetospheric modeling. In: *Quantitative modeling of magnetospheric processes*, Geophys. Monogr. Ser. Vol. **21**, W.P. Olson, ed.: p 340. Washington, D.C.: AGU 1979
- Young, D.T.: Near-equatorial magnetospheric particles between  $\sim 1$  eV and  $\sim 1$  MeV. *Rev. Geophys. Space Phys.* (in press)
- Young, D.T., J. Geiss, H. Balsiger, P. Eberhardt, A. Ghielmetti, Rosenbauer, H.: Discovery of  $He^{2+}$  and  $O^{2+}$  ions of terrestrial origin in the outer magnetosphere. *Geophys. Res. Lett.* **4**, 561, 1977
- Young, D.T., H. Balsiger, Geiss, J.: Observed increase in the abundance of kilovolt  $O^+$  in the magnetosphere due to solar cycle effects. *Adv. Space Res.* Vol. 1, No. 1, 309, 1981a
- Young, D.T., S. Perraut, A. Roux, C. de Villedary, R. Gendrin, A. Korth, G. Kremser, Jones, D.: Wave-particle interactions near  $\Omega_{He^+}$  observed on GEOS 1 and 2: 1. Propagation of ion cyclotron waves in  $He^+$ -rich plasma. *J. Geophys. Res.* **86**, 6755, 1981b
- Young, D.T., H. Balsiger, Geis, J.: Correlations of magnetospheric ion composition with geomagnetic and solar activity. *J. Geophys. Res.* **87**, 9077, 1982

Received November 16, 1982; Accepted January 27, 1983

## Review Article

Energetic Particle Signatures  
Near Magnetospheric Boundaries\*

M. Scholer

Max-Planck-Institut für Physik und Astrophysik, Institut für extraterrestrische Physik, 8046 Garching, Federal Republic of Germany

**Abstract.** Two aspects of magnetospheric energetic particles have gained increasing attention in recent years: firstly their signatures, in particular the anisotropy, have been used in order to study the behaviour of magnetospheric boundaries, and secondly the particles themselves have been analyzed in order to determine their acceleration mechanism. The first aspect is particularly useful when studying the structure and the temporal behaviour of the magnetopause and when investigating such processes as reconnection. The acceleration of particles has been found to be important at the boundary of the plasma sheet. This paper presents a review of recent ISEE observations of energetic ions and electrons near the magnetopause and near the boundary of the plasma sheet.

**Key words:** Magnetospheric boundaries – Magnetospheric energetic particles – Magnetopause – Plasma sheet

## Introduction

The behaviour of energetic particles in the outer magnetosphere has been studied extensively for two decades. In particular, observations of these particles have been used in order to determine their acceleration sites, but they have also been used as remote sensors in order to probe magnetospheric boundaries, as the magnetopause and the plasma-sheet boundary. Spurred on by the high-quality data returned from the ISEE satellites the topic of energetic particles near magnetospheric boundaries has gained new interest. In this report, we will review recent progress made on the structure of the magnetopause and the plasma-sheet boundary layer utilizing ISEE energetic particle observations.

Density Gradients Near Magnetopause  
and Remote Sensing

Due to their large gyroradius, energetic ions are ideally suited to probe magnetospheric boundaries to large distances from the satellite, i.e. up to two gyroradii. This concept has first been applied successfully near the magnetopause by Konradi and Kaufmann (1965) and Kaufmann

and Konradi (1969; 1973). Assuming the magnetopause to be a perfectly absorbing boundary, Williams (1979a, 1980) has analyzed ISEE 1 three dimensional energetic particle distributions to infer magnetopause distances, orientations, and velocities. The concept is shown schematically in Fig. 1, taken from a paper by Fritz and Fahrenstiel (1982). Let us assume that the magnetic field points in the  $z$  direction in a GSE (geocentric solar equatorial) coordinate system. A detector scanning in the ecliptic plane is measuring an azimuthal ion distribution as shown in Fig. 1a as the dark line.

The azimuthal scan exhibits a large anisotropy indicating that the satellite is close i.e. within two gyroradii of a strong particle density gradient. Superimposed is a square

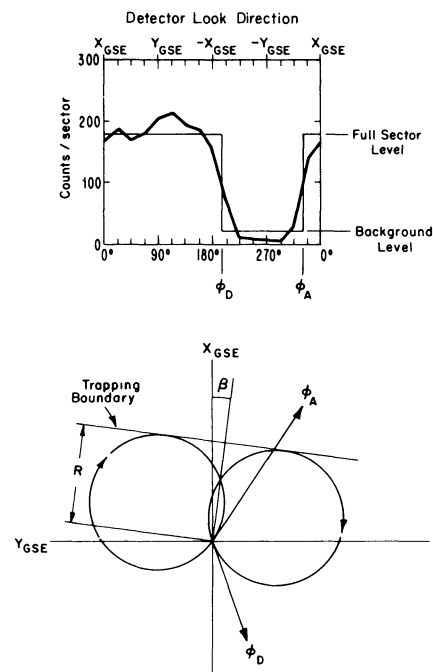


**Fig. 1.** Technique for determining trapping boundary parameters near the subsolar magnetopause. At the top of the figure is the 16 sector normalized partially-trapped  $>24$  keV ion distribution. Superimposed is a square wave fit from which the angles  $\phi_D$  and  $\phi_A$  are obtained. The drop in count rate from  $\phi_D$  to  $\phi_A$  is interpreted as scattering from a trapping boundary as shown in the lower portion of the figure. From these angles, the perpendicular distance  $R$  and orientation angle  $\beta$  to the trapping boundary are obtained (Fritz and Fahrenstiel, 1982)

\* Based on an invited review paper given at the Symposium on Plasma and Energetic Particles in the Magnetosphere, EGS Meeting, 23–27 August 1982, Leeds, U.K.

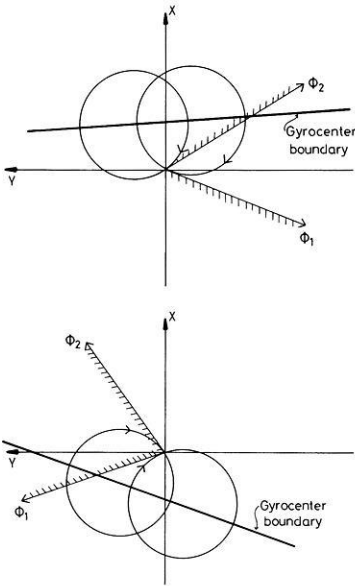


**Fig. 2.** Schematic representation of the sensing of a sharp gradient in gyrocenter density from the inside (upper part) and outside (lower part) of the particle distribution

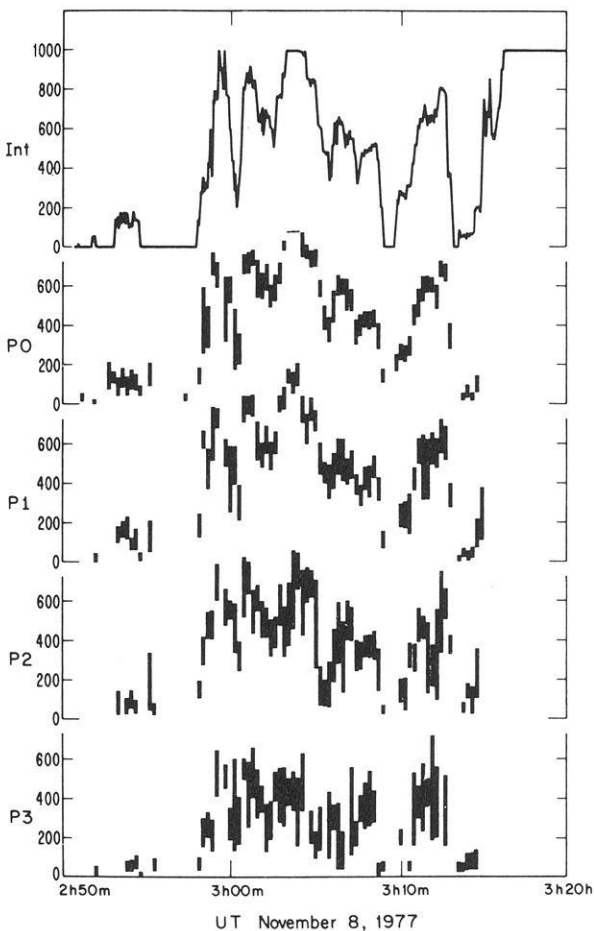


**Fig. 3.** Comparative trapping boundary distances. The distances to the trapping boundary computed for each energy channel are plotted as a function of time. P0-P3 channels have 15 s resolution. The integral > 24 keV channel has 4 s resolution and error bars have been omitted for clarity (Fritz and Fahrenstiel, 1982)

wave fit from which the angles  $\varphi_A$  and  $\varphi_D$  are derived. These angles are interpreted as the arrival directions at the satellite of the last magnetospheric particles which are completing their gyromotion without contacting the absorbing boundary. This geometry is depicted in Fig. 1 b, where it is seen that particles with arrival directions counter clockwise from  $\varphi_A$  to  $\varphi_D$  can complete their gyroorbits while those from  $\varphi_D$  to  $\varphi_A$  will contact the boundary and are absorbed. The angles  $\varphi_D$  and  $\varphi_A$  allow a unique determination of the perpendicular distance  $R$  and orientation angle  $\beta$  to the plane absorbing boundary. Williams (1979a) has assumed the magnetopause itself to be the absorbing boundary, although Williams (1980) cautioned that such an identification of the magnetopause is only valid in the sense that one is identifying the last magnetic field line which contains a trapped type particle distribution. Therefore, Fritz and Fahrenstiel call this boundary the trapping boundary and there are indeed cases in Williams (1980) where this boundary is earthward of the magnetopause as determined from the magnetic field measurements (e.g., 4 December 1977 magnetopause crossing).

We should like to avoid the concept of an absorbing boundary altogether and refer instead to the sensing of a sharp density gradient. We have to be more specific and differentiate between a gradient in number density and a gradient in gyrocenter density. Figure 2 shows schematically the sensing of a sharp gradient of the gyrocenter density. Let us assume the magnetic field is in the  $z$ -direction and there are no particles with a gyrocenter sunward (positive  $x$ -direction) of the gyrocenter boundary. The satellite is at the center of the coordinate system. Particles with arrival directions  $\varphi_1$  and  $\varphi_2$  are particles whose gyrocenters are just inside the gyrocenter boundary. Particles with arrival directions clockwise from  $\varphi_1$  to  $\varphi_2$  have their gyrocenter earthward of the gyrocenter boundary. Particles with arrival directions counter clockwise from  $\varphi_1$  to  $\varphi_2$  must have their gyrocenters sunward of the gyrocenter boundary and as the gyrocenter density is zero here, these arrival directions are empty. The lower frame of Fig. 2 shows that the satellite is observing particles at certain arrival directions even if it is outside of the region of gyrocenter density, i.e. the satellite is probing the boundary from the outside. The distance to this boundary is half the distance to the absorbing boundary introduced in Fig. 1. It may well be that this sharp gradient in gyrocenter density is due to an absorbing boundary (magnetopause, last closed field line, etc.), but this is not necessarily so.

Fritz and Fahrenstiel (1982) found that the plasma boundary layer occasionally penetrates up to several hundred kilometers earthward of the trapping boundary as determined by energetic ions. If the trapping boundary determines the position of the last closed field line, the occurrence of magnetosheath plasma earthward of the trapping boundary would be inconsistent with current merging theories. However, the last closed field line is probably determined more closely by the gyrocenter boundary introduced above. This boundary is one gyroradius earthward of the trapping boundary introduced by Fritz and Fahrenstiel, so that there would be no overlap between boundary layer and closed field lines.

The investigations of Williams (1979a, 1980) and Fritz and Fahrenstiel (1982) revealed the existence of 100–400 s waves with amplitudes of a few hundred kilometers of the trapping boundary and, by inference, of the magnetopause.

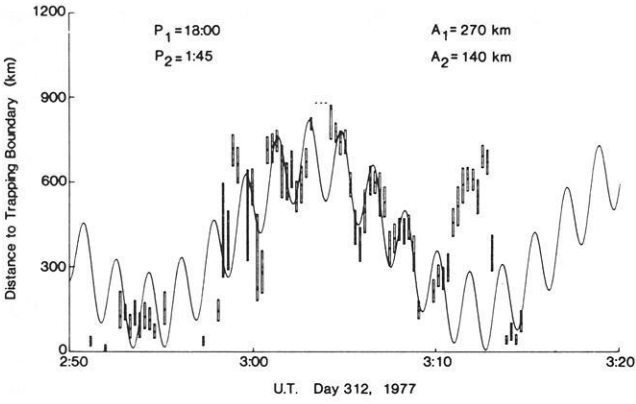


**Fig. 4.** Periodicity in  $R$ . A double period sinusoid with periods of 105 s and 18 min and amplitudes of 140 km and 270 km is superimposed on the trapping boundary distances obtained for the P0 channel. The 105 s periodicity is identified with waves on the boundary, while the 18 min component is used to fit an apparent inward “breathing” mode motion (Fritz and Fahnenstiel, 1982)

Figure 3, taken from Fritz and Fahnenstiel (1982), shows for a particular inbound magnetopause crossing of ISEE 2 the distance from the satellite to the trapping boundary as derived from the remote sensing with ions of different energies. The energy bins are labeled P0 to P3 and range from  $>24 \sim 70$  keV. The channel labeled Int is an integral channel above 24 keV. One can clearly see the oscillatory motion of the trapping boundary. In order to derive the

periodicities in  $R$ , Fritz and Fahnenstiel have fitted a double period sinusoid to the data of Fig. 3. The result is shown in Fig. 4. The periods of the sinusoids are 105 s and 18 min, with amplitudes of 140 km and 270 km. The authors suggest that the 105 s periodicity is due to waves on the boundary whereas the 18 min periodicity is a “breathing” motion of the magnetopause as a whole. The concept of a wavy structure of the trapping boundary is supported by two more observations: Williams (1980) has shown that the orientation angle  $\beta$  (defined as a clockwise rotation of the tangent to the magnetopause in the  $X_{SE}, Y_{SE}$  plane from the  $-Y_{SE}$  axis) shows significant variations. Figure 5 from Williams (1980) shows for five magnetopause crossings the orientation angle versus time for consecutive 1-min intervals as indicated. Also shown are suggested periodic variations with the respective period in seconds. Figure 5 shows the regular presence of variations in the orientation angle of the trapping boundary which are consistent with boundary waves in the few hundred second period range. A second observation suggesting a wavy structure of the boundary is the different boundary distance obtained from the sounding with different ion energies. As can be seen from Fig. 3, distances obtained with high energy ions (P3) are consistently lower than distances obtained from low energy ions ( $>24$  keV). Fahnenstiel (1981) has suggested that in the case of a wave geometry, the aspect ratio of the wave could be such that the trough of the wave is accessible to the smaller gyroradius ions, whereas the higher energy ions come into contact with the wave crest. This is shown schematically in Fig. 6.

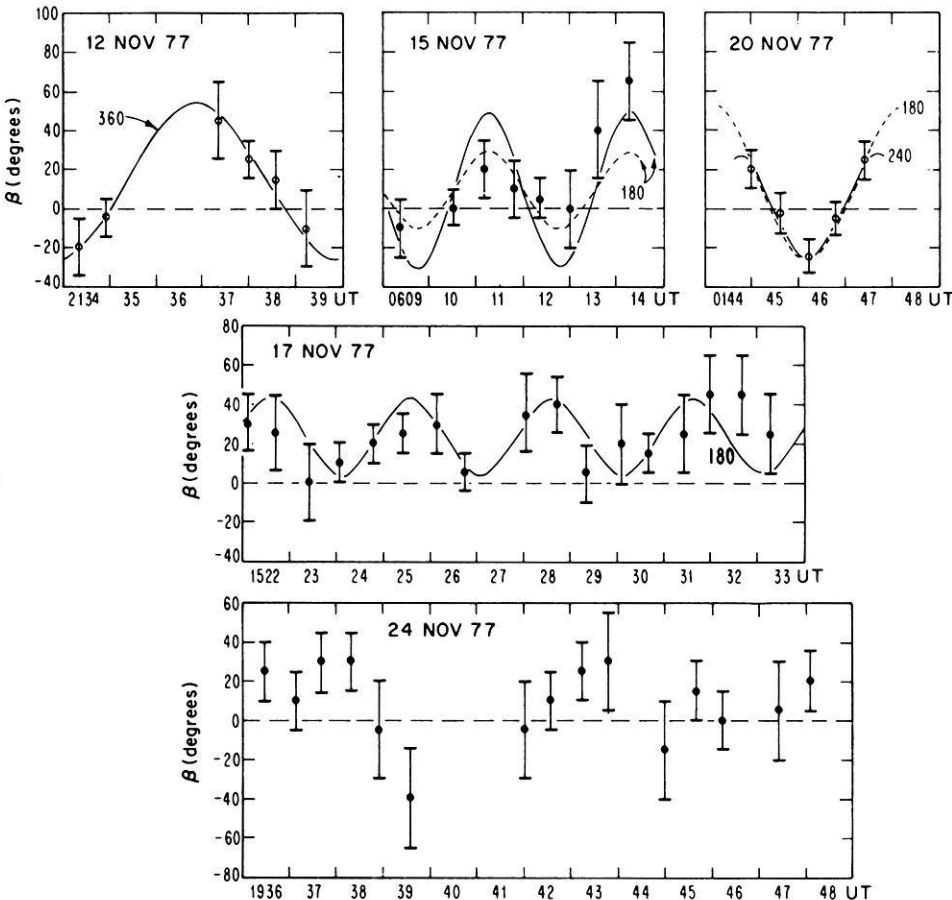


**Fig. 5.** Five time intervals for which nearly contiguous determinations of the magnetopause orientation angle could be made.  $\beta$  is plotted versus time for consecutive 1-min intervals as indicated. Periodic variations with the indicated period in seconds are shown for reference. Two amplitudes at a 180-s period are shown in the 15 November 1977 panel (Williams, 1980)

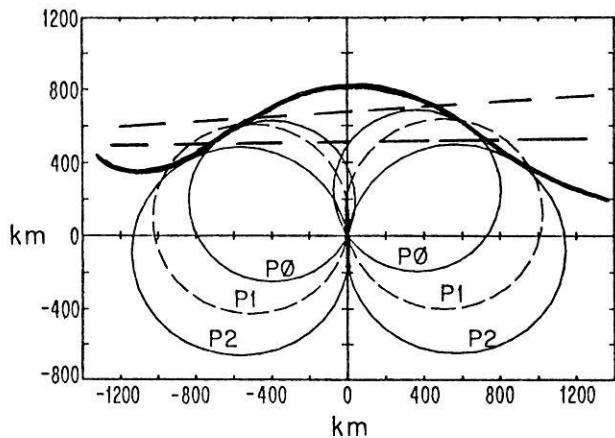


Fig. 6. Sounding of the wave crest and trough at the magnetopause by ions with different gyroradii (Fahnenstiel, 1981)

### Energetic Particles and Reconnection

Energetic ions are often found to constitute a layer outside of the magnetopause. Williams (1979b), Richter et al. (1979) and Lanzerotti et al. (1979) reported the existence of an energetic ion layer outside the magnetopause. Recently, Scholer et al. (1981) investigated energetic particle behaviour during magnetopause crossings which have been identified by Sonnerup et al. (1981) as reconnection events, i.e. where the rate of change of the tangential momentum of the plasma as it flows across the magnetopause layer is equal to the net tangential Maxwell stress. Figure 7 shows the time behaviour of the magnetic field (magnitude and direction) and of the energetic protons during an outbound magnetopause crossing on 8 September 1978 as shown in Scholer et al. (1981). It can be seen that the energetic particle population extends well within the magnetosheath. In addition the satellite encounters several burst-like energetic particle events in the magnetosheath. Before interpreting these observations we would like to discuss what a satellite should observe near a magnetopause which is a rotational discontinuity. A satellite crossing the magnetopause above or below an  $x$ -type neutral line will encounter reconnected field lines up to the outer reconnection separatrix. If magnetospheric trapped particles are escaping along the reconnected field lines, they should be observable up to the separatrix, which is on the magnetosheath side of the magnetopause. Scholer et al. (1981) interpreted these observations of energetic ions outside the magnetopause as a crossing of the region between magnetopause and outer separatrix. Figure 8 is a schematic representation of an interplanetary magnetic field line reconnected to a field line of the Earth's dipole. If magnetospheric particles escape along reconnected field lines a satellite crossing the reconnection region above the neutral line should observe particles streaming antiparallel to the magnetosheath field and a satellite crossing below the neutral line should observe particles streaming parallel to the magnetosheath field. This is indeed observed: Fig. 9 shows spatial distributions in the ecliptic together with the projection of the magnetic field. Outside the magnetosphere (e.g. 044:58–045:14 UT) the particles are streaming antiparallel to the field consistent with a reconnection line south of the satellite as determined from the plasma measurements by Paschmann et al. (1979) (note that Fig. 9 shows the intensity in the instrument look direc-

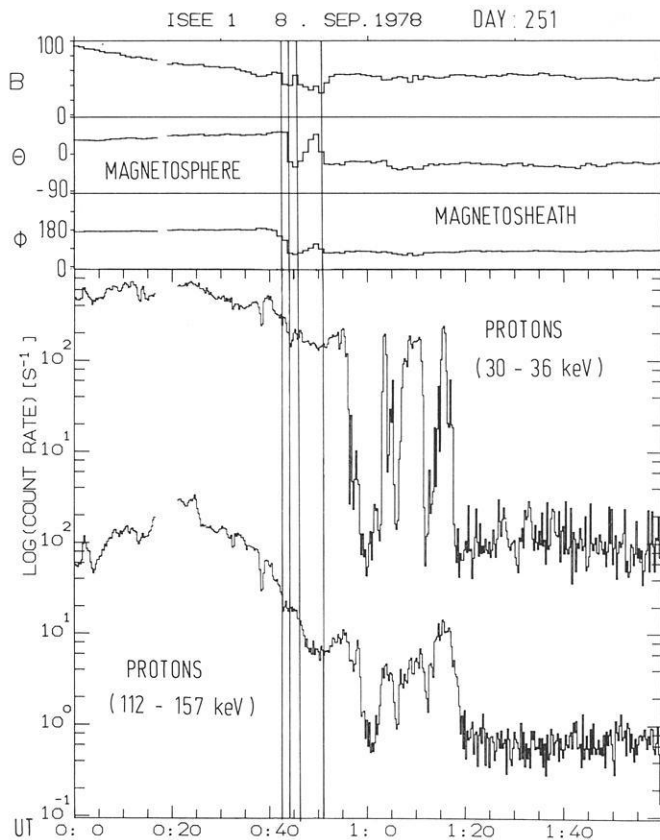


Fig. 7. Time behaviour of magnetic field magnitude and direction during a magnetopause crossing (three top panels) and time profile of 30–36-keV and 112–157-keV protons (bottom panel). Between the first two and the second two vertical lines a magnetopause is identified from magnetic field and plasma data (Scholer et al., 1981)

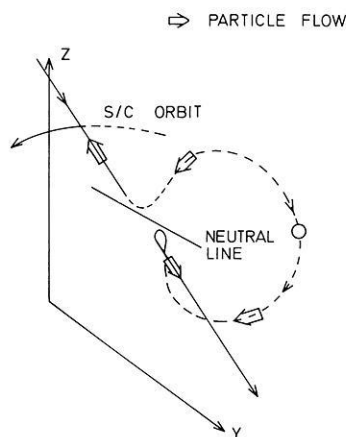
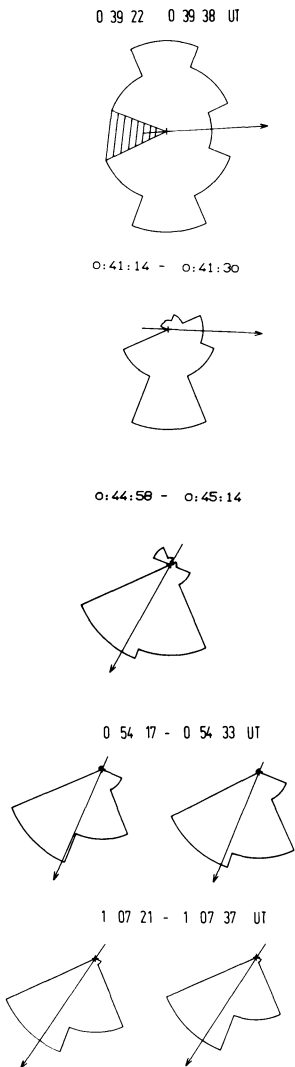


Fig. 8. Schematic representation of an interplanetary magnetic field line reconnected to a field line of the Earth's dipole and corresponding outflow of magnetospheric particles (Scholer et al., 1981)

tion). Sonnerup et al. (1981) have shown that when the satellite is crossing south of the reconnection line particles are indeed streaming parallel to the field.

Williams and Frank (1980) presented indirect evidence for open field lines within the magnetosphere. They found field-aligned asymmetries in the energetic ion distributions at satellite positions inside the magnetosphere close to the

ISEE 1 8 SEPT 78 DAY 251



**Fig. 9.** Energetic proton ( $\sim 30$  keV) distributions observed at three different times (from top to bottom: within the magnetosphere, in the layer outside the magnetopause, and in a magnetosheath burst). The distributions to the right are Compton-Getting-transformed into a coordinate system moving with the component of the magnetosheath plasma velocity perpendicular to the magnetic field. Arrows indicate the projection of the magnetic field into the ecliptic. The Sun is to the left of the figure (Scholer et al., 1981)

magnetopause. Scholer et al. (1982a) re-examined the 8 September 1978 event in order to determine the field line topology inside the magnetopause. When the satellite approached the magnetopause from the inside they first observed trapped distributions between certain look phases and missing particles at the other phases with respect to the local magnetic field. This indicates that the spacecraft is inside the last closed field line, but within 2 gyroradii of it. The following three-dimensional scan (each scan of the instrument takes 36 s) shows no particles at certain phase angles, at the other phase angles the particles in the  $60^\circ$ – $90^\circ$  pitch angle range are depleted, so that the field line passing through the satellite is unable to mirror and trap these ions below the satellite. However, as also empha-

sized by Eastman and Frank (1982), before and even for some time after the magnetopause crossing of 8 September 1977 the energetic electrons exhibit a pancake like distribution (i.e. peaked at a pitch angle of  $90^\circ$ ), indicating a trapped population and thus closed field lines.

Daly and Fritz (1982) have solved this apparent puzzle and have shown how trapped-like electrons can be maintained on open field lines together with streaming ions. They have investigated the idea that the electrons could be trapped by magnetic mirroring from the increased field in the magnetosheath. Figure 10 from Daly and Fritz (1982) shows the total magnetic field plotted against time around the magnetopause crossing (which at ISEE 2 occurred during a data gap). Also indicated are times of streaming ions and electrons. The magnetic field is seen to have a minimum shortly before the magnetopause crossing and increases again in the magnetosheath. Assuming a maximum magnetosheath field strength of  $B_m = 59$  nT for all field lines crossed by the satellite Daly and Fritz (1982) converted all values of  $B < B_m$  into an angle  $\alpha$ , that represents the edge of the expected loss cone in that field. This angle is shown on the right of Fig. 10. No particles are expected at a pitch angle less than  $\alpha$ , particles between  $\alpha$  and  $90^\circ$  are returning from the magnetosheath after mirroring, particles between  $90^\circ$  and  $180^\circ - \alpha$  are coming from the magnetosphere and will be reflected back and particles above  $180^\circ - \alpha$  can come from a source deeper in the magnetosphere and will be lost in the magnetosheath. Measured upper and lower cutoff angles in the electron distributions as shown in Fig. 10 indeed follow the field strength curve rather closely. Figure 11 is a reconstruction of the field line geometry proposed by Daly and Fritz (1982). The vertical line in the middle is the magnetopause and the bars between some of the field lines indicate the mirroring points for those particles with a pitch angle of  $90^\circ$  in the steady magnetosheath field. These particles are trapped on the field line between the bars, i.e. the satellite will observe close to the magnetopause inside as well as outside a trapped electron distribution. The reason that energetic protons are not similarly trapped is their much larger (43 times greater) gyroradius. In a field of 55 nT, 36 keV protons have a gyroradius of 500 km which is of the same order as the thickness of the magnetopause current layer as determined by Russell and Elphic (1978). It is thus unlikely that the ions can follow the bend in the field line adiabatically, so that the mirror hypothesis does not apply.

Magnetosheath particles are not only transmitted into the magnetosphere and thus form the boundary layer but they can also be reflected due to interaction with the current layer. Sonnerup et al. (1981) found that some magnetosheath particles are accelerated in the magnetopause layer and are reflected back into the magnetosheath, forming a population having  $\sim 20\%$  of the total sheath density just outside the current layer. Similarly, energetic magnetospheric ions can be accelerated in the current layer and are reflected back into the magnetosphere. Scholer and Ipavich (submitted 1983) have presented some evidence for the acceleration and reflection of energetic ring current ions at the magnetopause. Figure 12 shows 64-s-averaged spatial distributions of energetic protons around the final magnetopause crossing on 5 July 1978. These distributions are measured in the ecliptic plane; the Sun is to the left of the figure and the intensity is plotted in the instrument look direction. From the plasma and magnetic field data it has

1978-SEP-8 DAY 251

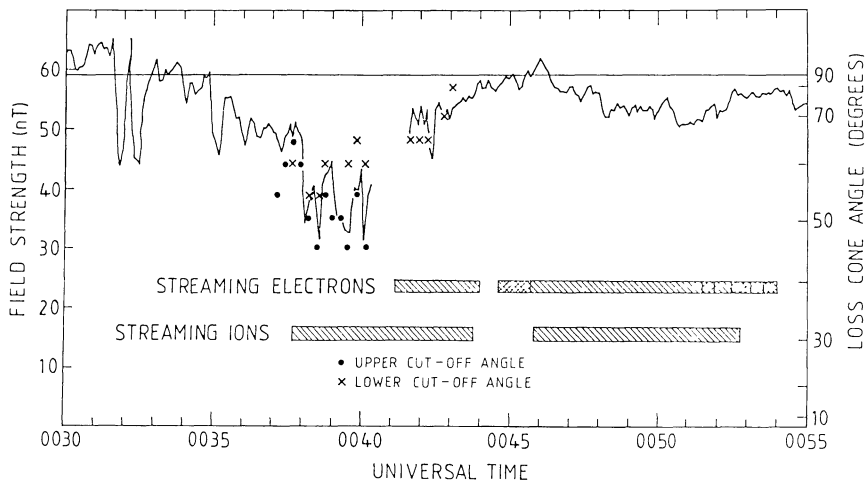


**Fig. 10.** Total magnetic field plotted against time, from 0030 to 0055 UT on 8 September 1978. On the left is the magnetic field scale, on the right the corresponding loss cone angle based on a mirroring field of 59 nT. Also indicated are times of streaming ions and electrons; the times of heavier shading for the electrons indicate very intense streaming. Measured upper and lower cutoff angles in the electron distributions are also plotted via use of the angle scale on the right (Daly and Fritz, 1982)

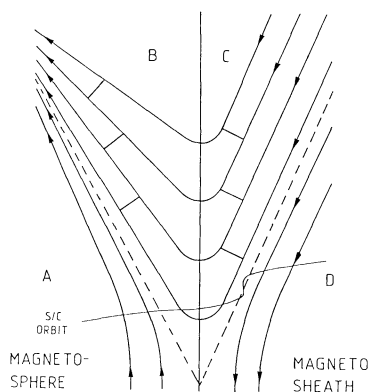


**Fig. 11.** Reconstruction of the field line geometry and spacecraft trajectory. The vertical line in the middle is the magnetopause, the lines with arrows are field lines. The bars between some of the field lines indicate the mirroring points for those particles with a pitch angle of 90° in the steady magnetosheath field, these particles are trapped on the field line between the bars. A horizontal curve represents the spacecraft's trajectory. The dashed lines and the magnetopause separate regions A, B, C, and D of different field line topology (Daly and Fritz, 1982)

been established that the satellite was north of a possible x-type neutral line (Sonnerup et al., 1981). As outlined above the satellite should be observed inside the magnetosphere, i.e. when the magnetic field is pointing from dusk to dawn (light arrow), a streaming of the magnetospheric particles out of the magnetosphere antiparallel to the magnetic field. The anisotropies are, however, opposite to those expected from the simple picture of magnetospheric particles leaking out along open field lines. Scholer and Ipavich (submitted 1983) suggested that part of the magnetospheric ions are reflected and accelerated at the magnetopause current layer so that at a constant energy one might observe higher fluxes of particles streaming away from the current layer parallel to the field than towards the current layer antiparallel to the field. Figure 13 from Scholer and Ipavich shows, to the left, phase space densities of protons antiparallel to the magnetic field within the magnetosphere. Let us assume that the open flux tubes contract over the magnetopause at the speed  $V_F$ . In a system moving with velocity  $V_F$  particles gain or lose no energy during reflection and

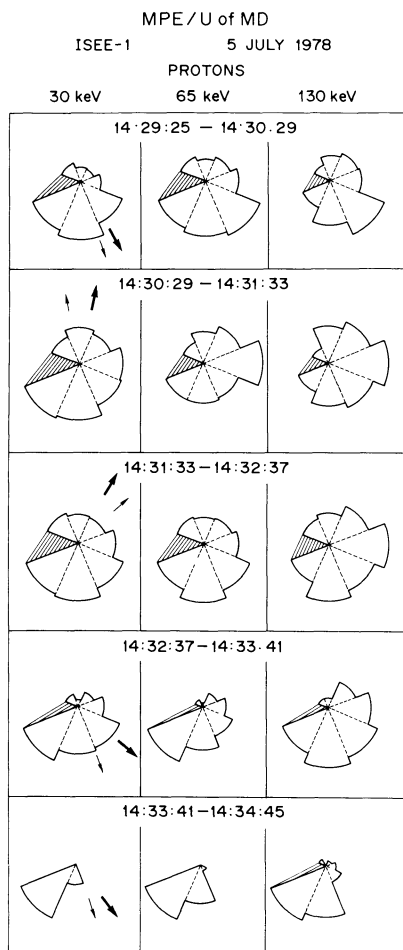


**Fig. 12.** Consecutive 64 s-averaged spatial distributions of ~30 keV, ~65 keV, and ~130 keV protons in the ecliptic plane during a multiple magnetopause crossing. The Sun is to the left of the Figure, the Sun sector is shaded. Also shown is the projection of the magnetic field into the ecliptic plane (light arrow) as well as the projection of the velocity vector (heavy arrow) into that plane (Scholer and Ipavich, 1983)

transmission since there is no electric field and the field lines are at rest. The distribution of the reflected particles is then found by constructing the mirror image of the input distribution about the field line speed multiplied with the

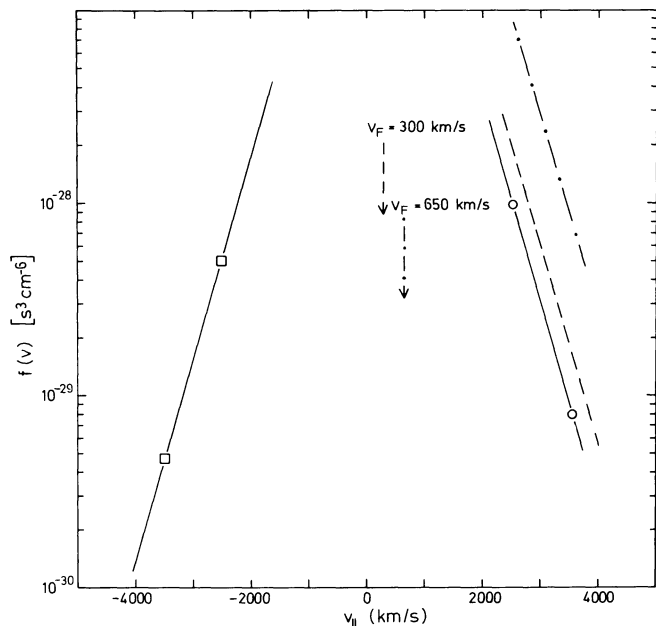


**Fig. 13.** Open squares: phase densities of protons antiparallel to the magnetic field. Dashed distribution results from the solid distribution by mirroring at  $v_F = 300$  km/s, dashed-dotted distribution results by mirroring at 650 km/s. Open circles are measured phase space densities parallel to the field and can be obtained from dashed-dotted distribution by multiplying with 0.1 or from dashed distribution by multiplying with 0.5, respectively (Scholer and Ipavich, 1983)

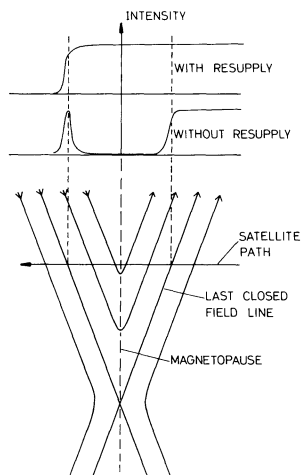


**Fig. 14.** Schematic representation of the reconnection configuration at the magnetopause. At the top are shown particle intensity profiles as measured during a satellite crossing if there is either resupply or no resupply of particles on open field lines

reflection coefficient. Figure 13 shows distributions mirrored at 300 km/s (dashed) and 650 km/s (dashed-dotted). Assuming either 50% or 10% reflection efficiency one can easily obtain the measured phase space densities of particles flowing within the magnetosphere away from the current layer (open squares).

Before leaving the subject of steady state reconnection at the magnetopause it should be emphasized that magnetospheric particles have to be continuously replenished on

open field lines. Scholer et al. (1981) noted that a field line should be empty after reconnection within two bounce periods i.e. within approximately 1 min. A satellite crossing outbound, north of a neutral line should essentially observe particles up to the inner separatrix, no particles between inner and outer separatrix and an intensity increase close to the outer separatrix. This is shown schematically in Fig. 14. Since such a drop in intensity is never observed, but the profiles look rather as at the top of Fig. 14, a rather efficient continuous re-supply mechanism on open field lines must be postulated.

### Flux Transfer Events

A feature found for the first time by the ISEE satellites and associated with the magnetopause are the so-called flux transfer events (FTE's). The FTE's are evident from characteristic signatures in the magnetic field data and have been interpreted by Russell and Elphic (1978; 1979) as magnetic flux tubes interconnected with the magnetospheric field. Daly et al. (1981), Scholer et al. (1982b), and Speiser and Williams (1982) have investigated energetic particle signatures during magnetic flux transfer events. Figure 15 from Scholer et al. (1982b) shows, for a magnetopause crossing on 8 November 1977, from top to bottom, the plasma density, the three components of the magnetic field in the boundary normal system:  $\mathbf{N}$  is the vector outward and normal to the magnetopause,  $\mathbf{L}$  is the GSM (geocentric solar magnetospheric)  $z$ -axis projected onto the magnetopause, and  $\mathbf{M}$  is given by  $\mathbf{N} \times \mathbf{L}$ . A positive excursion of the  $\mathbf{N}$  component, followed by a negative excursion before returning to zero, is indicative of magnetic flux transfer events in the magnetosheath. The lower panels show spin-averaged energetic protons and electrons. During the two FTE's from 0212–0215 UT and 0233–0238 UT there are clear particle enhancements of both protons and electrons, although the electron intensity is considerably below the intensity well within the magnetosphere. From the spatial distributions of protons and electrons within the FTE's shown in Fig. 16 it can be seen that the protons are streaming antiparallel to the magnetic field (the projection into the ecliptic is shown by an arrow) whereas the electrons exhibit a more or less isotropic distribution. The ion distributions are consistent with a picture of magnetospheric particles leaking out into a magnetosheath magnetic flux tube which is connected to the magnetospheric field. A qualitative sketch of such a flux tube topology has been given by Speiser and Williams (1982) and is shown in Fig. 17. Speiser and Williams used a one-dimensional, quasi-static model to follow particle orbits from the magnetosphere into the sheath, and map the distribution function using Liouville's theorem. They found good agreement between their model and the observations in the sheath if they assumed the presence of an inward pointing normal magnetic field component and the absence of a tangential electric field. The latter fact may indicate that what one observes in FTE's is the peeling off of a well-defined flux tube that underwent reconnection some time in the past. Speiser and Williams (1982) and Scholer et al. (1982b) observed quasi-trapped (QT) distributions when entering and leaving FTE's. Speiser and Williams (1982) interpreted these QT-distributions as the more slowly outward-moving particles with large pitch angles that get left behind by the faster particles with smaller pitch angles when a flux tube becomes

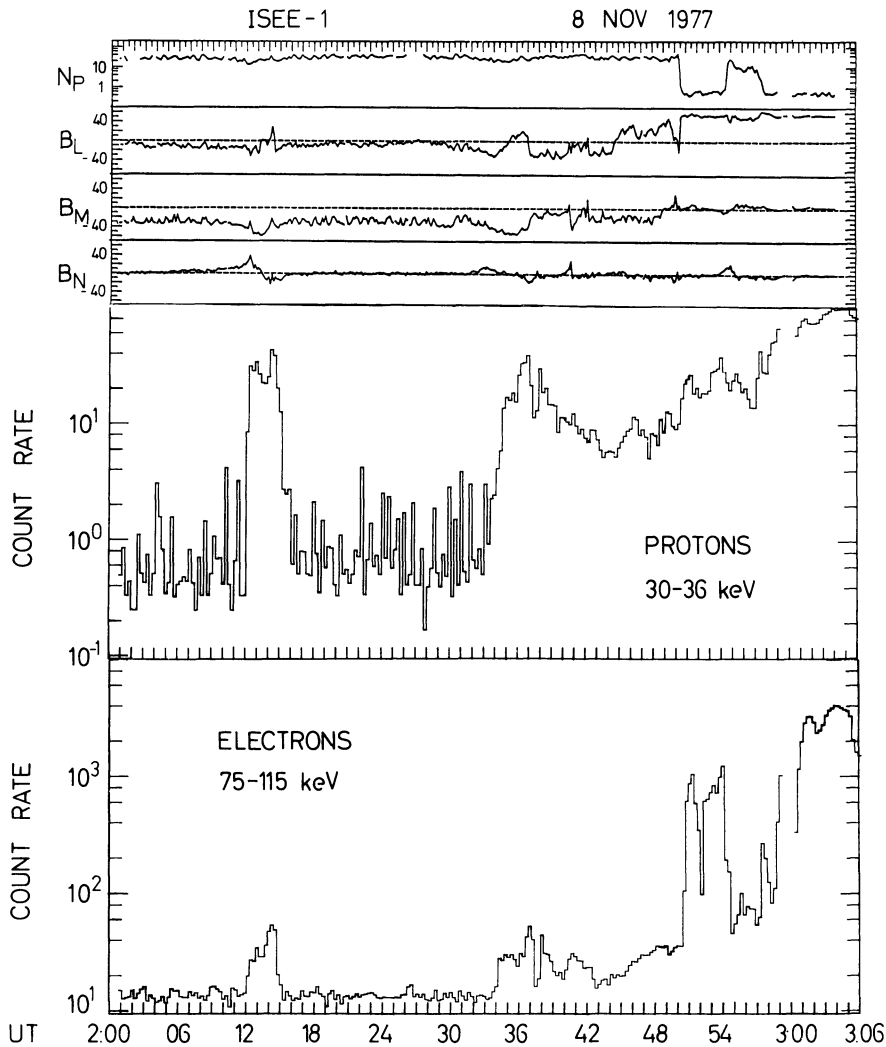


**Fig. 15.** From top to bottom: Plasma density; magnetic field components  $B_L$ ,  $B_M$ ,  $B_N$  energetic protons and energetic electrons during the magnetopause crossing on 8 November 1977 (Scholer et al., 1982b)

opened. This implies that the reconnection process is still occurring while one observes the event i.e. one sequentially samples older and younger open field lines when crossing an FTE. Scholer et al. (1982b), on the other hand, claim that they observed particles mainly at  $90^\circ$  pitch angle when entering the flux tube from above as well as when leaving the flux tube below where one should expect to cross freshly opened flux tubes. They suggest that at the boundary of the FTE's the magnetosheath field is draped around the flux tube and may lead to grad  $B$  drifts and nonadiabatic particle motion.

Daly and Keppler (1982) have reported that events previously designated inclusion events inside the magnetopause have energetic particle signatures similar to those observed during flux transfer events. Already Williams (1980) identified these events as close encounters of the satellite with the last closed field line. Figure 18 shows energetic particle data (two top panels) and magnetic field data in the boundary normal coordinate system during an inbound magnetopause crossing on 10 November 1977. During the two events in the magnetosphere, at 1503 and 1512 UT, the magnetic field N-component shows negative and positive excursions as during the FTE's in the magnetosheath. The ion intensity decreases somewhat and the pitch angle distribution is such that the ions are steaming antiparallel to

the field. The electron intensity drops to the same low level as in the flux transfer events. Daly and Keppler (1982) concluded that these events in the magnetosphere are also flux transfer events viewed from the other side of the magnetopause. This supports the interpretation of flux transfer events as isolated flux tubes in the magnetosphere which connect to the magnetosheath through the magnetopause. Daly and Keppler (1982) have suggested that the same resupply rate for protons and electrons together with the considerably smaller bounce time of the electrons could explain the low levels of electron flux in the FTE's inside and outside the magnetosphere. A different explanation has been given by Scholer et al. (1982b). They argue from the observation of isotropic electron distributions that strong scattering could result in a diffusion type leakage of the electrons along the open flux tubes so that large flux differences between magnetosphere and magnetosheath can be maintained.

Before leaving the subject of energetic particles at the magnetopause we should like to mention the magnetopause energetic electron layer. Such a permanent layer was found by Baker and Stone (1977) along the distant magnetotail and by Meng and Anderson (1975) and Domingo et al. (1977) at high latitudes near the dayside magnetopause and poleward of the polar cusp.

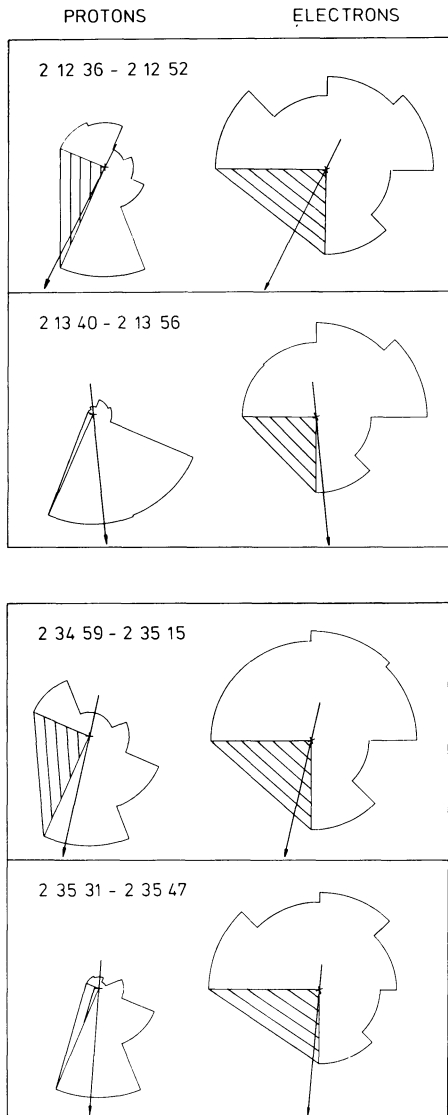


**Fig. 16.** Energetic proton (30–36 keV) and electron (75–115 keV) distributions observed during two flux transfer events on 8 November 1977. The intensity is plotted linearly in the instrument look direction (Scholer et al., 1982b)

### Energetic Ion Observations of the Plasma Sheet Boundary Layer

Energetic ions in the plasma sheet have been studied for many years. Their characteristic features have been used to infer the acceleration site, temporal evolution of the source, net energetic particle transport, electric fields and magnetic field topology. For a recent review on the topic of energetic particle bursts in the Earth's magnetotail see Krimigis and Sarris (1979). Here, we are not concerned with energetic particles in the magnetotail in general but with the recently detected thin layer of non-thermal particles streaming highly collimated along the tail field at the edge of the plasma sheet.

First observations of energetic protons and alpha particles streaming at the edge of the plasma sheet towards the Earth were reported by Möbius et al. (1980). Figure 19, taken from Möbius et al., shows on the left side proton and alpha particle spectra in two sectors of the instrument

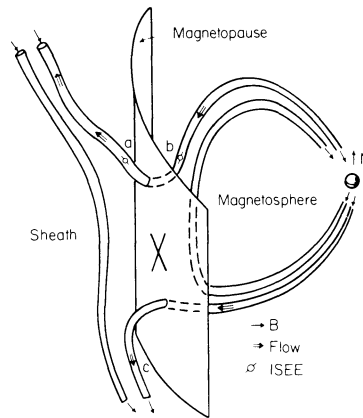


**Fig. 17.** Schematic representation of flow and field directions for flux transfer events (Speiser and Williams, 1982)

which is scanning in the ecliptic plane. Angular distributions of  $\sim 65$  keV/charge protons and alpha particles are shown in the right half of Fig. 19. The sector numbering is such that sector 2 is looking tailward, sector 4 is looking towards dawn, etc. The data are shown consecutively in time from top to bottom, and the angular distribution display shows the counting rate on a linear scale. The particles are streaming predominantly earthward and the spectra of both protons and alpha particles exhibit a maximum of the flux between  $\sim 65$  and  $\sim 130$  keV/charge during the first appearance of the particles. Furthermore, the alpha particle layer is confined within the proton layer. The deviation of the anisotropy from the Earth-Sun direction during the first encounter of the plasma sheet energetic ion layer can be explained by the effect of the density gradient perpendicular to the magnetic field at the boundary.

A detailed investigation of the energetic ions at the edge of the plasma sheet has been performed by Williams (1981). The three-dimensional measurements showed strong streaming and beam-like characteristics at each transition from low to high and high to low intensities in the energetic particle population. The azimuthal asymmetries indicate that the energetic ion streaming is located within  $\sim 2,000$  km of the plasma sheet edge. In general, when encountering the plasma sheet, streaming ions are first observed in the earthward direction at higher energies and the spectrum turns over towards lower energies. Later in the event earthward flowing particles are also observed at lower energies. At the same time as low energy earthward ion jetting is seen, tailward directed fluxes of higher energy ions are detected. These tailward streaming beams are the result of mirror point reflection of the earthward moving ion population. Williams (1981) explained the observation of peaked spectra in terms of a model where a source supplying energetic ions comes in contact with the field line going through the satellite position somewhere tailward of the satellite. Figure 20 from Williams (1981) illustrates the appearance of energetic ion beams at the satellite location due to the propagation of ions from a source with a power law spectrum a distance  $d$  away. The left side shows a  $E^{-3}$  differential energy spectrum and normalized arrival time ( $1/v_{\parallel} = T/d$ ,  $v_{\parallel}$  parallel velocity of ion) curves for pitch angles of  $0^{\circ}$  and  $60^{\circ}$ . The panels to the right show the time evolution of the spectra observed with an instrument located some distance  $d$  away. In this model peaked spectra

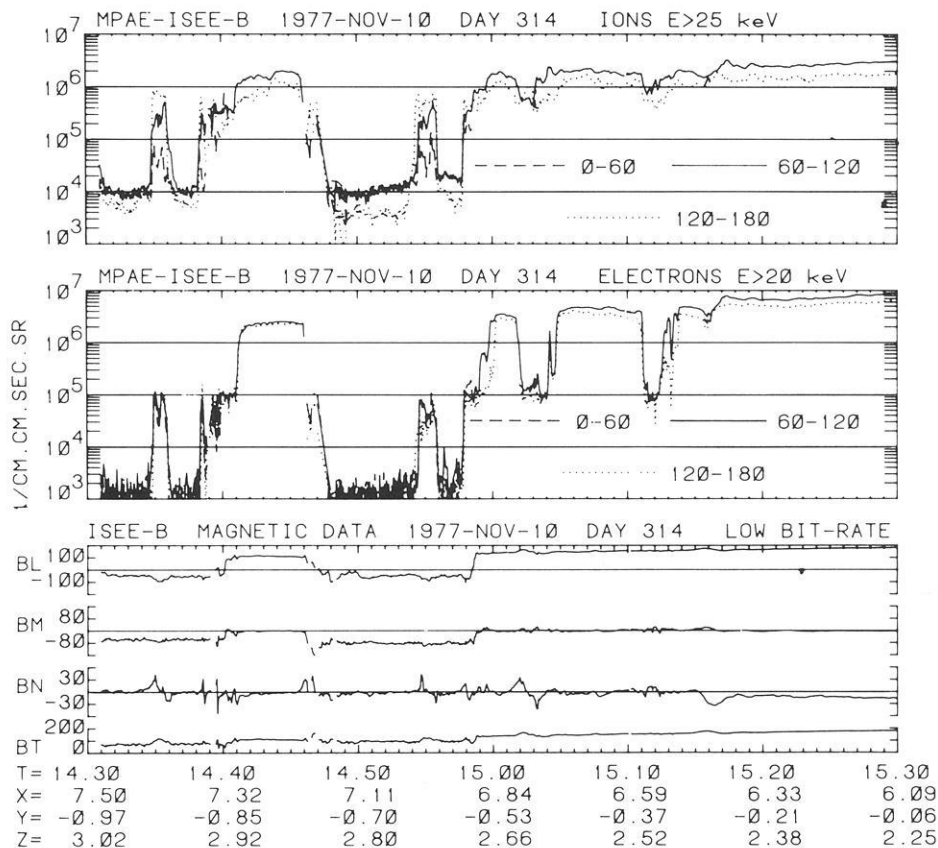


**Fig. 18.** Ion and electron data ( $E_i > 25$  keV,  $E_e > 20$  keV) plotted against time from 1430–1530 UT on 10 November 1977, and divided into three pitch angle ranges of  $60^\circ$  width each. Inside magnetosphere (1440–1447 and after 1459) the range  $0^\circ$ – $60^\circ$  is not sampled by this detector. The lower panel shows the magnetic field data, in boundary normal components, from Elphic and Russell (1979).  $BT$  is the unit of field strength is the nano-tesla. The set of four numbers beneath the plot contains the universal time (h and min) and the satellite position (in geocentric solar ecliptic coordinates, in Earth radii) (Daly and Keppler, 1982)

evolving in time and pitch angle are simply due to propagation effects from a time-variable source. Williams (1981) does not propose any specific source mechanism but concludes that the variable nature of the source can be due to a time-variable source, a spatially moving source or random encounters of the spacecraft flux tube with a steady source. This purely kinematical model is illustrated schematically in Fig. 21. Note, however, that while a time-variable source and a spatially moving source can result in the same energy dispersion effects at the satellite position, the spatial structure of the boundary layer is totally different. In the first case (time-variable source) bursts of energetic ions are produced intermittently somewhere in the tail while in the second case (moving source) there are layers of ions with different velocities which will move across the satellite position.

Another explanation of the peaked spectra has been given by Andrews et al. (1981a, b) in terms of the well-known velocity filter effect of a cross-tail electric field. Figure 22a illustrates how this dispersion arises. Field aligned particles of low and high speeds  $V_1$  and  $V_2$  are ejected from a source  $S$  close to the neutral sheet. The  $\mathbf{ExB}$  drift causes both particles to drift down with speed  $V_D$  so that their trajectories lie at different angles to the magnetic field  $\mathbf{B}$ . Thus the energetic ions are spatially dispersed such that the most energetic particles lie furthest from the neutral sheet. A satellite moving towards the neutral sheet will observe successively particles to lower and lower energies. Andrews et al. (1981a, b) have combined this velocity dispersion effect with the tailward motion of the source. In Fig. 22b a source moves from position  $S_1$  to position  $S_2$ . During this time particles of

slow and high speed ( $V_1$  and  $V_2$ ) have reached, under the influence of the  $\mathbf{ExB}$  drift, the end points of the arrows  $V_1$  and  $V_2$ , respectively. The connection of the endpoints of  $V_1$  and  $V_2$  with the source position  $S_2$  then defines upward moving fronts of slow and fast particles. Eventually the satellite will be crossed by these layers of particles of different energy. Figure 22c demonstrates how slow earthward moving particles and fast tailward moving particles can be observed simultaneously. For simplicity we neglect the motion of the source and consider only the  $\mathbf{ExB}$  drift effect. Particles of slow velocity  $V_2$  are ejected from a source at position  $S$ . Their velocity and the  $\mathbf{ExB}$  drift velocity then defines a line  $D_2$  where particles with the velocity  $V_2$  can be found. Particles of higher velocity  $V_1$  can be found at a line  $D_1$  further away from the neutral sheet. Let us assume that these particles are adiabatically reflected in the near-Earth magnetic field. They will then move along a line  $D_1$ , which intersects the line  $D_2$  at some location. A satellite at this location will observe simultaneously earthward jetting ions of velocity  $V_2$  and tailward moving particles of velocity  $V_1$ . Due to tailward motion of the source regions with different particle velocity will move across the satellite. Knowing the expansion speed of the boundary, which is due to tailward retreat of the source, the cross-tail electric field can be determined from the timing of the occurrence of ions with different velocities. Andrews et al. (1981b) obtained from a particular plasma sheet boundary crossing of ISEE 2 electric field values between 0.2 and 0.9 mV/m.

Neither Williams (1981) nor Andrews et al. (1981a, b) have suggested any particular source mechanism for the energetic particles. Forbes et al. (1981) studied plasma data

ISEE-1 MPE/UoMd  
19. APRIL 1978

- PROTONS
- ▲ ALPHAPARTICLES

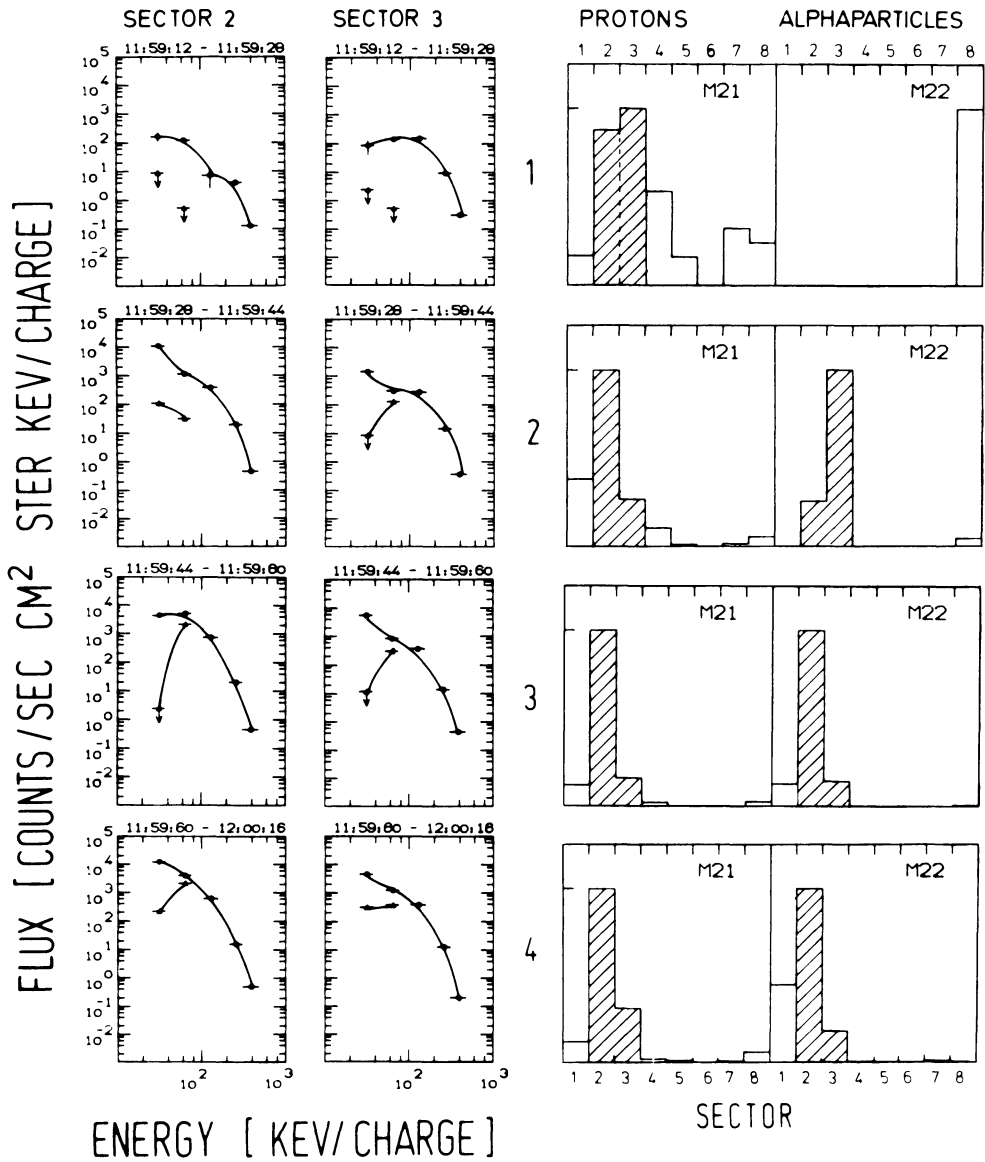
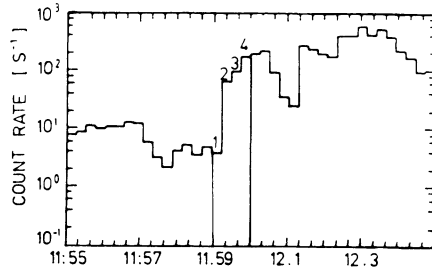


**Fig. 19.** (Left) Energy spectra of protons and alpha particles in sectors 2 and 3 together with (right) the angular distributions of 60-keV/q protons and alpha particles at the encounter of the plasma sheet (Möbius et al., 1980)

from ISEE 1 and 2 during a crossing of the plasma sheet boundary. They inferred an upward motion of the plasma sheet boundary of  $20 \pm 10$  km/s and found at the same time plasma velocities of  $\sim 30 \pm 10$  km/s toward the midplane of the plasma sheet. The upward advance of the surface of the plasma sheet in the presence of a downward convective flow induced by a dawn to dusk electric field in the tail requires the tailward motion of an energetic particle source. The source moves onto new magnetic field lines which map progressively deeper into the tail. Forbes et al. (1981) suggest that this motion of the source onto new

magnetic field lines is due to the tailward retreat of a magnetic neutral line and that particle acceleration is due to magnetic reconnection.

Andrews et al. (1981 a) applied the remote sensing technique with energetic particles to the plasma sheet boundary. They found upward speeds of the plasma sheet expansion of  $\sim 50$  km/s. From this, together with the observation of detached flux spikes preceding the main plasma sheet entry, a boundary structure has been proposed where the surface of the plasma sheet is corrugated with boundary waves propagating horizontally. Although the sheet expands slowly

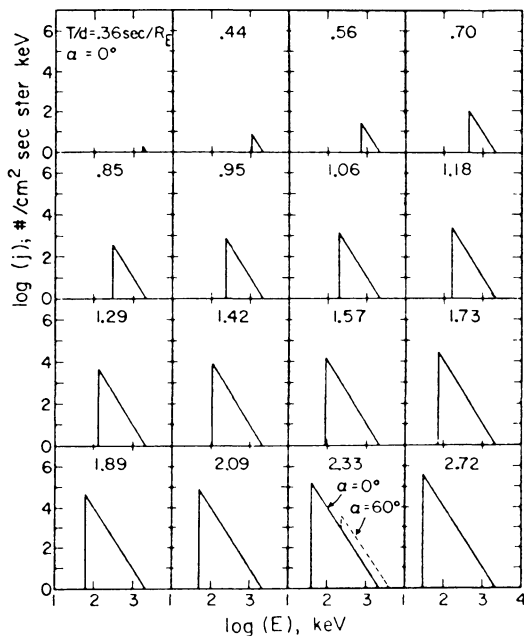
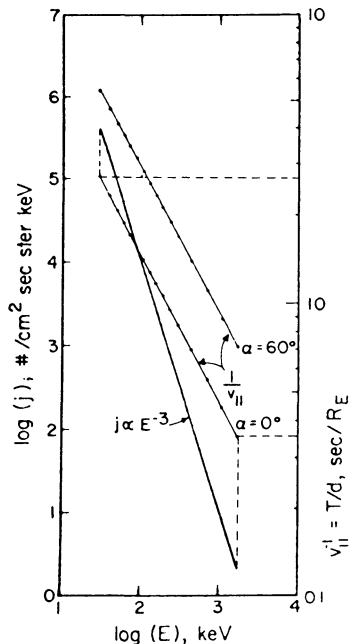


**Fig. 20.** Illustration of the appearance and evolution of “peaked” energy spectra observed by the ISEE 1 medium energy particles instrument due to propagation effects from a representative  $E^{-3}$  source. The left panel shows the  $E^{-3}$  source along with normalized propagation time,  $v_{\parallel}^{-1} = T/d$ , curves for the ISEE 1 instrument. The propagation time curves are shown for pitch angles  $\alpha = 0^\circ$  and  $60^\circ$ . The sixteen panels on the right show the time evolution of the instrument response for ions at  $\alpha = 0^\circ$  based on propagation from an  $E^{-3}$  source an arbitrary distance,  $d$ , away. Actual arrival times for these spectra are obtained by multiplying the  $T/d$  values by the source distance,  $d$ . One panel shows an  $\alpha = 60^\circ$  response for comparison. The concept illustrated by this figure is used with detector sampling characteristics and variable source parameters to explain inclined beams at the plasma edge (Williams, 1981)

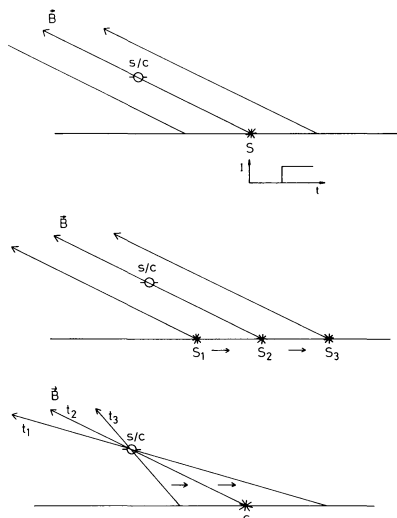


**Fig. 21.** Schematic representation of the occurrence of a time variable source (top), a spatially moving source (middle) or random encounters of the flux tube through the satellite with a source in the geomagnetic tail

the large tilt angles produced by the waves can lead to high vertical speed components.

Spjeldvik and Fritz (1981) have reported multiple plasma sheet encounters during an ISEE 1 plasma sheet boundary crossing. Figure 23 shows high resolution ion (24–44.5 keV) and electron (22–39 keV) observations from these authors. Several separate peaks are visible in the ion data and the peaks are typically 2–6 min apart. The ions are characterized by strong spin modulation indicating no observable fluxes when looking earthward and high fluxes when looking tailward. Since the instrument is scanning from north to south and back in 72 s, these peaks are in addition modulated by the scan motion as indicated by the scan position at the bottom of each panel. Only the interior of the last peak shows that the fluxes are essentially isotropic with only a modest spin modulation, i.e. the satel-

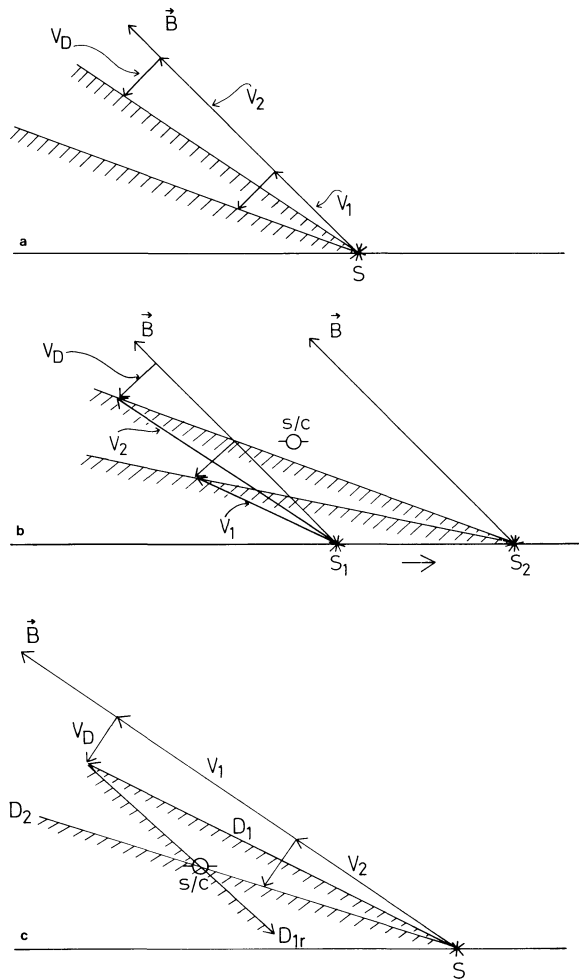


**Fig. 22 a.** Diagram to illustrate how the  $\mathbf{ExB}$  drift causes energy dependent boundaries in the tail. **b** Diagram to illustrate how a tailward retreating source together with the  $\mathbf{ExB}$  drift causes upward moving energy dependent boundaries. **c.** Trajectories of particles which can be observed at the satellite when near-earth reflection is included

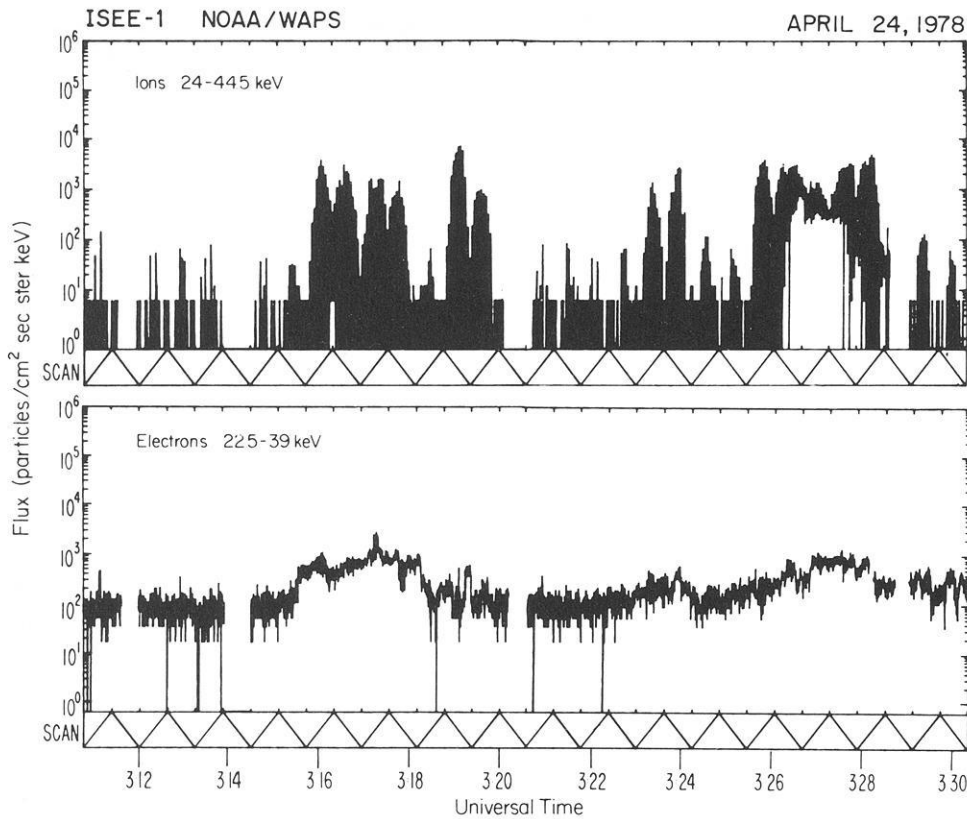


**Fig. 23.** High-resolution ion and electron observations from the lowest ion (24–44.5 keV) and electron 22.5–39 keV channels for ISEE 1 on day 114 (April 24) 1978. The peaks are modulated by the scan motion, as indicated by the scan position at the bottom of each panel. Notice the difference between the three first peaks where look direction modulation from zero flux from the Earth to high flux from the tail direction is seen, and the fourth peak which shows shoulders of similar field alignment and an interior of nearly isotropic fluxes (little look direction modulation). (Lower panel). Corresponding electron observation shows no such distinct features (Spjeldvik and Fritz, 1981)

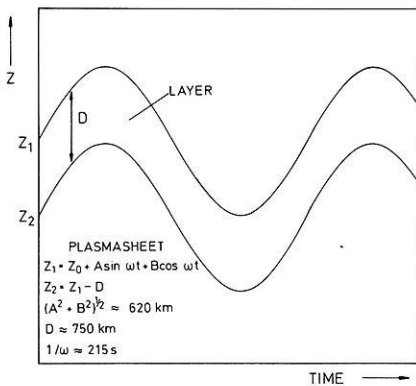


**Fig. 24.** Schematic representation of the plasma sheet boundary motion

lite is now beyond the boundary layer in the interior of the plasma sheet.

Spjeldvik and Fritz (1981) have interpreted the multiple crossings of the energetic ion layer in terms of large-scale waves of the boundary superimposed on the general plasma sheet thickening associated with the substorm process. Assuming that these waves are not travelling along the plasma sheet boundary but are only normal to the plasma sheet surface, the distance of the flow layer-lobe transition from the neutral sheet can be described by a sinusoid in time superimposed on the unperturbed surface position (see Fig. 24). The same holds for the flow layer-plasma sheet interior transition which is supposed to have a distance  $D$  from the lobe-flow layer transition. From the data for the last crossing shown in Fig. 23, Spjeldvik and Fritz (1981) obtain a layer thickness of 750 km, a wave amplitude of  $\sim 620$  km and a wave period of  $\sim 216$  s.

## Conclusions

Energetic particles have been used successfully in order to study magnetospheric boundaries like the magnetopause and the plasma sheet boundary. Such studies require ideally high temporal and good energy and angular resolution and  $4\pi$  coverage. The diagnostic value of energetic particles lies in the fact that due to their large gyroradii these particles can probe magnetospheric boundaries to larger distances. Such measurements have revealed the “wavy” structure of the magnetopause. Furthermore, by using energetic ions of magnetospheric origin as field line tracers the magnetic field topology near magnetospheric boundaries can be inferred.

It cannot be determined from energetic particle measurements alone whether the magnetopause is a rotational or tangential discontinuity. However, the observation of certain signatures of energetic particles near the magnetopause has added confidence to the identification of reconnection events. Similarly, the observation of energetic magnetospheric ions in flux transfer events has given strong support to the suggestion that these are flux tubes interconnected with the geomagnetic field.

The magnetic field near the magnetopause can change magnitude and direction over one gyroradius of an energetic ion. This is particularly true close to an  $x$ -type neutral line in a reconnection configuration or when magnetosheath field lines are draped around a flux tube connected with the magnetospheric field. In order to make further use of energetic ions as topology tracers their nonadiabatic behaviour in such magnetic field configuration has to be studied. Important contributions in this respect have been given by Speiser et al. (1981), Speiser and Williams (1982) and Daly (1983).

Magnetospheric ions are not only observed in the magnetosheath during reconnection events or in flux transfer events but are a more common feature outside the magnetopause. Their occurrence leads to several new questions which have not been attacked so far. In particular, it might be possible that while plasma and field measurements rely on the local occurrence of reconnection, energetic magnetospheric particles in the magnetosheath may be a signature of reconnection occurring much further away from the measuring site. A statistical analysis of their occurrence pattern may give important information about the magnetopause on a more global basis.

The energetic ion beams at the edge of the plasma sheet are of great importance for the process of plasma sheet recovery following magnetospheric substorms. It has been suggested that the thickening of the plasma sheet during recovery is caused by the populating of field lines previously devoid of energetic plasma with new particles from the neutral line region in the distant tail. Due to the tailward retreat of the neutral line and the continuous reconnection process, the plasma sheet builds up and thickens. Detailed study of the energetic ion beams may shed light on the origin of the plasma sheet.

## References

- Andrews, M.K., Keppler, E., Daly, P.W.: Plasma sheet motions inferred from medium-energy ion measurements. *J. Geophys. Res.* **86**, 7543–7556, 1981 a
- Andrews, M.K., Daly, P.W., Keppler, E.: Ion jetting at the plasma sheet boundary: simultaneous observations of incident and reflected particles. *Geophys. Res. Lett.* **8**, 987–990, 1981 b
- Baker, D.N., Stone, E.C.: The magnetopause electron layer along the distant magnetotail. *Geophys. Res. Lett.* **4**, 133–136, 1977
- Daly, P.W., Williams, D.J., Russell, C.T., Keppler, E.: Particle signature of magnetic flux transfer events at the magnetopause. *J. Geophys. Res.* **86**, 1628–1632, 1981
- Daly, P.W., Fritz, T.A.: Trapped electron distributions on open magnetic field lines. *J. Geophys. Res.* **87**, 6081–6088, 1982
- Daly, P.W., Keppler, E.: Observation of a flux transfer event on the earthward side of the magnetopause. *Planet. Space Sci.* **30**, 331–337, 1982
- Daly, P.W.: Remote sensing of energetic particle boundaries. *Geophys. Res. Lett.*, in press, 1983
- Domingo, V., Page, D.E., Wenzel, K.P.: Energetic relativistic electrons near the polar magnetopause. *J. Geophys. Res.* **82**, 2327–2336, 1977
- Eastman, T.E., Frank, L.A.: Observations of high-speed plasma flow near the Earth's magnetopause: evidence for reconnection? *J. Geophys. Res.* **87**, 2187–2201, 1982
- Fahnenstiel, S.C.: Standing waves observed at the dayside magnetopause. Preprint, NOAA-ERL, Boulder, Colorado, 1981
- Fritz, T.A., Fahnenstiel, S.C.: High temporal resolution energetic particle soundings at the magnetopause on November 8, 1977, using ISEE 2. *J. Geophys. Res.* **87**, 2125–2131, 1982
- Forbes, T.G., Hones, E.W., Bame, S.J., Asbridge, J.R., Paschmann, G., Schopke, N., Russell, C.T.: Evidence for the tailward retreat of a magnetic neutral line in the magnetotail during substorm recovery. *Geophys. Res. Lett.* **8**, 261–264, 1981
- Kaufmann, R.L., Konradi, A.: Explorer 12 magnetopause observations: Large-scale nonuniform motion. *J. Geophys. Res.* **74**, 3609–3627, 1969
- Kaufmann, R.L., Konradi, A.: Speed and thickness of the magnetopause. *J. Geophys. Res.* **78**, 6549–6568, 1973
- Konradi, A., Kaufmann, R.L.: Evidence for rapid motion of the outer boundary of the magnetosphere. *J. Geophys. Res.* **70**, 1627–1637, 1965
- Krimigis, S.M., Sarris, E.T.: Energetic particle bursts in the Earth's magnetotail. In: *Dynamics of magnetosphere*, S.-I. Akasofu, ed.: pp 599–630, Dordrecht: D. Reidel Publ. Co. 1979
- Lanzerotti, L.J., Krimigis, S.M., Bostrom, C.O., Axford, W.I., Lepping, R.P., Ness, N.F.: Measurements of the plasma flow at the dawn magnetopause by Voyager 1. *J. Geophys. Res.* **84**, 6483–6488, 1979
- Meng, C.-I., Anderson, K.A.: Characteristics of the magnetopause energetic electron layer. *J. Geophys. Res.* **80**, 4237–4243, 1975
- Möbius, E., Ipavich, F.M., Scholer, M., Gloeckler, G., Hovestadt, D., Klecker, B.: Observations of a nonthermal ion layer at the plasma sheet boundary during substorm recovery. *J. Geophys. Res.* **85**, 5143–5148, 1980
- Paschmann, G., Sonnerup, B.U.Ö., Papamastorakis, I., Schopke, N., Haerendel, G., Bame, S.J., Asbridge, J.R., Gosling, J.T., Russell, C.T.: Plasma acceleration at the Earth's magnetopause: evidence for reconnection. *Nature* **282**, 243–246, 1979
- Richter, A.K., Keppler, E., Axford, W.I., Denskat, K.U.: Dynamics of low energy electrons (>17 keV) and ions (>80 keV) in the vicinity of the low-latitude duskside magnetopause: Helios 1 and 2 observations. *J. Geophys. Res.* **84**, 1453–1463, 1979
- Russell, C.T., Elphic, R.C.: Initial ISEE magnetometer results: magnetopause observations. *Space Sci. Rev.* **22**, 681–715, 1978
- Russell, C.T., Elphic, R.C.: ISEE observations of flux transfer events at the dayside magnetopause. *Geophys. Res. Lett.* **6**, 33–36, 1979
- Scholer, M., Ipavich, F.M., Gloeckler, G., Hovestadt, D., Klecker, B.: Leakage of magnetospheric ions into the magnetosheath along reconnected field lines at the dayside magnetopause. *J. Geophys. Res.* **86**, 1299–1304, 1981
- Scholer, M., Daly, P.W., Paschmann, G., Fritz, T.A.: Field line topology determined by energetic particles during a possible magnetopause reconnection event. *J. Geophys. Res.* **87**, 6073–6080, 1982 a
- Scholer, M., Hovestadt, D., Ipavich, F.M., Gloeckler, G.: Energetic protons, alpha particles, and electrons in magnetic flux transfer events. *J. Geophys. Res.* **87**, 2169–2175, 1982 b
- Scholer, M., Ipavich, F.M.: Interaction of ring current ions with the magnetopause. *J. Geophys. Res.*, 1983
- Sonnerup, B.U.Ö., Paschmann, G., Papamastorakis, I., Schopke, N., Haerendel, G., Bame, S.J., Asbridge, J.R., Gosling, J.T., Russell, C.T.: Evidence for magnetic field reconnection at the Earth's magnetopause. *J. Geophys. Res.* **86**, 10049–10067, 1981
- Speiser, T., Williams, D.J., Garcia, H.: Magnetically trapped ions as a source of magnetosheath energetic ions. *J. Geophys. Res.* **86**, 723–732, 1981
- Speiser, T., Williams, D.J.: Magnetopause modelling: flux transfer events and magnetosheath quasi-trapped distributions. *J. Geophys. Res.* **87**, 2177–2186, 1982
- Spjeldvik, W.N., Fritz, T.A.: Energetic ion and electron observations of the geomagnetic plasma sheet boundary layer: Three-dimensional results from ISEE 1. *J. Geophys. Res.* **86**, 2480–2486, 1981
- Williams, D.J.: Magnetopause characteristics inferred from three-dimensional energetic particle distributions. *J. Geophys. Res.* **84**, 101–104, 1979 a
- Williams, D.J.: Observations of significant magnetosheath anti-solar energy flow. *J. Geophys. Res.* **84**, 2105–2108, 1979 b
- Williams, D.J., Frank, L.A.: ISEE-1 charged particle observations indicative of open field lines near the subsolar region. *J. Geophys. Res.* **85**, 2037–2042, 1980
- Williams, D.J.: Magnetopause characteristics at 0840–1040 hours local time. *J. Geophys. Res.* **85**, 3387–3395, 1980
- Williams, D.J.: Energetic ion beams at the edge of the plasma sheet – ISEE 1 observations plus a simple explanatory model. *J. Geophys. Res.* **86**, 5507–5518, 1981

# Recent ISEE Observations of the Magnetopause and Low Latitude Boundary Layer: A Review\*

M.A. Saunders

Blackett Laboratory, Imperial College, London SW7 2BZ, U.K.

**Abstract.** ISEE-1 and 2 satellite observations at the dayside magnetopause have enabled important progress to be made on the solar wind/magnetosphere coupling problem. The ISEE results have emphasized the significance of reconnection and have indicated that the process can occur both in a quasi-steady form and in an unsteady (flux transfer event (FTE)) manner. The detection of FTEs on open field lines within the magnetosphere, the discovery of reverse polarity FTEs, and the observation that FTEs can be associated closely with intervals of quasi-steady reconnection flow, all support further the view that FTEs are reconnection phenomena. Indeed, a sharp distinction need not exist between FTEs and the type of reconnection event described as quasi-steady.

**Key words:** Magnetopause – Low latitude boundary layer – Reconnection – Flux transfer events

## Introduction

The magnetopause or the outer boundary of the Earth's magnetic field, is the location of some of the most fundamental, yet arguably the most controversial processes in magnetospheric physics: that is those which effect the transfer of solar wind mass and momentum to the terrestrial magnetosphere. There is little doubt now that the solar wind does supply a significant fraction of the mass, and a dominant amount of the momentum and energy involved in magnetospheric motion. In particular it drives the magnetospheric convection system, which is central to our understanding of the macroscopic distribution of plasmas and electromagnetic fields (both DC and AC) within the magnetosphere (see Cowley, 1982; Southwood, in press).

The controversy, which has persisted despite the twenty years of in situ satellite measurements, concerns the exact form that the coupling takes. Discussion has centred principally around two mechanisms: the first involving magnetic reconnection between solar and terrestrial magnetic fields as described first by Dungey (1961), and the second involving a "viscous-like" interaction, with diffusion of solar plasma across the magnetopause (Axford and Hines, 1961). The continuing debate, and especially the lack of direct

empirical evidence in favour of reconnection, led Lemaire and Roth (1978) to suggest a hybrid coupling model involving "impulsive penetration" of solar wind plasma irregularities into the magnetosphere.

Shortly after the latter suggestion was made, the ISEE-1 and 2 satellites began providing the first high time and 3D resolution plasma data from the dayside magnetopause, where the primary coupling interactions are believed to take place. These measurements have thrown considerable light on the solar wind/magnetosphere coupling problem, and a discussion of the most recent ISEE results on this topic will form the basis of this review. For a thorough assessment of magnetopause and low latitude boundary layer research prior to mid-1982, the reader is referred to the review by Cowley (1982).

The new ISEE results have involved largely reconnection and, to reflect this emphasis, the paper divides as follows. Two sections describe the in situ evidence from ISEE that dayside reconnection occurs both in a quasi-steady form (next section) and as a transient, patchy (flux transfer event) process (subsequent section), with brief theoretical descriptions of the expected signatures in the field and plasma data included in each case. The next section considers the ISEE observations pertaining to the low latitude boundary layer and offers a fresh interpretation for the pulsed boundary layer features reported by Scokoppe et al. (1981). In the penultimate section the relative importance of the different coupling processes at the magnetopause are assessed in terms of the cross-magnetosphere potential to which each gives rise. Conclusions and important remaining questions comprise the last section.

## Quasi-Steady Reconnection

Although the temporal and spatial characteristics of reconnection have yet to be established, early results suggest that at times it occurs in the large scale quasi-steady manner envisaged by Dungey (1961) and described subsequently by Petschek (1964) and Levy et al. (1964). Twelve examples of quasi-steady reconnection have been published to date (Paschmann et al., 1979; Sonnerup et al., 1981; Gosling et al., 1982), with further cases identified but not yet reported (G. Paschmann, pers. comm., 1982).

Before reviewing this evidence, let us first briefly consider the signatures in the electromagnetic field and plasma which one would expect to see when steady subsolar reconnection is occurring. Figure 1 shows a cross-section through

\* Based on an invited review paper given at the Symposium on Plasma and Energetic Particles in the Magnetosphere, EGS Meeting, 23–27 August 1982, Leeds, U.K.

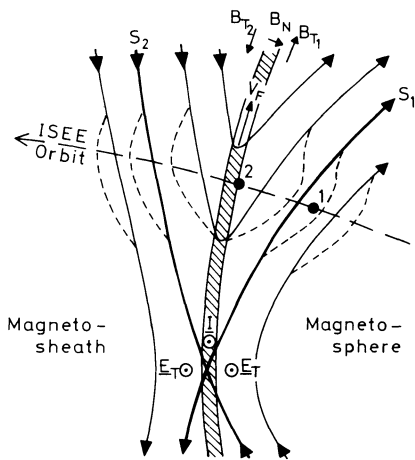


**Fig. 1.** Meridian cross-section of the dayside magnetopause illustrating the signatures of steady subsolar reconnection for antiparallel external and internal magnetic fields. The field lines are shown as solid lines, with the dashed lines denoting the field distortions which may occur following a short pulse of stronger reconnection which erodes extra flux

the dayside magnetopause current layer (shown hatched), covering a region from slightly south, to well north of, a reconnection  $X$ -line. The significance of the dashed field lines in the vicinity of the ISEE satellites (marked 1 and 2) will be explained later. Those magnetosheath and magnetosphere field lines connected to the  $X$ -line are called separatrices and are marked by an  $S$ .

The electromagnetic effects associated with reconnection are a magnetic field component  $B_N$  normal to the boundary, and an electric field  $E_T$  tangential to the current sheet. These two effects change the momentum of inflowing magnetosheath plasma through an acceleration process which can be pictured as similar in action to a slingshot. Maxwell field tension forces the sharply bent open flux tubes to shorten by contracting polewards at the speed  $V_F = E_T/B_N$ , thereby causing plasma acceleration through the release of magnetic field energy (Cowley, 1979; 1980). The plasma acceleration can be understood in an equivalent manner without recourse to the moving field line picture, as due to the  $\mathbf{I} \times \mathbf{B}_N$  body force. Electromagnetic energy is liberated to the plasma in the current layer (at the rate  $\mathbf{I} \cdot \mathbf{E}_T$ ) because the magnetopause current  $\mathbf{I}$  has a component parallel to  $\mathbf{E}_T$ . In addition to plasma acceleration the other characteristic plasma feature of subsolar reconnection is a mixing of magnetosheath and magnetospheric plasmas along the open flux tubes.

With these basic theoretical ideas in mind, let us now consider the ISEE data showing the first in situ evidence that reconnection occurs in a quasi-steady form. "Quasi-steady" in this context means that reconnection persists for longer than the five minutes required to set up a flow of open flux tubes over the entire dayside boundary. The most studied example occurred on 8 September 1978, during an outbound passage at a GSM local time and northern latitude of  $\sim 1140$  h and  $\sim 26^\circ$ .

Plasma and magnetic field data are displayed for both ISEE-1 and 2 separately in Fig. 2 (also see Paschmann

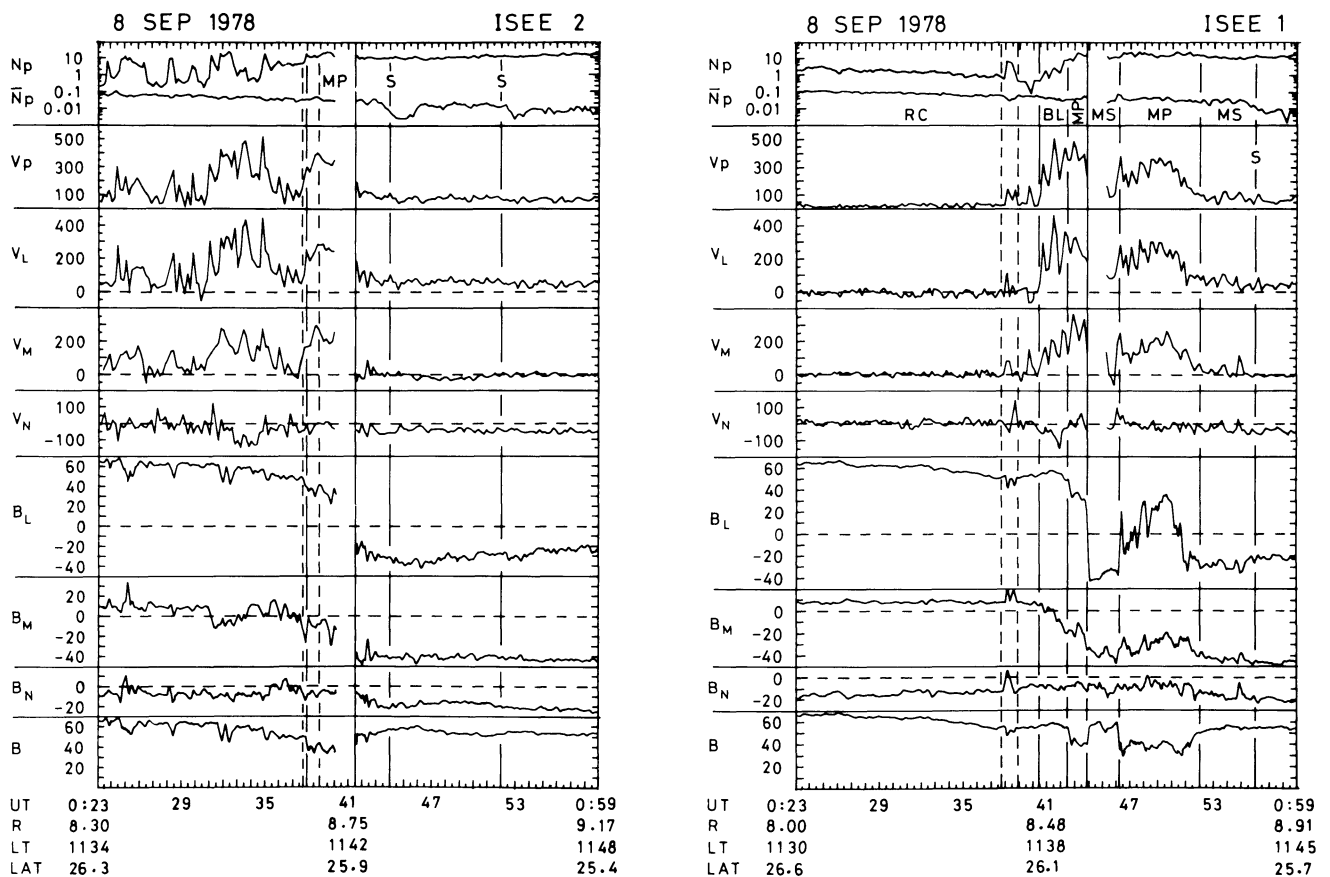


**Fig. 2.** Plasma and magnetometer data from (left) ISEE 2 and (right) ISEE 1 for thirty-six min during the outbound magnetopause crossing on 8 September 1978. Each satellite's position is given (at the bottom) in terms of geocentric radial distance (R) in earth radii, and GSM local time (LT) and latitude (LAT)

et al., 1979 and Sonnerup et al., 1981). The plasma parameters are 3D recordings with 12 s resolution, and the magnetometer data are 12 s averages plotted every 4 s. The top panel shows  $Np$ , the total plasma number density ( $\text{cm}^{-3}$ ), and  $\bar{N}p$ , the density of energetic (8–40 keV) ions. Below are plotted  $Vp$ , the plasma bulk flow speed ( $\text{km s}^{-1}$ ),  $B$ , the magnetic field strength (nT), and the Cartesian components of the flow and field expressed in boundary normal coordinates (Russell and Elphic, 1978). In this coordinate system  $\hat{N}$  is the estimated outward normal to the magnetopause,  $\hat{L}$  points north such that the GSM  $\hat{z}$  axis lies in the  $L-N$  plane, while  $\hat{M}$  completes the orthogonal triad and points westward. The normal used in Fig. 2 has GSM components (0.768,  $-0.312$ , 0.560) and is the minimum variance normal employed by Sonnerup et al. (1981). It differs in direction by  $24^\circ$  relative to the Fairfield (1971) model magnetopause normal (0.953,  $-0.050$ , 0.297) for the satellite location. The data are subdivided by vertical lines according to the main plasma regions and boundaries identified by Sonnerup et al. (1981): the ring current (RC), boundary layer (BL), magnetopause current layer (MP), and the magnetosheath (MS). The lines marked  $S$  denote the location of the outer reconnection separatrix inferred from the presence of energetic ring current ions in the magnetosheath. The significance of the interval bracketed by dashed lines at  $\sim 00:38.30$  UT will be discussed later. The satellite separation in LMN coordinates during the interval was  $\sim (300, 1,300, -1,500)$  km measured from ISEE 2 (the lead satellite) to ISEE 1.

The striking feature of the data is the high speed flow seen by both satellites in the boundary layer and in the region marked as magnetopause. These speeds are 5–10 times greater than those recorded later in the magnetosheath, and as the positive values of  $V_L$  and  $V_M$  show, the plasma acceleration is directed northward and dawnward (also see Eastman and Frank, 1982). The vector change in plasma momentum across the magnetopause matches expectations for the effect of “slingshot” acceleration from the release of magnetic field stress on open flux tubes (Paschmann et al., 1979). This acceleration is interpreted as quasi-steady because high speed flows are seen intermittently (due to boundary motion) at one or other satellite for at least half an hour. The presence in the vicinity of the magnetopause of an inward-pointing normal magnetic field component of 5–10 nT is clear also. A negative  $B_N$  is consistent with a satellite location north of the reconnection  $X$ -line, as also is the streaming anti-parallel to  $B$  of the energetic magnetospheric ions seen in the magnetosheath (Sonnerup et al., 1981; Scholer et al., 1981; 1982; Daly and Fritz, 1982). The detection of energetic ring current ions well outside the magnetopause with no discontinuity in density at the boundary (Fig. 2), and the fact that the plasma density in the boundary layer is intermediate between magnetosheath and ring current values, both imply a mixing of plasmas along open flux tubes.

In short, there exists virtually a complete set of reconnection signatures. The only missing item is a direct measurement of the tangential electric field, which is due to the relevant instrument being in an unfavourable mode during the interval. One observation has proved puzzling though, and that is the behaviour of the energetic electrons (tens of keV and greater) reported by Eastman and Frank (1982) and Scholer et al. (1982). These show a trapped distribution on field lines which the high speed flows and

streaming energetic ions imply are open. Since trapped electron distributions are characteristic of closed field lines, Eastman and Frank (1982) and Eastman et al. (submitted) disagree that reconnection is occurring, favouring instead an interpretation based on the impulsive penetration model of Lemaire and Roth (1978). However, Daly and Fritz (1982) present evidence that electrons may be trapped on open field lines, due to magnetic mirroring about the field strength minimum which occurs in the magnetopause current sheet (Fig. 2). Although reconnection theory predicts such a field depression, it would be interesting to investigate the behaviour of the energetic electrons in other reconnection events to establish whether similar behaviour occurred.

The tangential electric field is another feature which needs investigation in the other reconnection events. Tangential electric fields have been reported for a few ISEE magnetopause encounters (Mozer et al., 1978; 1979; Fahleson et al., 1979) but none of these cases correspond to intervals of quasi-steady reconnection. For the boundary crossing on 20 November 1977, which has received the most study in regard to DC electric field behaviour, Mozer et al. (1978; 1979) report an average  $E_T$  of  $1.7 \text{ mV m}^{-1}$  and a local power dissipation to the plasma of  $\sim 70 \mu\text{W m}^{-2}$ . However, no significant plasma flow acceleration is observed in this case (Sonnerup et al., 1981), a discrepancy the reason for which is not understood.

As mentioned earlier, in addition to the 8 September 1978 case, eleven other ISEE dayside magnetopause crossings have been published to date with properties suggestive of quasi-steady reconnection. As well as these examples, many further instances of reconnection have been identified in ISEE data where the process, rather than appearing quasi-steady, seems to occur in a transient, patchy manner, referred to as “flux transfer events” or FTEs (Russell and Elphic, 1978). FTEs form the next topic of discussion but it is appropriate to mention them first briefly here, as the data in Fig. 2 contain an observation which may have a significant bearing on their nature. FTEs can occur in close association with intervals of quasi-steady reconnection flow (Paschmann et al., 1982 (their Fig. 3); Rijnbeek et al., 1982) so there could be a physical connection between the two processes. The data enclosed by the dashed vertical lines at  $\sim 00:38.30$  UT in Fig. 2 are an instance of such association. These observations suggest a basis for the physical connection for as ISEE 1 is encountering an FTE, ISEE 2 located 1,500 km nearer the magnetopause, apparently sees quasi-steady reconnection flow. Further discussion of this point is reserved for later.

### Flux Transfer Event Reconnection

The first suggestion that reconnection may occur as a localised, transient process, was made by Haerendel et al. (1978) following analysis of HEOS 2 magnetometer data from the dayside low latitude boundary layer. ISEE dayside observations have confirmed this suggestion, though the data published to date indicate that patchy or unsteady reconnection occurs in the equatorial vicinity, rather than near the cusps as originally envisaged.

The discovery of signatures in the ISEE data indicative of isolated reconnected magnetic flux tubes was first reported by Russell and Elphic (1978; 1979) and Elphic and Russell (1979). These “flux transfer events” (FTEs) were

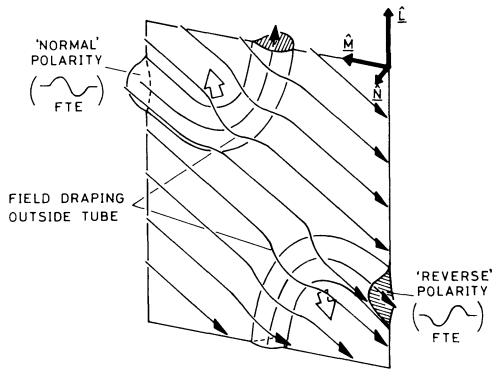


**Fig. 3.** Schematic view (from the magnetosheath) of two open FTE flux tubes shortly after a localised reconnection event at the dayside magnetopause. The southerly contracting open tube gives rise to the recently discovered “reverse” polarity FTE. The LMN coordinate directions are included for reference in the top right hand part of the sketch. (Figure is after Rijnbeek et al., 1982)

initially identified from their characteristic signal in the magnetic field when expressed in boundary normal (LMN) coordinates; namely, a bipolar (positive followed by negative) perturbation in  $B_N$ , together with a northward tilting of the magnetosheath field. Previous interpretational work (Russell and Elphic, 1978; Paschmann et al., 1982; Cowley, 1982) has shown that these properties are characteristic of reconnection occurring on a short-scale.

The origin of the FTE  $B_N$  signal can be understood with the aid of Fig. 3 (after Rijnbeek et al., 1982) which shows a sketch of the dayside subsolar magnetopause shortly after a localised reconnection event has occurred near the equator in the centre of the diagram. A southerly ( $-L$ ) and easterly ( $-M$ ) directed group of magnetosheath field lines has reconnected with the northerly directed magnetospheric field, so that the magnetic tension force causes the two parts of the reconnected open tube to contract along the magnetopause in the directions indicated by the open arrows. This contraction gives rise to perturbations in the overlying magnetosheath plasma and field. A satellite observing the northwards moving open tube will see a positive perturbation in the magnetic field component normal to the magnetopause as the tube approaches, and a negative perturbation as it recedes. The southward moving open tube, however, will give rise to a reverse  $B_N$  signature, that is, negative followed by positive, and a reverse polarity FTE will be seen. Within the open tubes deflections in the plasma flow and field direction should occur (Cowley, 1982; Rijnbeek et al., 1982). In particular, the magnetosheath ends of the tubes will be pulled towards the Earth's field direction, while the magnetospheric ends will be pulled similarly towards the direction of the magnetosheath field. The plasma flow inside the northerly moving open tube should be deflected northward and westward relative to the ambient magnetosheath flow, while the plasma flow within the southerly contracting open tube should be perturbed southwards and eastwards.

Nearly all the flux transfer events reported in the literature to date were observed soon after ISEE satellite launch in the late autumn of 1977, when ISEE was sampling northern GSM latitudes of typically  $20^\circ$ – $40^\circ$ . These FTEs all possess the positive followed by negative  $B_N$  polarity expected for open tubes moving north following reconnection

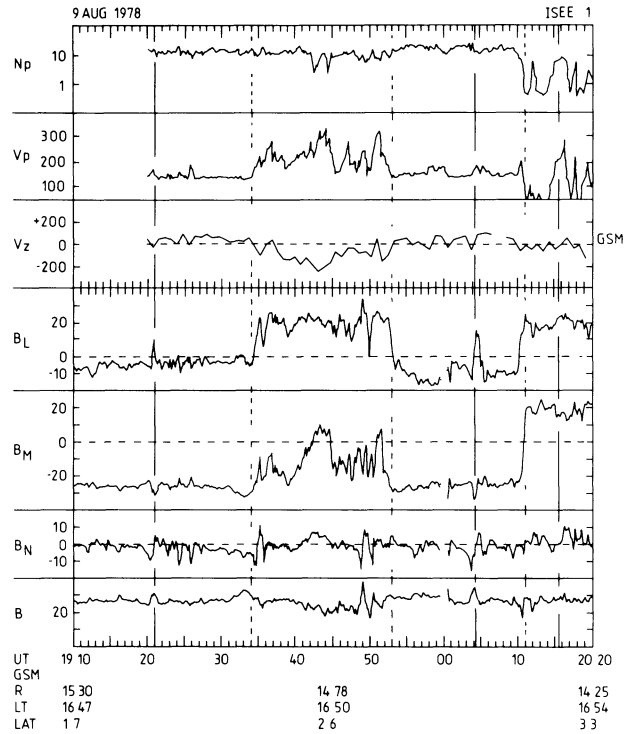


**Fig. 4.** ISEE 1 plasma and magnetic field measurements of the magnetopause region for the inbound crossing on 9 August 1978. The plotted parameters and their units are identical to those described for Fig. 2, except  $V_z$ , which is the GSM  $z$  (northward) component of the plasma velocity ( $\text{km s}^{-1}$ ). “Reverse” polarity FTEs are denoted by the vertical guidelines at  $\sim 19:21$  and  $\sim 20:04$  UT, while the dashed line at  $\sim 20:11$  identifies the magnetopause. (Figure is after Rijnbeek et al., 1982)

near the equator. The first report of a negative or reverse polarity FTE has been given recently by Rijnbeek et al. (1982). The data presented by these authors are shown in Fig. 4 and come from the inbound ISEE boundary pass on 9 August 1978 which occurred only  $2^\circ$  above the GSM equator. Plasma measurements (taken from Sonnerup et al., 1981) are shown above magnetometer recordings plotted in boundary normal coordinates. This boundary crossing has added interest because Sonnerup et al. (1981) identify the interval between 19:34 and 19:53 UT as one where quasi-steady reconnection was occurring. In particular it is the only example published so far where the satellite was situated south of the reconnection region. This is indicated in Fig. 4 by the southward deflection in direction of the accelerated plasma flows.

In the magnetosheath both before and after the interval of quasi steady reconnection, unsteady reconnection was occurring in the form of flux transfer events at  $\sim 19:21$  and  $\sim 20:04$  UT. These FTEs display all the characteristics described by Russell and Elphic (1978; 1979) and Paschmann et al. (1982), except that here the  $B_N$  polarity is negative to positive, and the magnetosheath plasma flow is deflected southward (albeit at one data point). From the discussion earlier, the latter properties are those expected for open FTE flux tubes located south of the reconnection region and connected to the Earth's southern hemisphere. The energetic ion streaming which accompanies both events also is consistent with connection to the southern hemisphere (P.W. Daly, pers. comm., 1982). Thus the FTE and

quasi-steady reconnection properties both indicate that reconnection was occurring north of the satellite. Although Rijnbeek et al. (1982) only discussed the one event, reverse polarity flux transfer events are observed during several other boundary crossings near or south of the GSM equator (Berchem and Russell, 1982; R.P. Rijnbeek, pers. comm., 1982).

### Low Latitude Boundary Layer Observations

The origin of the low latitude boundary layer (LLBL), the region containing tailward flowing plasma earthward of and adjacent to the magnetopause with characteristics intermediate between the magnetosheath and magnetosphere, is clearly basic to our understanding as to how solar wind momentum is transferred to the magnetosphere. Satellite observations prior to ISEE generally indicated that diffusion of each plasma population across the magnetopause was the primary LLBL formation mechanism (Hones et al., 1972; Akasofu et al., 1973; Eastman et al., 1976; Haerendel et al., 1978; Eastman and Hones, 1979). High resolution plasma measurements recorded by ISEE in the LLBL have also been interpreted as indicating an origin involving diffusion (Hones et al., 1982; Eastman et al., submitted). Skopke et al. (1981) also claim consistency with diffusion providing the diffusion coefficient is sufficiently large. However, it is not proven that diffusion is always the source of the layer. When reconnection is occurring a plasma population is set up interior to the magnetopause with properties similar to that of a diffusively driven boundary layer. The major distinction when reconnection is dominant is that the boundary layer flow may exceed the exterior flow speed because the plasma is subjected to the  $\mathbf{I} \times \mathbf{B}_N$  force as it penetrates the magnetopause.

The fact that several ISEE boundary layer crossings agree in detail with the occurrence of quasi-steady reconnection, indicates that in these cases diffusion was not the main boundary layer source. The existence of magnetosheath FTEs also implies a boundary layer origin not involving diffusion. Indeed, a scan of the Los Alamos/Garching ISEE fast plasma data shows that bursts of plasma acceleration, accompanied by "sharp-edged" pulses of magnetosheath plasma, are a common boundary layer feature, and often possess a 1–2 min timescale similar to that reported for magnetosheath flux transfer events.

Since FTEs were discovered in the magnetosheath, early work concentrated on their magnetosheath characteristics. However, if the interpretation suggested by Russell and Elphic (1978) involving localised magnetic reconnection across the magnetopause is correct, each magnetosheath FTE should have a counterpart feature inside the magnetosphere (see Fig. 3). The latter should appear as a pulse of accelerated magnetosheath plasma and possess magnetic field perturbations similar to those which accompany magnetosheath FTEs, except that in this case the field should be pulled towards the sheath field direction if the sheath flow is sub-Alfvénic (Cowley, 1982). In the absence of magnetic mirroring on open field lines the energetic particles should exhibit streaming along  $\mathbf{B}$ , as in magnetosheath FTEs.

The first reports of magnetospheric FTEs with the above properties have recently been made by Daly and Keppler (1982) and Paschmann et al. (1982). A possible

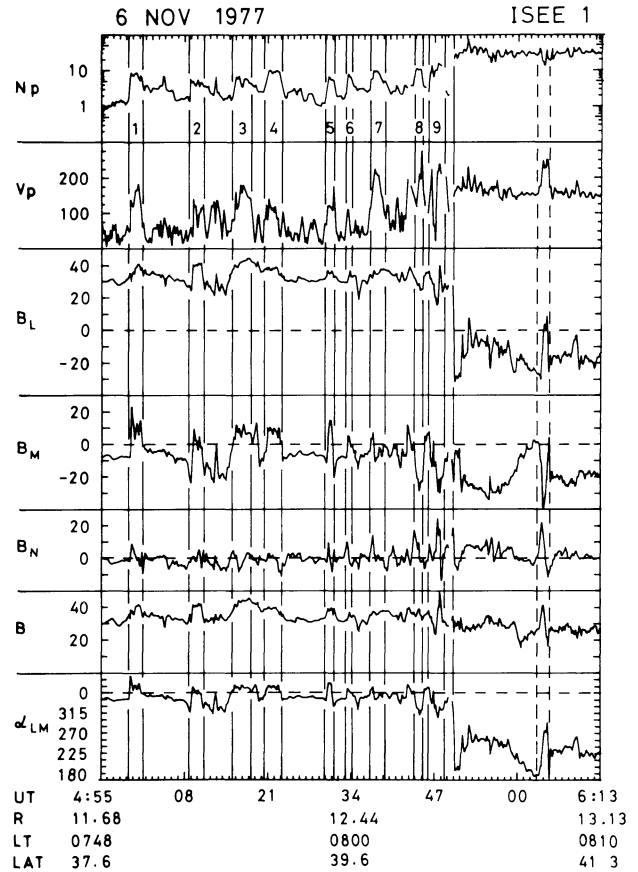


Fig. 5. ISEE 1 plasma and magnetometer recordings for the 6 November 1977 outbound crossing of the low latitude boundary layer and magnetopause. With the exception of  $\alpha_{LM}$ , the field angle in the LM plane, the plotted parameters are the same as described previously. The main intervals (or "pulses") of flowing boundary layer plasma are marked by vertical lines and numbered near the top of the diagram. A magnetosheath FTE is bracketed by the dashed guidelines at  $\sim 06:04$  UT

example of another counterpart feature was noted by Rijnbeek et al. (1982) and is marked in Fig. 4 by the right-hand vertical guideline. This feature is associated with a pulse of accelerated plasma, a reverse polarity (negative/positive) perturbation in  $B_N$  and a slight tilting of the boundary layer field towards the magnetosheath field direction. Clearer examples of internal FTEs exist in the ISEE LLBL crossing which has received most study to date, the 6 November 1977 outbound pass. This dawn flank northern latitude boundary layer passage has been studied by Skopke et al. (1981) and Paschmann et al. (1982). The interpretation given below is based on ideas developed by the author together with S.W.H. Cowley and D.J. Southwood.

ISEE 1 plasma and magnetometer data for a 78 min interval spanning the boundary layer and magnetopause regions on 6 November 1977 are shown in Fig. 5. The plasma data are 3D measurements with 12 s resolution, and the field recordings are displayed in boundary normal coordinates using a normal calculated by approximating the magnetopause as a tangential discontinuity. This normal differed in direction by  $20^\circ$  relative to the Fairfield (1971) model normal employed by Skopke et al. (1981) but the conclusions described below are independent of which normal is used. The bottom panel shows the field angle

$\alpha_{LM}$  in the LM plane (tangential to the magnetopause) defined in the same manner as the angle  $\alpha'_B$  displayed by Scokpe et al. (1981) (see their Fig. 3), with  $\alpha_{LM}=0^\circ$  directed along **L** (northward) and  $\alpha_{LM}=90^\circ$  pointing towards **M** (westward).

At the start of the interval shown in Fig. 5 ISEE was in the tenuous plasma sheet plasma (also see Scokpe et al., 1981). The boundary layer (BL) plasma of magnetosheath origin was encountered first at  $\sim 04:59$  UT, and is identified by the sharp increase in density and bulk flow speed. The magnetopause, indicated by the sharp reversal in  $B_L$  was crossed only once at  $\sim 05:50$  UT. During the intervening 51 min, nine (numbered from left to right) quasi-periodic "pulses" of boundary layer plasma were observed, each having a distinctive saw-tooth or square-wave density profile. The latter feature, and the density profile for pulse (9), are clearer in the higher time resolution 2D density data published in Scokpe et al. (1981). This publication also shows that the bulk flow in the pulses was generally directed tailwards.

Turning attention to the lower panels in Fig. 5, and in particular to the  $\alpha_{LM}$  plot, it is clear that the BL pulses are accompanied by well defined rotations in the magnetic field. The principal field perturbations occur in the **M** or east-west component. During pulses (1) to (6)  $B_M$  increases sharply and the field, as indicated in the  $\alpha_{LM}$  plot, rotates tailwards by  $\sim 30^\circ$ . In the Hones et al. (1982) BL field perturbation terminology, this field tilting would be described as "reverse draping". While a consistent  $B_M$  deflection is not observed in pulse (7), pulses (8) and (9), closest to the magnetopause, show  $B_M$  tilts directed opposite to those seen in the earlier pulses. The field now rotates sunward by  $\sim 30^\circ$  relative to the ambient field direction at 04:55 UT. This deflection is towards the magnetosheath field direction, as expected for field pulling if the magnetopause is open and the sheath flow is sub-Alfvénic (see Fig. 3).

Another feature which distinguishes the pulses closest to the magnetopause is their larger plasma flow speeds. The bulk flow is enhanced by 50–100 km s<sup>-1</sup> relative to the background magnetosheath level and to flow speeds in pulses (1) to (6). A similar speed increase also occurred in the magnetosheath associated with the prominent flux transfer event marked by the vertical dashed lines at  $\sim 06:04$  UT. Inside the FTE the field clearly tilts towards the ambient magnetospheric direction. One should also note that  $B_N$  deflections similar to those which accompany this magnetosheath FTE, occur in the vicinity of pulses (5) to (9). Furthermore, the duration of the BL pulses is very similar to that reported typically for magnetosheath FTEs of 1–2 min. In view of these similarities it is difficult not to believe that, at least, pulses (8) and (9) are on open tubes and are closely related to magnetosheath FTEs (see also Paschmann et al., 1982). This conclusion is supported by the Lindau energetic particle data (kindly supplied by P.W. Daly) which show strong streaming of the energetic ( $>25$  keV) ions antiparallel to **B** inside pulses (8) and (9), and in the magnetosheath FTE, thus indicating open tubes connected to the Earth's northern hemisphere. Furthermore, all the boundary layer pulse flux tubes are nearly empty of energetic ( $>20$  keV) electrons.

Accepting that pulses (8) and (9) correspond to the magnetospheric ends of open FTE fluxtubes, the question arises as to the origin of the earlier pulses where the field tilts the other way and the flow speeds are lower. In theory

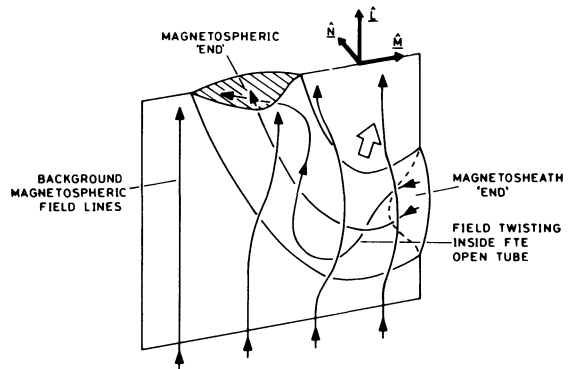


Fig. 6. Sketch of a tailward and northward propagating FTE observed from inside the magnetosphere. The field within the open tube is shown twisted as implied by the observed  $B_N$  perturbations. It is suggested that these "internal" FTEs may correspond to the BL "pulses" reported, for example, by Scokpe et al. (1981)

these features could arise from diffusive plasma entry at northern high latitudes, as Hones et al. (1982) discuss. However, this would mean different source mechanisms for the early and late BL pulses, when it is very tempting to see the data as a connected sequence of pulse encounters across the BL region.

A possible explanation for the change in character of field tilting as the magnetopause is approached is embodied in Fig. 6, which illustrates how one might visualise a BL FTE observed from inside the magnetosphere. The magnetosphere and magnetosheath "ends" of the open tube are indicated in the sketch; a satellite outside the magnetopause would see the latter as a magnetosheath FTE. Field tension, shown by the open arrow, causes the reconnected BL flux tube to tilt sunwards relative to the background magnetospheric field, thus producing a negative  $B_M$  perturbation. As the reconnected tube contracts northward along the magnetopause it distorts the ambient field and thus gives rise to the bipolar positive to negative  $B_N$  perturbation discussed above. However, as Paschmann et al. (1982) and Cowley (1982) independently point out, this draping effect can not be the sole cause of the  $B_N$  signal, since there would be then zero  $B_N$  field inside the open tube, whereas the observed signals resemble sinusoids and certainly do possess an interior  $B_N$  component. This implies that the field lines are twisted about the FTE flux tube axis due to a field-aligned current flowing along the open tube. The field twisting is indicated in Fig. 6 by the wavy field line.

A field-aligned current can explain why the field tilting in the earlier boundary layer pulses was opposite to that seen in the pulses closest to the magnetopause. Figure 6 shows that if the twist in the interior field becomes large enough, tailward tilting of the field could occur in the flux-tube section furthest from the magnetopause. Evidence for strong spatial structure inside the 6 November 1977 BL pulses is indicated by the simultaneous observation of oppositely directed field tilts at ISEE 1 and 2 for a brief interval during pulse (9) (data not shown). Apart from this instance, however, the ISEE 1 and 2 plasma and field data are very similar throughout the BL passage, indicating that satellite separations much greater than the  $\sim 500$  km existing at the time are generally necessary to examine the spatial structure inside BL pulses. A study of dual satellite

data for the autumn and early winter of 1978, when ISEE separations near the magnetopause much exceeded 500 km, should be productive. A further point favouring the notion of field twisting in FTEs is that reversals in the direction of field tilt, as in the 6 November 1977 BL pulses, are observed also in magnetosheath FTEs. A clear example is seen in Fig. 15 of Elphic and Russell (1979) (also see Fig. 2 of Paschmann et al., 1982).

Having discussed the physical properties of FTEs in the magnetosheath and boundary layer, let us now consider further the observation noted above, that during the 8 September 1978 boundary crossing ISEE 1 sees an FTE while ISEE 2, located approximately 1,500 km nearer the magnetopause, apparently observes quasi-steady reconnection flow. Referring to Fig. 2 and the interval in question at  $\sim 00:38.30$  UT, the FTE is identified with the prominent  $B_N$  perturbation and is associated with a pulse of accelerated boundary layer plasma a decrease in the energetic ( $> 8$  keV) ion density and a dropout in the flux of energetic ( $> 20$  keV) electrons (see Fig. 8 of Scholer et al., 1982 for the latter information). These properties coupled with a deflection in field direction by  $\sim 15^\circ$  away from the magnetosheath field direction and an in/out plasma flow component normal to the magnetopause, are similar to those which accompanied pulses (1) to (6) in the November 1977 boundary layer crossing (Sckopke et al., 1981). Although the  $B_N$  perturbation is not of the "classic" FTE type, a bipolar  $B_N$  signal is observed when the data are plotted using either the Fairfield (1971) model magnetopause normal or a tangential discontinuity normal. It is interesting to note that ISEE 2, as also did ISEE 1 later, observed FTE-like signals before encountering the region of quasi-steady reconnection flow. For example, weak FTE signatures exist in the ISEE 2  $B_N$  record at  $\sim 00:25$  and  $\sim 00:28$  UT, each associated with a pulse of magnetosheath plasma.

These facts raise the question as to whether a sharp distinction can really be drawn between FTEs and the type of event discussed by Sonnerup et al. (1981) and referred to as "quasi-steady" reconnection. Cowley (1982) suggests that the two phenomena may simply represent different regions on a continuous spectrum of space and time scales. If variations occur in the rate at which reconnection erodes magnetic flux, one might expect bulges containing extra flux to form. As these bulges contract polewards in the reconnection flow they would give rise to FTE signals in the overlying magnetosphere and magnetosheath field regions but not in the central open field line region between. The dashed lines in Fig. 1 indicate schematically the distortion to the steady state reconnection field pattern envisaged due to the change in flux tube cross-section accompanying a pulse of increased eroded flux. Although Fig. 1 is drawn for antiparallel internal and external magnetic fields, similar field distortions would occur in cases where the fields are not strictly antiparallel. In this context, the ISEE satellite positions in Fig. 1 apply for the interval at 00:38 UT on 8 September 1978. Before and after the field bulge encounter, ISEE 1 is located earthward of the inner separatrix  $S_I$ , but crosses it as the bulge is passing. The plasma flow at ISEE 1 is dominated largely by an in/out motion associated with the bulge passage, but it is curious why the accelerated flows at ISEE 2 are substantially larger (see Fig. 2). While the interpretation outlined above is tentative, it provides a framework for empirical study.

## Reconnection or Diffusion: Which Process Dominates?

This review has highlighted the recent experimental evidence for magnetic field reconnection at the dayside magnetopause. Although some readers may disagree with this choice of emphasis, the ISEE satellite results have pointed up the significance of reconnection. This in situ evidence should be added to the large mass of indirect evidence accumulated during the past twenty years (Cowley, 1982). By its very nature a diffusive coupling process can not explain the accelerated plasma flows which a short scan of the ISEE Los Alamos/Garching plasma data shows are present commonly in the boundary layer.

It should be emphasized, however, that boundary layers also exist when the magnetosheath magnetic field is directed northward and there is no evidence either for quasi-steady or FTE reconnection. Clear examples of such BLs, which appear thick, unstructured and lacking in plasma acceleration, are seen in Fig. 1 of Russell and Elphic (1978) (also see Fig. 1 of Paschmann et al. 1978) and in Fig. 4 of Eastman et al. (submitted). The occurrence of boundary layers when the IMF is northward indicates that reconnection is not the only solar wind/magnetosphere coupling mechanism. For example, Reiff et al. (1981), in a study comparing the cross polar cap potential drop (typically 50–100 kV), measured by low altitude satellites with solar wind parameters, identify a background value of  $\sim 30$  kV that is independent of IMF orientation. They suggest that this voltage could be associated with a mechanism other than reconnection, although it may include a residual potential arising from earlier intervals when IMF  $B_Z$  was southward, due to the inertia of the coupled atmosphere-ionosphere-magnetosphere convection system. To reduce the effect of such inertial lag, Wygant et al. (submitted) studied polar cap potentials following prolonged periods ( $\sim 3$  h) of northward IMF. They found that the voltage then declined to about 20 kV, a value which is comparable to the maximum in situ estimate for the convection potential generated by tailward closed flux tube transport in the low latitude boundary layer. For example, let us consider the 6 November 1977 boundary layer passage shown in Fig. 5. If, as Sckopke et al. (1981) favour, these boundary layer observations are on closed field lines, the typical pulse bulk speed ( $\sim 150$  km s $^{-1}$ ), field strength ( $\sim 40$  nT) and estimated layer width ( $\sim 6,000$  km), and the fact that such flows are present for roughly a third of the time, give a voltage of  $\sim 12$  kV, or  $\sim 24$  kV for dawn and dusk BLs combined. However, if as suggested here these BL flows are mainly on open field lines, then  $\sim 24$  kV is clearly an upper limit for the convection potential generated by non-reconnection processes. Similarly the combined voltage values of  $\sim 5$ –25 kV suggested by the flank BL observations reported by Eastman (1979), Eastman and Hones (1979) and Eastman et al. (submitted), also should be considered upper limits for the voltage arising from closed BL flux tube motion. Thus, as observations at both low and high altitudes indicate that non-reconnection processes provide only a small, though possibly significant, fraction of the total magnetospheric voltage, diffusion at the magnetopause may be, at best, only of moderate importance in driving magnetospheric flows (also see Cowley (1982) for a detailed discussion of this topic).

In contrast, quasi-steady and FTE reconnection can easily give rise to voltages of the correct order for driving

magnetospheric convection. The preliminary evidence available so far (Sonnerup et al., 1981) indicates that quasi-steady reconnection can occur over a broad region of the dayside magnetopause, covering roughly four hours of local time either side of noon (a linear dimension of  $\sim 25 R_E$ ). Using the inferred tangential electric field for the 8 September 1978 reconnection event of  $\sim 1 \text{ mV m}^{-1}$ , gives a total voltage across this region of  $\sim 150\text{--}200 \text{ kV}$ , which is a factor of 2–3 greater than typical cross-magnetosphere values. Although this voltage is an upper limit, since the instantaneous longitudinal extent of the reconnection region may be restricted, the value is compatible with reconnection playing a major role in magnetospheric dynamics.

The transfer of magnetic flux associated with FTEs also contributes a significant voltage. Russell and Elphic (1978) estimate the magnetic flux eroded by a single FTE to lie in the range  $2 \times 10^6$  to  $3 \times 10^7 \text{ Wb}$ . From the limited data published so far, FTEs recur typically on a 5–20 min time-scale, so if  $\sim 10^7 \text{ Wb}$  is transferred every  $\sim 10$  min, the mean voltage associated with the process is  $\sim 20 \text{ kV}$ . If the local time extent of an FTE is restricted, this value will be a lower limit, because not every FTE may be seen at a particular magnetopause location. In summary, the fact that total magnetospheric voltages of  $\sim 50\text{--}100 \text{ kV}$  may be obtained readily from the observed reconnection processes but not from diffusively driven closed flux tube motion in the LLBL, supports the view that reconnection is the dominant process in coupling the solar wind to the magnetosphere and in driving magnetospheric convection.

### Conclusions and Key Remaining Questions

The major factor which limited magnetopause studies prior to ISEE was the time resolution and 2D nature of satellite plasma instrumentation. The high time resolution 3D fast plasma experiments on ISEE have provided the first convincing in situ evidence for quasi-steady (or large-scale) reconnection. More commonly though, reconnection seems to occur as a small-scale or localised process in the form of flux transfer events (FTEs), which can have either a normal or a reverse polarity, depending upon whether the net motion of the open flux tube is north or south. The discovery of FTEs on open tubes within the magnetosphere, and the fact that most of the quasi-steady reconnection events published to date have clear FTEs in close association, (in one instance ISEE 1 observes an FTE simultaneous to ISEE 2 apparently seeing quasi-steady reconnection), is additional evidence that FTEs are reconnection phenomena. These recent findings strengthen the view that reconnection is the dominant mechanism for coupling solar wind mass and momentum to the magnetosphere.

An important remaining question concerns the IMF conditions under which reconnection takes place, and in particular, the factor determining whether it occurs as a quasi-steady or FTE process, if indeed a sharp distinction exists at all between these two phenomena. The only controlling parameter apparent so far is the dependence on IMF  $B_z$ : all the reconnection events and FTEs published to date occur when IMF  $B_z$  is near to zero or negative. A topic also requiring further investigation is the location of the reconnection region: is it situated near the equator as Dungey (1961) predicted and as all the in situ evidence available so far largely supports, or does it also occur in the cusps as Haerendel et al. (1978) suggested? One also

wishes to determine the source of the field-aligned currents which accompany FTEs, and to investigate where these currents close in the magnetosphere. Are they, for example, compatible in direction and magnitude with the low altitude Region 1 field-aligned currents as Cowley (1982) suggests? These are some of the present questions in a fascinating and rapidly progressing subject.

*Acknowledgements.* This study was performed during the course of a U.K. S.E.R.C. postdoctoral research award. Special thanks are due to D.J. Southwood and S.W.H. Cowley for numerous helpful and generous discussions. It is a pleasure also to thank G. Paschmann (MPE) and C.T. Russell (UCLA) for allowing their data to be used in this work.

### References

- Akasofu, S.-I., Hones, E.W., Jr., Bame, S.J., Asbridge, J.R., Lui, A.T.Y.: Magnetotail and boundary layer plasmas at a geocentric distance of  $\sim 18 R_E$ : Vela 5 and 6 observations. *J. Geophys. Res.* **78**, 7257–7274, 1973
- Axford, W.I., Hines, C.O.: A unifying theory of high-latitude geophysical phenomena and geomagnetic storms. *Can. J. Phys.* **39**, 1433–1464, 1961
- Berchem, J., Russell, C.T.: A survey of flux transfer events on the dayside magnetopause. Abstract booklet, COSPAR meeting, Ottawa, Canada, p. 219, 1982
- Cowley, S.W.H.: The formation and properties of boundary layers downstream from neutral lines in an open magnetosphere. In: Magnetospheric boundary layers, Rep. ESA SP-148, B. Battrick, ed., pp. 333–342. Noordwijk, Netherlands: ESA 1979
- Cowley, S.W.H.: Plasma populations in a simple open model magnetosphere. *Space Sci. Rev.* **26**, 217–275, 1980
- Cowley, S.W.H.: The causes of convection in the Earth's magnetosphere: a review of developments during the IMS. *Rev. Geophys. Space Phys.* **20**, 531–565, 1982
- Daly, P.W., Keppler, E.: Observation of a flux transfer event on the earthward side of the magnetopause. *Planet. Space Sci.* **30**, 331–338, 1982
- Daly, P.W., Fritz, T.A.: Trapped electron distributions on open magnetic field lines. *J. Geophys. Res.* **87**, 6081–6088, 1982
- Dungey, J.W.: Interplanetary field and the auroral zones. *Phys. Rev. Lett.* **6**, 47–48, 1961
- Eastman, T.E.: The plasma boundary layer and magnetopause layer of the Earth's magnetosphere. Ph.D. thesis, Los Alamos Sci. Lab., Los Alamos, New Mexico, 1979
- Eastman, T.E., Hones, E.W., Jr.: Characteristics of the magnetospheric boundary layer and magnetopause layer, as observed by IMP 6. *J. Geophys. Res.* **84**, 2019–2028, 1979
- Eastman, T.E., Frank, L.A.: Observations of high speed plasma flow near the Earth's magnetopause: evidence for reconnection? *J. Geophys. Res.* **87**, 2187–2202, 1982
- Eastman, T.E., Hones, E.W., Jr., Bame, S.J., Asbridge, J.R.: The magnetospheric boundary layer: site of plasma, momentum and energy transfer from the magnetosheath into the magnetosphere. *Geophys. Res. Lett.* **3**, 685–688, 1976
- Eastman, T.E., Popielawska, B., Frank, L.A.: Three-dimensional plasma observations near the outer magnetospheric boundary. *J. Geophys. Res.* (submitted)
- Elphic, R.C., Russell, C.T.: ISEE-1 and -2 observations of the magnetopause. In: Magnetospheric boundary layers, Rep. ESA SP-148, B. Battrick, ed., pp. 43–50. Noordwijk, Netherlands: ESA 1979
- Fahleson, U.V., Fälthammar, C.-G., Lindqvist, P.-A., Mozer, F.S., Torbert, R.B., Gonfalone, A., Pedersen, A.: Quasistatic electric fields observed during a number of magnetopause crossings by ISEE-1. In: Magnetospheric boundary layers, Rep. ESA SP-148, B. Battrick, ed., pp. 51–65. Noordwijk, Netherlands: ESA 1979
- Fairfield, D.H.: Average and unusual locations of the Earth's mag-

- netopause and bow shock. *J. Geophys. Res.* **76**, 6700–6716, 1971
- Gosling, J.T., Asbridge, J.R., Bame, S.J., Feldman, W.C., Paschmann, G., Sckopke, N., Russell, C.T.: Evidence for quasi-stationary reconnection at the dayside magnetopause. *J. Geophys. Res.* **87**, 2147–2158, 1982
- Haerendel, G., Paschmann, G., Sckopke, N., Rosenbauer, H., Hedgcock, P.C.: The frontside boundary layer and the problem of reconnection. *J. Geophys. Res.* **83**, 3195–3216, 1978
- Hones, E.W., Jr., Asbridge, J.R., Bame, S.J., Montgomery, M.D., Singer, S., Akasofu, S.-I.: Measurements of magnetotail plasma flow made with VELA 4B. *J. Geophys. Res.* **77**, 5503–5522, 1972
- Hones, E.W., Jr., Sonnerup, B.U.Ö., Bame, S.J., Paschmann, G., Russell, C.T.: “Reverse draping” of magnetic field lines in the boundary layer. *Geophys. Res. Lett.* **9**, 523–526, 1982
- Lemaire, J., Roth, M.: Penetration of solar wind plasma elements into the magnetosphere. *J. Atmos. Terr. Phys.* **40**, 331–335, 1978
- Levy, R.H., Petschek, H.E., Siscoe, G.L.: Aerodynamic aspects of the magnetospheric flow. *Am. Inst. Aeronaut. Astronaut. J.* **2**, 2065–2076, 1964
- Mozer, F.S., Torbert, R.B., Fahleson, U.V., Fälthammar, C.-G., Gonfalone, A., Pedersen, A.: Electric field measurements in the solar wind, bow shock, magnetosheath, magnetopause and magnetosphere. *Space Sci. Rev.* **22**, 791–804, 1978
- Mozer, F.S., Torbert, R.B., Fahleson, U.V., Fälthammar, C.-G., Gonfalone, A., Pedersen, A., Russell, C.T.: Direct observation of a tangential electric field component at the magnetopause. *Geophys. Res. Lett.* **6**, 305–308, 1979
- Paschmann, G., Sckopke, N., Haerendel, G., Papamastorakis, I., Bame, S.J., Asbridge, J.R., Gosling, J.T., Hones, E.W., Jr., Tech, E.R.: ISEE plasma observations near the subsolar magnetopause. *Space Sci. Rev.* **22**, 717–737, 1978
- Paschmann, G., Sonnerup, B.U.Ö., Papamastorakis, I., Sckopke, N., Haerendel, G., Bame, S.J., Asbridge, J.R., Gosling, J.T., Russell, C.T., Elphic, R.C.: Plasma acceleration at the Earth’s magnetopause: evidence for reconnection. *Nature* **282**, 243–246, 1979
- Paschmann, G., Haerendel, G., Papamastorakis, I., Sckopke, N., Bame, S.J., Gosling, J.T., Russell, C.T.: Plasma and magnetic field characteristics of magnetic flux transfer events. *J. Geophys. Res.* **87**, 2159–2168, 1982
- Petschek, H.E.: Magnetic field annihilation. AAS-NASA symposium on the physics of solar flares. *NASA SP-50*, 425–439, 1964
- Reiff, P.H., Spiro, R.W., Hill, T.W.: Dependence of polar cap potential drop on interplanetary parameters. *J. Geophys. Res.* **86**, 7639–7648, 1981
- Rijnbeek, R.P., Cowley, S.W.H., Southwood, D.J., Russell, C.T.: Observations of “reverse polarity” flux transfer events at the Earth’s dayside magnetopause. *Nature* **300**, 23–26, 1982
- Russell, C.T., Elphic, R.C.: Initial ISEE magnetometer results: magnetopause observations. *Space Sci. Rev.* **22**, 681–715, 1978
- Russell, C.T., Elphic, R.C.: ISEE observations of flux transfer events at the dayside magnetopause. *Geophys. Res. Lett.* **6**, 33–36, 1979
- Scholer, M., Ipavich, F.M., Gloeckler, G., Hovestadt, D., Klecker, B.: Leakage of magnetospheric ions into the magnetosheath along reconnected field lines at the dayside magnetopause. *J. Geophys. Res.* **86**, 1299–1304, 1981
- Scholer, M., Daly, P.W., Paschmann, G., Fritz, T.A.: Field line topology determined by energetic particles during a possible magnetopause reconnection event. *J. Geophys. Res.* **87**, 6073–6080, 1982
- Sckopke, N., Paschmann, G., Haerendel, G., Sonnerup, B.U.Ö., Bame, S.J., Forbes, T.G., Hones, E.W., Jr., Russell, C.T.: Structure of the low latitude boundary layer. *J. Geophys. Res.* **86**, 2099–2110, 1981
- Sonnerup, B.U.Ö., Paschmann, G., Papamastorakis, I., Sckopke, N., Haerendel, G., Bame, S.J., Asbridge, J.R., Gosling, J.T., Russell, C.T.: Evidence for magnetic field reconnection at the Earth’s magnetopause. *J. Geophys. Res.* **86**, 10049–10067, 1981
- Southwood, D.J.: Wave generation in the terrestrial magnetosphere. *Space Sci. Rev.* (in press)
- Wygant, J.R., Torbert, R.B., Mozer, F.S.: Comparison of S3-3 polar cap potential drops with the interplanetary magnetic field and models of magnetopause reconnection. *J. Geophys. Res.* (submitted)

Received November 15, 1982; Revised version January 19, 1983  
Accepted January 27, 1983

# Motion of Flux Transfer Events on 10 November 1977 Determined by Energetic Particles on ISEE 2\*

P.W. Daly and E. Keppler

Max-Planck-Institut für Aeronomie, D-3411 Katlenburg-Lindau 3, Federal Republic of Germany

**Abstract.** The medium energy particle spectrometer on board ISEE 2 has been used to measure the orientation and motion of the flux transfer events (FTEs) seen at the inbound magnetopause crossing on 10 November 1977. The method used is a simple version of the remote sensing technique using azimuthal asymmetries of ion intensities, that has previously been used to sound the magnetopause. During these events, the particle intensity was high enough that the secondary detectors, looking out of the ecliptic plane, could also be used, in spite of their much lower geometry factors. Only ions with pitch angles near  $90^\circ$  were employed, which eliminates some of the uncertainties of the method. The FTEs are seen to approach the spacecraft from the magnetopause side, with a northward component of velocity, and to retreat towards the magnetopause, also with a northward component. This is consistent with the picture of FTEs as isolated flux tubes in the magnetosheath connected to the magnetosphere which then move poleward to release magnetic tension. The northward motion has earlier been deduced only from the magnetic signature and is observed here directly for the first time. The speed of the FTEs is of the order of 100 km/s, and the size is of the order of an earth radius.

**Key words:** Magnetopause – Flux transfer event – Energetic particles – Remote sensing

## Introduction

Flux transfer events (FTEs) were discovered by Russell and Elphic (1979) in the magnetic data from the ISEE spacecraft during dayside magnetopause crossings. They were first observed in the magnetosheath, near the magnetopause, and were interpreted from the magnetic signature as a localised flux tube connected to the magnetosphere, being pulled poleward (northward in these cases) by the magnetic tension of the bent field line. That FTEs were indeed interconnected to the magnetosheath was confirmed by Daly et al. (1981) who showed that they were accompanied by streaming magnetospheric ions. The direction of streaming indicated connection to the northern hemisphere, consistent with the deduced northward motion. FTEs have since been dis-

covered inside the magnetopause (Daly and Keppler, 1982) and with so-called 'reverse' magnetic signatures, indicative of southward motion (Rijnbeek et al., 1982). Further energetic particle data have been presented by Scholer et al. (1982), as well as plasma and magnetic data (Paschmann et al., 1982), and plasma wave data (Anderson et al., 1982). Modelling of the events by tracing ion trajectories through the magnetopause has been carried out by Speiser et al. (1981) and by Speiser and Williams (1982).

In this work two FTEs from the 10 November 1977 inbound magnetopause crossing are analysed to determine the orientation and motion of the energetic particle boundaries. The method used is that of remote sensing by means of azimuthal asymmetries in the energetic ion intensities. This technique, based on the finite gyro-radii of the particles, was introduced by Kaufman and Konradi (1969) to sound the magnetopause and was first employed using the particle spectrometer on board ISEE 1 by Williams (1979). Further work has been published by Williams et al. (1979) and Williams (1980). Fritz and Fahrenstiel (1982) and Fritz et al. (1982) have used the ISEE 2 instrument to probe the magnetopause, while Andrews et al. (1981) have used the same device to measure plasma sheet motions. Daly (1982) has presented a critique of how the method should be employed at different types of boundaries, using more than one gyro-radius. These criticisms do not apply to the present work, since only ions at pitch angle  $90^\circ$ , and thus at only one gyro-radius, will be analysed.

## Instrumentation

The medium energy particle spectrometer on board the ISEE spacecraft is described elsewhere (Williams et al., 1978), but the main points will be summarised here. The primary instrument on ISEE 2 (WAPS, Wide Angle Particle Spectrometer) consists of a silicon surface barrier detector with a geometry factor of  $0.01 \text{ cm}^2 \text{ sr}$  to detect ions, looking at a direction  $82^\circ$  to the spin axis. A magnetic field sweeps electrons into separate detectors. The energy threshold for protons is 25 keV, for electrons 20 keV. Four secondary sets of detectors with lower geometry factors (factor of 80) are mounted at  $10^\circ$ ,  $44^\circ$ ,  $136^\circ$ , and  $170^\circ$  to the spin axis. These detectors are designated NAPS (Narrow Angle Particle Spectrometer) 1, 2, 3, and 4 respectively. Normally the NAPS detectors have too low a count rate to be useful at the outer magnetosphere, but since the events to be discussed here have unusually high intensities, measurements from these detectors will be included in this analysis.

\* Based on a paper given at the Symposium on Plasma and Energetic Particles in the Magnetosphere, EGS Meeting, 23–27 August 1982, Leeds, U.K.

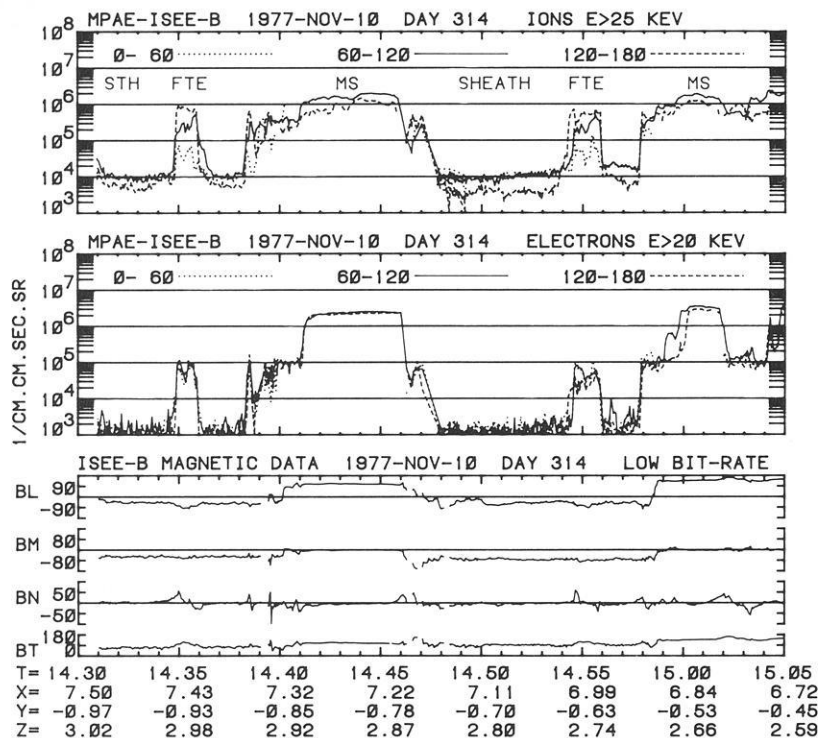


**Fig. 1.** Ion and electron intensities, in three pitch angle ranges, from the WAPS detector on ISEE 2, plotted against time from UT 1430 to 1505 on 10 November 1977, during an inbound pass of the magnetopause. Also included are the magnetometer data in the boundary normal coordinate system (LMN). *BT* is the magnitude of the magnetic field; *T* is the universal time; *X*, *Y*, *Z* are the satellite's GSE coordinates in earth radii

Directional information is obtained by sorting the count rates during one spin (3 s) into sectors, the number of which depends on data format and bit-rate. The number of sectors for the WAPS during the events in this paper is 8. This directional resolution within the spin plane (which is also the plane of the ecliptic) is supplemented by use of the NAPS detectors looking out of the spin plane. The NAPS detectors are not sectorized at this time, that is, they yield only one measurement averaged over the entire spin.

## Data

Figure 1 shows ion and electron data on 10 November 1977 from UT 1430 to 1505, during an inbound pass of the ISEE 2 satellite. Also shown are the magnetic field data from the U.C.L.A. magnetometers, plotted in the boundary normal coordinate system (LMN) of Russell and Elphic (1979). The spacecraft is in the magnetosheath until UT 1440 (*BL* < 0, marked *STH*), in the magnetosphere until 1447 (*BL* > 0, marked *MS*), is again in the magnetosheath until 1459, when it enters the magnetosphere for the final time. The particle data are from the WAPS detector only, and are divided into 3 pitch angle ranges of width 60° each, plotted as dotted, solid, and dashed lines. The FTEs at UT 1435 and 1455 have the characteristic magnetic signature, where the component normal to the magnetopause, *BN*, goes first positive then negative before returning to zero. There are several other FTEs during this time interval, including one inside the magnetosphere at UT 1502, but only the first two mentioned will be treated in this work. These two events are accompanied by increases in the ion and electron intensities. The ion intensities are close to their magnetospheric values and are greatest in the direction anti-parallel to the magnetic field (dashed line highest in upper panel of Fig. 1). The electrons are fairly isotropic and of much lower intensity than in the magnetosphere. They presumably escape from the opened field line much more

quickly than the ions, leaving an isotropic background population.

## Remote Sensing

What is not shown in Fig. 1 are the azimuthal asymmetries about the magnetic field. That is, at two different directions making the same angle to the magnetic field there can be different intensities observed. This effect is caused by the particle's finite gyro-radius plus a density gradient. As explained by Daly (1982), the particle intensity should be a function only of pitch angle and position of the gyro-center. Particles detected at the spacecraft at constant pitch angle but different gyro-phase angles have different gyro-center locations and can therefore have different intensities. For this work we consider the intensity to be a step function, to be either high or low. Different sectors can switch at different times, allowing us to determine the orientation, and thus direction of motion, of the particle boundary of the FTE.

The direction of the magnetic field in the magnetosheath is essentially along the geocentric solar ecliptic (GSE) *Y* axis, with a small inclination (17°) towards  $-Z$  and  $+X$ . Thus sector 1 of the ISEE 2 WAPS instrument, which looks towards  $+X$ , sector 5, which looks towards  $-X$ , the NAPS 1 detector, which looks along  $+Z$ , and NAPS 4, which looks along  $-Z$ , are all close to 90° to the field line. The intensities of the ions in these four directions are shown in Figs. 2 and 4, for 5 min intervals covering the FTEs at UT 1435 and 1455, respectively. The various curves have been shifted vertically to separate them, and have been labelled with arrows according to the flow direction of the corresponding particles in the GSE *XZ* plane. With *Z* upwards and *X* to the right, then NAPS 4 detects upward moving particles, WAPS sector 1 observes those moving to the left, WAPS sector 5 those to the right, and NAPS 1 sees those going downwards.

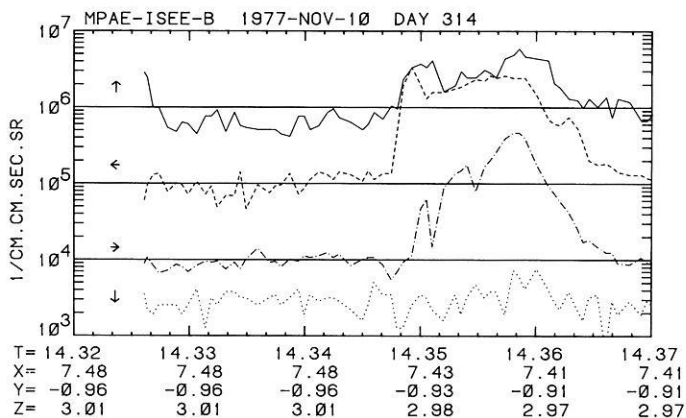


**Fig. 2.** Ion intensities in four directional channels which look perpendicular to the magnetic field, plotted against time for 5 minutes containing the FTE at UT 1435. The channels are shifted vertically to separate them

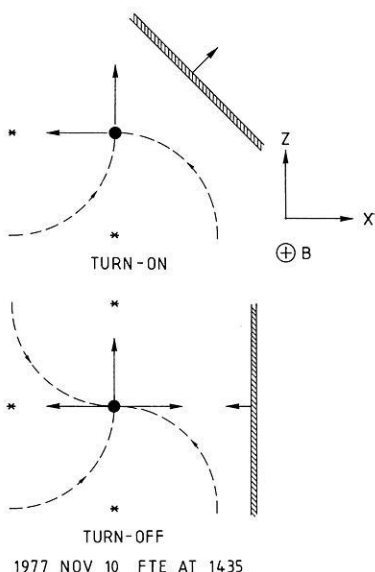


**Fig. 3.** Representation in the GSE  $XZ$  plane of those channels which have high intensities at the beginning and end of the FTE at UT 1435, showing also the deduced orientation of the particle boundary

From Fig. 2 it can be seen that for the FTE at UT 1435 the upward and leftward moving ions switch from low to high before the those in the other directions. At the end of the event the upward particles remain high longer, while the left and rightward particles decrease together. These two situations are illustrated in the  $XZ$  plane in Fig. 3. In the upper part of the diagram the beginning of the FTE is shown, with ions moving upwards and to the left. A quarter of each gyro-orbit is plotted as a dashed line, and the corresponding gyro-centers are marked with a star. The event turns on with particles whose gyro-centers are located below and to the left of the spacecraft; that is, the particle boundary must be oriented from lower right to upper left, as indicated by the shaded bar, and is moving towards the upper right. At the end of the event, the lower part of Fig. 3, the upward moving particles, those with their gyro-center to the left, persist longest, and those moving left and right, with centers below and above, are lost together. The boundary is vertical, as shown, and moves to the left.

A similar analysis can be performed for the FTE at

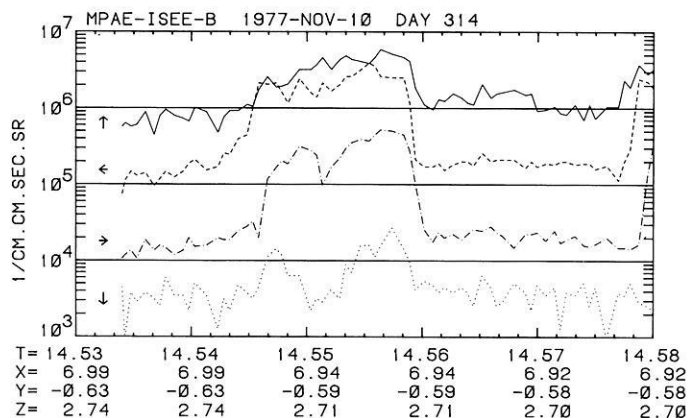


**Fig. 4.** The same as Fig. 2, but for the 5 minute period containing the FTE at UT 1455

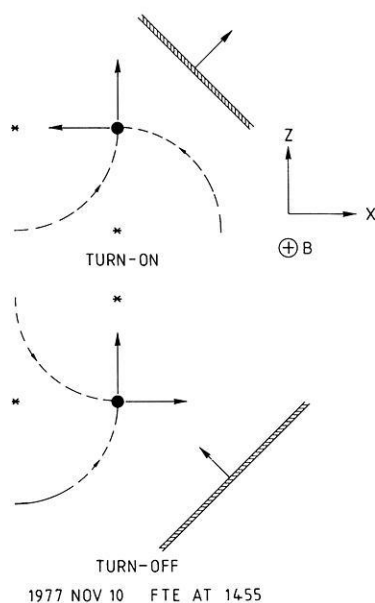


**Fig. 5.** The same as Fig. 3, but for the FTE at UT 1455

UT 1455. Figure 4 shows the plot against time of the intensities of the four directions perpendicular to the magnetic field. Again those moving upwards and to the left turn on before the others, and the upward moving particles turn off last. This time, however, the rightward moving ions tend to last one spin longer than the leftward ones. The representation in the  $XZ$  plane is given in Fig. 5. The upper part is the same as in Fig. 3, but the lower part, the end of the event, has been drawn to reflect the asymmetry between the rightward and leftward moving ions: the boundary is oriented from lower left to upper right and moves to the upper left. The inclination from vertical is perhaps exaggerated.

## Discussion

The four directional channels of the ISEE 2 ion detector which are perpendicular to the magnetic field see the onset and end of the flux transfer events at different times, allowing one to determine the orientation of the particle bound-

ary. The determination is very rough, to within half a quadrant in the plane normal to the field, in this case the GSE  $XZ$  plane. In both cases the event begins with the particle boundary moving along the positive  $X$  and  $Z$  axes, that is coming from the magnetopause and from the south. Both events end with the boundary moving along the negative  $X$  axis (towards the magnetopause), and in the second case at 1455, also along the positive  $Z$  axis. The  $L$  axis of the LMN coordinate system (Russell and Elphic, 1979), which is identified as north, is inclined  $21^\circ$  to the left of the  $Z$  axis. Thus all the boundary motions in Figs. 3 and 5 have a northward component.

Paschmann et al. (1982) have classified both these FTEs as their type A, meaning the field is more southwards during them than in the magnetosheath, contrary to the predictions of the simple picture. Their explanation is that these are shallow penetrations of the events, seeing only the draping of the ambient field outside the reconnected flux tube itself. They point out that this is not consistent with the observation of magnetospheric particles unless these can leak outside. Such a leakage is postulated for the remote sensing method, but such particles must exhibit gyro-phase asymmetries. That particle distributions without such asymmetries are observed at some time during each FTE demonstrates that the reconnected flux tube must have been encountered. For the FTE at 1435, this encounter is about 20 s long, whereas for the one at 1455 it is 60 s. We conclude that the reconnected flux tube was fully penetrated, at least briefly, and that the magnetic field in these events is more complicated than that derived from simple pictures. Certainly the field aligned current which is required to explain the normal component signature (Paschmann et al., 1982; Rijnbeek et al., 1982) would also produce a southward component even fully inside the FTE.

An estimate of the velocity of the events can be made from the size of the gyro-radius and the time of passage of the particle boundary. The average energy of the ions (assuming protons) in the  $>25$  keV integral channel is 37 keV (spectral index during the FTEs is 4, Daly et al., 1981) and the field is 100 nT, which makes the gyro-radius 275 km. From Figs. 2 and 4 one sees that the particle boundary takes roughly 10 s to cross all the channels, a distance of two gyro-radii. The velocity is then of the order of 55 km/s. This however is the velocity along the normal of the boundary surface. If the FTE is moving in the plane of the magnetopause and the particle boundary is inclined  $45^\circ$  to the real direction of motion, then the velocity of the FTE is  $55/\sin(45) = 78$  km/s. The duration of the FTE is about 2 min, which would mean its physical size is 9,400 km. These calculations are order of magnitude only.

## Summary and Conclusions

The particle boundaries of the flux transfer events are seen to sweep over the spacecraft with a velocity of the order of 100 km/s, from the magnetopause and the south, and to retreat towards the magnetopause and to the north. The size of the event is of the order of an earth radius. The original picture of Russell and Elphic (1979), in which FTEs were bloated flux tubes moving northward on the outer surface of the magnetopause, is confirmed by this direct observation of the motion of the associated particle boundaries. This analysis is made possible for the events at the crossing of 10 November 1977 because the ion intensities

were high enough for the NAPS detectors to be useful, and because the magnetic field was so oriented that four directional sectors could be found looking perpendicular to it.

*Acknowledgements.* We wish to thank C.T. Russell of U.C.L.A. for kindly providing the magnetometer data. The ISEE particle spectrometer has been constructed with the support of the Max-Planck-Gesellschaft zur Förderung der Wissenschaft e.V. and of the Bundesministerium für Forschung und Technologie under grant RV-14-B-30/73.

## References

- Anderson, R.R., Harvey, C.C., Hoppe, M.M., Tsurutani, B.T., Eastman, T.E., Etcheto, J.: Plasma waves near the magnetopause. *J. Geophys. Res.* **87**, 2087–2107, 1982
- Andrews, M.K., Keppler, E., Daly, P.W.: Plasma sheet motions inferred from medium-energy ion measurements. *J. Geophys. Res.* **86**, 7543–7556, 1981
- Daly, P.W.: Remote sensing of energetic particle boundaries. *Geophys. Res. Lett.* **9**, 1329–1332, 1982
- Daly, P.W., Keppler, E.: Observations of a flux transfer event on the earthward side of the magnetopause. *Planet. Space Sci.* **30**, 331–337, 1982
- Daly, P.W., Williams, D.J., Russell, C.T., Keppler, E.: Particle signature of magnetic flux transfer events at the magnetopause. *J. Geophys. Res.* **86**, 1628–1632, 1981
- Fritz, T.A., Fahrenstiel, S.C.: High temporal resolution energetic particle soundings at the magnetopause on November 8, 1977, using ISEE 2. *J. Geophys. Res.* **87**, 2125–2131, 1982
- Fritz, T.A., Williams, D.J., Paschmann, G., Russell, C.T., Spjeldvik, W.: The magnetopause as sensed by energetic particles, magnetic field, and plasma measurements on November 20, 1977. *J. Geophys. Res.* **87**, 2133–2138, 1982
- Kaufman, R.L., Konradi, A.: Explorer 12 magnetopause observations: Large scale non-uniform motion. *J. Geophys. Res.* **74**, 3609–3627, 1969
- Paschmann, G., Haerendel, G., Papamastorakis, I., Scopke, N., Bame, S.J., Gosling, J.T., Russell, C.T.: Plasma and magnetic field characteristics of magnetic flux transfer events. *J. Geophys. Res.* **87**, 2159–2168, 1982
- Rijnbeek, R.P., Cowley, S.W.H., Southwood, D.J., Russell, C.T.: Observations of “reverse polarity” flux transfer events at the earth’s dayside magnetopause. *Nature* **300**, 23–26, 1982
- Russell, C.T., Elphic, R.C.: ISEE observations of flux transfer events at the dayside magnetopause. *Geophys. Res. Lett.* **6**, 33–36, 1979
- Scholer, M., Hovestadt, D., Ipavich, F.M., Gloeckler, G.: Energetic protons, alpha particles, and electrons in magnetic flux transfer events. *J. Geophys. Res.* **87**, 2169–2175, 1982
- Speiser, T.W., Williams, D.J.: Magnetopause modelling: flux transfer events and magnetosheath quasi-trapped distributions. *J. Geophys. Res.* **87**, 2177–2186, 1982
- Speiser, T.W., Williams, D.J., Garcia, H.A.: Magnetospherically trapped ions as a source of magnetosheath energetic ions. *J. Geophys. Res.* **86**, 723–732, 1981
- Williams, D.J.: Magnetopause characteristics inferred from three-dimensional energetic particle distributions. *J. Geophys. Res.* **84**, 101–104, 1979
- Williams, D.J.: Magnetopause characteristics at 0840–1040 hours local time. *J. Geophys. Res.* **85**, 3387–3395, 1980
- Williams, D.J., Keppler, E., Fritz, T.A., Wilken, B., Wibberenz, G.: The ISEE 1 and 2 medium energy particles experiment. *IEEE Trans. Geosci. Electron.* **GE-16**, 270–280, 1978
- Williams, D.J., Fritz, T.A., Wilken, B., Keppler, E.: An energetic particle perspective of the magnetopause. *J. Geophys. Res.* **84**, 6385–6396, 1979

*Review Article***On the Dynamics of the Ring Current\***

B. Hultqvist

Kiruna Geophysical Institute P.O. Box 704, S-98127 Kiruna, Sweden

**Abstract.** The present knowledge of the ring-current population is first briefly summarized, with emphasis on the lower energies. It is then shown that in the February 1979 magnetic storm  $O^+$  ions of  $\leq 17$  keV energy contributed considerably to the energy density of the ring current in its entire altitude range. They probably dominated the dayside ring current, from an energy density point of view, in the early phase of the storm. It is argued that these  $O^+$  ions, observed in the dayside magnetosphere in the early phase of the storm, were extracted directly from the dayside ionosphere over a wide latitude interval. The likely importance, from an energy density point of view, of  $O^+$  ions in the ring current at higher energies ( $> 17$  keV) where the composition has not, as yet, been investigated, is finally discussed.

**Key words:** Ring current – Energetic particles in magnetosphere –  $O^+$  ions

**Introduction**

The cause of the world-wide depression of the geomagnetic field intensity during the main phase of magnetic storms, which has been studied for more than a hundred years (Adams, 1880; 1881; Ellis, 1880), is a westward-directed ring current flowing around the Earth. In the last two decades spacecraft borne instruments have demonstrated that the ring current is due to strong increases, in the range  $L=2-7$ , in the fluxes of electrons and ions which drift around the earth and give rise to the westward current (Hoffman and Brachen, 1967). The ions contribute most to the current and the magnetic field depression is proportional to the energy density of the ring-current plasma (Sckopke, 1966). A fairly complete distribution function for the ring-current ions, determined as a function of  $L$ , was first obtained less than ten years ago by Explorer 45 (Williams and Lyons, 1974).

When the Explorer 45 payload was planned and built the ring-current ions were assumed to be virtually all protons, so the lack of a composition-determining instrument on board was not considered to be important. The first energetic-ion mass-spectrometer measurements in

space, made by the Lockheed group on low-orbiting satellites, were reported in 1972 (Shelley et al., 1972) and the then astonishing result was that, during magnetic storms, the precipitated energetic-ion fluxes in the 0.7–12 keV energy range sometimes contained even higher fluxes of  $O^+$  ions than of  $H^+$ . These observations raised the question of whether the then dominating view, of the ring-current particles as brought into the inner magnetosphere by convection and diffusion from greater distances on the night side (the plasma sheet and the tail), was the whole truth or whether direct injection from the ionosphere might contribute significantly (Shelley et al., 1972, and others later).

Williams (1979; 1981) has recently summarized the development of our understanding of the ring current during the seventies. He has emphasized the importance of composition determinations in a figure and a table reproduced here (Fig. 1 and Table 1). Both Fig. 1 and Table 1 demonstrate effectively the lack of knowledge of the composition of the majority of the ring-current particles. Only for the low and high energy tails of the ring-current ion population have direct measurements of the composition been possible hitherto. Figure 1 also indicates the effect of part of the ions being  $O^+$  instead of  $H^+$  (dashed curve) and demonstrates that the quiet-time ring current has a harder energy spectrum than the storm-time one. It should be emphasized that the profiles in Fig. 1 are based on Explorer 45 observations before and during one single magnetic storm, in December 1971, which was a large one (Dst reached  $-190$  nT), and that smaller storms may show different profiles, especially in the inner part of the ring-current region where differences in the penetration depth of the injected particles become apparent.

After Explorer 45 only a few satellites have provided detailed ring current information. Balsiger et al. (1980) and Balsiger (1981) have analysed GEOS 1 data for two storms covering the energy range from a few tens of eV to a few hundreds of keV. The ring current composition below 17 keV, during the recovery phase of magnetic storms, has been studied by Balsiger et al. (1980) on the basis of GEOS observations and by Lundin et al. (1980) with Prognoz-7 data, with slightly different emphasis. Their results are summarized by Williams (1981). Lennartsson et al. (1981), Peterson et al. (1981), Sharp et al. (1983) and others have recently published results of ISEE 1 measurements of the composition of the ions below 17 keV in the ring-current region as well as in the plasmasheet, adjacent to the ring current and at great distances. They have all demonstrated

\* Based on an invited review paper given at the Symposium on Plasma and Energetic Particles in the Magnetosphere, EGS Meeting, 23–27 August 1982, Leeds, U.K.

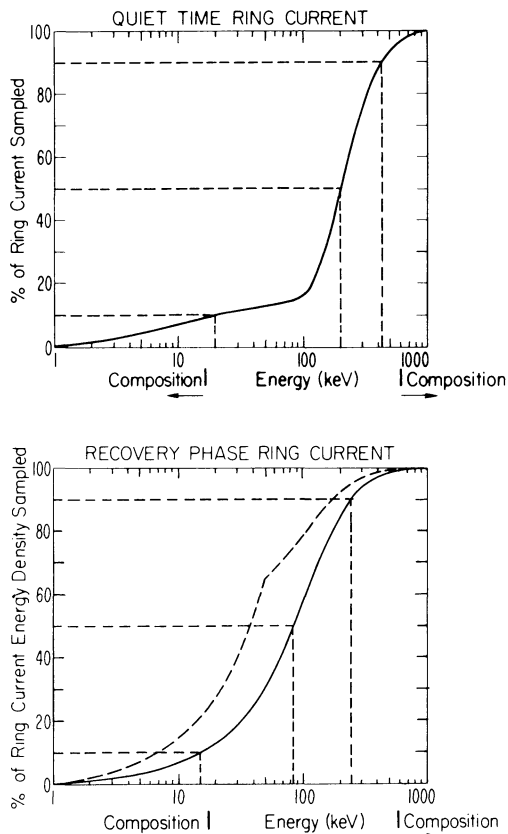


**Fig. 1.** Cumulative percentage of ring current energy density vs energy for pre-storm and early recovery phases of the major geomagnetic storm on 17 December 1971, as observed by means of Explorer 45 (After Williams, 1981). Solid curves assume all ions are protons. For the dashed curve in the lower diagram all ions below 50 keV have been assumed to be  $O^+$  ions and all ions above 50 keV, protons.

**Table 1.** Ring current composition summary (after Williams, 1979)

Energy (keV)	Technique	H	He	C	O	Comments <sup>a</sup>	Source preference
$\lesssim 17$	Direct observation	×	×		×	Low altitude; synoptic surveys; trapped and precipitated; energy, latitude, and time dependence in relative abundances	Ionosphere
$\lesssim 30-50$	Inference	×	×		×	Equatorial decay rates-charge exchange comparisons; recovery phase; time dependence in relative abundances	?
50-100						No information; centrum of ring current energy distribution is in 50-100 keV range	?
$\sim 100-1,000$	Inference	×				Equatorial intensity profile-cross L diffusion comparisons; steady state and recovery phase	?
$\gtrsim 600$	Direct observation	×	×	×	×	High altitude; energy, altitude, and time dependence in relative abundances	Solar Wind

<sup>a</sup> Depending on energy, altitude, and time of observation, it is possible for any of the ions indicated to dominate the ion distribution

that, in the energy range studied,  $O^+$  ions of ionospheric origin constitute an important part of the hot magnetospheric plasma, from a number density point of view, during disturbed conditions.

None of these authors have dealt with the question of the importance of the observed, fairly low-energy, ring-current ions for the magnetic effects of the ring current, i.e. of the variation of the energy density distribution with energy and  $L$ . This review addresses that question as one of its main concerns (although the data available is very limited). In fact there is very little data published on this matter, which may be partially due to the fact that, in order to obtain a cross cut through the whole ring-current region, eccentric orbit satellites are needed. Most satellites in recent years have had very eccentric orbits, which means long orbital periods and generally only one passage through a storm-time ring current per magnetic storm (GEOS-1 is the exception). With highly-eccentric-orbit satellites one thus needs good luck to have a good satellite passage through the ring-current population in the appropriate phase of a storm. The present report is largely based on a fairly detailed analysis of one single such "lucky" observation of the day-side ring current in the early main phase of the 21 February 1979 magnetic storm by means of Prognoz 7. The approach is different and complementary to those of the studies referred to above.

### Energy Density Distributions

For the reasons mentioned above (and possibly others) very few observations of the distribution of the energy density in the ring current against energy and radial distance have been published. The question we address in this section is the following: Are the heavy ions of ionospheric origin in the ring current, observed hitherto only below 17 keV for technical reasons, of any importance for the magnetic

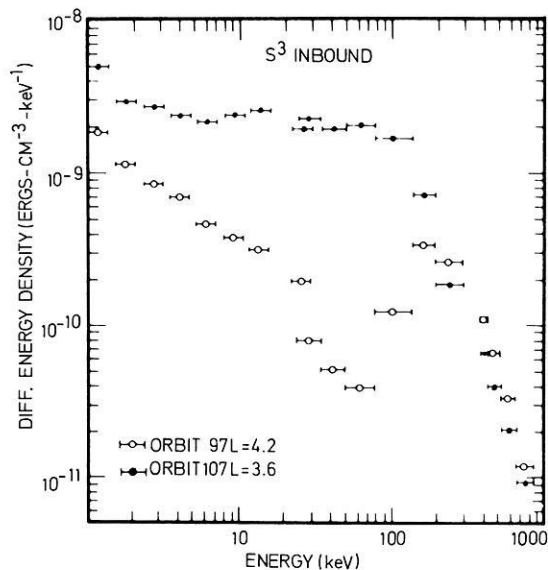


**Fig. 2.** Ion energy density spectra (protons assumed) measured by Explorer 45 during pre-storm quiet-time (orbit 97) and during early recovery phase (orbit 102) for the 17 December 1971 geomagnetic storm. (From Smith and Hoffman, 1973)

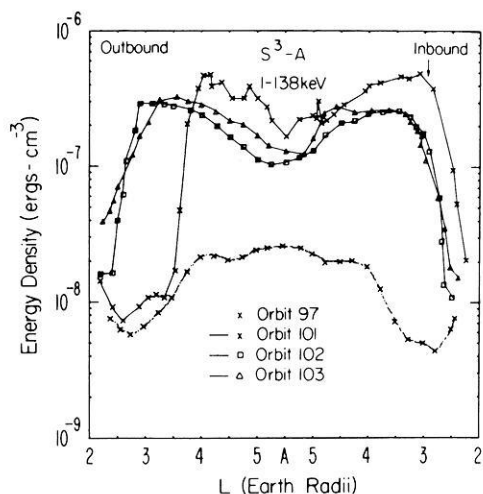


**Fig. 3.** Proton energy density radial profiles as measured by Explorer 45 ( $S^3$ -A) during pre-storm quiet (orbit 97), main phase injection (orbit 101), and recovery phase (orbits 102 and 103) for the 17 December 1971 geomagnetic storm. (From Smith and Hoffman, 1973)

effect associated with the storm-time ring current, or is the magnetic disturbance completely dominated by the higher energy ions in the main part of the ring-current energy range. As this question is of some general interest we will discuss how far we can get in answering it on the basis of the limited published data available.

The most complete data set (except for composition) for the energy density distribution, as a function of energy and  $L$ , during different phases of a magnetic storm is that obtained with Explorer 45 during the December 1971 storm (Smith and Hoffman, 1973). This was a large storm ( $|\text{Dst}|_{\text{max}} = 190$  nT). The observations were made in the evening-midnight sector. This storm is also discussed by Williams (1979). Two figures of Smith and Hoffman (1973) are reproduced here as Fig. 2 and 3, as they summarize well the energy density distribution as function of energy

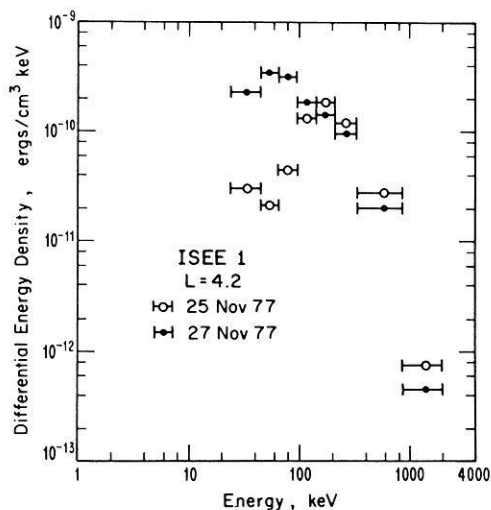


**Fig. 4.** Ion energy density spectra obtained by ISEE 1 during pre-storm quiet-time (25 November 1977) and during recovery phase (27 November 1977). (After Williams, 1981)

(Fig. 2) and of  $L$  and the variations of the energy density distribution in the course of such a large storm (Fig. 3). The values shown in these two figures are based on the assumption that the ions were protons. If the ions were heavier than protons the energy density values were higher (Williams, 1979).

During the smaller geomagnetic storm in November 1979 ( $|\text{Dst}|_{\text{max}} = 100$  nT), the ISEE-1 medium energy experiment measured the differential energy density distributions above 24 keV (protons assumed) shown in Fig. 4 before the storm and in its recovery phase (Williams, 1981). The observations were made near noon (1030 LT in the first pass). The quiet-time data before the storm agree well with the quiet-time data before the big storm shown in Fig. 2. The recovery-phase energy densities in Fig. 4 are an order of magnitude lower than in the large storm case in Fig. 2. This may, to some smaller extent, be due to the fact that the Fig. 4 data were obtained somewhat later in the storm than the data in Fig. 2, but mainly to the lower intensity of the storm.

Energy densities as a function of  $L$  for the November 1977 storm are shown in Fig. 5 (after Williams, 1981). It corresponds to Fig. 3 for the December 1971 storm but covers only energies  $\geq 24$  keV. The ions are assumed to be protons. Fig. 5 also provides information about how the changes of the energy density are distributed between the 24–210 keV and 210–2,080 keV energy ranges. The energy density increases at lower energies (24–210 keV) and decreases at higher energies. This behaviour is similar to that shown in Fig. 2 and is discussed in detail by Lyons and Williams (1976). The main storm-time effect in phase space is an enhancement of densities at values of the first adiabatic invariant ( $\mu$ ) below the  $\mu$ -value of the density maximum seen in the quiet-time data. Above this  $\mu$ -value of maximum density (corresponding to  $\sim 150$  keV energy at  $L \sim 4$ ) phase space densities remain constant (Williams, 1981).

Whereas there are very large increases of 1–138 keV ions at  $L = 3$  in the large storm case of Fig. 3, there is no increase in the 24–210 keV range at  $L = 3$  in the smaller storm data

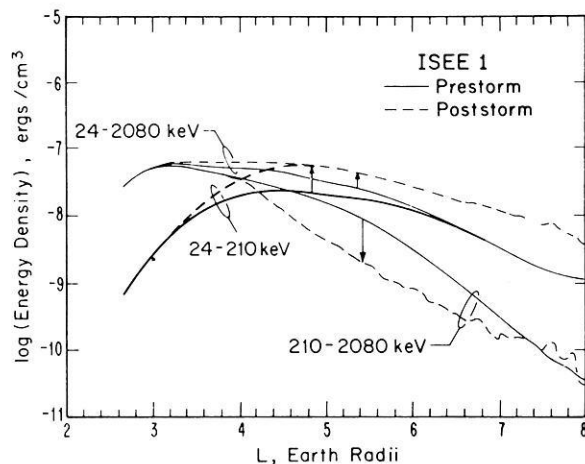


Fig. 5. Pre-storm (25 November 1977) and post-storm (27 November 1977) energy densities vs  $L$  value. (After Williams, 1981)

in Fig. 5. This illustrates that the injection depth of the ring-current plasma is strongly related to the intensity of the magnetic storm.

Detailed observations of the ion distributions below 30 keV, including composition (0.2–17 keV), in the dayside magnetosphere, near noon, during a  $|Dst|_{\max} = 100$  nT storm were made by means of Prognoz-7 on 21 February 1979 (Lundin et al., 1982a; Hultqvist, 1982, 1983). The Prognoz-7 measurements were taken before Dst reached its minimum value, whereas the ISEE-1 measurements shown in Figs. 4 and 5 were obtained after the Dst minimum. One may expect the obtained density values in both cases to be somewhat lower than the peak value during the storm. According to Fig. 3, order of magnitude differences between densities in main phase and (early) recovery phase are not expected in the central part of the ring current, during several hours around the storm peak.

It is somewhat unclear how low in energy  $O^+$  ions could be detected by means of the solid state detectors on ISEE 1 used by Williams (1981). The lower energy limit may have been as high as 100 keV. We may therefore assume, as an extreme alternative, that Williams's data give practically only the proton content of the ring current. As the heavy ions of ionospheric origin most likely decrease in relative importance with energy above the present measuring limit of the mass spectrometers (17 keV), this limitation is not likely to affect the comparisons of ring current energy density contributions from different energy ranges very much. Even if it should turn out in the future that  $O^+$  ions play a major role in the main part of the ring current energy density distribution (50–100 keV) also a comparison of the relative contribution to the magnetic effect by the presently observed ring-current ions of ionospheric origin (of energies below 17 keV) to that of the proton component of the ring current is of interest. In fact, if ionospheric ions should turn out to be of major importance in magnetic storms near the peak of the energy density distribution also, the general conclusion of the discussion in this section concerning the importance of ionospheric ions in the ring current is only amplified.

The fact that the ISEE data and Prognoz 7 data were obtained in two different storms is of course a serious drawback. However, as the Dst value is considered to be a rather good measure of the total energy in the ring current, we

may expect that the two storms were quite equal in this respect at the storm peaks. If there were a higher  $O^+$  content in the ring current in February 1979 than in November 1977 because of the solar cycle effect on the  $O^+$  density below 17 keV energy demonstrated by Young (1980) and Young et al. (1982), we have in the discussion below compared the energy density of the  $O^+$  ions below 17 keV with a too high energy density of protons above 24 keV and the relative figures of the importance of  $O^+$  ions for the magnetic effect of the ring current should rather be somewhat higher than found. Unless  $O^+$  ions play a dominating role in the 50–100 keV range (which is unlikely) this difference is not expected to change the general qualitative conclusions we draw.

Prognoz-7 data from the early main phase of the February 1979 storm are shown in Fig. 6a. The format is quite different from that in earlier figures, partly due to the inclusion of composition information, but the energy density in the units of Figs. 3 and 5 ( $\text{erg}/\text{cm}^3$ ) of  $H^+$  and  $O^+$  ions can easily be obtained from the data in Fig. 6 by combining the density ( $N_i \text{ m}^{-3}$ ) and temperature ( $T_i \text{ K}$ ) values according to  $\epsilon_i (\text{erg}/\text{cm}^3) = 2.07 \cdot 10^{-22} N_i (\text{m}^{-3}) \cdot T_i (\text{K})$ . The characteristic energy of each ion species is given as a temperature (although the distributions are generally not Maxwellian). More detailed energy distribution data is contained in Fig. 7a. Prognoz-7 crossed the ring current boundary inbound at 1130 UT at a geocentric distance of  $8.6 R_E$ . The solar magnetic (SM) latitude was  $35^\circ$  and the SM longitude  $350^\circ$  (i.e. MLT  $\sim 1120$ ).

Figures 6b and 7b show the similar data sets for a fairly undisturbed period. Dst had the values  $-23$ ,  $-25$ ,  $-21$ ,  $-14$ ,  $-11$ ,  $-14$  nT in the six hour interval centered on the time of the satellite crossing of the magnetopause ( $\sim 1750$  UT). The magnetopause crossing occurred at a geocentric distance of  $11 R_E$ , at  $10^\circ$  SM longitude (i.e. MLT  $\sim 1240$ ) and at  $\sim 45^\circ$  SM latitude. The only major difference between the conditions in which the two data sets of Figs. 6a and 6b were obtained was evidently the magnetospheric disturbance level. The main differences between the storm main phase and the low disturbance data are the higher number densities (for the energy range 0.2–17 keV) in the storm situation both inside ( $\sim 2 \text{ cm}^{-3}$  and  $\sim 0.4 \text{ cm}^{-3}$  respectively) and outside ( $30 \text{ cm}^{-3}$  and  $10 \text{ cm}^{-3}$ ) the ring current boundary and – more remarkable – the complete domination during the storm time passage of  $O^+$  ions below 17 keV in the entire dayside magnetosphere. The  $O^+$  density in the outer magnetosphere is an order of magnitude higher in Fig. 6a than in Fig. 6b and there is an  $O^+$  density increase at least in as far as  $L \sim 3$ , whereas the  $H^+$  density is not very much changed. Nor are the  $H^+$  (crosses) and  $O^+$  (circles) temperatures (0.2–17 keV) very much different in the storm main phase from those in the undisturbed situation, except in the innermost part where the  $O^+$  temperature is lower in the storm than in the undisturbed situation (MeV electrons give rise to a strongly dominating background along part of the low altitude trajectory in Fig. 6a, UT  $\sim 1545 - \sim 1635$ , which has not been eliminated from the data.)

Let us now compare the energy density information for  $\leq 17$  keV contained in Figs. 6a and 6b with that for  $\geq 24$  keV in Fig. 5.

At  $L=3$  the pre-storm energy density value ( $\epsilon$ ) is shown in Figure 5 to be  $\sim 2 \cdot 10^{-9} \text{ erg}/\text{cm}^3$  for 24–210 keV ions (assumed to be protons) and  $\sim 5 \cdot 10^{-8}$  for 210–2,080 keV

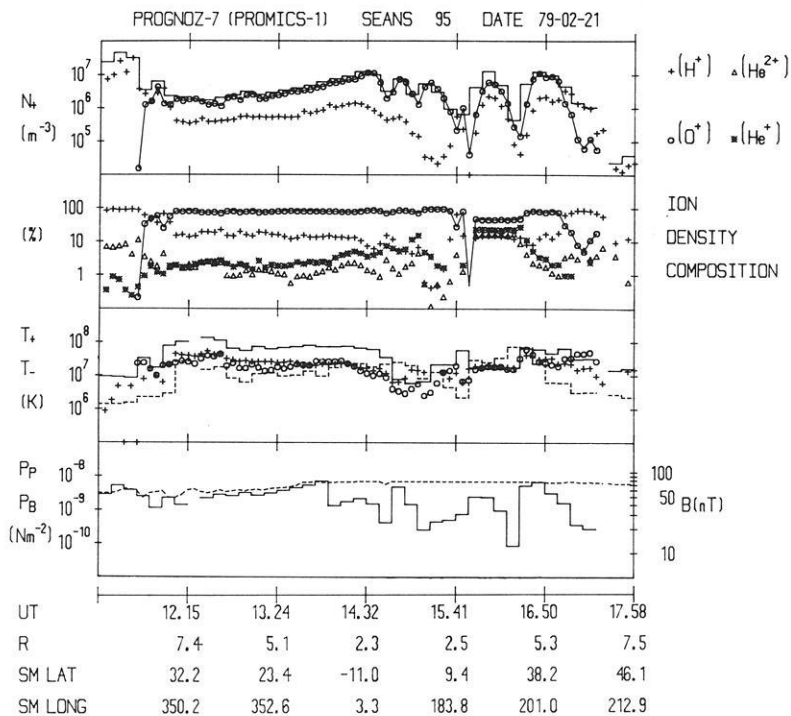
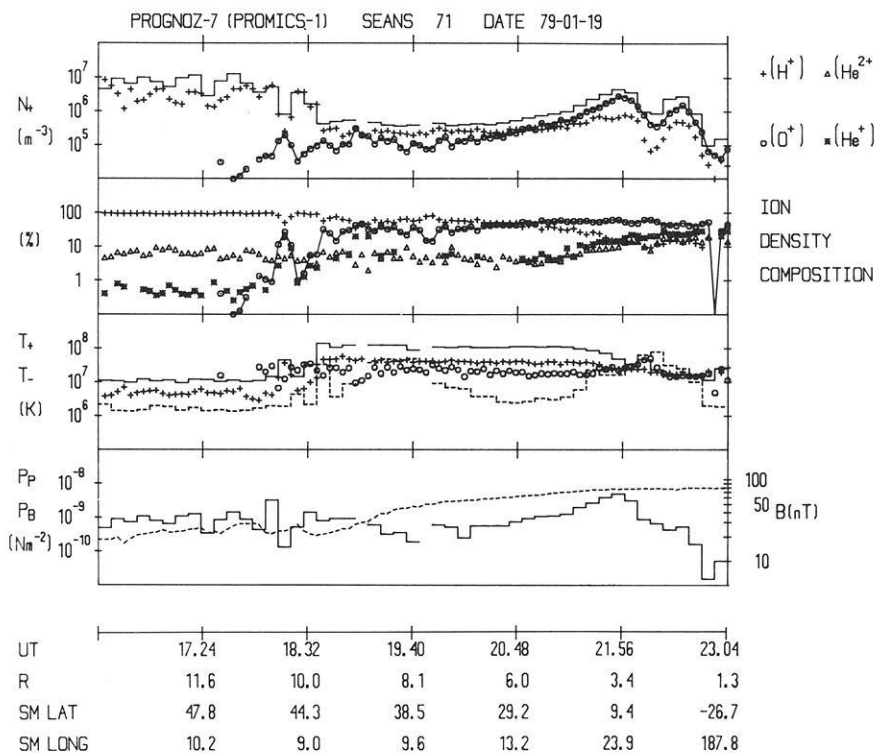


**Fig. 6a** An example of a storm time situation in the dayside magnetosphere when  $O^+$  ions dominated over other ion species. Between  $\sim 1545$  and  $\sim 1635$  UT MeV electrons gave rise to a dominating background which has not been eliminated from the data shown. The upper panel shows the ion number density ( $N_+$ ) as deduced from the  $E/q$  spectrometers assuming the ions were all protons (solid lines). Plus signs (+) represent the density of  $H^+$  as deduced from the perpendicular ICSs (assuming isotropy) and circles (o) represent the number density of  $O^+$  using all ICSs. The second panel from the top represents the percentages of the four major ion constituents with respect to the total number density (logarithmic scale used). The third panel shows the temperatures of ions (solid line) and electrons (broken line) as deduced from the  $E/q$  electron and ion spectrometer data fitted onto Maxwellians. In the same panel the "perpendicular"  $H^+$  (+) and  $O^+$  (o) temperatures have been plotted. The fourth panel shows the ion plasma pressure (solid line) and magnetic field pressure (dotted line). The time and space coordinates (in Solar Magnetic, SM, coordinates) are given along the horizontal axis.



**b** An example of observations in the dayside magnetosphere during fairly low disturbance conditions. At the lowest altitudes MeV electrons produce a dominating background which has not been eliminated from the data shown in the figure. The format is the same as in **a**

ions. The 0.2–17 keV ion data for the low disturbance level in Fig. 6 give a value of  $\sim 4 \cdot 10^{-9}$  erg/cm<sup>3</sup>, i.e. comparable with, but somewhat larger than, the 24–210 keV energy density and an order of magnitude lower the energy density of the higher energy ions ( $\geq 210$  keV).

Whereas at  $L=3$  there is no change from prestorm to recovery phase for 24–210 keV ions in Fig. 5, the 0.2–17 keV ions in Fig. 6 show an increase of  $\epsilon$  to  $4 \cdot 10^{-8}$  erg/cm<sup>3</sup> in the *early main phase*, practically all

carried by  $O^+$  ions. This value is about the same as the energy density of the entire high energy part of the ring current plasma at that L value. The Prognoz observations thus indicate that in (small) magnetic storms there is an injection even at  $L=3$  of  $O^+$  ions into the dayside ring current in the early main phase of the storm, representing about as much energy density as the quiet-time (and storm-time; small storms) high-energy particles ( $> 210$  keV). That Williams did not see any increase at all in his low energy



## PROMICS-1 LOW-SPEED

SEANS 71 DATE : 79-01-19 START TIME : 17-27

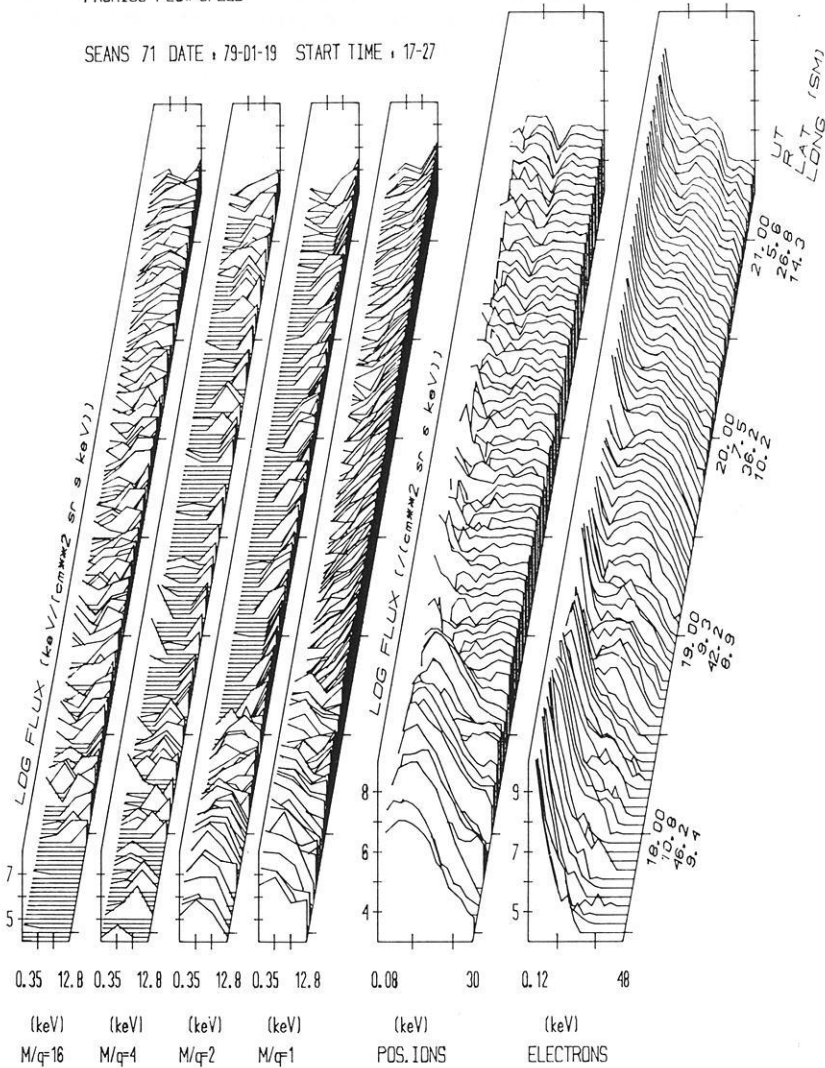


Fig. 7b

predict quantitatively what effect the difference in storm time between the ISEE-1 and Prognoz-7 observations may have. At  $L=8$  we are outside the main part of the ring current and the contribution to the magnetic field depression at the Earth's surface is generally small.

To summarize this section: We have, in the main part of the dayside ring current ( $L=5$ ) of a small storm, found rough agreement with Williams' (1979, 1981) results for the nightside ring current in a large storm concerning the contribution to the total ring current energy density by  $O^+$  ions below 17 keV energy ( $\sim 20\%$ ). At the inner edge ( $L=3$ ) we have found an  $O^+$  population of  $\leq 17$  keV energy contributing about as much as all ions above 24 keV (protons assumed) to the energy density. At the outer edge ( $L=8$ ) the low energy  $O^+$  ions have also been shown to be a major contributor to the energy density. On the whole, the  $\leq 17$  keV  $O^+$  ions have thus been found to play a considerable role in the magnetic effect in the early main phase of the small-storm, dayside ring current investigated.

The Prognoz-7 observations were made in the rising phase of solar activity. There is a strong solar cycle variation of the average  $O^+$  density below 17 keV at the geostationary orbit with  $O^+$  ions playing a larger role the higher

the solar activity (Young, 1980; Young et al., 1982). Near solar activity minimum, the  $O^+$  contribution to the ring current energy density is therefore expected to be lower than in the example discussed above and in peak years of the solar cycle it is expected to be higher.

### On the Sources of the Ring Current

For a discussion of the composition, with source considerations, of the high energy part of the ring current population, which may be an important component of the quiet-time ring current, the reader is referred to Spjeldvik and Fritz (1978a, b, d) and Williams (1979). Here we shall only deal with the observations of the low energy part of the storm-time ring current distribution in the dayside magnetosphere by means of Prognoz-7, which were discussed from an energy density point of view in the previous section. As justification for the origin of the ions we use the fact that there are very few  $O^+$  ions in the solar wind and very many of them in the ionosphere.

As mentioned earlier, the possibility of the ionosphere being an important source of magnetospheric ions was suggested after the first observations by the Lockheed group

of  $< 12$  keV  $O^+$  ions being precipitated into the atmosphere during magnetic storms, even at fairly low magnetic latitudes (Shelley et al., 1972). The first ion mass spectrometer flown to great altitudes on GEOS-1 by the Bern group demonstrated the occurrence of substantial fluxes of ionospheric  $O^+$  ions in the ring current (Geiss et al., 1978; Balsiger et al., 1980). Lundin et al. (1980) demonstrated the dominance of  $O^+$  ions for energies less than 17 keV in the inner part of the ring current ( $L \leq 4$ ) during the recovery phase of magnetic storms, in agreement with the inference by Lyons and Evans (1976) of heavy ion dominance below 50 keV in the later part of storms. That ionospheric  $O^+$  ions are ejected locally with high fluxes into the magnetosphere along auroral latitude magnetic field lines, was first demonstrated convincingly by the S3-3 measurements (Shelley et al., 1976; Ghielmetti et al., 1978).

Even against the background of the previous observations outlined above, the data in Fig. 6a are rather surprising in that the number density and energy density of  $O^+$  ions below 17 keV are an order of magnitude higher than the corresponding densities of protons in practically the entire dayside magnetosphere, from near the magnetopause to an  $L$ -value well below 3. (In the innermost part MeV-electron background counts are present in Fig. 6a). A comparison with the low disturbance situation illustrated in Fig. 6b demonstrates, as mentioned before, that the storm-time situation differs from it in that the  $O^+$  density has been increased by an order of magnitude whereas the  $H^+$  density and the temperatures are not very much changed.

That the  $O^+$  ions below 17 keV energy in the dayside ring current during the early main phase of a fairly small magnetic storm, which are shown in Figs. 6a and 7a, are of ionospheric origin, is of course without doubt. But we can say a lot more about their path to where they were observed by analysing the observations in some detail (Lundin et al. 1982a, Hultqvist, 1982, 1983).

First, the  $\leq 17$  keV ionospheric ions shown in Fig. 6a are not likely to have reached the inner magnetosphere via the plasma mantle (fairly generally supposed to be a major source of the plasma sheet and, by inward convection, of the ring current). Lundin et al. (1982a) have analysed observations of the plasma mantle during the same passage of Prognoz-7 through the magnetosphere in which the Figure 6a data were taken and have found that the  $O^+$  density in the mantle was of the order of 10% or less as compared with  $\sim 90\%$  in the dayside magnetosphere.

Secondly, the  $O^+$  ions in the dayside magnetosphere, at least in the inner part, are not likely to originate in a plasma injection population on the nightside associated with the magnetic storm, because there was not enough time for them to drift to the noon sector (unless the convection field was unreasonably high). The Dst decrease started only at 06 UT and Dst reached  $-90$  nT between 08 and 09 UT after which it increased again, indicating a low convection field intensity after 09 UT.

Thirdly, the Prognoz-7 observations on the nightside during the same passage showed that the  $O^+$  density was lower there than on the dayside.

It can therefore be concluded that the  $O^+$  ions observed by Prognoz-7 in the dayside magnetosphere on February 21, 1979 were extracted from the ionosphere on the dayside (Hultqvist, 1982, 1983).

Hultqvist (1983) has also concluded that the source region on the dayside had a very wide extension in  $L$ , arguing

that if the source were limited to a fairly narrow  $L$  range one would expect to see an uneven  $O^+$  distribution over  $L$  along the satellite trajectory, unless the limited  $L$  range source were at the inner edge of the ring current, i.e. at  $L=2-3$ , or if the convection electric field in the dayside magnetosphere were dominantly dusk-dawn directed instead of dawn-dusk directed, both of which alternatives are highly unlikely, according to all experience. Observations of source regions for ionospheric ions which are very wide in  $L$  have been reported (Lundin et al., 1982b).

On the basis of a comparison of the observations summarized in Figure 6a with existing knowledge about the altitude distribution of cold ionospheric ions, Hultqvist (1983) has found that the hot  $O^+$  ions in the dayside ring current cannot have been produced by accelerating cold  $O^+$  ions in the outer parts of the field tubes. There are not sufficient numbers of cold  $O^+$  ions available in the magnetosphere. In order to find sufficient numbers of cold  $O^+$  ions to accelerate, the extraction has in fact to occur below 1,000 km altitude in the ionosphere. Moore (1980) has presented strong arguments, based on basic charge exchange considerations, for the main extraction region being located below the neutral O/H cross-over altitude (500–1,500 km). Hultqvist's (1983) observational results thus confirm his basic arguments.

We therefore conclude that the  $\leq 17$  keV  $O^+$  ions, which dominated the dayside ring current from an energy density point of view, in the early main phase of the February 1979 storm (see previous section), were directly injected from the dayside ionosphere. This does not mean that ions directly extracted and accelerated out of the ionosphere were likely to carry most of the total ring current energy. For that part of the ring current ions which have energies near the peak of the differential energy density distribution, acceleration processes are required that produce ions well above the energies that characterize the dayside  $O^+$  population shown in Figs. 6a and 7a.

### On the Acceleration Processes

Most of what we know about the processes that accelerate ions out of the ionosphere has been learnt from the measurements of the S3-3 satellite (see Mozer et al., 1980, and Sharp and Shelley, 1981, for reviews) but recently Prognoz-7 has also contributed (Lundin et al., 1982b). A very brief summary of the results may be as follows:

- Strongly field aligned outflowing ion beams are produced by electrostatic acceleration, mainly above 5,000 km altitude along high-latitude magnetic field lines (Ghielmetti et al., 1978; Gorney et al., 1981). The composition of the upflowing ions has been found to vary from more than 90% protons to more than 90% oxygen ions.
- There are also mechanisms that accelerate ions perpendicularly to the magnetic field lines and give rise to conical pitch angle distributions (conics). These processes are assumed to be associated with ion cyclotron waves (Ungstrup et al., 1979, and others).
- The accelerated ions generally do not move adiabatically to the equatorial plane (and on towards mirroring or precipitation). Pitch angle scattering or transverse acceleration occurs between an altitude of an earth radius, or less, and the equatorial plane which is sufficiently strong to make the beams wide (Borg et al., 1978; Kaye et al., 1981). The

processes may work differently on various ion species (Collin et al., 1981). The largest altitude at which narrow (adiabatically moving) beams have been observed hitherto is  $\sim 5 R_E$  (Lundin et al., 1982b).

Although the processes mentioned above can both extract  $O^+$  ions below 1,000 km altitude and give them keV energies at greater altitudes, the observations do not fit very well to a model with low-altitude perpendicular acceleration due to ion-cyclotron waves and field-aligned acceleration in a simple potential drop at greater heights. Some of the problems are the following: Field aligned electron distributions coming together with field aligned ions from the same hemisphere, reported first by Borg et al. (1978), have been found in a large fraction of ion bursts near the equatorial plane by means of the SCATHA satellite (Kaye et al., 1981); The wide energy spectra observed, illustrated in Fig. 7, are not consistent with the main acceleration occurring in a simple potential drop, where all ions obtain the same energy increase. If a potential drop acceleration is important strong secondary effects must exist that modify energy spectra (and pitch angle distributions) greatly.

Even if, as we have seen in previous sections, direct extraction and acceleration of ions out of the ionosphere contribute significantly to the ring current and plasma sheet energy content, it is obvious, as mentioned before, that different kinds of acceleration processes from those discussed above are required for providing the higher energy particles of the ring current. The energy of charged particles can be increased only by electric fields. The electric fields may have different characteristics in different phases of magnetic storms. When there are fast variations in the geomagnetic field, induced electric fields may be important. They may well produce ions in the entire energy range up to the highest energies in the ring current (Heikkila and Pellinen, 1977; Pellinen and Heikkila, 1978; Heikkila et al., 1979). There does not seem to be any favouring of heavy ions over protons in the acceleration due to induced electric fields.

The potential dawn-dusk electric field generated by the solar wind flowing by the Earth gives rise to inward convection of the plasma on the nightside. When the convection electric field decreases after the injection period the particles find themselves in trapped orbits. Substorms generally inject plasma to  $L=4-5$ , while flux increases at  $L < 4$  are significant only during magnetic storms. The adiabatic energy increase cannot be larger than that corresponding to the entire voltage difference between the dawn and dusk sides of the magnetosphere. This is, of the order of 50 kV in substorms but it may be much larger during magnetic storms, up to a few hundred kV in the most intense injection period. The ratio of the particle energy in the original and final location is, for equatorially mirroring ions, the same as the ratio of the magnetic field intensities in the two locations (adiabatic compression). This is also the energy increase associated with loss-free radial diffusion of such particles. For equatorial pitch angles different from  $90^\circ$ , the energy increase is lower. By non-adiabatic diffusion processes some particles may reach  $L$  values lower than those corresponding to the potential difference over the magnetosphere and thereby obtain higher energies, but this is a slower process than convection.

Lyons and Williams (1980) have suggested, on the basis of Explorer 45 observations, that the flux increases of ring current particles at  $L \leq 4$  during geomagnetic storms result

simply from an inward displacement of the pre-existing trapped particle distribution a few  $R_E$  further out and that ions need not be brought from greater distances in the plasmashet or the tail as has been generally thought (Axford, 1969; Williams, 1972).

The observation by means of the ISEE 1 satellite of large amounts of ionospheric ions in the plasma sheet during magnetic storms (Peterson et al., 1981) makes it natural to expect that the high energy ions in the central ring current region come from the plasmashet, having been accelerated during the inward transport (e.g. Balsiger, 1983). We shall therefore consider briefly some relations between the main part of the ring current ion population (from an energy density point of view) and the observations of the plasmashet composition by Peterson et al. (1981).

The ISEE 1 measurements have shown the existence of percentages even above 50 of  $O^+$  ions in the plasmashet, out to  $20 R_E$ , during magnetic storms. During the 21 February 1979 storm, 71%  $O^+$  ions (below 17 keV) were recorded at  $20 R_E$  (Peterson et al., 1981), whereas only one to a few tens of percent  $O^+$  ions were observed at closer distances (Lennartson et al., 1981). During quiet conditions only one or a few percent of  $O^+$  ions have been found in the plasmashet. The  $O^+$  ions observed in the plasmashet during the February 1979 storm obviously had been extracted from the ionosphere on the night side of the earth in a similar way to that discussed for the dayside above. Although no characteristic energy values are reported for the greatest distances, we may assume that the  $O^+$  ions had a mean energy of a few keV, as further in (Lennartsson et al., 1981).

If an ion mixture of the kind mentioned were brought, by convection, into the central ring-current region ( $L=4-5$  for small storms; see Fig. 5) their mean energy would be increased by adiabatic compression. The amount of energy increase depends on the origin of the ions. Those which are brought into the central ring current in the expansive phase of the storm were located only a few earth radii further out before the storm ( $L=5-7$ , say; Lyons and Williams, 1980). The plasmashet ions from greater distances, which were extracted from the ionosphere in the early phase of the storm may, if they are pitch angle scattered away from the loss cone, take up a smaller or larger fraction of the electric potential difference over the magnetosphere. This energization is expected to work identically on all ions of equal energy irrespective of mass. This is brought about by the gradient and curvature drift of the ions across equipotential surfaces of the convection field. Before the storm the ionospheric ion content in this region was generally low (e.g. Balsiger et al., 1980; Petersen et al., 1981; Balsiger, 1983) unless there had been significant disturbances well before the storm. We may thus expect that the ion mixture that is injected into the central part of the ring current by the strong convection field existing in the early storm phase before Dst reaches its minimum value, contains relatively low percentages of  $O^+$  ions. Those ions which arrive in the  $L=5-7$  region by extraction from the ionosphere in the early phase of the storm have typical mean energies of a few keV and they have their energy increased, by the convection to  $L=4-5$ , by less than an order of magnitude. Thus, they do not reach the central part of the energy density versus energy distribution of the ring current (50–100 keV). Most ions located in the plasmashet at greater distances than  $7 R_E$  at or after the storm onset convect past the earth at fairly great distances and never

reach the trapped orbit region, even after its expansion, when Dst has passed its minimum.

We thus expect the main part of the ring current ion population (50–100 keV) in the  $L \sim 4\text{--}5$  range to consist of ions of energies of a few tens of keV located in the  $L$  range 5–7 when the storm main phase starts. Those ions have generally reached the source region mentioned in a period with a lower activity level than during the storm and have thus obtained a lower potential energy increase from the convection electric field than storms provide. The highest energies present between  $L = 5$  and 7 have reached there from outside by non-adiabatic diffusion processes, as their forbidden regions at low activity level are likely to be larger than  $7 R_E$  (or they have been accelerated locally by some unknown process). Most of the ions are however expected to have reached the source region ( $L = 5\text{--}7$ ) by convection and have therefore obtained energy increases from the adiabatic motion in a fairly low disturbance convection field. As the potential difference between the dawn and dusk flanks of the magnetosphere in fairly quiet conditions is typically only a few tens of kV, the typical ion energy increase when reaching the source region is expected to be of the order ten keV. The original energy of the ions at great distances in the plasmashet may thus be the determining factor in whether ions, at least some of them, reach energies between 50 and 100 keV when they arrive in the central ring-current region after further acceleration in the storm convection electric field of the magnetosphere. That is the basis for the following discussion of the possible importance of an acceleration process which favours heavy ions entering the plasmashet from the mantle. Its real importance remains to be determined.

Charged particles may get into the inwardly convecting part of the magnetospheric tail, the plasma sheet, by way of the plasma mantle, reaching the neutral current sheet where they may be accelerated before they start convecting towards the Earth. To reach the mantle they either have to enter the dayside boundary layer, where they may be accelerated in the magnetopause current layer, or they may be extracted from the ionosphere in the cusp region more or less directly into the mantle. Having entered the mantle they are expected to stay in it, provided they have a field aligned speed that is not higher than the flow speed of the plasma and the magnetic field lines at the magnetopause of the open magnetosphere (see Cowley, 1980, for a detailed discussion of the open magnetosphere model). (If the magnetic field lines along the high-latitude nightside magnetopause do not pass through the magnetopause into the magnetosheath, as Prognos-7 observations indicate that they generally do not do (Lundin et al., 1982a), this limiting velocity condition does not apply directly. Even then there should be some velocity criterion for the ions to meet in order to reach the current layer in the tail at distances where convection towards the Earth occurs.) After the current layer acceleration, the adiabatic compression follows (discussed above) as an effect of the convection electric field.

A circulation process thus exists in the magnetosphere which “pumps up” the energy of the particles. This process tends to provide more energy to heavy ions than to protons, because the acceleration process in the current layers gives approximately the same velocity increase to the ions independently of mass.

As mentioned before, in order to stay in the magneto-

spheric circulation loop, the particles have to have sufficiently low field aligned velocities. As the acceleration in the current sheets at the magnetopause and in the neutral sheet of the tail tends to be directed along the field lines, the majority of the ions are not expected to make more than one round trip through the convection cycle, if the limiting field aligned velocity condition applies. Some of them may be scattered into the cycle again by nonadiabatic processes after having made one (or more) round trips and may thereby achieve very high energies. We shall briefly consider, a little more quantitatively, what effect the ion mass may have on this energization process associated with the magnetospheric circulation.

A typical flow velocity along the mantle magnetopause of plasma and magnetic field lines is 250 km/s. This corresponds to an energy of  $O^+$  ions moving along the field lines of 5.2 keV.  $O^+$  ions in the mantle with lower energies will certainly not leave the magnetosphere but higher energy  $O^+$  ions may, if the field lines are open. For protons the corresponding energy is 16 times lower: 0.32 keV. In a neutral sheet current layer with a flow velocity of say 200 km/s (e.g.  $E = 0.2$  mV/m and  $B = 1$  nT)  $O^+$  and  $H^+$  ions with the above-mentioned energies, along the field lines, may be accelerated up to a maximum field-aligned velocity of 650 km/s (Cowley, 1980) which corresponds to an energy of 35 keV for  $O^+$  ions but only 2.2 keV for  $H^+$  ions. If such ions are convected inward by a potential convection electric field, which may correspond to a potential difference across the magnetosphere of one or a few hundred kilovolts during the early intense injection phase of magnetic storms but to only a few tens of keV in fairly quiet conditions, they will pick up a larger or smaller fraction of that potential difference, depending upon where they start out. This means that ions of energies near the peak in the differential energy density distribution of the ring current (50–100 keV depending upon ions mass and storm strength; see Fig. 1) can be produced in one round trip through the magnetospheric circulation system more easily if the ions are  $O^+$  than if they are  $H^+$  ions. We therefore may expect that the relative energy density contribution to the ring current of  $O^+$  is larger than the  $O^+$  number density fraction of the plasma mantle, if acceleration in one or more current layers is important anywhere in the circulation loop through the magnetosphere. The  $O^+$  ions are also expected to achieve higher energies than  $H^+$  ions in all diffusive transport processes into the ring-current region, provided there is a current layer acceleration to start with. For instance, if a 35 keV  $O^+$  ion (accelerated as mentioned above) is scattered to  $90^\circ$  pitch angle and brought from the tail with  $B = 10$  nT, say, to a distance of  $\sim 5 R_E$  in the equatorial plane ( $B \sim 250$  nT) it will obtain an energy of almost an MeV, whereas a proton transported to the same place after maximum acceleration in the current layer would have an energy of only 55 keV. Radial diffusion is a much slower process than the convection and is not expected to play a major role in determining the temporal development of the ring current during the more active phases of magnetic storms.

Lundin et al. (1980) have shown that the plasma mantle contains  $O^+$  during disturbed conditions but not during quiet conditions. The peak relative abundances of  $O^+$  amount to a few tens of percent (number density). 5–10%  $O^+$  is rather representative for disturbed conditions. The

number density distribution within the plasma mantle is generally very uneven in time/space. According to what has been argued above, concerning the favouring of  $O^+$  ions compared to protons in current layer acceleration, we may thus expect that, of those ions which get into the plasmasheet and ring current from the mantle, a larger fraction of the  $O^+$  ions than of the  $H^+$  ions achieve energies in the range 50–100 keV. Those plasmasheet ions which have not experienced any current layer acceleration region are generally not likely to have energies in this range, according to the above discussion, unless they have had time to diffuse into the central ring current region. Also ions streaming into the tail in the magnetospheric high latitude lobes (Sharp et al., 1981) may reach the current layer of the neutral sheet in the tail and be accelerated in the way discussed.

The  $O^+$  ions in the storm-time mantle may come more or less directly from the ionosphere (Lundin et al., 1982a) or they may originate in the dayside ring-current population, which has been extracted from the ionosphere in the early phase of the storm, as described in earlier sections. Such ions drift to the dayside magnetopause in the dawn-dusk directed convection field. There they are accelerated and ejected along the field lines, some of them in the direction of the earth. After mirroring in or near the cusp they enter the plasma mantle and stay there (provided their field-aligned velocity component is not larger than the flow velocity at the magnetopause; see above) until they finally reach the tail neutral sheet. As the convection cycle time of magnetic field lines from the dayside magnetopause through mantle, tail and plasma sheet, back to the dayside is expected to be several hours, even for moderate penetration into the magnetosphere of the field lines (not reaching the permanently trapped ring-current region) during storm conditions (see e.g. Cowley, 1980), we may expect to see more energetic  $O^+$  ions (which have passed through the circulation process, after extraction from the ionosphere at the beginning of the storm) in the dayside ring current only several hours after the start of the storm main phase and mostly only in the outer parts of the ring-current region where the ions are not permanently trapped.

If the high energy ions in the storm-time ring current are accelerated mainly by inductive electric fields there does not seem to be any strong favouring of heavy ions within the energy range where the majority of the ring-current ions are found, as mentioned above. Observations of the composition of the ring-current ions above 20 keV may thus also tell us something about the dominating acceleration process(es).

### Concluding Remarks

In this report the importance of ionospheric ions in the ring current has been emphasized. The observational basis for the above discussion is very recent and quite limited in some respects. It suffers in particular from the lack of composition determinations for the main part of the ring-current population (between 17 and ~200 keV). Several of the conclusions drawn above are therefore rather hypothetical. It will be most interesting to see the results of the mass determination of the entire ring-current population which the AMPTE and Viking satellites are expected to carry out in the fall of 1984.

### References

- Adams, W.G.: Comparison of curves of the declination magnetographs at Kiev, Stonyhurst, Coimbra, Lisbon, Vienna and St. Petersburg. *Brit. Assoc. Rep.*, 201, 1880
- Adams, W.G.: On magnetic disturbances and earth currents. *Brit. Assoc. Rep.*, 463, 1881
- Axford, W.I.: Magnetospheric convection. *Rev. Geophys.* **7**, 421, 1969
- Balsiger, H., Eberhardt, P., Geiss, J., Young, D.T.: Magnetic storm injection of 0.9–16 keV/e solar and terrestrial ions into the high altitude magnetosphere. *J. Geophys. Res.* **85**, 1645, 1980
- Balsiger, H.: Composition of hot ions (0.1–16 keV/e) as observed by the GEOS and ISEE mass spectrometers and inferences for the origin and circulation of magnetospheric plasmas. *Adv. Space Res.* **1**, 289, 1981
- Balsiger, H.: On the composition of the ring current and the plasmasheet and what it tells about the sources of these hot plasmas. In: *High latitude space plasma physics*, B. Hultqvist and T. Hagfors, eds. New York: Plenum Publ. Corp. 1983
- Borg, H., Holmgren, L.-Å., Hultqvist, B., Cambou, F., Reme, H., Bahnsen, A., Kremser, G.: Some early results of the keV plasma experiment on GEOS-1. *Space Sci. Rev.* **22**, 511, 1978
- Collin, H.L., Sharp, R.D., Shelley, E.G., Johnson, R.G.: Some general characteristics of upflowing ion beams over the auroral zone and their relationship to auroral electrons. *J. Geophys. Res.* **86**, 6820, 1981
- Cowley, S.W.H.: Plasma populations in a simple open model magnetosphere. *Space Sci. Rev.* **26**, 217, 1980
- Ellis, W.: Correspondence in phenomena in magnetic storms. *Nature* **23**, 33, 1880
- Geiss, J., Balsiger H., Eberhardt, P., Walker, H.P., Weber, L., Young, D.T., Rosenbauer, H.: Dynamics of magnetospheric ion composition as observed by the GEOS mass spectrometer. *Space Sci. Rev.* **22**, 537, 1978
- Ghielmetti, A.G., Johnson, R.G., Sharp, R.D., Shelley, E.G.: The latitudinal, diurnal and altitudinal distributions of upflowing energetic ions of ionospheric origin. *Geophys. Res. Lett.* **5**, 59, 1978
- Gorney, D.J., Clarke, A., Croley, D.R., Fennell, J.F., Luhmann, J.M., Mizera, P.F.: The distribution of ion beams and conics below 8000 km. *J. Geophys. Res.* **86**, 83, 1981
- Heikkila, W.J., Pellinen, R.J.: Localized induced electric field within the magnetotail. *J. Geophys. Res.* **82**, 1610, 1977
- Heikkila, W.J., Pellinen, R.J., Fälthammar, C.-G., Block, L.P.: Potential and inductive electric fields in the magnetosphere during auroras. *Planet. Space Sci.* **21**, 1383, 1979
- Hoffman, R.A., Brachen, P.A.: Higher – order ring currents and particle energy storage in the magnetosphere. *J. Geophys. Res.* **72**, 6039, 1967
- Hultqvist, B.: Recent progress in the understanding of the ion composition in the magnetosphere and some major question marks. *Rev. Geophys. Space Phys.* **20**, 589, 1982
- Hultqvist, B.: On the origin of the hot ions in the disturbed dayside magnetosphere. *Planet. Space Sci.* **31**, 173, 1983
- Kaye, S.M., Johnson, R.G., Sharp, R.D., Shelley, E.G.: Observations of transient  $H^+$  and  $O^+$  bursts in the equatorial magnetosphere. *J. Geophys. Res.* **86**, 1335, 1981
- Lennartsson, W., Sharp, R.D., Shelley, E.G., Johnson, R.G., Balsiger, H.: Ion composition and energy distribution during 10 magnetic storms. *J. Geophys. Res.* **86**, 4628, 1981
- Lundin, R., Lyons, L.R., Pissarenko, N.: Observations of the ring current composition at  $L=4$ . *Geophys. Res. Lett.* **7**, 425, 1980
- Lundin, R., Hultqvist, B., Pissarenko, N., Zackarov, A.: The plasma mantle: Composition and other characteristics observed by means of the Prognoz-7 satellite. *Space Sci. Rev.* **31**, 247, 1982a
- Lundin, R., Hultqvist, B., Dubinin, E., Zackarov, A., Pissarenko, N.: Observations of outflowing ion beams on auroral field lines at altitudes of many earth radii. *Planet. Space Sci.*, in press 1982b

- Lyons, L.R., Evans, D.S.: The inconsistency between proton charge exchange and the observed ring current decay. *J. Geophys. Res.* **81**, 6197, 1976
- Lyons, L.R., Williams, D.J.: Storm associated variation of equatorially mirroring current protons, 1–800 keV at constant first adiabatic invariant. *J. Geophys. Res.* **81**, 216, 1976
- Lyons, L.R., Williams, D.J.: A source for the geomagnetic storm main phase ring current. *J. Geophys. Res.* **85**, 523, 1980
- Moore, T.E.: Modulation of terrestrial ion escape flux composition (by low-altitude acceleration and charge exchange chemistry). *J. Geophys. Res.* **85**, 2011, 1980
- Mozer, F.S., Cattell, C.A., Hudson, M.K., Lysak, R.L.K., Temerin, M., and Torbert, R.B.: Satellite measurements and theories of low altitude auroral particle acceleration, *Space Sci. Rev.* **27**, 155, 1980
- Pellinen, R.J., Heikkila, W.J.: Energization of charged particles to high energies by an induced substorm electric field within the magnetotail. *J. Geophys. Res.* **83**, 1544, 1978
- Peterson, W.K., Sharp, R.D., Shelley, E.G., Johnson, R.G., Balsiger, H.: Energetic ion composition of the plasmashet. *J. Geophys. Res.* **86**, 761, 1981
- Schopke, N.: A general relation between the energy of trapped particles and the disturbance field near the Earth. *J. Geophys. Res.* **71**, 3125, 1966
- Sharp, R.D., Carr, D.L., Peterson, W.K., Shelley, E.G.: Ion streams in the magnetotail. *J. Geophys. Res.* **86**, 4639, 1981
- Sharp, R.D. and Shelley, E.G.: Magnetosphere-ionosphere coupling through the auroral acceleration region. Report, Lockheed Palo Alto Research Labs., Palo Alto, Calif., 1981
- Sharp, R.D., Johnson, R.G., Lennartsson, W., Peterson, W.K., Shelley, E.G.: Hot plasma composition results from the ISEE-1 spacecraft. In: Energetic ion composition in the Earth's magnetosphere, R.G. Johnson, ed. Tokyo, Japan: Terra Scientific Publishing Co. and Dordrecht, Holland: D. Reidel Publishing Co. 1983
- Shelley, E.G., Johnson, R.G., Sharp, R.D.: Satellite observations of energetic heavy ions during a geomagnetic storm. *Geophys. Res.* **77**, 6104, 1972
- Shelley, E.G., Sharp, R.D., Johnson, R.G.: Satellite observations of an ionospheric acceleration mechanism. *Geophys. Res. Lett.* **3**, 654, 1976
- Smith, P.H., Hoffman, R.A.: Ring current particle distributions during the magnetic storms of December 16–18, 1971. *J. Geophys. Res.* **78**, 4731, 1973
- Spjeldvik, W.N., Fritz, T.A.: Energetic ionized helium in the quiet time radiation belts: Theory and comparison with observation. *J. Geophys. Res.* **83**, 654, 1978a
- Spjeldvik, W.N., Fritz, T.A.: Theory for charge states of energetic oxygen ions in the earth's radiation belts. *J. Geophys. Res.* **83**, 1583, 1978b
- Spjeldvik, W.N., Fritz, T.A.: Quiet time observations of equatorially trapped mega-electronvolt radiation belt ions with nuclear charge  $Z=4$ . *Z. Geophys. Res.* **83**, 4401, 1978c
- Ungstrup, E., Klumpar, D.M., Heikkila, W.J.: Heating of ions to superthermal energies in the topside ionosphere by electrostatic ion cyclotron waves. *J. Geophys. Res.* **84**, 4289, 1979
- Williams, D.J.: Sources, losses and transport of magnetospherically trapped particles. In: The magnetosphere, E.R. Dyer and J.G. Roederer, eds., p. 66. Dordrecht, Holland: D. Reidel 1972
- Williams, D.J.: Ring current composition and sources. In: Dynamics of the magnetosphere, S.-I. Akasofu, ed., p. 407. Dordrecht, Holland: D. Reidel 1979
- Williams, D.J.: Ring current composition and sources: On update. *Planet. Space Sci.* **29**, 1195, 1981
- Williams, D.J., Lyons, L.R.: The proton ring current and its interaction with the plasmopause: Storm recovery phase. *J. Geophys. Res.* **74**, 4195, 1974
- Young, D.T.: Synoptic studies of magnetospheric composition. Paper submitted to the philosophisch-naturwissenschaftlichen Fakultät of the University of Bern in partial fulfillment of the requirements for obtaining the "venia docendi", Bern, Feb. 1980
- Young, D.T., Balsiger, H., Geiss, J.: Correlations of magnetospheric ion composition with geomagnetic and solar activity. *J. Geophys. Res.* **87**, 9077, 1982

Received October 14, 1982; Revised January 7, 1983;  
Accepted January 27, 1983

# Ionic Composition of the Earth's Radiation Belts\* \*\*

W.N. Spjeldvik

Cooperative Institute for Research in Environmental Sciences, University of Colorado, Boulder, CO 80309, USA and Nordmann Research Ltd. Boulder, CO 80303, USA

**Abstract.** Several different ion species have been positively identified in the earth's radiation belts. Besides protons, there are substantial fluxes of helium, carbon and oxygen ions, and there are measurable quantities of even heavier ions. European, American and Soviet space experimenters have reported ion composition measurements over wide ranges of energies: at tens of keV (ring-current energies) and below, and at hundreds of keV and above. There is still a gap in the energy coverage from several tens to several hundreds of keV where little observational data are available. In this review emphasis is placed on the radiation belt ionic structure above 100 keV. Both quiet time conditions and geomagnetic storm periods are considered, and comparison of the available space observations is made with theoretical analysis of geomagnetically trapped ion spatial, energy and charge state distributions.

**Key words:** Radiation belts – Ion composition – Spacecraft data – Geomagnetic field – Radial diffusion – Charge exchange – Magnetic storms – Ion anisotropy – Trapped radiation.

## Introduction

The region of space occupied by the earth's radiation belts contains substantial fluxes of particles ranging in energy from below an electronvolt to above 100 MeV. No single spacecraft particle detector is capable of covering this great energy range, so a combination of detectors must be used, each with its own advantages and limitations. A particularly difficult type of measurement is the mass discriminating detection of ions between a few tens of keV and several hundred keV energies. Instruments that cover these energies have now been devised, but not yet flown in space.

The ionic composition of the radiation belts is both complex and time variable. Besides protons there are substantial fluxes of helium, carbon, nitrogen, oxygen

and even heavier ions. Theory predicts that at the higher energies in the MeV range the charge states of these ions should primarily be among the higher attainable. Unlike the energetic electron component of the trapping region, the ion fluxes are generally not distributed into an inner and an outer zone, but rather fill the entire stable trapping region with a peak flux location according to the ion energy. Early in-situ magnetospheric observations unambiguously determined the presence of energetic ions heavier than protons (Krimigis and Van Allen, 1967; Krimigis et al., 1970; Van Allen et al., 1970; Shelley et al., 1972). Subsequent experimental work gave much more detailed information about the distribution of these ions with the observable trapping region parameters: *L*-shell, energy and pitch angle (Sharp et al., 1974a, b, 1976a, b, 1977a, b, Shelley et al., 1974, 1976a, b, 1977; Johnson et al., 1974, 1975, 1977, 1978; Fritz and Williams, 1973; Fritz, 1976; Fritz and Wilken, 1976; Fritz et al., 1977; Fritz and Spjeldvik, 1978, 1979; Spjeldvik and Fritz, 1978a, b, c, d, 1981a, b, c; Blake, 1973, 1976; Blake et al., 1973, 1980; Blake and Fennell, 1981; Fennell et al., 1974; Lundin et al., 1980; Hovestadt et al., 1972a, b, 1978a, b, 1981; Mogro-Campero, 1972; Panasyuk et al., 1977, Panasyuk, 1980; Panasyuk and Vlasova, 1981). At hundreds of keV and MeV energies, when comparison is made between protons and heavier ions at equal total ion energy, the dominance of the heavy ions is indicated in segments of the radiation belts; on the other hand, flux comparisons at equal energy per nucleon generally favor protons. At lower energies, the recent works of Lundin et al. (1980), Lennartsson et al. (1981), Lennartsson and Sharp (in press 1982) and Young et al. (1982) demonstrate the variability of the ring current ionic composition during different geomagnetic and solar conditions. Significant variations of the high energy trapped ion composition are also known to take place, at least during some magnetic storms (e.g. Spjeldvik and Fritz, 1981a, b, c).

In recent years it has become clear that energetic heavy ions are particularly effective in causing internal damage to spacecraft memory and control systems (J.B. Blake, personal communication, 1980; McNulty, 1981; Adams and Partridge, 1982). Thus the detailed study of these ions is of practical as well as academic interest.

This review is organized into two experimental observation sections where quiet and disturbed time data are presented, a theory section where the physics of ra-

\* Based on an invited review paper given at the Symposium on Plasma and Energetic Particles in the Magnetosphere, EGS Meeting, 23-27 August 1982, Leeds, UK

\*\* Work done at the NOAA Space Environment Laboratory, Boulder, Colorado, USA

diation belt heavy ions is outlined together with modeling results, a section comparing these theoretical predictions with the available ion data, and a concluding section that discusses near-future research trends. An unavoidable bias in the selection of papers referred to is due to the author's research inclinations and the fact that it is not possible to read every paper in the field. Observational results from ion mass spectrometers are the subject of the companion review by Young (1983) (see also previous reviews by Shelley, 1979; Johnson, 1979); the present paper will therefore limit its scope to radiation belts ions above  $\sim 100$  keV per ion.

## Experimental Observations at Quiet Times

### *Instrumentation*

Significant technological advances in spacecraft borne instrumentation have occurred during the last decade obviating, in many cases, the uncertainty pertaining to the ionic identity. By virtue of the paucity of instruments utilizing solid state detectors, quite complicated detector systems have also been devised. Among the earliest problems were the distinction between energetic ions and electrons, suppression of electromagnetic radiation effects and particles penetrating the sides of the detector head. Ion fluxes can be deduced by comparing the counts in two identical solid state detector systems of which one has a thin metal foil across the entrance aperture, or by having a permanent "broom"-magnet in the collimator of a single detector head or by actively using such a magnet with multiple detectors to form a magnetic spectrometer. To some extent, particle species separation can also be achieved by precise pulse height discrimination. A common type of energetic ion detector flown by numerous groups during the seventies is the twin-element solid state design (Fritz and Cessna, 1975; Panasyuk et al., 1977). By combining the information on the energy deposited in both of the AlSiAu detectors it is possible, within a certain energy range, to determine both ion energy and mass. Such instruments have been flown on numerous spacecraft, and this type of detector system can be operational from several hundred keV per ion to tens of MeV per ion, with ion identification, and down to  $\sim 14$  keV per ion, without mass discrimination, depending on the detector thickness and the design of the adjoining pulse height discrimination system. For measurements of more energetic ions, multiple detector configurations have been designed, generally with increasing detector thickness away from the collimator opening; known absorbers may also be placed between the detector elements (forming a range telescope). Shielding against unwanted radiation can be done by passive means (thick walls) or by an active system (e.g. guard ring scintillators); for a review of energetic particle instruments, see Spjeldvik (1981a).

More modern designs elicit a three parameter ion analysis by measuring both the energy deposited in each of two or more detectors and the time of flight between two of them. From this one obtains a more precise ion identification; however, very fast electronic circuits are necessary in order to measure the particle transit time over path lengths as short as  $\sim 10$  cm or

less (Williams et al., 1978). A hybrid instrument combining a proportional counter, solid state detector and a scintillator was successfully used by Hovestadt and Vollmer (1971) on the S3-2 spacecraft for measuring very energetic ions and low energy cosmic rays. A variation of this instrument, which also utilizes an electric field deflection in a 20 kV potential field, was included in the ISEE-1 and ISEE-3 payloads (Hovestadt et al., 1978a). This instrument also permits information about the ionic charge states to be gathered. The energy coverage is primarily in the multi-MeV per ion range. New instruments are currently being developed to extend the data coverage towards lower energies to bridge the gap between the upper energy limit of spacecraft mass spectrometers, which is typically a few tens of keV (Balsiger et al., 1976), and the practical lower energy bound of the mass discriminating solid state detector systems, which is typically 600 keV per ion (Fritz, 1979). Since no data are available from these new instruments, their discussion is deferred to the last section of this review.

The disadvantage with most of the older "proton" (i.e. total ion) detectors is the fact that the ion species remains undetermined. The instruments were most often beam-calibrated with protons, and the mistaken conclusion may be drawn that the observed ions in space are only protons. The latter may only be a valid conclusion in conjunction with other collaborative evidence, such as simultaneous mass-spectrometer or solid state mass discriminating detector data. However, much of the "proton" observation presented in the early literature really represents ion counts within the proton channel passbands, so it is possible that neither the species identification nor the quoted ion energy is correct. This should be kept in mind while re-examining and utilizing older ion ("proton") data.

### *Radiation Belt Protons*

Equatorial observations of radiation belt ion ("proton") fluxes between 78.6 keV and 22 MeV per ion are shown in Fig. 1. These data were obtained with two, separate, twin-element solid state detectors on Explorer 45 (Fritz, 1979; Spjeldvik, 1981a) during the early half of June 1972. The use of a thin solid state detector element for the higher energy passbands and suitable pulse height discriminator logic made most of the data channels insensitive to incident electrons. The ion flux averages shown in this figure (from Fritz and Spjeldvik, 1979) were constructed statistically over  $\sim 50$  quiet-time spacecraft passes, assuming that the ions are indeed protons. Evidence to that effect is only circumstantial; the theoretical calculations of Spjeldvik (1977) demonstrated that the Explorer 45 quiet-time ion data at  $\sim 100$  keV- $\gtrsim 1$  MeV could only be simulated by theoretical calculations if these ions were protons and not helium or oxygen ions. It was also found that the radial flux maximum is systematically displaced towards lower energies with increasing ion energy in this range. Spectrally, the Explorer 45 equatorial ion (proton) observations generally show steep spectra above  $\sim 100$  keV at  $L$ -shells beyond  $L \sim 4.5$ , and a spectral maximum is formed at a few hundred keV at the lower  $L$ -shells. Such positive spectral gradients could be un-

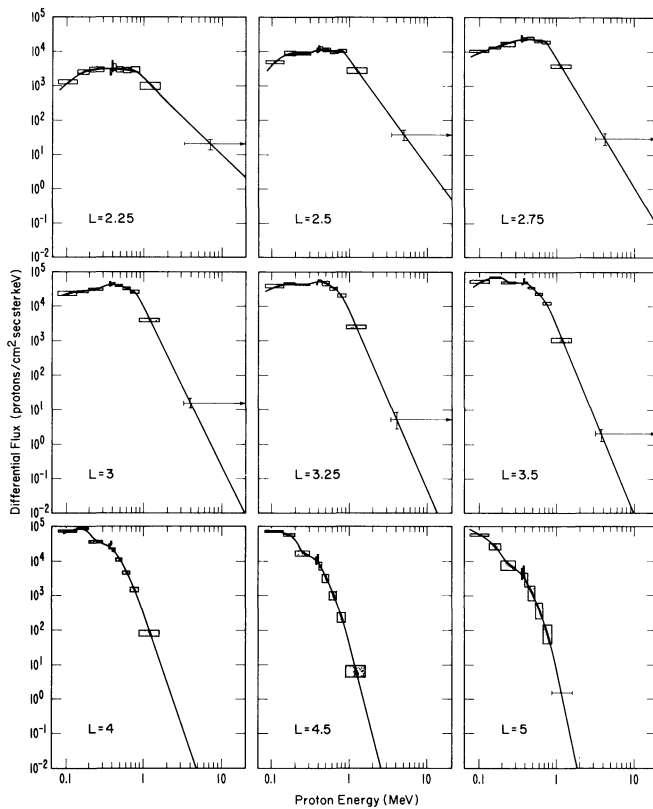


**Fig. 1.** Energy spectra of equatorial radiation belt protons in the range 0.1–20 MeV deduced from Explorer 45 observations during the geomagnetically quiet period 5–15 June 1972. The data extend over  $L$  shell of 2.25, 2.5, 2.75, 3, 3.26, 3.5, 4, 4.5, and 5. The solid curve in each panel is drawn as the best fit to the data points for the differential energy channels and as an analytic approximation to the quasi-integral channel (see Fritz and Spjeldvik, 1979). The data are represented by the energy passband (horizontal extent) and the standard deviations (vertical extent)

stable to plasma wave growth, but that aspect has yet to be fully explored in the radiation belts.

### Helium Ions

Instruments capable of discriminating heavy ions from protons have been flown on a number of spacecraft, including Injun-4, Injun-5, Ogo-4, Explorer 45, ATS-6, S3-2, Cosmos-900, Molniya-2 and many others. Figure 2 shows examples of the proton and helium ion results obtained where four of the channels (effective at 1–50 MeV) measured protons and two of the channels (effective at 4–60 MeV per ion) measured helium ions. The orbits of Cosmos-900 and Molniya-2 were such that substantial ranges of  $B/B_0$ -values were sampled ( $B$  being the magnetic induction at the spacecraft and  $B_0$  its equatorial value on the same field line). When converted to flux units results from this class of instruments have been quite revealing, and we have learned that ions with nuclear charge  $Z > 1$  can be dominant at certain energies and locations in the trapping region (Fritz and Wilken, 1976; Panasyuk et al., 1977; Fritz and Spjeldvik, 1979). A comparative result from the ATS-6 spacecraft is illustrated in Fig. 3 (from

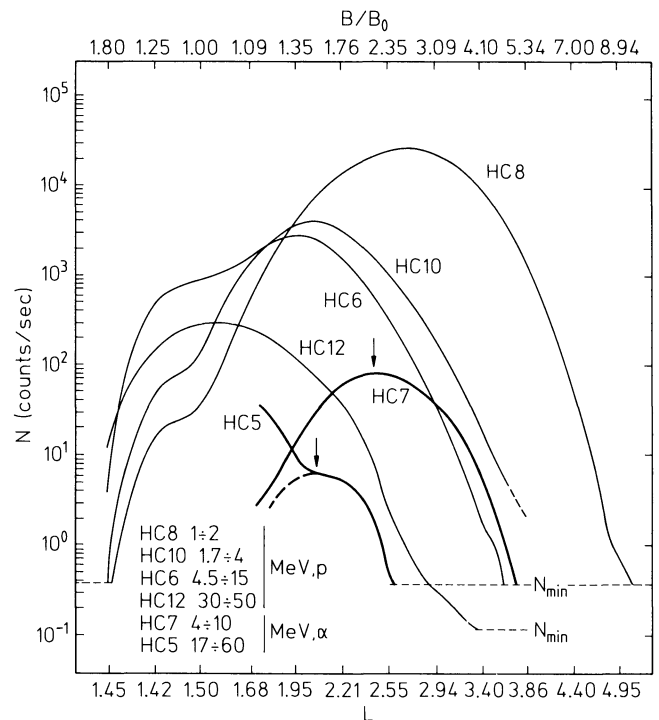


**Fig. 2.** Ion (proton) observations presented as radial profiles in four passband: HC8 at 1–2 MeV, HC10 at 1.7–4 MeV, HC6 at 4.5–15 MeV and HC12 at 30–50 MeV; and alpha-particle (helium ion) observations in two passbands: HC7 at 4–10 MeV per ion and HC5 at 17–60 MeV per ion. The data were obtained with the Molniya-2 spacecraft (for details, see Panasyuk et al., 1977)

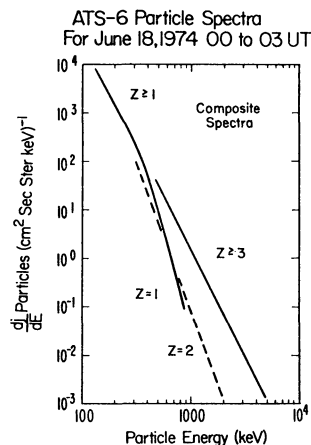


**Fig. 3.** Equatorial heavy ion spectra monitored with the satellite ATS-6 in the geostationary orbit at  $L=6.6$ . The instruments did not permit determination of ion charge states but did discriminate between ion mass. The leftward solid curve represents  $Z \geq 1$  ions at  $E < 350$  keV and  $Z=1$  ions (i.e. protons) at higher energies. The simultaneous spectral observations indicate that heavy ions ( $Z \geq 3$ ) dominates at energies above a few hundred keV per ion. These data are taken during a disturbed period on 18 June, 1974 (from Fritz and Wilken, 1976), but similar results also apply for quiet conditions, (e.g. Spjeldvik and Fritz, 1978b)

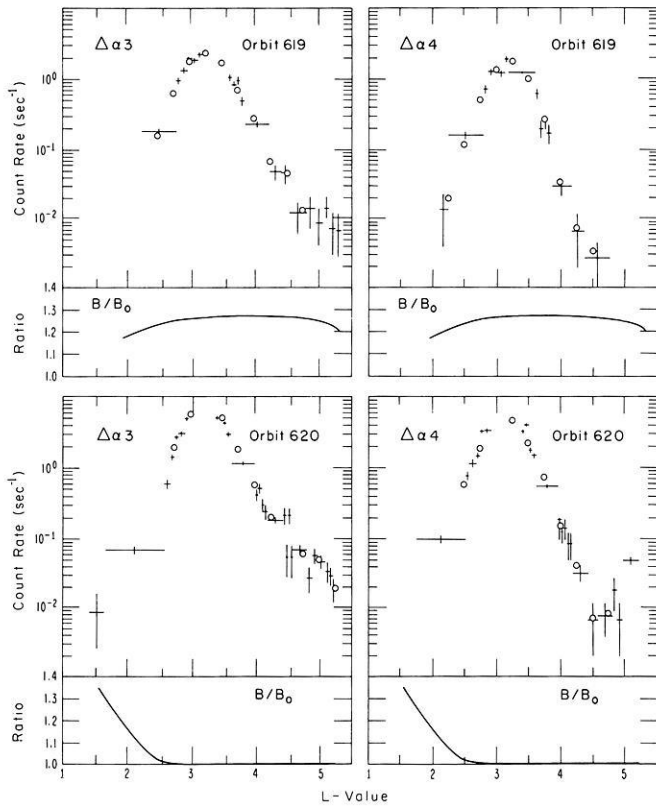


**Fig. 4.** Radial profiles of helium ions in the earth's radiation belts as observed with Explorer 45 during two consecutive outbound spacecraft passes on June 1, 1972. The passbands are:  $\Delta\alpha 3$ : 1.16–1.74 MeV per ion and  $\Delta\alpha 4$ : 1.74–3.15 MeV per ion. The data are represented by crosses where the horizontal error bar indicates the accumulation  $L$ -shell interval and the vertical error bars the statistical uncertainty in the data. The circles are interpolation points used in the subsequent analysis. The sub-panels indicate the  $B/B_0$ -values of the spacecraft location where  $B/B_0=1$  for the exact geomagnetic equator (Fritz and Spjeldvik, 1978)

Fritz and Wilken, 1976) where measurements of helium ions, CNO (carbon nitrogen, oxygen) ions are compared with those of protons using mass discriminating data channels. It is evident that at this (geostationary) location the  $Z > 1$  ions dominate over protons when compared at equal total ion energy for energies beyond  $\sim 1$  MeV.

Observations of radiation belt helium ions at the geomagnetic equator over a range of  $L$ -shells extending from the top of the atmosphere to  $L \sim 5.2$  were made with Explorer 45. Four examples of radial helium ion profiles in the lower MeV energy range are shown in Fig. 4 together with the orbital  $B/B_0$ -values (Fritz and Spjeldvik, 1978). Notice that the helium ion count rates are generally higher when the orbit is close to the magnetic equatorial plane (lower panels in this figure). To assess the quiet time structure of radiation belt helium ions, a statistical study was made of  $\sim 50$  Explorer 45 spacecraft orbits through the heart of the trapping region. Fritz and Spjeldvik (1979) found that the radial distributions are fairly narrow with a peak around  $L \sim 3.25$  and (full width half maximum) (FWHM) of  $\Delta L \sim 0.5$ , at energies in the lower MeV range. Ra-

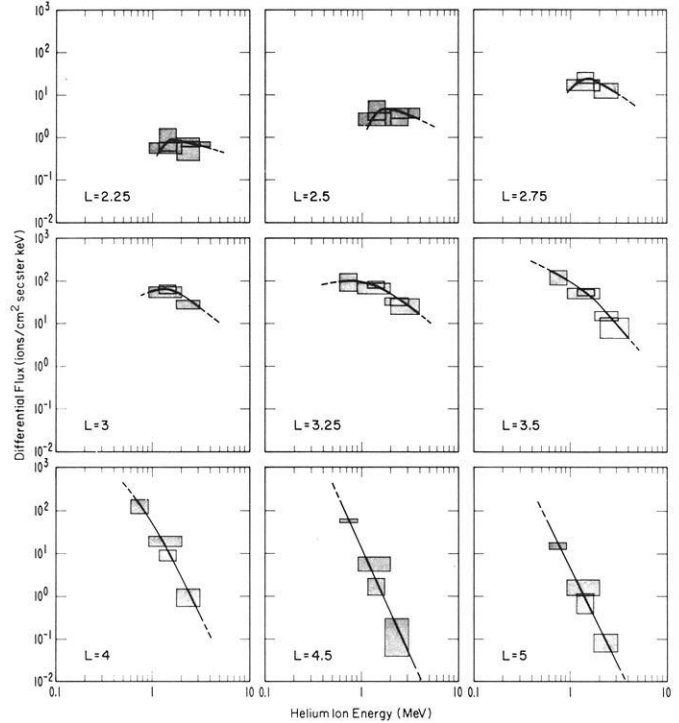


**Fig. 5.** Energy spectra of equatorial radiation belt helium ions deduced from mass selective ion observations on Explorer 45 during the geomagnetically quiet period 1–15 June, 1972. The spectral coverage corresponds to unambiguous helium ion observations in the  $\Delta\alpha 3$  and  $\Delta\alpha 4$  channels (1.16–1.74 and 1.74–3.15 MeV per ion) and heavy ion observations ( $Z \geq 2$ ) in the  $\Delta\alpha 1$  and  $\Delta\alpha 2$  channels. The data are given at  $L=2.25, 2.5, 2.75, 3, 3.25, 3.5, 4, 4.5$  and  $5$  (Fritz and Spjeldvik, 1979)

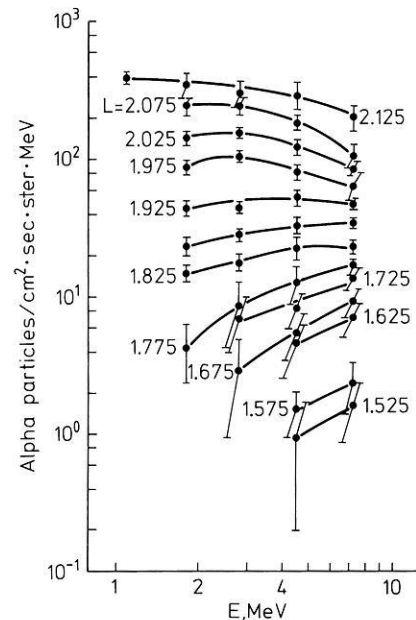


**Fig. 6.** Differential energy spectra of energetic helium ions in the inner radiation belt. The  $L$ -shell coverage extends from  $L = 1.525$  to  $L = 2.125$  with  $B/B_0 \approx 1.3$ . These data were obtained with the OV1-19 spacecraft (from Blake et al., 1973)

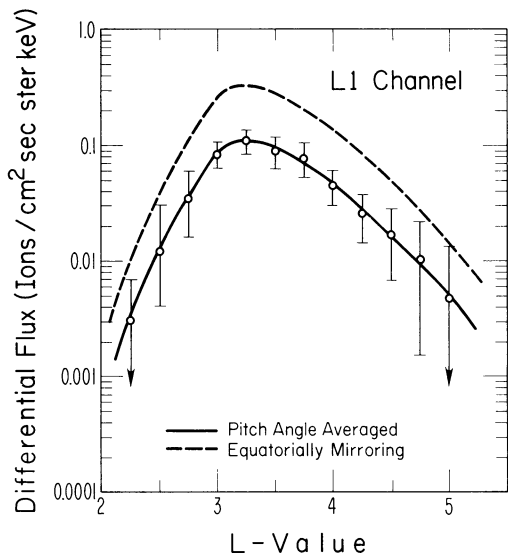


**Fig. 7.** Radial profile of the Explorer 45 quiet time observations in channel L1 during the period June 1–15, 1972. The solid line shows the pitch angle averaged observation, and the vertical error bars indicate the standard deviation in the data set at each quarter integral  $L$  shell. The dashed line depicts the calculated equatorially mirroring flux assuming that the observed heavy ions are atomic oxygen ions. The energy passband is 1.82–4.8 MeV per ion (from Spjeldvik and Fritz, 1978d)

diation belt helium ion spectra are exhibited in Fig. 5 (from Fritz and Spjeldvik, 1979) where the horizontal error indications depict the width of the passbands and the vertical error bars the statistical uncertainty. Similar to that of protons, the helium ion spectra are found to be quite steep beyond  $L \sim 4$ , and at lower  $L$ -shells a

noticeable hardening is seen which results in fairly flat spectra with a possible spectral turnover below  $L \sim 3$ ; the latter cannot be stated with certainty from these data. However, corroborating data at lower  $L$ -shells (from Blake et al., 1973) shown in Fig. 6 do indeed demonstrate the positive spectral slopes of MeV helium ions below  $L \sim 2$  at the geomagnetic equator.

#### CNO and Heavier Ions

The pulse height discriminator systems of two element solid state detectors can also be designed to distinguish CNO and heavier ions from the lighter ones, at least at some energies. Fig. 7 depicts the results from Explorer 45 at 1.8–4.8 MeV per ion for CNO ions (Spjeldvik and Fritz, 1978d). It was found that the CNO radial profile is broader than that of helium ions; some of this apparent width could be due to the wide energy acceptance ( $\Delta E = 3$  MeV). Unfortunately, only one CNO ion data channel on Explorer 45 had high enough count statistics to be used in the analysis, and this prevents information about the spectral shapes of CNO ions with this spacecraft.

Ions heavier than oxygen could not be determined with certainty from the Explorer 45 instruments during quiet times. Spjeldvik and Fritz (1981c) have placed an upper limit of  $\sim 0.1$  ions/cm<sup>2</sup> s ster integrated over energies beyond  $\sim 10$  MeV per ion for ions with nuclear charge  $Z \geq 9$  during the period 1–15 June 1972.

#### Observations of Carbon and Oxygen Ions in Discrete Channels

The twin detector instruments described in the foregoing are not able to distinguish between the ionic charge

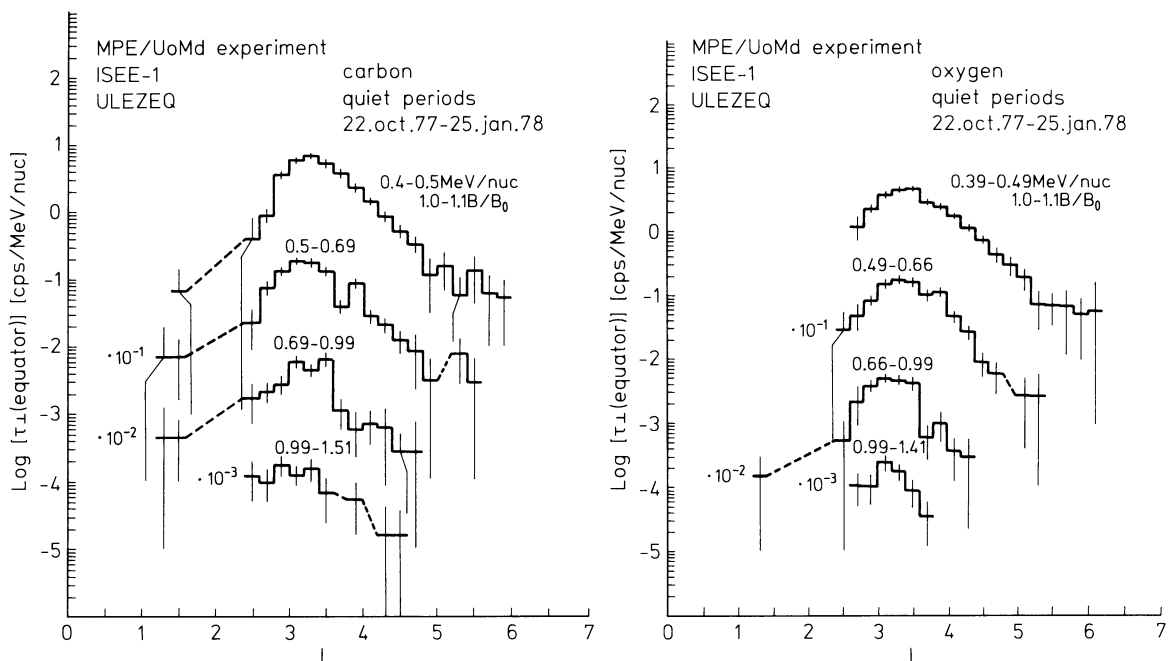


**Fig. 8.** Observations of carbon and oxygen ions in distinct passbands made with the ULEZEQ detector system on the ISEE-1 spacecraft averaged over a number of selected quiet periods during 22 October 1977 through 25 January 1978. *Left panel:* Carbon ion data in four passbands 4.80–6.00, 6.00–8.28, 8.28–11.88 and 11.88–18.12 MeV per ion. *Right panel:* Oxygen ion data in four passbands: 6.24–7.84, 7.84–10.56, 10.56–15.84 and 15.84–22.56 MeV per ion (for details, see Hovestandt et al., 1981)

states, and the discrimination between carbon, nitrogen and oxygen ions is also very difficult owing to the similar behavior of these ions in the MeV range. An instrument able to carry out measurements with both mass and charge resolution in the MeV range was flown on ISEE-1. Using data from this instrument, Hovestadt et al. (1978b) were, for the first time, able to report separate measurements of the carbon and oxygen ion fluxes in the earth's radiation belts. This instrument is also capable of measuring helium ions with significant energy resolution at  $E=0.39$ – $2.18$  MeV per nucleon in six passbands (multiplication by four gives the total ion energy). As one might expect, they found that the more energetic helium ions have their flux maxima at lower  $L$ -shells.

The results for C and O ions deduced from ISEE-1 observations are shown in Fig. 8. For each ion species there are four data channels. For carbon ions these are:  $E=0.40$ – $0.50$ ,  $E=0.50$ – $0.69$ ,  $E=0.69$ – $0.99$  and  $E=0.99$ – $1.51$  MeV per nucleon, and multiplication by 12 gives the total carbon ion energy passbands. For oxygen ions these are almost identical:  $E=0.39$ – $0.49$ ,  $E=0.49$ – $0.66$ ,  $E=0.66$ – $0.99$  and  $E=0.99$ – $1.41$  MeV per nucleon, and multiplication by 16 gives the total oxygen ion energy passbands. For both ion species one observes an inward shift of the flux peak location with increasing ion energy. The count-rate comparison also shows that both C and O ions are present in substantial quantities.

#### Ion Abundance Comparisons

It is of interest to compare the flux intensities of protons with those of the heavier ions, and the relative abundances of the heavy ions. Figure 9 shows the results of calculating the ratio of helium ion flux to that of protons using the Explorer 45 statistical average during 1–15 June 1972 (from Fritz and Spjeldvik, 1979). The shaded areas indicate the estimated uncertainty in the final result. This comparison, which was made at equal total ion energy, demonstrates that the He/p ratio well exceeds unity in the outer radiation zone at the higher energies. At  $L=5$ , say, the value of this ratio is  $\sim 10$  at 3 MeV per ion. A significant variation of the He/p ratio is also evident in recent Soviet results; Fig. 10 shows data reported by Panasyuk et al. (1977) using observations made with the Molniya-2 spacecraft. Although these data do not pertain to the geomagnetic equator or to fixed  $B/B_0$ -values, the same trend is evident, namely a strong increase in the He/p ratio with higher  $L$ -shells. The lower part of this figure also shows the observed He/p ratio calculated at equal energy per nucleon for the same spacecraft orbit. Statistical results have also been obtained for the He/p ratio using the Explorer 45 quiet-time observations in the geomagnetic equatorial plane ( $B/B_0 \cong 1$ ). These results, which are shown in Fig. 11, demonstrate that the He/p values at equal energy per nucleon are small, usually in the range  $10^{-3 \pm 1}$  at these  $L$ -shells and that a systematic energy variation is seen with a minimum located at several hundred KeV per nucleon. This minimum is not evident in the results of Panasyuk et al. (1977) quoted above, this could be due to the Molniya-2 orbit or it could be a temporal feature dependent on the injection and diffusion pre-history of these particles. One should

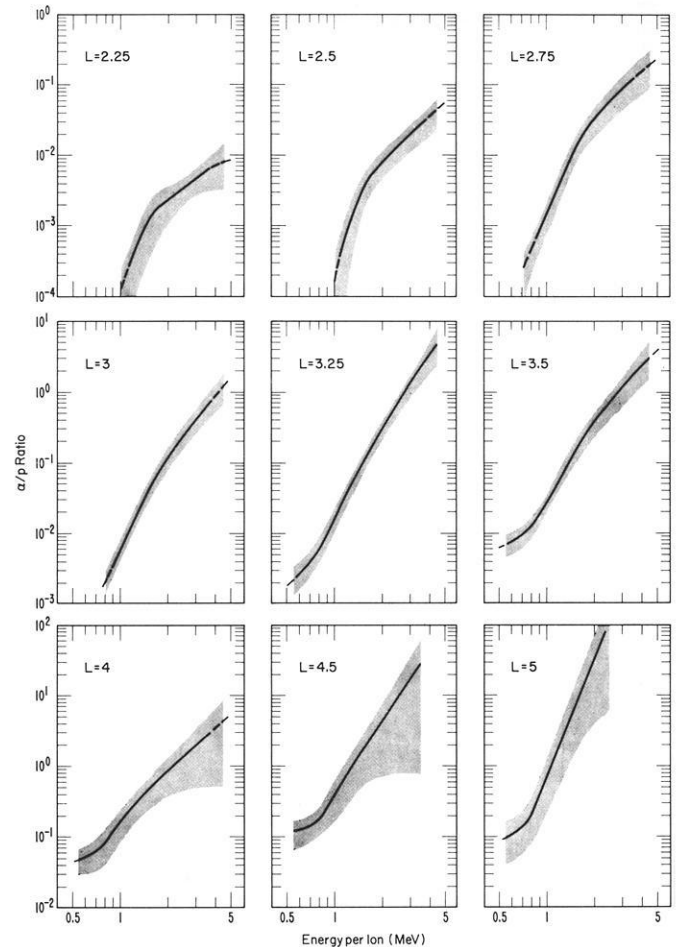


**Fig. 9.** Calculated quiet time equatorial He/H (or  $\alpha/p$ ) ion flux ratio in the earth's radiation belts during geomagnetically quiet conditions. The data were reduced based on simultaneous ion (most likely proton) and helium ion data obtained with the Explorer 45 spacecraft during 1–15 June 1972. The ratios are given at equal total ion energy in the range 0.5 to 5 MeV per ion, and the shaded areas depict the statistical uncertainty in the derived ratios (Fritz and Spjeldvik, 1979)

point out that the observed He/p ion flux ratio values at equal energy per nucleon are more than an order of magnitude lower than the solar wind He/p abundance ratio which (by number density) can vary from less than 1% to more than 10% with perhaps a mean of  $\sim 4\%$  (e.g. Hirschberg, 1973, 1975). For further details of the solar wind ion composition see Bame et al. (1975).

It is of interest to compare the CNO/p ion flux ratio, and the statistical results from Explorer 45 for CNO ions given in Fig. 7 together with the proton data in Fig. 1 yield the comparison (at equal total ion energy) shown in Fig. 12 (from Spjeldvik and Fritz, in press 1982). As in the case of the He/p ratio, the CNO/p ratio at equal energy per ion also shows a significant positive gradient with  $L$ -shell, and such that the CNO/p ratio exceeds unity at  $L > 4.5$ . This observed trend, from the 50-orbit statistical data of Explorer 45 during 1–15 June 1972, is also consistent with the ion abundance result from ATS-6 at the geostationary orbit at  $L \sim 6.6$  shown in Fig. 8. When compared at equal en-

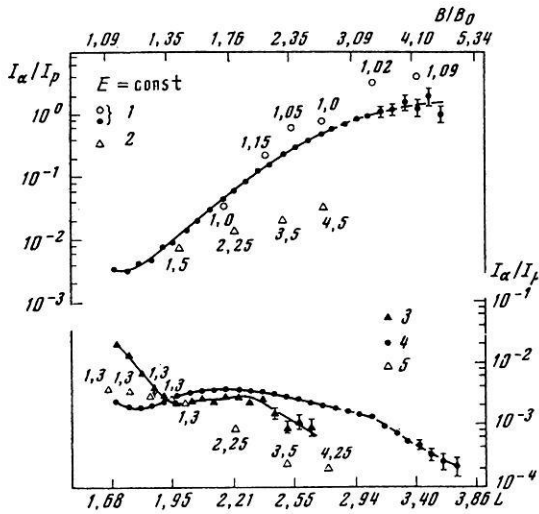


**Fig. 10.** Determination of the He/H ratio versus  $L$ -shell based on data from the Molniya-2 spacecraft and comparison with OV1-19 data. The upper abscissa scale also indicates the  $B/B_0$ -values along the Molniya-2 orbit for all solid (filled) data symbols. *Upper curves:* The He/H ratio at equal energy per ion: solid circles are Molniya-2 data at 4.5–15 MeV per ion and open circles are Molniya-2 data for another spacecraft pass closer to the magnetic equator (with  $B/B_0$ -values indicated for each data point). Open triangles show the comparative data from OV1-19 at 5.55 to 9 MeV per ion; the  $B/B_0$ -values for this spacecraft orbit are also indicated for each data point. *Lower curves:* The He/H ratio at equal energy per nucleon: Solid triangles denote Molniya-2 data at 4.5–15 MeV per nucleon and solid circles denote Molniya-2 data at 1–2 MeV per nucleon. For comparison also OV1-19 data are shown as the open triangles; the  $B/B_0$ -values for this spacecraft orbit are also indicated for each data point

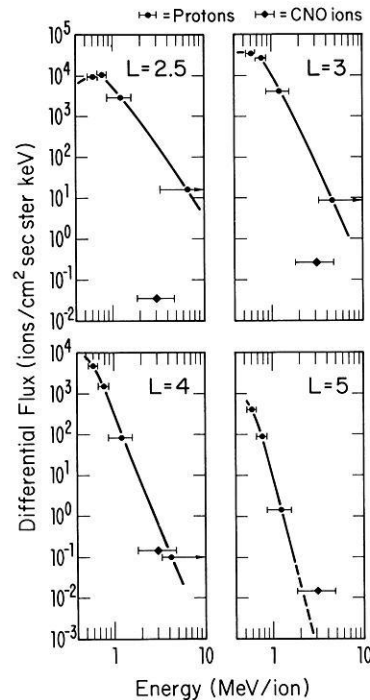


**Fig. 12.** Comparison of quiet time ion (most likely proton) and CNO ion fluxes in the earth's radiation belts at  $L=2.5, 3, 4$  and  $5$  using simultaneous observations made with Explorer 45 during 5–15 June 1972. The horizontal bars depict the energy passbands for the different ion species (from Spjeldvik and Fritz, 1982)

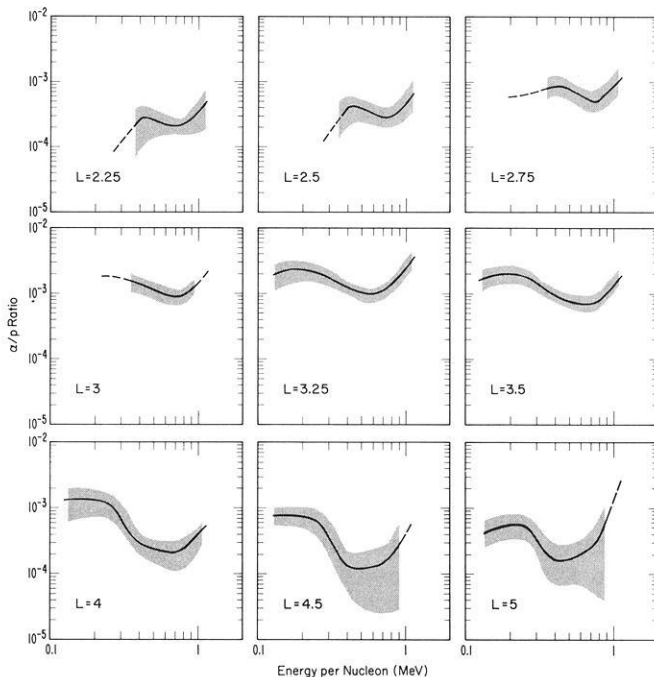


**Fig. 11.** Calculated equatorial quiet time He/H ion flux ratios at equal energy per nucleon in the earth's radiation belts. The results utilize the same data base as given in Fig. 16, and the shaded areas depict the statistical uncertainty in the derived results

ergy per nucleon, the CNO/p ratio would be very small throughout most of the radiation belts, however.

It is well known that if the MeV heavy ions in the radiation belts have their origin in the sun (via the solar wind or solar energetic particles) or in low energy galactic cosmic rays then, by the elemental abundance, the geomagnetically trapped C and O ion flux intensities should be roughly comparable. If these ions had their source in the terrestrial atmosphere/ionosphere (via the polar wind and/or upward auroral ion jets followed by acceleration to MeV energies) then the C/O flux ratio would be very small, of the order  $\sim 10^{-5}$  (e.g. Blake, 1973). It is here assumed that some unknown (implausible) process does not exist that could strongly favor C over O ions.

It is quite clear that the fluxes of carbon and oxygen ions are of comparable intensity, however; and thus, pending confirmation by independent means, the results of Hovestadt et al. (1978b, 1981) illustrated in Fig. 8 establish the extraterrestrial origin for MeV radiation belt ions. A detailed co-comparison is given in Fig. 13 which gives the C/O flux ratio at equal energy per nucleon. At  $L=2.8$ – $3.8$  this ratio varied between 1.3 at 400 keV per nucleon to 4.1 at 1.2 MeV per nucleon. When such comparison is made at equal total ion energy the ratio is about unity (within a factor of two). Although these ISEE-1 results are given for a single pass through the radiation belt trapping region, one would expect to find long term stability during quiet times (as evidenced by the Explorer 45 data discussed above). This contrasts the ion composition results obtained by the mass spectrometers, at tens of keV en-

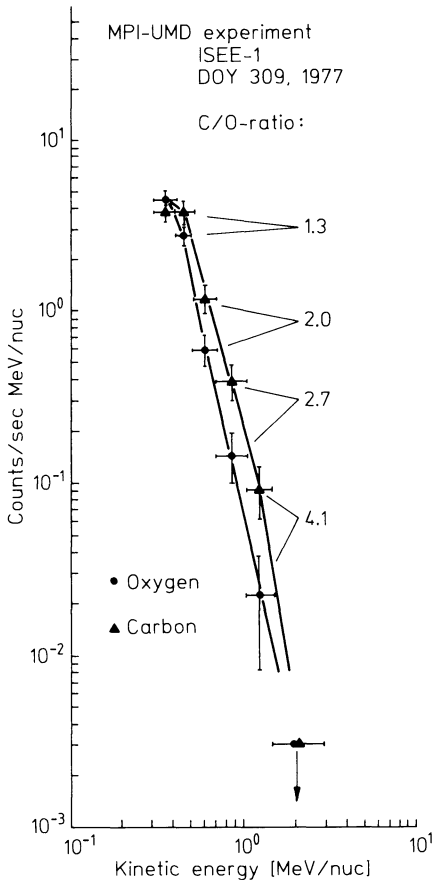


**Fig. 13.** Direct comparison of simultaneously derived spectra of carbon and oxygen ions in the earth's radiation belts at  $L = 2.8$ – $3.8$ . The data were obtained with the ULEZEO detector system on the ISEE-1 spacecraft. These comparisons were made at equal energy per nucleon (from Hovestadt et al., 1978b)

ergies and below, where substantial time variability on the time scale of hours and days in the ionic composition is found (Lyons and Moore, 1981; Lundin et al., 1980; Lennartsson et al., 1981; Lennartsson and Sharp, 1982).

#### Ion Anisotropies

Observed pitch angle anisotropies of energetic electrons have yielded significant insight into the dynamical processes operating on these particles (Lyons et al., 1971, 1972; Lyons and Thorne, 1973). Studies of anisotropy characteristics of energetic ions could likewise give valuable information about scattering processes and plasma waves such as ion-cyclotron waves. Joselyn and Lyons (1976) have delineated the energy ranges and spatial locations of such interactions for protons; however, much work remains to be done, both from the theoretical and experimental sides, for different ion species.

Specific studies of angular particle distributions have been made by Williams and Lyons (1974a, b), and Lyons and Williams (1975, 1976). Statistically, during a two-week geomagnetically quiet period, the proton anisotropies have been determined from the Explorer

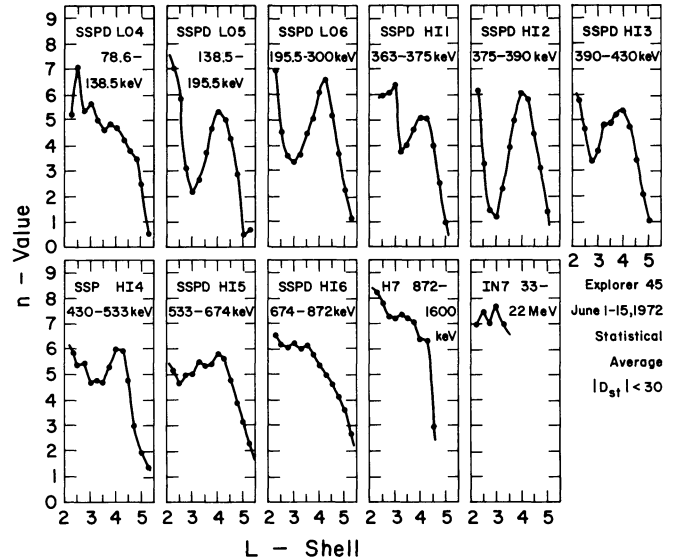


**Fig. 14.** Determination of the pitch angle anisotropy  $n$ -value based on the assumed functional relation  $j(\alpha_0) = j(\pi/2) \sin^n \alpha_0$ . The data represents a statistical average of  $\sim 50$  Explorer 45 passes through the radiation belts when  $|D_{st}| < 30$  nT during 1–15 June 1972

45 data by plotting the observed omnidirectional fluxes versus the  $B/B_0$ -parameter (Fritz and Spjeldvik, 1979) and those results show that the proton pitch angle distributions become somewhat more anisotropic with lower  $L$ -shells and with higher energies but also that some deviations from a monotonic trend occurs at some  $L$ -shells and energies. Plotting these data versus  $L$ -shell with  $\Delta L = 0.25L$  resolution yields the result shown in Fig. 14. In this graph the  $B/B_0$ -dependences have been reduced to a single parameter fit, assuming a functional relation

$$J = J_0 \sin^n \alpha_0 = J_0 (B/B_0)^{-n/2}$$

where  $\alpha$  is pitch angle, subscript-0 denotes equatorial ( $B/B_0 = 1$ ) quantities,  $J$  is ion flux, and the exponent (anisotropy index)  $n$  is the single parameter anisotropy information. One should, of course, be aware that not every pitch angle distribution in the trapping region can be parametrized this way. Injection effects,  $L$ -shell splitting, preferential angular scattering at some pitch angles and  $B$ -field time variability are examples of processes that may produce other types of angular distributions. Nevertheless, much of the radiation belt ion pitch angle distributions are to a first approximation expressible by such a functional relation. A secondary reason for plotting the proton data this way is that it facilitates direct comparison with other ion species where complete pitch angle distributions may not be available, but where an  $n$ -index often can be deduced.

The corresponding Explorer 45 anisotropy record for energetic helium ions in the lower MeV range has been studied by Fritz and Spjeldvik (1978). As in the case of protons, these statistical data appear to be reasonably well matched by the above assumed functional form. For MeV helium ions no systematic  $L$ -shell variation of the anisotropy  $n$ -index is deduced, and this is

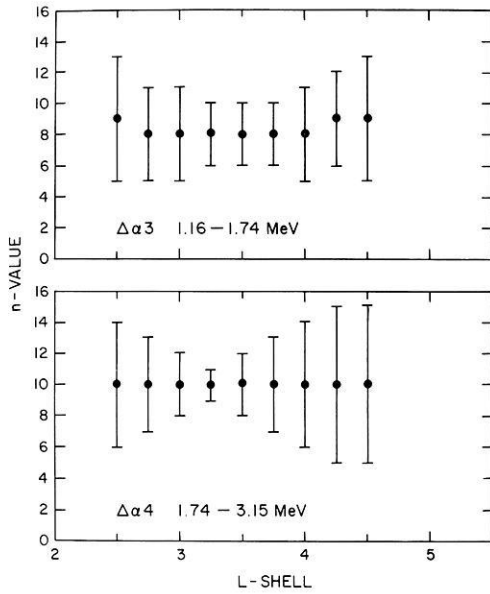


**Fig. 15.** Equatorial helium ion anisotropy radial profile using the same data as given in Fig. 23 but with a resolution of  $\Delta L = 0.25$  from  $L=2.5$  to  $L=4.5$ . The  $n$ -values are given with estimated errorbars according to the data spread at a given  $L$ -shell

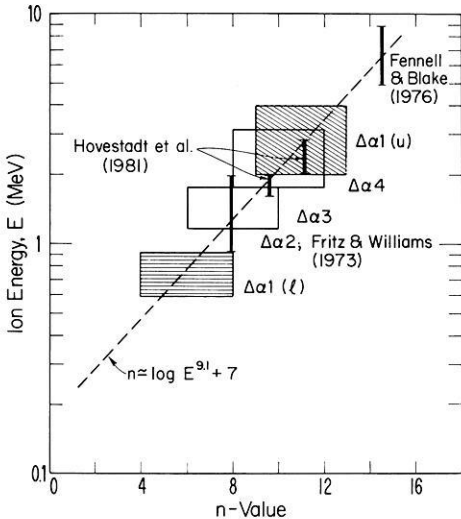


**Fig. 16.** Equatorial derivation of an empirical energy dependence of the radiation belt helium ion anisotropy index  $n$  based on results from several spacecraft. A functional relation  $n \approx 7 + 9.1 \log E$  with  $E$  in MeV per ion is deduced (from Fritz and Spjeldvik, 1982)

explicitly illustrated in Fig. 15 (from Fritz and Spjeldvik, 1982) although the errors bars are large enough to allow for significant variation. Of course the energy coverage is limited, and one cannot exclude an  $n(L)$ -dependence at other helium ion energies. There is, however, a systematic variation of the  $n$ -index with helium ion energy. That finding is illustrated in Fig. 16 where a dependence  $n(E) \sim 7 + 9.1 \log(E/E_0)$  is deduced with  $E_0 = 1$  MeV. This empirical fit appears to provide a fair description of all the Explorer 45, ISEE-1 and S3-2 helium ion anisotropy data within the plasmasphere.

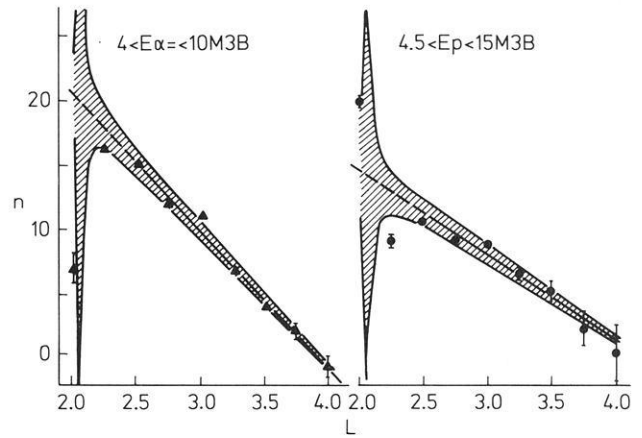


**Fig. 17.** Pitch angle anisotropy index  $n$  versus  $L$ -shell of observation, but for varying  $B/B_0$ -value with  $L$ -shell. The data were obtained with the Molniya-2 spacecraft on 25 October 1975. *Left panel:*  $n$ -value versus  $L$ -shell for 4–10 MeV per ion helium ions (1–2.5 MeV/nucleon). *Right panel:*  $n$ -value versus  $L$ -shell for 4.5–15 MeV ions (assumed to be protons) (from Panasyuk and Vlasova, 1981)

In contrast to these results, Panasyuk and Vlasova (1981) have deduced a rather strong dependence of the  $n$ -index with  $L$ -shell. Their result is reproduced in Fig. 17 and is based on proton and helium ion data from the Molniya-2 spacecraft where wide proton and helium ion data channels, 4.5–15 and 4–10 MeV per ion, respectively, were used. It is conceivable that at the higher  $L$ -shells primarily the lower energy protons and helium ions are measured, while at the lower  $L$ -shells the counts would come from the more energetic ions (as one might expect from theoretical considerations). If so, then an energy dependence can be seen as an apparent  $L$ -dependence and vice versa. The Molniya-2 data were reduced using only two spacecraft orbits from which a two point anisotropy determination was made; this could leave the result sensitively dependent on the accurate orbit parameters and the magnetic field model; the latter was taken as a dipole. M. Panasyuk (personal communication, 1982) has also pointed out that if the distribution fails to follow a  $\sin^n \alpha_0$  dependence at large  $B/B_0$  values then unreliable  $n$  versus  $L$  determinations could result. The differences between the Explorer 45 and the Molniya-2 results were intriguing enough to pursue the investigation further, however. Figure 18 shows the results of plotting all available helium pitch angle anisotropy information versus  $L$ -shell, regardless of the ion energy. The data are clearly significantly less well ordered, and it is difficult to deduce a common  $L$ -shell variation of the  $n$ -index for helium ions. In particular, the very low  $n$ -values deduced by Panasyuk and Vlasova (1981) at  $L > 3.5$  (the helium ion fluxes would become isotropic just below  $L=4$ ) are not supported by the other data. On the other hand, the high  $n$ -values observed near  $L \sim 2.5$  by these researchers agree well with the observations of Fennell and Blake (1976).

A recent result by Blake and Fennell (1981) indeed shows that a single  $n$ -value does not describe the helium anisotropy at large  $B/B_0$ -values. Their result is given in Fig. 19 for helium ions at 392–960 keV per ion

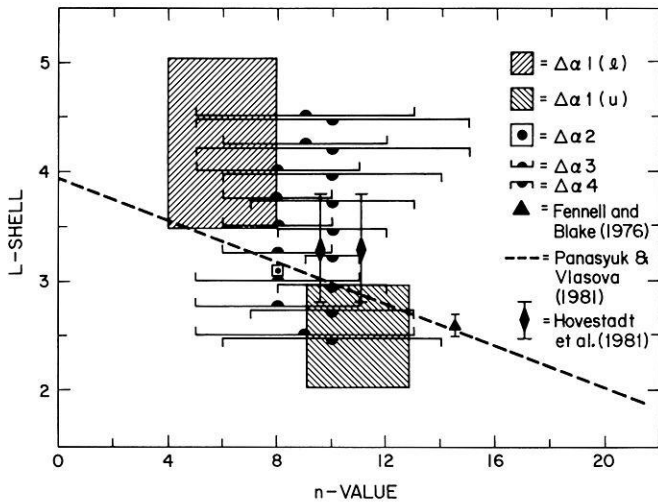


**Fig. 18.** Plotting of  $n$ -value versus  $L$ -shell regardless of helium ion energy from many experiments. Explorer 45 quiet time data:  $\Delta\alpha 1(l)$  at 0.59–0.91 MeV per ion,  $\Delta\alpha 1(u)$  at 2.00–3.99 MeV per ion,  $\Delta\alpha 2$  at 0.91–2.00 MeV per ion,  $\Delta\alpha 4$  at 1.74–3.15 MeV per ion. Also shown are data from Fennell and Blake (1976), Panasyuk and Vlasova (1981) and Hovestadt et al. (1981)

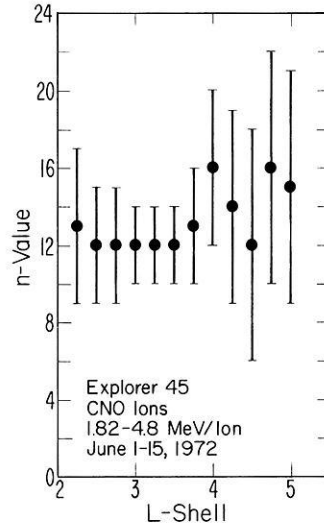


**Fig. 20.** Variation  $n$ -value with  $L$ -shell for CNO ions at 1.82–4.8 MeV per ion. The data were obtained with Explorer 45 during the geomagnetically quiet period 1–15 June 1972. To lowest order little significant variation of  $n$  with  $L$  can be discerned

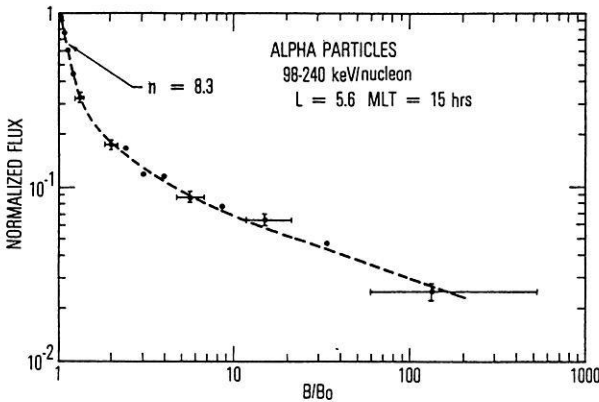


**Fig. 19.** Anisotropy information at large  $B/B_0$ -value for helium ions at 392–960 keV per ion at  $L=5.6$  and  $MLT=15$  hours given by Blake and Fennell (1981). These data were obtained with the SCATHA spacecraft. Notice that a simple relation  $J = J_{eq} (B/B_0)^{-n/2}$  is a poor fit to the data at  $B/B_0 \geq 2$  while  $n=8.3$  is a fair fit at  $1 \lesssim B/B_0 \lesssim 2$

(98–240 keV per nucleon) and shows that near the geomagnetic equator the pitch angle anisotropy is describable by  $n \sim 8.3$  (for  $B/B_0 < 1.6$ ) while a much smaller  $n$ -value describes the larger distances from the geomagnetic equator. Thus, measurements made at varying  $B/B_0$ -values would also be expected to give an apparent  $n(L)$ -dependence, particularly when the  $B/B_0$ -range covers the transition between the two different anisotropy levels.

The pitch angle anisotropy is also substantial for CNO ions. In a statistical study of Explorer 45 data, Spjeldvik and Fritz (1978d) found  $n$ -values typically in the range 10–12 at 1.8–4.8 MeV per ion (for oxygen ions) on the geomagnetic equator. Figure 20 shows the  $n$ -values deduced from these quiet time observations

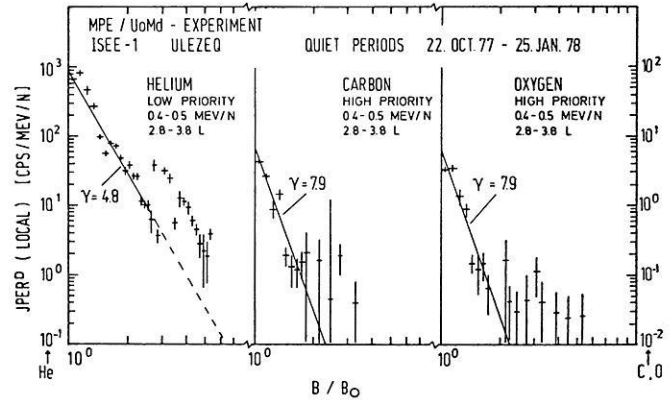


**Fig. 21.** The observed  $B/B_0$ -dependence of helium, carbon and oxygen ions obtained with the ULEZEQ detector system on the ISEE-1 spacecraft. *Left panel:* Helium ion data at 1.6–2.0 MeV per ion (0.4–0.5 MeV per nucleon) for which an  $n$ -value of 9.6 ( $\gamma = n/2 = 4.8$ ) is deduced for  $B/B_0 \lesssim 2$ . *Middle panel:* Carbon ion data at 4.8–6.0 MeV per ion (0.4–0.5 MeV per nucleon) for which an  $n$ -value of 15.8 ( $\gamma = n/2 = 7.9$ ) is deduced. *Right panel:* Oxygen ion data at 6.4–8.0 MeV per ion (0.4–0.5 MeV per nucleon) for which an  $n$ -value of 15.8 ( $\gamma = n/2 = 7.9$ ) is deduced. The data were averaged over the  $L$ -shell interval  $L=2.8$ –3.8. Notice deviations from the simple  $(B/B_0)^{-n/2}$  form at  $B/B_0 \geq 2$  (Hovestadt et al., 1981)

during 1–15 June 1972. To lowest order, there is not a reliable variation of  $n$  with  $L$ , although some slight non-regularity in the vicinity of  $L=4$  to 5 is seen.

Data from the ISEE-1 spacecraft extend the quiet-time ion anisotropy information for a number of different ion species. Figure 21 from Hovestadt et al. (1981) demonstrates that, at comparable energies per nucleon (0.4–0.5 MeV per nucleon), carbon and oxygen ions are substantially more anisotropic than helium ions where  $n_{He} \sim 9.6$  and  $n_C$  and  $n_O \sim 15.8$  measured at  $L$

=2.8–3.8. Of course, seen in total ion energy, the carbon and oxygen ions are factors of 3 and 4 times as energetic as the helium ions.

One may conclude that energetic heavy ions in the earth's radiation belts are consistently highly anisotropic.

### Observations During Magnetic Storms

A few studies have addressed the radiation belt ion composition during disturbed conditions such as magnetic storms. The qualitative behavior of the proton (ion) component at tens and hundreds of keV energies has long been studied. Davis and Williamson (1963, 1966) found that while lower energy ion fluxes, at tens to hundreds of keV, were enhanced during magnetic storms, higher energy ion fluxes in the MeV range were often decreased. Söraas and Davis (1968) recognized the importance of analyzing the phase space density at fixed first and second adiabatic invariants. Non-monotonic features in radial distributions of the phase space density are attributable to internal sources, "injections" or to time variations in the boundary conditions, i.e. to more rapid flux variations in the outer radiation zone. It is now recognized that the storm-time ion flux enhancements commonly observed at lower radiation belt energies represents the ion injection while the high energy decreases are often due to adiabatic adjustment of the magnetic field. An example of such storm-time variations is shown in Fig. 22 where ion (proton) energy density from Explorer 45 is depicted, and similar variations have been observed with ISEE-1 and other spacecraft (Williams and Lyons, 1974a, b; Lyons and Williams, 1976; Williams, 1980, 1981, in press 1982; Burke, 1981). Open circles depict pre-storm data and closed circles the storm time observations. When these data are reanalyzed in terms of the phase space densities themselves adiabatically mapped by the magnetic field variations (D.J. Williams, personal communication, 1980; Burke, 1981) the high energy flux decreases can be adequately accounted for as being a mere adiabatic adjustment. A similar situation also exists for storm-time energetic electrons (West et al., 1973, 1979, 1981; Spjeldvik and Thorne, 1975; Lyons and Williams, 1975).

Acceleration of pre-existing lower energy particles can in many cases explain "injections" as observed with instruments of finite energy bandwidth. A cross- $L$  non-diffusive displacement preserving the first two adiabatic invariants can appear as a "source" for the geomagnetic storm, main-phase ring current (i.e. Lyons and Williams, 1980). This result emphasizes the need for clear distinction between physical transport from one topologically different region of the magnetosphere to another, on one hand, and essentially in-situ redistribution in velocity space, on the other hand. Both processes have in the past been labeled "injections".

From studies of data obtained by spacecraft in low and high altitude orbits it is recognized that all ion species are not injected proportionally to their pre-storm radiation belt ionic abundance. Randall (1973) has given a detailed account for the observed He/p ratio variations observed at low altitudes during a magnetic storm. Unfortunately, because of the off-equatorial ob-

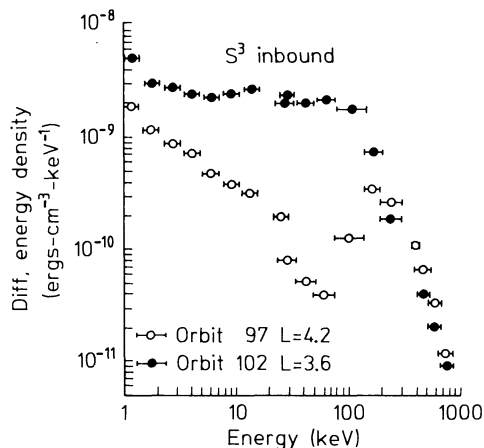


**Fig. 22.** Stormtime variation of ring current and radiation belt ion energy density observed with Explorer 45 during the quiet time (pre-storm) orbit 97 in December 1971 (open circles) and the stormtime values a day later (orbit 102). Both recordings were made in the interior of the trapping region (from Williams, 1979)

ervation location one could not with certainty distinguish between actual abundance variations and species dependent pitch angle distribution adjustments. With data from the later Explorer 45 satellite, in an essentially equatorial orbit, it was recognized that important ionic composition variations do indeed take place during at least some magnetic storms. In a series of papers, Spjeldvik and Fritz (1981, a, b, c) described the variations of the MeV heavy ion fluxes during a sequence of four magnetic storms that occurred during June through December 1972. The  $D_{st}$ -record for this time depicts four storm periods with significant  $D_{st}$ -excursions by well over 100 nT. The August 1972 magnetic storm differed from the June, September and October/November storms by a quite irregular time history of the  $D_{st}$ -index. The August 1972 storm was associated with very major solar flares which had significant effects throughout the solar system (Hoffman et al., 1975; Lanzerotti and MacLennan, 1974; Hakura, 1976; Nakagawa, 1976; Bhonsle et al., 1976; Malitson et al., 1976; Rao, 1976; Simnett, 1976; Miller, 1976; Matsushita, 1976; Smith, 1976; Vaisberg and Zastenker, 1976; Intrilligator, 1976; Cahill, 1976; Reagan et al., 1981). Solar wind ions can also be significantly accelerated in shock wave disturbances (e.g. Pesses et al., 1979; Gosling et al., 1980; Scholer et al., 1980).

### Helium Ion Flux Variations

Enhanced fluxes of energetic helium ions in the MeV range appear fairly suddenly in the heart of the trapping region during at least some magnetic storms. The left panel of Fig. 23 shows the time history of 1.74–3.15 MeV per ion helium ion fluxes at the geomagnetic equator during June through December 1982 at a nominal (undisturbed)  $L=3$ . These Explorer 45 data show the varying influence of the different magnetic storms on helium ions. Spjeldvik and Fritz (1981a) found that the June 1972 magnetic storm had its principal effect on MeV helium ions beyond  $L \sim 3.5$  where the trapped fluxes became enhanced by almost an order of magni-

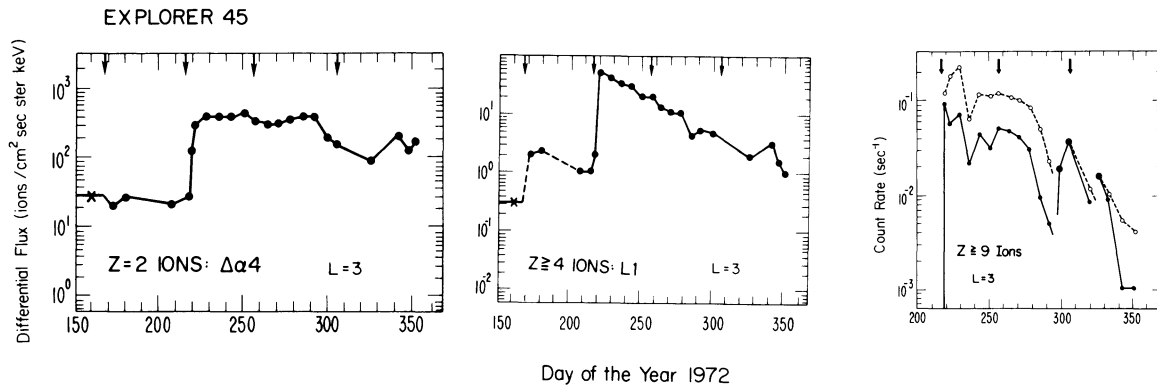


**Fig. 23.** Evolution of radiation belt helium ion ( $Z=2$ ) and CNO ion ( $Z\geq 4$ ) flux intensities, and  $Z\geq 9$  ion count rates at 1.74–3.15 MeV per ion, 1.8–4.8 MeV per ion (for oxygen ions) and  $\geq 10$  MeV per ion respectively during the four major magnetic storms that occurred during June–December, 1972. The data were obtained with Explorer 45 at  $L=3$

tude. At lower  $L$ -shells little effect was seen. In contrast, the August 1972 magnetic storm provided a substantial MeV helium ion flux increase onto  $L$ -shells well below  $L\sim 2.5$ . At  $L=2.5$  the trapped helium flux enhancement was a factor of  $\sim 30$  while at higher  $L$ -shells significant increases were also seen. The subsequent magnetic storms in September and October/November 1972 produced little observable effects on the MeV radiation belt helium ions below  $L\sim 5$ . The most likely reason is that any injection provided by these storms was much smaller than that of the August 1972 storm and therefore did not appear evident compared with the prolonged after-effect of the August 1972 magnetic storm. It is possible, of course, that these later two magnetic storms did not inject MeV helium ions. All fluxes are either equatorial ( $B/B_0=1$ ) or have been mapped to  $B/B_0=1$  using angular distribution information.

#### Variations of CNO and Heavier Ions

The corresponding record for MeV CNO ions is shown in the middle panel of Fig. 23. These data pertain to somewhat higher energies, 1.8–4.8 MeV per ion for oxygen ions. The CNO ion flux enhancement was noticeable as low as  $L=2.5$  for the June 1972 magnetic storm (Spjeldvik and Fritz, 1981b), and the most prominent increase is seen between  $L=3$  and  $L=4.5$  for this storm. As in the case of helium ions, the CNO ion fluxes were greatly enhanced during the August 1972 magnetic storm. The relative increase was particularly spectacular at  $L\sim 2.5$  where almost three orders of magnitude relative flux enhancement was observed, and a large increase in the trapped fluxes was also seen at  $L=3$ . In comparison to the August 1972 magnetic storm MeV CNO ion injection, the September and October/November 1972 magnetic storms provided little changes in the flux levels except possibly at the highest  $L$ -shells. The data were mapped to  $B/B_0=1$ ; for details, see Spjeldvik and Fritz (1981b).

While the June 1972 magnetic storm did not provide an enhancement of the fluxes of  $Z\geq 9$  ions at  $E>10$  MeV above the intensity level observable with the Explorer 45 instruments, the August 1972 magnetic storm provided a substantial injection of the  $Z\geq 9$  ions.

This is illustrated in the right panel of Fig. 23 which depicts the time evolution of these ion fluxes during and following that storm for a nominal  $L$ -shell of  $L=3$  at  $L<2.5$  and  $L>3.5$  the fluxes were generally too low to have usable count statistics. Data on the angular distribution are sketchy, and in this figure an attempt was made to establish the trapped  $Z>9$  fluxes at the geomagnetic equator as function of time by mapping the observed fluxes at the actual  $B/B_0$ -locations (in the range  $1\leq B/B_0\lesssim 1.4$ ) to  $B/B_0=1$ . The dashed line shows the result of that exercise assuming a relation  $J=J_0\sin^{10}\alpha_0$  (for details, see Spjeldvik and Fritz, 1981c). Although there are sufficient count statistics to establish the presence of these ions, some of the non-smoothness also results from the small number of counts, at best a few counts per minute. The precise identity of these ions could not be determined with the Explorer 45 heavy ion detector telescope, but expectations from the solar energetic particle emission observations at higher energies (i.e. Webber et al., 1975) suggest that magnesium and silicon ions might be the ones observed. The instrument was not able to distinguish between heavy (atomic) ions such as ions of Mg, Si, Fe etc., and molecular ions (from the lower ionosphere) such as  $\text{NO}^+$ ,  $\text{O}_2^+$ , etc.; no known mechanism is capable of accelerating ionospheric ions to tens of MeV energies in the earth's radiation belts, however. It is nevertheless worth noting that very energetic molecular ions have been observed in Jupiter's magnetosphere (i.e. Hamilton et al., 1980). A detailed study of solar particle anisotropy, rigidity spectra and propagation characteristics for a different event has been carried out by Debrunner and Lockwood (1980), and MaSung et al. (1980) report mean ionization states of energetic particles in the vicinity of the earth's magnetosphere. The charge states of these ions are found to be high, and comparable to those of the solar corona (c.f. Jordan, 1969).

#### Observed Post-Storm Ion Flux Decay

From the time evolution of the heavy ion fluxes, a typical post-storm ion flux decay time may be estimated. When the time evolution is transport dominated it is of interest to determine whether the net radial diffusion is

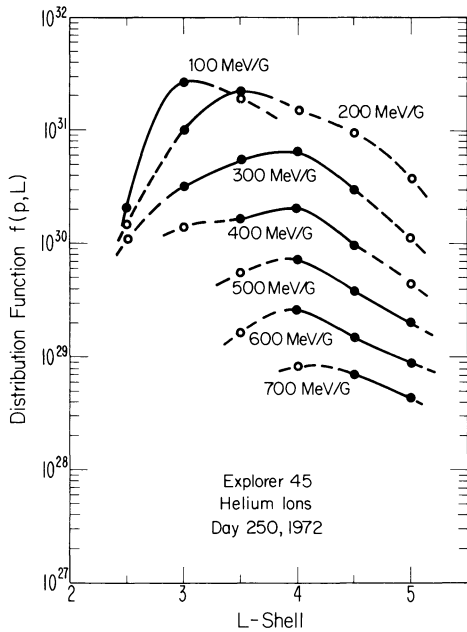


**Fig. 24.** Distribution function  $f(p, L)$  for day 250 (Sept. 6), 1972, calculated from the MeV helium ion flux observations made by Explorer 45 in the Earth's radiation belts. Solid lines and solid circles are from interpolations in the observed data, dashed lines and open circles are from graphic extrapolations in the spectral plots. With the flux  $j(E, L)$  given in ions/cm<sup>2</sup> s sr keV the distribution function  $f(p, L) = p^{-2} j_1(E, L)$  is plotted in units of ions s/cm<sup>4</sup> g<sup>2</sup> sr keV; multiplication with  $6.25 \times 10^8$  gives cgs units (ions s<sup>3</sup>/g<sup>3</sup> cm<sup>6</sup>)

inward or outward. The equatorial net radial diffusion flux can be determined from  $\Phi = -D_{LL} L^{-2} \frac{\partial f(\mu, L)}{\partial L}$

where  $f(\mu, L)$  is the instantaneous ion distribution function at equatorial pitch angle  $\alpha_0 = \pi/2$ . When  $\partial f/\partial L > 0$  net inward transport is indicated, and that is usually the case during quiet times when the radiation belt internal losses are offset by inward diffusion across an outer zone boundary location. When  $\partial f/\partial L < 0$  net outward radial diffusive transport is indicated. Figure 24 shows the deduced helium ion radial profile of the distribution function for a range of  $\mu$ -values corresponding to energies in the lower MeV range. It is clear that beyond  $L \sim 3$  the  $\partial f/\partial L$  values are generally negative showing net outward helium ion transport during the post-storm period following the August 1972 magnetic storm period. Since generally the radial diffusion coefficient increases strongly with higher  $L$ -shells ( $D_{LL} \sim L^{1.0}$  for magnetic radial diffusion, e.g. Schulz and Lanzerotti, 1974), cross- $L$  transport can be an important loss mechanism for MeV ions during this period. Eventually the MeV ions diffusing out from beyond  $L \sim 3.5$  will encounter the magnetopause (on the dayside) or the magnetotail (on the nightside) and thus be lost from the trapping region.

Figure 25 depicts the observed helium ion, CNO ion and  $Z \geq 9$  ion decay times. The helium ion decay times, shown in the left panel, vary from  $\sim 7$  days at  $L = 5$  to  $> 100$  days at  $L \sim 2.5$ . A comparison with theoretical predictions based on Coulomb collision energy degradation, ion charge exchange loss times and typical

cross- $L$  transport time scale is also provided. In this context it should be noted that the Coulomb energy degradation times used here are just those of single particle energy degradation, i.e.  $\tau_{cc} \sim \left(\frac{1}{E} \frac{dE}{dt}\right)^{-1}$ .

In principle, the actual time scale would be the ensemble average determined from the distribution function itself,

i.e.  $\tau_{EA} = f \left( \left\langle \frac{\Delta E}{\Delta t} \right\rangle \frac{\partial f}{\partial \mu} \frac{\partial \mu}{\partial E} \right)^{-1}$ , and such a refinement

should be included in future work. The charge exchange loss times were calculated from an assumed (theoretical) distribution over the ionic charge states. While helium ions are subject to at least three different charge state altering reactions,  $\text{He}^+ \rightarrow \text{He}^{++}$ ,  $\text{He}^{++} \rightarrow \text{He}^+$  and  $\text{He}^+ \rightarrow \text{He}$ , only the last of these produces loss of the ion by "untrapping" it from the magnetic field control. Thus the charge exchange loss rate is determined, in part, from the relative distribution in the different ionic charge states  $\tau_{CE} = \tau_{10} (f_1 / \sum_i f_i)^{-1}$

where the distribution function subscripts denote the charge state numbers.  $\tau_{10}$  is just  $(\sigma_{10} V [H])^{-1}$  where  $\sigma_{10}$  is the charge exchange cross section for  $\text{He}^+ \rightarrow \text{He}$ ,  $V$  is ion speed and  $[H]$  is the neutral hydrogen exosphere number density. For the Explorer 45 helium ion channel used in Fig. 25 (1.16–1.74 MeV per ion) a good agreement between the observed post-storm decay times and theoretical expectations is found; similar agreements were found for other helium ion energies (Spjeldvik and Fritz, 1981a).

This type of analysis was also done for CNO ions, and the results were compared with theoretical time scales for oxygen ions. The observed decay times varied from  $\sim 6$  days at  $L = 5$  to  $\sim 40$  days at  $L = 3.5$ . This is shown in the middle panel of Fig. 25 for the 1.8–4.8 MeV per ion CNO data. At first glance it might seem that the observed decay times are longer than the theoretically predicted Coulomb collision times at  $L < 4$ . However, the CNO data channel is quite wide, and it is expected that the CNO ion fluxes within this energy range should be primarily  $> 4$  MeV ions at  $L < 3$  while primarily  $< 2$  MeV ions at  $L > 4$  (Spjeldvik and Fritz, 1978d, 1981b). Thus, invoking this theoretical spectral expectation, the decay data are indeed consistent with theory.

It is more difficult to analyze the  $Z \geq 9$  ions since the ion identity is unknown and there is also a lack of information about the basic charge exchange cross sections of such ions ( $Z \geq 9$ ) in an atomic hydrogen gas. For a review of known cross sections, see Clafin (1970) and Spjeldvik (1979), and references therein. The actual observed decay time scales for the  $> 10$  MeV,  $Z \geq 9$  ions are shown in the right panel of Fig. 25 with error bars corresponding to the uncertainty in the data given in Fig. 23. The decay times range from  $\sim 13$  days at  $L = 3.25$  to  $\sim 54$  days at  $L = 2.25$ . Typically these decay times are short, on the order of a few tens of days with a monotonic decrease of the time scales with higher  $L$ -shells. A comparison with the expected cross- $L$  transport times in Fig. 25 reveals that at the  $L$ -shells where the  $Z \geq 9$  ion data were obtained  $\tau_{decay} \ll \tau_{diffusion}$ . On the other hand, both  $\tau_{Coulomb}$  and  $\tau_{charge\ exchange}$  should increase with increasing  $L$ -shell (because of the decreasing

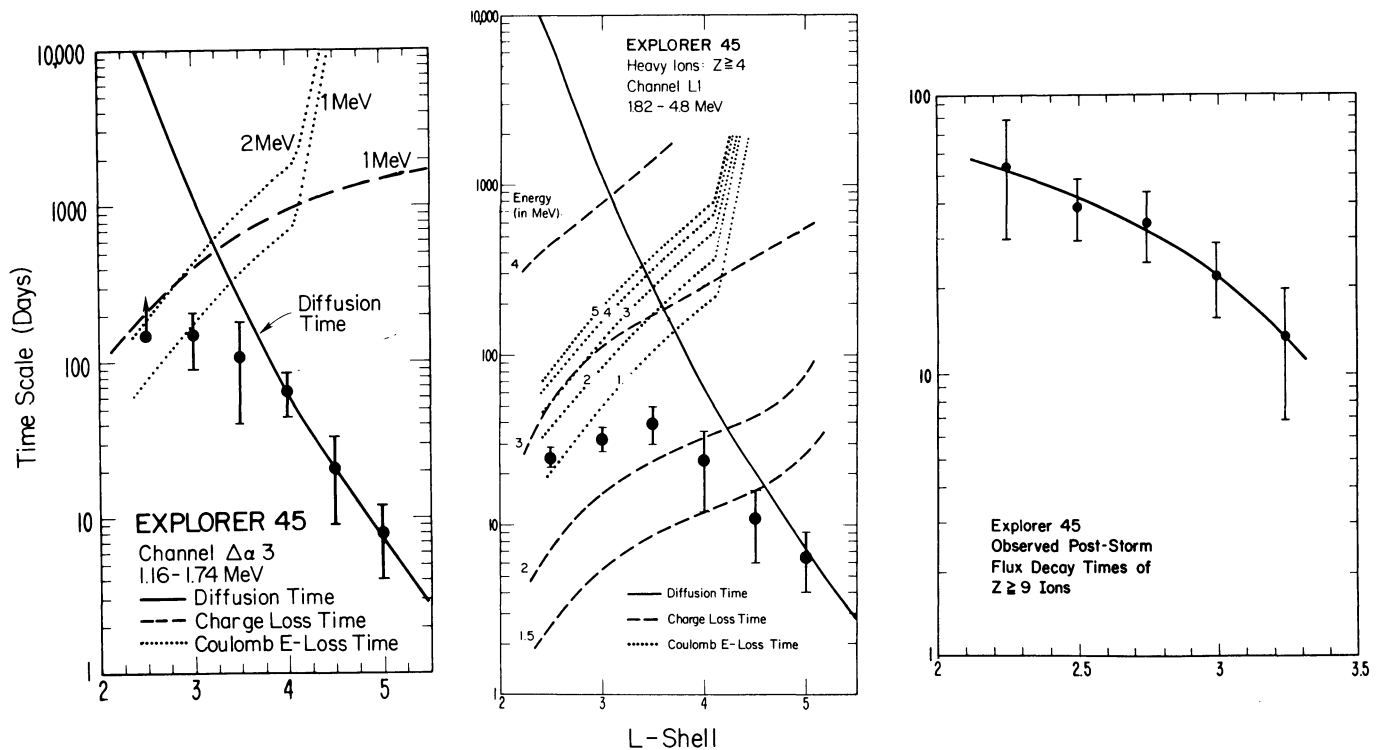


**Fig. 25.** Time scales of the observed helium ion, CNO ion and  $Z \geq 9$  ion decay following the August 1972 magnetic storm ion injection. The three panels show the data for the  $\Delta\alpha 3$ , L1 and  $Z \geq 9$  ion channels at 1.16–1.74 MeV per ion for helium, 1.8–4.8 MeV per ion for oxygen and  $\geq 10$  MeV per ion for  $Z \geq 9$  ions respectively. The vertical error bars show the estimated uncertainty in the time scale determination stemming from statistical variations and the infrequent ‘accelerated’ mode data sampling. Time scales longer than  $\sim 3$  months cannot unambiguously be determined because of the statistical spread. Likewise time scales shorter than a few days are difficult to resolve. The solid lines are lines of deduced radial diffusion times following an  $L^{-10}$  dependence and normalized to the data; and from the helium ion decay record one may estimate radial diffusion times of  $6.67 \times 10^7 L^{-10}$  days on  $L$  shells well beyond  $L=3.5$  with corresponding uncertainty as indicated by the error bars. Theoretical charge exchange and Coulomb energy degradation times scales are also shown (dashed and dotted lines); for details, see Spjeldvik and Fritz (1981 a, b, c)

exospheric neutral atomic hydrogen concentration [ $H$ ]). Thus it would appear that the theory used so far successfully for He and CNO ions at a few MeV energies cannot explain the decay of the  $Z \geq 9$  ions at  $E \geq 10$  MeV per ion. The reason for this was suggested by Hoverstadt et al. (1981) who pointed out that the gyro-radii for these very energetic heavy ions become so large that the Alfvén criterion for the validity of the adiabatic radiation belt approximation is no longer fulfilled. These ions are thus exhibiting a non-adiabatic (or quasi-adiabatic) behavior for which the theory still has to be developed, for example by studying the non-adiabatic ion trajectories (e.g. Störmer, 1955). The net result might be to lower the residence times in the trapping region.

### Theoretical Considerations

Theoretical studies of the motion of high energy particles in the earth’s magnetic field were carried out early in the century by Störmer and his contemporaries; their work, summarized in the book by Störmer (1955), followed the single particle trajectory tracing approach. The particles were thought to originate in the sun and follow deterministic trajectories in the earth’s dipolar-like magnetic field. In the general case, this is a difficult

mathematical problem, and even for a static geomagnetic field, no explicit analytic solution has been found. Great simplification can be achieved over much of the energy range of interest for the earth’s radiation belts when the three approximate periodic motions of trapped particles are considered (Alfvén and Fälthammar, 1963). The fluctuating nature of the geomagnetic field causes perturbations in these periodic motions, leading to particle energy changes, pitch angle scattering and radial transport. The general theory for these processes is well established, e.g. reviews by Fälthammar (1968), Hess (1968), Roederer (1970), Schulz and Lanzerotti (1974), Schulz (1975), Spjeldvik (1979), Lyons (1979). Calculations of radiation belt particle fluxes have also been carried out based on the diffusion theory (Nakada and Mead, 1965; Cornwall, 1972; Lyons and Thorne, 1973; Spjeldvik, 1977; Spjeldvik and Fritz, 1978 a, b; Spjeldvik, 1981 b).

The recognition that heavy ions play an important role in the radiation belts has led to greater emphasis on the precise ionic composition (Cornwall and Schulz, 1979) and to consideration of the different ionic charge states (Spjeldvik, 1979). In the following the current status of radiation belt ion modeling is outlined, emphasizing the macroscopic properties and the use in developing predictive models of the inner magnetosphere.

Trapped radiation belt ions are subject to fluc-

tuations in the large scale geoelectric and geomagnetic fields, and they may interact with various modes of plasma waves. In a macroscopic sense, this leads to radial diffusion and pitch angle diffusion. Energy degradation by Coulomb collisions cause a “flow” in velocity space and charge exchange reactions may lead to sudden untrapping of the ions. The overall effect of these processes may be written as a multi-mode diffusion equation

$$\begin{aligned} \frac{\partial f_i}{\partial t} = & \frac{\partial}{\partial \phi} \left[ D_{\phi\phi} \frac{\partial f_i}{\partial \phi} \right] + \frac{\partial}{\partial z} \left[ D_{zz} \frac{\partial f_i}{\partial z} \right] \\ & + \frac{\partial}{\partial J} \left[ \left\langle \frac{\Delta J}{\Delta t} \right\rangle_i f_i \right] + \frac{\partial}{\partial \mu} \left[ \left\langle \frac{\Delta \mu}{\Delta t} \right\rangle_i f_i \right] \\ & + \sum_j A_{ji} f_j - \sum_j A_{ij} f_i + S_i. \end{aligned} \quad (1)$$

$S$  represents a particle source internal to the trapping region, and  $\mu$ ,  $J$  and  $\phi$  are the three adiabatic invariants,  $z$  is the canonical pitch angle variable where  $z = \phi y' T(y) dy'$  and  $y = \sin \alpha_0$  where  $\alpha_0$  is the equatorial pitch angle and  $z$  is given approximately by

$$z \approx 1/2(1-y^2)T(0) - \frac{4}{11}[T(0)-T(1)](1-y^{11/4})$$

with  $T(y)$  being the bounce time dependence of equatorial pitch angle (Hamlin et al., 1961; Schulz, in press 1981).  $\langle \Delta J / \Delta t \rangle_i$  and  $\langle \Delta \mu / \Delta t \rangle_i$  are the stochastic degradation rates in the  $\mu$  and  $J$  invariants caused by Coulomb collisions and  $A_{ij}$  is the charge exchange factor for transformation from state  $i$  to state  $j$  (e.g. Cornwall, 1972; Spjeldvik, 1979). For protons there is just one charge state ( $i=1$ ) and the last two terms reduce to  $-A_{10}f_1$ . Although it is, in principle, possible to solve this equation, there is no analytic solution expressible by a known function for the general case. Even a purely numerical solution is laborious since a four-dimensional parameter space spanned by  $\mu$ ,  $J$ ,  $\phi$  and  $i$  plus time must be considered. The solution in this general case has not yet been obtained, and every numerical simulation has studied simplified cases. A steady-state time independent approximation is most often used.

Lyons and Thorne (1973), in their steady state radial diffusion study of radiation belt electrons, replaced the pitch angle diffusion term with  $\frac{\partial}{\partial z} \left[ D_{zz} \frac{\partial f_1}{\partial z} \right] \approx -\frac{f_1}{\tau_p(E, L)}$  where  $\tau_p(E, L)$  is the overall electron precipitation lifetime versus scattering into the atmospheric

bounce loss cone. They also replaced  $\frac{\partial}{\partial \mu} \left( \left\langle \frac{\Delta \mu}{\Delta t} \right\rangle f_1 \right)$  by  $-\frac{f_1}{\tau_{coul}}$  where  $\tau_{coul}$  is the single particle Coulomb collision “life time” defined from  $\tau_{coul} \approx \left( \frac{1}{E} \frac{dE}{dt} \right)^{-1}$ . Of course, the correct ensemble time scale for an arbitrary equatorial pitch angle  $\alpha_0$  is defined as

$$\tau_{EL} = \left( \frac{1}{f_i} \left[ \frac{\partial}{\partial \mu} \left( \left\langle \frac{\Delta \mu}{\Delta t} \right\rangle f_1 \right) + \frac{\partial}{\partial J} \left( \left\langle \frac{\Delta J}{\Delta t} \right\rangle f_1 \right) \right] \right)^{-1},$$

but such a quantity cannot be specified a priori since it depends on the solution to the diffusion problem itself. For electrons there is no charge exchange process to consider. A significant simplification also comes from considering only one pitch angle, most often the equatorially mirroring particles only (i.e. where  $J \equiv 0$ ) are studied. These considerations reduced the electron problem of Lyons and Thorne (1973) to a one-dimensional approximate case of radial transport only. Although the accuracy of some of their simplifications may be called into question, their solution retained much of the essential physics, and they obtained results in good agreement with in-situ electron observations.

In modeling protons and other ions Nakada and Mead (1965), Cornwall (1972), Blake et al. (1973), Spjeldvik (1977) and Spjeldvik and Fritz (1978a, b) retained the radial diffusion term, the Coulomb collision term, and the charge exchange term(s). But they also restricted attention to equatorially mirroring ions, and for energetic ions the pitch angle scattering term was neglected altogether (by assuming  $D_{zz} \sim 0$ ). Figure 26 shows an ex-

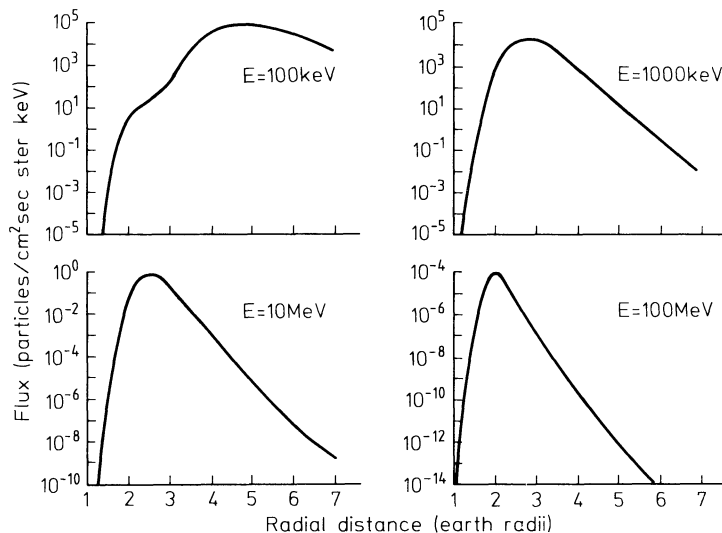


**Fig. 26.** Theoretical radial profiles of energetic radiation belt proton fluxes calculated from the steady state model of Spjeldvik (1977) with outer radiation zone boundary conditions assigned at  $L=7$ . The results are shown for 100 and 1,000 keV, and 10 and 100 MeV. These curves were computed based on the exospheric neutral hydrogen model of Tinsley (1976) and with radial diffusion coefficients as described in Spjeldvik (1977). No pitch angle scattering was allowed and only equatorially mirroring protons were considered

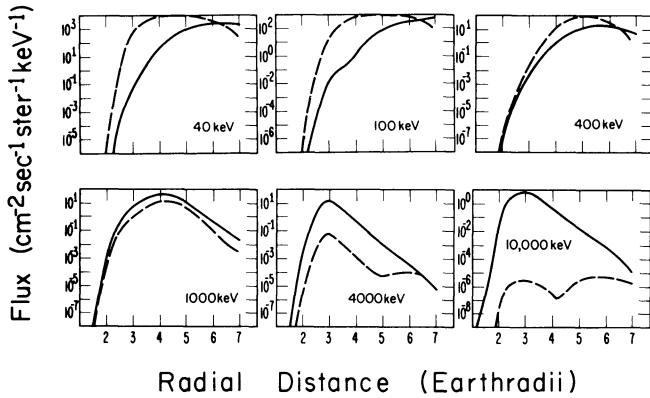


**Fig. 27.** Theoretical radial profiles of radiation belt helium ion fluxes calculated from the steady state model of Spjeldvik and Fritz (1978a) with outer zone boundary conditions assigned at  $L=7$ . Dashed curves depict charge state 1 (i.e.  $\text{He}^+$ ) while solid curved depict charge state 2 (i.e.  $\text{He}^{++}$ ), and the curved are given for 40, 100, 400, 1,000, 4,000 and 10,000 keV per ion. The relative charge state distribution indicates the dominance of  $\text{He}^{++}$  above  $\sim 1$  MeV per ion while  $\text{He}^+$  are most abundant at lower energies

ample of the proton model result for  $\alpha_0 = \pi/2$  (from Spjeldvik, 1977). These calculations reproduce the well known observational result that protons are not distributed into two belts, but occupy a single radiation zone encompassing the entire trapping region, and such that the more energetic protons have their flux peak at the lower  $L$ -shells. Spectrally, these calculations show that the proton spectra in the interior of the radiation belts turn over and exhibit positive  $\partial j/\partial L$ -values (with  $j(E, L) = p^2 f(p, L)$  where  $p$  is the proton momentum) at the lower energies.

A similar treatment of energetic helium ions gave the theoretical distributions illustrated in Fig. 27 (from Spjeldvik and Fritz, 1978a): Notice that the lowest helium ion charge state is dominant below  $\sim 1$  MeV while the second charge state is most important above this energy. This result is essentially independent of the ion charge state boundary condition applied in the outer radiation zone, thus charge state redistribution processes resulting from collisions between the energetic ions and exospheric particles are important in most of the trapping region. Qualitatively the theoretical helium ion fluxes also peak at lower  $L$ -shells with increasing ion energy, and their spectra show positive  $\partial j/\partial L$ -values below  $\sim 1$  MeV at  $L \lesssim 3.5$ . Some interesting spectral features arise from the combined influences of energy-dependent radial diffusion and energy dependent losses. The parameter used for radial diffusion (Cornwall, 1972) leads to preferential loss of helium ions at  $\sim 100$ – $1,000$  keV total ion energy; for details, see Spjeldvik and Fritz (1978a). The theoretical results are probably not strictly valid below  $\sim 100$  keV since convective processes may be more important than diffusion at and below ring current energies.

Two examples of model results for oxygen ions are depicted in Fig. 28. In the left panels a flux boundary condition was imposed at  $L=6.6$  under the assumption that only  $\text{O}^+$  was present (corresponding to a purely ionospheric ion source at all energies), and in the right

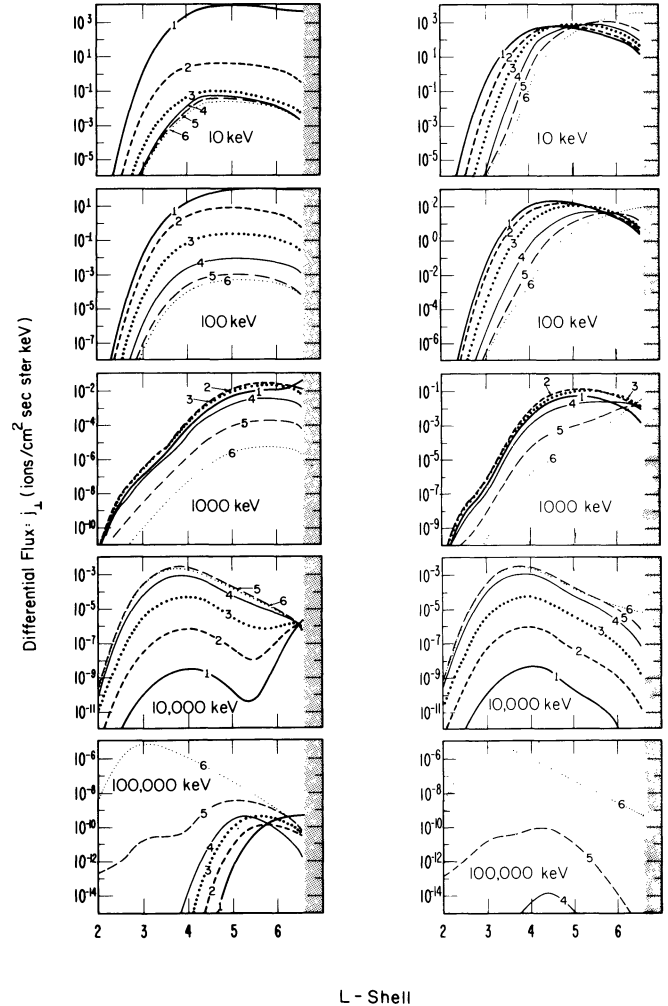


**Fig. 28.** Computed atomic oxygen ion fluxes in the earth's radiation belts assuming an ionospheric source of  $\text{O}^+$  at the outer zone boundary (left panels) or alternating a solar source of  $\text{O}^{6+}$  ions at the outer boundary (right panels). The six lowest positive charge states are permitted, and the diffusion coefficients have the same values as in the calculations in Figs. 26 and 27. Charge state numbers are given on the curves. The panels show radial profiles at 10, 100, 1,000, 10,000 keV per ion. Detailed description of the theoretical calculations are found in Spjeldvik and Fritz (1978b)

panels the identical spectra were taken at  $L=6.6$  but with solely  $\text{O}^{6+}$  present (an implicit assumption of an extraterrestrial ion source). The calculated oxygen ion fluxes and charge state distributions in the interior of the radiation belts were found to be fairly similar in both cases, however, except near the outer zone boundary. This is explicitly shown in Fig. 29 for 4 MeV oxygen ions subject to the ionospheric (left panel) and solar wind (right panel) source assumptions. Notice that below a charge state redistribution zone of width  $\Delta L \sim 1.5$   $L$ -shell units a characteristic charge state distribution is formed. In this case with  $\text{O}^{4+}$  ions dominant. For specific details about expected charge state distribution properties and the uncertainties in the calculations from which they are derived, see the review by Spjeldvik (1979).

In all the model calculations carried out so far for

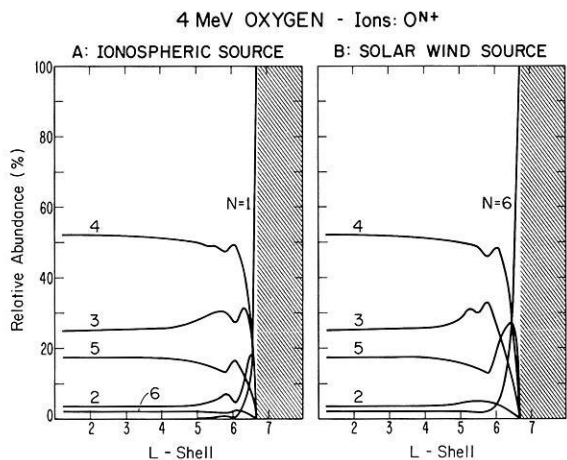


**Fig. 29.** Normalized charge state distributions for 4 MeV atomic oxygen ions in the Earth's radiation belts. The left panel assumes solely  $O^+$  in the outer radiation zone and the right panel assumes solely  $O^{+6}$  at  $L=6.6$ , corresponding to ionospheric and solar wind ion sources respectively. It can be seen that at  $L$ -shells below a narrow transition zone ( $\Delta L \sim 1.5$ ) the charge state distributions become practically independent of the ion source characteristics and that at this energy the fourth charge state predominates the charge state distribution

radiation belt ions, rates of radial transport due to fluctuations in the large scale electric and magnetic fields have assumed that the fluctuation power spectra follow  $P(\nu) \approx \nu^{-2}$  dependences (where  $\nu$  is the fluctuation frequency). That may not always be the case (Arthur et al., 1978; Holzworth and Mozer, 1979), and whenever the power is not exactly  $-2$ ,  $D_{\phi\phi}$  (or equivalently  $D_{LL}$ ) will depend on  $\mu$  (and possibly  $J$ ). Westphalen and Spjeldvik (1982) have suggested a method by which the time averaged  $\mu$ -dependence of  $D_{\phi\phi}$  may be deduced from inner zone ( $L \sim 1.2$ ) trapped particle spectra in the keV and lower MeV range, below the energy range where the cosmic ray albedo neutron decay source (CRAND) is important. The actual determination of  $D_{\phi\phi}(\mu, J)$  remains to be implemented, however. Detailed investigations of a number of theoretical aspects of the inner edge of the radiation belts have recently been

made by Jentsch and Wibberenz (1980) and Jentsch (1981), but are beyond scope of the present review.

Figure 30 shows a comparison of theoretically computed proton, helium and oxygen ion fluxes at  $E=0.1-20$  MeV per ion. Notice that in the heart of the radiation belts,  $L=3.25$ , theory predicts that protons should be the dominant ion species from  $\sim 100$  to  $\sim 1,000$  keV per ion while helium and oxygen ions should be more numerous when compared at equal total ion energy in the MeV range. The curves are drawn for three different values of the magnetic radial diffusion coefficient, with one fixed electric radial diffusion coefficient, and given observed outer zone boundary conditions; for details see Spjeldvik and Fritz (1978b). Much of the Explorer 45 ion composition data for equatorially mirroring ions support these theoretical results over the limited energy range where the data are available. However, a critical test can only be made when simultaneous proton and heavy ion data are available over a much more extensive energy range. Further studies of the ISEE spacecraft data would be in order.

### Comparison of Theory and Observation

Ionic composition observations have been made over two energy ranges, below a few tens of keV and above several hundred keV. Figure 31 (from Williams, 1980) shows the quiet time integral radiation belt particle energy density. It can be seen that the main contribution to the energy density comes from the intermediate energies where our current composition knowledge is lacking. There is much evidence supporting the idea that a substantial fraction of the lower-energy ring current ion population is of ionospheric origin (Lundin et al., 1980; Lennartsson et al., 1981; Lennartsson and Sharp, in press 1982; Williams, 1980; Young et al., 1982), perhaps mixed with solar wind ions, and that the higher energy ions are of extraterrestrial origin (e.g. Hovestadt et al., 1978b). Below  $\sim 20$  keV per ion observations point to  $H^+$ ,  $He^+$ ,  $O^+$ ,  $O^{++}$  in variable relative abundances, and above  $\sim 500$  keV per ion the observations reveal ions of hydrogen, helium, carbon, oxygen and heavier ions. The energetic heavy ions are also

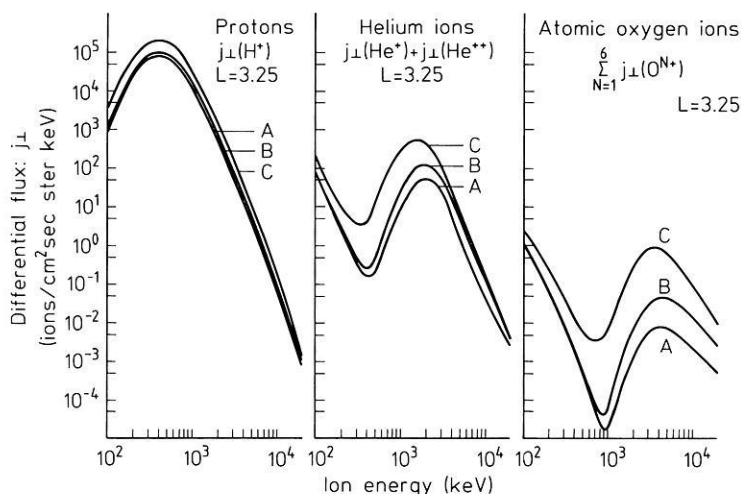


**Fig. 30.** Theoretical ion composition of the earth's radiation belts. Sensitivity comparison of protons, helium ions, and oxygen ions due to variations in the magnetic diffusive ion transport rate as quantified by the magnetic diffusion coefficient  $D_{LL}^{(M)}$ . The spectral curves shown for each ion species represent a flux summation over all applicable charge states at an  $L$ -shell of 3.25, where the ion fluxes generally maximize in the lower range. The spectral coverage in these panels extends over the energy range 100 keV to 20 MeV per ion. The curves labeled A, B, and C correspond to  $D_{LL}^{(M)}$  values of  $2 \times 10^{-10} \times L^{10}$ ,  $10^{-9} \times L^{10}$ , and  $10^{-8} \times L^{10} R_E^2/\text{day}$ , respectively, with  $D_{LL}^{(E)}$  taken as  $2 \times 10^{-6} \times L^{10}/(L^4 + (\mu_M/i)^2) R_E^2/\text{day}$  where  $\mu_M$  is measured in MeV/Gauss and  $i$  is the ionic charge state number

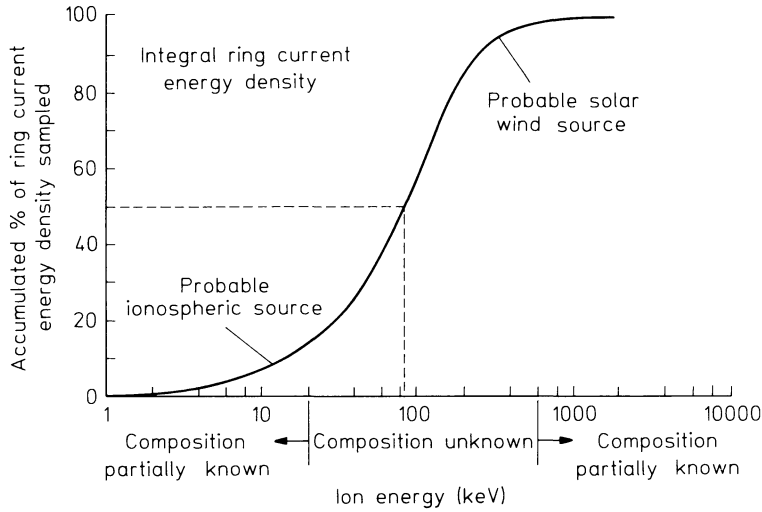


**Fig. 31.** Integral ring current and radiation belt energy density for quiet time conditions. Indicated are the energy ranges where partial information about the ionic composition is available from experimental data. The contribution to the trapped particle energy density is greatest where this curve is steepest, and that energy range coincides with the energy range where the actual radiation belt composition is unknown

observed to be in the higher charge states (D. Hovestadt, personal communication, 1979).

Unfortunately, most instruments do not permit the determination of the precise ionic charge state distribution. At a given ion energy, the total contribution of a given ion species,  $j = \sum_i j_i$ , is measured. To compare the theoretically calculated particle distributions with such observations requires the summation of the theoretical results over all ionic charge states. The radiation belt transport and loss relation (1) then yields:

$$\begin{aligned} \frac{\partial f}{\partial t} = & \frac{\partial}{\partial \phi} \left[ D_{\phi\phi} \frac{\partial f}{\partial \phi} \right] + \frac{\partial}{\partial z} \left[ D_{zz} \frac{\partial f}{\partial z} \right] \\ & + \frac{\partial}{\partial J} \left[ \left\langle \frac{\Delta J}{\Delta t} \right\rangle f \right] + \frac{\partial}{\partial \mu} \left[ \left\langle \frac{\Delta \mu}{\Delta t} \right\rangle f \right] \\ & - Af + S \end{aligned} \quad (2)$$

where quantities with no charge state subscript are averaged over all the available ionization states. The ion pitch angle and radial diffusion coefficients become:

$$\begin{aligned} D_{\phi\phi} = & \sum_i D_{\phi\phi i} \frac{\partial f_i}{\partial \phi} \bigg/ \sum_i \frac{\partial f_i}{\partial \phi}, \\ D_{zz} = & \sum_i D_{zz i} \frac{\partial f_i}{\partial z} \bigg/ \sum_i \frac{\partial f_i}{\partial z} \end{aligned} \quad (3)$$

while the energy degradation effects on the first and second adiabatic invariants is now described by:

$$\begin{aligned} \left\langle \frac{\Delta \mu}{\Delta t} \right\rangle = & \sum_i \left\langle \frac{\Delta \mu}{\Delta t} \right\rangle_i f_i / \sum_i f_i, \\ \left\langle \frac{\Delta J}{\Delta t} \right\rangle = & \sum_i \left\langle \frac{\Delta J}{\Delta t} \right\rangle_i f_i / \sum_i f_i, \end{aligned} \quad (4)$$

For the distribution of a given ion species summed over all charge states the charge exchange expressions reduce to a simple weighted loss term where

$$A = A_{10} f_1 / \sum_i f_i, \quad (5)$$

$$f = \sum_i f_i, \quad (6)$$

and

$$S = \sum_i S_i. \quad (7)$$

As a consequence, one may apply, to the summed distribution function  $f$ , an equation similar to that of the distribution function  $f_i$  for individual charge states but where the proper coefficients are weighted by the charge state distribution and its derivatives.

In general, the different coefficients vary significantly with the ionic charge state. As an example, the Cornwall (1972) model radial diffusion coefficients  $D_{LL}$  (simply related to  $D_{\phi\phi}$  by a Jacobian transformation) for electric fluctuations may be written in the form

$$D_{LLi}^{(E)} = C^{(E)} \frac{L^{10}}{L^4 + (\mu_M/i)^2} \quad (8)$$

where the sub-coefficient  $C^{(E)}$  depends on the electric field fluctuation magnitude (and has values in the range  $2 \times 10^{-6} - 2 \times 10^{-5} R_E^2$  per day) and  $\mu_M$  is the magnetic moment in MeV per Gauss. This expression is valid for equatorially mirroring particles;  $D_{LLi}^{(E)}$  and  $D_{LLi}^{(M)}$  vary somewhat with equatorial pitch angle (e.g. Schulz, 1975). At multi-MeV energies the second term in the denominator of (8) dominates and thus  $D_{LLi}^{(E)} \propto i^2$  where  $i$  is the ionic charge state number, and in the high energy limit

$$D_{LL}^{(E)} \simeq C^{(E)} L^{10} \mu_M^{-2} \sum_i i^2 \frac{\partial f_i}{\partial L} \bigg/ \sum_i \frac{\partial f_i}{\partial L}. \quad (8)$$

In this limit the ionic charge state distribution is biased towards the higher charge states attainable, and for this reason the effective radial diffusion coefficient may become quite large. A similar situation may exist for ion pitch angle diffusion although the specific details remain to be investigated.

It is also worth noting that the effective rate of ion loss through charge state neutralization (e.g. the process  $\underline{Q}^+ + H \rightarrow \underline{Q} + H^+$ ; where underlining denotes the energetic particle) scales with the ratio  $f_1 / \sum_i f_i$ . This implies that when  $f_1 \ll f_i$  for  $i \geq 2$ , the time scale of ion loss due to charge exchange will be very long. Coulomb

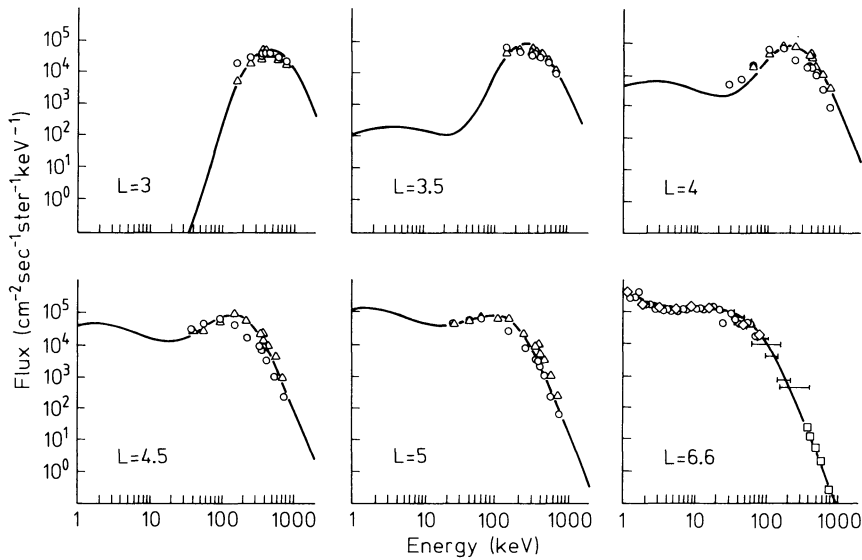


**Fig. 32.** Radiation belt proton energy spectra; comparison of theoretical and observed energy spectra in the keV energy range at  $L$  values of 3, 3.5, 4, 4.5, 5, and 6.6. The spectrum at  $L=6.6$  constitutes the adopted boundary condition on the theoretical calculations based on data taken from a number of experiments on the satellite ATS 6 in geostationary orbit (Fritz et al., 1977). The data at the lower  $L$  values are taken from quiet time observations on board the satellite Explorer 45. Because an increasing number of detector channels are judged unreliable with decreasing  $L$  values, the spectral distribution of valid data is less extensive at the lower  $L$  shells (for details, see Spjeldvik, 1977)

collisions, on the other hand, generally have an energy degradation rate following an  $i^2$  dependence (Rossi and Olbert, 1970). Thus, ions in the higher ionic charge states will be degraded in energy at a rate higher than those in the lower charge states; e.g. an  $O^{6+}$  ion will have an energy degradation rate 36 times higher than an  $O^+$  ion at the same energy. Consequently, one would expect the spectral shapes of such ions to vary with charge state.

The charge state information for geomagnetically trapped ions cannot be used to infer the ion origin conclusively. Spjeldvik and Fritz (1978b) have demonstrated that charge state altering reactions soon transform the ionic charge state according to internal radiation belt processes. To some limited extent a similar situation might exist for the elemental abundance of trapped ions, since mass dependent processes can change the relative abundances. The latter process is particularly important below a few hundred keV ion energies.

Given suitable boundary conditions in the outer radiation zone, it is possible to compute numerically the radiation belt theoretical distributions of several different ion species. Since these ions are subject to mass and charge dependent interactions with the plasmasphere and exosphere, their relative abundance will result from a combination of source strength and internal radiation belt processes.

Figure 32 shows a direct comparison of proton (ion) observations from Explorer 45 at  $L \leq 5$  and ATS-6 at  $L = 6.6$ , and theoretical proton spectra at different  $L$ -shells. The outer zone proton fluxes were modeled from the ATS-6 observations so critical comparison can be made only at lower  $L$ -shells. Unfortunately, the coverage of uncontaminated Explorer 45 data is substantially less at the lower  $L$ -shells, particularly below  $L \sim 3$ . Nevertheless, the comparison shows a fair agreement, strengthening the idea that the 100–1,000 keV ions are protons. This finding can be further tested by attempting to match the fluxes of another ion species with the proton (ion) data, and this was done by Spjeldvik (1977) who found it difficult to accomplish such a match unless rather extreme assumptions on the rate of radial diffusion together with virtual absence of protons

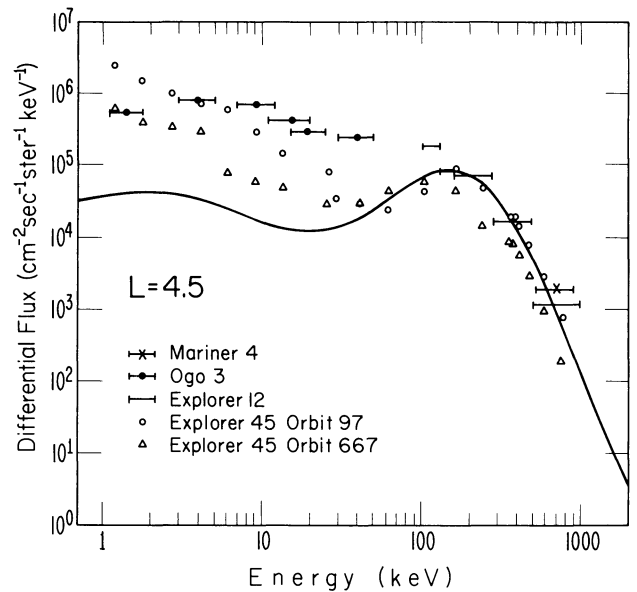


**Fig. 33.** Comparison between Explorer 45 ion observations at  $L=4.5$  and data from OGO 3, Explorer 12, and Mariner 4. Also shown are the theoretically predicted proton fluxes shown as the solid curve. Ion observations at tens of keV may not be protons (see the text). At this  $L$ -shell the Explorer 45 data below 40 keV are judged questionable (Spjeldvik, 1977)

were adopted. Thus, the available indirect evidence supports the finding that these ions probably are protons, and to the extent of the valid data from Explorer 45 there is a good agreement between theory and observation at radiation belt energies. There is no agreement at ring current energies ( $E < 100$  keV), however. That is depicted in Fig. 33 which compares the theoretical proton spectrum at  $L=4.5$  with data from Mariner 4, OGO-3, Explorer 12 and Explorer 45. Presumably some of this discrepancy below  $\sim 100$  keV stems from the possibility that the majority of these ions may not be protons, and some from the effect of non-diffusive transport process operating at these energies.

A similar comparison can also be made for the heavier ions, but only over a short energy range. Figure 34

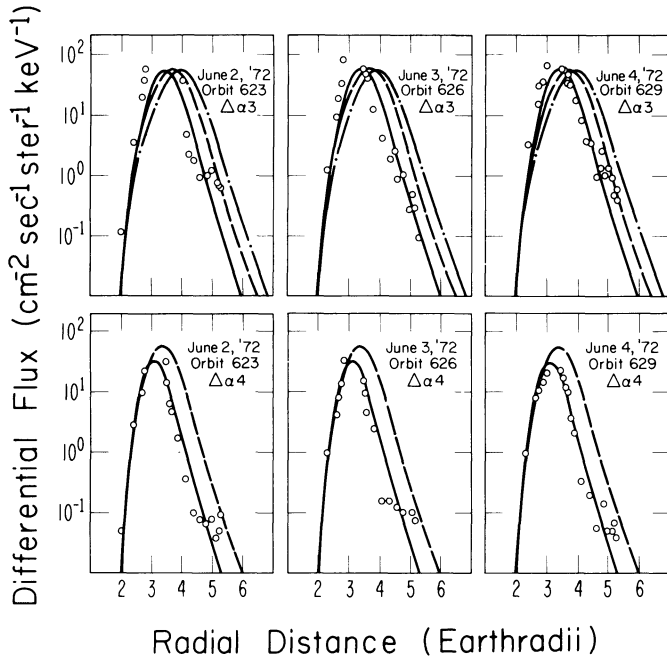


**Fig. 34.** Radiation belt helium ion radial profiles; comparison between theory and experiment. Circles are observed differential fluxes from the heavy ion experiment on Explorer 45 averaged over the energy passbands  $\Delta\alpha 3$  (1.16–1.74 MeV) and  $\Delta\alpha 4$  (1.74–3.15 MeV) on three consecutive geomagnetically quiet days, June 2–4, 1972. The lines are theoretical predictions. For the  $\Delta\alpha 3$  channels (upper panels) the theoretical curves represent differential fluxes at 2 MeV (solid), 1.5 MeV (dashed) and 1.2 MeV (dot-dashed). For the  $\Delta\alpha 4$  channels (the lower panels) the theoretical curves represent differential fluxes at 3 MeV (solid) and 2 MeV (dashed) (for details, see Spjeldvik and Fritz, 1978a)

depicts a comparison of Explorer 45 helium ion observations at 1.16–1.74 and 1.74–3.15 MeV per ion with theoretical results at 1.2, 1.5 and 2, and 2 and 3 MeV per ion respectively. The agreement is quite good for the three quiet days of data used here. A much more critical comparison would be to extend the energy range, particularly towards lower energies where the theory predicts spectral turnover below  $\sim 1$  MeV. The comparison of oxygen ion theoretical radial distribution and available CNO data is given in Fig. 35, and in spite of the uncertainty in the theoretical curves owing to the input parameter estimates (most notably in the charge exchange cross sections, Spjeldvik and Fritz, 1978b) a fair agreement was achieved. As in the case of helium ions, there is a need for more critical comparison. The data on carbon and oxygen ions now available from the new instruments on ISEE-1 can be used for this purpose when data from suitable spacecraft orbits close to the geomagnetic equatorial plane are selected.

#### Future Outlook

The last decade has been one of increasing emphasis on precise ionic measurements in the earth's radiation belts. Foremost has been the desire to establish the ion identity and their individual spectral and anisotropy

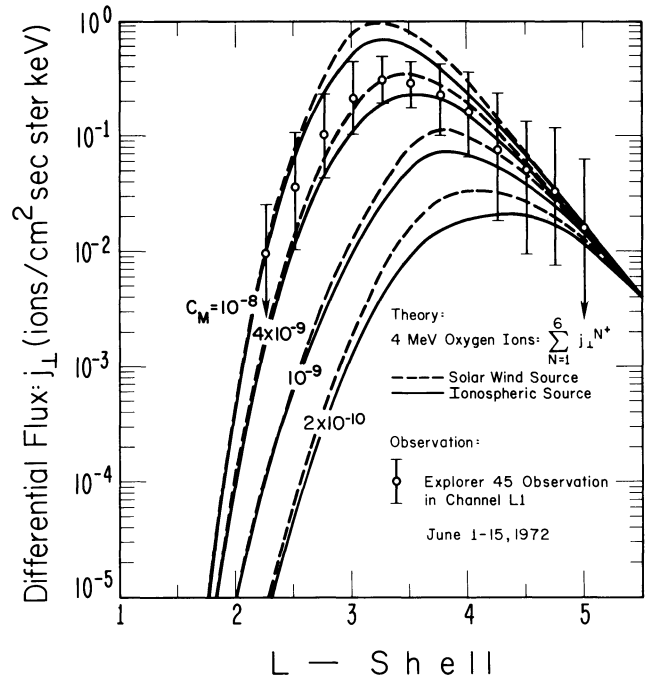


**Fig. 35.** Radiation belt oxygen ion radial profile; comparison between theory and observation. The lines indicate computed radial profiles of 4 MeV oxygen ions summed over all charge states in the earth's radiation belts. The solid curves assume an ionospheric source of  $O^+$  and the outer zone boundary and show the profiles for  $C_M = 2 \times 10^{-10}$ ,  $C_M = 10^{-9}$ ,  $C_M = 4 \times 10^{-9}$ , and  $C_M = 10^{-8} R_E/\text{day}$  where  $D_{LL}^{(M)} = C_M L^{1.0}$ . The dashed curves assume a solar wind source of  $O^{6+}$  at the outer zone boundary and show the profiles for the same values of  $C_M$ . Data on oxygen ions obtained from the L1 channel on the satellite Explorer 45 are also indicated. The detector passband is 1.82–4.8 MeV per ion for oxygen ions

characteristics. Development of fast pulse resolution electronic circuitry for spacecraft use has enabled researchers to develop time-of-flight instruments where not only the differential ( $dE/dx$ ) and total ( $E$ ) energy deposition of energetic ions incident on solid state detectors could be measured, but also the ionic orbital flight time over a fixed path length within the instrument. Several such instruments have been built and flown. Details of future heavy ion detectors now being developed for the NASA/OPEN mission have been published (Spjeldvik, 1981a; Wilken et al., 1982). Besides three solid state detectors and an ion flight path, such instruments utilize electrostatic deflection of (low energy) secondary electrons emitted by the thin detectors. That eliminates the need for magnets (a weight saving), and microchannel plates provide position sensitive secondary electron measurements. These instruments are expected to provide good mass and energy information from about 200 keV per ion to tens of MeV.

A problem encountered in the in-situ measurements of minor species is related to the often low geometric factor of the instrument. Ions at tens of keV energies can be deflected by a strong electrostatic field (as is commonly done in some mass spectrometer design), and the principle now being invoked is to make the instrument aperture into an annular (ring) shape such that incoming ions are deflected and focused onto a

smaller area detector (D. Bryan and D. Hardy, personal communications, 1980). An instrument now also being developed for the Swedish/VIKING and the NASA/OPEN mission uses this annular (toroidal) aperture geometry (Wilken et al., 1982), and incoming ions are first deflected by a (variable) electric field, then post-accelerated by a known amount and finally detected in a solid state detector. This type of instrument bears the promise of closing the now existing gap in our ability to determine the ion identity at upper ring current energies. Other ion detectors may also be under development, but their current state of design and proprietary considerations preclude a discussion here. Nevertheless, it can be anticipated that the ionic mass and charge composition of the earth's radiation belts will be studied intensively during the coming years.

*Acknowledgements.* The author has benefitted from many years of collaboration with Dr. Theodore A. Fritz, and from the hospitality of the research division at the NOAA/Space Environment Laboratory in Boulder, Colorado. The work was supported by NASA grants S-50897G and W-14595. Useful discussions with Dr. D. Hovestadt are gratefully acknowledged.

## References

- Adams, J.H., Partridge, K.: Do trapped heavy ions cause soft upsets on spacecraft? NRL Memorandum Report 4846, Naval Research Laboratory, Washington, D.C., 20375, 1982
- Alfvén, H., Fälthammar, C.-G.: Cosimal electrodynamics. Oxford, United Kingdom. Clarendon Press 1963
- Arthur, C.W., McPherron, R.L., Lanzerotti, L.J., Webb, D.C.: Geomagnetic field fluctuations at synchronous orbit, 1. Power spectra. *J. Geophys. Res.* **83**, 3859, 1978
- Balsiger, H., Eberhardt, P., Geiss, J., Ghielmetti, A., Walker, H.P., Young, D.T., Loidl, H., Rosenbauer, H.: A satellite-borne ion mass spectrometer for the energy range 0 to 16 keV. *Space Science Instrumentation* **2**, 499, 1976
- Bame, S.J., Asbridge, J.R., Feldman, W.C., Montgomery, M.D.: Solar wind heavy ion abundances. *Solar Phys.* **43**, 463, 1975
- Bhonsle, R.V., Degaonkar, S.S., Alurkar, S.K.: Ground-based solar radio observations of the August 1972 events. *Space Sci. Rev.* **19**, 475, 1976
- Blake, J.B., Fennell, J.F., Schulz, M., Paulikas, G.A.: Geomagnetically trapped alpha particles: 2. The inner zone. *J. Geophys. Res.* **78**, 5498, 1973
- Blake, J.B.: Experimental test to determine the origin of geomagnetically trapped radiation. *J. Geophys. Res.* **78**, 5822, 1973
- Blake, J.B.: On the ionic identity of the ring current particles. *J. Geophys. Res.* **81**, 6189, 1976
- Blake, J.B., Fennell, J.F., Hovestadt, D.: Measurements of heavy ions in the low-altitude regions of the outer zone. *J. Geophys. Res.* **85**, 5992, 1980
- Blake, J.B., Fennell, J.F.: Heavy ion measurements in the synchronous altitude region. *Planet. Space Sci.* **29**, 1205, 1981
- Burke, W.J.: An overview of radiation belt dynamics. In: Proceedings of the Air Force Geophysics Laboratory workshop on the Earth's radiation belts: January 26-27, 1981, R.C. Sagalyn, W.N. Spjeldvik and W.J. Burke, eds., pp.9-46. Air Force Systems Command, AFGL-TR-81-0311, Hanscom AFB, Massachusetts, 1981
- Cahill, L.J., Jr.: Response of the magnetosphere during early August 1972. *Space Sci. Rev.* **19**, 703, 1976
- Claflin, E.S.: Charge exchange cross sections for hydrogen and helium ions incident on atomic hydrogen: 1 to 1,000 keV. Report TR-0059 (6260-20)-1, The Aerospace Corporation, El Segundo, California, July 1970
- Cornwall, J.M.: Radial diffusion of ionized helium and protons: A probe for magnetospheric dynamics. *J. Geophys. Res.* **77**, 1756, 1972
- Cornwall, J.M., Schulz, M.: Physics of heavy ions in the magnetosphere. In: *Solar System Plasma Physics*, C.F. Kennell, L.J. Lanzerotti and E.N. Parker, eds. North-Holland Publ. 1979
- Davis, L.R., Williamson, J.M.: Low energy trapped protons. *Space Sci. Rev.* **3**, 365, 1963
- Davis, L.R., Williamson, J.M.: Outer zone protons. In: *Radiation trapped in the Earth's magnetic field*, B.M. McCormac, ed. Dordrecht, Holland: D. Reidel Publ. Co. 1966
- Debrunner, H., Lockwood, J.A.: The spatial anisotropy, rigidity spectrum and propagation characteristics of the relativistic solar particles during the event on May 7, 1978. *J. Geophys. Res.* **85**, 6853, 1980
- Fälthammar, C.-G.: Radial diffusion by violation of the third adiabatic invariant. In: *Earth's particles and fields*, Ed.: B.M. McCormac, ed.: p.157. New York: Reinhold Publishing 1968
- Fennell, J.F., Blake, J.B., Paulikas, G.A.: Geomagnetically trapped alpha particles: 3. Low-altitude alpha-proton comparisons. *J. Geophys. Res.* **79**, 521, 1974
- Fennell, J.F., Blake, J.B.: Geomagnetically trapped alpha particles. In: *Magnetospheric particles and fields*, B.M. McCormac, ed.: p.149. Dordrecht, Holland: D. Reidel Publ. Co. 1976
- Fritz, T.A., Williams, D.J.: Initial observations of geomagnetically trapped alpha particles at the equator. *J. Geophys. Res.* **78**, 4719, 1973
- Fritz, T.A., Cessna, J.R.: ATS-6 NOAA low energy proton experiment. *IEEE, transactions on aerospace and electronic systems*, **AES-11**, 1145, 1975
- Fritz, T.A.: Ion Composition. In: *Physics of the Solar planetary environments*, D.J. Williams, ed.: p.716. Washington, D.C.: American Geophys. Union 1976
- Fritz, T.A., Wilken, B.: Substorm generated fluxes of heavy ions at the geostationary orbit. In: *Magnetospheric particles and fields*, B.M. McCormac, ed.: p.171. Dordrecht, Holland: D. Reidel Publ. Co. 1976
- Fritz, T.A., Arthur, C.W., Coleman, P.J., Jr., Cummings, W.D., DeForest, S.E., Erickson, K.N., Konradi, A., Masley, A.J., Mauk, B.H., McIlwain, C.E., McPherron, R.L., Paulikas, G.A., Pfitzer, K.A., Reasoner, D.L., Satterblom, P.R., Su, S.Y., Walker, R.J., Whipple, E.C., Jr., Winckler, T.R.: Significant Initial Results from ATS-6. NASA Technical Paper 1101, Goddard Space Flight Center, Maryland, 1977
- Fritz, T.A., Spjeldvik, W.N.: Observations of energetic radiation belt helium ions at the geomagnetic equator during quiet conditions. *J. Geophys. Res.* **83**, 2579, 1978
- Fritz, T.A.: The S<sup>3</sup> solid state proton detector experiment. Technical Memorandum, NOAA, U.S. Dept. of Commerce, Washington, D.C., 1979
- Fritz, T.A., Spjeldvik, W.N.: Simultaneous quiet time observations of energetic radiation belt protons and helium ions: The equatorial  $\alpha/\rho$ -ratio near 1 MeV. *J. Geophys. Res.* **84**, 2608, 1979
- Fritz, T.A., Spjeldvik, W.N.: Pitch angle distributions of geomagnetically trapped MeV helium ions during quiet times. *J. Geophys. Res.* **87**, 5095, 1982
- Gosling, J.T., Asbridge, J.R., Bame, S.J., Feldman, W.C., Paschmann, G., Sckopke, N.: Solar wind ions accelerated to 40 keV by shock wave disturbances. *J. Geophys. Res.* **85**, 744, 1980
- Hakura, Y.: Interdisciplinary summary of solar/interplanetary events during August 1972. *Space Sci. Rev.* **19**, 411, 1976
- Hamilton, D.C., Gloeckler, G., Krimigis, S.M., Bostrom, C.O.,

- Armstrong, T.P., Axford, W.I., Fan, C.Y., Lanzerotti, L.J., Hunten, D.M.: Detection of energetic hydrogen molecules in Jupiter's magnetosphere by Voyager 2: Evidence for an ionospheric plasma source. *Geophys. Res. Lett.* **7**, 813, 1980
- Hamlin, D.A., Karplus, R., Vik, R.C., Watson, K.M.: Mirror and azimuthal drift frequencies for geomagnetically trapped particles. *J. Geophys. Res.* **66**, 1, 1961
- Hess, W.N.: The radiation belt and magnetosphere. Waltham, Massachusetts: Blaisdell Publishing Co. 1968
- Hirshberg, J.: Helium abundance in the sun. *Rev. Geophys. Space Phys.* **11**, 115, 1973
- Hirshberg, J.: Composition of the solar wind: Present and past. *Rev. Geophys. Space Phys.* **13**, 1059, 1975
- Hoffman, R.A., Cahill, L.J., Jr., Anderson, R.R., Maynard, N.C., Smith, P.H., Fritz, T.A., Williams, D.J., Konradi, A., Gurnett, D.A.: Explorer 45 (S<sup>3</sup>-A) observations of the magnetosphere and magnetopause during the August 4-6, 1972 magnetic storm period. *J. Geophys. Res.* **80**, 4287, 1975
- Holzworth, R.H., Mozer, S.F.: Direct evaluation of the radial diffusion coefficient near  $L=6$  due to electric field fluctuations. *J. Geophys. Res.* **84**, 2559, 1979
- Hovestadt, D., Vollmer, O.: A satellite experiment for detecting low energy heavy cosmic rays. *Proceedings of the 12th International Conference on Cosmic Rays* **4**, 1608, 1971
- Hovestadt, D., Häusler, B., Scholer, M.: Observations of energetic particles at very low altitudes near the geomagnetic equator. *Phys. Rev. Lett.* **28**, 1340, 1972a
- Hovestadt, D.E., Achtermann, E., Ebel, B., Hausler, B., Paschmann, G.: New observations of the proton population of the radiation belt between 1.5 and 104 MeV. In: *Earth's magnetospheric processes*, B.M. McCormac, ed.: p.115. Dordrecht, Holland: D. Reidel Publ. Co. 1972b
- Hovestadt, D., Gloecker, G., Fan, C.Y., Fisk, L.A., Ipavich, F.M., Klecker, B., O'Gallagher, J.J., Scholer, M., Arbinger, H., Cain, J., Hofner, H., Kunne, E., Laeverenz, P., Tums, E.: The nuclear and ionic charge distribution particle experiments on the ISEE-1 and ISEE-C spacecraft. *IEEE, Transactions Geoscience Electronics* **GE16**, 166, 1978a
- Hovestadt, D., Gloecker, G., Fan, C.Y., Fisk, L.A., Ipavich, F.M., Klecker, B., O'Gallagher, J.J., Scholer, M.: Evidence for solar wind origin of energetic heavy ions in the Earth's radiation belt. *Geophys. Res. Lett.* **5**, 1055, 1978b
- Hovestadt, D., Klecker, B., Mitchell, E., Fennell, J.F., Gloecker, G., Fan, C.Y.: Spatial distribution of  $Z \geq 2$  ions in the outer radiation belt during quiet conditions. *Adv. Space Res.* **1**, 305, 1981
- Intriligator, D.S.: The August 1972 solar-terrestrial events: Solar wind plasma observations. *Space Sci. Rev.* **19**, 629, 1976
- Ivanova, T.A., Maslov, V.D., Panasyuk, M.I., Sosnovets, E.N.: Radiation measurements on the Cosmos-900 Satellite: 3. Spectrometry of protons and Alpha-particles with energies greater than 1 MeV/nucleon. *Kosmicheskie Issledovaniya* **18**, 567 1980
- Jentsch, V., Wibberenz, G.: An analytic study of the energy and pitch angle distribution of inner-zone protons. *J. Geophys. Res.* **85**, 1, 1980
- Jentsch, V.: On the role of external and internal source in generating energy and pitch angle distributions of inner-zone protons. *J. Geophys. Res.* **86**, 701, 1981
- Johnson, R.G., Sharp, R.D., Shelley, E.G.: The discovery of energetic He<sup>+</sup> ions in the magnetosphere. *J. Geophys. Res.* **79**, 3135, 1974
- Johnson, R.G., Sharp, R.D., Shelley, E.G.: Composition of the hot plasmas in the magnetosphere. In: *Physics of the Hot Plasma in the Magnetosphere*, B. Hultqvist and L. Stenflo, eds: p.45. New York: Plenum Publ. Co. 1975
- Johnson, R.G., Sharp, R.D., Shelley, E.G.: Observations of the ring current composition during the 29 July 1977 magnetic storm. *EOS, Trans. Am. Geophys. Union* **58**, 1217, 1977
- Johnson, R.G., Sharp, R.D., Shelley, E.G.: Observations of ions of ionospheric origin in the storm-time ring current. *Geophys. Res. Lett.* **5**, 59, 1978
- Johnson, R.G.: Energetic ion composition in the Earth's magnetosphere. U.S. National Report to the IUGG, David E. James, ed. *Rev. Geophys. Space Phys.* **17**, 696, 1979
- Jordan, C.: The ionization equilibrium of elements between carbon and nickel. *Monthly Not. R. Astron. Soc.* **142**, 501, 1969
- Joselyn, J.A., Lyons, L.R.: Ion cyclotron wave growth calculated from satellite observations of the proton ring current during storm recovery. *J. Geophys. Res.* **81**, 2275, 1976
- Krimigis, S.M., Van Allen, J.A.: Geomagnetically trapped alpha particles. *J. Geophys. Res.* **72**, 5779, 1967
- Krimigis, S.M., Verzariu, P., Van Allen, J.A., Armstrong, T.P., Fritz, T.A., Randall, B.A.: Trapped energetic nuclei  $Z \geq 3$  in the Earth's outer radiation zone. *J. Geophys. Res.* **75**, 4210, 1970
- Lanzerotti, L.J., MacLennan, C.G.: Solar particle observations during the August 1972 event. In: *Correlated interplanetary and magnetospheric observations*, D.E. Page, ed.: p. 587, Dordrecht-Holland, D. Reidel Publ. Co. 1974
- Lennartsson, W., Sharp, R.D., Shelley, E.G., Johnson, R.G., Balsiger, H.: Ion composition and energy distribution during 10 magnetic storms. *J. Geophys. Res.* **86**, 4628, 1981
- Lennartsson, W., Sharp, R.D.: A comparison of the near equatorial ion composition between quiet and disturbed conditions. *J. Geophys. Res.*, in press 1982
- Lundin, R., Lyons, L.R., Pissarenko, N.: Observations of the ring current composition at  $L$ -values less than 4. *Geophys. Res. Lett.* **7**, 425, 1980
- Lyons, L.R., Thorne, R.M., Kennel, C.F.: Electron pitch angle diffusion driven by oblique Whistler-mode turbulence. *J. Plasma Phys.* **6**, 589, 1971
- Lyons, L.R., Thorne, R.M., Kennel, C.F.: Pitch angle diffusion of radiation belt electrons within the plasmasphere. *J. Geophys. Res.* **77**, 3455, 1972
- Lyons, L.R., Thorne, R.M.: Equilibrium structure of radiation belt electrons. *J. Geophys. Res.* **78**, 2142, 1973
- Lyons, L.R., Williams, D.J.: The storm and poststorm evolution of energetic (35-560 keV) radiation belt electron distributions. *J. Geophys. Res.* **28**, 3985, 1975
- Lyons, L.R., Williams, D.J.: Storm-associated variations of equatorially mirroring ring current protons, 1-800 keV, at constant first adiabatic invariant. *J. Geophys. Res.* **81**, 216, 1976
- Lyons, L.R.: Plasma Processes in the Earth's radiation belts. In: *Solar System plasma physics*, C.F. Kennel, L.J. Lanzerotti and E.N. Parker, eds. North-Holland Publ. Co. 1979
- Lyons, L.R., Williams, D.J.: A source for the geomagnetic storm main phase ring current. *J. Geophys. Res.* **85**, 523, 1980
- Lyons, L.R., Moore, T.E.: Effects of charge exchange on the distribution of ionospheric ions trapped in the radiation belts near synchronous orbit. *J. Geophys. Res.* **86**, 5885, 1981
- Malitson, H.H., Fainberg, H.H., Stone, R.G.: Hectometric and kilometric solar radio emission observed from satellites in August 1972. *Space Sci. Rev.* **19**, 511, 1976
- Ma Sung, L.S., Gloecker, G., Fan, C.Y., Hovestadt, D.: Observations of the mean ionization states of energetic particles in the vicinity of the Earth's magnetosphere. *J. Geophys. Res.* **85**, 5983, 1980
- Matsushita, S.: Ionospheric and thermospheric responses during August 1972 storm — A review. *Space Sci. Rev.* **19**, 713, 1976
- McNulty, P.J.: Radiation effects on electronic systems. In: *Proceedings of the Air Force Geophysics Laboratory workshop on the Earth's radiation belts: January 26-27,*

- 1981, R.C. Sagalyn, W.N. Spjeldvik and W.J. Burke, eds.: pp.99-124. Air Force Systems Command, AFGL-TR-81-0311, Hanscom AFB, Massachusetts, 1981
- Miller, F.D.: Solar-cometary relations and the events of June-August 1972. *Space Sci. Rev.* **19**, 739, 1976
- Mogro-Campero, A.: Geomagnetically trapped carbon, nitrogen and oxygen nuclei. *J. Geophys. Res.* **77**, 2799, 1972
- Nakada, N.P., Mead, G.D.: Diffusion of protons in the outer radiation belt. *J. Geophys. Res.* **70**, 4777, 1965
- Nakagawa, Y.: Flares of August 1972: Analysis of dynamics. *Space Sci. Rev.* **19**, 459, 1976
- Panasjuk, M.I., Reizman, S.Ya., Sosnovets, E.N., Filatov, V.N.: Experimental results of proton and alpha-particle measurements at energies more than 1 MeV/nucleon in the radiation belts. *Geomagn. Aeron.* **15**, 887, 1977
- Panasjuk, M.I., Sosnovets, E.N.: Radiation measurements on the Cosmos-900 satellite: 3. Spectrometry of protons and alpha-particles with energies greater than 1 MeV/nucleon. *Kosmicheskie Issledovaniya* **18**, 567, 1980
- Panasjuk, M.I.: Charge state of energetic ions, (in Russian). *Kosmicheskie Issledovaniya* **18**, 83, 1980. English translation in: *Cosmic Research*, **18**, 64, 1980
- Panasjuk, M.I., Vlasova, N.A.: Anisotropy of fluxes of protons and alpha particles with energies greater than 4 MeV in the radiation belts. *Cosmic Research*, **19**, 52, 1981
- Pesses, M.E., Tsurutani, B.T., Van Allen, J.A., Smith, E.J.: Acceleration of energetic protons by interplanetary shocks. *J. Geophys. Res.* **84**, 7297, 1979
- Randall, B.A.: Time variation of magnetospheric intensities of outer zone protons, alpha particles and ions ( $Z > 2$ ). University of Iowa, Report 73-3, 1973
- Rao, U.R.: High energy cosmic ray observations during August 1972. *Space Sci. Rev.* **19**, 533, 1976
- Reagan, J.B., Meyerott, R.E., Nightingale, R.W., Gunton, R.C., Johnson, R.G., Evans, J.E., Imhof, W.L., Heath, D.F., Krueger, A.J.: Effects of the August 1972 solar particle events on stratospheric ozone. *J. Geophys. Res.* **86**, 1473, 1981
- Roederer, J.G.: Dynamics of geomagnetically trapped radiation. New York: Springer-Verlag 1970
- Rossi, B., Olbert, S.: Introduction to the physics of space. New York: McGraw-Hill 1970
- Scholer, M., Ipavich, F.M., Gloekler, G., Hoverstadt, D.: Conditions for acceleration of energetic ions  $\geq 30$  keV associated with the Earth's bow shock. *J. Geophys. Res.* **85**, 4602, 1980
- Schulz, M., Lanzerotti, L.J.: Particle diffusion in the radiation belt. New York: Springer-Verlag 1974
- Schulz, M.: Geomagnetically trapped radiation. *Space Sci. Rev.* **17**, 481, 1975
- Schulz, M.: Pitch angle diffusion in canonical coordinates: A theoretical formulation. *Astrophys. Space Sci.*, in press 1981
- Sharp, R.D., Johnson, R.G., Shelley, E.G., Harris, K.K.: Energetic  $O^+$  ions in the magnetosphere. *J. Geophys. Res.* **79**, 1844, 1974a
- Sharp, R.D., Johnson, R.G., Shelley, E.G.: Satellite measurements of auroral alpha particles. *J. Geophys. Res.* **79**, 5167, 1974b
- Sharp, R.D., Johnson, R.G., Shelley, E.G.: The morphology of energetic  $O^+$  ions during two magnetic storms: Temporal variations. *J. Geophys. Res.* **81**, 3283, 1976a
- Sharp, R.D., Johnson, R.G., Shelley, E.G.: The morphology of energetic  $O^+$  ions during two magnetic storms: Latitudinal variations. *J. Geophys. Res.* **81**, 3292, 1976b
- Sharp, R.D., Shelley, E.G., Johnson, R.G.: A search for helium ions in the recovery phase of a magnetic storm. *J. Geophys. Res.* **82**, 2361, 1977a
- Sharp, R.D., Johnson, R.G., Shelley, E.G.: Observation of an ionospheric acceleration mechanism producing energetic (keV) ions primarily normal to the geomagnetic field direction. *J. Geophys. Res.* **82**, 3324, 1977b
- Shelley, E.G., Johnson, R.G., Sharp, R.D.: Satellite observations of energetic heavy ions during a geomagnetic storm. *J. Geophys. Res.* **77**, 6104, 1972
- Shelley, E.G., Johnson, R.G., Sharp, R.D.: Morphology of energetic  $O^+$  in the magnetosphere. In: *Magnetospheric physics*, B.M. McCormac, ed.: pp.135-139. Dordrecht, Holland: D. Reidel Publ. Co. 1974
- Shelley, E.G., Sharp, R.D., Johnson, R.G.: Satellite observations of an ionospheric acceleration mechanism. *Geophys. Res. Lett.* **3**, 654, 1976a
- Shelley, E.G., Sharp, R.D., Johnson, R.G.:  $He^{++}$  and  $H^+$  flux measurements in the dayside cusp: Estimates of convection electric field. *J. Geophys. Res.* **81**, 2363, 1976b
- Shelley, E.G., Sharp, R.D., Johnson, R.G.: Ion composition in the quiet time magnetosphere. *EOS, Trans. Am. Geophys. Union* **58**, 1217, 1977
- Shelley, E.G.: Heavy ions in the magnetosphere. *Space Sci. Rev.* **23**, 465, 1979
- Simnett, G.M.: Solar cosmic radiation during August 1972. *Space Sci. Rev.* **19**, 579, 1976
- Smith, E.J.: The August 1972 solar-terrestrial events: Interplanetary magnetic field observations. *Space Sci. Rev.* **19**, 661, 1976
- Söraas, F., Davis, L.R.: Temporal variations of the 100 keV to 1,700 keV trapped protons observed on satellite Explorer 26 during the first half of 1965. NASA/Goddard Space Flight Center, Report X-612-68-328, Maryland, 1968
- Spjeldvik, W.N., Thorne, R.M.: The cause of storm after effects in the middle latitude D-region. *J. Atmos. Terr. Phys.* **37**, 777, 1975
- Spjeldvik, W.N.: Equilibrium structure of equatorially mirroring radiation belt protons. *J. Geophys. Res.* **82**, 2801, 1977
- Spjeldvik, W.N., Fritz, T.A.: Energetic ionized helium in the quiet time radiation belts: Theory and comparison with observation. *J. Geophys. Res.* **83**, 654, 1978a
- Spjeldvik, W.N., Fritz, T.A.: Theory for charge states of energetic oxygen ions in the Earth's radiation belts. *J. Geophys. Res.* **83**, 1583, 1978b
- Spjeldvik, W.N., Fritz, T.A.: Composition of the hot plasma in the inner magnetosphere: Observations and theoretical analysis of protons, helium ions and oxygen ions. *Space Research*, **XVIII**, 317, 1978c
- Spjeldvik, W.N., Fritz, T.A.: Quiet time observations of equatorially trapped megaelectronvolt radiation belt ions with nuclear charge  $Z \geq 4$ . *J. Geophys. Res.* **83**, 4401, 1978d
- Spjeldvik, W.N.: Expected charge states of energetic ions in the magnetosphere. *Space Sci. Rev.* **23**, 499, 1979
- Spjeldvik, W.N.: State of the art of energetic particle measurements in the Earth's magnetosphere. In: *Proceedings of the Air Force Geophysics Laboratory workshop on the Earth's radiation belt: January 26-27, 1981*, R.C. Sagalyn, W.N. Spjeldvik and W.J. Burke eds.: pp.125-208. Air Force Systems Command, AFGL-TR-81-0311, Hanscom AFB, Mass., 1981a
- Spjeldvik, W.N.: Modelling of magnetically trapped radiation in the inner magnetosphere of the Earth. In: *Proceedings of the Air Force Geophysics Laboratory workshop on the Earth's radiation belts: January 26-27, 1981* R.C. Sagalyn, W.N. Spjeldvik and W.J. Burke, eds.: pp. 245-270. Air Force Systems Command, AFGL-TR-81-0311, Hanscom AFB, Mass., 1981b
- Spjeldvik, W.N., Fritz, T.A.: Observations of energetic helium ions in the Earth's radiation belts during a sequence of geomagnetic storms. *J. Geophys. Res.* **86**, 2317, 1981a
- Spjeldvik, W.N., Fritz, T.A.: Energetic heavy ions with nuclear charge  $Z \geq 4$  in the equatorial radiation belts of the Earth: Magnetic storms. *J. Geophys. Res.* **86**, 2349, 1981b
- Spjeldvik, W.N., Fritz, T.A.: Observations of ions with nucle-

- ar charge  $Z \geq 9$  in the inner magnetosphere. *J. Geophys. Res.* **86**, 7749, 1981c
- Spjeldvik, W.N., Fritz, T.A.: Experimental determination of geomagnetically trapped energetic heavy ion fluxes. In: Energetic ion composition of the Earth's magnetosphere, *Advances in Earth and Planet. Sci.*, **5**, R.G. Johnson, ed. Tokyo: Terra Scientific Publishing, in press 1982.
- Störmer, C.: *The Polar Aurora*. Oxford: Clarendon Press 1955
- Tinsley, B.A.: Evidence that the recovery phase ring current consists of helium ions. *J. Geophys. Res.* **81**, 6193, 1976
- Vaisberg, O.L., Zastenker, G.N.: Solar wind and magnetosheath observations at earth during August 1972. *Space Sci. Rev.* **19**, 687, 1976
- Van Allen, J.A., Randall, B.A., Krimigis, S.M.: Energetic C, N, O nuclei in the Earth's outer radiation zone. *J. Geophys. Res.* **75**, 6085, 1970
- Webber, W.R., Roelof, E.C., McDonald, F.B., Teegarden, B.J., Trainor, J.: Pioneer 10 measurements of the charge and energy spectrum of solar cosmic rays during 1972 August. *Astrophys. J.* **199**, 482, 1975
- West, H.I., Jr., Buck, R.M., Walton, J.R.: Electron pitch angle distributions throughout the magnetosphere as observed with OGO-5. *J. Geophys. Res.* **78**, 1064, 1973
- West, H.I., Jr., Buck, R.M., Davidson, G.: Study of energetic electrons in the outer radiation belt regions using data obtained by the LLL spectrometer on OGO-5 in 1968. Lawrence Livermore Laboratory Report **UCRL-52807**, California, 1979
- West, H.I., Jr., Buck, R.M., Davidson, G.T.: The dynamics of energetic electrons in the Earth's outer radiation belt during 1968 as observed by the Lawrence Livermore National Laboratory's spectrometer on OGO-5. *J. Geophys. Res.* **86**, 2111, 1981
- Westphalen, H., Spjeldvik, W.N.: On the energy dependence of the radial diffusion coefficient and spectra of inner radiation belt particles: Analytic solutions and comparison with numerical results. *J. Geophys. Res.* **87**, 8321, 1982
- Wilken, B., Fritz, T.A., Stüdemann, W.: Experimental techniques for ion composition measurements in space. *Nuclear Instruments and Methods* **196**, 161, 1982
- Williams, D.J., Lyons, L.R.: The proton ring current and its interaction with the plasmopause: Storm recovery phase. *J. Geophys. Res.* **79**, 4195, 1974a
- Williams, D.J., Lyons, L.R.: Further aspects of the proton ring current interaction with the plasmopause: Main and recovery phases. *J. Geophys. Res.* **79**, 4791, 1974b
- Williams, D.J., Keppler, E., Fritz, T.A., Wilken, B., Wibberenz, G.: The ISEE 1 and 2 medium energy particle experiment. *IEEE, Transactions on Geoscience Electronics* **GE-16**, 270, 1978
- Williams, D.J.: Ring current composition and sources. In: *Dynamics of the magnetosphere*, S.I. Akasofu, ed.: pp.407-424. Dordrecht, Holland: D. Reidel Publ. Co. 1980
- Williams, D.J.: Ring current composition and sources: An update. *Planet. Space Sci.* **29**, 1195, 1981
- Williams, D.J.: The Earth's ring current: Causes, generation and decay. *Space Sci. Rev.*, in press 1982
- Young, D.T., Balsiger, H., Geiss, J.: Correlations of magnetospheric ion composition with geomagnetic and solar activity. *J. Geophys. Res.*, in press 1982
- Young, D.T.: Ion composition and dynamics at ring current energies. *J. Geophys.* (this issue), 1983

Received November 12, 1982; Revised version February 10, 1983

Accepted February 10, 1983

# Energy and Charge Distribution of Energetic Helium Ions in the Outer Radiation Belt of the Earth\*

B. Klecker<sup>1</sup>, D. Hovestadt<sup>1</sup>, M. Scholer<sup>1</sup>, G. Gloeckler<sup>2</sup>, F.M. Ipavich<sup>2</sup>, and C.Y. Fan<sup>3</sup>

<sup>1</sup> Max-Planck-Institut für Physik und Astrophysik, Institut für extraterrestrische Physik, D-8046 Garching, Federal Republic of Germany

<sup>2</sup> University of Maryland, Department of Physics and Astronomy, College Park, MD 20742, USA

<sup>3</sup> University of Arizona, Department of Physics, Tucson, AZ 85721, USA

**Abstract.** We report the first direct determination of the charge states of energetic helium ions in the outer radiation belt. Our measurements, in the range  $L=3-4$ , revealed unexpected high fluxes of singly ionized helium below 1 MeV/nucleon: We found a  $\text{He}^+/\text{He}^{2+}$  ratio of  $0.4 \pm 0.1$  at  $L=3.3$  with a steep decrease to  $\sim 0.04$  at  $L=3.7$  at energies of 0.50–0.57 MeV/nucleon. The data were obtained with the MPE/UoMd experiment aboard the ISEE-1 spacecraft during a near equator ( $B/B_0 < 1.025$ ) perigee pass on 17 Nov 1977. The observations suggest that fast cross- $L$  transport during magnetic storms and non-adiabatic motion may play an important role for the distribution of helium ions at MeV energies in the outer radiation belt.

**Key words:** Earth's outer radiation belt – Helium ionic charge composition – Radial diffusion

## Introduction

The observation of ions heavier than protons in the Earth's radiation belt has been recognized for a long time as providing a test for our understanding of radiation belt acceleration, propagation and loss processes (Cornwall, 1972; Krimigis, 1973; Blake, 1973). In addition, these tracer ions give unique insight into the sources of the trapped radiation: Large  $\text{He}^+$  and  $\text{O}^+$  fluxes at suprathermal energies as discovered at low altitudes and in the storm-time ring current (Shelley et al., 1972; Sharp et al., 1974, 1977; Balsiger et al., 1980) suggest strongly that the ionosphere is an important source of the trapped radiation. At somewhat higher energies ( $\geq 0.4$  MeV/nucleon) the first unambiguous measurement of carbon and oxygen ions reported by Hovestadt et al. (1978a) revealed a C/O-ratio of  $\sim 1$  at  $L > 2.7$ , thus given strong support for the idea of an extraterrestrial source of these more energetic trapped ions in the outer radiation belt. Furthermore, there is now increasing evidence that heavy ions are not always a minor species but may also in part determine the radiation belt dynamics: Tinsley (1976) and Lyons and Evans (1976), for example, pointed out that at ring-current energies  $Z > 1$  ions (possibly  $\text{He}^+$ ) rather than protons may be the dominant species.

Observations on the distribution of energetic helium in the Earth's radiation belt have been reported by many authors (Blake and Paulikas, 1972; Fritz and Williams, 1973; Fennell et al., 1974; and more recently by Fritz and Spjeldvik, 1978; Hovestadt et al., 1978a, 1981a; Blake et al., 1980; Spjeldvik and Fritz, 1981). These observational results have been complemented by extensive numerical calculations, modeling the transport of energetic ions in the radiation belt (Cornwall, 1972; Spjeldvik and Fritz, 1978a, b). These computations demonstrated the fundamental importance of charge exchange reactions for the distribution of heavy ions in the stationary radiation belt.

The model calculations predict, that, at low energies ( $< 0.25$  MeV/nuc) and small  $L$ -values ( $L \lesssim 3$ ), singly ionized helium is more abundant than doubly ionized helium. At higher energies ( $> 0.5$  MeV/nuc), however, doubly ionized helium dominates over  $\text{He}^+$ . These results are derived for a quiet magnetosphere assuming steady state conditions. If nonstationary transport during geomagnetically disturbed time periods plays a significant role, deviations from the stationary charge state distributions can be expected. A direct measurement of the ion charge states in the MeV energy range was, until recently, beyond experimental capabilities. In this paper we report the first direct measurement of the charge states of helium at energies  $> 0.5$  MeV/nucleon obtained with the Max-Planck-Institut/University of Maryland experiment aboard the ISEE-1 spacecraft in 1977.

## Satellite and Instrumentation

The data were obtained with the Ultra-Low-Energy-Z-E-Q measuring analyzer (ULEZEQ) of the Max-Planck-Institut/University of Maryland experiment on ISEE-1.

The ISEE-1 satellite was launched into an eccentric orbit with an initial apogee of  $\sim 23 R_E$ , a perigee of  $\sim 600$  km, an inclination of  $28.7^\circ$  and a period of  $\sim 57$  h. During the first months of the mission the spacecraft moved, during one out of five low altitude passes, close to the geomagnetic equator over an extended range of  $L$ -values. Thus it is possible to study the characteristics of equatorially mirroring ions in great detail.

The ULEZEQ sensor is mounted with its look direction perpendicular to the spin axis of ISEE-1, which is spinning nearly perpendicular to the ecliptic plane at  $\sim 20$  rpm. The sensor combines the energy/charge determination in an electrostatic deflection analyzer with a  $dE/dx$  vs  $E$  measurement

\* Based on a paper given at the Symposium on Plasma and Energetic Particles in the Magnetosphere, EGS Meeting, 23–27 August 1982, Leeds, U.K.

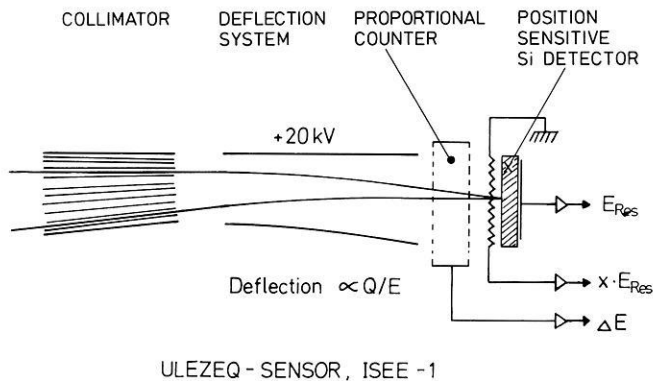


Fig. 1. Cross-sectional view of the ULEZEQ sensor on ISEE-1

Table 1. ULEZEQ Response<sup>a</sup>

Rate-ID	Particle	Energy range	Comment
UHP 1	proton	0.45–1.2 MeV/nuc	Rate channel
UHP 2	proton	1.20–3.0 MeV/nuc	Rate channel
UHA	helium	0.25–3.0 MeV/nuc	Rate channel
UHH	Z > 2	> 0.3 MeV/nuc (O)	Rate channel
		> 0.2 MeV/nuc (Fe)	Rate channel
HE 1	helium	0.42–0.50 MeV/nuc	PHA events, normalized with UHA-rate.
HE 2	helium	0.50–0.57 MeV/nuc	
HE 3	helium	0.57–0.67 MeV/nuc	
HE 4	helium	0.67–0.95 MeV/nuc	

<sup>a</sup> Geometrical Factor:  $\sim 0.02 \text{ cm}^2 \text{ sr}$

to derive both the ionic and nuclear charge as well as the energy of the particles between 0.3 and 3 MeV/nucleon. A schematic cross section of the sensor is shown in Fig. 1. For ions passing through the multislit collimator and the electrostatic deflection analyzer and stopping in the position sensitive solid state detector (PSD), three parameters are measured: (1) the energy loss,  $\Delta E$ , in a thin window, flow-through, proportional counter (PC), (2) the deflection,  $x$ , and (3) the residual energy,  $E_{Res}$ , in the position sensitive detector. These three parameters, in principle, unambiguously determine the nuclear charge  $Z$ , the ionic charge  $Q$ , and the energy  $E$  of the incoming ion. The energy response of the sensor is summarized in Table 1. A detailed description of the experiment may be found elsewhere (Hovestadt et al., 1978 b).

### Charge Determination

The ionic charge  $Q$  can be derived from the position signal ( $x \cdot E_{Res}$ ) and the incident energy ( $E_{in}$ ) of the particles. However, due to non-uniformities in the resistive layer (palladium) of the position sensitive detector, which were established after the launch of ISEE-1, the position signal does not depend linearly on the actual deflection of the particles. In order to regain the position calibration we evaluated the position response of the PSD of our experiment on ISEE-1 using in-flight data obtained during a large solar flare in September 1978. Figure 2 shows the position response for  $\text{He}^{2+}$  as a function of incident energy. The corresponding response of the PSD of our sensor of identical design on ISEE-3 is shown for comparison. The unit of the position response corresponds to the maximum deflection of the ions. Figure 2 indicates that the position signal

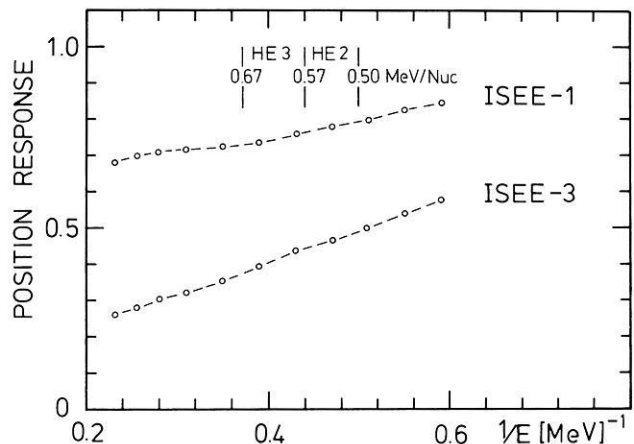


Fig. 2. Position response of the position sensitive detectors on ISEE-1 and ISEE-3, respectively. Data obtained for a large solar flare (day 268 0:00–270 11:00 UT, 1978) have been used

of the PSD on ISEE-1 becomes insensitive to the actual deflection at energies  $\geq 0.7 \text{ MeV/nucleon}$ . We restricted the charge analysis therefore to the energy range 0.5–0.67 MeV/nucleon, where the charge resolution, although degraded relative to ISEE-3, is sufficient to separate clearly the helium charge states. This energy range has been subdivided into two energy bins, denoted HE 2 and HE 3, in Fig. 2.

### Observations

We analyzed the helium charge state distribution during the low altitude pass of ISEE-1 on 17 Nov 1977. This orbit was selected because the magnetosphere was reasonably quiet during this day ( $Kp < 3$ ,  $DST > -50 \gamma$ ) and the time period met our requirements of (1) having good data coverage and high time resolution due to high data rate and (2) ISEE-1 being close to the geomagnetic equator. It should, however, be noted that the preceding period of 6 days was not quiet with an average  $Kp$  index of  $\sim 4$  and a maximum  $Kp$  value of  $6^-$  for 6 h. During the time period analyzed, ISEE-1 was very close to the equator ( $B/B_0 < 1.025$ ). This is essential for the present analysis: Due to the pitch angle distribution of equatorially mirroring helium ions, which is sharply peaked at  $90^\circ$  (Fritz and Williams, 1973; Blake et al., 1980; Hovestadt et al., 1981 a; Fritz and Spjeldvik, 1982), the counting statistic for off-equator passes would not be sufficient for a detailed charge analysis with good spatial resolution.

We restricted our analysis to  $L > 3.2$  in order to minimize the influence of the background due to the high fluxes of energetic protons. Figure 3 shows a typical example of the  $\Delta E$  versus  $E_{Res}$  pulse height matrix obtained during the time period 20:46–20:51 UT on 17 Nov 1977, ( $L = 3.6$ – $3.8$ ). HE 1, HE 2, HE 3, and HE 4 denote four boxes along the He-track used for the evaluation of helium energy spectra. The energy scale indicates the incident energy of  $^4\text{He}$  ions. This pulse height matrix demonstrates that protons, pile-up counts produced by protons, and helium ions are clearly separated. Note that the number of events along the proton track is considerably reduced relative to the helium and proton pile-up counts. This is due to the electronic selection system which significantly suppresses all counts in the shaded lower left area of the matrix.

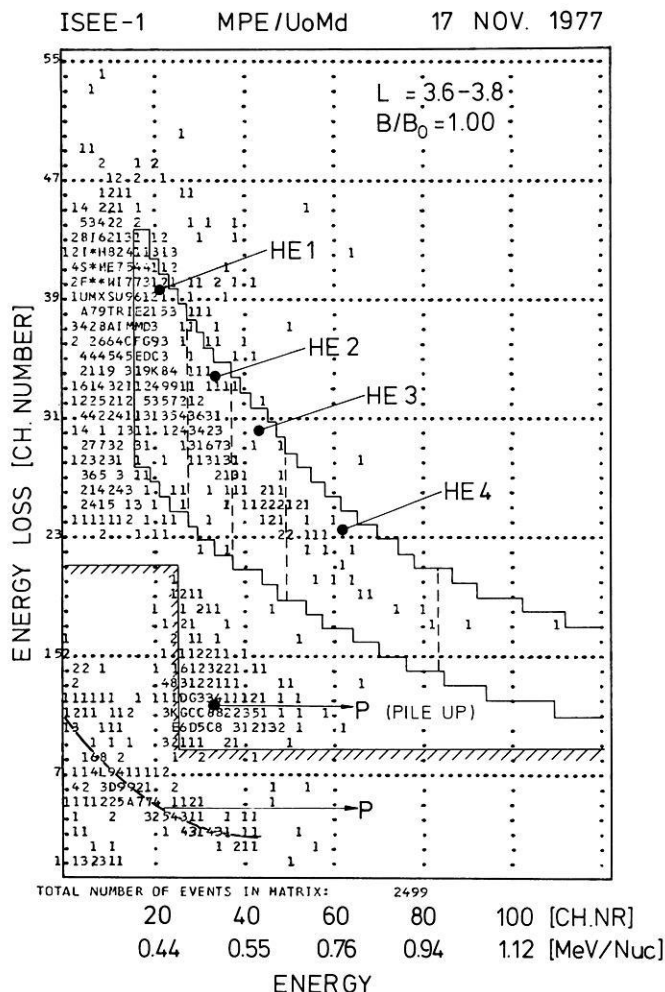


**Fig. 3.** Energy loss versus residual energy pulse-height matrix accumulated during the near equator perigee pass of ISEE-1 on 17 Nov 1977, (20:46–20:51 UT)

### Helium Charge Analysis

Ionic charge histograms for helium ions are derived by first preselecting the helium in the  $\Delta E$  versus  $E_{Res}$  pulse height matrix and subsequently converting the position signal into a charge scale using the results of the ISEE-1 in-flight calibration as described above. In Fig. 4 helium charge histograms are presented for two energy ranges (0.5–0.57, 0.57–0.67 MeV/Nuc, labelled HE 2 and HE 3 in Fig. 3) and for four  $L$ -intervals between  $L=3.2$  and  $L=4.0$ . We find a significant amount of singly ionized helium at low  $L$ -values ( $L \lesssim 3.6$ ) in both energy ranges with a drop of the  $\text{He}^+/\text{He}^{2+}$ -ratio down to the sensitivity level of the experiment at  $L \gtrsim 3.6$ . The maxima of the charge histograms at the higher energy range (right panel) are not centered at integral charge state numbers. This reflects the uncertainties in the charge determination of helium which become larger with increasing energy. The  $L$ -dependence of the  $\text{He}^+/\text{He}^{2+}$ -ratio in the energy range 0.50–0.57 MeV/nucleon is shown more quantitatively in Fig. 5. The  $\text{He}^+/\text{He}^{2+}$ -ratios have been derived by fitting two gaussians to the corresponding charge histograms  $H(Q)$  of Fig. 4, using a least square fit procedure with 5 free parameters:

$$F(Q) = \alpha_0 + \alpha_1 \exp \left[ - \left( \frac{Q - 0.5Q_2}{\Delta Q} \right)^2 \right] + \alpha_2 \exp \left[ - \left( \frac{Q - Q_2}{\Delta Q} \right)^2 \right]. \quad (1)$$

$F(Q)$  is optimized with respect to the coefficients  $\alpha_1$ ,  $\alpha_2$ , and a possible background  $\alpha_0$  using a linear regression procedure. The width of the charge distribution (characterized by  $\Delta Q$ ) and the center of the  $\text{He}^{2+}$  distribution ( $Q_2$ ) are adjusted by an iterative method to allow for small variations in the instrumental parameters.

The resulting minimum variance double gaussian  $F(Q)$  is shown in Fig. 4 (dashed lines). The  $\text{He}^+/\text{He}^{2+}$ -ratios are calculated by numerically integrating the gaussian fits to the distributions of  $\text{He}^+$  and  $\text{He}^{2+}$ . The errors as given in Fig. 5 are derived as a combination of the standard deviation of the fit and the statistical errors resulting from the integrals of the  $\text{He}^+$  and  $\text{He}^{2+}$  distribution, respectively. It can be seen in Fig. 5 that the  $\text{He}^+/\text{He}^{2+}$ -ratio drops from  $0.4 \pm 0.1$  at  $L=3.2-3.4$  to  $0.075 \pm 0.03$  at  $L=3.4-3.6$  and to  $\sim 0.04$  at  $L > 3.6$ .

### Energy Spectra and Distribution Function

Perpendicular differential helium fluxes ( $j_{\perp}$ ) at the equator ( $B/B_0 < 1.025$ ) are presented in Fig. 6. These fluxes have been derived from spin averages of the helium pulse height matrices and of the total helium counting rate, using the given angle between the spacecraft spin axis and the local magnetic field direction. For the pitch-angle distribution of helium ions the functional form  $j(\alpha) = j_{\perp} \cdot \sin^n(\alpha) = j_{\perp} \cdot (B/B_0)^{n/2}$  has been assumed, where  $\alpha$  is the pitch angle of the particles. For  $n$  a value of 10 has been used which is in good agreement with experimental results in this energy range (Blake et al., 1980; Hovestadt et al., 1981a; Fritz and Spjeldvik, 1982). The helium pulse height counts are converted to  $j_{\perp}$  on a 64 s time basis. Figure 6 shows that the helium spectra steepen considerably with increasing  $L$ -value with a spectral index  $\gamma = -4.3$  at  $L=3.5$  and  $\gamma = -7.1$  at  $L=3.9$ . With the spectra of equatorially mirroring helium ions as a function of  $L$ -value we are able to calculate the distribution function  $f \sim j_{\perp} \cdot L^3$  for several values of the first adiabatic invariant  $\mu$ . Figure 7 shows the distribution function of helium for several values of the magnetic moment  $\mu$  (200–600 MeV/Gauss). Above  $L \sim 3.5$  these curves have a positive slope indicating an inward radial transport of these ions. It should be noted that this result is derived for the total ( $\text{He}^+ + \text{He}^{2+}$ ) helium population. The individual distribution functions of  $\text{He}^+$  and  $\text{He}^{2+}$  cannot be calculated because the ionic charge analysis is only possible for a very limited energy range, as discussed above.

### Discussion

The results of our analysis of the energy spectra and ionic charge composition of helium during the near equator perigee pass of ISEE-1 on 17 Nov 1977, can be summarized as follows:

- significant fluxes of singly ionized helium ( $\text{He}^+/\text{He}^{2+} = 0.4 \pm 0.1$ ) have been observed at low  $L$ -values ( $L = 3.3$ )
- the  $\text{He}^+/\text{He}^{2+}$ -ratio exhibits a sudden decrease from a value of  $\sim 0.4$  at  $L=3.3$  to  $\sim 0.04$  at  $L=3.7$

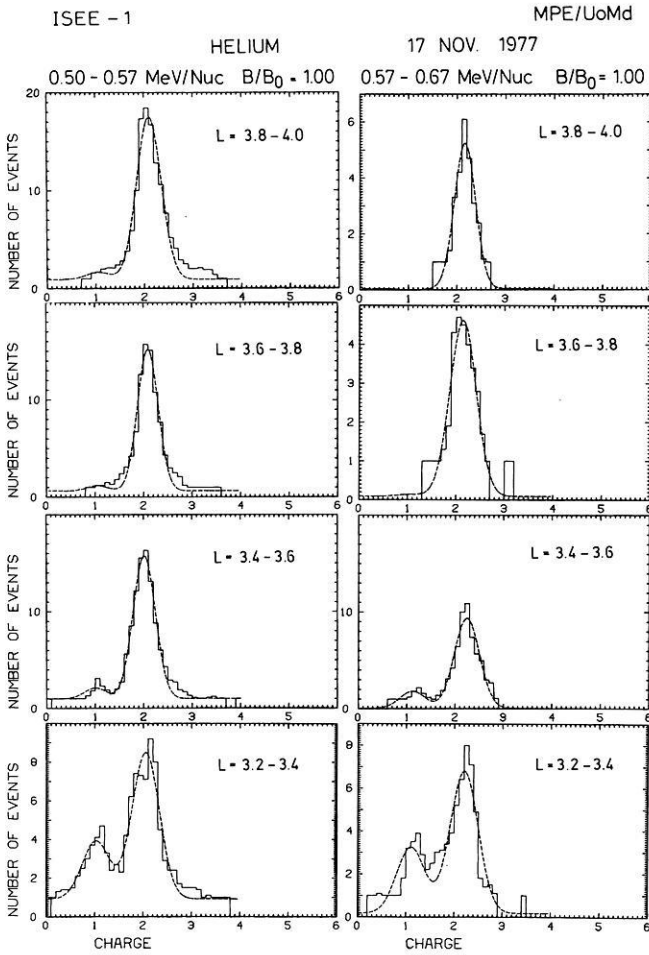


**Fig. 4.** Helium charge histograms in the energy range 0.50–0.67 MeV/nuc obtained on ISEE-1 during the near equator perigee pass on 17 Nov 1977

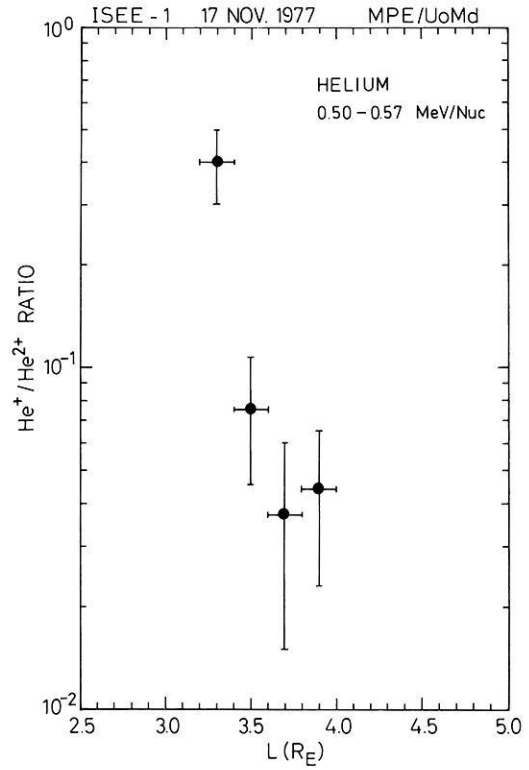


**Fig. 5.**  $\text{He}^+ / \text{He}^{2+}$ -ratio in the energy range 0.50–0.57 MeV/nuc as a function of  $L$ -value. The ratios are derived from the double-gaussian fit shown in Fig. 4 (left panels)

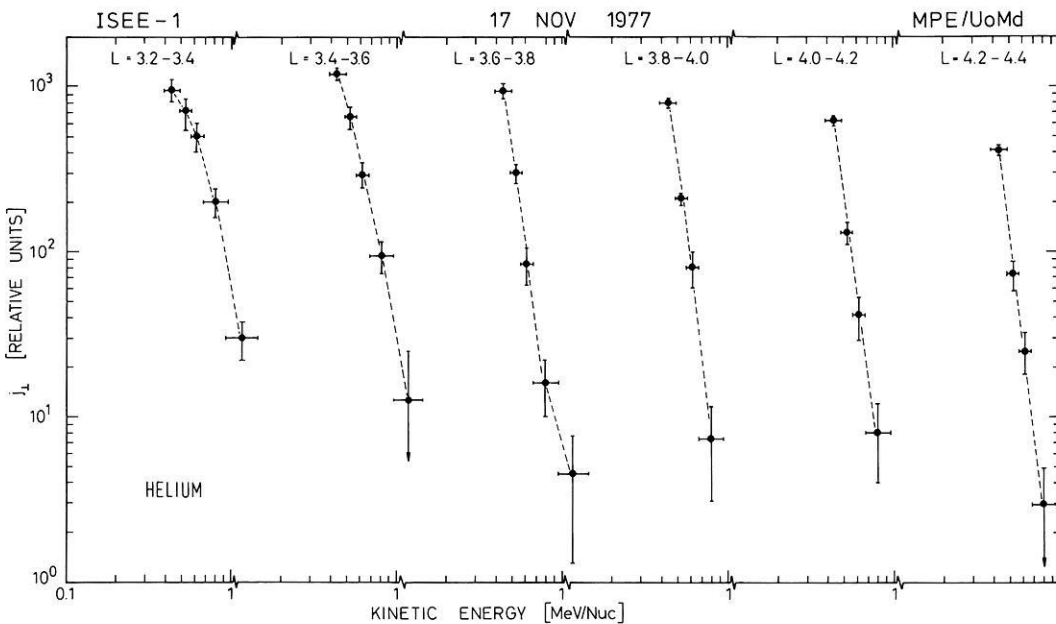


**Fig. 6.** Helium energy spectra in the  $L$ -range 3.2–4.4 as obtained on ISEE-1 during a near equator perigee pass ( $B/B_0 < 1.025$ ) on 17 Nov 1977

- the helium energy spectra at the equator become steeper with increasing distance from the Earth
- the distribution function  $f(\mu, L)$  of helium, evaluated at constant magnetic moment (200–600 MeV/Gauss) exhibits a positive radial gradient for  $L \gtrsim 3.5$ .

Among these results the most striking feature is the high  $\text{He}^+/\text{He}^{2+}$ -ratio at  $L=3.3$  and the steep decrease towards higher  $L$ -values. The positive slope of the helium distribution function  $f(L)$  and the steepening of the spectra with increasing distance from the Earth are, at least qualitatively, consistent with conventional steady state radial diffusion models, where the particle distribution is determined by cross- $L$  diffusion from an outer boundary to the inner radiation belt and by losses due to charge exchange reactions and coulomb interactions. However, the sudden decrease of the  $\text{He}^+/\text{He}^{2+}$ -ratio as observed between  $L=3.3$  and

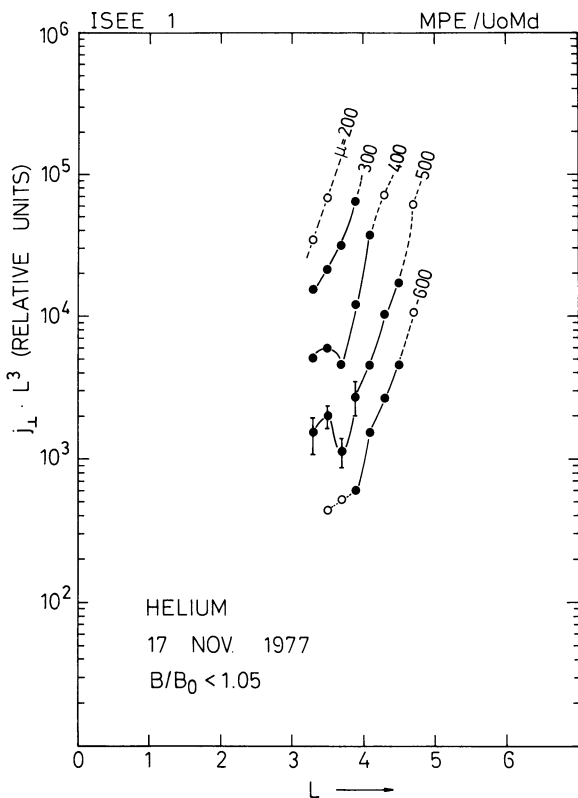


**Fig. 7.** Distribution function of helium derived at constant magnetic moment. Open circles indicate that extrapolations of the energy spectra as shown in Fig. 6 have been used

3.7 during the perigee pass on 17 Nov 1977, seems to be not consistent with such a stationary model.

The numerical calculations of Spjeldvik and Fritz (1978a, 1981) showed that, for steady state conditions, the  $\text{He}^+/\text{He}^{2+}$ -ratio at 0.5 MeV/nucleon is almost constant with  $L$ . Spjeldvik and Fritz (1981) obtained  $\text{He}^+/\text{He}^{2+} \sim 0.02\text{--}0.03$  between  $L=3$  and 5. Cornwall (1972) also obtained  $\text{He}^+/\text{He}^{2+} \sim \text{const}$  with  $L$  but with a much higher value of  $\sim 0.5\text{--}1.0$  between  $L=3$  and 4.5 at 0.5 MeV/nucleon. However, this discrepancy may be due to the different boundary conditions in  $\mu$ -space and/or to different values of the charge exchange cross sections used by Cornwall (1972). Furthermore, the upper boundary in  $\mu$ -space was, in his calculation, at  $\mu=880$  MeV/Gauss and thus may strongly influence the results at 0.5 MeV/nucleon, which corresponds to  $\mu > 230$  MeV/Gauss for  $L > 3.3$ .

Both model calculations revealed small variations of the  $\text{He}^+/\text{He}^{2+}$ -ratio with  $L$  which are certainly much less than the factor of  $\sim 10$  observed during the perigee pass on 17 Nov 1977. Qualitatively, only a small variation of the  $\text{He}^+/\text{He}^{2+}$ -ratio with radial distance (at constant energy) can be expected, because in this range of energies and  $L$ -values the  $\text{He}^+/\text{He}^{2+}$ -ratio is determined predominantly by charge exchange reactions. This is due to the fact that at  $L \sim 3\text{--}4$  and  $E \sim 0.5$  MeV/nucleon, the typical time scales for coulomb energy degradation, charge exchange losses, and diffusive transport during magnetospherically quiet times are much larger than the time scales for charge exchange reactions. This is illustrated in Table 2 which shows typical transport and loss time scales for energetic helium ions in the radiation belt. The time scales for coulomb losses ( $\tau_{cb}$ ) and charge exchange losses ( $\tau_{CE}$ ) are taken from Spjeldvik and Fritz (1981). The time scale for diffusive transport ( $\tau_D$ ) has been calculated adopting

$$D_{LL} = 2 \times 10^{-10} \cdot L^{10} + 2 \times 10^{-5} \cdot L^{10} / (L^4 + (\mu/Q)^2) [R_e^2/d] \quad (2)$$

for the radial diffusion coefficient, where the first term is due to magnetic field fluctuations and the second term arises from electric field fluctuations;  $\mu$  and  $Q$  are the magnetic moment in MeV/Gauss and the ionic charge, respectively. The same function  $D_{LL}$  has been used by Spjeldvik (1977) and by Spjeldvik and Fritz (1978a) for their model calculations of proton and helium ion distributions in the quiet time radiation belt and resulted in a reasonably good fit to their quiet time experimental data. The time scales for charge exchange reactions  $\tau_{12}(\text{He}^+ \rightarrow \text{He}^{2+})$  and  $\tau_{21}(\text{He}^{2+} \rightarrow \text{He}^+)$  have been calculated with

$$\tau_{ij} = [\sigma_{ij} \langle H \rangle v]^{-1} \quad (3)$$

**Table 2.** Typical transport and loss time scales for energetic helium ions in the radiation belt

$L$	$E$ (MeV/nuc)	$\tau_{cb}^a$ (days)	$\tau_{CE}^a$ (days)	$\tau_D^b$		$\tau_{21}$ (days)	$\tau_{12}$ (days)
				$\text{He}^+$ (days)	$\text{He}^{2+}$ (days)		
2.95	0.5	412	54,500	21,400	6,420	151	2.2
3.55	0.5	965	71,400	7,100	2,700	290	4.2
4.0	0.5	1,660	115,000	2,990	1,420	433	6.3
4.45	0.5	19,000	174,000	1,250	730	590	8.6
5.05	0.5	308,000	240,000	404	292	900	14.5

<sup>a</sup> Spjeldvik and Fritz, 1981

<sup>b</sup> Calculated with Eq. (2)

using the charge exchange cross sections ( $\sigma_{ij}$ ) given in Spjeldvik and Fritz (1978a) and assuming a neutral hydrogen density ( $\langle H \rangle$ ) of the Earth's exosphere (at a temperature of 950° K) as given by Tinsley (1976). The time scales derived with (3) will, of course, rely strongly on the accuracy of the charge exchange cross sections used. The cross sections compiled by Spjeldvik and Fritz (1978a), however, seem to agree reasonably well with experimental values (Allison, 1958; Pivovar et al., 1962).

From Table 2 it can be seen that the dominant (smallest) time scales, determining the relative abundance of  $\text{He}^+$  and  $\text{He}^{2+}$ , are  $\tau_{12}$  and  $\tau_{21}$  and that the dominant loss process for  $\text{He}^+$  in this range of energy and radial distance is the  $\text{He}^+ \rightarrow \text{He}^{2+}$  charge exchange reaction with a time scale  $\tau_{12}$  of only  $\sim 6$  days at  $L=4$ . Because of this small time scale it is unlikely that small variations of the parameters used for the model calculations may result in drastic changes of the radial dependence of the  $\text{He}^+/\text{He}^{2+}$ -ratio. However, non-stationary processes on time scales  $\tau \sim \tau_{12}$  could result in large deviations from the stationary distribution of helium ions.

### Non-Stationary Processes

The perigee pass on 17 Nov 1977 is in the recovery phase of a magnetic storm ( $DST \sim -75$  nT) with increased geomagnetic activity (maximum  $Kp \sim 6^-$ ) starting about 6 days before our measurement. Therefore, it is conceivable that non-stationary processes such as direct injection of helium ions into the region  $L \sim 3.2-3.6$  or fast (adiabatic) cross- $L$  transport may be important. The latter has been proposed, for example by Lyons and Williams (1980), to explain sudden temporal changes of the trapped proton distribution in the outer radiation belt. Below we will discuss both possibilities briefly.

(1) *Direct Injection of Energetic Solar Helium Ions.* Although the possibility of direct trapping of solar particles has been discarded until recently (Krimigis, 1970; Blake and Paulikas, 1972), the study of helium ions during magnetic storms by Spjeldvik and Fritz (1981) appears to suggest that non-diffusive injection processes occasionally play an important role during geomagnetic disturbances following large solar particle events. Furthermore, large abundances of singly ionized helium in low energy solar flare particles ( $\text{He}^+/\text{He}^{2+} \sim .20$ ) have been discovered recently (Hovestadt et al., 1981b). However, neither shortly before nor after the perigee pass under discussion has an intensity increase of the low energy solar ion population been observed in interplanetary space. Therefore, we conclude that direct injection of solar particles is not very likely to constitute the source of  $\text{He}^+$  observed on 17 Nov 1977, although it may be important for the 4 Aug 1972 event studied by Spjeldvik and Fritz (1981).

(2) *Fast Cross- $L$  Drift of the Ions:* Lyons and Williams (1980) explained flux increases in the trapped low energy ion population observed during geomagnetic storms at  $L=2.5-4$  by an inward drift of the ions, driven by an equatorial azimuthal electric field. The time scale of this process is of the order of the drift period and would be sufficiently fast to transport singly ionized helium down to  $L=3.3$ . However, Lyons and Williams (1980) did not observe an inward drift at energies  $\geq 100$  keV. The latter fact is a natu-

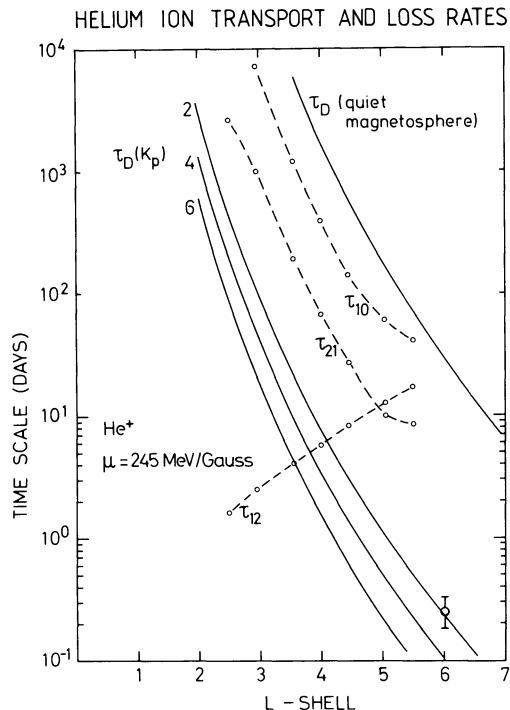


**Fig. 8.** Typical time scales for helium charge exchange reactions (circles, interpolated by dashed lines) and diffusive radial transport during magnetospherically quiet times and disturbed time periods (heavy lines). All time scales have been calculated for helium ions with  $\mu = 245$  MeV/Gauss, the diffusion time scales have been calculated for  $\text{He}^+$

ral consequence of the proposed drift mechanism which is effective only for ions with a drift period comparable to or larger than the time scale for which large azimuthal electric fields exist (typical a few hours, the time scale of a magnetic storm). The drift period of equatorially mirroring non-relativistic ions in a dipole field is given by

$$\tau_{drift} = 0.73 \cdot \frac{Q}{E} \cdot \frac{1}{L} \text{ hours,} \quad (4)$$

where  $E$  is the energy of the ions in MeV. Thus, the drift period at 2 MeV for singly ionized helium at  $L=3.5$  is only 6 min and a factor of 20 smaller than the drift period of 100 keV protons. Therefore it seems unlikely that this process could lead to effective radial transport in the energy range of our observations.

(3) *Fast Diffusive Transport.* Another possibility is a fast diffusive transport of the helium ions. During the 4 days of increased geomagnetic activity preceding our measurement the  $Kp$  index was  $\sim 5$  for a 24 h time period with a maximum value of  $6^-$  for 6 h. It is conceivable that the radial diffusion coefficient was greatly increased and, consequently, the time scale for radial diffusion was significantly reduced during this time period, as illustrated in Fig. 8. The three curves labelled  $Kp=2, 4, 6$  show the time scale for radial diffusion assuming nonstationary radial transport ( $\mu = \text{const}$ ) by azimuthal electric field fluctuations. For the equatorial power spectra  $P(\nu)$  of electric field fluctuations an empirical formula of Mozer (1971) has been used which takes into account the  $Kp$ -dependence of  $P(\nu)$ :

$$P_i(\nu) = 100 \cdot \frac{200}{\nu} \exp(0.4 Kp) \nu^{-1.6 \pm 0.3} (\text{mV})^2 / \text{m}^2 \text{Hz} \quad (5)$$

$P_i(\nu)$  is the power in the  $i$ th component of the perpendicular (azimuthal and radial) electric field fluctuations at the equator and  $\nu$  the particle drift frequency in cph. The relation between the electric field power spectrum and the diffusion time scale is given by (Fälthammar, 1965):

$$\tau_D \sim \frac{4B_0^2}{P(\nu)} \quad (6)$$

Taking the first Fourier component and the maximum value in the allowed parameter range of (5), we calculated the minimum value of  $\tau_D$  for singly ionized helium at 245 MeV/Gauss. The data point at  $L=6$  has been calculated from another measurement of electric field power spectra by Holzworth and Mozer (1979) during a time period with an average  $Kp$  index of  $\sim 2$ . The typical time scale  $\tau_D$  obtained with (2) for a quiet magnetosphere is shown for comparison. Also shown in Fig. 8 are the time scales  $\tau_{10}$ ,  $\tau_{12}$ , and  $\tau_{21}$  for charge exchange reactions, evaluated with (3) at constant magnetic moment  $\mu = 245$  MeV/Gauss, which corresponds to  $E = 0.53$  MeV/nucleon at  $L = 3.3$ . It is evident from Fig. 8 that fast cross- $L$  diffusion of low energy helium ions during magnetospherically disturbed time periods on time scales comparable with the charge exchange time scale  $\tau_{12}$  seems to be possible. At low energies and large radial distances, however, helium ions are expected to be predominantly singly ionized with  $\text{He}^+/\text{He}^{2+} > 1$  at  $L \gtrsim 4$  and  $E \lesssim 0.25$  MeV/nucleon (Spjeldvik and Fritz (1978a)). Thus it is conceivable that due to fast diffusive radial transport the high  $\text{He}^+/\text{He}^{2+}$ -ratios which most likely exist at large  $L$ -values in the lower energy range, will appear at low  $L$ -values in the high energy range. There, singly ionized helium can be observed for a few days before it decays by charge-exchange with neutral hydrogen of the earth's exosphere. The high  $\text{He}^+/\text{He}^{2+}$  observed at  $L = 3.2$ – $3.6$  could, therefore, be explained, at least qualitatively, by nonstationary processes in the magnetosphere. Whether this scenario provides a quantitative explanation for both the high  $\text{He}^+/\text{He}^{2+}$ -ratio at  $L = 3.3$  and the sudden decrease above  $L = 3.3$  can be verified only by solving the time dependent transport equations for  $\text{He}^+$  and  $\text{He}^{2+}$ , including the simultaneous radial diffusive transport, the charge exchange processes and Coulomb energy loss as discussed above. However, such an analysis has not yet been performed.

In addition to time dependent effects, non-adiabatic processes, as the violation of the first adiabatic invariant, may play an important role. This has been suggested by Hovestadt et al. (1978a) in order to explain the absence of iron ( $\text{Fe}/\text{O} < 0.01$ ) at energies of 0.4–1.5 MeV/nucleon in the trapping region of the outer radiation belt. A simple criterion, which can be used to separate adiabatic and non-adiabatic particle motion, is the Alfvén criterion which states that for adiabatic motion the gyroradius  $\rho$  of the particles has to be small compared with the scale length of the perpendicular magnetic field gradient:

$$\rho \cdot \left| \frac{\nabla B}{B} \right| \lesssim 0.1.$$

The gyroradii of iron and oxygen ions at the same energy/nucleon differ by only a factor of  $\sim 2$ . Therefore, if the interpretation of Hovestadt et al. (1978a) holds, small differences in rigidity result in large intensity differences of the trapped particle distribution. The gyroradii of  $\text{He}^+$  and  $\text{He}^{2+}$  in the energy range of our measurements are compa-

rable to the gyroradii of iron and oxygen in the energy range investigated by Hovestadt et al. (1978a). Rigidity dependent processes which suppress iron ions relative to oxygen and carbon in the outer radiation belt must therefore also influence the distribution of singly ionized helium relative to doubly ionized helium.

In summary, we found high abundances of singly ionized helium ( $\text{He}^+/\text{He}^{2+} = 0.4 \pm 0.1$ ) at  $L = 3.3$  during one perigee pass of ISEE-1 on 17 Nov 1977, with a sudden decrease of the  $\text{He}^+/\text{He}^{2+}$  ratio by a factor of  $\sim 10$  between  $L = 3.3$  and 3.7. We have shown that non-stationary and/or non-adiabatic processes may play an important role for the distribution of helium ions in the outer radiation belt. To clarify whether this is a persistent feature, a more systematic study of singly and doubly ionized helium during quiet and disturbed time periods is currently in progress.

*Acknowledgements.* The authors are grateful to the many individuals at the Max-Planck-Institut and the University of Maryland who have contributed to the success of the ISEE-mission. In particular, we thank J. Cain, H. Höfner, E. Künneth, P. Laeverenz, and E. Tums for designing and preparing the experiment for launch. We acknowledge helpful discussions with W.N. Spjeldvik. This work has been supported by NASA under contract NAS5-20062 and by the Bundesministerium für Forschung und Technologie, FRG, under contract number RC14-B8/74.

## References

- Allison, S.K.: Experimental results on charge-changing collisions of hydrogen and helium atoms and ions at kinetic energies above 0.2 keV, *Rev. Mod. Phys.* **30**, 1137–1168, 1958
- Balsiger, H., Eberhardt, P., Geiss, J., Young, D.T.: Magnetic storm injection of 0.9 to 16 keV/e solar and terrestrial ions into the high-altitude magnetosphere. *J. Geophys. Res.* **85**, 1645–1662, 1980
- Blake, J.B., Paulikas, G.A.: Geomagnetically trapped alpha particles, 1. Off-equator particles in the outer zone. *J. Geophys. Res.* **77**, 3431–3440, 1972
- Blake, J.B.: Experimental test to determine the origin of geomagnetically trapped radiation. *J. Geophys. Res.* **78**, 5822–5824, 1973
- Blake, J.B., Fennell, J.F., Hovestadt, D.: Measurements of heavy ions in the low-altitude regions of the outer zone. *J. Geophys. Res.* **85**, 5992–5996, 1980
- Cornwall, J.M.: Radial diffusion of ionized helium and protons; a probe for magnetospheric dynamics. *J. Geophys. Res.* **77**, 1756–1770, 1972
- Fälthammar, C.G.: Effects of time-dependent electric fields on geomagnetically trapped radiation. *J. Geophys. Res.* **70**, 2503–2516, 1965
- Fennell, J.F., Blake, J.B., Paulikas, G.A.: Geomagnetically trapped alpha particles, 3. Low altitude outer zone alpha-proton comparisons. *J. Geophys. Res.* **79**, 521–528, 1974
- Fritz, T.A., Williams, D.J.: Initial observations of geomagnetically trapped alpha-particles at the equator. *J. Geophys. Res.* **78**, 4719–4723, 1973
- Fritz, T.A., Spjeldvik, W.N.: Observations of energetic radiation belt helium ions at the geomagnetic equator during quiet conditions. *J. Geophys. Res.* **83**, 2579–2583, 1978
- Fritz, T.A., Spjeldvik, W.N.: Pitch angle distributions of geomagnetically trapped MeV helium ions during quiet times. *J. Geophys. Res.* **87**, 5095–5101, 1982
- Holzworth, R.H., Mozer, F.S.: Direct evaluation of the radial diffusion coefficient near  $L = 6$  due to electric field fluctuations. *J. Geophys. Res.* **84**, 2559–2566, 1979
- Hovestadt, D., Gloeckler, G., Fan, C.Y., Fisk, L.A., Ipavich, F.M., Klecker, B., O'Gallagher, J.J., Scholer, M.: Evidence for solar

- wind origin of energetic heavy ions in the earth's radiation belt. *Geophys. Res. Lett.* **5**, 1055–1057, 1978 a
- Hovestadt, D., Gloeckler, G., Fan, C.Y., Fisk, L.A., Ipavich, F.M., Klecker, B., O'Gallagher, J.J., Scholer, M., Arbinger, H., Cain, J., Höfner, H., Künne, E., Laeverenz, P., Tums, E.: The nuclear and ionic charge distribution particle experiments on the ISEE-1 and ISEE-C spacecraft. *IEEE, Transaction on Geoscience Electronics*, **GE-16**, 166–175, 1978 b
- Hovestadt, D., Klecker, B., Mitchell, E., Fennell, J.E., Gloeckler, G., Fan, C.Y.: Spatial distribution of  $Z \geq 2$  ions in the outer radiation belt during quiet conditions. *Adv. Space Res.* **1**, 305–308, 1981 a
- Hovestadt, D., Gloeckler, G., Klecker, B., Ipavich, F.M., Fan, C.Y., Fisk, L.A., O'Gallagher, J.J., Scholer, M.: Singly charged energetic helium emitted in solar flares. *Astrophys. J.* **246**, L81–L84, 1981 b
- Krimigis, S.M.: The charge composition aspect of energetic trapped particles. In: *Solar-Terrestrial Relations*, p. 207. Calgary, Canada: University of Calgary 1973
- Krimigis, S.M.: Alpha particles trapped in the earth's magnetic field. In: *Particles and fields in the magnetosphere*, B.M. McCormac, ed.: p. 364. Dordrecht, Holland: D. Reidel Publ. Co. 1970
- Lyons, L.R., Evans, D.S.: The inconsistency between proton charge exchange and the observed ring current decay. *J. Geophys. Res.* **81**, 6197–6200, 1976
- Lyons, L.R., Williams, D.J.: A source for the geomagnetic storm main phase ring current. *J. Geophys. Res.* **85**, 523–530, 1980
- Mozer, F.S.: Power spectra of the magnetospheric electric field. *J. Geophys. Res.* **76**, 3651–3667, 1971
- Pivovarov, L.I., Tubaev, V.M., Novikov, M.T.: Electron loss and capture by 200–1500 keV helium ions in various gases. *Soviet Physics JETP*, **14**, 20–24, 1962
- Sharp, R.D., Johnson, R.G., Shelley, E.G., Harris, K.K.: Energetic  $O^+$  ions in the magnetosphere. *J. Geophys. Res.* **79**, 1844–1850, 1974
- Sharp, R.D., Shelley, E.G., Johnson, R.G.: A search for helium ions in the recovery phase of a geomagnetic storm. *J. Geophys. Res.* **82**, 2361–2366, 1977
- Shelley, E.G., Johnson, R.G., Sharp, R.D.: Satellite observations of energetic heavy ions during a geomagnetic storm. *J. Geophys. Res.* **77**, 6104–6110, 1972
- Spjeldvik, W.N.: Equilibrium structure of equatorially mirroring radiation belt protons. *J. Geophys. Res.* **82**, 2801–2808, 1977
- Spjeldvik, W.N., Fritz, T.A.: Energetic ionized helium in the quiet time radiation belts: Theory and comparison with observation. *J. Geophys. Res.* **83**, 654–662, 1978 a
- Spjeldvik, W.N., Fritz, T.A.: Theory for charge states of energetic oxygen ions in the earth's radiation belts. *J. Geophys. Res.* **83**, 1583–1594, 1978 b
- Spjeldvik, W.N., Fritz, T.A.: Observations of energetic helium ions in the earth's radiation belts during a sequence of geomagnetic storms. *J. Geophys. Res.* **86**, 2317–2328, 1981
- Tinsley, B.A.: Evidence that the recovery phase ring current consists of helium ions. *J. Geophys. Res.* **81**, 6193–6196, 1976

Received December 3, 1982; Revised version February 2, 1983  
Accepted February 17, 1983

# High Energy Electrons at Altitudes 500 km Near the Equator\*

L. Just<sup>1</sup>, K. Kudela<sup>1</sup>, A.A. Gusev<sup>2</sup>, and G.I. Pugacheva<sup>2</sup>

<sup>1</sup> Institute of Experimental Physics, Slovak Academy of Sciences, Solovjevova 47, 040 00 Košice, Czechoslovakia

<sup>2</sup> Institute of Nuclear Physics, Moscow State University, Moscow 117234, USSR

**Abstract.** Measurements provided by a high-energy electron spectrometer on board a low altitude polar orbiting satellite allowed the determination of fluxes of electrons with energy above 100 MeV which were stably trapped or quasi-trapped in the radiation belt at  $L = 1.13-1.16$ . Relatively high fluxes of trapped electrons at minimum-B-equator are reported,  $(18,200 \pm 2,000) \text{ m}^{-2} \cdot \text{s}^{-1} \cdot \text{sr}^{-1}$  and  $(10,400 \pm 1,500) \text{ m}^{-2} \cdot \text{s}^{-1} \cdot \text{sr}^{-1}$  for  $>100 \text{ MeV}$  and  $>300 \text{ MeV}$ , respectively. The sharp increase of the electron flux with decreasing B in the region, where stably trapped particles are detected, corresponds to pitch angle distribution at the equator of the form  $J(\theta) \sim \sin^n \theta$ , where  $n = 65 \pm 15$ . The shape of the pitch angle distribution, together with relatively high fluxes of electrons, supports the assumption that they are generated due to the decay of particles produced in interaction of high energy protons trapped in the inner radiation belt with the residual atmosphere.

**Key words:** High energy electrons – Radiation belt of Earth – Intercosmos 17 satellite

## Introduction

Although the characteristics of electrons with energies up to several MeV trapped in the Earth's radiation belt at low altitudes have been studied for many years (for instance Imhof and Smith, 1965), the picture of electron population at higher energies is not so complete to date.

The existence of a radiation belt composed of electrons with energies above 100 MeV was suggested by Grigorov (1977). Further, the measurements on board Cosmos 490 and Salyut 6 confirmed this assumption (Basilova et al., 1978; Basilova et al., 1982a, b, c; Galper et al., 1981).

This paper follows the works mentioned above and extends the analysis of high energy electrons in the equatorial region using the experimental material obtained during measurements by the apparatus SEZ-10 on board Intercosmos-17 satellite.

\* Based on a paper given at the Symposium on Plasma and Energetic Particles in the Magnetosphere, EGS Meeting, 23-27 August 1982, Leeds, U.K.

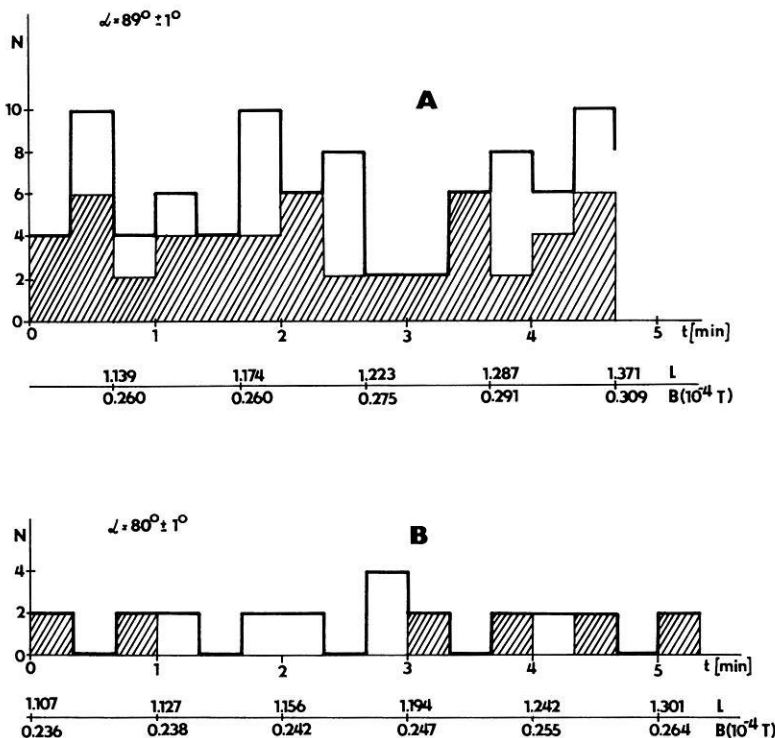


**Fig. 1a and b.** Number of counts of the telescope without the lead filter (*full line*) and with the filter (*thin line*) corresponding to the electrons  $E_e > 100 \text{ MeV}$  plus relativistic protons and relativistic protons, respectively. Accumulation is taken for 20 s because of low statistics:  
**a** region with  $B = (0.285 \pm 0.035) \cdot 10^{-4} \text{ T}$   $\alpha = 89^\circ \pm 1^\circ$   
**b** region with  $B = (0.241 \pm 0.005) \cdot 10^{-4} \text{ T}$   $\alpha = 80^\circ \pm 1^\circ$

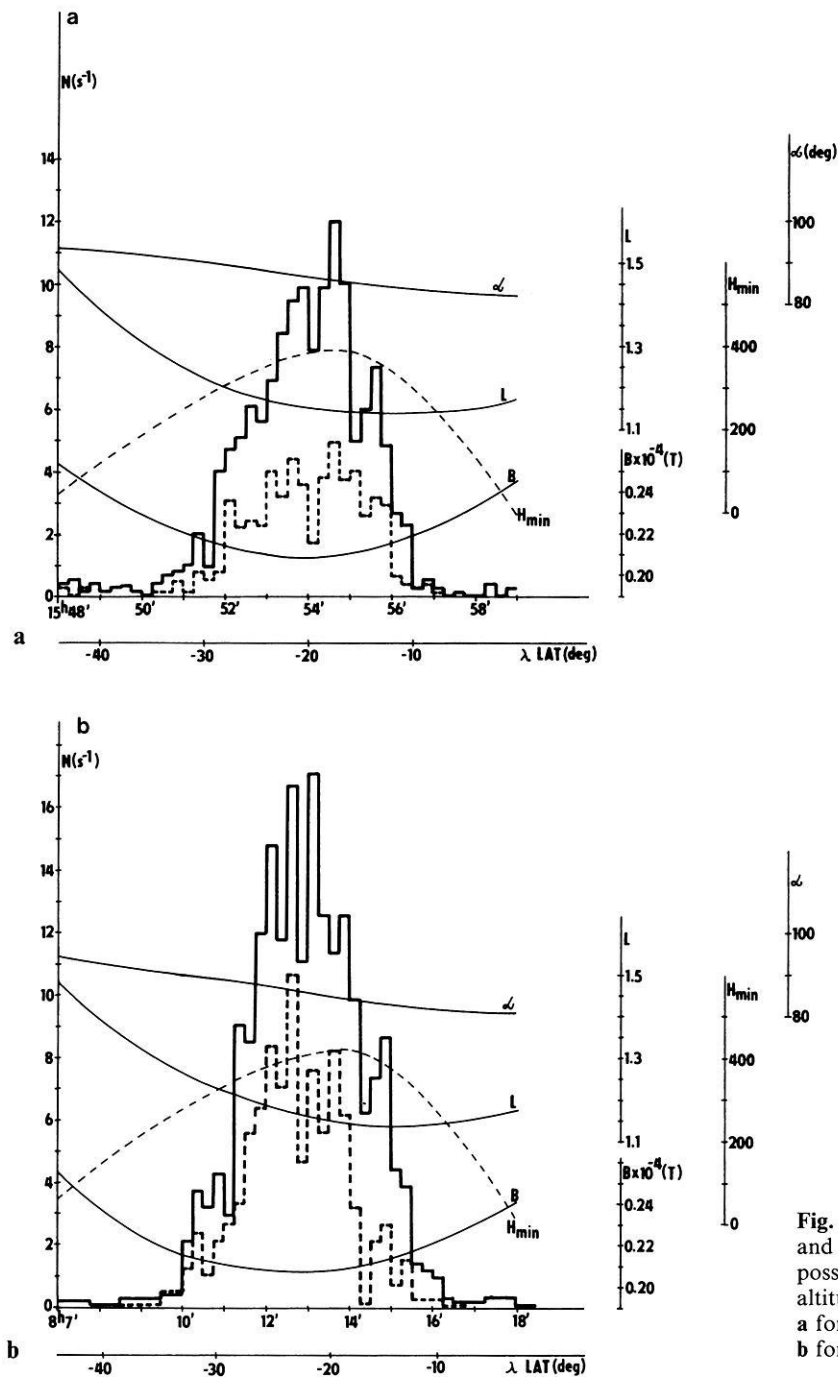


Fig. 2a and b. Registration of  $\geq 100$  MeV electrons (—) and  $\geq 300$  MeV (---) for passes when data recording was possible with 0.3 s resolution. Given are  $L$ ,  $B$ , minimum altitude of mirror points  $H_{min}$  and pitch angle  $\alpha$ .

a for 13. Dec. 1977, 15.48–16.00 UT

b for 17. Jan 1978, 08.07–08.18 UT

## Experiment

The satellite Intercosmos-17 had a circular orbit with altitude 500 km and inclination  $83.5^\circ$ . The apparatus SEZ-10 placed on board the satellite was a spectrometer for electrons with energies 0.1–300 GeV. The detector consists of two telescopes, one of them under a lead filter with a thickness corresponding to 3 radiation length units. Electrons impacting on the filter produce electron-photon cascade and are not registered in the detector of singly charged particles. The flux of electrons is determined as the difference of counting rates between the telescope without the lead filter and the one with it. The filter changed its position periodically above the two telescopes.

The telescopes consist of scintillators, a Cherenkov detector and an energy detector of the sandwich type combined of lead and scintillator sheets – the shower calorimeter. The telescope without the filter measures the flux of electrons and protons, the telescope with the filter detects the slightly attenuated flux of protons. The attenuation coefficient  $K = 0.93 \pm 0.02$  was obtained experimentally in calibration by the beam of protons with energy 1.24 GeV. It is supposed that  $K$  is independent of proton energy. The detector of energy has 8 intergral energy levels with threshold energies 0.1, 0.3, 1, 3, 10, 30, 100 and 300 GeV, respectively. A more detailed description of the apparatus is presented in (Grigorov et al., 1978).

The opening angle of the telescope was  $22^\circ$  and the

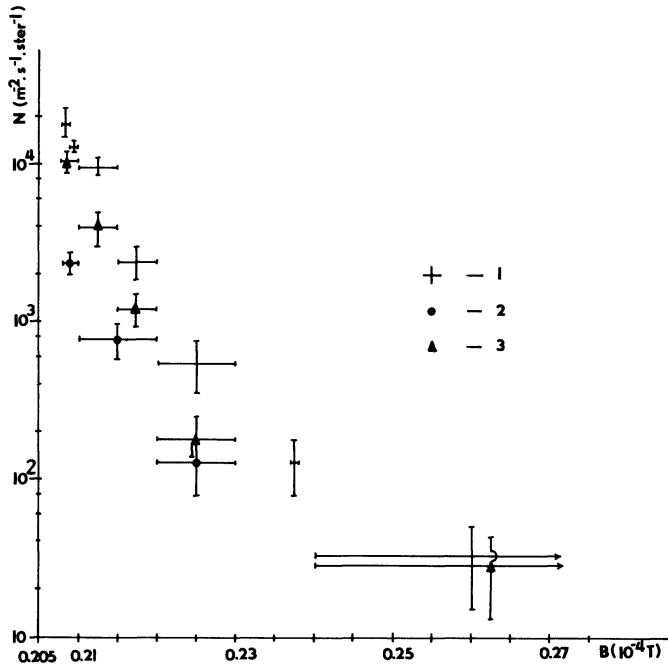


Fig. 3. Dependence of counting rate of electron detectors on  $B$  for the interval  $L=1.13-1.16$ .

1. -  $E_e > 100$  MeV and  $\alpha = 87^\circ \pm 3^\circ$
2. -  $E_e > 100$  MeV and  $\alpha = 81^\circ \pm 1^\circ$
3. -  $E_e > 300$  MeV and  $\alpha = 87^\circ \pm 3^\circ$

geometrical factor of the detector was  $7 \text{ cm}^2 \cdot \text{sr}$ . The axis of the telescope was oriented perpendicularly to the orbital plane. This fact allowed the determination of the flux of particles with relatively high pitch angles. For given  $L$ , the value of the angle  $\alpha$  between the axis of the detector and local  $\vec{B}$  depends on the longitude. For our analysis, where  $L < 1.4$ , the value of  $\alpha$ , computed from the knowledge of  $B$  components and orientation of the detector, had a minimum value of  $65^\circ$ .

### Observations

Individual passes of the satellite through the low latitude region can give the picture of the electron fluxes which are stably trapped or quasi-trapped in the radiation belt. Boundaries of trapping, quasi-trapping and albedo particles are given as lines in the  $L$ - $B$  plane or  $L$ - $\alpha_{min}$  plane, where  $\alpha_{min}$  denotes the pitch angle of the particles at the peak of the given field line. By the term "trapped" for given  $L$  we mean particles for which the line of mirror points is not lower than 60 km above the Earth (Basilova et al., 1982a) at any longitude. Albedo particles have a maximum altitude of their mirror points at 60 km. Particles for which  $B$  is between the values of boundaries described, are quasi-trapped.

Here we are analyzing fragments of orbits, through the region  $L=1.10-1.40$ . Two examples of recording of the counting rate are given in Fig. 1. In the basic telemetry regime they are accumulated counts in 5 s intervals in both telescopes, with and without the lead filter. The fragments of the orbit correspond to that part of  $L$ - $B$  plane where stable trapping is not possible and only quasi-trapped and/or albedo particles can be registered here. More clearly, the geomagnetic field model IGRF 1975 gives, for the alti-

tude 500 km and for  $L=1.15$ , the region of stable trapping defined above in  $B < 0.233 \cdot 10^{-4}$  T and for  $L=1.30$   $B < 0.248 \cdot 10^{-4}$  T. The given  $L$  shell reaches the satellite at higher  $B$  on the top pass of Fig. 1 than on the bottom one. The difference is in the orientation of the detector. For the upper part of Fig. 1  $\alpha$  changes its value from  $90.9^\circ-88.9^\circ$  while at the lower part  $\alpha=80.0^\circ-81.4^\circ$ . The comparison of the two passes shows the dependence of the flux of quasi-trapped electrons on angle  $\alpha$ .

Because of the relatively low counting rate corresponding to the flux of electrons  $E_e > 100$  MeV in the quasi-trapping region, the detailed analysis of the flux profile in narrow  $L$  intervals is impossible. Coming to the region of lower  $B$ , where stably trapped particles may also be present, the flux of electrons increases. The basic telemetry regime is able to measure reliably only up to 6 counts per s, and this makes a limit for using this regime only up to approximately  $H_{min} = 100$  km for orientations of the detector with angle  $\alpha = 90 \pm 6^\circ$ .

Several orbits through the region of low  $B$  (for  $L$  up to  $L=1.16$ , practically to minimum- $B$ -equator) in the Brazil magnetic anomaly were examined carefully, especially those with an alternative telemetry regime, when counts are accumulated in 0.3 s intervals. The profiles of electron fluxes with  $E_e > 100$  MeV and  $E_e > 300$  MeV, respectively, obtained in two passes through the region with low  $B$  are presented in Fig. 2a, b. The flux increases sharply at  $B < 0.21 \times 10^{-4}$  T in comparison with that of quasi-trapped electrons.

Combination of the two telemetry regimes gives the possibility of obtaining the altitude profile, i.e. the dependence of electron flux on  $B$  for a given  $L$ . We have chosen the interval  $L=1.13-1.16$ , because at these  $L$  we can measure, at altitude 500 km, particles practically at the minimum  $B$  value. On the other hand we must take a finite width  $\Delta L$  because of low statistics.

Compilation of the data obtained from 23 passes of the  $L$  region mentioned above at various longitudes and in two  $\alpha$  intervals, for 5 s recordings, together with passes of the satellite through the low  $B$  region in the Brazil magnetic anomaly, for 0.3 s recordings, is presented on Fig. 3.

A very sharp dependence of the flux on  $B$  up to  $0.24 \times 10^{-4}$  T is seen. Fitting the data for  $\alpha = 90 \pm 6^\circ$  as  $B^{-n/2}$  we obtain the value of  $n = 65 \pm 15$ . From that we can estimate the pitch angle distribution at the equator as  $\sin^n \theta$ , where  $\theta$  is the equatorial pitch angle of the particles. In the stably trapping region the strong pitch angle dependence may also be deduced from the significant change of flux with angle  $\alpha$ .

### Discussion and Conclusion

Analysis of 23 passes of the satellite Intercosmos-17 through the near-equatorial region allowed the determination, for  $L=1.13-1.16$ , of fluxes of quasi-trapped, as well as of stably trapped electrons. Typical values of the quasi-trapped electron flux are, for  $\alpha = 90 \pm 6^\circ$ ,  $33 \pm 24 \text{ m}^{-2} \cdot \text{s}^{-1} \cdot \text{sr}^{-1}$  and  $27 \pm 23 \text{ m}^{-2} \cdot \text{s}^{-1} \cdot \text{sr}^{-1}$  for  $>100$  and  $>300$  MeV respectively (see the values centered near  $B = 0.26 \cdot 10^{-4}$  T in Fig. 3). No significant dependence on  $B$  was obtained for quasi-trapped particles.

A sharp increase of flux, for  $\alpha = 90 \pm 6^\circ$ , consistent with  $B^{-n/2}$ , where  $n = 65 \pm 15$ , is seen for a decrease of  $B$  under

the limit of stable trapping. The highest fluxes registered were  $(18,200 \pm 2,000) \text{ m}^{-2} \cdot \text{s}^{-1} \cdot \text{sr}^{-1}$  and  $(10,400 \pm 1,500) \text{ m}^{-2} \cdot \text{s}^{-1} \cdot \text{sr}^{-1}$  for  $> 100 \text{ MeV}$  and  $> 300 \text{ MeV}$ , respectively. They were detected for  $L = 1.15$  and  $H_{min} = 420 \text{ km}$ .

Clear dependence of the electron flux on pitch angle is detected for the stably trapped particles.

The high fluxes of electrons registered here and the shape of their pitch angle distribution, with the high energy protons at the lower edge of the radiation belt, (Fischer et al., 1977) are difficult to explain only as a result of an interaction of primary cosmic rays with the atmosphere of the Earth, as was suggested for fluxes of electrons registered under the radiation belts. It is possible that the source of relatively high fluxes of energetic electrons is the interaction of high energy protons ( $E > 1 \text{ GeV}$ ) of the inner radiation belt with the residual atmosphere. Preliminary estimates show that the results of measurements presented here are not in contradiction with this assumption.

Further progress in understanding production and loss mechanisms for the high energy electron component in the equatorial region needs to extend the statistics of passes of the satellite through the low latitudinal region as well as careful estimation of electron production due  $\mu \rightarrow e$  decay of charged pions created by high energy protons from inner radiation belt in interaction with the atmosphere. Spectral characteristics as well as more detailed pitch angle distributions of electrons for various  $L$  in comparison with high energy proton spectra given for instance by Hovestadt et al. (1972) and Valot and Engelmann (1973) are needed.

*Acknowledgements.* The authors would like to thank Dr. S.N. Kuznetsov for his valuable discussions on the results presented here.

## References

- Basilova, R.N., Grigorov, N.L., Kogan-Laskina, E.I., Pugacheva, G.I.: Registration of electrons with energy  $\sim 100 \text{ MeV}$  trapped by the magnetic field of the Earth. *Pisma v ZETF* (in Russian) **27**, 278–282, 1978
- Basilova, R.N., Gusev, A.A., Kogan-Laskina, E.I., Pugacheva, G.I.: The boundaries of quasitrapping region of residual radiation near equator. *Kosmicheskie issledovania* (in Russian) **20**, 300–304, 1982a
- Basilova, R.N., Kogan-Laskina, E.I., Pugacheva, G.I., Energy spectra of quasitrapped electrons with  $E \geq 100 \text{ MeV}$  according to data of COSMOS-490 satellite. *Geomagn. Aeron.* (in Russian) **22**, 129–131, 1982b
- Basilova, R.N., Gusev, A.A., Pugacheva, G.I., Titenkov, A.F.: High energy electrons in the inner radiation belt of the Earth. *Geomagn. Aeron.* (in Russian), **22**, 671–672, 1982c
- Fischer, H.M., Auschrat, V.W., Wibberenz, G.: Angular distribution and energy spectra of protons of energy  $5 \leq E \leq 50 \text{ MeV}$  at the lower edge of the radiation belt in equatorial latitudes. *J. Geophys. Res.* **82**, 537–547, 1977
- Galper, A.M., Grachev, V.M., Dmitrienko, V.V., Kirillov-Ugryumov, V.G., Lyakhov, V.A., Ryumin, V.V., Ulin, S.E., Schwetz, N.I.: Registration of enhanced fluxes of high energy electrons in the region of Brazil magnetic anomaly. *Kosmicheskie issledovania* (in Russian) **19**, 645–647, 1981
- Grigorov N.L.: On the possibility of existence of Earth's radiation belt of electrons with energies above  $100 \text{ MeV}$ . *Doklady AN SSSR* (in Russian) **234**, 810–813, 1977
- Grigorov, N.L., Gusev, A.A., Zatsepin, V.I., Pugacheva, G.I., Savenko, I.A., Titenkov, A.F., Shirayeva, V.Ya., Dorcoman, D., Marin, A., Blazh, K.: Spectrometer for investigation of electrons with  $E_e = 100 \text{ MeV} - 100 \text{ GeV}$  in cosmic ray composition. *Kosmicheskie issledovania* (in Russian) **16**, 609–613, 1978
- Hovestadt, D., Achtermann, E., Ebel, B., Häusler, B., Paschmann, G.: New observations of the proton population of the radiation belt between  $1.5$  and  $104 \text{ MeV}$ . In: *The Earth's magnetospheric processes*, B.M. McCormac, ed: p 118. Dordrecht, Holland: D. Reidel 1972
- Imhof, W.L., Smith, R.V.: Longitudinal variations of high energy electrons at low altitudes. *J. Geophys. Res.* **70**, 569–577, 1965
- Valot, P., Engelmann, J.: Pitch angle distribution of geomagnetically trapped protons for  $1.2 \leq L \leq 2.1$ . *Space Res.* **8**, 675–682, 1973

Received November 16, 1982; Revised version February 25, 1983  
Accepted March 8, 1983